UNIVERSITÀ DEGLI STUDI DELL'INSUBRIA
Facoltà di Scienze Matematiche Fisiche e Naturali
Dottorato in Fisica
XXIII ciclo

OPTIMISATION OF THE BOLOMETRIC PERFORMANCES OF THE CUORE-0/CUORE AND LUCIFER DETECTORS FOR THE NEUTRINOLESS DOUBLE BETA DECAY SEARCH

Thesis submitted by:
Claudia Rusconi

A doctoral dissertation in partial fullfillment
of the requirements to obtain the Degree of
Doctor Philosophiae in Physics

July 2011

Supervisor: Prof. A. Giuliani
Program coordinator: Prof. P. Ratcliffe

SUMMARY

INTRODUCTION 10
Chapter 1. NEUTRINOS: TO STANDARD MODEL AND BEYOND 13
1.1. The portrait of the neutrino as a Standard Model particle 14
1.2. Neutrino oscillations and leptonic mixing matrix 16
1.2.1. Neutrino mass hierarchy 19
1.3. The importance of being a Majorana particle 21
1.4. Neutrinoless double beta decay: the final frontier 25
1.4.1. Experimental approaches to 0νββ 31
1.4.1.1. The experimental sensitivity to $m_{\beta\beta}$ 32
1.4.2. 0νββ: state of the art 37
1.4.2.1. The Heidelberg-Moscow experiment 37
1.4.2.2. The NEMO-3 experiment 39
1.4.2.3. The Cuoricino experiment 40
Chapter 2. BOLOMETRICALLY SEEKING NEUTRINOLESS DOUBLE BETA DECAY 43
2.1. The next-generation 0νββ experiments 43
2.2. Bolometers 48
2.3. Ideal bolometer model 50
2.3.1. The Absorber 52
2.3.1.1. Phonon thermalization process 53
2.3.1. Phonon Sensors 56
2.4. Composite bolometer model 61
2.4.1. Static behaviour 62
2.4.2. Dynamic behaviour 64
2.5. Noise sources in bolometric detectors 68
Chapter 3. TOWARDS THE CUORE SINGLE MODULE 70

3.1. General description 71
3.1.1. The background of the Cuoricino experiment 71
3.1.2. The CUORE single module 73
3.2. TeO_2 crystal absorbers 75
3.2.1. The nuclide: ^{130}Te 75
3.2.2. The compound: TeO_2 crystals 75
3.2.2.1. TeO_2 crystal properties 76
3.2.3. TeO_2 crystal production 77
3.3. Doped semiconductors 81
3.3.1. Thermistors 81
3.3.1.1. Production 81
3.3.1.2. Characterization 89
3.3.2. Heaters 93
3.3.2.1. Production 94
3.3.2.2. Characterisation 97
3.3.3. Semiconductor coupling 98
3.3.3.1. Chips-to-absorber coupling 98
3.3.3.2. Electric connections 99
3.4. The holder 101
3.4.1. Copper structure 101
3.4.2. PTFE supports 103
3.5. Modelling the CUORE bolometers 103
3.6. From a floor to nineteen towers: the CUORE detector 106
3.6.1. The CUORE Tower Assembly Line (CTAL) 108
3.6.1.1. The gluing glove box 109
3.6.1.2. The Assembly Glove Boxes 109
3.7. CUORE background and sensitivity 113
3.8. CUORE-0 115
Chapter 4. CHARACTERISATION OF THE CUORE-0 AND CUORE THERMISTORS 117

4.1. Experimental setup 119
4.2. Data collection 123
4.3. Temperature calibration 126
4.4. Data analysis 133
4.4.1. Some consideration on the Temperature Scales 143
4.4.2. General comments on the results 147
Chapter 5. CUORE-0/CUORE CRYSTAL AND THERMISTOR VALIDATION 153
5.1. Validation protocol for the CUORE crystal production 153
5.2. CUORE Crystal Validation Runs 156
5.2.1. Manual detector assembly 157
5.2.2. CCVR spectra 163
5.1. Bulk contamination of the CUORE crystals 166
5.1.1. ^{210}Po bulk activity 166
5.1.2. U/Th bulk contaminations 169
5.1.3. ^{40}K bulk contamination 170
5.1.4. ^{210}Pb activity 171
5.2. Surface contamination of the CUORE crystals 173
5.2.1. U/Th surface contaminations 175
5.3. Extrapolation to CUORE background 177
5.4. Performances of CCVR bolometers 180
5.4.1. Energy resolution of CCVRs 180
5.4.2. Pirro curves 185
5.4.3. Pulse shapes 189
Chapter 6. THERMISTOR-TO-ABSORBER COUPLING 193
6.1. Need to change 193
6.2. Constraints to the gluing process 200
6.2.1. The glue 201
6.2.2. The geometry of the epoxy interface 204
6.2.3. Restrains on environmental conditions 205
6.3. Innovations in the CUORE-0/CUORE gluing line 207
6.3.1. Mixing of the bi-component epoxy 208

6.3.2. Dispensing of the mixed epoxy ... 210
6.3.2.1. The air-free dispenser ... 215
6.3.2.2. The pneumatic glue dispenser ... 219
6.3.3. Comparison between dispensing techniques ... 222
6.3.4. Sensor positioning ... 223
6.4. The final CUORE-0/CUORE gluing line ... 226
6.4.1. Introduction of automated elements ... 227
6.4.2. Optimisation of the glue handling ... 230
6.4.3. Optimization of the Z-pos ... 233
6.4.4. Optimization of the zero point location ... 233
6.4.5. The gluing procedure ... 236
Chapter 7. SCINTILLATING BOLOMETERS ... 240
7.1. The basic idea ... 241
7.2. The LUCIFER experiment ... 245
7.2.1. The candidate isotopes ... 245
7.2.2. The LUCIFER detector ... 247
7.3. Detectors: Three Different Ones ... 250
7.4. ZnSe-Ge detector ... 256
7.4.1. ZnSe-Ge aboveground: the COMO run ... 256
7.4.1.1. Event identification ... 259
7.4.1.2. Energy calibration of the heat channel ... 259
7.4.1.3. Rejection efficiency and quenching factor ... 263
7.4.2. ZnSe-Ge underground: the LNGS run ... 265
7.4.2.1. Event Discrimination ... 266
7.4.2.2. Light Detector ... 268
7.5. ZnSe-Si detector ... 270
7.6. $ZnMoO_4$-Ge detector ... 272
7.6.1.1. Event identification ... 276
7.6.1.2. Energy calibration of the heat channel ... 278
7.6.1.1. Rejection efficiency and quenching factor ... 278
7.6.1.1. Light detector ... 281

CONCLUSIONS 282
List of abbreviations 283
List of Figures 285
List of Tables 299
Bibliography 304

INTRODUCTION

In the nowadays astroparticle physics, many of the most interesting open questions involve neutrinos.

The solution of the neutrino flavour oscillation puzzle, thanks to the SuperKamiokaNDE and SNO experiments, pointed out the necessity to go beyond the Standard Model of the particle physics by realizing that neutrinos have masses. In fact the oscillations can be understood only if a mixing mechanism, similarly to what happens in the hadronic field, is assumed, which leads to the introduction of neutrino mass eigenstates that combine in to flavour eigenstates by means of a mixing matrix. But oscillations are sensitive only to the square mass difference of the neutrino masses, therefore they cannot give any information about the absolute neutrino mass scale and on the ordering of their masses. Moreover, the fact that neutrino are neutral and massive, allows the hypothesis that, differently from all the other elementary particles, which are Dirac objects, they can be identical to their own antiparticles, being Majorana particles.

Which is the absolute neutrino mass scale? Which is the neutrino mass hierarchy? And, above all, are neutrinos Dirac or Majorana particles? Neutrinoless double beta decay investigation can give an answer to these questions.

The double beta decay (DBD) is a rare nuclear process in which a nuclide transforms in a stable daughter by the simultaneous emission of two electrons. This transition can occur in principle for 35 nuclei, whose ordinary single beta decay is unfavourable or energetically forbidden. Because DBD is a second order process of the weak interaction, it is a very low probability transition, so the candidate parent nuclei have a very long lifetime.

Usually two decay modes are considered: the two-neutrino double beta decay ($2\nu\beta\beta$), predicted by the Standard Model and already observed in several nuclides, in which two antineutrinos are also present in the final state; and the neutrinoless double beta decay ($0\nu\beta\beta$), which, foreseeing no neutrino in the final state, violates the lepton number conservation and is possible only if the neutrino is a massive Majorana particle. The probability of this rare decay to occur depends on the so-called effective Majorana mass, $m_{\beta\beta}$,

which is related to the neutrino mass eigenstate through the element of the neutrino mixing matrix.

In principle the experimental signature of the 0νββ is clearly identifiable: a peak at the Q-value of the transition, enlarged only by the finite energy resolution of the detector, in the spectrum obtained by summing over the energies of both the electrons emitted in the decay. Among the different techniques suitable to approach the 0νββ, bolometers probed to be a very powerful tool for searching this extremely rare decay, as demonstrated by the results of the Cuoricino experiment: thanks to its tower made of ~60 TeO_2 bolometers, containing ^{130}Te as DBD isotope, Cuoricino set one of the most sensitive limits on 0νββ, investigating the so-called quasi-degenerate pattern of neutrino masses.

To go further this amazing result, big efforts are required to improve the bolometric technique in order to start exploring the inverted hierarchy region of neutrino masses. Due to the rarity of the decay, huge quantities of nuclides must be observed for long times, and in an environment free of radioactive contaminants whose counting rates could mask the ones searched for.

CUORE is the natural prosecutor of Cuoricino: with 19 towers, each of 52 TeO_2 bolometers, it will not be just a big version of the previous experiment: in fact the increase of the number of detectors (and therefore of the source mass) of a factor ~20 is not sufficient to reach the desired sensitivity on the $m_{\beta\beta}$. A review of all the aspects of the bolometers is necessary, in terms of the parameters related more directly to the sensitivity of the experiment, as well as of the detection performances. A particular care is devoted to reduce the background by avoid the radioactive contamination and re-contamination of the detector components. This requires the selection of high-purity raw materials, the development of dedicated cleaning procedures and the tower construction in a clean-room environment. Moreover, for having a high reproducibility in the detector performances among the huge number of bolometers to be produced, a new assembly line is also needed, with the introduction of some automated elements.

An intermediate step will precede the beginning of CUORE: its first tower will be cooled-down and measured as a stand-alone experiment, with the beginning of data-taking foreseen in the winter of 2011. CUORE-0 will provide a test the new CUORE assembly line, and a high-statistics check of the improvements to reduce the radioactive background and to improve the bolometric behaviour of the detectors, but it will also be a powerful experiment on its own, capable of improving the limit on $m_{\beta\beta}$ fixed by Cuoricino.

Besides these “passive methods” of background reduction, the modularity of the final CUORE array will provide another tool for the background suppression, thanks to the

rejection of simultaneous events in different detector elements, which cannot be ascribed to a 0νββ.

A real "active method" for suppressing the background is the use of the scintillating bolometers technique: the simultaneous detection of heat and scintillation light for the same event allows rejecting α particles with 100% efficiency, since the ratio between the photon and phonon yield is much different for α than for β/γ interactions. This possibility, that cannot be applied to CUORE bolometers because the TeO_2 has no scintillating properties, is at the basis of LUCIFER experiment.

The aim of this recently proposed project is the search of 0νββ decay of candidates with a Q-value higher than 2.6 MeV, i.e. outside the natural gamma radioactivity range, since in this case alphas are the only really disturbing background sources. A complete elimination of αs for these candidates could easily lead to specific background levels of the order of 10^{-3} counts/(keV·kg·y) or lower. The most probable candidate isotopes for the LUCIFER experiment are ^{82}Se, ^{100}Mo, ^{116}Cd and the selection of their scintillating compound has been already started.

My PhD activity of the last three years, presented here, was performed in the framework of both CUORE-O/CUORE and LUCIFER experiment. In the first case my work focused on the optimization of the single bolometer elements, i.e. the sensor and the absorber, as well as their coupling, aiming at an increase of both bolometric performances and radio-purity: the behaviour of the CUORE-0/CUORE temperature sensors has been analysed and the uniformity of protocols for the production and processing of energy absorbers has been tested; moreover a dedicated study for the optimization and the automation of the coupling between the energy absorbers and the sensors, which is a delicate point in the determination of performance reproducibility. The tuning of all of these aspects, as will be seen in the course of this thesis, is necessary for CUORE to reach the goal of sensitivity to $m_{\beta\beta}$ in the range of inverted hierarchy.

Regarding LUCIFER, my PhD work was concentrated on the selection of materials to be used for the scintillating bolometers: different scintillating crystals and light detectors has been tested for evaluating their capability in discriminating α from β/γ events, in order to find the best combination suitable for the experiment.

Chapter 1.
NEUTRINOS: TO STANDARD MODEL AND BEYOND

Relax
I need some information first
Just the basic facts[1]

The discovery of the electron and the radioactivity in general at the end of the 1890s gives start to the nuclear and subnuclear physics era that, by investigating matter deeper and deeper, allows the identification of a wide range of particles and an accurate comprehension of the interactions among them, building what nowadays is called the Standard Model of particle physics (SM).

According to this model, the basic bricks of matter are six quarks and six leptons, with their related antiparticles, all of them being fermionic particles (i.e. with spin=½) interacting through four fundamental forces. In the modern quantum field theory, these interactions are mediated by the exchange of integer spin particles, the boson vectors.

The SM certainly is not the final step of the process attempting to unify the physics laws in a single, elegant theory. There are several phenomena whose explanation is not included into the model, and also a lot of the SM parameters, as the particle masses, are not predicted but introduced "manually" on the basis of experimental measurements. Moreover, one of the main outcomes of the SM, the unification of the electromagnetic force and the weak force in a unique interaction, has opened the way to the so called great unification theories (GUT).

Starting from the first steps towards the SM until now, when the physicists try to go beyond to this milestone, the investigation of neutrinos has been extremely significant, even if, among the elementary particles, they are surely the most elusive.

The fact that neutrinos have nonzero mass has been the first experimental evidence of

[1] (227).

new physics beyond the SM. That astonish result of the past century is now well understood, but many questions regarding some neutrino property are still open: which is the real neutrino mass scale? Are neutrinos Dirac particles, as all the elementary particles in the SM, or their nature is different from the other bricks of the universe? The investigation of a rare nuclear transition, known as Double Beta Decay, can give hints to the solution of neutrino puzzle.

1.1. The portrait of the neutrino as a Standard Model particle

Having nor colour neither electrical charge, neutrinos don't undergo to strong and electromagnetic interactions; their mass is assumed to be null, therefore they are not subject of gravitation. Hence neutrinos interact only by weak force and so they are a privileged way for studying this interaction.

The neutrino was introduced for the first time to physics by W. Pauli in 1930 (1), as an artifice for justifying J. Chadwick's observations on the so-called β rays. This radiation is made by the electrons emitted in a β decay, a nuclear process in which an atom with mass number A and atomic number Z transforms into an isobar with A and Z+1. The energetic spectrum of the emitted electrons is a continuous and cannot be explain in terms of a two body observed in the final state (the daughter nucleus and the electron). Therefore Pauli supposed a third particle to be present in the final state, carrying the missing energy, and called it "neutron".

This hypothetical particle was renamed "neutrino" by E. Fermi after the discovery of the "real" neutron in 1932; Fermi also used both these particles, together with the proton, to advance his effective theory on β decay as a three-body decay: $n \rightarrow p + e^- + \bar{\nu}_e$ (2).

Nevertheless the neutrino remained a hypothesis for the following twenty years, until C. Cowan and F. Reines (3), in 1956, verified the existence of neutrino induced β reactions: $\bar{\nu}_e + p \rightarrow n + e^+$. Using a reactor as a source (Uranium fission fragments are rich in neutrons and undergoes to β decay emitting of electrons and antineutrinos) for compensating the low statistics of the process, a rate of few events per hour was observed on a target of $CdCl_2$ and water.

In the same year T. Lee and C. Yang put forward the hypothesis of the parity violation in weak processes (4), then confirmed by several experiments (one above all, the C. Wu one, (5)). That opened the way to the so called V-A theory of weak interactions.

In 1958 M. Goldhaber measured the negative helicity (i.e. the projection of the particle's spin onto the direction of its momentum) of neutrinos (6) and, in the following years, B. Pontecorvo ideas (7), together with the experiments performed at the Brookhaven accelerator, showed the existence of two different neutrino flavours: ν_e and ν_μ (8).[2]

Muonic neutrinos played a very important role in 1973: the observation of processes $\nu_\mu N \rightarrow \nu_\mu N$ in the Gargamelle bubble chamber at CERN (9) showed the existence of weak neutral current events, i.e. mediated by the vector boson Z^0 as postulated (together with weak charged current events and $W^\pm$ bosons) in the electroweak theory by S. Glashow, S. Weinberg and A. Salam (10), (11), (12). These bosons were then directly produced in 1983 using the $p\bar{p}$ collider SPS at CERN (13), (14), (15).

The construction of e^+e^- colliders (LEP at CERN and SLC at Stanford) and more powerful $p\bar{p}$ collider (Tevatron at Fermilab) at the end of the 1980s allowed a high statistics production of Z and W and therefore a deep investigation of their properties. In particular, at LEP, from the decay width of the Z^0 resonance, it was obtained that the number of light neutrino families (i. e. with $m_\nu < \frac{1}{2} m_Z$), N_ν is equal to 3 (see Figure 1-1).

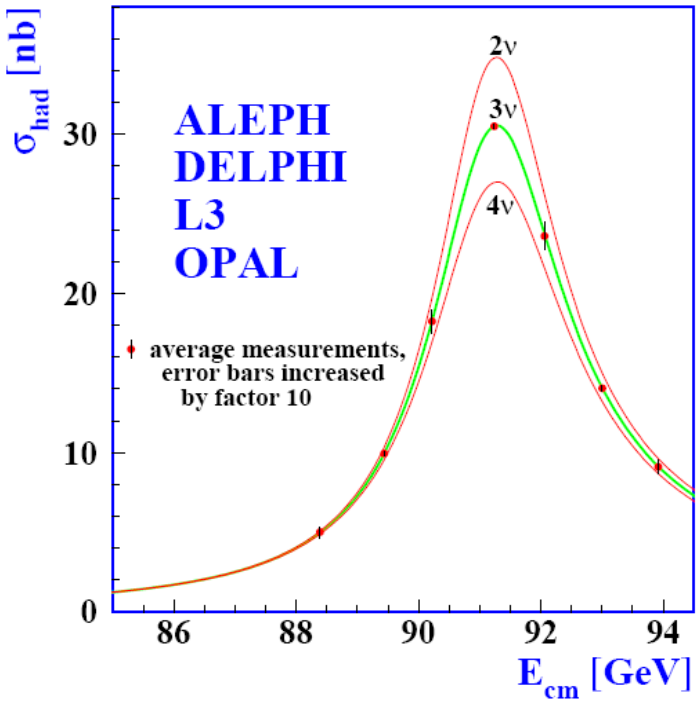

Figure 1-1. Measurement of the cross section of hadron production at the Z resonance. The curves show the expected cross section for two, three and for neutrino families coupled with Z in the SM, assumed neutrino mass to be negligible (16).

[2]The existence of the ν_τ was implied after the detection of the tau particle in the second half of the 1970s at SLAC, but its experimental observation happened only in the year 2000 (219).

1.2. Neutrino oscillations and leptonic mixing matrix

In the previously quoted experiments the neutrino sources are β-decaying elements (in particular at nuclear reactors, producing $\bar{\nu}_e$) and accelerators (producing ν_e, $\bar{\nu}_e$, ν_μ, $\bar{\nu}_\mu$). Other two important neutrino sources are the sun and the atmosphere, from which firstly came out the oscillation phenomena. In fact, in 1968 the chlorine-based R. Davis' Homestake experiment (17) for measuring the solar electron neutrino flux observed a deficit of approximately 2/3 with respect to the prediction of the Standard Solar Model (18).

Its result, afterwards confirmed by other radiochemical experiments (GALLEX, SAGE, GNO) starting from the '90s (19), suggested to Bruno Pontecorvo the idea of solar electron neutrinos oscillating into other flavours (20) but the confirmation to this theory arrived only at the beginning of the new millennium with the Sudbury Neutrino Observatory (SNO) experiment (21).

Differently from the radiochemical experiments, able to measure only to ν_e flux, SNO is sensitive both to electron neutrinos, thanks to charged current reaction on Deuterium, and to all the three flavours together, by measuring neutral current reactions. The results from the first process confirm the solar ν_e deficit, while the total ν flux measured by neutral current process is in agreement with the theoretical prediction: this means that there is a non-electron component in the solar neutrino flux, but these other-flavoured neutrinos cannot be produced by the sun itself.

Slightly before, the Super-KamiokaNDE experiment (22) in the '90, studying the atmospheric neutrino, observed a difference between the flux of downward-going and the flux of upward-going ν_μ, explained by their oscillation into ν_τ.

These results from solar and atmospheric neutrinos were also confirmed by using artificial neutrino sources: for example KamLAND first discovered the disappearance of reactor-produced $\bar{\nu}_e$ (23), while the $\bar{\nu}_\mu$ disappearance was observed by the long-baseline neutrino beam K2K experiment (24) and then their outcomes have been improved by other reactor or long baseline experiments, such as CHOOZ (25) and MINOS (26).

The solar and atmospheric neutrino flux deficit can be explained assuming that neutrinos change their flavour while propagate, but it is possible only if there are massive.

If neutrinos have mass, there will be neutrino mass eigenstates, ν_i, i = 1, 2, 3, each with mass m_i, whose time-evolution is:

$$|\nu_i\rangle_t = e^{-iE_i t}|\nu_i\rangle_0.$$

1-1

To change from the flavour eigenstate basis $|\nu_\alpha\rangle$, with α = e, μ, τ, to the mass eigenstate one $|\nu_i\rangle$ and vice versa, let's introduce a unitary matrix U so it is possible to write each flavour eigenstate as a mass eigenstates superposition:

$$|\nu_\alpha\rangle = \sum_i U^*_{\alpha i} |\nu_i\rangle$$

1-2

In particular, if U is a diagonal matrix, the sum becomes a one to one correspondence between a precise mass state and a flavour state, i. e. $m(\nu_\alpha) = \delta_{\alpha i}\, mi$.

Hence the probability for a massive neutrino, travelling a distance L in vacuum, in a time t, with momentum p, to oscillate from the flavour state ν_α to the flavour state ν_β is:

$$P(\nu_\alpha \to \nu_\beta) = \left|\langle \nu_\beta | \nu_\alpha \rangle_t\right|^2 = \left|\sum_i U^*_{\alpha i}\, e^{-iE_i t} U_{\beta i}\right|^2$$

$$= \delta_{\alpha\beta} - 4\sum_{i>j} \Re\left(U^*_{\alpha i} U_{\beta i} U_{\alpha j} U^*_{\beta j}\right) \sin^2\left(\frac{\delta\phi_{ij}}{2}\right) + 2\sum_{i>j} \Im\left(U^*_{\alpha i} U_{\beta i} U_{\alpha j} U^*_{\beta j}\right) \sin\left(\delta\phi_{ij}\right).$$

1-3

$\delta\phi_{ij}$ is the relative phase between two states, i, j after a time t and it is given by:

$$\delta\phi_{ij} = \left(E_i - E_j\right)t = \frac{\left(E_i^2 - E_j^2\right)}{\left(E_i + E_j\right)} t = \frac{\left(m_i^2 - m_j^2\right)}{\left(E_i + E_j\right)} t = \frac{\left(\Delta m_{ij}^2\right)}{\left(E_i + E_j\right)} t.$$

1-4

Because the mass difference among neutrino states is very small if compared to all the momenta and energies of the particle, it is possible to define $E \equiv \frac{1}{2}(E_i + E_j)$ and, taking into account that $L = t \cdot p/E$, one obtains:

$$\delta\phi_{ij} = \frac{\left(\Delta m_{ij}^2\right)}{2p} L.$$

1-5

Neutrino flavour changing is a quantum interference phenomenon.

It is easy to see that the oscillation probability is different from zero only if Δm_{ij}^2 is not null and if the *U* matrix is not diagonal. Therefore the evidence of oscillations strictly implies

that neutrinos are massive particle and the lepton mixing. The U matrix is exactly the leptonic mixing matrix, also called PMNS matrix, from the initials of B. Pontecorvo, Z. Maki, M. Nakagawa e S. Sakata who introduced and developed the oscillation theory.

Considering the three known flavour states and three mass states, the U matrix can be written as:

$$U = \begin{array}{c} \\ \nu_e \\ \nu_\mu \\ \nu_\tau \end{array} \begin{array}{c} \begin{array}{ccc} \nu_1 & \nu_2 & \nu_3 \end{array} \\ \begin{bmatrix} c_{12}c_{13} & s_{12}c_{13} & s_{13}e^{-i\delta} \\ -s_{12}c_{23}-c_{12}s_{23}s_{13}e^{i\delta} & c_{12}c_{23}-s_{12}s_{23}s_{13}e^{i\delta} & s_{23}c_{13} \\ s_{12}s_{23}-c_{12}c_{23}s_{13}e^{i\delta} & -c_{12}s_{23}-s_{12}c_{23}s_{13}e^{i\delta} & c_{23}c_{13} \end{bmatrix} \end{array}$$

1-6

It depends on four parameters: three mixing angles and one complex phase introducing the CP violation in the leptonic sector.

The existing neutrino oscillation data allow to determine the parameters which drive the solar neutrino and atmospheric neutrino oscillations, $\Delta m^2_{solar}=\Delta m^2_{12}$, θ_{12}, and $\Delta m^2_{atm}=|\Delta m^2_{31}|\sim|\Delta m^2_{23}|$, θ_{32}, with a relatively good precision (but not the sign of Δm^2_{atm}), and to obtain rather stringent limits on the angle θ_{13}. The best fit values and the 3σ allowed ranges of all the parameters are collected in Table 1-1.

These results imply that $\theta_{23}\sim\pi/4$, $\theta_{12}\sim\pi/5.4$ and $\theta_{13} \lesssim \pi/13$, making the PMNS matrix drastically different from the CKM quark mixing matrix (27). At present no experimental information on the Dirac and Majorana CP violation phases in the neutrino mixing matrix is available. Thus, the status of CP symmetry in the lepton sector is unknown. If $\theta_{13}\neq 0$ the Dirac phase δ can generate CP-violation effects in neutrino oscillations (28), (29), (30).

Parameter	Best Fit	3σ
Δm^2_{12} [10^{-5} eV^2]	$7.59^{+0.23}_{-0.18}$	7.03 - 8.27
$\lvert\Delta m^2_{13}\rvert$ [10^{-3} eV^2]	$2.40^{+0.12}_{-0.11}$	2.07 - 2.75
$\sin^2\theta_{12}$	$0.318^{+0.019}_{-0.016}$	0.27 - 0.38
$\sin^2\theta_{23}$	$0.50^{+0.07}_{-0.06}$	0.36 - 0.67
$\sin^2\theta_{13}$	$0.01^{+0.013}_{-0.009}$	≤ 0.053

Table 1-1. Best fit values with 1σ errors and the 3σ allowed intervals for the three-flavour oscillation parameters from global data including solar, atmospheric, reactor (KamLAND and CHOOZ) and accelerator (K2K and MINOS) experiments (31).

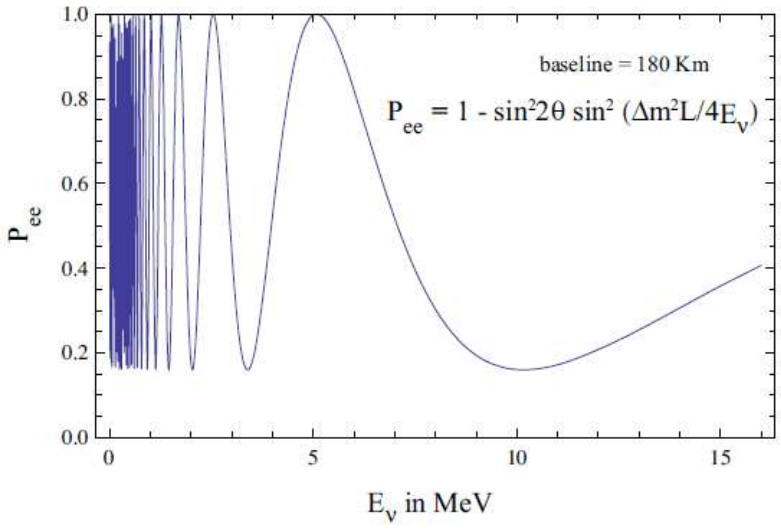

Figure 1-2. The ν_e survival probability $P(\nu_e \rightarrow \nu_e)$ (Eq. 1-3) in the 2-neutrino scenario as a function of the neutrino energy for L=180 km, $\Delta m^2=7.0\cdot10^{-5}$ eV^2 and $\sin^2 2\theta=0.84$ (32).

1.2.1. Neutrino mass hierarchy

The various oscillation experiments identify a couple of mass eigenstates, ν_1 and ν_2, divided by a small mass difference, and a third eigenstate ν_3, very far from the other two. The first couple explains the solar neutrino oscillations, while the second one is responsible of the atmospheric oscillations (it is possible to explain oscillation data in term of a 2-neutrino scenario because θ_{13} is very small. An example of ν_e survival probability in this scenario is displayed in Figure 1-2). From the oscillations data it is also possible to estimate the flavour component of each mass eigenstate (Figure 1-3).

The sign of Δm^2_{solar} leads to $m_2>m_1$ but, because the sign of Δm^2_{atm} is not measured, determining the position of m_3 with respect to m_1 and m_2 is not possible. Furthermore, being neutrino oscillations sensitive only to the neutrino mass squared differences, they cannot give any information about how much the mass squared spectrum is above zero.

With this situation, three different mass hierarchies are possible:

- ✓ Normal Hierarchy, where $m_1 \ll m_2 \ll m_3$. In this case, $m_3 \sim \sqrt{\Delta m^2_{atm}} \sim 0.04$-$0.05$eV, $m_2 \sim 0.009$ eV, $m_1 \sim 0$ (Figure 1-3, left).
- ✓ Inverted Hierarchy, where $m_1 \sim m_2 \sim \sqrt{\Delta^2_{atm}} \gg m_3$ (Figure 1-3, right).
- ✓ Quasi-Degenerate Hierarchy, where $m_1 \sim m_2 \sim m_3$ with small mass differences responsible of the oscillations.

Because oscillation experiments are not enough to define an absolute neutrino mass scale, other kinds of experiments are required for completing the neutrino mass scenario.

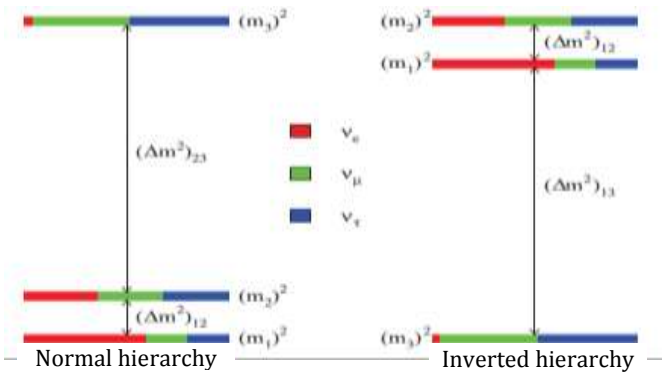

Figure 1-3. Three neutrino mass squared spectrum in case of normal (left) and inverted (right) hierarchy, with the estimation of the flavour components of each mass eigenstate, according to oscillations data (33).

The first method is to study the single beta decay spectrum, whose end-point is modified in shape by neutrino mass. This type of experiment has no theoretical assumption on neutrinos and is completely model-independent. It is sensitive to the quantity:

$$m_\beta = \sqrt{\sum_{i=1}^{3} |V_{ei}^2| m_i^2}.$$

1-7

The most sensitive result in this field has been obtained by the Mainz and Troitsk experiment, fixing an upper limit of 2.5 eV (95% C.L.) to m_β (34).

A second way to understand neutrino masses comes from cosmological observations (the formation of Large Scale Structure and the presence of anisotropies in the Cosmic Microwave Background) that can probe the quantity:

$$m_{cosmo} = m_1 + m_2 + m_3.$$

1-8

This evaluation is not connected to weak mechanisms but it is strongly related to cosmological models, therefore it needs independent verifications. Presently the limit on the sum of m_i is m_{cosmo}<0.67 eV (95% C.L.) (35).

Last but not least the neutrinoless double beta decay ($0\nu\beta\beta$), a rare nuclear decay that is not foreseen in the SM and, if observed, will state important information not only about the neutrino absolute mass scale, but also on the neutrino nature. Being this kind of experiment the framework in which this PhD thesis has been developed, the $0\nu\beta\beta$ will be discussed in detail in Section 1.4.

1.3. The importance of being a Majorana particle

In the Standard Model, neutrinos are described as left-handed massless particles, associated to the charged leptons. Therefore the observation of neutrino oscillations opens the way to new theories able to expand the SM and explaining not only why neutrinos have mass, but also why their mass is so small if compared with the other particles. One way for achieving this result is questioning the assumption that the neutrino is a fermion of the same kind of the other elementary particles of the SM, i.e. a Dirac particle.

A Dirac fermion is a particle well differentiated from its own antiparticle; a Majorana fermion, instead, is a particle identical to its own antiparticle. For all the quarks and the charged leptons the difference between particle and antiparticle is carried by the electric charge; being neutrinos neutral, for them this difference is no more obvious.

The possibility of having neutrinos as Majorana particles shows up in the mass terms of their Lagrangian precluded to the others fermion. Generally, the Lagrangian of a fermionic field, ψ, from which the Dirac equation describing the particle evolution is derived, is:

$$\mathcal{L} = \bar{\psi}\left(i\gamma^{\mu}\partial_{\mu} - m_D\right)\psi = \bar{\psi}i\gamma^{\mu}\partial_{\mu}\psi - m_D\bar{\psi}\psi,$$

1-9

where the first term corresponds to the kinetic energy, while the second one, called "Dirac term", is the mass term. Decomposing the field ψ in its left and right chirality components (ψ_L and ψ_R respectively), the Dirac mass term becomes:

$$-\mathcal{L}_D = m_D\bar{\psi}\psi = m_D(\bar{\psi}_L\psi_R + \bar{\psi}_R\psi_L) = m_D\bar{\psi}_L\psi_R + \ h.c.^{3}$$

1-10

For neutrinos it is possible to introduce another mass term still holding the Lorentz invariance, i.e. $\psi^T C^{-1}\psi$ (here T denotes transposition and C is the charge conjugation matrix) but that, unlikely to the Dirac mass term, is not invariant under a phase transformation $\psi \rightarrow e^{i\alpha}\psi$, so it doesn't imply the existence of a conserved charge, as happens instead for Dirac particles. Because $\psi^C \equiv C\bar{\psi}^T$, this new mass term, called Majorana term, can be written as:

$$-\mathcal{L}_M = \frac{1}{2}(m_M\bar{\psi}\psi^C + m_M^*\bar{\psi}^C\psi) = \frac{1}{2}m_M\bar{\psi}\psi^C + \ h.c.,$$

1-11

[3] From here now h.c. means hermitian conjugate.

where m_M (taken as real) is called Majorana mass. Using again left and right projections and considering that $(\psi_{L,R})^C = (\psi^C)_{R,L}$, one left and one right Majorana mass terms are obtained:

$$-\mathcal{L}_{m_L} = \frac{1}{2} m_L \left(\overline{\psi^C}\right)_R \psi_L + h.c. \qquad \text{and} \qquad -\mathcal{L}_{m_R} = \frac{1}{2} m_R \left(\overline{\psi^C}\right)_L \psi_R + h.c$$

1-12

Hence, the more general mass term, i.e. the Dirac-Majorana term, is:

$$-\mathcal{L}_{D-M} = m_D[\bar{\psi}_L \psi_R] + \frac{m_L}{2}\left[\psi_L \left(\overline{\psi^C}\right)_R\right] + \frac{m_R}{2}\left[\left(\overline{\psi^C}\right)_L \psi_R\right] + h.c.$$

1-13

Let's now introduce two new fields, ϕ_1 and ϕ_2, in order that:

$$\phi_1 = \frac{\psi_L + (\psi^C)_R}{\sqrt{2}} \qquad \text{and} \qquad \phi_2 = \frac{\psi_R + (\psi^C)_L}{\sqrt{2}}.$$

1-14

They describe Majorana objects, because $\phi_1{}^C = \phi_1$ and $\phi_2{}^C = \phi_2$; using these fields it is possible to rewrite the mass term as:

$$-\mathcal{L}_{D-M} = m_D(\bar{\phi}_2\phi_1 + \bar{\phi}_1\phi_2) + m_L\bar{\phi}_1\phi_1 + m_R\bar{\phi}_2\phi_2 = \bar{\Phi}[M]\Phi,$$

1-15

where Φ is a column vector with components ϕ_1 and ϕ_2, and $[M] = \begin{bmatrix} m_L & m_D \\ m_D & m_R \end{bmatrix}$ is the neutrino mass matrix that can be diagonalized with a rotation in the space of vector Φ, represented by the matrix Z. The elements of the diagonal matrix $\mathcal{D}$=ZMZ^T are the eigenvalues of M, i.e. m_ν and M_N, so $\mathcal{D}$ can be used to rewrite the mass term. In this case the fields are expressed by the components of the vector $F \equiv \begin{bmatrix} \nu \\ N \end{bmatrix} = Z^{-1}\Phi$, which are still Majorana objects.

Hence:

$$-\mathcal{L}_{D-M} = m_\nu \bar{\nu}\nu + M_N \bar{N} N.$$

1-16

In other words, the eigenstates of the combination of Dirac and Majorana mass terms are two distinct Majorana particles, ν and N, with mass m_ν and M_N.

The matrix eigenvalues are:

$$\begin{matrix} m_\nu \\ M_N \end{matrix} = \frac{1}{2}\left[(m_L + m_R) \mp \sqrt{(m_L - m_R)^2 + 4m_D^2}\right].$$

1-17

According to the values of the Dirac or Majorana masses, different cases arise. For example, if $m_L=m_R=0$, we have $m_\nu=-M_N=m_D$ and there are two degenerate mass eigenstates that give a Dirac mass term: in other words, a Dirac fermion is a special case of the superposition of two Majorana fermions.

A very interesting case is the one with $m_L=0$ and $m_D \ll m_R$, that leads to:

$$m_\nu \cong {m_D^2}/{m_R} \qquad \text{and} \qquad M_N \cong m_R,$$

1-18

i.e. one particle, ν, has an extremely small mass m_ν and corresponds to the light neutrino, while the other is a very heavy neutral lepton[4]. That explanation of the lightness of the neutrinos because of a big Majorana mass m_R is called See-Saw mechanism.

This procedure can be easily extended to three flavour neutrinos: F becomes a six component vector ($\nu_{1\ldots3}$, $N_{1\ldots3}$) and $m_{L,R,D}$ are matrixes.

The Majorana nature of neutrinos implies also a modification in the leptonic mixing matrix: it was defined unless a phase factor that lives the lepton eigenstates unchanged, because they were considered as Dirac fermions. But that redefinition is no more possible for Majorana neutrinos and so the mixing matrix becomes:

$$V = U \times A =$$
$$= \begin{bmatrix} c_{12}c_{13} & s_{12}c_{13} & s_{13}e^{-i\delta} \\ -s_{12}c_{23}-c_{12}s_{23}s_{13}e^{i\delta} & c_{12}c_{23}-s_{12}s_{23}s_{13}e^{i\delta} & s_{23}c_{13} \\ s_{12}s_{23}-c_{12}c_{23}s_{13}e^{i\delta} & -c_{12}s_{23}-s_{12}c_{23}s_{13}e^{i\delta} & c_{23}c_{13} \end{bmatrix} \times \begin{bmatrix} e^{i\frac{\alpha_1}{2}} & 0 & 0 \\ 0 & e^{i\frac{\alpha_2}{2}} & 0 \\ 0 & 0 & 1 \end{bmatrix}.$$

1-19

The phases α_1 and α_2 are known as Majorana phases, besides the Dirac phase, δ, similar to the one existing in the quark mixing matrix.

The See-Saw mechanism plays an important role in the context of cosmology, in particular in the explanation of the baryon-antibaryon asymmetry, i.e. the excess of matter over antimatter in the universe (36):

[4] Until now there is no evidence of other neutral lepton with mass lower than 80GeV.

$$\eta \equiv \frac{n_B - n_{\bar{B}}}{n_\gamma} = (6.15 \pm 0.25) \cdot 10^{-10}$$

1-20

Is difficult to justify this tiny difference as an initial condition at the beginning of the big-bang, so a mechanism is needed that generated dynamically the baryon asymmetry at a certain stage of the universe evolution. There is a set of requirements (known as the Sakharov conditions, (37)) that this interaction must fulfil in order to generate the baryon asymmetry: it must violate the baryon number conservation, as well as the C and C-P conservation, and it has to be out of the thermal equilibrium.

It is not possible to fulfil these requirements in the framework of the Standard Model. Within the extension of the SM several theories arise; one of the most favourable is the baryogenesis through leptogenesis: lepton number might be violated by some non SM physics, giving rise to a lepton asymmetry, which is converted into the observed baryon asymmetry by a sphaleron process[5].

The thermal leptogenesis (38), (37), (39), (36), (40) is an implementation of a baryogenesis through leptogenesis scenario that satisfies the Sakharov conditions in the SM with just the addition of the heavy singlet right-handed neutrinos foreseen in the See-Saw.

These heavy neutrinos N, produced in the Big-Bang, being Majorana particles, can decay into lepton or an antilepton. Since a CP violation is expected, the decays $N \rightarrow \ell^- + H^+$ and $N \rightarrow \ell^+ + H^-$ (where $H^\pm$ are the SM Higgs particles) would have different rates, producing a universe with a different number of leptons and antileptons. Then the sphaleron process converts this lepton asymmetry into a baryon asymmetry; CP-violation is due to the Yukawa interactions of the right-handed neutrinos with the SM lepton doublets and out-of-equilibrium is induced by the right-handed neutrino decays.

Therefore, by confirming the existence of Majorana masses and the Majorana character of neutrinos the observation of $0\nu\beta\beta$ would be evidence in favour of the See-Saw, hence of thermal leptogenesis.

[5] A sphaleron (from the greek *σφαλερός* meaning "ready to fall") is a time independent solution to the electroweak field equations of the Standard Model; it is a non-perturbative process that doesn't conserve baryon number, B, or lepton number, L, but conserve L-B. Geometrically, a sphaleron is simply a saddle point of the electroweak potential energy (in the infinite dimensional field space).

"In electroweak gauge theory, the vacuum state is infinitely degenerate, and the different substates are separated by energy barriers. Through a quantum tunneling process, the system can move to a different vacuum substate which has nonzero baryon number. This process is heavily-suppressed at low energies (below the so-called sphaleron mass of ~ 10 TeV), so it is not expected to occur in Nature today, but is feasible at earlier points in the universe's history. The sphaleron process is non-perturbative, so a true Feynman diagram can't be drawn for it [...]. This process trades three leptons, one from each generation, for nine quarks, three within each generation, and one of each colour per generation. L and B are not conserved separately [...] though the quantum number B – L is. In a sense, this process generates a baryon excess out of a lepton excess [...]." (218).

As briefly introduced, a consequence of the Majorana nature of neutrinos is that the leptonic number, L, is no more a conserved quantity, unlike in the SM.

In fact, in the description of SM processes, L=1 denotes negative charged leptons and neutrinos, L=-1 is for positive charged leptons and antineutrinos and L=0 is for not leptonic particles, and neutrinos and antineutrinos can be distinguished according to the leptonic number they should have in order that L is conserved in the reaction. For example, let's consider the decay $\pi^+ \rightarrow \mu^+ + \nu_\mu$: because $L(\pi^+)=0$ and $L(\mu^+)=1$, ν_μ should be a neutrino that will produce a μ^+ while interacting in the detector. On the other side, in the process $\pi^- \rightarrow \mu^- + \bar{\nu}_\mu$, $\bar{\nu}_\mu$ is an antineutrino that will create a μ^- in a following interaction[6]. This behaviour seems to underline that neutrino and antineutrino are two well distinct particles, in opposition to what should happens if they were Majorana particles.

The same situation can also be seen in a different way by mean of the helicity; in the π^+ decay, the ν_μ is produced in a negative helicity state (LH), while in the π^- decay the $\bar{\nu}_\mu$ comes out with positive helicity (RH); hence ν_μ e $\bar{\nu}_\mu$ are different because they are created in a opposite helicity state (even if, for a given helicity, they are the same particle) and, while interacting, they will produce a μ^+ and a μ^- respectively.

Therefore, the particle defined "neutrino" when the conservation of L is assumed is a LH state of a Majorana neutrino, and an "antineutrino" is a RH state of the same particle.

As a matter of fact, a massive particle cannot be a pure helicity state, so a neutrino producing a negative charged lepton will have a small component of RH helicity.

These remarks are fundamental for the comprehension of the key phenomena in the investigation of the Dirac/Majorana nature of neutrinos, i.e. the neutrinoless double beta decay ($0\nu\beta\beta$). This process, being the central topic of this PhD work, will be detailed treated in the next section.

1.4. Neutrinoless double beta decay: the final frontier

Double beta decay (DBD) is a rare, spontaneous nuclear process consisting in a father nucleus (A, Z) that transforms into a stable daughter with the same mass number but with nuclear charge increased by two units: (A, Z+2).

This transition, first proposed by Maria Goeppert-Mayer in 1935 (41), can in principle occur for 35 nuclei, whose ordinary single beta decay is suppressed by a large change of the nuclear spin-parity state or energetically forbidden (if the intermediate (A, Z+1) nucleus has

[6] Neutrino mixing and oscillations are not considered here, for simplicity, and ν_μ is a mass eigenstate.

a binding energy greater than the (A, Z) and (A, Z+2) nuclei). Because DBD is a second order process of the weak interaction, it is a very low probability transition, so the candidate parent nuclei have a very long lifetime, as can be seen in Table 1-2.

Usually two different DBD modes are considered. In the first one the transition is characterised by the emission of two electrons and two antineutrinos, and so it is called two-neutrino double beta decay (2νββ):

$$(A, Z) \rightarrow (A, Z+2) + 2e^- + 2\bar{\nu}. \qquad 1\text{-}21$$

This process, for which the lepton number is conserved, can be understood in terms of two simultaneous neutron decays, as can be seen from Figure 1-4a. It is predicted by the Standard Model and it has been already observed in several nuclides (see Table 1-2).

In the second mode the process will have just the two electrons in the final state:

$$(A, Z) \rightarrow (A, Z+2) + 2e^-. \qquad 1\text{-}22$$

This is called neutrinoless double beta decay (0νββ): it violates the lepton number conservation (ΔL=2) and is possible only if the neutrino is a massive Majorana particle, definitely implying new physics beyond the SM. It can be explained by two consecutive steps:

$$\begin{aligned} (A, Z) &\rightarrow (A, Z+1) + e^- + \bar{\nu}_e \\ (A, Z+1) + \nu_e &\rightarrow (A, Z+2) + e^- \end{aligned} \qquad 1\text{-}23$$

A neutron decays emitting a RH $\bar{\nu}_e$ that is then absorbed as a LH ν_e, starting the second part of the process. This is the so-called mass mechanism. The neutrino emitted at one weak interaction vertex and absorbed at the other one, as the intermediate nuclide with all its excited states, is a virtual particle. This is possible if the neutrino and the antineutrino are the same particle that should be massive in order to be in a mixed helicity state and allowing the helicity flip. The process is sketched in Figure 1-4b.

There are also other mechanisms which can induce the 0νββ process: right-handed currents with the exchange of both light and heavy neutrinos, or the exchange of other more exotic particles. In addition, the neutrinoless process can be accompanied by the emission of a Majoron (a hypothetical neutral pseudoscalar particle with zero mass, associated with the spontaneous breaking of the local or global B–L symmetry).

Isotope	2νββ half-life [y]	0νββ half-life [y]	
$^{48}Ca \rightarrow {}^{48}Ti$	$4.4 \cdot 10^{19}$	$> 1.5 \cdot 10^{21}$ (42)	
$^{76}Ge \rightarrow {}^{76}Se$	$1.5 \cdot 10^{21}$	$> 1.9 \cdot 10^{25}$ (43)	$> 1.6 \cdot 10^{25}$ (44)
$^{82}Se \rightarrow {}^{82}Kr$	$0.9 \cdot 10^{20}$	$> 2.1 \cdot 10^{23}$ (45)	
$^{96}Zr \rightarrow {}^{100}Mo$	$2.3 \cdot 10^{19}$	$> 1.0 \cdot 10^{21}$ (46)	
$^{100}Mo \rightarrow {}^{100}Ru$	$7.1 \cdot 10^{18}$	$> 5.8 \cdot 10^{23}$ (45)	$> 5.5 \cdot 10^{23}$ (47)
$^{116}Cd \rightarrow {}^{116}Sn$	$2.8 \cdot 10^{19}$	$> 1.7 \cdot 10^{23}$ (48)	
$^{128}Te \rightarrow {}^{128}Xe$	$1.9 \cdot 10^{24}$	$> 8.6 \cdot 10^{22}$ (49)	
$^{130}Te \rightarrow {}^{130}Xe$	$6.8 \cdot 10^{20}$	$> 2.8 \cdot 10^{24}$ (50)	
$^{136}Xe \rightarrow {}^{136}Ba$	$> 8.1 \cdot 10^{20}$	$> 1.2 \cdot 10^{24}$ (51)	
$^{150}Nd \rightarrow {}^{150}Sm$	$8.2 \cdot 10^{18}$	$> 1.8 \cdot 10^{22}$ (52)	

Table 1-2. Summary of the most sensitive direct searches for 2νββ and 0νββ. Limits are at 90% C.L. All the 2νββ half-lives come from (53), except the limit on ^{136}Xe, that is taken from (54). The references for the 0νββ half-lives are reported directly in the table.

Nevertheless it has been demonstrated (55) that, whatever is the mechanism driving the 0νββ decay, this transition requires that the neutrino is a massive Majorana particle.

From the experimental point of view, an effective way to distinguish the 0νββ from the 2νββ is to measure the energy of the two electrons emitted in the decay and to analyse the shape of the two electron sum energy spectrum. In fact, because the 2νββ is a four-body decay, it will be a continuous spectrum between 0 and the total energy available in the decay, the Q-value, with a maximum around ⅓Q. On the contrary, in case of the neutrinoless decay, all the kinetic energy is carried by the two electrons (neglecting nuclear recoil) and the spectrum will result in a sharp peak centred at the transition energy (Figure 1-5), whose width depends on the energy resolution of the detector.

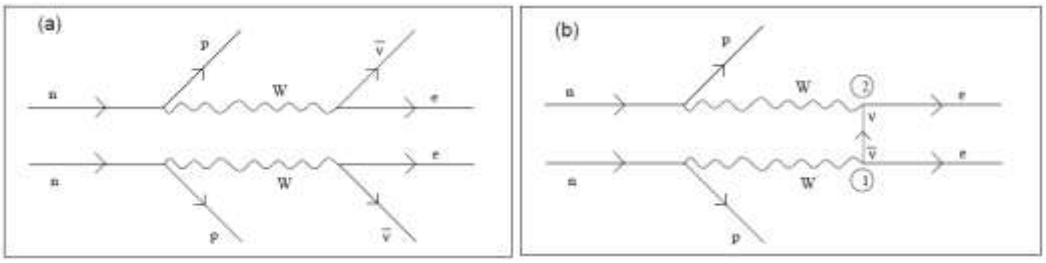

Figure 1-4. Feynman diagrams for the 2νββ (a) and 0νββ (b) decay channels. In the latter, an antineutrino is produce at the vertex 1 and a neutrino is absorbed at vertex 2.

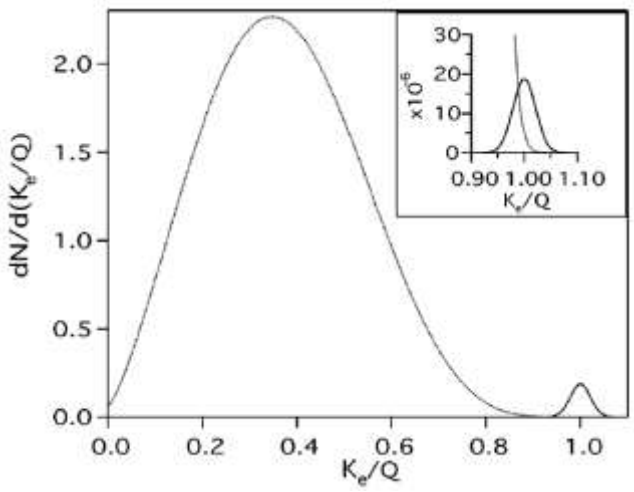

Figure 1-5. Spectra of the sum of the two electron kinetic energies, K_e: he 2νββ (dotted curve) is normalised to 1, while the 0νββ (solid curve) is normalised to 10^{-2} (10^{-6} in the inset, to underline the contribution of the 2νββ as a background to the 0νββ). All spectra are convolved with energy resolution of 5% (56).

The 0νββ decay rate is usually expressed using the general relation derived from Fermi's golden rule (57):

$$R_{0\nu} = \frac{1}{T^{0\nu}_{1/2}} = G_{0\nu}(Q,Z)|M_{0\nu}|^2 m^2_{\beta\beta},$$

1-24

where $G_{0\nu}(Q,Z)$ is the two electron phase-space integral, that can be exactly calculated and scales as Q^5, and $M_{0\nu}$ is the nuclear matrix element; both parameters depend on the 0νββ candidate. $m_{\beta\beta}$ is the effective neutrino mass:

$$m_{\beta\beta} = \left| \sum_{i=1}^{3} |U_{ei}|^2 m_i e^{i\alpha_i} \right|.$$

1-25

Here the U_{ei} are the neutrino mixing matrix elements, m_i are the neutrino mass eigenstates and the α_i are the Majorana phases introduced in equation 1-19. Their presence implies that cancellations are possible, and if the neutrino is a Dirac particle the cancellation is total (it is equivalent to a couple of degenerate Majorana neutrinos with opposite phases), so that the decay doesn't take place.

It is possible to relate the effective Majorana mass, $m_{\beta\beta}$, with the lightest mass eigenstate, m_{light}, which is determined according to the mass hierarchy. For example, considering the normal hierarchy, where $m_{light}=m_1$, one obtains:

$$m_{\beta\beta} = |cos^2\theta_{12}cos^2\theta_{13}e^{i\alpha_1}m_1 + sin^2\theta_{12}cos^2\theta_{13}e^{i\alpha_2}\sqrt{\Delta m_{12}^2 + m_1^2}$$
$$+ sin^2\theta_{13}e^{-2i\delta}\sqrt{|\Delta m_{13}^2| + m_1^2}|.$$

1-26

Here θ_{12}, θ_{13} and δ are the mixing angles and phase, and $\alpha_{1,2}$ are the Majorana phases appearing in Eq. 1-19. Using angle and squared-mass difference values from oscillation experiments, for a given set of phases, an allowed region of $m_{\beta\beta}$ in function of m_{light} is determined. A plot of $m_{\beta\beta}$ in case of normal hierarchy and inverted hierarchy with phases from 0 to 2π is shown in Figure 1-6. It is clear from this plot that finding a value for $m_{\beta\beta}$ will at last fix the neutrino mass hierarchy, setting a range for the absolute neutrino mass values.

Eq. 1-24 shows that measuring the half-life of the decay is not enough to obtain the value of $m_{\beta\beta}$. While the phase-space factors, $G_{0\nu}(Q,Z)$, are exactly computable (see Figure 1-8), this is not the case for the Nuclear Matrix Elements, $M_{0\nu}$.

Several models have been proposed for carrying on this theoretical calculation; actually the most accredited are the Quasiparticle Random Phase Approximation (QRPA), that is developed in different frameworks such as Renormalized QRPA or proton-neutron QRPA (see, for example, (58), (59)), the Interacting Shell Model (ISM) (60) and, recently, also the Microscopic Interacting Boson Model (IBM-2) (61). The results obtained with these calculations are collected in Figure 1-7.

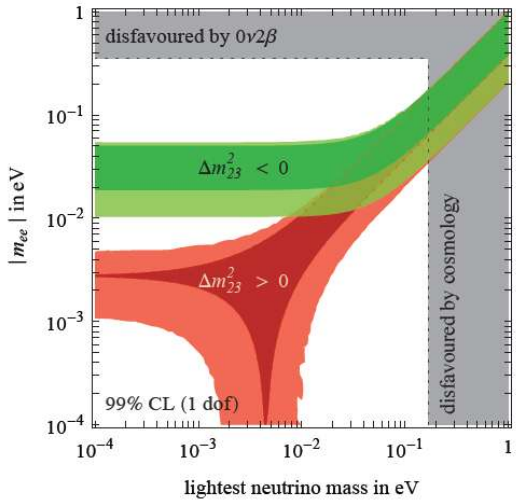

Figure 1-6. 99% CL expected ranges as function of the lightest neutrino mass for mββ (here m_{ee}) using recent data from oscillation experiments. The green region corresponds to the inverted hierarchy ($m_{light} = m_3$) while the red one is for the normal hierarchy ($m_{light} = m_1$). The darker regions at the centre of both areas show how the ranges would shrink if the oscillation values were known with negligible errors (36).

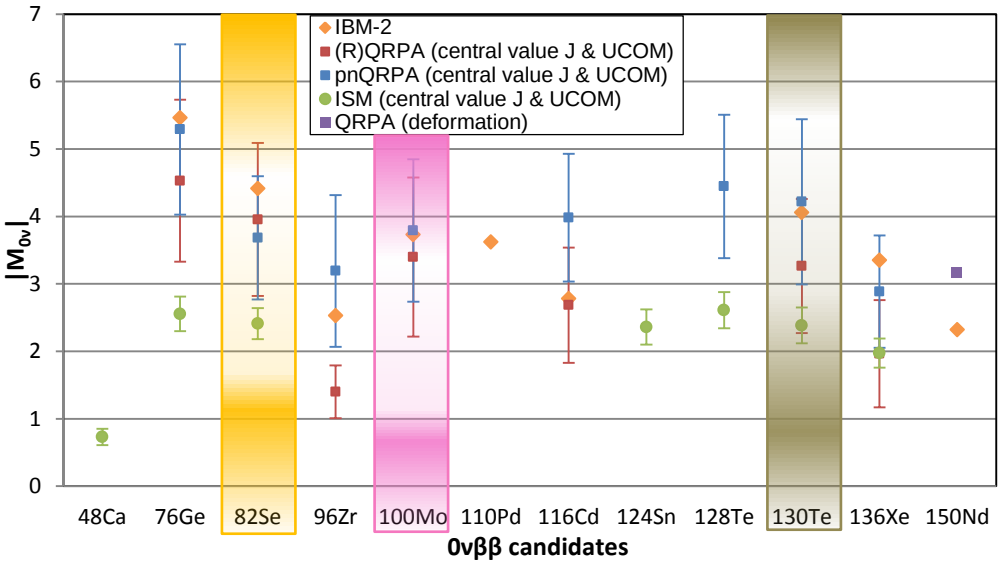

Figure 1-7. 0νββ nuclear matrix elements calculated for some 0νββ candidates with the Microscopic Interacting Boson Model (IBM-2) (61), the Quasiparticle Random Phase Approximation (QRPA) in both renormalized QRPA (58) and proton-neutron QRPA (59) frameworks, and in a recent work taking into account nuclear deformation for the ^{150}Nd (62), and the Interacting Shell Model (ISM) (60). When a range is present, the central mark for each NME range indicates only the mean of the maximum and minimum values of the range, and is intended solely to guide the eye. The range limits are obtained identifying the minimum and the maximum NME values among the two NME ranges calculated with Jastrow and UCOM Short Range Correlation, and the central value is obtained averaging the range limits. All matrix elements are in dimensionless units. The three coloured bands highlight the isotopes considered in this PhD work.

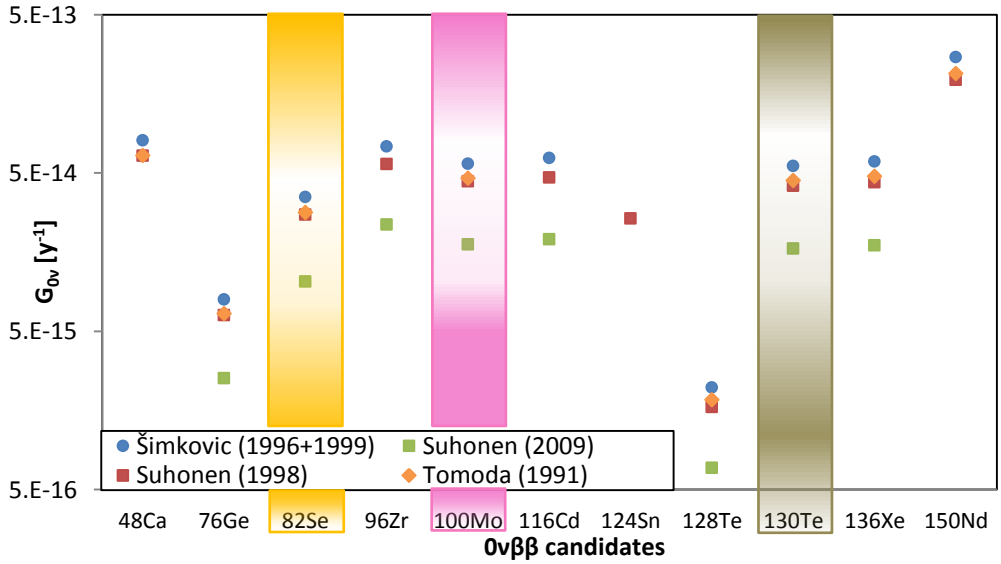

Figure 1-8. Phase-space factors for some 0νββ candidates, calculated from the electron wavefunctions according to (63) with r_0=1.1 fm and g_A=1.25 for the blue-round series (Simkovic, (64), (65)) and with r_0=1.2 fm and g_A=1.25 for the green-square series (Suhonen-1998, (66)); the yellow-rhomb series (Tomoda) is obtained from (67), with r_0=1.2 fm and g_A=1.25: the value listed in (67) are in [$y^{-1}fm^2$] unit, being multiplied by a factor $4R^2$ ($R= r_0A^{1/3}$) to match the definition of the nuclear matrix element and the neutrino potential in (67). The phase space factors in the red-squared series (Suhonen-2009) are deduced from the decay time $T_{1/2}$ reported in (59) with r_0=1.2 fm and g_A=1.00. The three coloured bands highlight the isotopes considered in this PhD work.

Presently, no best-model exists, being difficult to estimate the correctness and the accuracy of the calculations, that are complicated and involves several steps, because they are not connected to other nuclear process that allows a simple verification. Even the comparison with the 2ν-channel presents unclear points, mostly because of the different role played by neutrinos in the two processes. In this situation, one possibility is to consider the spread of the theoretical values of the Nuclear Matrix Element as a measure of their uncertainty; actually this is the main source of uncertainty in the value of $m_{\beta\beta}$ obtained by the various experiments. However a convergence of the $M_{0\nu}$ from the different models has been observed in the last years. A confrontation among the $M_{0\nu}$ results from different models is displayed in Figure 1-7.

1.4.1. Experimental approaches to 0νββ

Even if the 0νββ experimental signature is very simple, a peak at the Q-value in the two electron sum energy spectrum, finding it is not simple at all. The observation of this small effect and the demonstration that it corresponds really to the searched decay is a challenging task and imposes severe constraints on the experiment design.

The peak is superimposed to a continuum background, to which contributed also the 2νββ, whose tail extends in the region of interest (56). A detector with good energy resolution is therefore mandatory for distinguish the peak, together with strategies to control the natural radioactivity and cosmogenic background, as underground production and operating of the detector. In addition to the two-electron sum peak evaluation, the event reconstruction providing the kinematic of the single electron would be useful to reduce the background and to give information about the 0νββ mechanism driving the decay (57).

In the present DBD experimental scenario it is possible to distinguish two main approaches to the 0νββ search (68): the calorimetric technique, with the source embedded in the detector itself, and the external-source approach, in which source and detector are two separate systems. Both methods have pros and contra: the calorimetric approach is an intrinsically high efficiency method, so large source masses are possible; and also, with the proper choice of the detectors (bolometers or Ge diodes), it can reach a very high energy resolution (of the order of 0.1%). But there are of course constraints on detector materials (and so on the investigable nuclei) and reconstructing the event topology is difficult.

On the contrary, the external source approach allows a precise event topology reconstruction, which lead to background identification (except for the 2νββ). With this method it is also possible to investigate several candidate nuclei at the same time with the

same detector, and different experimental techniques can be profitably combined: scintillation, TPC, drift chamber, magnetic field and TOF. But there is the problem of the auto-absorption in the source, that makes difficult to use large source masses, and the energy resolution is poor (order of 10%) limited by the fluctuation of the energy deposed by the electrons in the source itself.

The exploration of different techniques and several sources is mandatory to reduce the experimental systematic in the results.

1.4.1.1. The experimental sensitivity to $m_{\beta\beta}$

In order to compare the different experiments, it is useful to provide an analytical expression for the half-life to which an experiment investigating a certain nucleus with a given level of background is sensitive. The sensitivity to the lifetime, $S_{0\nu}$, can be defined as the lifetime corresponding to the minimum detectable number of particles over the background at a certain confidence level. It can be derived from the radioactive decay law:

$$N(t) \sim N_0 \cdot \left(1 - \ln 2 \cdot \frac{t}{T_{1/2}^{0\nu}}\right)$$

1-27

where N_0 is the number of nuclei at t=0 and $T^{0\nu}{}_{1/2} \ll t$ (as confirmed from the present limits on 0νββ life-times –see Table 1-2). From this, the number of 0νββ decays expected in the measuring time t, $N_{\beta\beta}$, becomes:

$$N_{\beta\beta} = \frac{M \cdot N_A \cdot a}{W} \cdot \ln 2 \cdot \frac{t}{T_{1/2}^{0\nu}} \cdot \varepsilon$$

1-28

where M is the source mass, N_A is the Avogadro number, a is the isotopic abundance of the parent nuclide, W is the molecular weight of the source, ε the detector efficiency.

If no decays are observed in the measuring time, $N_{\beta\beta}$ is the background fluctuation in the energy region under investigation, and $T^{0\nu}{}_{1/2}$ expresses the limit on the decay half-life.

To detect $N_{\beta\beta}$ in an energy window ΔE corresponding to the energy resolution of the detector, the presence of radioactive background must be considered. The number of background events B in a time t and in an interval equal to the energy resolution ΔE, centred at the Q-value of the decay, is given by:

$$B = b \cdot M \cdot t \cdot \Delta E,$$

1-29

where b is the background rate measured in counts/(kg·keV·y) and M is again the source mass. In this case, it has been assumed that the background under the 0νββ-peak is independently measured and is approximately constant. In case that ΔE is very large, this approximation is less valid because events from 2νββ decay can enter the interval ΔE. Moreover, the number of background events, considered as scaling with the source mass, will follow a Poissonian distribution.

The minimum number of events that are needed to reach a certain significance of the peak (a certain C.L.) is given by the probability that the fluctuation of background events is equal to the peak:

$$N_{\beta\beta} = n_\sigma \cdot \sqrt{B}$$

1-30

Here n_σ is the number of standard deviations corresponding to a given Confidence Level (for example, a C.L. of 99.73% corresponds to n_σ=3).

Inserting Eq. 1-28 and Eq. 1-29 in Eq. 1-30, one obtains the sensitivity of an experiment with non-zero background rate:

$$S_{0\nu} = \frac{4.174 \times 10^{26}}{n_\sigma} \cdot \left(\frac{a}{W}\right) \sqrt{\frac{M \cdot t}{b \cdot \Delta E}} \cdot \varepsilon_{\Delta E}$$

1-31

The lifetime sensitivity can be translated into the neutrino mass sensitivity; using the 0νββ decay rate expression in case of mass mechanism (Equation 1-24) together with the lifetime sensitivity, one gets:

$$S(m_{\beta\beta}) \propto \frac{1}{G_{0\nu}^{1/2} |M_{0\nu}|} \cdot \left(\frac{b \cdot \Delta E}{M \cdot T}\right)^{1/4}.$$

1-32

From Eq. 1-32 it is clear that the most relevant factor that influences the sensitivity on the effective Majorana mass is the nuclide choice, being the set-up parameters under a forth root.

The isotope selection should be driven by several considerations. First of all the Q-value, i.e. the decay's transition energy, considering that the space phase factor, $G_{0\nu}$, depends on Q^5; the higher the Q-value assures a bigger the probability for the decay to occur, but also that the 0νββ-peak will be far from the natural-radioactivity region, that ends with the 2.6 MeV γ-peak of ^{208}Tl from the ^{232}Th decay chain. Above this energy there are only extremely rare high energy γ from ^{214}Bi.

Also the nuclear dynamics, expressed by the nuclear matrix element, is relevant: even if the spread of the $M_{0\nu}$ for different candidates is not wide, for some nuclei the disagreement among the various theories is bigger, while for other there is no more than one calculation.

Usually, to deal with these aspects, the nuclear factor of merit, F_N, is introduced, defined as the product of the squared modulus of the nuclear matrix element and the phase space factor of the decay:

$$F_N = G_{0\nu} \cdot |M_{0\nu}|^2 \qquad 1\text{-}33$$

A list of some 0νββ candidate with the corresponding Q-value is depicted in Figure 1-9, while the corresponding nuclear matrix elements and phase-space factors are collected in Figure 1-7 and Figure 1-8.

To understand the importance of having a high isotopic abundance let's consider an experiment, running for 1 year, whose detectors have energy resolution ΔE=10 keV, efficiency ε=1 and an overall background level of 1 count/(keV·kg·yr): the minimum number of candidate nuclei required to this experiment for detecting half-lives higher than 10^{26} years is $5 \cdot 10^{27}$. This means that natural isotopic abundances of a few per cent are not enough for this purpose.

The problem can be overcome by the isotopic enrichment, but it is to be considered that it is a complex and expensive procedure that can also introduce radioactive contaminants in the detector. Figure 1-10 shows the isotopic abundance of some nuclei candidates to 0νββ decay. All the isotopic abundances are similar, with the exception of the one of Te, that is very high.

Of course, selecting a certain isotope fixes (or limit) the type of detector to be used in the experiment: not all the material, for example, can become a bolometer (see Table 1-3).

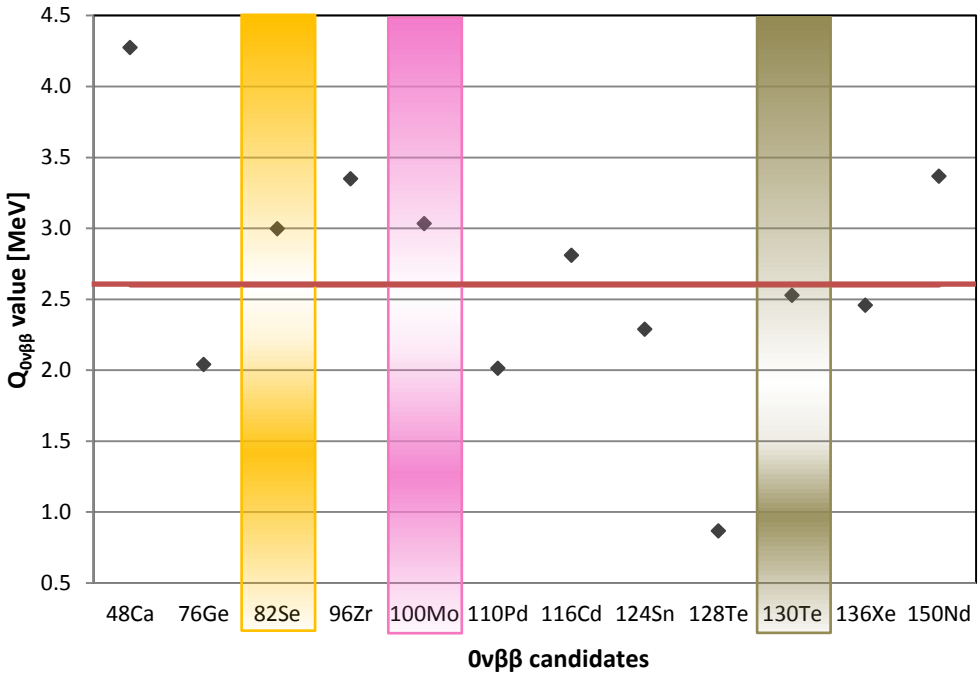

Figure 1-9. Q-values of some candidate nuclei to 0νββ (69), (70). The three coloured bands highlight the isotopes relevant in this PhD work. As a reference, the red line denotes the 2.6 MeV γ-peak of ^{208}Tl, corresponding to the end-point of natural radioactivity.

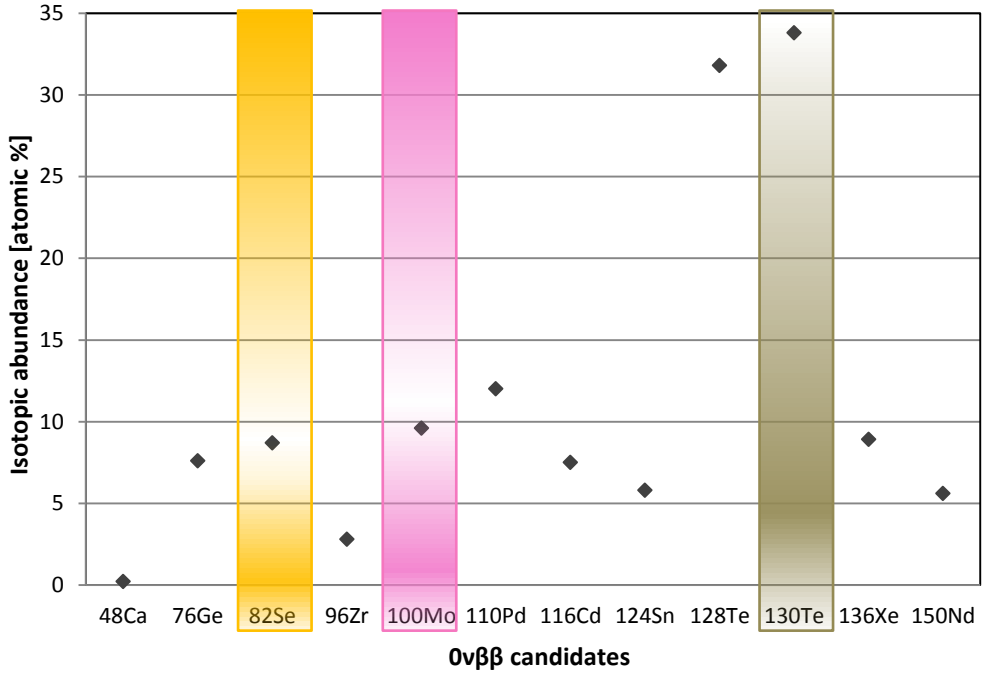

Figure 1-10. The isotopic abundance of some nuclei candidate to 0νββ (71), (72). The three coloured bands highlight the isotopes relevant in this PhD work.

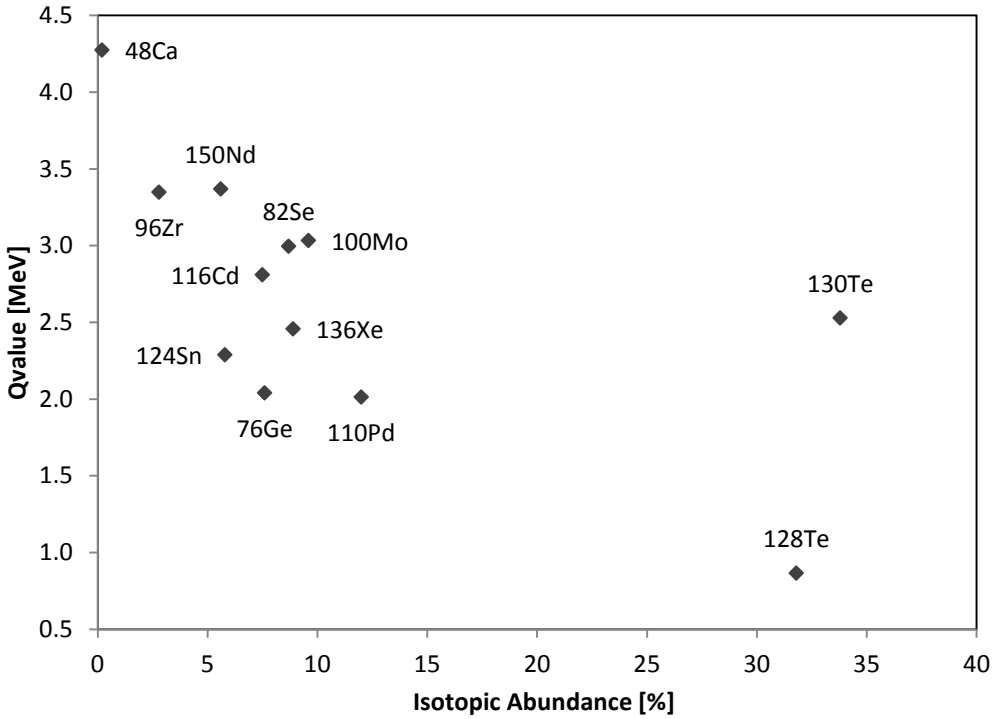

Figure 1-11. Q-value versus isotopic abundance for some 0νββ candidate nuclides.

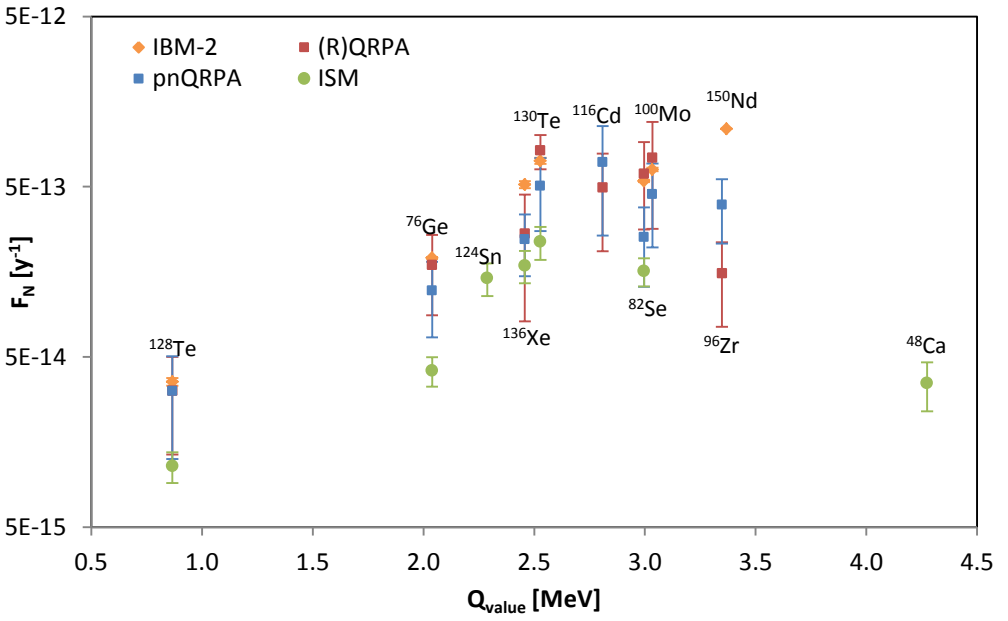

Figure 1-12. Nuclear form factors (defined by Eq. 1-33) for some 0νββ candidates. As in the NME plot (Figure 1-7), the central mark of each F_N range indicates the mean of the maximum and minimum values of the range, and is intended solely to guide the eye. The error bars show the full extent of each range. The reference used for the calculation are: IBM-2: (61) ($M_{0\nu}$), and (66), (67) ($G_{0\nu}$); (R)QRPA: (58) ($M_{0\nu}$) and (64), (65) ($G_{0\nu}$); pnQRPA: (59) ($M_{0\nu}$) and (66), deduced from $T_{1/2}$ in (59) ($G_{0\nu}$) ISM: (60) ($M_{0\nu}$) and (66) ($G_{0\nu}$). For details see the caption of Figure 1-7 and Figure 1-8.

Candidate nuclide	Materials successfully tested as bolometers
$^{48}Ca \rightarrow {}^{48}Ti$	**CaF_2, $CaMoO_4$**
$^{76}Ge \rightarrow {}^{76}Se$	Ge
$^{82}Se \rightarrow {}^{82}Kr$	**ZnSe**
$^{96}Zr \rightarrow {}^{100}Mo$	ZrO_2
$^{100}Mo \rightarrow {}^{100}Ru$	**$PbMoO_4$, $CaMoO_4$, $SrMoO_4$, $CdMoO_4$, $ZnMoO_4$,** Li_2MoO_4, $MgMoO_4$,
$^{116}Cd \rightarrow {}^{116}Sn$	**$CdWO_4$, $CdMoO_4$**
$^{130}Te \rightarrow {}^{130}Xe$	TeO_2
$^{136}Xe \rightarrow {}^{136}Ba$	---
$^{150}Nd \rightarrow {}^{150}Sm$	---

Table 1-3. Successfully tested bolometric materials for DBD search; the compounds written in bald are good scintillators at low temperatures.

Despite all these considerations, what emerges confronting the characteristic of different 0νββ candidates is that there is no a "best-isotope", having all same pros and cons: for example ^{48}Ca has a high Q-value but a low isotopic abundance, and so on. Figure 1-11 and Figure 1-12 empathize this concept, showing both isotopic abundance and the nuclear factor F_N versus the Q-value of some 0νββ candidates. Except for few nuclei, the isotopes are concentrated in a small area in both graphs. This allows exploring several sources and using different techniques, enlarging the 0νββ experimental scenario.

1.4.2. 0νββ: state of the art

The present 0νββ search is dominated by three recently concluded experiments: Heidelberg-Moscow, NEMO3 and Cuoricino.

These projects are different in the source investigated and in the detecting technique, but have some comparable elements, such as the measuring time and the total mass of the source, and explored the same region of the possible neutrino mass patterns. In the next sub-sections their features and results will be briefly presented.

1.4.2.1. The Heidelberg-Moscow experiment

The Heidelberg-Moscow (HM) experiment (73), running in the Nineties and now over, belong to the calorimetric technique, investigating the 0νββ of ^{76}Ge in ^{76}Se by meaning of five

high-purity Ge-diodes enriched at 86% in ^{76}Ge, with an active mass of 10.96 kg corresponding to a source strength of 7.6×10^{25} ^{76}Ge nuclei.

The detectors operated in the underground site of Laboratori Nazionali del Gran Sasso (LNGS), Italy, with an high energy resolution, typically 4 keV FWHM, achieving very low background level (0.17 counts/(keV·kg·y) around Q-value) that has been further improved by a factor 5 using Pulse Shape Discrimination (PSD) techniques for rejecting events in coincidence among different diodes. With a statistics of 35.5 kg·y in ^{76}Ge, the limits on the half-life and on the effective Majorana mass are $T^{0\nu}_{1/2}$ <1.9×10^{25} y and $m_{\beta\beta}$ <0.3-0.6 eV (depending on the nuclear matrix elements chosen for the analysis) respectively.

However in 2001 few members of the HM collaboration claimed evidence of a 0νββ-peak (74) that nowadays gives $T^{0\nu}_{1/2}=2.23^{+0.44}_{-0.31}\cdot10^{25}$ y at 6σ; this would translate in $m_{\beta\beta}$=(0.32±0.03) eV (75), (76), (77), (78), (79), (80). The energy spectrum is reported in Figure 1-13. Of course the claim raised scepticism in the Double Beta Decay community, including a large part of the HM collaboration itself (81), (82), (83), (84), (85), mostly due to the fact that the identification of the background in the region of the peak is not clear. Because the HM experiment is now over, a definitive word about the claim will be given only by the very sensitive next generation 0νββ projects: in particular, the first phase of the GERDA experiment (86), whose data taking on ^{76}Ge has recently begun, will be able to verify the claim.

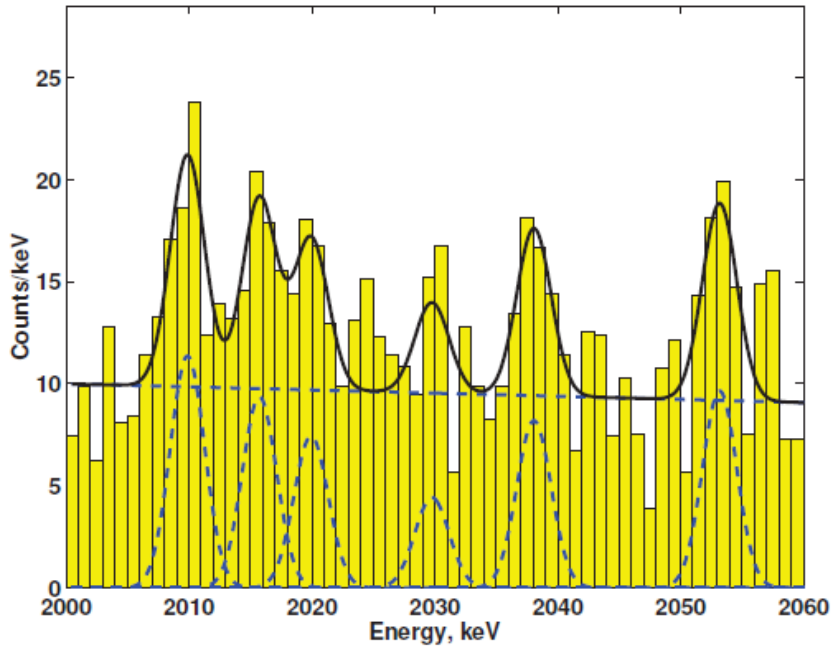

Figure 1-13. Energy spectrum measured by the Heidelberg-Moscow experiment in the $Q_{\beta\beta}{}^{0\nu}$ region (78).

1.4.2.2. The NEMO-3 experiment

The Neutrino Ettore Majorana Observatory (NEMO-3) (87), concluded in January 2011 after effective 5 years of data collection (88), was the most sensitive DBD experiment belonging to the external source technique.

The set-up, installed underground in the Laboratoire Souterrain de Modane (France), is divided in twenty sectors, allowing the study of many nuclides at the same time, such as ^{100}Mo, ^{82}Se, ^{150}Nd, ^{116}Cd, ^{130}Te, ^{96}Zr, ^{48}Ca.

The experiment is based on the direct detection of the two electrons emitted in the decay that cross a magnetised tracking volume made of Geiger counter cells and release their energy in a calorimeter based on plastic scintillator.

In this way, in addition to the two-electron sum peak, the experiment can reconstruct the two-electron angular distribution and the energy spectrum of the single electron, becoming sensitive also to the mechanism driving the 0νββ decay (57). The energy resolution ranges from 11% to 14.5%.

The best efforts have been made on ^{100}Mo and ^{82}Se nuclei, resulting in the presently most precise values on their 2νββ half-lives (see Table 1-2, central column) and providing also lower limits on their 0νββ half-lives (see Table 1-2, right column), corresponding to a lower limit on the effective Majorana mass of 0.8–1.3 eV and 1.4–2.2 eV respectively, according to the nuclear matrix element used (89).

An example of the energy sum spectrum of the two electrons, of the angular distribution of the two electrons, and of the single energy spectrum of the electrons for the ^{100}Mo is displayed in Figure 1-14.

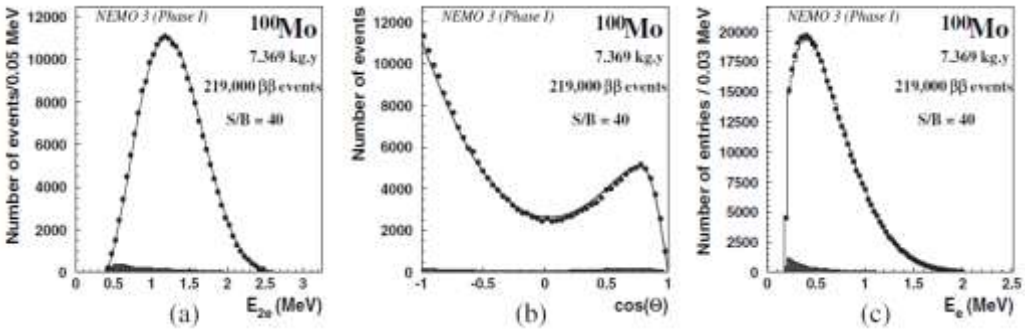

Figure 1-14. (a) Energy sum spectrum of the two electrons, (b) angular distribution of the two electrons, and (c) single energy spectrum of the electrons, after background subtraction from ^{100}Mo with 7.369 kg·yr exposure. The solid line corresponds to the expected spectrum from 2νββ simulations and the shaded histogram is the subtracted background computed by Monte Carlo simulations. The signal contains 219 000 ββ events and the signal-to-background ratio is 40 (90).

1.4.2.3. The Cuoricino experiment

In the underground site of LNGS, from 2003 to summer 2008, the Cuoricino detector (91) searched for the 0νββ decay of ^{130}Te using the bolometric technique, providing one of the best present limit on $m_{\beta\beta}$ and prepared the way for one of the most promising next-generation 0νββ searches: the CUORE experiment, that constitutes the framework of this PhD thesis. For this reason in this section just a brief description of the Cuoricino detector and the bolometric technique will be given, and then these subject will be detailed in Chapter 2 and Chapter 3.

The operating principle of a bolometer is very simple: the energy deposited in the detector by a nuclear event is measured by recording the temperature increase of the detector as a whole. In order to make this extremely small heating appreciable and to reduce all the intrinsic noise sources, the detector must be operated at very low temperatures, of the order of 10 mK for large masses. In the Cuoricino detector the absorber is a TeO_2 crystal and the thermal pulses are read by Neutron Transmutation Doped Ge thermistors.

The Cuoricino array (Figure 1-15) is a tower made of 62 TeO_2 bolometers arranged in thirteen floors, for a total detector mass of ~41 kg, corresponding to a source strength of 5.0×10^{25} ^{130}Te nuclei. The mechanical structure of tower is made of OFHC copper, to which bolometers are connected by means of PTFE holders. The detector was cooled down in a dilution refrigerator to a temperature of ~8 mK.

Figure 1-15. The thirteen floors of the Cuoricino tower. Eleven floors are made with four bolometers whose absorber size is 5x5x5cm^3, while the remaining two are composed by six 3x3x6cm^3 detectors. Among these small crystals, two have been enriched at 82% in ^{130}Te and other two at 75% in ^{128}Te.

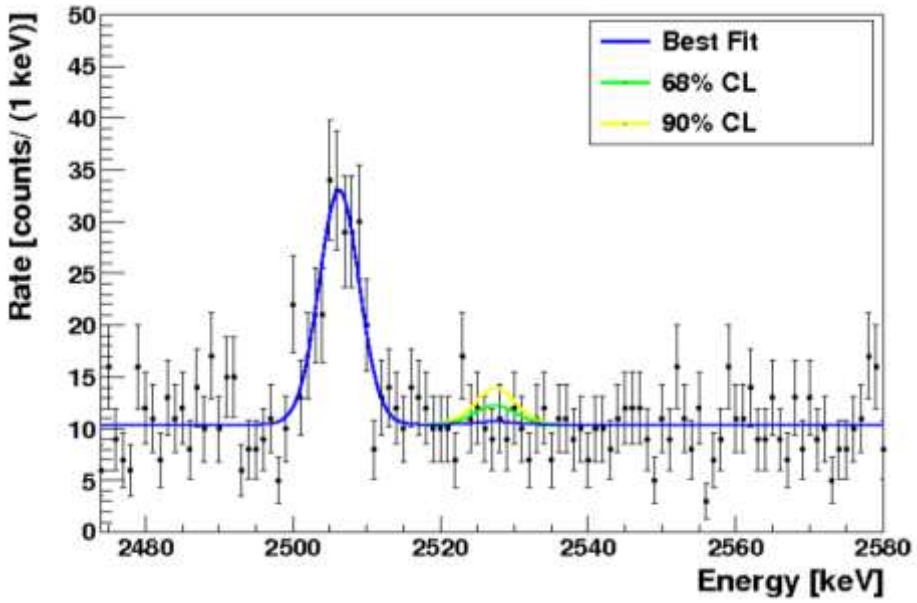

Figure 1-16. Best fit, 68% and 90% confidence intervals for the total statistics superimposed on the Cuoricino sum spectrum in the 0νββ region (50).

A very low background, of the order of 0.18 counts/(keV·kg·y) was obtained in the 0νββ decay region and the energy resolution is about 8 keV FWHM, quite reproducible in all the crystals. The spectrum collected in the Double Beta Decay region is shown in Figure 1-16.

The obtained limit on the ^{130}Te half-life is $T^{0\nu}_{½} < 2.8 \cdot 10^{24}$ y, corresponding to a sensitivity on the effective Majorana mass of 0.3-0.7 eV (50), depending on the adopted nuclear matrix element.

Despite its sensitivity comparable to the one of the HM experiment, Cuoricino cannot disprove the ^{76}Ge claim due to the discrepancies in the nuclear matrix element calculations. This can be seen inserting the nuclear factor of merit, F_N, defined by Eq 1-33, in the expression of the effective Majorana mass (Eq. 1-24). This will give:

$$m_{\beta\beta} = \frac{1}{\sqrt{T^{0\nu}_{1/2} \cdot F_N}},$$

1-34

that allows comparing Ge results with the Te results without any dependence on $m_{\beta\beta}$:

$$T^{0\nu}_{1/2}\left(^{130}Te\right) = T^{0\nu}_{1/2}\left(^{76}Ge\right) \cdot \frac{F_N\left(^{76}Ge\right)}{F_N\left(^{130}Te\right)}.$$

1-35

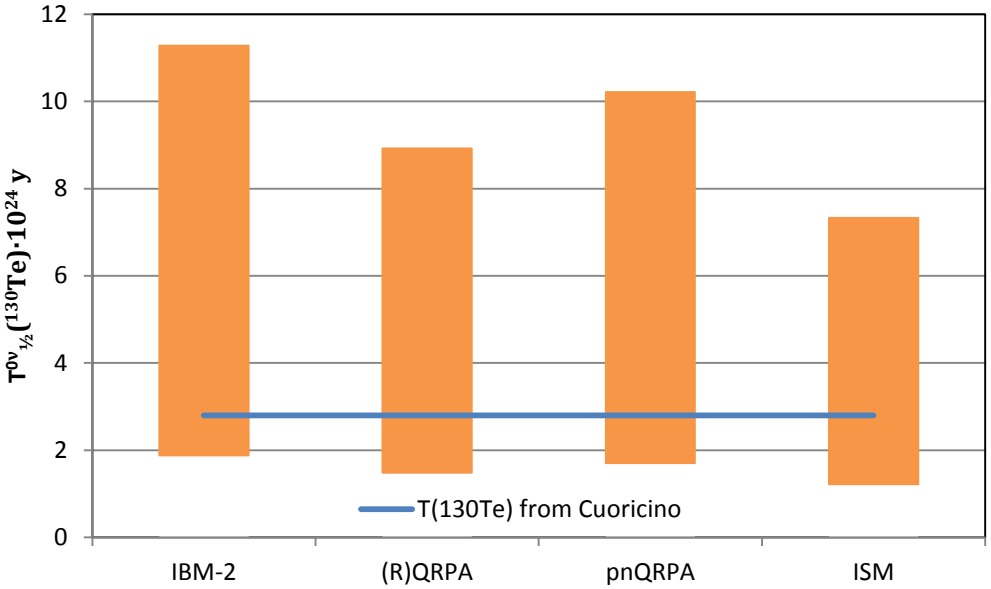

Figure 1-17. Comparison between the Cuoricino limit on ^{130}Te $T^{0\nu}_{1/2}$ and the ^{76}Ge claim from the HM experiment claim expressed in terms of $T^{0\nu}_{1/2}$ (^{130}Te) as stated from Eq. 1-35. The orange horizontal line represents the Cuoricino limit where the blue columns are the range of the limit of the ^{130}Te obtained from the ^{76}Ge claim by using nuclear factor taken from IBM-2, (R)QRPA, pnQRPA and ISM nuclear matrix element calculation (see Figure 1-12 for the details of the F_N calculation and references).

This confrontation results in different intervals, according to the nuclear matrix element chosen for the calculation of the nuclear factor. Figure 1-17 shows the bands corresponding to the ^{76}Ge claim translated into the Cuoricino results according to four most quoted nuclear matrix calculations. As can be easily seen, the present Cuoricino limit is well inside these intervals, but cannot exclude them in any nuclear model.

Chapter 2.
BOLOMETRICALLY SEEKING NEUTRINOLESS DOUBLE BETA DECAY

We're lost. Unless you've got something that can smell neutrinos.[7]

In the previous Chapter the current results on 0νββ search have been described, showing how presently the experiments are just investigating the quasi-degenerate hierarchy of neutrino mass (see Figure 2-1), being their sensitivity to the effective Majorana mass around 500 meV. Now the 0νββ community is addressing its efforts to reach the inverted hierarchy region and this means improving the sensitivity of at least one order of magnitude. To understand the efforts required to reach this target, the characteristics of an experiment that should be improved to enhance the discovery potential of a detector will be presented in this Chapter. In particular the attention will be focused on the Cuoricino experiment and its bolometers, being the optimisation of these detectors towards the CUORE and LUCIFER experiments the main subject of this dissertation. Therefore a detailed description of bolometers and their operation will be discussed here.

2.1. The next-generation 0νββ experiments

To reach the inverted hierarchy region, the sensitivity should be improved by one order of magnitude, i.e. $S(m_{\beta\beta})$ ~50 meV while $S(m_{\beta\beta})$ ~10 meV is needed to exclude it. Exploring the direct hierarchy region requires to gain at least one order of magnitude more in the sensitivity.

From Eq. 1-31 and Eq. 1-32 it is evident that, fixed the 0νββ candidate (possibly with a high Q-value, as discussed in Section 1.4.1.1), the half-life sensitivity can be improved by acting on the source mass (M), the measuring time (t), the energy resolution (ΔE), the background level (b) and, eventually, if not already exploited, the isotopic abundance (a).

[7] (228).

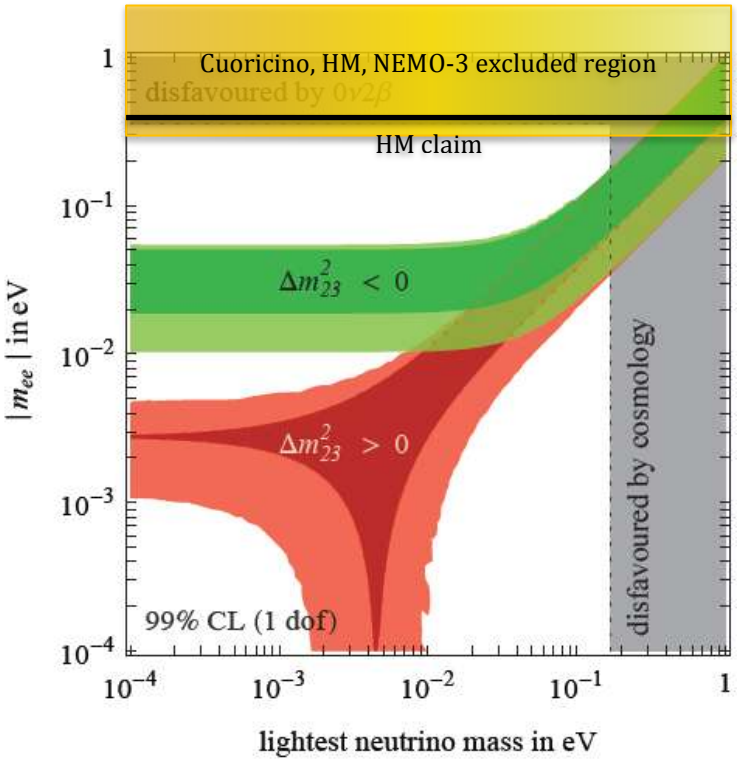

Figure 2-1. The status of the actual 0νββ searches in terms of explored neutrino mass hierarchy regions. Being the present experimental sensitivity to the effective Majorana mass about 500 meV, only the Quasi-Degenerate hierarchy region has been probed, as shown by the yellow band. The black line denotes the central value of the HM claim.

Among them, the less influent is the measuring time. As can be seen by the following comparisons:

$$\frac{S_{0\nu}(4\ year)}{S_{0\nu}(1\ year)} \cong 2 \qquad \text{and} \qquad \frac{S_{0\nu}(20\ year)}{S_{0\nu}(5\ year)} \cong 2, \tag{2-1}$$

after an initial improvement thanks to few years of data taking, gaining another factor two in the sensitivity requires a detector live-time of 20 years, hardly reachable by the experiments.

The present 0νββ sources have masses of some tenth of kg. To have a sensible improvement in the sensitivity the source mass should increase of one order of magnitude:

$$\frac{S_{0\nu}(500\ \text{kg})}{S_{0\nu}(50\ \text{kg})} \cong 3. \tag{2-2}$$

This enlargement is difficult in particular for the external-source experiments, because of the possibility of self-absorption in the source, but in general it is an expensive and complicated solution; another possibility, instead of having a bigger source is to use an enriched source, even if also this opportunity is complex.

Nevertheless this effort is mandatory: considering only candidate nuclei with high Q-value (as the ones in Figure 1-9), approaching the inverted hierarchy region means searching for 1-10 counts/(y·ton), while fully covering it means to be sensitive to 0.1-1 counts/(y·ton), fixing the size of the future experiments from hundreds of kg to 1 ton of isotope.

This imposes also severe constraints on the background level, b, that should be close to 0 for the entire live-time of the experiment. For searches with ΔE(FWHM) ~1 keV this requirement translate in to b ~1 counts/(keV·y·ton), while the target is even more ambitious for experiments with worse energy resolution, where however the most critical role is played by 2νββ decay.

There are various sources that give rise to these spurious counts such as environmental β and γ radioactivity, cosmic rays, neutrons, radon and contamination of the materials composing the detectors and their shielding.

The γ background, coming from natural contaminations in ^{238}U and ^{232}Th of the materials that surround the detectors can be easily avoided thanks to the choice of a high Q-value isotope as a 0νββ source. The case of ^{238}U and ^{232}Th internal contaminations has to be dealt with more carefully, in particular for non-homogeneous (or passive) detectors, while, under certain assumptions, it does not play a significant role for homogeneous detectors (Ge-diodes and bolometers): α decays, in fact, will produce the full energy peak, well above the most interesting $Q_{\beta\beta}$ values, while all the β–γ events of these two radioactive chains (except the contribution of ^{234} Pa from the ^{238}U chain) can be recognized through coincidences with the α emission that precedes (or follows) them (see Figure 2-2).

The cosmic ray contribution to background can be reduced by conducting the 0νββ deep underground, where the only surviving cosmic-ray particles are the muons, that can produce high energy neutrons, bremsstrahlung γ-rays and electromagnetic showers. A muon veto can help in controlling this background component.

The best known cosmogenic isotope is ^{60}Co, which is a common contaminant in Copper, the material commonly used in shielding 0νββ experiments because it is the cleanest solid material available (92). Because its high production rates at the Earth surface and its long half-life (5.3 y) ^{60}Co is able to remain in the apparatus and potentially create background after the materials have been placed underground. These backgrounds can be

mitigated by purifying the radioactive isotope from the host material and then minimizing its exposure above ground.

Low energy neutrons produced by environmental radioactivity can induce (n,γ) reactions, that leads to radioactive nuclei, in materials close to or inside the detectors with gamma energies up to 10 MeV; furthermore, high energy neutrons generated by μ-induced spallation reactions can release several MeV by direct interaction in the detectors.

The so called "surface contamination" background plays a role in almost all detectors, but it is in particular crucial for fully active detectors, as in the case of bolometers; it is composed by the α particles, emitted from radioactive nucleus located within few μm of a surface facing the detector, that lose part, or even all, of their energy in the few microns of this dead layer before reaching the detector.

The resulting energy spectrum will be a continuum between 0 and 4–8 MeV (the common α energy), covering, unfortunately all the possible $Q_{\beta\beta}$ values. Furthermore, the same mechanism holds in the case of surface contaminations on the detector itself. This α-induced background represents the main source of background for the Cuoricino experiment. These surface contaminations are usually one order of magnitude smaller (93) with respect to the sensitivity available with the best commercial detectors (namely High purity Silicon Barrier Detectors), making impossible their measurement.

All of these background sources must be considered when selecting the detector materials and technology in order the experiment will be able to test the inverted hierarchy region of neutrino masses, together with the fact that this technology should deal with about one ton of source.

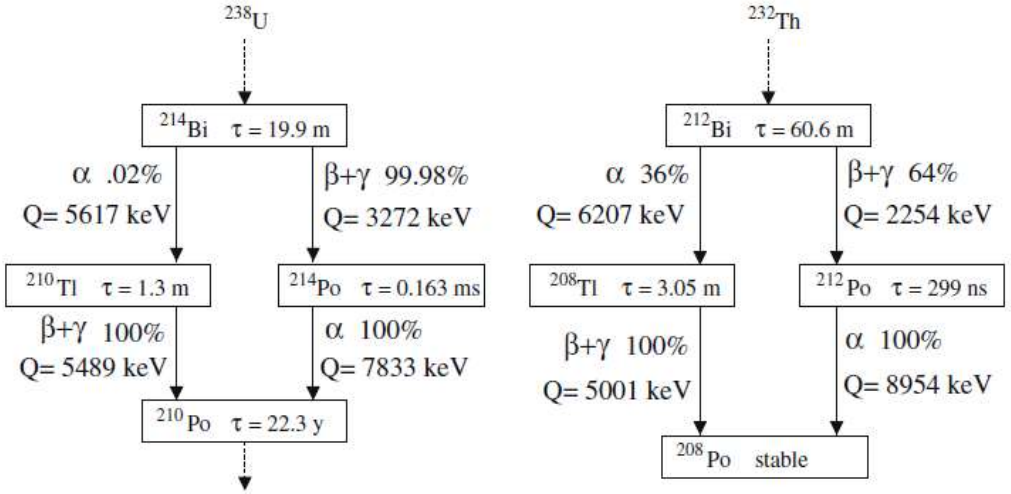

Figure 2-2. High energy β-γ decays of the ^{238}U and ^{232}Th chains preceded (or followed) by an α emission. Using delayed α coincidences, β-γ decays can be identified (94).

Experiment	Isotope	Technique	ΔE [% at Q_{val}]		Bkg rate [c/(keV·kg·y)]	Mass [kg]
CUORE (95), (96), (97)	^{130}Te	Bolometers	0.18	R	$4 \cdot 10^{-2}$	200
				O	$1 \cdot 10^{-3}$	400
EXO (98), (99), (100), (101)	^{136}Xe	Liquid Xe	3.3	R	$1 \cdot 10^{-3}$	160
				O	$5 \cdot 10^{-4}$	1000
GERDA (102), (103), (104), (105)	^{76}Ge	Ge-diodes	0.16	R	$1 \cdot 10^{-2}$	35
				O	$1 \cdot 10^{-3}$	100
KamLAND-Zen (106), (107)	^{136}Xe	Liquid Scint	9.5	R	$5 \cdot 10^{-4}$	360
				O	$1 \cdot 10^{-4}$	1000
NEXT-100 (108), (109)	^{136}Xe	TPC	0.7	R	$2 \cdot 10^{-4}$	90
				O	$6 \cdot 10^{-5}$	1000
SNO+ (110), (111), (112)	^{150}Nd	Liquid Scint	6.5	R	$1 \cdot 10^{-3}$	50
				O	$5 \cdot 10^{-4}$	500
SuperNEMO (113), (114), (115)	^{82}Se	Tracko-calo	4.0	R	$4 \cdot 10^{-4}$	25
				O	$6 \cdot 10^{-5}$	100

Table 2-1. Several proposed next generation 0νββ experiments: for each proposal, the isotope that will be used, together with estimates for detector performance parameters (FWHM energy resolution, detection efficiency and background rate per unit of energy, time and 0νββ isotope mass) are given. The background estimates and the 0νββ source mass include both a reference ® and an optimistic (O) scenario (116).

Among the several next-generation proposed or under-construction experiments (see Table 2-1), the CUORE project is one of the most sensitive (116). It is the natural prosecutor of the Cuoricino experiment, with a mass twenty times greater and a target level of background two orders of magnitude lower. The details of the experiment, being the main framework in which this PhD works has been done, will be discussed in Chapter 3. In particular the great efforts that have been carried on in the material selection will be presented in Chapter 5.

Further improvements in the background rate would require, probably, active suppression methods such as the scintillating bolometers, a very promising development of the calorimetric approach. The simultaneous detection of heat and scintillation light for the same event allows rejecting α-particles with 100% efficiency, since the ratio between the photon and phonon yield is different for α than for β and γ interactions. Such technique, actually carried on by the LUCIFER project, may permit a reduction of the background rate down to 10^{-3} counts/(keV·kg·y) or better and will be discussed in Chapter 7.

Both the CUORE and LUCIFER experiments are based on the bolometric technique, which has been briefly presented in the discussion about the Cuoricino detector. In order to understand the efforts and the improvements needed to go toward the CUORE experiment, that aims to explore the inverted mass pattern of neutrino masses with the same typology of detector, and the innovation introduced by the LUCIFER experiment, a detailed description of bolometers and their operation will be presented in the next Section.

2.2. Bolometers

The use of Low Temperature Detectors (LTD) in the field of nuclear physics research and radioactivity measurements was proposed in 1934 by F.E. Simon (117), while the first detection of an alpha particle with such as device happened fifteen years later, thanks to the work made by Andrews and his collaborators (118). But other thirty years have to pass for the use of bolometric technique in the search of DBD to be proposed by E. Fiorini and T.O. Niinikoski in 1984 (119). The high energy resolution, combined to the versatility in the choice of materials, make bolometers extremely suitable in the field of $0\nu\beta\beta$ search.

The bolometric technique can be considered young, with only twenty-six years of activity in fundamental physics research; its potentialities have not been fully explored yet, and there is room for the improvement of current performances. In particular the development from the Cuoricino to the CUORE bolometers will be treated in Chapter 3

Bolometers are low temperature detectors (LTD) made of an absorber, where the particle energy is released, producing excitations, and a sensor that converts them into a signal. Here in particular devices are considered in which the particle detection is mediated by phonons, the quasiparticles associated to crystal lattice vibrations (and therefore called Phonon Mediate Detectors, PMDs). Because the energy of such as excitations is very low («10 meV), these detectors must operate at very low temperature (10-100 mK), for preventing the thermal generation of phonons that cud mimic or hide a real particle signal.

A PMD is a very efficient device if considered that almost all the energy deposed in a detector is converted in phonons. For example, let's consider a 1 keV electron deposing all its energy in a detector: in case of a semiconductor detector, only the 30% of the electron energy will produce ionization, while the remaining creates phonons; for a scintillator detector all the electron energy is converted in electron-hole pairs, but the efficiency in the light output production is 5-15%; if the electron is detected by hitting a nucleus, no more than 6% of its recoil energy will be create ionization.

Moreover, because the energy w needed for creating phonons is lower with respect to the energy for creating other signal mediators (such as ionization or electron-hole pairs), bolometers have excellent performances in particle detection. The number of mediators N created by a particle releasing energy E in the detector is:

$$N = \frac{E}{w}.$$

2-3

For example, in a scintillator detector w is about 100 eV, in case of gas detector, for the production of an electron-ion pair, w∼30 eV whereas in a solid state detector w ∼3 eV. Of course as lower is the minimum energy required for generating a mediator, as lower will be the minimum detectable energy released in the detector: that makes bolometers particularly suitable for low-energy particle detection.

Having a small w implies also having a better energy resolution, because, for the same energy release, a bigger amount of mediators is created, increasing the statistics associated to the single event. Assuming a Poisson statistics, for which the standard deviation for a measurement of N events is $\Delta N=\sqrt{N}$ (i.e. assuming that the intrinsic energy resolution is limited only by statistical fluctuation of the produced mediator number), the FWHM energy resolution ΔE, using Eq. 2-3, is given by:

$$\frac{\Delta E}{E} = 2.35\frac{\Delta N}{N} = 2.35\sqrt{\frac{Fw}{E}};$$

2-4

F is the Fano factor, generally lower than 1 (120), taking into account the deviation from the poissonian statistics.

The theoretical energy resolution of a bolometer is very high if compared to others kinds of detectors. For example, a 1 g Si bolometer operating at 20 mK will have ΔE <1 eV, i.e. two order of magnitude better of the best Si(Li) diode; or a 1 kg Ge bolometer at 10 mK could measure γ rays with ΔE ∼10 eV, i.e. two order of magnitude better of a Ge diode.

This thermodynamic limit can be reached by a real bolometer only if the statistical fluctuations due to others deposing energy mechanism (such as metastable electron-hole states) are minimized and there are no dominant contribution from the noise sources (see Section 2.5).

2.3. Ideal bolometer model

The first bolometers were proposed as perfect calorimeters, able to thermalize (i.e. to convert in heat) all the energy released in the absorber. This is an idealization of their behaviour, which is more complex, but it is enough to describe their main features as rare event detectors.

In a first approximation a bolometer made of an absorber, where the impinging particle transmits its energy to phonons, coupled to a sensor, which is sensitive to the resulting rise in temperature and converts it in another physical quantity, such as a current or a voltage signal, can be roughly modelled as a heat capacity C linked by means of a thermal conductance G to a heat bath at the constant temperature T_0 (Figure 2-3). This model is called monolithic because there is just one overall heat capacity C taking into account the contributions of both the absorber and the sensor. A more complex model will be presented in Section 0. The heat bath's capacity is considered as infinite.

If T(t) is temperature of the absorber at the time t, assuming $\Delta T=|T(t)-T_0| \ll T_0$ corresponds to state that C and G has no dependence on T. Therefore the temporal evolution of an energy E deposed in the absorber and instantaneously thermalized is:

$$\Delta T(t) = \frac{E}{C}\exp\left(-\frac{t}{\tau}\right), \qquad 2\text{-}5$$

where $\tau=C/G$ is the thermal relaxation time.

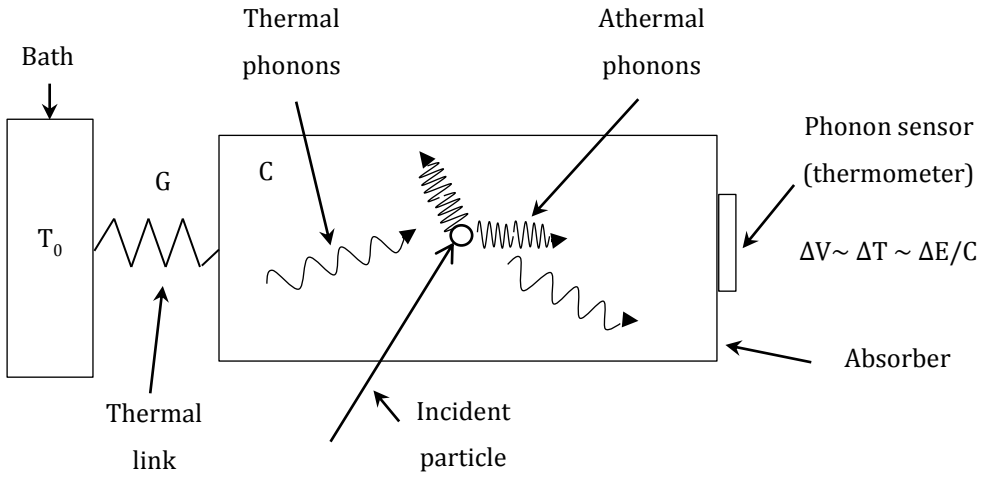

Figure 2-3. Schematic model of a bolometer.

According to the approximation, the maximum value of the temperature variation is:

$$T_{max} \propto \frac{E}{C}.$$

2-6

It follows that lower is the thermal capacity, higher will be the signal amplitude. For energy depositions in the keV-MeV range, appreciable signals with respect to statistical fluctuations can be obtained by working at very low temperature (10-100 mK). On the contrary, a release of 1 MeV energy in a 1 mole absorber at room temperature corresponds to a temperature variation of order of 10^{-15} K, impossible to be measured.

Heat capacity is also relevant for the thermal relaxation time τ and its reduction leads to fast signals. At the same time, however, τ should be long compared to the time scale of the transmission of the signal to the sensor, which is of order a few ms for the bolometers considered here: for this reason, bolometers cannot stand counting rates higher than Hz.

From this simple model is possible to see the important role played by the heat capacity in the definition of the detector energy resolution. Assuming that all the deposed energy is converted in phonons, the energy resolution is limited only by the fluctuations of thermal phonons exchanged with the bath trough the conductance G. If the average energy needed to create a phonon is $w = k_B T$, and using also Eq. 2-6, Eq. 2-3 becomes:

$$N = \frac{C(T)}{k_B}.$$

2-7

As a consequence, from Eq. 2-4, the energy resolution becomes:

$$\Delta E \cong \Delta N \cdot k_B T \cong \sqrt{k_B C(T) T^2}.$$

2-8

The first constraints on the design of a bolometric detector arise, hence, from the previous discussion: the operation at low temperatures and the selection of materials with low capacity are a must. Reminding that the monolithic model is a rough, introductive approximation, and that a more sophisticated picture is reserved to the final part of this same chapter, the constitutive elements of a bolometric detector will be presented in the next sections. The discussion will be general, and will be related to its specific application in the Cuoricino and CUORE experiments only in Chapter 3.

2.3.1. The Absorber

As previously introduced, the most relevant parameter of a bolometer it is the overall heat capacity that has to be small enough to obtain big and fast signals in response to an energy deposition. The specific heat c(T) of a crystal at low temperature can be expressed as a sum of two contributions:

$$c(T) = c_r(T) + c_e(T),$$

2-9

coming from the crystal lattice (c_r) and from the electrons (c_e). In dielectric diamagnetic materials only the lattice contribution is present and it is determined by the Debye law:

$$c_r(T) = \frac{12}{5}\pi^4 N_A k_B \left(\frac{T}{\Theta_D}\right)^3$$

2-10

where k_B is the Boltzmann constant, N_A the number of Avogadro and Θ_D is the Debye temperature that characterises each crystal. This law, valid for $T<\Theta_D$, can be translated into an expression for the heat capacity:

$$C(T) = \beta \frac{m}{M}\left(\frac{T}{\Theta_D}\right)^3.$$

2-11

Here β =1944 J/(K·mol), m is the absorber mass and M is its molecular weight.

For metals instead the specific heat at low temperature is dominated by the electronic contribution. For conducting materials, the conduction electrons behaviour is described by a Fermi gas, therefore:

$$c_e(T) = \frac{\pi^2}{\Theta_D} ZR \frac{T}{\Theta_F},$$

2-12

where Z, R e Θ_F are the number of conducting electron in the atom, the gas constant and the Fermi temperature respectively.

This contribution is different in case of superconductive materials at a temperature lower than their critical temperature, T_c. For them, in fact, it holds:

$$c_e(T) = K_s exp\left[-2\left(\frac{T_c}{T}\right)\right],$$

2-13

where K_s is a constant that depends on the material. However this contribution to the specific heat is negligible with respect to the lattice one when $T \ll T_c$.

Therefore the best materials for bolometer absorbers have to be selected among dielectric and diamagnetic crystals with high Debye temperature Θ_D or among superconductors with critical temperatures higher than the working temperature.

2.3.1.1. Phonon thermalization process

Thermal phonons are the final product of a long process that occurs after an energy release in the absorber and are the heat signal read by the phonon detector linked to the absorber. The process in which the energy transfer from the particle to the crystal occurs follows essentially two channels: the nuclear and the electronic ones (121).

In the nuclear channel, crystal lattice vibrations are produced by nuclear scattering; but also structural damaging of the lattice can result, in which part of the energy can be stored and therefore will not be converted into phonons, worsening the energy resolution of the detector.

In the electronic channel, the energy transfer occurs thanks to a sequence of scattering processes that slows down the incident particle in a distance from the interaction point ranging from μm to mm, according to the kind of particle (heavy or electrons). This produces many electron-hole pairs with a very high spatial density and energy, that start interacting with each other and spreading quickly in the crystal, until they reach a density similar to the one of the lattice impurities. At this point the charge carriers undergo scattering processes with the impurities, loosing energy until a quasi-equilibrium situation is reached and the carrier energy continue degrading via direct interaction with the crystal lattice, generating finally phonons. Also in this channel a fraction of the initial energy can be lost and therefore not converted into phonons. This is due mainly because of three mechanisms: radiative ricombinations of the electron-hole pairs with the escape of the emitted photons; non-radiative ricombinations taking too long time with respect to the signal formation; permanent trapping of electrons and holes in impurity sites or lattice defects. Nevertheless the fraction of energy transferred to the lattice is large and phonons are created through different mechanisms depending on the electron-hole pair density and on their energy.

A scheme of the global process for the phonon creation is depicted in Figure 2-4.

After the production, the phonons undergo different processes until they reach a thermal distribution (schematized in Figure 2-6). At the beginning phonons have high energy and low momentum on the optical branch and depart from the particle interaction region beginning a decreasing cascade of the phonon energy. According to energy and momentum conservation, in a very short time (10-100 ps) the optical phonons decay in two longitudinal acoustic phonons (LA) having half the energy of the initial phonon (of the order of the Debye energy) and opposite momentum (122), (123). Also the electron-hole recombination occurring at impurity levels contribute to this phonon population.

Therefore the final result is a phonon system, mainly LA with energy of the order of $h\nu_D$, where ν_D is the Debye cut-off frequency of the crystal, that then undergoes further energy-degradation via phonon-phonon interaction, producing transverse acoustic (TA) phonons, whose decay is forbidden by the momentum conservation law. Therefore other mechanisms should occur, able to degrade phonon energy and also to induce the conversion of the TA phonons, otherwise stable, in to LA phonons, so they can thermalize. These processes are scattering on impurities and reflection on crystal surfaces (see Figure 2-5).

After other decays phonons are able to cross the whole crystal without further decaying and are therefore called ballistic phonons, and can reach the crystal surface (124); here they will interact with the phonon sensor connected to the absorber generating athermal contribution to the signal. The ones that are not collected are reflected by surfaces and they finally thermalize.

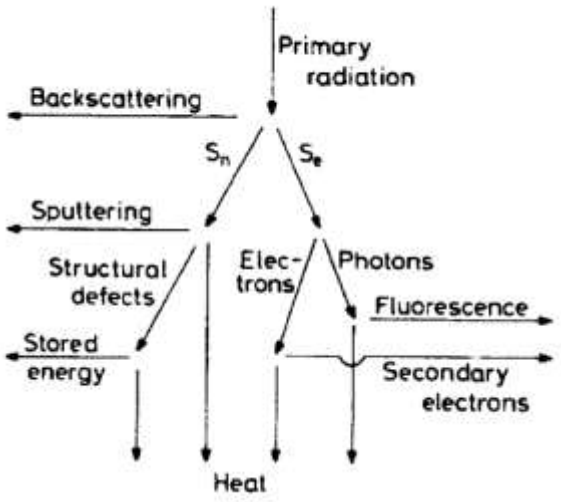

Figure 2-4. Simplified diagram of the energy flow due to incident radiation within an absorber. S_n is the nuclear channel while S_e is the electronic one. Only the energy appearing as heat at the bottom of the diagram will contribute to the phonon creation (125).

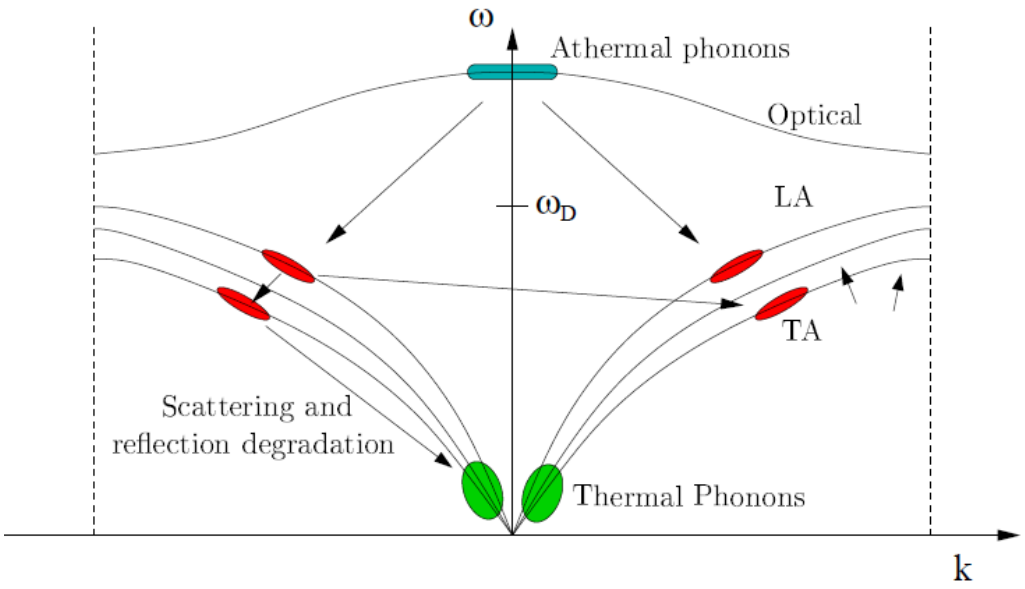

Figure 2-5. Model of the thermalisation process of phonons after their production in the absorber.

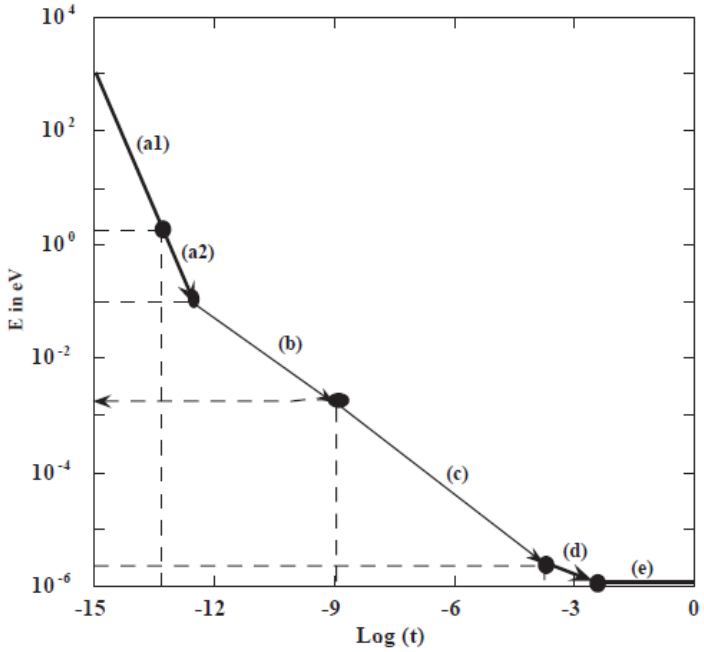

Figure 2-6. Typical average phonons energy versus time (a1) and (a2) recoil of electrons and nuclei with creation of electron–hole pairs and mostly high-energy optical and Debye phonons; (b) rapid decay of phonons by successive creation of lower energy pair of acoustic phonons, each process conserving both energy and momentum. At the end of (b), phonons propagate ballistically and reach the surface of the absorbing crystal; (c) interaction with the surface, creation of athermal signal, (d) rise of thermal signal; (e) is the return to equilibrium temperature (34).

2.3.1. Phonon Sensors

Because the energy release in the absorber results in both athermal and thermal phonons, two kind of phonon sensors can be conceived: ballistic phonon sensors, for detecting the phonons at their first interaction with the absorber surface, and thermal phonon sensors, with the aim of having a complete thermalization of the released energy in reasonable time.

Assuming the thermalization time to be finite, the development of the thermal signal in the sensor can be defined as:

$$\Delta T(t) = \frac{E}{C(T)} \frac{\tau}{\tau - \tau_H} \left[\exp\left(-\frac{t}{\tau}\right) - \exp\left(-\frac{t}{\tau_H}\right) \right], \qquad 2\text{-}14$$

where τ and τ_H are time constants accounting for the fact that the temperature increase is not instantaneous and depends on the constructive characteristics of the sensor.

According to the absorber dimensions (sub-millimetric or macroscopic) the decay times of these detectors correspond to the thermal relaxing time, which is of the order of msec or sec, respectively. Concerning the rise times, they are dominated by the speed of sound in the crystal in case of monolithic bolometers or by the heat propagation through the absorber-sensor interface for composite bolometers; therefore they range between 100 nsec and 10 μsec for the first case and 100 μsec - 10 msec for the second. It holds that the total time of the heat pulses is determined by the relaxing times and therefore that thermal detector can stand counting rates not higher than few Hz. Several types of devices able to detect thermal phonons exist, the most common being Semiconductor Thermistors (ST) and Transition Edge Sensors (TES). Because the firsts are the one used in the CUORE experiment, the description of the phonon sensors will be focused on them.

A thermistor is essentially a semiconductor whit a dopant concentration very close to the metal-insulator transition (MIT) resulting in a strong dependence of the conducibility on the temperature (therefore on the thermal phonons). Measuring its resistance corresponds to a temperature variation detection.

Semiconductors are covalent solids with the valence band completely full and the conduction band completely empty at the absolute zero. Their energy gap between the valence and conduction bands is no more than 2 eV. In an intrinsic semiconductor conduction can happen because of thermal excited electrons in the in the conduction band and to the corresponding number of holes in the valence band. It is possible only if the

activation energy is equal or larger than the energy gap, and it is possible for working temperature is very low with respect to room temperature, since $k_B T(300\ K) \sim 0.025$ eV. The fraction of intrinsic carrier (electrons or holes) in the (conduction or valence) band depends exponentially on the temperature:

$$n = p = \frac{\left(2\pi k_B T \sqrt{m_e m_h}\right)^{3/2}}{4(\pi h)^3} e^{-\frac{E_g(T)}{2k_B T}}.$$

2-15

Here k_B is the Boltzmann constant, m_e and m_h are the effective mass of electrons and holes, respectively, and Eg is the energy gap between conduction and valence band, that depends with the temperature according to:

$$E_g(T) = E_g(0) - \frac{\alpha T^2}{(T + \beta)},$$

2-16

where $E_g(0)$ is the energy gap value at 0 K and α, β two constants (126).

When the semiconductor is doped, the impurities introduce new energy levels just below the conduction band (in case of donor impurities) or just above the valence band (in case of acceptor impurities).

At low temperature (<10 K) the extrinsic carrier concentration dominates with respect to the intrinsic carrier concentration, therefore donor impurities introduce an n-type (or electronic) conductivity, while acceptors corresponds to a p-type (or hole) conductivity. The whole conductivity behaviour will depend on the difference between acceptor and donor impurity concentrations, i.e. the doping level, p-n.

Let's consider the case of an n-type doping: at room temperature almost all the dopant atoms are ionised and their "lost" electrons can reach the conduction band thanks to the energy received from the lattice vibrations. These electrons are therefore free to move around the crystal. On the contrary, at cryogenic temperature, the conduction band is almost empty, resulting in a reduced electric conducibility of the material.

A particular critical concentration of dopant does exist, beyond which a semiconductor shows a metallic behaviour whatever the temperature. This doping level denotes the so called Metal-Insulator Transition (MIT) (127) and corresponds to a concentration of donor atoms so that the wave functions of their outer electrons can overlap.

In this way the electrons are no more confined and a new conducting mechanism arises, apart from the passing in the valence band: the electrons can now jump from a donor site to another one (hopping mechanism) (128).

For this to happen, a certain level of compensation is required, i.e. a certain ratio between the acceptor and donor concentration (N_A and N_D respectively), defined by:

$$K = \frac{N_A}{N_D},$$

2-17

in order to have holes in correspondence of donor atoms and enhancing the electron mobility, determining the density of states near the Fermi energy.

If the doping level is just below the MIT dopant concentration, the conducting hopping mechanism is due to quantum-mechanical tunnelling through the potential barrier separating the dopant sites activated by phonon mediation (as sketched in Figure 2-7).

Essentially, two conducting regimes can be distinguished:

- ✓ short range hopping (SRH), in which the tunnelling hopping mechanism happens between two spatially close sites because the phonon-electron interaction and the presence of a free donor centre;
- ✓ variable range hopping (VRH), that dominates at very low temperature (<< 10 K) and is characterized by a hopping mechanism between two energetically close sites, if they are located in a narrow range around the Fermi energy: this implies that carriers can migrate also on far sites (129).

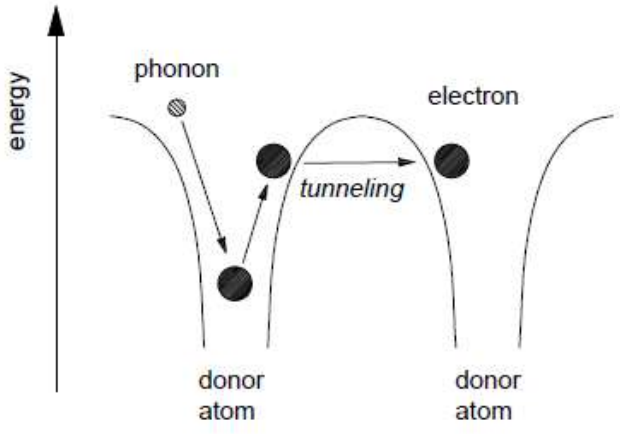

Figure 2-7. A scheme of the tunnelling hopping conduction mechanism in semiconductor mediated by phonon in case of doping slightly below the MIT concentration.

For both conducting regimes, the dependence of the resistivity ρ with the temperature is given by:

$$\rho(T) = \rho_0 \exp\left(\frac{T_0}{T}\right)^{\gamma},$$

2-18

where γ is ¼ in SRH and ½ in VRH; the latter corresponds to the formation of a gap in the density of the electron states near the Fermi energy because of the Coulombian repulsion among the electrons (130).

The CUORE temperature sensors are devices operating in the VRH regime, therefore Eq. 2-18 will occur several times in the following Chapters, especially in Chapter 3 and Chapter 4, and it will be referred as "VRH law", while the parameter R_0 and T_0, to be determined experimentally for each device, will be named "VRH parameters". The uniform doping, absolutely necessary for having all the devices operating in the same way, is achieved by using the Neutron Transmutation Doping (NTD) technique, as described in Section 3.3.1.1. In particular, for the CUORE thermistors, the expression of the resistance R(T) as a function of the resistivity is given by:

$$R(T) = \rho(T)\frac{l}{s} = \frac{\rho_0 l}{s}\exp\left(\frac{T_0}{T}\right)^{\gamma} = R_0 \exp\left(\frac{T_0}{T}\right)^{\gamma},$$

2-19

where $R_0=\rho_0 \cdot l/s$ and l, s are the distance between the electrical contacts and the thermistor section respectively.

The VRH does not describe entirely the thermistor behaviour. In fact at low temperature, for a reason not yet well understood, the thermal coupling between electrons and the lattice in the thermistor is weakened. A phenomenological model has been proposed, known as Hot Electron Model (HEM) (131) for explaining the non-linearity of the VRH conduction, thanks to the introduction of a thermal conductance, $G_{e\text{-}ph}$, between phonons and electrons. According to this model, the conducting electrons make a thermal system at a certain temperature T_e, connected to the phonon bath by $G_{e\text{-}ph}$, which is at the temperature T_{ph}. When a power P is injected into the system, T_e results larger than T_{ph}.

Because conduction electrons and phonons of the lattice form two separate systems connected by a finite thermal conductance, the thermistor resistivity will not depend on the lattice temperature, but only on T_e. This modifies Eq. 2-18 in:

$$\rho(T) = \rho_0 \exp\left(\frac{T_0}{T_e}\right)^{1/2}.$$

2-20

A parameter characterizing the thermistor performances is the sensitivity defined as:

$$A = \left|\frac{dlogR(T)}{dlogT}\right|,$$

2-21

that measures the ability of the sensor to convert small variation in temperature (fractions of mK) in appreciable resistance variations. Usually the sensitivity for a semiconductor thermistor ranges between 1 and 10 and, for the particular case of Eq. 2-19, it becomes:

$$A = \gamma\left(\frac{T_0}{T}\right)^{\gamma}.$$

2-22

When energy is deposed in the absorber, which has a temperature T_b, a thermal pulse is generated, as expressed in Eq. 2-14 using the rough monolithic approximation; it can be converted into an electric signal by means of the thermistor bias circuit, that leads a current I going across the sensor.

Considering the basic circuit shown in Figure 2-8, the relationship between the voltage signal ΔV, the parameters of the thermistor and the deposited energy E is given by:

$$\Delta V = \frac{R_L}{R_L + R} \cdot V \cdot A \cdot \frac{\Delta T_b}{T_b} \sim \frac{E}{C \cdot T_b} \cdot A \cdot \sqrt{P \cdot R}$$

2-23

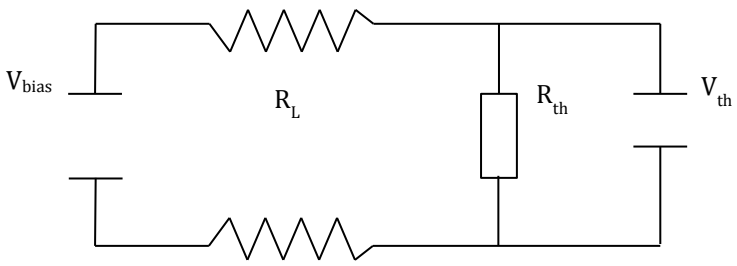

Figure 2-8. A sketch of the basic thermistor bias circuit.

2.4. Composite bolometer model

Now that the basic principles of the energy absorber and of the temperature sensor are known, a more refined bolometric model can be presented. The aim of this section is to provide a basic understanding of the static and dynamic behaviour of macro-bolometers, aiming at the explanation of their use in experiments on 0νββ. Also, the instruments will be given to face the optimization work that will be detailed in this thesis, from Chapter 3 to Chapter 6. The thermal model presented here will be described in its main aspects for the sake of a better comprehension of the next topics; a detailed treatment is found in (132).

The simplified monolithic model has just been presented in Section 2.3, while introducing to the bolometric technique: in that thermal picture, the detector is seen as a single heat capacity C connected to the heat bath by means of a conductance G. The monolithic model has already been labelled as limited and incapable of accounting for the real signal structure. The first adjustment to the real case consists in separating the detector in its two main components, the absorber and the thermistor; each of them will be described by means of a heat capacity and will be linked to the other elements of the system through a heat conductance. This evolution of the model is still not sufficient, however, as it neglects any non-linearities in the behaviour of the thermistor. For example, the HEM (see Section 2.3.1) separates the phonon system from the electron one inside the temperature sensor: the two systems are connected by a thermal conductance weaker than the one among the electrons, and therefore they reach distinct temperatures following power injection.

Summing up, the bolometric detector under discussion here can be described by an enhancement of the monolithic model that takes into account, at least, the following terms:

- ✓ the heat bath, which is the thermal reference point;
- ✓ the absorber, connected by means of distinct conductances to the heat bath and to the phonon system of the thermistor;
- ✓ the phonon system of the thermistor, connected by means of distinct conductances to the heat bath and to the thermistor's electronic system, which is uncoupled due to the HEM picture;
- ✓ the electron system of the thermistor, connected to the phonon system of the thermistor by a conductance.

The three-nodes system just sketched constitutes a composite model and is integrated by taking into account the characteristics of the electric circuit for thermistor polarization (Figure 2-8), for converting the temperature rise into electric signal. The behaviour of this kind of macro-bolometer will be analyzed now in both its static and dynamic behaviour.

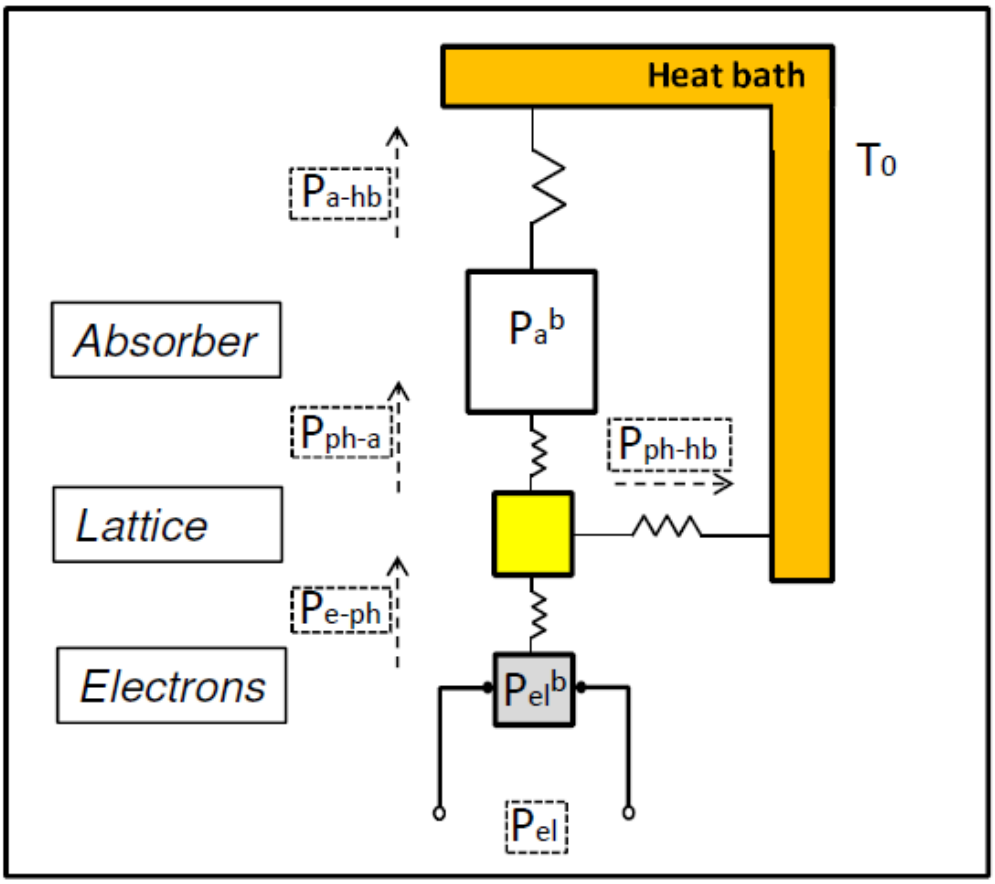

Figure 2-9. Composite thermal model with three nodes. The sign of powers flowing in the system is not known in principle, and they are fixed by convention.

2.4.1. Static behaviour

In ideal static conditions, when no electric power is injected in the system, all the nodes are expected to reach the same temperature T_0 of the heat bath; in the real case, localized background powers are always present and generate a thermal flow among the model's nodes, even when no energy is released in the absorber and the thermistor is not polarized. At least two parasitic powers, P_a^b and P_{el}^b, should be considered: the former is dissipated in the crystal absorber because of unavoidable micro-vibrations, while the second one can be correlated to parasitic currents induced by electromagnetic interferences. When the thermistor is polarized by the passage of an electric current I for signal read-out, Joule heating by means of an electric power P_{el} takes place in its electron system. In such conditions, describing the static behaviour of the modelled macro-bolometer means finding

the thermal equilibrium configuration reached by the network sketched in Figure 2-9. The power balance for the three nodes of the thermal system under discussion is:

$$\begin{cases} P_{el} + P_{el}^{b} = P_{e-ph} \\ P_{e-ph} = P_{ph-hb} + P_{ph-a} \\ P_{ph-a} + P_{a}^{b} = P_{a-hb} \end{cases}$$

2-24

where P_{el} can be expressed in terms of the elements in the polarization circuit pictured in Figure 2-8:

$$P_{el} = R(T_{el}) \cdot \left(\frac{V_{bias}}{R(T_{el}) + R_L} \right)$$

2-25

In the set of Eq. 2-25, the dependence on the different temperatures of the nodes can be made explicit by expressing the power P_{12} flowing between nodes 1 and 2 in function of T_1 and T_2, with $T_1 > T_2$. As confirmed by experimental measurements that will be reported in Section 3.5, the thermal conductances used in the model are expressed by a law of power in function of T:

$$G(T) = g_0 \cdot T^{\alpha}$$

2-26

The power flowing between the generic nodes 1 and 2 in the depicted thermal network can therefore be written as:

$$P_{12} = \int_{T_1}^{T_2} G(T) dT = \frac{g_0^{12}}{\alpha_{12} + 1} \cdot \left[T_1^{\alpha_{12}+1} - T_2^{\alpha_{12}+1} \right]$$

2-27

The thermal balance system (Eq. 2-24), rewritten in terms of Eq. 2-27, is non-linear and cannot be solved analytically. Its solution by means of numerical methods gives the temperature of each node, and both the resistance of the thermistor $R(T_{el})$ and the current flowing through it, then, can be calculated from the value T_{el}.

2.4.2. Dynamic behaviour

Once static conditions are known, the dynamic problem can be approached. It consists in finding the temporal evolution of a pulse generated by an energy deposition in the crystal absorber. When the monolithic model was presented in Section 2.3, a first-order approximation for the evolution in time of pulses was found in the case of a capacity C linked to the heat bath by a conductance G.

Although the composite model is more complex and should be treated independently, some considerations on the general signal structure can be drawn. The temperature variation generated by the particle interaction is defined starting from the static equilibrium configuration of the network, which is regained when the whole evolution of the thermal pulse is over; although approximate, this first picture shows that the characteristic times of a thermal pulse, linked to the constant $\tau = C/G$, are those of the thermal relaxation towards equilibrium, and that such relaxation is described by exponential functions.

The previous general view can be refined by specific reference to temperature variations in the composite model. Energy conservation in the time interval dt can be applied to the three nodes of the thermal network in Figure 2-9, obtaining the set of differential equations:

$$\begin{cases} -C_{el} \cdot \dfrac{dT_{el}}{dt} = -P_{el} - P_{el}^{b} + P_{e-ph} \\ -C_{ph} \cdot \dfrac{dT_{ph}}{dt} = -P_{e-ph} + P_{ph-hb} + P_{ph-a} \\ -C_{a} \cdot \dfrac{dT_{a}}{dt} = -P_{ph-a} - P_{a}^{b} + P_{a-hb} \end{cases}$$

2-28

$T_{el}(t)$, $T_{ph}(t)$ and $T_a(t)$ are the unknown temperatures of the thermistor's electron, thermistor's phonon and crystal absorber nodes; C_{el}, C_{ph} and C_a are their heat capacities, respectively, and depend on temperature with the general form:

$$C(T) = \mathrm{c} \cdot T^{\beta},$$

2-29

where c is a coefficient experimentally measured; the exponent β is equal to 3 for the absorber due to the Debye law and 1 for the electron system of the thermistor. The powers

P_{12} flowing in the system still have the form of Eq. 2-27. At time t = 0, the power $P_a = E \cdot \delta(0)$ is released instantaneously in the absorber, which implies the following conditions hold:

$$\begin{cases} T_{el}(0) = T_{el}^s \\ T_{ph}(0) = T_{ph}^s \\ T_a(0) = T_a^s + \dfrac{E}{C_a} \end{cases}$$

2-30

The superscripts "s" refer to the static equilibrium temperatures of the three nodes. A necessary remark is that the third equation, more specifically the initial condition $\Delta T_a = E/C_a$, is valid provided that the variation with temperature in the heat capacity of the absorber is negligible, and then $\Delta T \ll T$: the approximation is valid in the case under study but does not hold for absorbers with very small heat capacities or large energy depositions.

The set of equations 2-28, completed by the initial conditions 2-30 that correspond to an instantaneous release of energy E, can be solved only in a numerical way. However, opportune approximations can be made in order to linearize it:

1) the thermal pulse generated in the crystal absorber is treated as a small perturbation of the work point determined by the static problem. In other words, the power flowing from the heat bath to the generic node j in dynamic conditions can be written as:

$$\int_{T_{hb}}^{T_j} G(T)dT = \int_{T_{hb}}^{T_j^S+\Delta T} G(T)dT = \int_{T_{hb}}^{T_j^S} G(T)dT + \int_{T_j^S}^{T_j^S+\Delta T} G(T)dT \sim \int_{T_{hb}}^{T_j^S} G(T)dT + G(T_j)\cdot\Delta T$$

2-31

In the previous equation, T_j^S is the temperature of the generic node j determined in static equilibrium conditions, and ΔT is the temperature variation during pulse evolution. The "small perturbation" approximation relies on the assumption that heat conductances and capacities do not change within the variation range of the pulses. In this way, the equations that describe the composite model's dynamic behaviour are rewritten in terms of heat capacities and thermal conductances evaluated at the temperatures in the operation point;

2) The heat capacity C_{ph} of the phonon system in the thermistor is considered negligible compared with the other ones; as will be evidenced in Section 3.5, the inequality $C_{ph} \ll C_{el} \ll C_a$ holds true for the CUORE bolometers.

These approximations allow solving analytically the dynamic problem and the resulting solution has the form:

$$T_{el}(T) = \frac{E}{C_a} \cdot K \cdot \left(e^{\lambda_1 t} - e^{\lambda_2 t}\right) + T_{el}^{s}$$

2-32

The constants K, λ_1, and λ_2 depend from the values of the heat capacities and conductances in the system evaluated at the temperatures T_j^s obtained from the solution of the static problem. However, the description of the composite model given in this section must be completed by incorporating some additional elements, such as the electrothermal feedback, the presence of parasitic capacitances in the bias circuit and the contribution of athermal phonons.

The electro-thermal feedback is the phenomenon that describe the non-linearity of the V-I relation in a biased thermistor, because the applied voltage produces a power dissipation P which increases the temperature and acts back on the resistance of the thermistor. It will be described in Section 3.3.1.2. As depicted by the first equation in the set 2-24, the power in the electron system is given by the sum of two terms: a static parasitic power and a Joule power $I^2 \cdot R(T_{el})$. The latter becomes smaller during the time-evolution of a thermal pulse because the rise in temperature due to particle interaction in the absorber leads to a decrease in the resistance of the thermistor: the lower the Joule power dissipated, the faster is the relaxation of T_{el} to its static equilibrium value T_{el}^{s}. This effect is relevant unless the power in the electron system is dominated by the parasitic term. Electro-thermal feedback is integrated in the model by introducing an effective thermal conductance between the electron and the phonon systems, which substitutes the G_{ph-el} used in the previous discussion:

$$G_{ph-el}^{*}(T_{el}^{s}) = G_{ph-el}(T_{el}^{s}) - \frac{I^2 \cdot R(T_{el}^{s}) \cdot A(T_{el}^{s})}{T_{el}^{s}}$$

2-33

A is the logarithmic sensitivity of the thermistor used. The use of the substitution of Eq. 2-33 incorporates the electro-thermal feedback effect in the system without altering the structure of the solution (Eq. 2-32).

Since bolometric detectors are operated in a cryogenic environment, the electric read-out of each thermistor requires that a pair of wires is brought up to the room temperature

electronics stage. Experimentally, parasitic capacitances are observed between the wires and between the wires and the ground. The second refinement of the composite thermal model consists therefore in integrating similar effects: this is done by including the presence of a capacitance-to-thermistor's resistance parallel configuration in the bias circuit (see Figure 2-10). Given a parasitic capacitance c_p, the differential equation that describes the variation in time of the voltage pulse at the terminals of the thermistor is given by:

$$\frac{dV}{dt} = \frac{1}{c_p R_L} \cdot \left[V_{bias} - \frac{R + R_L}{R} \cdot V \right]$$

2-34

This expression completes the set of equations 2-28 that describes the time evolution of the thermal pulse in the three nodes of the composite system. Summing up, the presence of a parasitic capacitance introduces in the system a new time constant $\tau_p = c_p R_L$, which cannot be neglected in the application under discussion: in the Cuoricino case, the typical operational values $c_p \sim 20 - 500$ pF and $R_L \sim 10$ GΩ lead to τ_p of even a few seconds, therefore comparable to the evolution times of thermal pulses.

The last refinement of the proposed composite model regards the contribution of athermal phonons with high energy of order $\hbar\omega_D$); they can degrade in thermal phonons by scattering with the absorber's surfaces or lattice impurities, but they can also reach directly the thermistor where they thermalize by interaction with conductance electrons. In this case, the initial condition $T_a(0) = T_a^S + E/C_a$ should be modified because the energy transfer of the interacting particle is now split in two contributions to both thermal and athermal phonons.

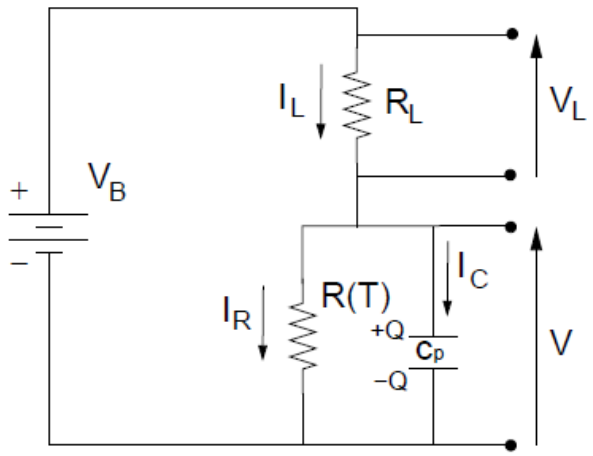

Figure 2-10. Bias circuit for the voltage read-out of the thermistor, corrected by the presence of a parasitic capacitance in parallel with the sensor's resistance.

2.5. Noise sources in bolometric detectors

To conclude the general picture of the bolometers, a brief description of the noise that can affect the detector performances will be here given. The noise sources can be divided in two categories: intrinsic noise, depending on the bolometer and its physical parameters, and extrinsic noise, related to the bias circuit, the read-out chain and the cryogenic system.

Intrinsic noise cannot be eliminated totally and limits the nominal energy resolution; it is due mainly to: The main sources of this kind of noise are:

- ✓ Johnson noise, that is the white noise generated by the fluctuation of charge carrier across the thermistor, considered as a resistive element. The power spectrum of this noise is:

$$\epsilon_R = \sqrt{4k_B RT},$$

2-35

where R is the thermistor resistance at the temperature T. Using the monolithic model, it is possible to demonstrate that the Johnson noise at low-frequency is reduced by the electro-thermal feedback.

- ✓ Thermodinamic or phonon noise, that limits the intrinsic energy resolution in case of complete energy thermalisation; it is caused by the fluctuation of the number of thermal phonons exchanged with the heat bath through the conductance G, creating random fluctuations in the absorber temperature.

  When Poisson statistics is assumed, an estimate of the fluctuation of the internal energy of the absorber is given by Eq. 2-8. In the case of the monolithic bolometer model, a detailed calculation of noise due to the intrinsic sources shows how that expression must be multiplied by a dimensionless factor ξ: has to be introduced (133):

$$\Delta E \cong \xi\sqrt{k_B C(T) T^2}.$$

2-36

The value of ξ depends on the details of the temperature sensor and of the temperature dependencies of the thermal conductance and of the heat capacity, and can be made of the order of the unity with a proper optimization work.

The extrinsic noise can depend on the cryogenic and electronic set-ups for the bolometer operation, such as, for example the Johnson noise due to the load resistance in the thermistor bias circuit (see Figure 2-8). Other sources of noise can be included in this category, such as electric microphonic noise, electromagnetic interferences, and mechanical microphonic noise. These aren't classifiable as intrinsic noise of the detectors or as consequence of the electronic read-out of bolometers but can seriously impact detector performance.

Chapter 3.
TOWARDS THE CUORE SINGLE MODULE

Brick by brick by brick by brick we're building[8]

Proposed since 1998 (134), the Cryogenic Underground Observatory for Rare Events (CUORE) (135), is one of the most sensitive next-generation experiments searching for 0νββ. The CUORE detector will consist of 988 TeO_2 bolometers arranged in 19 towers, resulting in a scaled-up version of the Cuoricino experiment (introduced in Section 1.4.2.3) that will exploit the experience and results gained from its predecessor while aiming at an improvement in sensitivity by roughly two orders of magnitude.

The elementary brick of the CUORE detector, usually called Single Module, is a single floor of a tower. The structure and the materials of the CUORE single module are almost the same as in Cuoricino but, because the CUORE goal is an extremely better sensitivity, huge efforts have been done to better the Single Module (see Section 3.1).

In particular, the improvements follow two ways: one is to decrease the background level to 10^{-2} counts/(keV·kg·y), more than one order of magnitude lower than what measured in Cuoricino, by a more careful selection of the construction materials, which will also undergo special cleaning treatments and be stored underground to minimize cosmic-ray activation. On the other hand, differently from Cuoricino that was totally "handmade", the CUORE detector will be built thanks to a devoted assembly line, with the purpose of increasing the uniformity among the performances of the one thousand detectors and having a faster and cleaner construction. Because of all the modifications introduced, before the construction of the entire CUORE detector, a single tower will be made, named CUORE-0, and cooled down in the Cuoricino refrigerator (see Section 3.8).

The revision of the Cuoricino Single Module towards the CUORE Single Module and the construction of CUORE-0, being the framework in which this PhD work developed, will be detailed in the present Chapter, with the aim of pointing out the elements that mostly contribute in increasing the sensitivity and presenting the optimisation work performed.

[8] (226).

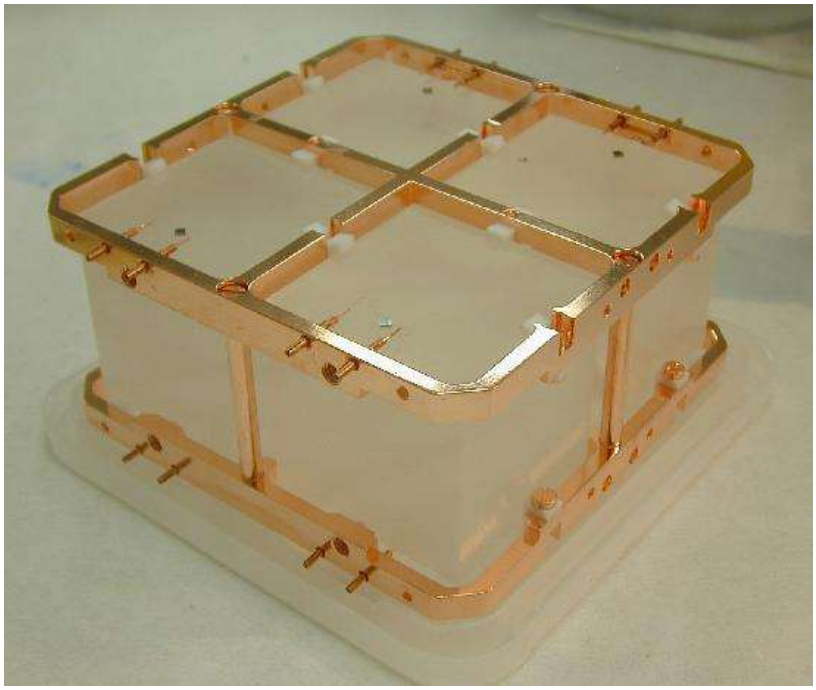

Figure 3-1. Picture of a Cuoricino Single Module.

3.1. General description

This Section will provide a general description of the CUORE-0/CUORE Single Module, focusing on the main elements constituting the bolometers and on the improvements made since Cuoricino; some of them, treated deeply in this thesis work, will be analysed thoroughly in the next chapters, while here a complete description of the Single Module will be given.

In order to understand the sources of background to be dealt with, and the related improvements made to overcome them, the Cuoricino background will be also briefly presented.

3.1.1. The background of the Cuoricino experiment

In Cuoricino two main contributions have been identified as responsible of the counting rate in the Region of Interest (ROI) (135), (91):

- ✓ About 30% of the background is ascribed to a ^{232}Th contamination in the cryostat. This background is due to multi-Compton events of the 2615 keV line of ^{208}Tl (belonging to the ^{232}Th chain) and appears to be the only purely gamma-

induced background in the ROI. Studies based on Monte Carlo simulations of the set-up and dedicated measurements (as the one described in (136)) indicates that this is the only source of background originated outside the detector, implying that the Cuoricino external shields are thick enough to reduce to negligible levels the contributions of muons, neutrons and environmental γs but the internal Roman lead shield surrounding the Cuoricino array is not sufficient to shield the detector from the radioactivity of the cryostat.

- ✓ The remaining 70% is ascribed to surface contaminations of the crystals and of the copper structure. Unlike other detectors, bolometers have no dead layer at their surface, therefore they are fully sensitive both to their own surface contamination and to that of the materials facing them (the Cuoricino array is held in vacuum and faces mainly copper parts). As a consequence also short range particles like αs and βs can reach (or escape from) the active volume of the detector, depositing therefore only a fraction of their energy in it. In this way also Th and U αs (which have typical energies > 4 MeV) can mimic a 0νββ decay. In the case of crystal surface contaminations this background can be efficiently rejected by the use of the anticoincidence cut (these are the events where the α/β particles exit the source crystal entering a nearby one), while degraded αs (namely alphas that release only part of their energy in the crystal) coming from the surface contamination of the materials directly facing the detectors create a flat background above the 2615 keV region. This contribution is the most difficult to deal with.

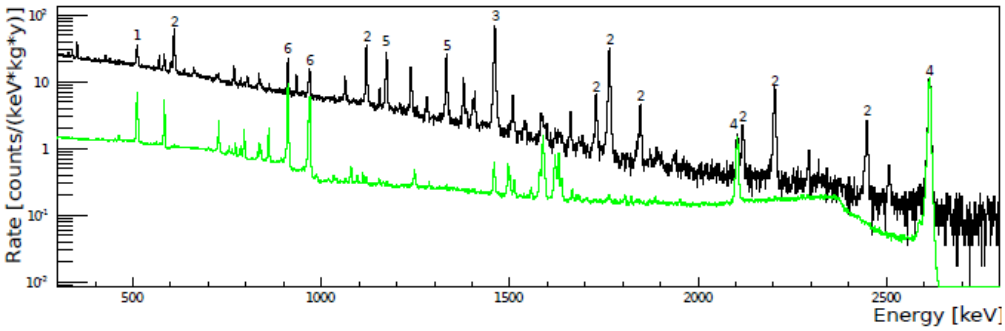

Figure 3-2. Anticoincidence total energy spectrum of all Cuoricino detectors (black). The most prominent peaks are labelled and come from known radioactive sources such as: e^+e^- annihilation (1), ^{214}Bi (2), ^{40}K (3), ^{208}Tl (4), ^{60}Co (5) and ^{228}Ac (6). The total energy spectrum of all Cuoricino detectors during calibration measurements is also shown (colour). For convenience, it is normalized to have the same intensity of the 2615 keV line of ^{208}Tl as measured in the non-calibration spectrum.

3.1.2. The CUORE single module

The basic module of the CUORE-0/CUORE detector, i.e. the single floor of a tower, is made by a 2x2 array of cubic TeO_2 crystal absorbers, each 50 mm on a side and mass 750 g, containing ^{130}Te as $0\nu\beta\beta$ source (see Sections 3.2.1 and 3.2.2). The crystals are produced by the Shanghai Institute of Ceramics Chinese Academy of Sciences (SICCAS – China), which also grew the Cuoricino ones. Several improvements have been achieved in terms of homogeneity and radio-purity of the production (described in Section 3.2.3), for reducing surface and bulk contaminations, requiring specific tests for the validation (discussed in detail in Chapter 5).

Each crystal is provided with a Neutron Transmutation Doped Ge thermistor, usually referred simply as NTD (see Section 3.3.1), that detects the temperature changes in the absorber thanks to the strong dependence of its resistance with the temperature. This dependence is strictly related to the doping of the thermistor, therefore a precise characterisation of the NTDs is mandatory (as will be dealt with in Chapter 4). The crystals are equipped also with heaters, heavily doped Si devices that provide fixed reference pulses for the bolometer response stabilisation (see Section 3.3.2).

The coupling of these elements to each crystal is made by a matrix of glue spots; this is a very delicate issue in the construction of the CUORE bolometers, because the formation of the signal depends strongly on it. There are several factors to deal with the thermistor-to-absorber coupling: the selection of the glue, the number of contact points between the doped chips and the crystal and so on, as introduced in Chapter 6; most of them have been studied and fixed since Cuoricino but, differently for the pilot experiment, the CUORE gluing will be done thanks to a semi-automatic system (see Section 3.3.3.1).

The crystals are mechanically and thermally coupled to an Oxygen-Free High Conductivity (OFHC) copper holder, acting as heat sink, thanks to PTFE pieces. The cleaning of all these materials is another important point of the CUORE assembly, as their surfaces facing the bolometers can be sources of degraded α that contributed dangerously to the background (as introduced in Section 2.1).

On the external side of the frames, copper pads, designed on Kapton boards, are fixed to carry the signal to the electronic read-out. The electrical connection between the doped semiconductors and the copper pad is made with 25 μm diameter gold wires, attached by means of the ball bonding and wedge bonding technique on the two different ends respectively (see Section 3.3.3.2).

A sketch of the CUORE Single Module can be found in Figure 3-3, while Figure 3-4 displays a scheme of a single CUORE bolometer, reporting pictures of its main components.

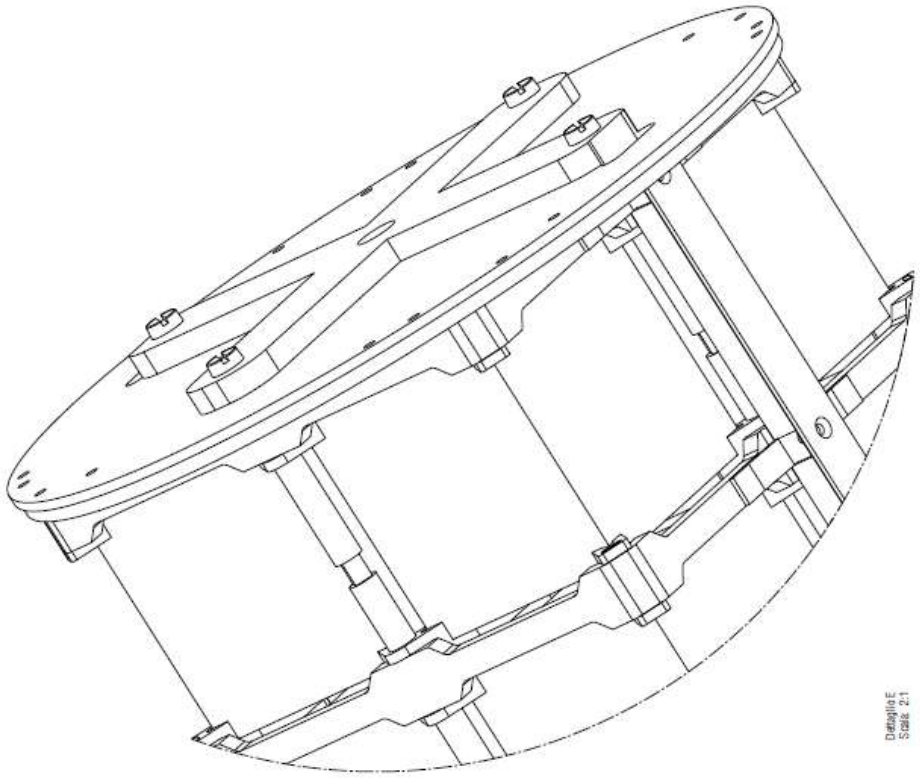

Figure 3-3. Drawing of a CUORE Single Module connected to the top plate of a tower.

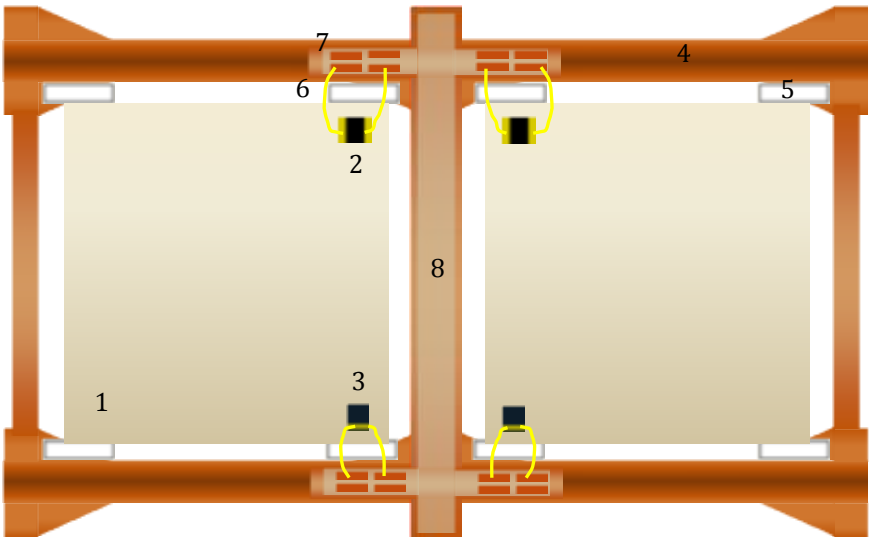

Figure 3-4. Sketch of a CUORE bolometer, with all its elements: 1) the TeO_2 crystal absorber; 2) the NTD-Ge thermistor, with wrap-around style gold pads; 3) the Si heater; 4) the copper frame acting as thermal bath; 5) the PTFE spacers, linking the absorber to the bath; 6) the gold wires, 7) the copper pad and 8) the wire tray for carrying out the electrical signal.

3.2. TeO_2 crystal absorbers

The Cuoricino and CUORE experiments search for the 0νββ decay of the ^{130}Te in ^{130}Xe.

The main advantage of this choice is the high natural isotopic abundance of the nuclide that makes the isotopic enrichment of the crystals not mandatory for the experiment. Observing the other features of the ^{130}Te, such as the Q-value or the results from the nuclear matrix element calculation, no strong disadvantages emerge. Another plus of the ^{130}Te is that its crystalline compound, the TeO_2, is particularly suitable for use in a cryogenic particle detector because of its crystal and thermal characteristics (Section 3.2.2.1).

3.2.1. The nuclide: ^{130}Te

The natural isotopic abundance of ^{130}Te is 33.8% (137), higher with respect to other 0νββ candidate nuclides, as can be seen in Figure 1-10. Because of this, enrichment is not mandatory for CUORE, but can be considered for the future, since it could be double the sensitivity (see Eq. 1-31 and Eq. 1-32), even if up to now no specific R&D in this direction has been carried on.

A second important feature of ^{130}Te is the Q-value (138): $Q_{0\nu\beta\beta}$=2527.01±0.32 keV. This value it is not the highest among the 0νββ candidates (as shown in Figure 1-9) but it is considerably large and that is good considering that the space phase factor, $G^{0\nu}$, depends on Q^5; the higher the Q-value, the bigger is the probability for the decay to occur. The ^{130}Te Q-value is not outside the region of the natural radioactivity, whose end-point correspond to the γ-peak of ^{208}Tl (due to the Thorium chain) at 2615 keV; nevertheless it is situated in a window of the spectrum characterized by low radioactivity, between the full energy and the Compton edge of the 2615 keV photon peak of ^{208}Tl, and out of the ^{238}U background.

3.2.2. The compound: TeO_2 crystals

A Tellurium compound exists that is particularly convenient for use in a cryogenic particle detector: it is known as paratellurite (TeO_2) and it forms dielectric and diamagnetic crystals for which, at few mK, the relatively high value of Debye temperature, T_D =232 K (139) (higher than for pure Te), yields a very low heat capacity, leading to large temperature signals and good energy resolution (see Eq. 2-6 and 2-8). Paratellurite (differently from the pure metallic Te) can also stand subsequent thermal cycles down to cryogenic temperatures.

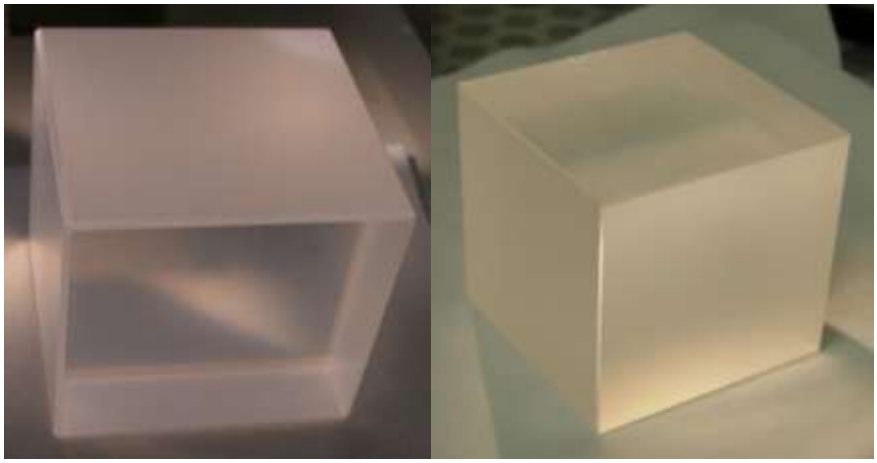

Figure 3-5. Pictures of the 5x5x5 cm^3 TeO_2 crystal produced by SICCAS for the CUORE-0 and CUORE experiments.

Moreover, the thermal expansion coefficient of TeO_2 crystal (140) is very close to that of copper, at least along the direction perpendicular to the growth axis, allowing copper to be used for the holder of the detector without placing too much strain on the crystals in the cooling process.

With paratellurite, large single crystals with good thermal and mechanical properties can be grown; together with the fact that Te dominates the compound with respect to the mass (about 80%), the choice of TeO_2 permits to have large quantities of this material.

Examples of TeO_2 crystal are shown in Figure 3-5.

3.2.2.1. TeO_2 crystal properties

Tellurium dioxide is found in nature in two mineral forms: tellurite (orthorombic) and paratellurite (α-TeO_2). The latter has a tetragonal symmetry D_4(422) and due to its useful acousto-optic properties, is commercially produced on a large scale. First crystal synthesis using Czochralski method was reported in 1968 (141). The first Bridgman growth of TeO_2 crystals was reported in 1985 (142). The structure of the crystal may be regarded as a distorted rutile structure with a doubling of the unit cell along the [001] direction where the positions of the tellurium are slightly shifted from the regular rutile positions (143).

Tellurium ion is fourfold coordinated by oxygen, the coordination polyhedron being a distorted trigonal bipyramid (144) with two different bond distances: 1.88 Å (short) and 2.12 Å (long). Each oxygen atom is bonded to two tellurium atoms with an angle of 140° between long and short bonds; other tellurium neighbours are at larger distances. Oxygen positions have no symmetry. Eight nonequivalent oxygen or interstitial sites and four

nonequivalent tellurium sites can be distinguished. The material is bi-refringent, optically active and highly transparent (145) in the range of 350 nm – 5 μm. TeO_2 is insoluble in water and has high refractive indices (n_o=2.274 and n_e=2.430 at λ=500 nm). The density of TeO_2 synthetic crystals is 6.04 g/cm^3, close to the density calculated from measured lattice constants: a=4.8088 Å and c=7.6038 Å. The melting point of commercially available TeO_2 99.99% purity powder is 733 °C.

3.2.3. TeO_2 crystal production

To reduce the presence of environmental radioactivity and radioactive contaminants in the detector, a high control of all the crystal production steps is required. In particular, to minimize the influence of long-lived, naturally occurring isotopes, such as ^{238}U, ^{232}Th, ^{40}K and their daughters, great care must be devoted to the selection of all materials and ancillaries used for the preparation of the TeO_2 crystals, i.e. a detailed monitoring of all materials, tools and facilities used for raw oxide synthesis and crystal growth.

Possible surface contamination must be controlled with great care by a strict selection of consumables and equipment used for chemical and mechanical processing of grown crystals. Materials and tools used in the packaging process must also be strictly controlled for the same reasons. Sea level transport and underground storage of prepared crystals are necessary in order to minimize their cosmogenic activation.

For accomplishing the task of having high radiopure TeO_2 crystals for the CUORE experiment, dedicated production lines for raw material synthesis, crystal growth and surface processing were built compliant with radio-purity constraints. Based on previous experience (146) and on a background goal of (10^{-2}-10^{-3}) counts/(keV·kg·y) for the CUORE experiment, limit values were defined for the concentration of radionuclides to be accepted in raw materials, consumables, reagents and intermediary products used for the production of TeO_2 crystals for CUORE. The values are reported in Table 3-1.

Production and certification protocols have been developed and high sensitivity measurements have been performed to check the radio-isotope concentrations in raw materials, reactants, consumables, ancillaries and intermediary products used for TeO_2 crystals production (147), as described in Section 5.1.

Furthermore the CUORE TeO_2 crystals have very strict specifications concerning dimensions, surface quality and crystallographic orientation. Crystals have cubic shape with (50±0.050) mm edges and chamfers of 0.5 mm. The average flatness of faces has to be <0.010

mm and cubic faces have to be oriented parallel to crystallographic planes ([001], [110], [1-10]) within ±1°. The crystals have two hard faces (<100>) and four soft faces (<110>).

Material	Category	Contamination limits
Metallic Te	Raw material	$^{238}U < 2*10^{-10}$ g/g $^{232}Th < 2*10^{-10}$ g/g $^{210}Pb < 10^{-4}$ Bq/kg $^{40}K < 10^{-3}$ Bq/kg $^{60}Co < 10^{-5}$ Bq/kg
Water and acids used for TeO_2 powder synthesis	Reagent	$^{238}U < 2*10^{-12}$ g/g $^{232}Th < 2*10^{-12}$ g/g
Water	Consumable	$^{238}U < 2*10^{-12}$ g/g $^{232}Th < 2*10^{-12}$ g/g
TeO_2 powder before crystal growth	Intermediary Product	$^{238}U < 2*10^{-10}$ g/g $^{232}Th < 2*10^{-10}$ g/g $^{210}Pb < 10^{-4}$ Bq/kg $^{40}K < 10^{-3}$ Bq/kg $^{60}Co < 4*10^{-5}$ Bq/kg $Pt < 10^{-7}$ g/g $Bi < 10^{-8}$ g/g
TeO_2 crystal, ready-to-use	Final product	$^{238}U < 3*10^{-13}$ g/g $^{232}Th < 3*10^{-13}$ g/g $^{210}Pb < 10^{-5}$ Bq/kg $^{60}Co < 10^{-6}$ Bq/kg
SiO_2 powder for crystal polishing and textile polishing pads	Consumables	$^{238}U < 4*10^{-12}$ g/g $^{232}Th < 4*10^{-12}$ g/g
Gloves, plastic bags, cleaning tissues, etc	Ancillaries	$^{238}U < 4*10^{-12}$ g/g $^{232}Th < 4*10^{-12}$ g/g

Table 3-1. Concentration limits for radioactive isotopes requested for raw materials, reagents, consumables and intermediary products used for the production of TeO_2 crystals (147).

The production process of TeO_2 crystals for CUORE is divided into two major phases, crystal synthesis and crystal polishing, which are then divided into several sub-processes. Bulk contamination is a risk in the crystal synthesis phase, while surface contamination is the main concern during the crystal processing.

The raw material synthesis and TeO_2 crystal growth methodology used for the CUORE crystal production are well known (148), (149). The key to obtain high purity crystals is making two successive crystal growth processes with two associated iterations of TeO_2 powder synthesis, as illustrated in Figure 3-6, and described in detail in (147). In this way the final radio-pure TeO_2 crystals are grown from a highly pure TeO_2 powder as raw material.

The TeO_2 powder used for the first growth is synthesized from metallic Te dissolved with aqua regia[9] and then precipitated with concentrated ammonia. After the washing and drying processes, the obtained raw dried powder is further calcinated at 680 °C in Pt crucibles for 24h in free atmosphere thus obtaining the raw calcinated powder used for the crystal growth. TeO_2 seeds used for the crystals growth along [001] direction are cut and oriented within 30' precision, shaped and washed using ultrapure water and reagents.

For the crystal growth, platinum crucibles are filled with the crystal seed and the raw calcinated powder, sealed and placed into alumina refractory tubes which at their turn are placed into modified Bridgman furnaces (149). Crucibles are heated to about 800-860 °C and kept at this temperature for several hours after which they are raised to a certain height in order to melt the top of the seed and keep the system still for 4h in order to create a stable solid–liquid interface.

The growth process is then driven by lowering the crucible at a rate of 0.6 mm/h and raising the furnace temperature by about 3 °C/h. At the end of the growth process the furnaces are cooled down to room temperature slowly in order to avoid crystals' cracks caused by thermal stress.

The high purity TeO_2 powder used for the second growth is prepared from selected regions of crystals obtained in the first growth. Selected TeO_2 crystalline pieces are dissolved with concentrated HCl and then precipitated with concentrated ammonia. The precipitate is further washed and dried at 80 °C. The ultra-pure dried powder thus obtained is further treated at 680 °C in a Pt crucible for 24 hours in free atmosphere to obtain the ultra-pure calcinated powder and a second growth process is executed following the same procedure as in the first one. Nevertheless, the tools and ancillaries used for the two growth processes are strictly separated in the frame of a radiopure crystals production protocol applied in the case of TeO_2 crystals for DBD application In the second phase of TeO_2 crystal production, the raw crystal ingots are subject to a rough mechanical processing (cutting, orienting and shaping) followed by the final surface treatment and packaging.

A preliminary mechanical process is performed to bring the crystal shape, dimensions and crystallographic orientation of faces very close to their nominal values. Then a final mechanic process is performed in a clean room, with also the purpose of deep cleaning the crystal's surfaces, which may have been contaminated during the rough mechanical processing.

The cleaning process is made in two steps, first by chemical etching and second by polishing. The polishing also smooths the crystal faces, possibly damaged by chemical

[9] (HNO_3 : HCl = 1:3).

etching. The targeted number of atomic layers to be taken away by these two procedures is on the order of 10^4 in order to eliminate all impurity atoms that may have adsorbed on the crystal's face and further diffused in its bulk.

A special vacuum packaging procedure was also defined in order to reduce surface radio-contamination risks, especially due to radon exposure in free atmosphere. After the clean room operation, crystals are packed and barcode labelled in a triple vacuum package and stored by groups of six crystals in polyethylene vacuum boxes. For long term storage, the packaged crystals are placed in a controlled environment with low-radon atmosphere (<10 Bq/m^3), monitored with two radon detectors, one inside and one outside the box.

The entire production process (schematised in Figure 5-1) is subject to a complex validation protocol (described in Chapter 5), which includes radio-purity certification procedures to be applied in each production phase and immediate actions to be taken in case of failure, including the halt of crystal production until the problem is solved.

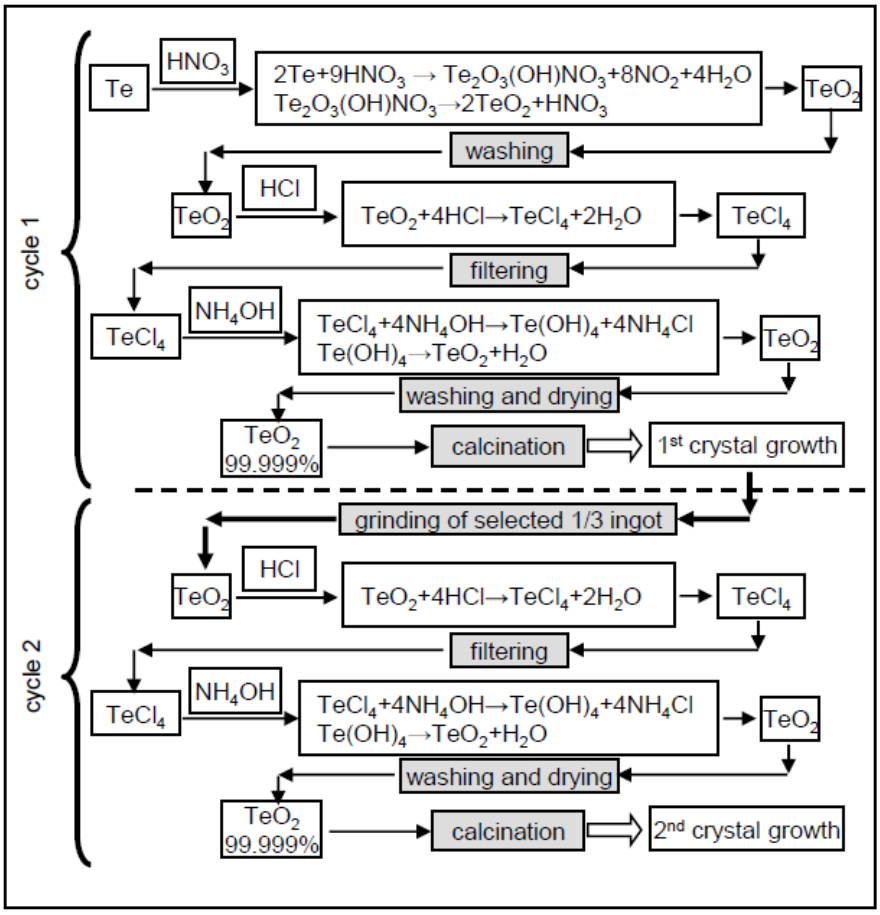

Figure 3-6. A scheme of the two successive crystal growth procedures.

3.3. Doped semiconductors

As previously introduced, CUORE-0/CUORE crystals are equipped with two different doped semiconductors for the detection of the temperature variation (the thermistor) and for the measurement stabilisation (the heater). To do properly their work, these essential bolometric elements must satisfy specific conduction properties at low temperature, which are determined by the doping level, as discussed in Section 2.3.1.

The doping operation is usually performed on wafers and the single devices are cut from the wafer afterwards. However it is difficult to achieve complete control on the doping level in the whole processed material: a successive characterization of the produced devices is therefore necessary.

In the following sections the main features, the production and the characterisation procedure of both CUORE-0/CUORE thermistors and heaters will be presented

3.3.1. Thermistors

As introduced in Section 2.3.1, the thermistors are devices whose resistivity has a stiff dependence on the temperature:

$$R(T) = \rho(T) \cdot \frac{1}{S} = R_0 e^{(T_0/T)^\gamma} \qquad 3\text{-}1$$

because their doping is just below the MIT regime and the conduction is dominated by the VHR mechanism with Coulomb Gap (that gives γ=0.5).

The CUORE-0/CUORE thermistors are designed and produced by a conjunct group composed by researchers of both the Lawrence Berkeley National Laboratory (LBNL) and the Department of Material Sciences at the University of California-Berkeley.

3.3.1.1. Production

Producing thermistors by doping semiconductors is a delicate issue because an extremely specific impurity concentration, very close to the metal-insulator transition, is required. Furthermore the doping must be uniform everywhere in the sample, because the probability for hopping to occur depends exponentially on the inter-dopant distance; therefore any fluctuations in the average local dopant concentration will lead to a change in

the distribution of the inter-dopant distance which in turn will results in fluctuations in the local hopping probability, translating in resistivity fluctuations (150). Moreover, because of the large amount of thermistors needed (at least one thousand for CUORE), the uniformity of the doping must be guaranteed on all the production samples.

The only process that can provide the most uniform dopants concentration in the sample is the Neutron Transmutation Doping (NTD) technique (see, for example (151) and Figure 3-7), developed at LBL (152), and initially used at most for silicon devices (153). In this method a semiconductor is doped by the partial nuclear transformation of its stable isotopes into dopants via thermal neutron capture. It is achievable by irradiating the samples of semiconductor crystals with a neutron flux in a nuclear reactor.

When a Ge wafer is inserted in a nuclear reactor, thermal neutrons are captured by three of the five isotopes contained in natural Ge. The occurring reactions are listed in Table 3-2. Because the process is lead at low temperature, the mobility of the impurities is very low (impurity conduction in the NTD germanium was experimentally studied in (154), (155)).

Because the growth of the Ge crystals is not sensitive to the small nuclear mass fluctuation of the Ge stable isotopes, they are randomly distributed in the semiconductor. Considering also that the absorption cross sections for neutron capture are very small, the "self" shadowing of the neutron flux inside the crystal is negligible. These two conditions, and the use of a thermal neutron source very large respect to the semiconductor size and whose flux vary very slow with the distance, assure the homogeneous doping in the Ge samples.

The NTD process involves epithermal neutron as well (i.e. neutron with energy just above the thermal one), therefore the concentration of dopant atoms is expressed by:

$$N_{dop} = m \cdot i.a. \cdot \frac{N_A \cdot (\sigma_T \Phi_T + \sigma_E \Phi_E)}{M} \cdot t,$$

3-2

where m is the wafer mass, i.a. is the isotopic abundance, M the molar mass of the target isotope, t is the irradiation time, σ_T, Φ_T and σ_E ,Φ_E are the thermal and epithermal neutron capture cross section and flux respectively.

Defining n_A the acceptor concentration and n_D the donor concentration, it is possible to introduce the net-doping concentration N_{net} and the compensation K:

$$N_{net} = n_A - n_D$$

3-3

$$K = \begin{cases} n_A/n_D \text{ for } n_D > n_A \\ n_D/n_A \text{ for } n_A > n_D \end{cases}$$

3-4

The control of the isotopic composition by adjusting the neutron flux, allows the control of the net-doping concentration and the compensation, as well as the conduction type (n or p). The NTD process in Ge creates both acceptors (the majority) and donors (in minor way), compensating dopant. The resultant material is p-Ge with compensation K showing certain scatter because of the role of the presence neutron in the doping.

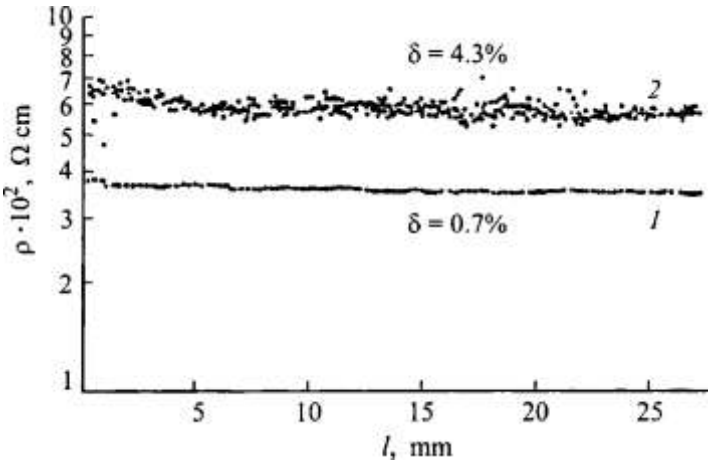

Figure 3-7. Microdistribution of the resistivity of reference resistances prepared from germanium by NTD method (1) and metallurgical method (2) (156).

i.a. [%]	N capture		σ_T [barn]	σ_E [barn]	$T_{½}$	
21	$^{70}Ge+n \rightarrow {}^{71}Ge+\gamma$		3.43	1.5		A
	↳ $^{71}Ga+\nu_e$	EC			11.4 d	
36	$^{74}Ge+n \rightarrow {}^{75}Ge+\gamma$		0.51	1.0		D
	↳ $^{75}As+\bar{\nu}_e$	β^-			83 min	
7.4	$^{76}Ge+n \rightarrow {}^{77}Ge+\gamma$		0.160	2.00		DD
	↳ $^{77}As+\bar{\nu}_e$	β^-			11.33 h	
	↳ $^{77}Se+\bar{\nu}_e$	β^-			38.8 h	

Table 3-2. Reactions occurring in the NTD process for a Ge wafer. In the first reaction Ga acceptor form, while the second and the third lead to donors and double donor respectively. σ_T and σ_E are the thermal and epithermal neutron capture cross section.

The presence in the reactor spectrum of fast, high-energy neutrons gives rise to nuclear transformations that creates radiation defects or even disordered regions in the samples. This problem is difficult to be avoided but it has been show that the production of the radioactive ^{68}Ge and ^{65}Zn is totally negligible for radioastronomy applications of NTD Ge thermistors in composite bolometers (157). Another problem due to the fast neutrons is the radiation damage of the sample, but that can be solved by an appropriate thermal annealing (400 °C for six hours in case of Ge).

The NTD procedure allows to obtain a concentration of dopants per neutron unity flux equal to $2.94 \cdot 10^{-2}$ cm^3 per neutron/(cm^2·s) for Ga and $8.37 \cdot 10^{-3}$ cm^3 per neutron/(cm^2·s) for As (158). Since the doping level of Ge has to be $\sim 1 \cdot 10^{17}$ atoms/cm^3, a very high reactor flux (stable in time and energy) is required for performing the doping in a reasonable time.

The evaluation of the quality of the doped material is possible only after the decay of the activation product ^{71}Ge, and about one year is necessary before the samples can be handled, introducing a delay before understanding if the wafers need more exposure. To overcome this difficulty, the Ge samples are always accompanied by foils of metal with long-lived (n,γ) radioactive daughter nuclei; in this way the neutron exposure of Ge can be determined accordingly with accuracy and uniformity of exposure is achieved.

After the reactor exposure, the radioactive decay period, and the heat treatment to repair the crystal structure, the NTD Ge wafer is cut to obtain pieces of the desired geometry. The thermistor size selected since the Cuoricino R&D (and test in the Cuoricino bolometers and in the following CUORE R&D) is 3x3x1 mm^3. Ohmic contacts are obtained by boron ion implantation followed by annealing and the deposition of a thin (200 Å) Pd adhesion layer and a thicker (1000-2000 Å) Au contact layer. In the Cuoricino thermistors the gold pad are on the two parallel 3x1 mm^2 sides and the electric contact are provided by 50 μm diameter gold wires welded to the gold pads with the ultrasonic ball-bonding technique (159).

The thermistor pad geometry and the wire diameter have been changed from Cuoricino to CUORE-0/CUORE due to technical and practical issues connected to the detector assembly (see Section 3.3.3.2). In the new thermistors (with size almost the same as in Cuoricino) the gold pads are not only lateral but extend also on the thermistor upper face, covering two small, parallel areas of about 0.2x3 mm^2. In this way the bonding procedure can be done not only on the thermistor side, but also in a frontal way. The gold wire chosen for the bonding of the new thermistors has a diameter of 25 μm. This kind of thermistor (sketched in Figure 3-8), with both lateral and frontal pads, is called “wrap-around”. An accurate discussion about the new CUORE-0/CUORE thermistor pad geometry, showing how it doesn’t affect the thermistor performances, can be found in (160).

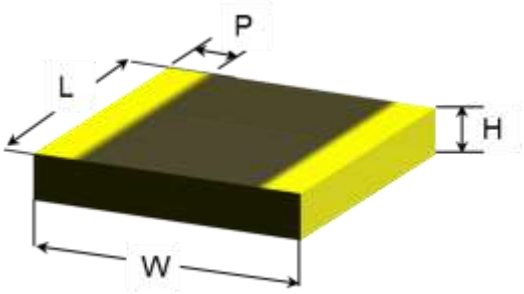

Figure 3-8. Sketch of a CUORE-0/CUORE thermistor. W is the width, i.e. the distance between the lateral gold pads (~2.95 mm); L is the length and (~2.90 mm); H is the height (~0.9 mm); P is the width of the gold pads (~0.2 mm).

All the CUORE-0 thermistors have been produced at LBL with some redundancy (120 samples) from two of the three 30 mm diameter, 3 mm thick Ge wafers composing the so-called #34 series, named 34B and 34C; the three wafers was irradiated together at the University of Missouri Research Reactor (MURR) in 1999 and then the 34B and 34C underwent to further irradiations in 2001.

#34 series belongs to a bigger set of several wafers irradiated for different amounts of time to obtain the desired neutron fluence. Each series was accompanied by a set of neutron fluence monitor isotopes having different half-lives and cross-sections for thermal and epithermal neutrons, for increasing the sensitivity to the neutron energy spectrum at the reactor. Table 3-3 reports the fluence data as reported by MURR or calculated from the monitor isotopes while the monitor isotopes used for the CUORE-0 wafers are collected in Table 3-4 and Table 3-5,. The details of the neutron fluence calculations are given in (161).

34B irradiation data	
Wafer mass [g]	25.6
Fluence requested to MURR [total n/cm^2]	$4.18 \cdot 10^{18}$
MURR reported flux time [h]	36.99
MURR reported flux [n/cm^2/s]	$6.43 \cdot 10^{12}$
MURR reported fluence (flux · hours) [n/cm^2]	$8.56 \cdot 10^{17}$
Thermal neutron fluence derived from monitor foils	$3.65 \cdot 10^{18}$
Epithermal neutron fluence derived from monitor foils	$1.01 \cdot 10^{16}$
Epithermal/Thermal fluences	0.003
Thermal neutron (only) fluence derived from monitor foils	$3.58 \cdot 10^{18}$
Thermal/(Thermal only) fluences	1.02

Table 3-3. Comparison of fluence data for 34B wafers reported from MURR and calculating using both thermal and epithermal neutron flux or considering only thermal fluence from the ^{59}Fe 1099 keV line.

Target	Product	σ_T [b]	σ_R [b]	$T_{½}$	i.a. [%]
^{103}Rh	^{104}Rh	11	80	4.36 m	100
^{58}Ni	^{59}Ni	4.6 (3)	2.20 (20)	$7.6 \cdot 10^4$ y	68.0769 (98)
^{62}Ni	^{60}Ni	14.5 (3)	6.60 (20)	101 y	3.6345 (17)
^{54}Fe	^{55}Fe	2.25 (18)	1.20 (20)	2.73 y	5.845 (35)
^{58}Fe	^{59}Fe	1.3	1.2	44.5 d	0.282 (4)
^{59}Co	^{60}Co	37.18 (6)	74.0 (20)	5.271 y	100
^{55}Mn	^{56}Mn	13.30 (20)	14.0 (3)	2.578 h	100
^{94}Zr	^{95}Zr	0.05	0.3	64.02 d	17.38 (28)

Table 3-4. Thermal and resonant cross sections for neutrons and the half-life of their products via (n,γ) reactions for isotopes used for neutron monitoring for the MURR irradiation.

Target	reaction	product	Q [MeV]	Avg c.s.	$T_{½}$ [day]
^{103}Rh	(n,2n)	^{102}Rh	10		
^{55}Mn	(n,2n)	^{54}Mn	11.5	1.80 e-4	314
^{103}Rh	(n,p)	^{103}Ru	14	114.8	39.27
^{58}Ni	(n,p)	^{58}Co	1.5	9.00 e-2	72
^{54}Fe	(n,p)	^{54}Mn	< 0	6.5 e-2	314

Table 3-5. Reaction for the fast-neutron monitors.

Measurements performed at LNGS also show that the residual activity of the NTD thermistors become fully tolerable in an experiment with thermal detectors already a few months after irradiation (162).

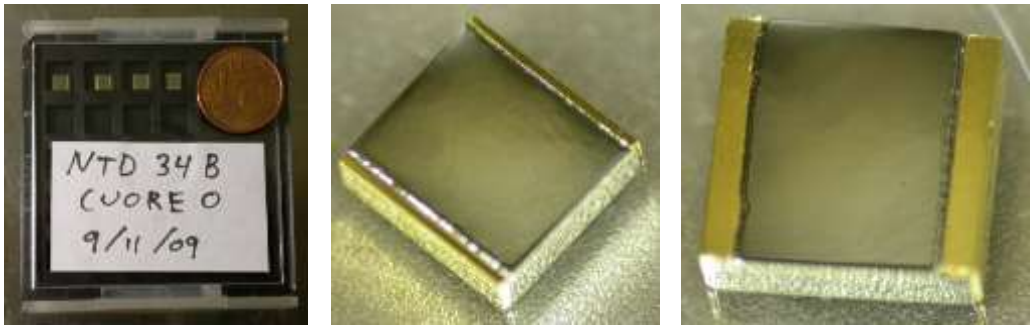

Figure 3-9. A box of CUORE-0 thermistors (left), a sample of 34B CUORE-0 thermistor (middle) and a sample of 34C CUORE-0 thermistor (right).

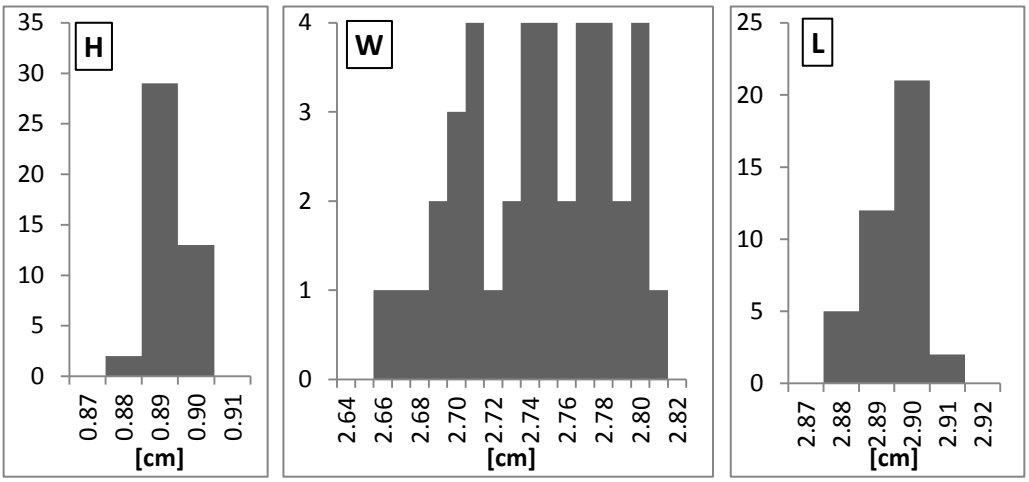

Figure 3-10. Spread in the size of the 34C CUORE-0 NTDs. The average values of the height, width and length are: <H> = 0.893 cm; <W>=2.745 cm; <L> = 2.895 cm. For the meaning of H, W, L, see Figure 3-8.

The 34C wafer was cut firstly in thermistors with size slightly smaller than the CUORE-0 specifications, to optimize the NTD yield of the wafer. Unfortunately this operation resulted in worse tolerance on the thermistor dimensions, therefore the following wafer, the 34B, was cut strictly in accordance with the CUORE-0 requirements, i.e. 3.0x2.9x0.9 mm^3, where the first number refers to the pad distance, and with ±75 μm uncertainty on each dimension. A picture of 34B and 34C thermistor samples is displayed in Figure 3-9 while the spreads in the 34C thermistor dimensions are collected in Figure 3-10.

The nuclear reactor selected for irradiating the CUORE wafers is different from the one used for past irradiation of Cuoricino and CUORE-0 wafers; the new facility is the Massachusetts Institute of Technology Nuclear Research Laboratory (MIT-NRL) and it was selected because it has a larger neutron flux with respect to the MURR ($1.69 \cdot 10^{12}$ neutrons/cm^2/s instead of $5.5 \cdot 10^{12}$ neutrons/cm^2), it can accommodate larger wafers (four 65 mm diameter 3 mm thick Ge wafers in one can) and make them rotate during the run to guarantee uniform irradiation, and the fast neutron flux is 1000 times lower than at MURR. Also in this case the incoming neutron fluxes are controlled by heavy metal foils monitors.

The Ge wafers for CUORE NTDs are 65 mm diameter, 3.2 mm thick and have a mass of 57.37 g; from each wafer about 700 3x3x1 mm^3 thermistors will be cut: the goal is to produce about 2500 thermistors having homogeneous properties, for a total number of 3.6 wafers to be irradiated. The starting high-purity Ge wafers for CUORE are different than those used for the Cuoricino and CUORE-0 NTDs, and they have likely two orders of magnitude less impurities with respect to the previous wafers.

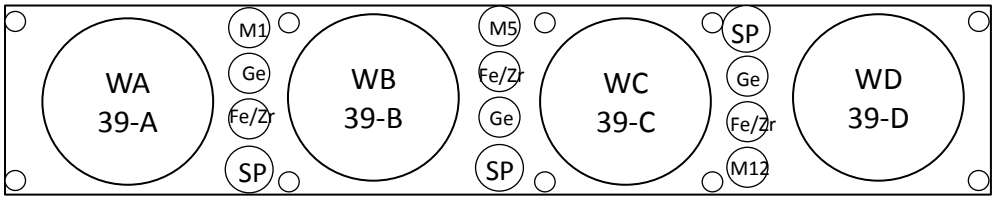

Figure 3-11. Sketch of the wafer holder for Ge wafer the irradiation at MIT-NRL. The location of the wafers (large circles) and the monitor isotopes (small circles) are shown.

Series	MIT-NRL reported fluence [n/cm^2]	Fluence measured from monitors [n/cm^2]	Monitor/MIT-NRL
#39	$3.586 \cdot 10^{18}$	$3.72 \cdot 10^{18}$	1.04
#40	$4.197 \cdot 10^{18}$	$4.30 \cdot 10^{18}$	1.03

Table 3-6. Comparison of the fluence data for #39 and #40 series from MIT-NRL and from the monitors.

Two sets of four CUORE wafers, named #39 and #40, were irradiated together between March 2006 and June 2007 in five steps to reach the 86% fluency of CUORE-0 wafers, then the #40 underwent two additional irradiation to reach 100%. A sketch of the holder for the irradiation of the wafer at MIT-NRL is depicted in Figure 3-11 while Table 3-6 collect the fluence data of both series.

Radioactivity measurements of the #39 and #40 wafers were performed at the Low Background Facility at Oroville in the first half of 2008. A spectrum from these counting is shown in Figure 3-12. #39 wafers were etched once with HF/HNO_3 before the measurement, #40 ones were etched twice. ^{68}Ge (1077 keV line from ^{68}Ga decay) and ^{65}Zn (1115 keV) were observed, indicating the presence of fast neutrons. There are also peaks associated with ^{110m}Ag (657 keV) and ^{60}Co (1173 keV); these surface contaminants are removed with etching.

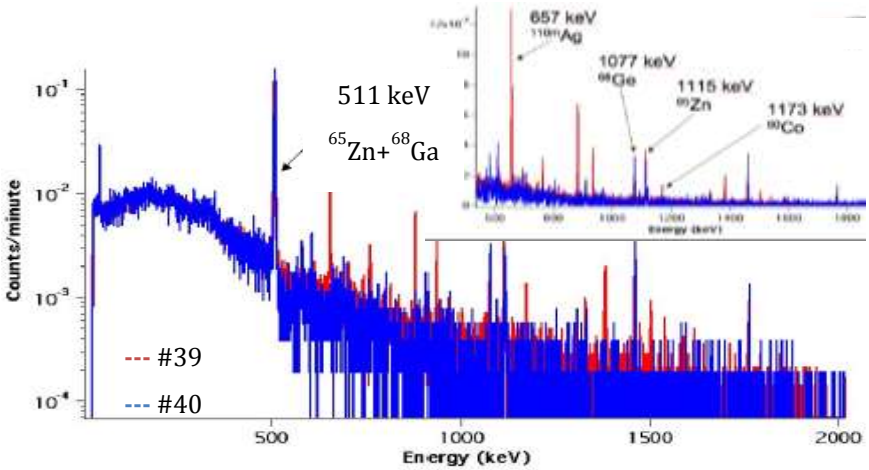

Figure 3-12. Spectrum from the radioactivity measurements of #39 and #40 wafers. In the inset, only the region above 600 keV is shown. The 1077 keV ^{68}Ge line, the 1115 keV ^{65}Zn line, the 657 keV ^{110m}Ag line and the 1173 keV ^{60}Co line are observed.

The fixed dimensions for the CUORE thermistors are the following: the width ranges between 3.040 and 2.870 mm, the length is 2.900±0.050 mm and the height is 0.9±0.050 mm. The gold pads are 0.200±0.020 mm large and the angle tolerance is 90±0.025 deg, while the planarity (with respect to two opposite sides) is ±0.010 mm. The width has a lower tolerance with respect to the other dimensions for improving the yield of thermistors produced from a single wafer. In fact the wafers are crowned and requiring a higher precision implies that the 60 mm diameter wafer should have to be cut in half along its ~3 mm thickness to make two wafers of <1.5 mm thick, that would then be ground and polished to 0.9 mm thickness, with a loss of about 1/3 of the material. The reason for quoting the as a range instead of a tolerance (2.955±0.085 mm) is due to the fact that a Gaussian width distribution centred at 2.955 mm is not expected because the shape of the wafer: the new NTDs are supposed to have mainly a width close to the lower bound of the range.

3.3.1.2. Characterization

The parameters R_0, T_0 and γ, appearing in the VRH law (Eq. 3-1), must be experimentally determined for each thermistor at its working temperature. This is done by coupling the thermistor to a low temperature heat sink with a heat-conductive epoxy and connecting it to a read-out system like the one shown in Figure 3-13. When a bias voltage V_{bias} is applied, a current flows through the device and, measuring the output voltage from the thermistor, it is possible to collect a V-I curve, usually called load curve (this procedure is described in detail for Si thermistors in (163)).

The load curve shows a linear behaviour at low biases but, increasing the current, the static resistance of the thermistor tends to decrease because the device undergoes heating for the injected electrical power. In fact, the bias applied to the thermistor creates a power P dissipated in the absorber through the thermal conductance, and therefore the absorber will reach the temperature:

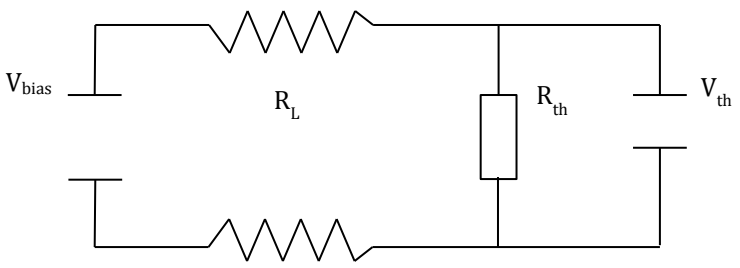

Figure 3-13. A sketch of the electronic readout system for the thermistor characterisation.

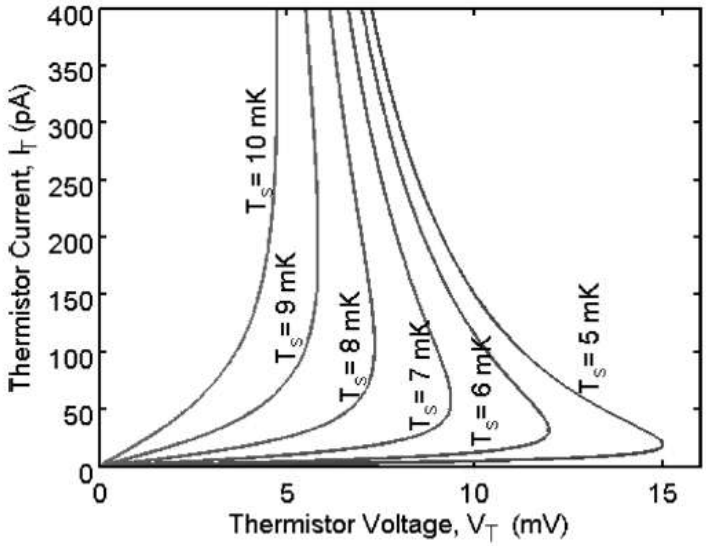

Figure 3-14. Simulated I-V curves at different temperatures of a Ge NTD thermistor having T_0 = 3.3 K, R0=1.15 (164).

$$T_B = T_0 + \frac{P}{G},$$

3-5

where T_0 is the heat sink temperature.

This decreases the slope of the I(V) curve that, under certain condition, presents a maximum voltage (called inversion point) and then change from positive to negative. Increasing again V_{bias}, an oscillating behaviour of the load curve appears, with the voltage remaining close to the inversion point. The self-heating phenomenon leading to the non-linearity of the curve is known as electrothermal feedback. The optimum operating biasing current occurs where the derivative dI/dV increases rapidly with increasing V_{bias}, maximizing the signal to noise ratio. The resistance is obtained from the linear part of the load curve the thermistor, and combining fit to a set of load curves at different base temperatures the R_0 and T_0 parameters of each thermistor are determined.

The thermistor electric signal for a temperature variation ΔT is given by:

$$|\Delta V| = V \cdot A \cdot \frac{\Delta T}{T},$$

3-6

where A is the thermistor sensitivity defined in Eq. 2-21 and Eq. 2-22.

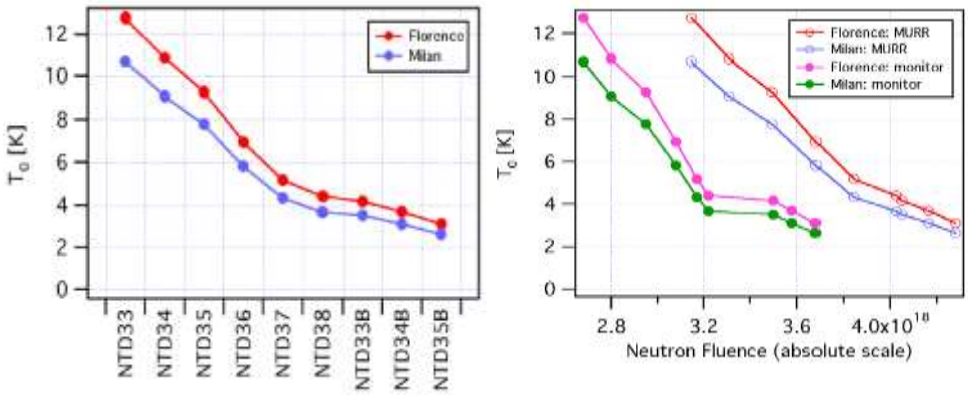

Figure 3-15. Left: T_0 measured by Milan and Florence for the NTD series irradiated at MURR. Right: T_0 measured by Milan and Florence as a function of the neutron fluence, as quoted from the MURR and calculated from the monitors.

The characterization of the 34B thermistors was done at the cryogenics laboratories in the universities of Milan and Florence, as happened also for the Cuoricino series and for the others irradiated at MURR. The two measurements resulted in two different absolute scales, but each measurement is consistent in of them, as can be seen from Figure 3-15. The results of both characterizations are collected in Table 3-7. For having a unique value for the VRH parameters a new characterization is required, to be performed with a general, reliable, temperature scale. This work has been done in the context of this thesis, and will be discussed in Chapter 4.

The thermistors from #39 and #40 series were characterized by the Florence and Como groups in 2008. The measurements confirm a different thermometry, already noticed in the past. However, in both measurements, the wafers resulted or too resistive and sensitive (#39), meaning that the fluence was too low or, on the contrary, too conductive and flat (#40), corresponding a too-high exposition, with respect to the CUORE goal. The resulting T_0 for different thermistor samples measured are collected in Table 3-8.

34B series characterisation	T_0 [K]	ρ_0 [Ω·mm]
Milan	3.111	1.04
Florence	3.68	0.869

Table 3-7. Results of the characterisation of the 34B series performed by the Milano and Florence group.

	T_0 #39 [K]			T_0 #40 [K]		
Milan	6.69	6.22		1.60	1.59	1.76
Florence	7.826	7.740	8.165	2.081	2.329	2.227

Table 3-8. T_0 resulting from the characterisations of the #39 and #40 series performed by the Milan and Florence group.

Figure 3-16 shows the average T_0 measured by the two different groups versus the neutron fluence obtained from the monitors. The latest three points (the "B"s) deviate from the expected T_0 behaviour. The straight lines correspond to a fit performed using the first three points and the CUORE series (labelled in bold in the graph). The change in the slope can be accounted by the epithermal content in the MURR flux varying in time, i.e. if the epithermal content increased for #36-#38 series and then for 33B-35B. The effects of different epithermal content in the flux can be appreciated in Figure 3-17 that shows how the expected N_{net} for the series irradiated at MURR and at MIT-NRL changes with the epithermal content.

Calculating the 34B neutron fluence from the fits gives $3.40 \cdot 10^{18}$ and $3.42 \cdot 10^{18}$ using the Florence and the Milan data respectively (they differ of 1%). Compared to this new 34B fluence, the #39 series is at 90% doping of 34B, while #40 series results to be 4% over-doped.

This discrepancy can be attributed to the neutron fluence measurements of the monitor from the MURR irradiation. Whatever the reason, in order to have the requested doping, a top-off procedure has been adopted to correct the doping produced in the first neutron exposition for #39 wafers. A new characterisation for the new doped samples is mandatory and it has been performed during this thesis work. The results are presented in Chapter 4.

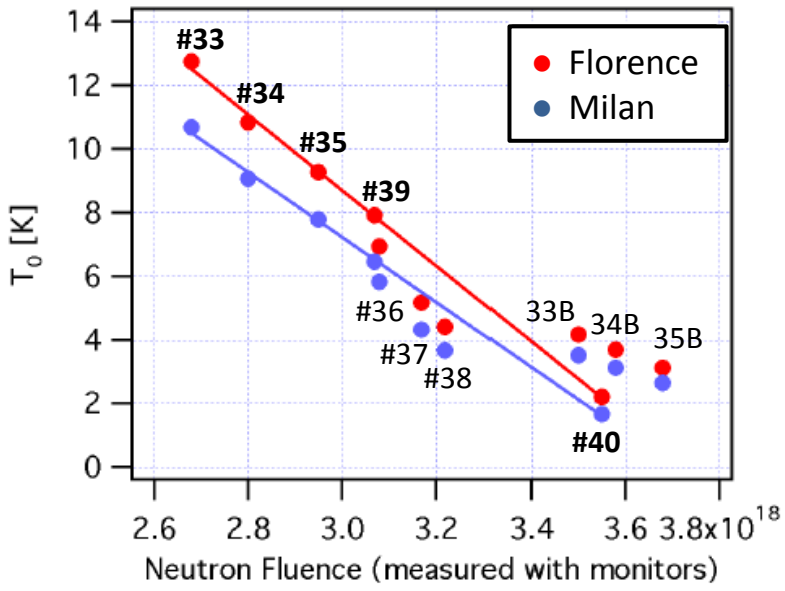

Figure 3-16. T_0 as a function of the neutron fluence measured by monitors. The lines correspond to the fits of the first three points (#33, #34, #35) together with the CUORE series (#39, #40) –all the points are labelled in bold. The fitted function is $T_0=a+fluence \cdot b$ and the parameters obtained are $a=44.315 \pm 0.887$, $b=-1.1869 \cdot 10^{-17} \pm 2.93 \cdot 10^{-19}$ for the Florence data and $a=37.907 \pm 0.719$, $b=-1.0225 \cdot 10^{-17} \pm 2.38 \cdot 10^{-19}$ for the Milan data.

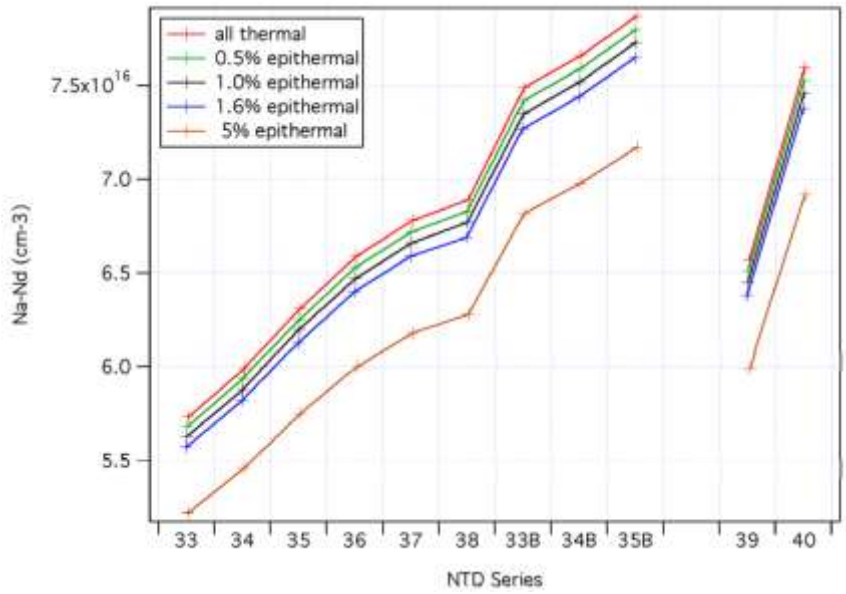

Figure 3-17. N_{net} doping for 0.5%, 1.0%, 1.6% and 5% epithermal flux for the wafers irradiated at MURR and at MIT-NRL.

3.3.2. Heaters

One of the critical points to deal with when operating a bolometric experiment for long periods is to maintain the detectors in conditions as stable as possible. Unfortunately the complicated cryogenic set-up required for operating the detectors at low temperatures shows intrinsic temperature instabilities: as a consequence, the baseline changes, a spread of the pulse amplitudes is generated and the energy resolution is worsened; a heat-sink temperature variation of 1/10000 is enough to affect this crucial parameter (165).

The relative temperature variations of the detector can be seen as a consequence of the relative temperature variations of the heat sink to which it is connected (166), according to:

$$\frac{dT_d}{T_d} = \frac{dT_{hs}}{T_{hs}} \cdot \left(\frac{T_{hs}}{T_d}\right)^{\beta},$$

3-7

where T_d and T_{hs} are the detector and heat sink temperature respectively, the differentials refer to small variations and β is the exponent appearing in the law:

$$G = T^{\beta-1},$$

3-8

expressing the temperature dependence of the thermal conductance G between the detector and the heat sink, and it is expected to be ~4 for a TeO^2 crystal coupled to the bath with PTFE pieces.

A specific method for the stabilization of each detector response is therefore required: the simplest idea is to use a pulser delivering periodically a fixed amount of energy in the detector, with a pulse-shape as similar as possible to the real signal (166). The study of the variation of the detector response for the same energy deposition, due to the cryogenic instabilities, can be used to correct off-line their effects.

The choice for the CUORE stabilisation is to adopt a heating element, named simply heater, as energy pulser, that, once thermally coupled to the crystal, is able to deliver reference Joule pulses in the detector.

The heater-based pulser is operated as follows: square voltage pulses are injected into the devices with a programmable pulse generator, tuning the amplitude and the time width (of order 1 ms, much shorter than the typical thermal signal rise time in CUORE detectors) in order to develop a few MeV thermal energy in the heater. The produced pulses can be equally spaced in time, with rates and amplitude tunable according to the experimental requirements, and they can be easily identified by software flags.

In order to inject a stable, almost instantaneous, reference amount of Joule power in the detector, the heater should have some specific characteristics: its resistance must be reasonably independent of temperature and applied voltage, and it must be higher than the one of connection wires (the range suitable for CUORE is from ~10 kΩ to ~10 MΩ); its heat capacity must be negligible compared to that of the detector; the relaxation time of the heat pulse delivered into the crystal must be much shorter than all the other typical thermal constants; and the signal formation due to Joule heating must simulate as much as possible a particle interaction, to assure that the pulse amplitude dependencies on time, baseline level and other operation conditions are the same for the two processes.

3.3.2.1. Production

The fabrication of the CUORE-0/CUORE heaters started in the frame of an R&D project for the realization of implanted silicon thermistors, to be used for the developement of microbolometers, in the context of a collaboration between the Milano bolometer group and the Italian research center on semiconductors Istituto Trentino per la Cultura (ITC-irst).

Steady resistances with the required values (from ~10 kΩ to ~10 MΩ) can be realized by means of semiconductor materials doped well above the Metal-to-Insulator transition

(127). Furthermore the resistive structure, which usually consists in a long, narrow, thin meander necessary to achieve reasonably high resistances, must be integrated in a small, easy to handle chip and finally thermally connected to the detector in a similar way as that adopted for the thermistors.

According to standard procedures, silicon thermistors fabricated by means of the silicon planar technology for neutrino mass experiments (163) are usually realized in form of wafers, each containing a fixed number of thermistors. This layout includes also suitable test structures, grouped in a so called "test strip", besides the devices of interest, allowing the control of the fabrication process and to measure room-temperature electrical parameters. The whole wafer, as well as the contact diffusion structure, is fabricated by applying the standard ion implantation technique, as below summarized (for further details see (167)):

At the end the sensitive portion of the ion implanted device consists in a kind of resistive meander, whose geometry can be adapted in order to vary the resistance R, once the resistivity ρ has been fixed by the doping level, taking into account that:

$$R = \frac{l}{w} \cdot \frac{\rho}{S},$$

3-9

where l and w are the length and the width of the doped region and S is the thickness of the doped area.

The CUORE heaters production, made at ITC-irst, consists in 15 wafers, each with 36x36 single elements, made according to a detailed procedure detailed described in (167) starting from a p-type monocrystallin silicon grown with the Czochralski method and using phosphorus as the doping element (the critical concentration for the Si:P system is $3.74 \cdot 10^{18}$ atoms/cm^3).

The single heater is a 2.33x2.4x0.52 mm^3 device provided with four Al pads, allowing to choose its resistance among four values (from a minimum of 100 kΩ to a maximum of 300 kΩ), selected by contacting different pairs of pads. In fact, since the whole meander structure has been realized with the same implantation procedure, it is expected to exhibit a uniform resistivity at low temperatures. As a result the pad-to-pad resistance should equal to 1/3 of the total value measured between the two pads placed at the extremities of the device, being the resistances between two adjacent pads equal. A scheme of the single heater is depicted in Figure 3-18 while pictures of some samples are collected in Figure 3-19.

The complete fabrication process, valid for all the 15 wafers, was identified during the previous test. The only still varying parameter is the implant dose, according to which the

wafers are split into three groups, as shown in Table 3-9. Therefore it is still possible to choose the best suited resistance value among the three groups.

The CUORE heater production is the first example of a massive fabrication of such devices using a standard procedure; because there are regions in the wafers in which the resistance varies strongly, a test of each heater that will be used in CUORE bolometers is mandatory, in order to have a sample of 2000 heaters as homogeneous as possible, as required for the implementation of the electronic system and the related software.

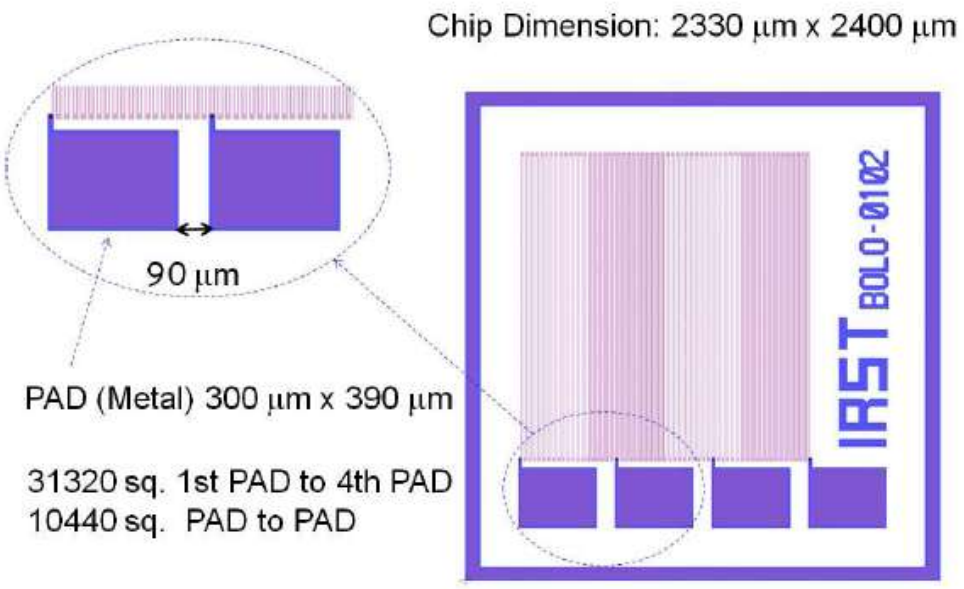

Figure 3-18. The structure of a heater of the CUORE production made at ITC-irst. The resistive meander is visible and the dimension and the ratio length/width are reported (165).

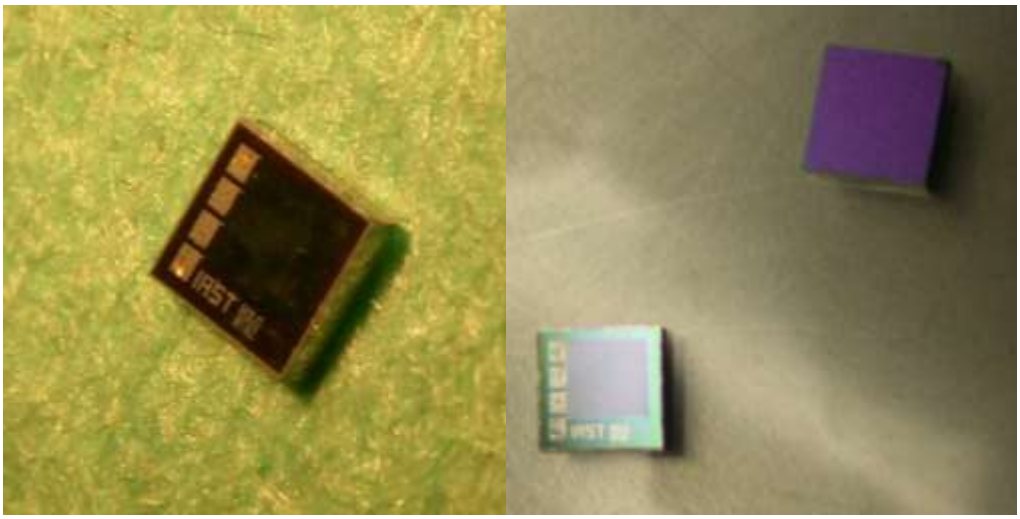

Figure 3-19. Samples of Si heaters from the CUORE production.

Implant	Dose [ions/cm^2]	Wafers
P 1/3	$5 \cdot 10^{15}$	1, 2, 3, 4, 5, 6, 7
P 2/3	$6 \cdot 10^{15}$	8, 9, 10, 11
P 3/3	$4 \cdot 10^{15}$	12, 13, 14, 15

Table 3-9. Splitting of the 15 CUORE wafers according to the implant dose.

3.3.2.2. Characterisation

The characterization of the CUORE heaters has to probe that the resistance of each heater, besides to be in the proper value range (~100 kΩ), is stable with temperature variations in conditions close to the cryogenic working temperatures of the bolometer, and also the uniformity of the implant by measuring the pads-to-pads low temperature resistances.

A mapping of the wafer areas is performed at ITC-irst immediately after production, by measuring the resistance values at room temperature to quantify the spreads of the resistance values throughout the wafer itself. An example of this mapping is shown in Figure 3-20.

Thanks to this room temperature preliminary characterisation it will be easier to select the heaters from "good" regions of the wafers. Nevertheless measuring two thousands of devices at temperatures of about 10 mK remains a huge and expensive work, in terms of money and time. Fortunately, exhaustive studies carried out in (167) pointed out a strong correlation between the results obtained at 77 K (the temperature of liquid nitrogen) and at lower temperatures: the correlation allowed determining a heater selection procedure based upon the measurements performed at liquid nitrogen temperature, speeding up the entire characterization process, that has been entirely carried out by the Como group between 2007 and concluded in 2010. Details of the procedure can be found in (168).

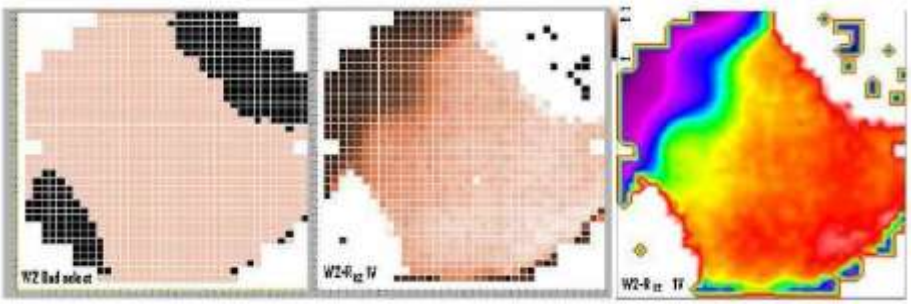

Figure 3-20. Examples of wafer mapping realized at ITC-irst using the results of room temperature characterisation: "bad-select" map, "shades" map and coloured map for wafer 2, measuring the heater resistances between pad 1 and 2 with 1 V of bias voltage (165).

3.3.3. Semiconductor coupling

To complete the description of the CUORE-0/CUORE single module it is necessary to deal with the connection between the various elements of the bolometer, i.e. with the mechanical and thermal link of the Ge thermistor and the Si heater with the absorber and their electric coupling. These connections have been changed a lot with respect to Cuoricino, and the difference between the past and the future approaches will be discussed in the following sections.

3.3.3.1. Chips-to-absorber coupling

The connection of both the thermistor and the heater to the TeO_2 crystal is made with a bi-component epoxy distributed in matrices of spots; for the thermistor the matrix is composed by nine dots, while the heater, being smaller, accommodates only five dots. Each glue spots has a diameter of about 750 μm and a height of 50 μm.

The distribution in separate dots compensates the differential thermal contractions between the material of each sensor and TeO_2, so that no fractures or detachment of the elements happen at low temperatures. Examples of gluing can be found in Figure 3-21.

This kind of coupling, as well as the choice of the glue (based on its low radioactivity and good thermal conduction) has been established since Cuoricino experiments. However in the construction of Cuoricino the gluing of the chips to the absorber was made manually, with the help of proper tools, and the resulting variability in quality led to a lack of reproducibility in the signal shape and detector performance; in the CUORE-0/CUORE instead it will be done thanks to a devoted semi-automatic line that has been designed and developed during this PhD work: a deep discussion about the requirements and the process of the bolometer element coupling is carried in Chapter 6.

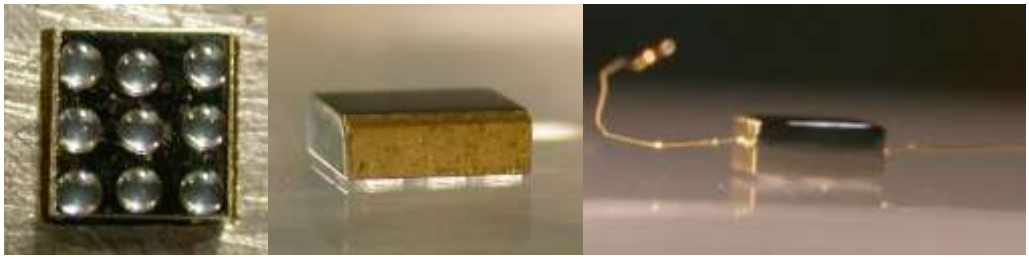

Figure 3-21. Examples of thermistors glued with nine glue dots made with a nine tip matrix.

3.3.3.2. Electric connections

In the Cuoricino and in the CUORE experiments the electric contacts are obtained with gold wires ball-bonded on the gold pads of the thermistors and on the aluminium pads of the heater. These connections are also thermal links to the heat bath, as the wires are then connected to Cu parts linked to the holder for electric read-out.

The ball-bonding technique is widely used in the microelectronic industry to perform the connection of metal wires (159). The process is allowed by the appropriate definition of a set of parameters, mainly force, power, time, temperature and ultrasonic energy, which are different according to the properties of the metallic interface. During ball-bonding, the wire is fed through a ceramic capillary set on the mobile part of a bonding machine; a gold ball with diameter ranging from 1.5 to 2.5 times the wire diameter is first formed by melting the end of the wire through electronic flame-off: its consistency, controlled by the flame-off and the tail length (the portion of wire elongating out of the capillary), is critical for successful bonding.

The so-called free-air ball is brought into contact with the bond pad. Adequate amounts of pressure, heat, and ultrasonic forces are then applied to the ball for a specific amount of time, forming the initial metallurgic weld between the ball and the bond pad; the ball bond itself is deformed into its final shape. The connection is favoured by the inter-diffusion of atoms in the interface.

The main difference between the Cuoricino and the CUORE approach to bonding is that in the past the gold wires were connected to the chips before their gluing onto the absorber, while for CUORE the bonding process has to be done after the gluing, and the best way for doing that is having thermistors with pads extending also in their upper face, to allow performing a frontal bonding, as anticipated in Section 3.3.1.1.

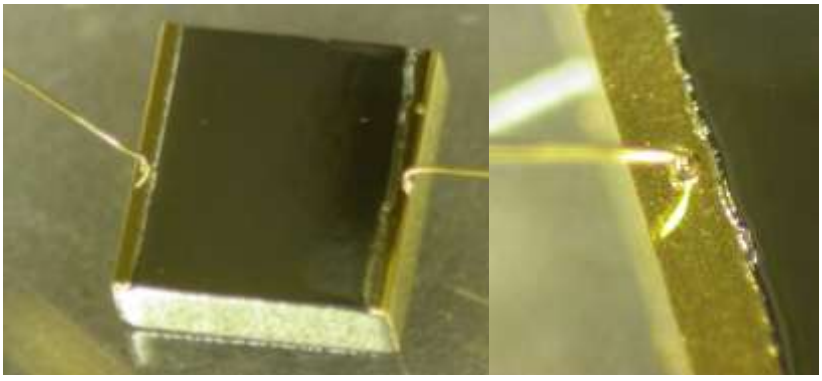

Figure 3-22. A wrap-around thermistor provided with frontal bonded gold wires.

This changing has several reasons: one is to make easier the gluing procedure, having no delicate wires to deal with; second, it is difficult to access the lateral gold pad once the thermistor is glued on the crystal, being not enough room for the ceramic capillary to work: in this case fixing a broken wire bond requires disassembling the tower to remove the affected crystal, removing the thermistor from the crystal, repairing the bonds on the thermistor, regluing the it to the crystal, and then rebuilding the tower.

The other main difference between the Cuoricino and the CUORE bonding is the gold wire diameter, that has been reduced from 50 μm to 25 μm. The reasons of this choice are due to the new way the gold wires are connected to the electronic read-out in CUORE. In Cuoricino the gold wires were manually inserted and crimped in Cu pins placed in the holder toward the thermistor itself. In this way the gold wires were about 1.5 cm long and disposed along an almost straight line. On the contrary the CUORE wiring is realised through special Cu tapes, named Flexible Flat Cable (FFC), glued to wire trays connected to the side of the entire tower: the gold wires are bonded directly on the Cu pads of the tape, performing an about 3 cm long arc; it is difficult to bond thick (50 μm) wires with this shape because their act as springs with high restoring forces, breaking the extremely delicate Au-Cu bonding. For this reason the CUORE-0/CUORE wires will be 25 μm diameter.

The details of the CUORE bonding procedure are given in Section 3.6.1.2.

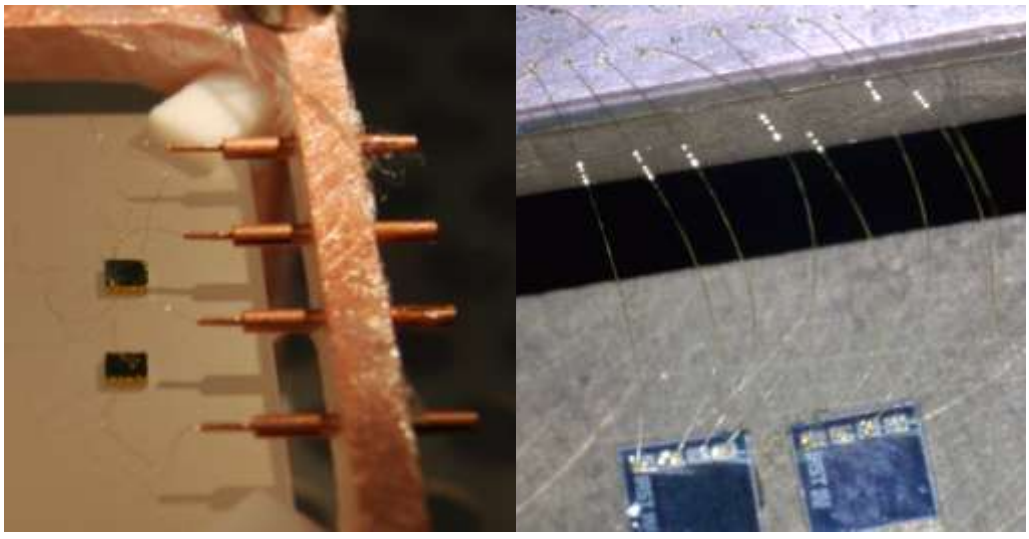

Figure 3-23. (Left) A Cuoricino style wiring: the 50 μm gold wires of the thermistors, attached before the gluing, are inserted and crimped in the small copper pins, which are on they turns connected to the copper holder. (Right) A CUORE-style wiring: the 25 μm gold wires are bonded to the heaters after their gluing and have to reach the Cu pad of the FFC stepping over the frame. The different lengths of the wire path can be observed.

3.4. The holder

The two main elements composing the Single Module holder are the copper structure, acting as heat sink, and the PTFE elements, devoted to the connection between the crystal and the heat sink. Because both these component touch or face the crystals, a huge attention is paid to their cleaning.

3.4.1. Copper structure

The copper holder for the Single Module of the CUORE detector is made of a bottom and a top frame spaced by four columns. When more than one module are assembled together, the copper frames will be in common between two adjacent floors. The frame is squared, 122 mm side, and it has in each corner a plug for placing the PTFE pieces (see Figure 3-24).

Copper is one of the larger materials by mass present in CUORE. Most of the copper is an Oxygen Free Electrolytic (OFE) alloy produced by Norddeutsche Affinerie (NA). Its radioactivity content was measured in LNGS to be $<1.6\cdot10^{-11}$ g/g in Th and $<4.3\cdot10^{-12}$ g/g in U. The base-temperature components will be machined from Electronic Tough Pitch (ETP1) alloy, a.k.a. NOSV. The NOSV copper has been chosen for its low hydrogen content, and it exhibits extremely low contamination levels (already verified several years ago by the Heidelberg group (169)) with upper limits of $2.4\cdot10^{-12}$ g/g for Th and $1.3\cdot10^{-12}$ g/g for U.

In Cuoricino a large fraction of the background in the ROI is ascribed to a deep (>5 μm) surface contamination in the copper of the mounting structure. This contamination, due to U or Th or Pb and their daughters, does not have a strong signature. Its most evident effect is the presence of a flat background in the energy spectrum extending from above the 2615 keV ^{208}Tl line up to 4 MeV, where the spectrum starts being dominated by alpha peaks.

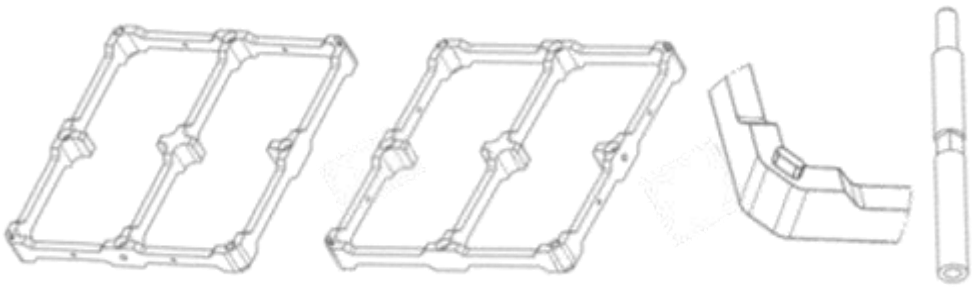

Figure 3-24. Drawings of the CUORE frames. From left to right: lower and upper frame for a four-crystal floor, detail of the plug for the PTFE pieces and a column.

For this reason different copper surface-treatment strategies has been pursued and final test to fix the cleaning procedure for CUORE copper took place in 2009–2010 with the Three Tower Test (TTT) (170).

The TTT detector consisted of three stacked 12-crystal towers separated from one another by copper shields, showed in Figure 3-25. The surfaces of the copper parts in each tower were cleaned using different procedures:

- ✓ the copper for the uppermost tower (T1) was treated following the procedure that produced the best result in previous R&D tests: the copper pieces were cleaned with soap, treated with H_2O_2+H_2O+citric acid and wrapped with seven layers of polyethylene.
- ✓ the middle tower (T2) was cleaned at LNGS by a new chemical process, starting with simple soap and water, followed by electroerosion with 85% phosphoric acid, 5% butanol, and 10% water, followed by chemical etching with nitric acid, and finally passivation with H_2O_2+H_2O+ citric acid.
- ✓ the copper for the lowermost tower (T3) was cleaned at Legnaro National Laboratory (LNL, Italy) with a procedure consisting of tumbling, electropolishing, chemical etching, and a magnetron plasma-cleaning technique.

The TTT was installed in the former Cuoricino cryostat and collected data from September 2009 through January 2010. The result of the TTT measurement was that the copper treatment adopted for T1 and T3 gave similar results, while the counting rate measured in T2, indicating that this technique is less effective in reducing copper surface contamination.

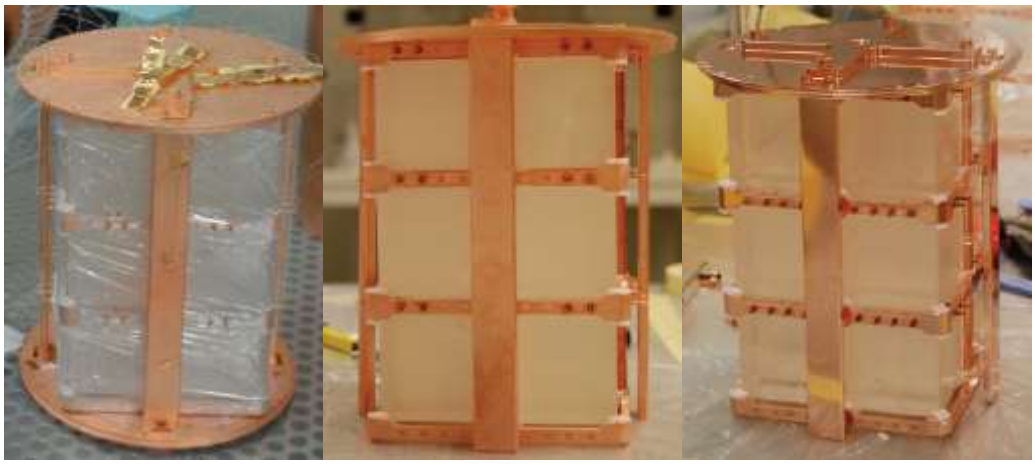

Figure 3-25. The three towers. From left to right: T1, wrapped in polyethylene, T2 cleaned at LNGS, T3 cleaned at Legnaro National Laboratory.

As a consequence, after the machining, the copper of the CUORE detector components will undergo the six stages of the Legnaro "ultra-cleaning" procedure, which aim is essentially to remove a tiny layer of the component surface, including dirt and impurities due to handling and machining. To preserve the tolerances of certain parts of the components (necessary for assembling the structure but not facing the crystals) specific protections were developed at Frascati National Laboratory of INFN.

A significant effort was dedicated to the logistics of the operation, as Cu is easily activated by cosmic rays: four months of exposure to cosmics is the maximum affordable before Cu activation is no longer negligible, so the parts must be stored underground whenever not undergoing machining or cleaning.

For this reason, some room has been reserved for the CUORE copper in the Baradello underground site near Como.

3.4.2. PTFE supports

The PTFE blocks supporting the crystals inside the Cu structure play an important role. The pieces must be made to precise dimensions to ensure that the correct pressure is placed on the crystals when cooled inside the cryostat.

Since the PTFE blocks will touch the crystals, they must be made from specially selected PTFE and their surfaces must be perfectly decontaminated before use. Before the machining the PTFE have been checked with neutron activation analysis obtaining the following upper limits for its radioactive contaminations: $1.1 \cdot 10^{-11}$ g/g for ^{232}Th and $3.0 \cdot 10^{-11}$ g/g for ^{238}U. All the blocks received from the manufacturer have been cleaned according to a devote protocol and stored under nitrogen at LNGS.

3.5. Modelling the CUORE bolometers

Section 2.4 focused on an overview of the bolometric technique with large-size absorbers. Now that the characteristics of the CUORE bolometers have been introduced, the composite modelling can be referred to this specific application. The thermal network corresponding to the composite picture and updated to the elements of the CUORE basic bolometer is sketched in Figure 3-26. The reference node of the model is the heat bath, here constituted by the copper holder, at temperatures of order ~10 mK during the operation of the detector. Thermal conductances G_j and heat capacities C_j all have the forms of power laws in T, as described by Eq. 2-26 and Eq. 2-29 with experimentally determined coefficients g_j

and c_j, and the other quantities required for a full definition of the CUORE basic bolometer are listed hereafter. Most of them have been measured for Cuoricino-like single module but are still valid for the CUORE-bolometers.

- ✓ The thermistor characteristic curve of the thermistors, expressed in terms of the VRH parameters R_0, T_0 and γ (see Eq. 3-1), that have to be experimentally determined, as stated in Section 3.3.1.2. Being the characterisation of the CUORE-0 and CUORE thermistor one of the subject of this PhD thesis the results will be presented in Chapter 4.
- ✓ The TeO_2 crystal's specific heat (C_{abs}). Dedicated measurements performed in Florence (139) confirmed the good agreement of its temperature dependence with Debye's law, and determined the Debye temperature as T_D=232 K.
- ✓ The crystal-to-heat bath thermal coupling ($G_{abs\text{-}bath}$), provided by the set of PTFE holders screwed to the Cu support structure. The measurement made in Milan (171), and specific to the Cuoricino design in terms of contact surface, gave the result:

$$G_{abs\text{-}bath}\,[W/K] = 4\times10^{-5}\cdot(T[K])^2 \qquad 3\text{-}10$$

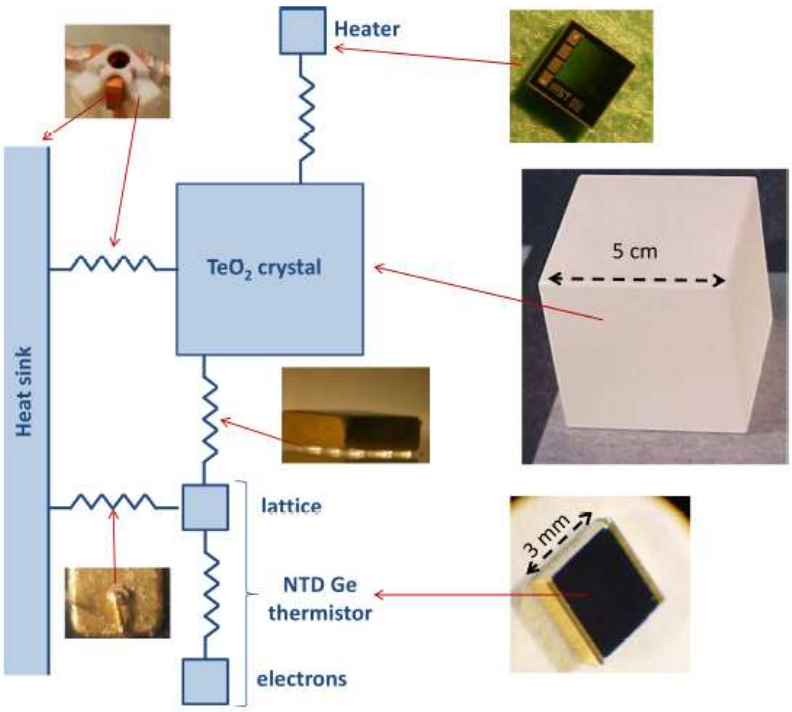

Figure 3-26. Schematic diagram of a CUORE bolometer, with a photo of each of its components.

- ✓ The thermal conductance of the glue spots in the thermistor/absorber interface ($G_{th\text{-}abs}$). The conductance measured for the bi-component epoxy used and for the peculiar geometry of its deposition is (171):

$$G_{th\text{-}abs}\ [W/(K\cdot spot)] = 2.6\times10^{-4}\cdot(T[K])^3 \qquad 3\text{-}11$$

- ✓ The specific heat of the lattice of the thermistors (C_{lat}), corresponding to the Ge specific heat:

$$C_{lat}\ [J/K\cdot mm^3] = 3\times10^{-9}\cdot(T[K])^3 \qquad 3\text{-}12$$

- ✓ The thermistor lattice-to-heat sink thermal coupling. It is due to the interface between Ge, which constitutes the sensor's bulk material, and Au, in form of side pads for signal read-out. The conductance is proportional to the single pad area:

$$G_{pad}\ [W/K\cdot mm^2] = 0.8\times10^{-5}\cdot(T[K])^{2.4} \qquad 3\text{-}13$$

- ✓ The thermal conductance in the electron-phonon uncoupled systems ($G_{ph\text{-}el}$). It is internal to the thermistor itself and its estimation is (171):

$$G_{ph\text{-}el}\ [W/K\cdot mm^3] = 7.8\times10^{-2}\cdot(T[K])^{4.37} \qquad 3\text{-}14$$

- ✓ The specific heat of the thermistor electron system (C_{el}), chosen to account for the observed rise times of thermal pulses and not measured directly:

$$C_{el}\ [J/K\cdot mm^3] = 1.1\times10^{-9}\cdot(T[K]) \qquad 3\text{-}15$$

- ✓ The background power acting on the crystal and on the electron system of the thermistor. No direct experimental measurements on these parameters have been performed; however, a few pW are seemed a reasonable value for the background power in the absorber, while fractions of pW are assumed for the electron system of the thermistor.

Model parameter	Value
C_{abs}	$2.3 \cdot 10^{-3} \cdot T^3$ [J/K]
C_{lat}	$2.7 \cdot 10^{-8} \cdot T^3$ [J/K]
C_{el}	$9.9 \cdot 10^{-9} \cdot T$ [J/K]
C_{pad}	$4.8 \cdot 10^{-5} \cdot T^{2.4}$ [W/K]
$C_{abs\text{-}bath}$	$4.0 \cdot 10^{-5} \cdot T^2$ [W/K]
$C_{ph\text{-}el}$	$7.0 \cdot 10^{-1} \cdot T^{4.37}$ [W/K]
$C_{th\text{-}abs}$	$1.6 \cdot 10^{-3} \cdot T^3$ [W/K]

Table 3-10. Values of the composite model parameters applied to the Cuoricino bolometers, considering 5x5x5 cm^3 absorbers and 3x3x1 mm^3 thermistors.

Calculations referred to the specific case of the single Cuoricino macro-bolometer are reported in Table 3-10. The values in the table are obtained from the parameters listed above, assuming crystal absorber with 5×5×5 cm^3 volume and Ge thermistor with 3×3×1 mm^3 size. A comparison among the heat capacities reported in the table confirms the approximation made in Section 2.4.2 to obtain an analytic solution for the dynamic behaviour of the modelled bolometer: the term C_{lat} is negligible respect to C_{el} and C_{abs}, at the operating temperature of the Cuoricino detector. There is no need to include the Si heater in the picture, as its heat capacity is properly designed to give a negligible contribution.

The composite model applied to the detectors discussed here will be also used in the context of this thesis, in particular in Chapter 6 for a qualitative evaluation of bolometric performances, as well as to make assumptions about the contributions brought in this regard by the single parameters.

3.6. From a floor to nineteen towers: the CUORE detector

The CUORE detector is a modular device made by 19 towers, all identical and closely packed in a cylindrically symmetric structure (see Figure 3-28, left). Each tower is made of 52 TeO_2 crystals, for a total number of $5 \cdot 10^{25}$ ^{130}Te nuclides for tower, arranged in 13 floors, each floors being a Single Module described before, with the copper frames in common between two adjacent planes. On the external side of the frames, 17 μm thick Cu strips glued on copper wire trays, are fixed to carry the signal to the electronic read-out. A scheme of the single CUORE tower is depict in Figure 3-27.

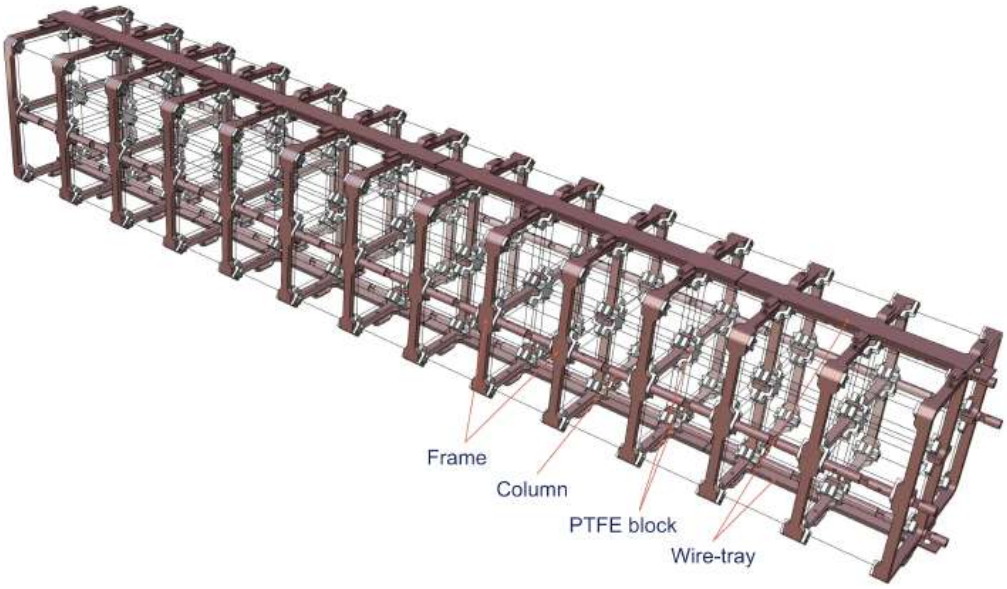

Figure 3-27. Scheme of a single CUORE tower.

The CUORE detector will be surrounded by a 6 cm thick Roman lead shield: differently from the modern lead, the Roman one has an extremely low contamination in ^{210}Pb (parent of ^{210}Bi) since it was separated from U more than 2000 years ago (hence ^{210}Pb had decayed while U is no more present to feed its production). The ^{210}Pb content of the Roman lead for CUORE was measured to be less than 4 mBq/kg (172). The bulk contamination of this lead was measured in LNGS on a 22.1 kg sample, resulting in upper limits on ^{232}Th and ^{238}U of 1.1·10-11 g/g and 7.7·10-11 g/g respectively. Similar values have been obtained with NAA.

The lead shield is also surrounded by two high-purity copper vessels (see Figure 3-28, right). The presence of these three shields will allow controlling the contribution of the experimental set-up to the background in the ROI.

Considering that the total mass of the CUORE bolometers will be about 750 kg, and adding 5+70 kg from the PTFE and the Cu parts constituting all the towers, it appears how the cooling down of the CUORE detector will be an operation at the limit of the present cryogenic technology.

A devoted a ^{3}He/^{4}He dilution refrigerator has been designed for this purpose with a system of 6 vessels at decreasing temperatures (300 K, 40 K, 4 K, 600 mK, 50 mK and 10 mK) aiming at maintaining the CUORE detector at the lowest possible temperature (~10 mK) while guaranteeing stable and radio-pure conditions for a very long time (years).

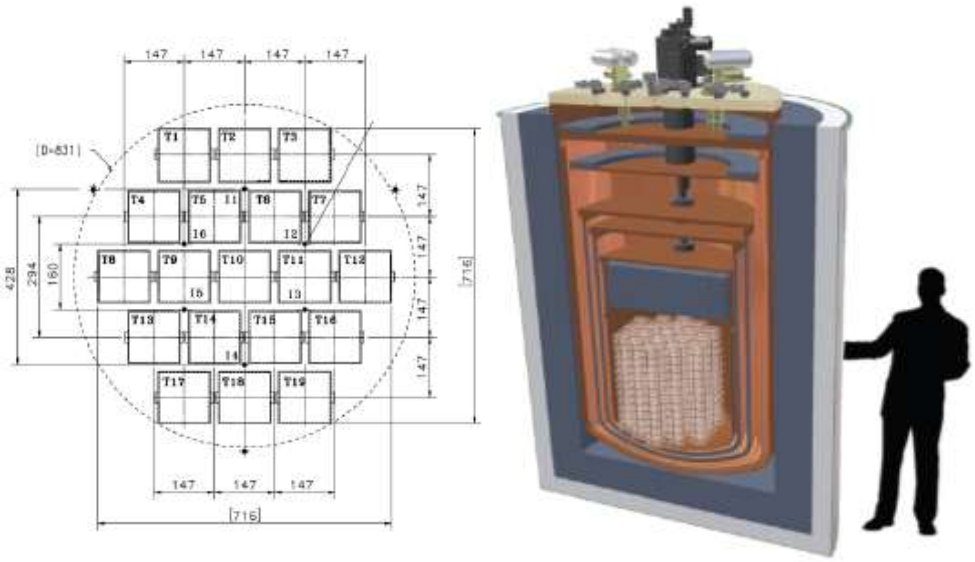

Figure 3-28. (Left) Layout scheme of the 19 towers of CUORE (top view). (Right) Drawing of the CUORE cryostat in cross-section, revealing the shielding and the array of towers.

3.6.1. The CUORE Tower Assembly Line (CTAL)

The assembly of the CUORE towers must be accomplished following very strict prescriptions, due to the extraordinary level of radio-purity required for a successful DBD experiment. This is done following a "zero contact" philosophy for the detector components i.e. no exposure to air to prevents possible Radon contamination and minimized contact (in space and time) with other materials, requiring a cleanroom assembly, and as little exposure to cosmic rays as possible, that requires a very careful logistic plans in order to reduce the time the detector parts spend aboveground.

The detector construction will undergo an easy-to-reproduce procedure: it will be semi-automatic and precisely timed for the NTD-to-crystal coupling, to obtain uniformity among detectors performances, and manual but strictly defined and tool-aided for the tower building, allowing the operator working in a safe, clean and fast way.

Therefore the tower construction is engineered around two units: the gluing station, which provide all the tools needed to glue the chips on the crystals, and an assembly line, an integrated set of tools devoted to the final assembly of the tower. Both units use glove boxes to provide a controlled atmosphere environment where the assembly actions can be safely performed. Each glove box has been specifically designed in order to meet the requirements of each single operation while minimizing the required time.

3.6.1.1. The gluing glove box

The quality of the glue spots (number of good spots, volumes of the drops, their height, diameter, pitch, air bubble inclusion, thickness after gluing etc...) is one of the most delicate aspects of bolometer assembly both with respect to its integrity after the cool down, and with respect to the bolometer response itself. Moreover, in case of a bad gluing the possibility to re-do the gluing on that crystal depends on our capability to restore the initial cleanness of the crystal once all the operations needed to remove the glue and/or the chip have been done. For these reasons the gluing of the thermistor and heater on each crystal will be accomplished in a glove-box, in a nitrogen gas atmosphere to avoid Rn, humidity and dust, by means of a partially automated system to obtain far more reproducible sensor-to-absorber couplings. This system has been designed during this PhD thesis work and will be discussed in Chapter 6.

3.6.1.2. The Assembly Glove Boxes

The assembly line runs around a common air tight box, named Garage , which will be used to safely store and handle the tower during all the assembly steps, plus some dedicated working volumes, i.e. the Glove Boxes (GB), able to variegate the geometry and the tools installed, depending on the specific operations to be carried out. The interface between these two different volumes, the Garage and the Glove Boxes, is the Universal Working Plane (UWP), an aluminium table, mounted on the garage top, presenting, on the upper surface all the manufacturing necessary to install the tools needed by the individual GBs and to seal the GBs themselves to the garage (see Figure 3-29).

The tower grows up on top of an assembly plate, part of the garage equipment, that can rotate or move up and down through an elevator with a rotating base, driven by a remote control. Speed and precision of the motion allow the operator to place the tower in the different positions required for the assembly actions that must be carried out. By using the vertical motion, the tower can be safely parked and sealed inside the garage at any time, both during standard procedures like the exchange of a glove box, or whenever the assembly must be interrupted for any reason (see Figure 3-29).

The first GB that is coupled to the UWP to proceed in the construction of the tower is the Mech GB (Figure 3-30) that will be used to mechanically assemble the structure of a single CUORE tower. This GB is now almost fully fabricated. A draft protocol for this assembly step has been written and checked with real actors. Most of the custom tools

needed in the assembly have been designed and produced; others have still to be definitively designed, together with the purging system, as already reported.

As soon as the tower structure is completed, the Mech GB is removed and substituted by the Cabling GB that allows placing the wire trays on the tower itself. This glove-box will be used also for the assembly of CUORE-0 radiation shield (Figure 3-31).

The next step is bonding the thermistors and the heaters to the pad of the wire trays. Due to the strong restrictions on materials coming from the radioactivity issue, the pads are made of copper instead of the more standard gold, because the gold deposition technique showed to be radioactive. This task is accomplished inside the Bonding GB in which a commercial bonding machine has been customized to work in vertical. Here many of the movements normally accomplished by the operator have been substituted by step motors, remotely controlled. The difficulties of bonding very small Cu pads with 25 μm gold wires, having the tower and the machine in a vertical position inside a glove box puts this procedure at the frontiers of the bonding capabilities.

Once the bonding is completed, the Cabling GB is used again to mount the covers of the wire trays. This ends the construction of the tower, that is then put in a nitrogen flushed Storage Box (Figure 3-29).

Figure 3-29. A mock-up tower closed in the Garage, with at the top the UWP (left) and the mock-up tower lifted from the Garage into the Storage Box thanks to the elevator (right).

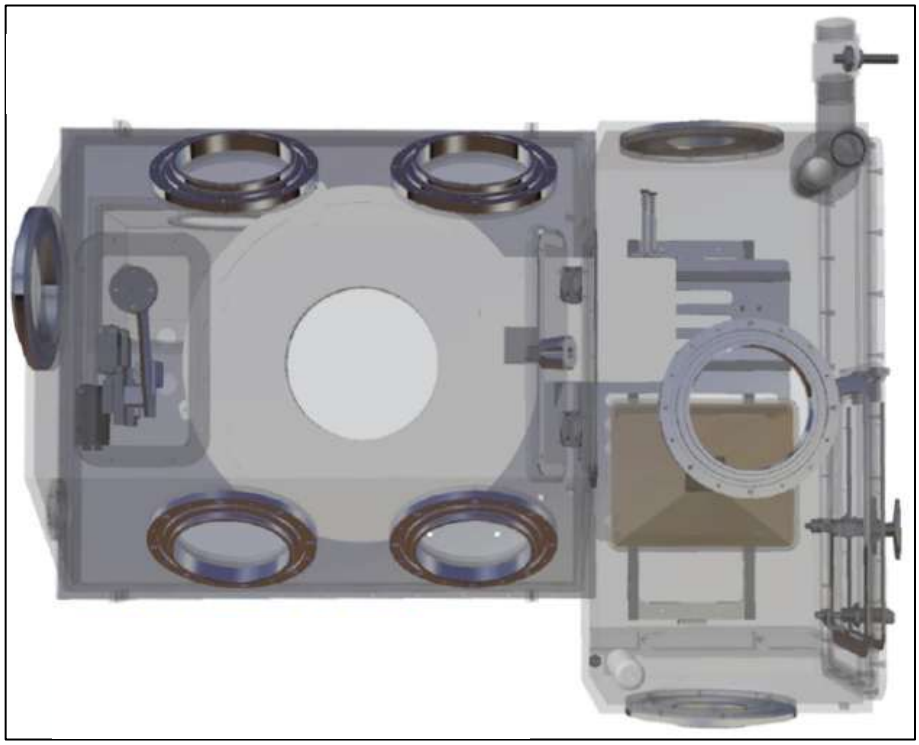

Figure 3-30. Schematic drawing of the Mech Box (top view).

Figure 3-31. Sketch of the Cabling Box (left) and the real GB on the top of the Garage (right).

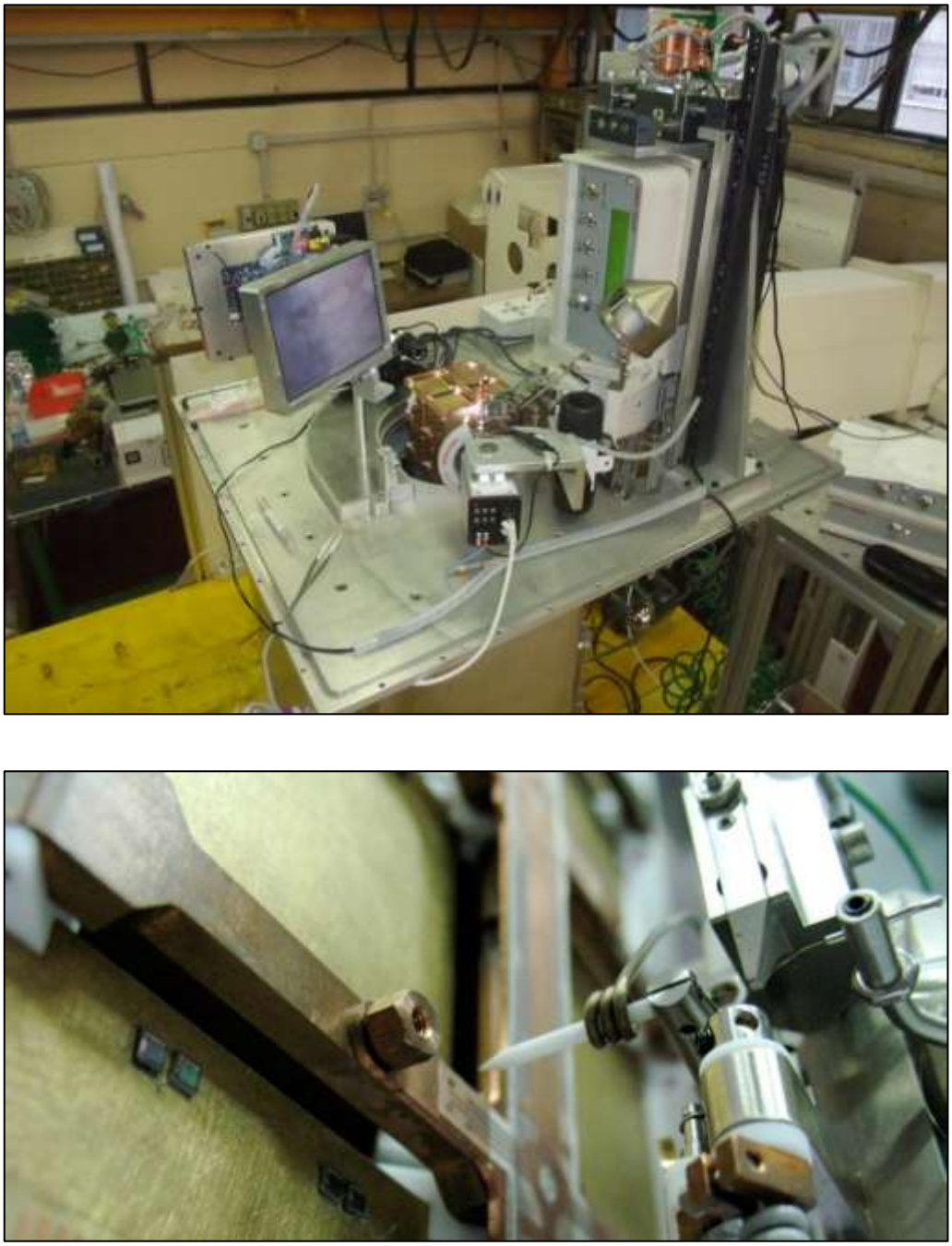

Figure 3-32. (Top) The instrumentation of the Bonding Box with the vertical bonding machine on the left and the camera and the screen on the right. (Bottom) A detail of the ceramic capillary approaching the mock-up tower for bonding tests.

3.7. CUORE background and sensitivity

The location, design, and construction of CUORE have been optimized to ensure the experiment attains the lowest backgrounds possible. The rock overburden provides 3200 m.w.e. of shielding against cosmic rays, while the cryostat has numerous internal and external lead shields to block natural environmental radiation. The apparatus will also be constructed from select materials which will undergo special cleaning treatments (especially for the surface of copper and TeO_2) and be stored underground to minimize cosmic-ray activation.

In addition to these methods of passive background suppression, to reduce to the lowest level the impact of surface contaminations, the detector has been designed with a compact structure, minimizing the amount of material and dead space between the crystals (namely the copper). Besides reducing the Cu induced background by having less copper facing the crystals, this strategy will render the detector more effective at active rejection of background events because the likelihood is increased that unwanted cosmic-rays and radioactive decays will produce simultaneous hits in multiple crystals, unlike 0νββ decays which should usually be confined to a single crystal. Moreover it will also improve the efficiency of the anticoincidence cut in reducing the effect of crystal surface contaminations: in the final design of the CUORE array the anticoincidence cut reduces by a factor >4 the background induced by Th or U crystal surface contamination.

Taking in account all of these factors, the CUORE target background of 10^{-2} counts/(keV·kg·y) looks feasible. Table 3-11 collects the contributions to the background from many detector parts. Considering this background and the one measured in Cuoricino, the gain in the life-time sensitivity (Eq. 1-31) is:

$$\frac{S_{0\nu}(0.01)}{S_{0\nu}(0.2)} \cong 4.5. \qquad 3\text{-}16$$

Material	Mass in CUORE	Expected b in the ROI
$Te0_2$ (surface)	741 kg	$< 2\cdot10^{-3}$ c/(keV·kg·y)
$Te0_2$ (bulk)		$< 5\cdot10^{-5}$ c/(keV·kg·y)
Copper (bulk)	900 kg	$< 1\cdot10^{-3}$ c/(keV·kg·y)
PTFE	5 kg	$< 3\cdot10^{-3}$ c/(keV·kg·y)
Roman Lead	50 kg	$< 4\cdot10^{-3}$ c/(keV·kg·y)

Table 3-11. Radioactivity levels of the detector major components and their effect on the 0νββ counting rate as predicted by the Monte Carlo simulation. In all cases there are only upper limits on the contaminations.

Considering also that the ^{130}Te mass is about 20 times than in Cuoricino, there is another gain in the sensitivity of:

$$\frac{S_{0\nu}(200\ \text{kg})}{S_{0\nu}(11\ \text{kg})} \cong 4.25.$$

3-17

The overall CUORE sensitivity to the life-time, assuming an energy resolution of 5 keV FWHM in the 0νββ region (91), a background rate of 10^{-2} counts/(keV·kg·y) and 5 year live time is:

$$S_{0\nu} = 2{\cdot}10^{26}\ \text{y}$$

3-18

(see Figure 3-33). This translates into a limit on the effective neutrino mass of:

$$m_{\beta\beta} < 36\text{-}84\ \text{meV},$$

3-19

according to the nuclear matrix element used, making CUORE start exploring the inverted hierarchy region of neutrino masses, as shown in Figure 3-34.

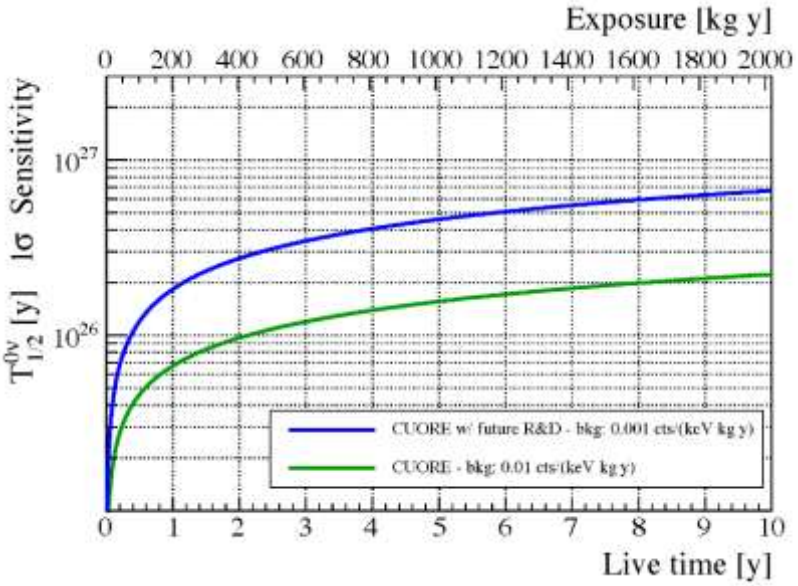

Figure 3-33. The CUORE sensitivity to the 0νββ half-life of ^{130}Te as a function of the measuring time, assuming a 5 keV FWHM energy resolution, in case of the realistic CUORE background of 10^{-2} counts/(keV·kg·y) (green, lower line) and of a target, optimistic background of 10^{-3} counts/(keV·kg·y) (blue, upper line).

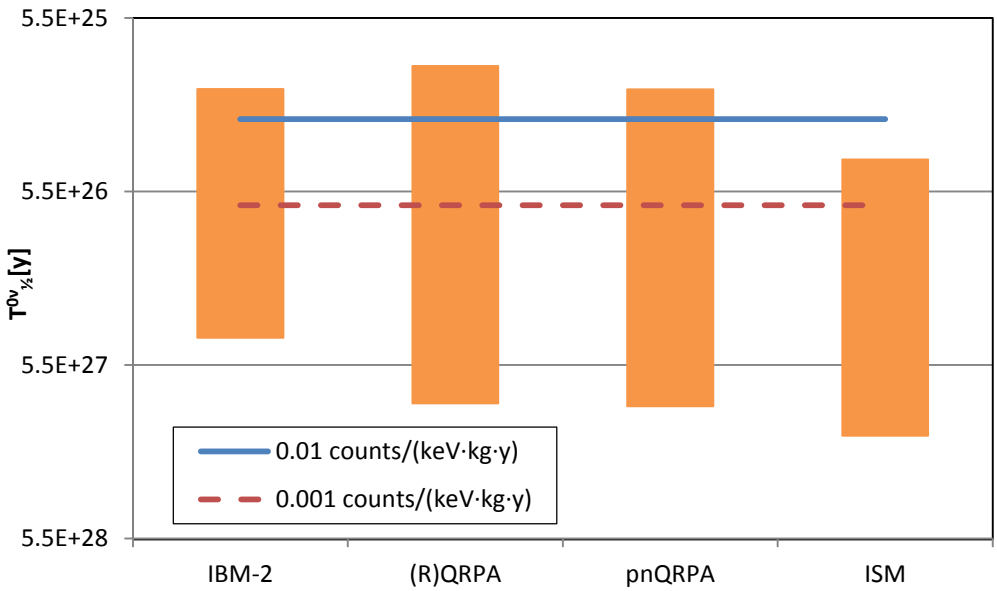

Figure 3-34. The inverted hierarchy region of neutrino mass spectra corresponds to an effective Majorana mass range between 50 meV and 10 meV (see Figure 1-6). Here this mass interval has been translated into ^{130}Te life-time using the nuclear form factors obtained from different nuclear matrix element calculations (see Figure 1-12) and is represented by the vertical orange bands. The CUORE sensitivities in case of a realistic background of 10^{-2} counts/(keV·kg·y) and of an optimistic background of 10^{-3} counts/(keV·kg·y) are superimposed onto these intervals (blue line and red dotted line respectively); assuming the realistic background, CUORE will be able to touch the inverted hierarchy region in most of the cases (i.e. according to three over four nuclear matrix element calculations) while it will deep explore this mass pattern in case the improvement on the reduction of the background will reach its optimistic target.

3.8. CUORE-0

The CUORE-0 detector will be the first step of the CUORE experiment. Its planned sensitivity will improve the limit set by Cuoricino in just a few months of data acquisition, making CUORE-0 one of the most sensitive 0νββ experiments worldwide.

The detector will consist of a complete CUORE tower: same material and assembly line of the CUORE detector will be used in its construction. Then the tower will be encapsulated in a dedicated copper shield (unlike what happens in CUORE where the 8mK-shield surrounds all the towers together to allow anti-coincidence cuts) and will be operated in the Cuoricino refrigerator in Hall A at LNGS. The detector base temperature will be about 8 mK.

The main goal of CUORE-0 is to guarantee a full test of the new CUORE assembly line. It will provide a check with high statistics of the detector improvements aiming at reducing the radioactive background and will test the improved uniformity of the bolometric behaviours. Moreover CUORE-0 will demonstrate operations critical to the success of the CUORE experiment. It will reveal flaws and inefficiencies in the assembly procedures and

permit a thorough exercise of the analysis framework. Most importantly this provides an opportunity to develop the skill sets necessary within the collaboration.

To allow a complete test of the CUORE readout chain, the Cuoricino cryostat was newly cabled with the same wires and thermalisation stages that will be used in CUORE. During the preparation of the CUORE-0 WT test maintenance has been performed on the cryogenic apparatus in order to prepare the system for the CUORE-0 3-years-run.

The CUORE-0 background has been predicted on the basis of the Cuoricino and Three Tower Test results. The 30% of the Cuoricino background in the ROI has been ascribed to the tail of the 2615-keV γ ray in the decay of ^{232}Th from the contamination of the cryostat copper shield (50). Because the cryostat will be the same also for CUORE-0, that will give an irreducible background of 0.06 counts/(keV·kg·y). Moreover, in the TTT a flat background between 3 and 4 MeV of 0.048±0.007(stat)±0.005(syst) counts/(keV·kg·y) has been measured (170); this background seems to extend till the 0νββ energy region, thus contributing to the residual background in the region of interest. Considering these factors, a realistic background for CUORE-0 has been estimated to be 0.12 counts/(keV·kg·y).

The corresponding sensitivity to the lifetime as a function of the live time of the experiment is given in Figure 3-35 assuming the irreducible background alone and the realistic background.

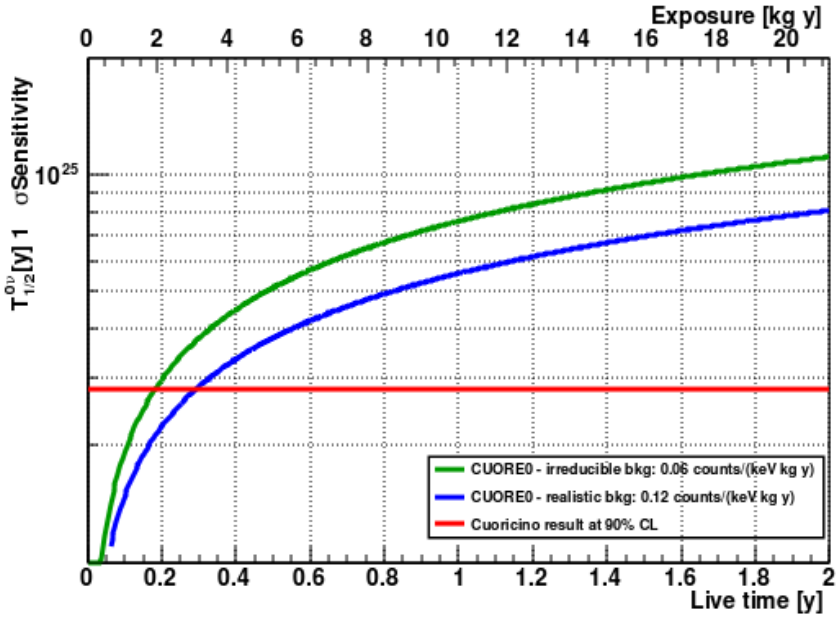

Figure 3-35. The CUORE-0 sensitivity to the 0νββ half-life of ^{130}Te as a function of the measuring time of the experiment assuming 5 keV FWHM as energy resolution in case of the realistic CUORE-0 background of 0.12 counts/(keV·kg·y) (blue, lower line) and in case the background is due only to the irreducible component derived from the cryostat (green, upper line). The Cuoricino limit is given as a reference (red, straight line).

Chapter 4.
CHARACTERISATION OF THE CUORE-0 AND CUORE THERMISTORS

íre ilqa yéva nótina, hostainiéva, yallumë:
ananta úva táre fárea, ufárea![10]

As introduced in 3.3.1.2, the aim of the NTD characterization is to derive the thermistor doping parameters by measuring the NTD resistance at different temperatures and performing a fit of the law R(T), which is derived by Eq. 2-18:

$$R(T) = R_0 exp\left(\frac{T_0}{T}\right)^{\gamma}.$$

4-1

In particular, for the CUORE-0 thermistor there is the necessity to verify that R_0 and T_0 are uniform among the NTDs and that these values are compatible with those obtained for the Cuoricino thermistors (173), i.e. that the CUORE-0 NTD resistances at the working temperature foreseen for the experiment are the same as in Cuoricino, in order to use the same electronics for the readout.

The CUORE-0 thermistor characterisation has been performed on some samples of 34B and 34C NTDs chosen by chance among the entire CUORE-0 thermistor production arrived in Como in September 2009.

Top-off series	Dose requested for top-off [n/cm^2]	Total dose [n/cm^2]	% of 34-B dose
39_A	$2.67 \cdot 10^{17}$	$3.34 \cdot 10^{18}$	98%
39_C 39_3	$3.35 \cdot 10^{17}$	$3.41 \cdot 10^{18}$	100%

Table 4-1. The doses for the three top-offs of the series #39. The dose of the 34B NTDs is $3.41 \cdot 10^{18}$.

[10] "When all is counted, and all numbered at last, /but yet it will not be enough, not enough." (225).

For the CUORE thermistors the situation is a little bit more complicated. Because the irradiation of the CUORE wafers resulted in too resistive (series #39) or too conductive (series #40) NTDs with respect to the CUORE target, a top-off procedure has been adopted to correct the R-T law of the #39 NTDs (see 3.3.1.1).

The purpose of the CUORE thermistor characterization run is then to check the two series of thermistors obtained from different top-offs of the #39, named 39A and 39C (the 39_3 came from a witness piece of Ge irradiated together with the 39C), and to test again the series #40. Their doping levels are collected in Table 4-1.

Some NTDs were cut from the wafers to be tested and were sent to Como in October 2009 (see Figure 4-1). These "witness" thermistors from the CUORE production are smaller than the final CUORE ones (3×2.4×1 mm^3 instead of 2.90×2.90×0.90 mm^3, where the second number refers to the distance between the pads –see 3.3.1.1.) and the gold pads for the electrical connections are only lateral (see Figure 4-2).

Figure 4-1. The complete set of the "witness" thermistors of the CUORE production.

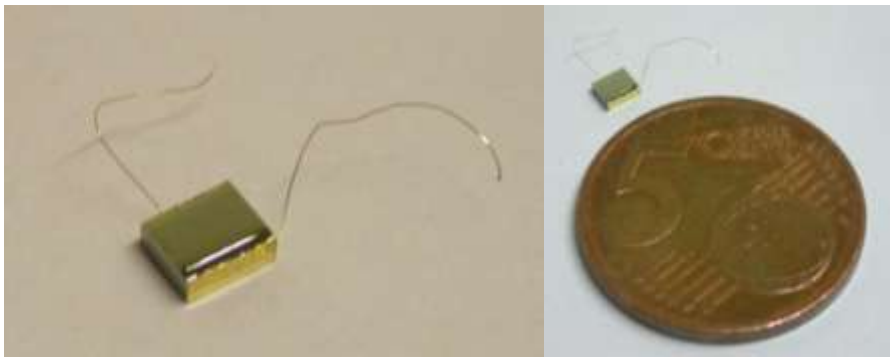

Figure 4-2. A CUORE "witness" thermistor. Its size (3×2.4×1 mm^3) is smaller than a standard CUORE-0 or CUORE thermistor and has only lateral gold pad instead of being wrap around type. Here 50 μm gold wires have already been bonded to the gold pads.

The “witness” thermistors were grouped in four boxes. Three of them contained four NTDs from each top-off of the wafer #39, while the last one, named 40A, contained six thermistors from series #40.

4.1. Experimental setup

The experimental setup is common for both CUORE-0 and CUORE thermistor characterisations. A copper holder, on which the thermistors will be fixed, is connected to the mixing chamber of the TBT cryostat at the Insubria cryogenic laboratory; a dedicated electronic and DAQ system provide the thermistor readout and the temperature stabilization.

The holder is composed by two parts: the first one allows the connection with the mixing chamber and carries the electrical contacts, while the second one accommodates the thermistors and a calibrated thermometer. They are mechanically connected with a small steel bar and thermally linked with copper wires.

The insulation of the thermistor housing is made by a Kapton layer, on which thin copper pads are glued, to provide electrical connections for the thermistors. The thermistor signals are then carried to the cryostat wiring by insulated constantan wires.

There are eleven slots for the thermistors in the mounting, displaced on its two opposite sides. Two of them are dedicated to reference thermistors, i.e. thermistors with a well know behaviour; they are a Cuoricino-type thermistor, named H31-B25, for an immediate comparison of the performances with the new thermistors, and the so-called BIG23H NTD, as auxiliary thermometer[11].

All the thermistors, provided with 50 μm diameter gold wires, are attached onto the Kapton mask with one spot of Varnish glue (174), while the gold wires are fixed to the copper contact pads with an Indium cold welding. A heater is also linked to the holder, for changing the temperature of the mounting by the injection of a fixed amount of power.

The Ge calibrate thermometer, a GR200A-30 from LakeShore Cryotronics (175), is placed at the bottom of the mounting, in a dedicated copper holder for its thermalisation, and it is read out by four wires. The entire holder is then closed in a cylindrical copper shield thermally connected to the mixing chamber. A scheme and some pictures of the holder can be found in Figure 4-3 and Figure 4-4.

[11] The BIG23H thermistor was calibrated in the past years by the Milan group using a Nuclear Orientation Thermometer (^{60}Co source) with very few points and imposing a VRH law with Coulomb gap (γ=0.5) for the T-R data fit. In particular, there is a serious uncertainty about the correct subtraction of the wire resistance in this calibration.

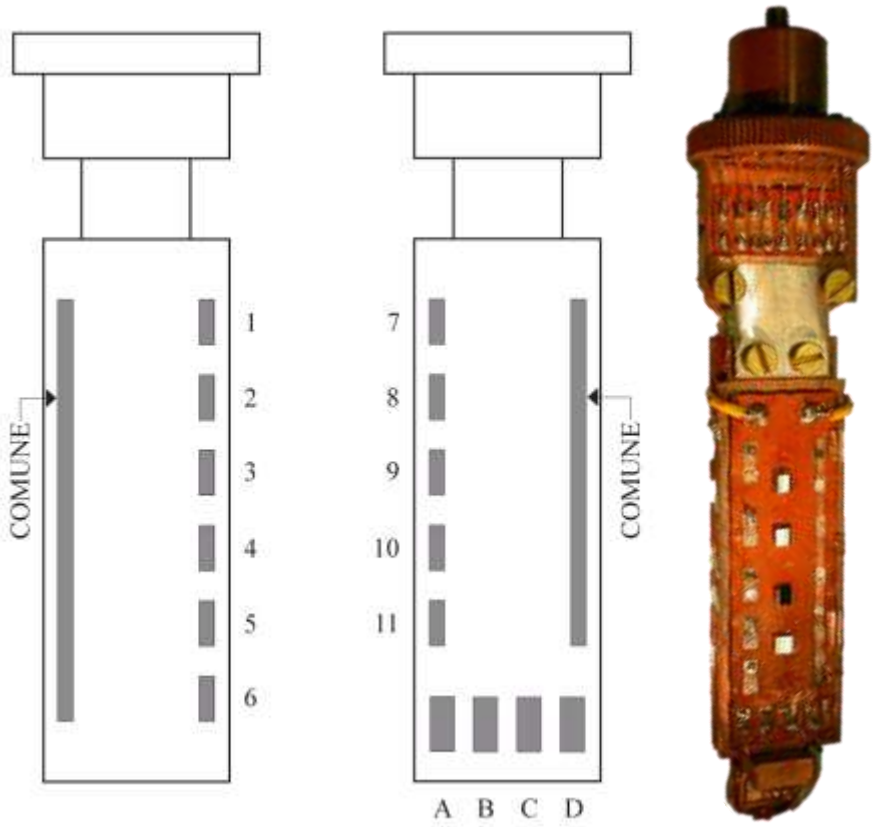

Figure 4-3. (Left/Middle) A scheme of both sides of the holder for the thermistor characterisations. Six thermistors can be accommodated on one side and five on the opposite one, for a total of eleven slots. The long, grey lines denote the common pad, while pads named A, B, C, D are the four contacts devoted to the calibrate thermometer four-wires read-out. (Right) A picture of one side of the holder. The top part is the one to be connected to the cryostat mixing chamber, while the bottom one is the thermometer holder.

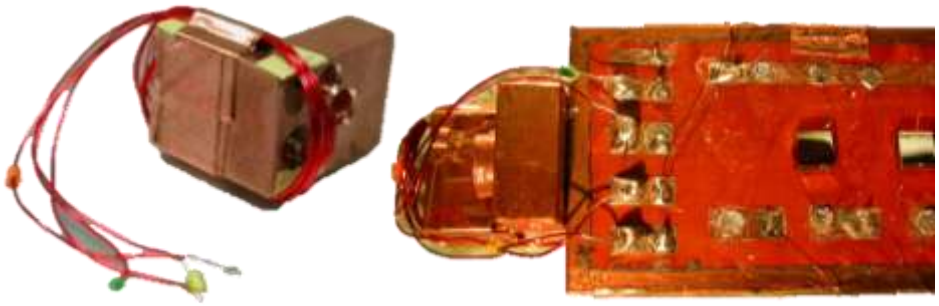

Figure 4-4. (Left) The calibrate thermometer is placed in its dedicated holder. (Right) The thermometer holder is fixed to the entire mounting. The Indium cold welding of the wires can be seen for both thermistors and thermometer.

The electronics for the thermistor read-out is summarized in Figure 4-5. The thermistors are biased with a symmetric circuit, then the signal is read differentially after a differential amplifier with fixed gain G = 218, to reduce the common noise. To have the maximum possible signal and a constant current passing through the thermistor, it is necessary that $R_L >> R_{bol}$, where R_{bol} is the thermistor resistance. At the usual cryogenic temperatures the thermistors have resistance between 1 and 100 MΩ, that requires R_L of order of GΩ.

Two multimeters measure the bias voltage output and the thermistor voltage output. It is possible to switch from one NTD channel to another thanks to a multiplexer on the same board where the load resistors are placed. The measure of the thermistor resistance $R_{bol}(T)$ at different biases is performed automatically by a devoted software controlling the electronics.

The calibrate thermometer resistance is read with the four-wires technique by an AVS-47 Resistance Bridge (176), which can measure resistances with voltage excitations as low as 10 μV; the AVS bridge is coupled to a PID temperature controller, the TS-530, connected to the heater on the mounting. To stabilize the thermistors at a desired temperature it is necessary to set the corresponding thermometer resistance value on the PID, which then tries to correct the error between this set point and the resistance value read by the AVS bridge by injecting a certain amount of power through the heater on the mounting, until the cryostat refrigerating action and the heating flow are in balance. The load curves are acquired after one hour from the stabilization, to ensure complete thermalisation of the samples.

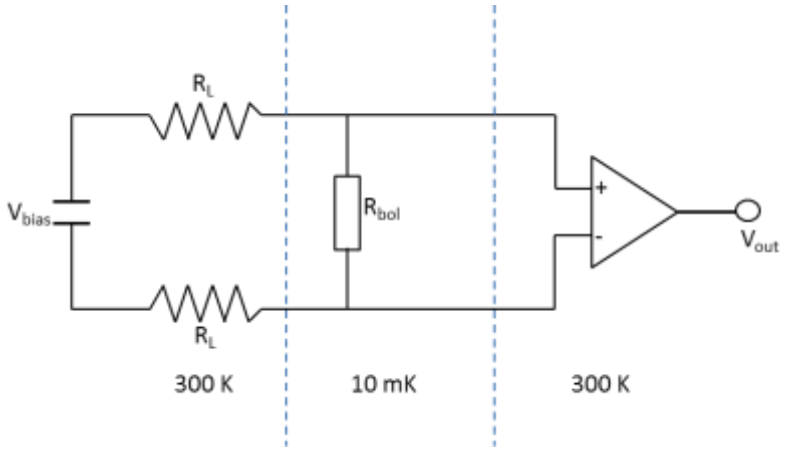

Figure 4-5. A scheme of the electronic readout system. The load resistance R_L can assume values from 0.01 MΩ to 2.07 GΩ. The temperatures at which each part of the circuit operates are also displayed.

As a rough check of the setup configuration the value of the thermometer resistance at the liquid He temperature (of the order of 30 Ω) has been measured and it is equal to that reported in the thermometer data sheet within a few mΩ.

Once the desired temperature has been reached, the software allows measuring the thermistor resistances sampling two V_{bias} intervals with two different R_L values, in order to accurately scan both the linear and the non-ohmic region of the load curve (see Figure 4-6). The limits of the two V_{bias} regions (named V_{min1}, V_{max1}, V_{min2}, V_{max2}) and the two corresponding load resistances (named R_{L1} and R_{L2}) are chosen taking in account that:

- ✓ V_{min1} should be as small as possible, to be compatible with the minimum observable signal variation;
- ✓ V_{max1} should be high enough to sample the entire ohmic region of the load curve;
- ✓ V_{min2} should allow a merging between the first and the second part of the sampling, taking in account the change in the load resistance. That means:

$$\frac{V_{max1}}{R_{L1}} \geq \frac{V_{min2}}{R_{L2}} \qquad 4\text{-}2$$

- ✓ V_{max2} should be as high as possible, below saturation.

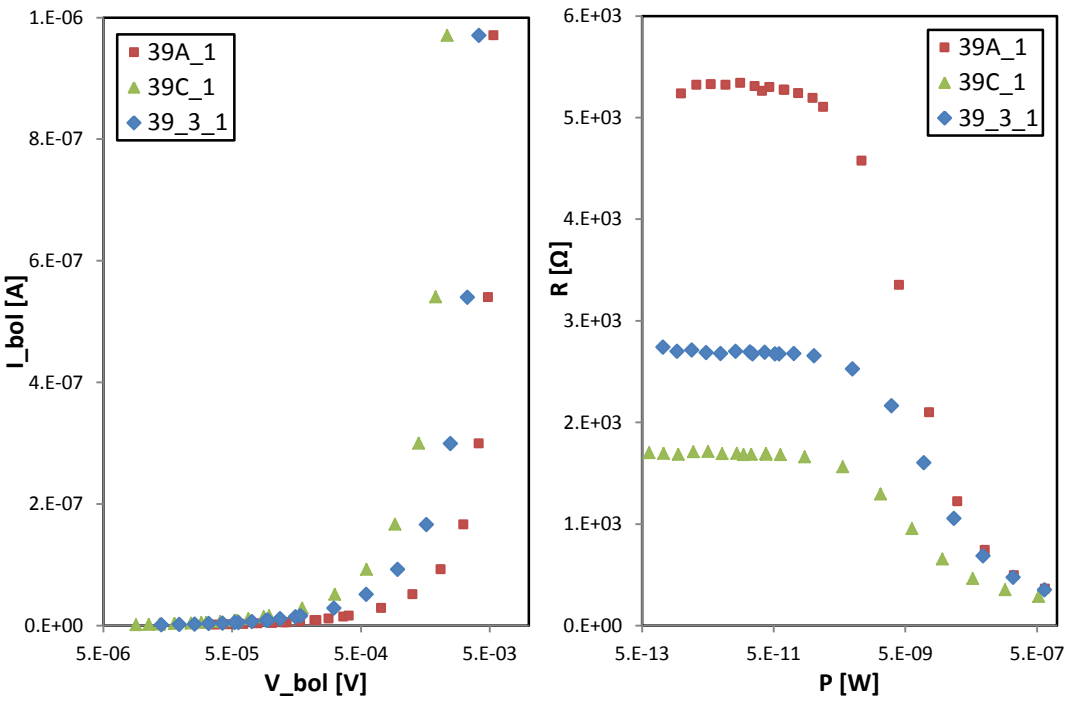

Figure 4-6. Typical V-I and R-P curves. In the R-P plot the plateau corresponds to the ohmic region.

Usually ten bias values have been sampled in each voltage ranges, spaced with a logarithmic scale. For every temperature steps the curve I_{bol} - V_{bol} (or equivalently R_{bol} - P_{bol}) has been collected for each thermistor. Typical V-I and R-P curves are shown in Figure 4-6. In the R-P plot the plateau corresponds to the ohmic region. At very low power, the measurement is noisy as the voltage variation is comparable with the preamplifier noise. Sometimes, a trend ascribable to the preamplifier leakage current can appear.

4.2. Data collection

The CUORE-0 thermistor calibration took place in September 2009 at the Insubria cryogenic laboratory. Load curves have been taken at eleven different temperature points for five CUORE-0 thermistors (just two from 34C wafer because one channel got lost, and three from 34B wafer) and the two reference thermistors. The remaining three slots were dedicated to the measurement of the wire resistances by connecting these pairs of pads with gold wires welded with Indium joints as for the thermistors. The read values of these shorted contacts resulted independent of the channels, giving an average wire resistance of 222.7 Ω, value that must be subtracted to all the measured thermistor resistances.

A map of the channels is reported in Table 4-2, while in Figure 4-7 the trend of the resistance of all thermistors versus the thermometer resistance is displayed.

The CUORE thermistor calibration took place in November 2009 at the Insubria cryogenic laboratory. During the measurement a sudden warming up of the cryostat occurred because of a He leakage into its IVC. For this reason the characterization was performed in two runs, one with eleven and one with nine temperature points, some of them repeated as a check of the re-establishing of the initial conditions, for a total of eighteen different temperature points. From now on, the two runs will be denoted CUORE-I and CUORE-II.

As can be seen from Figure 4-8 the thermistors didn't suffer for the re-cooling, with the exception of the BIG23H and, in a minor way, the first of the 39A thermistors. This discrepancy in the thermistor behaviour seems to be dependent on the position of the NTD on the copper holder, but it has been not understood yet.

Two thermistors for each group have been characterised (being the short circuits for the wire resistance measurements removed) together with the two reference thermistors, as shown in Table 4-3.

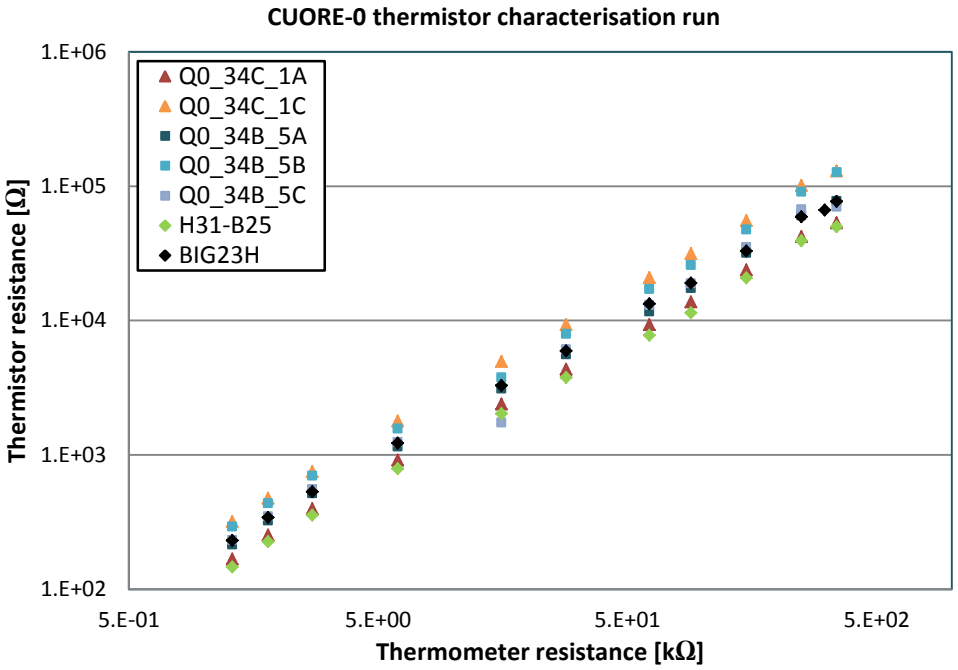

Figure 4-7. The resistance values for all the thermistors in the CUORE-0 characterisation run versus the thermometer resistance values are displayed.

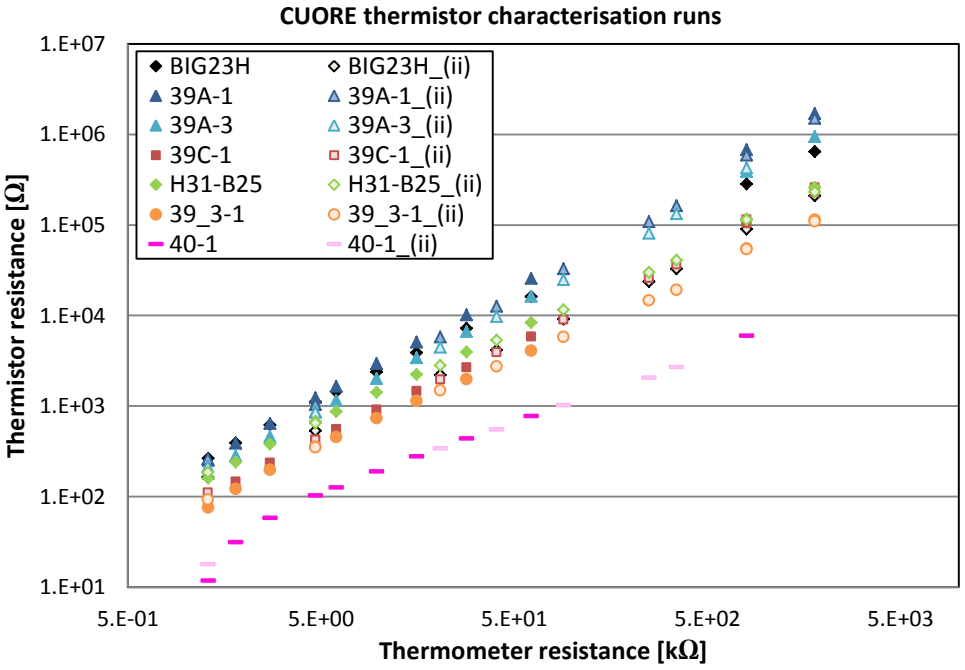

Figure 4-8. The resistance values for all the thermistors in both CUORE-I and CUORE-II characterisation runs versus the thermometer resistance values are displayed. The thermistors behave in the same way during the two runs except the BIG23H and, in a minor way, the 39A-1.

Channel	**1**	**2**	**3**	**4**	**5**	**6**
Side 1	BIG23H	S	Q0_34C_1A	Q0_34C_1B	Q0_34C_1C	S
Channel	**7**	**8**	**9**	**10**	**11**	////
Side 2	H31_B25	Q0_34B_5A	Q0_34B_5B	Q0_34B_5C	S	////

Table 4-2. The channel map of CUORE-0 NTD characterisation run. "S" stays for shorted contacts used for evaluating the wire resistance. Channel 4 was lost during the cool down.

Channel	**1**	**2**	**3**	**5**	**6**
Side 1	BIG23H	39A-1	39A-3	39-C-1	39-C-2
Channel	**7**	**8**	**9**	**10**	**11**
Side 2	H31-B25	39-3-1	39-3-2	40A-1	40A-2

Table 4-3. The channel map of CUORE NTD characterisation run. Channel 4 was not used because it was broken during the CUORE-0 characterisation run.

The thermistor resistance is obtained by averaging on the plateau points and the corresponding standard deviation is taken as a measurement of the resistance error. Generally, the error is around 5% of the resistance value, except for the series 40 samples, that have higher errors. The ohmic region is individuated by comparing the resistance error with the resistance reduction trend as the power increase.

All the temperature points for the three runs, i.e. the resistances at which the thermometer has been stabilized for the collection of the I-V curves, are shown in Table 4-4. The corresponding temperature calibration will be discussed in the following section.

R_{therm} [kΩ]	CUORE-0	CUORE-I	CUORE-II
1.30	✓	✓	✓
1.81	✓	✓	
2.72	✓	✓	
4.68		✓	✓
6.00	✓	✓	
9.75		✓	
15.7	✓	✓	
20.7			✓
28.4	✓	✓	
40.6			✓
61.3	✓	✓	
90.0	✓		✓
150	✓		
250	✓		✓
346	✓		✓
800		✓	✓
1800		✓	✓
2400			✓
Free fall	✓	✓	✓

Table 4-4. The thermometer resistance values at which the thermistor load curves have been collected, for each characterisation run.

4.3. Temperature calibration

The calibration data of the LakeShore thermometer have been provided by the factory (shown in Figure 4-9), which also supplied an interpolation of that data with Chebychev polynomials. The usable calibration range stops down to about 50 mK, i.e. about 30 mK above the lower temperature reachable with the TBT cryostat. From that the need to discuss about how to use the load curves acquired below 50 mK and/or how to extrapolate the calibration down to 20 mK. Looking at the calibration points a clear change in the trend below 90 mK is observable. the curve is less steep and looks less regular as well. This fact has two possible interpretations:

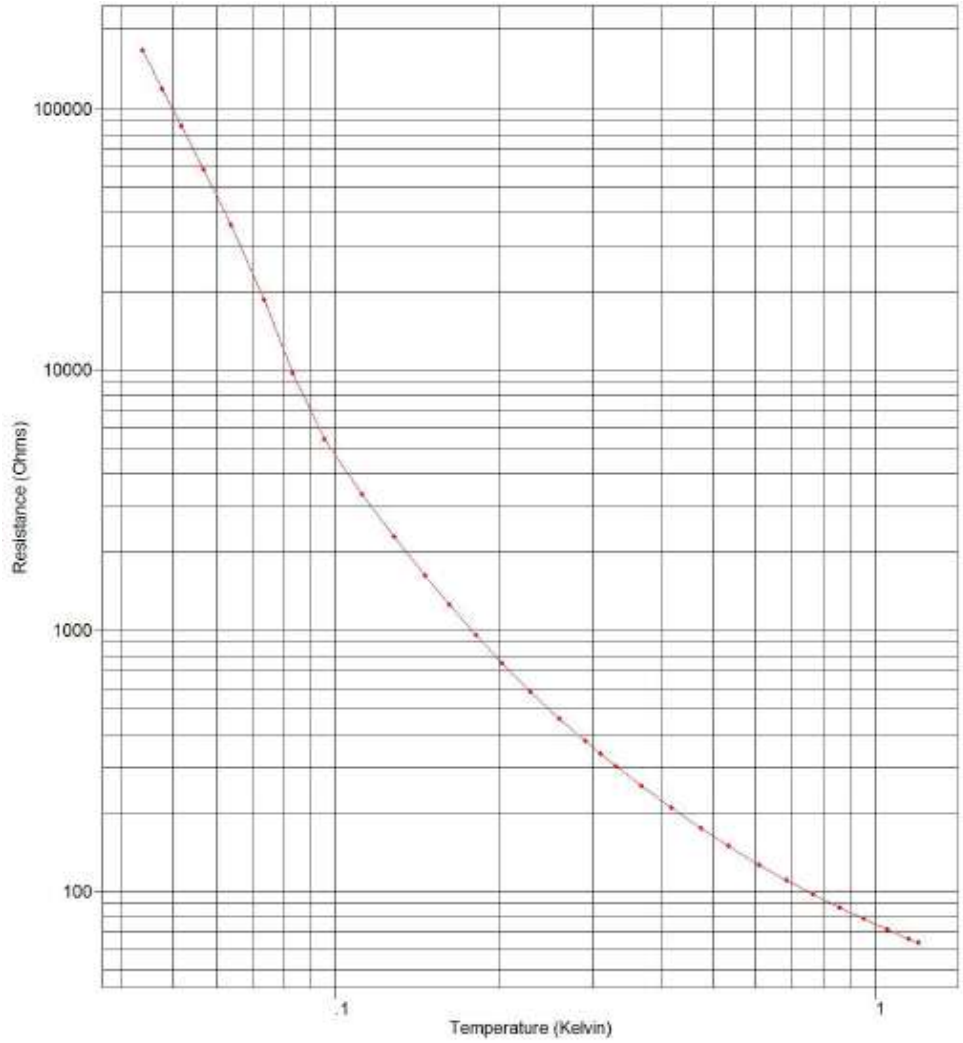

Figure 4-9. The calibration data for the Ge thermometer provided by the LakeShore company. A clear change in the slope of the curve is clearly observable at ~90 mK.

1) the curve is correct and reflects the real behaviour of the thermometer;
2) the thermometer was not correctly measured below 90 mK and it was in self-heating.

As for the first hypothesis, such a change is possible in particular if the Ge chip is not uniformly doped. Slight inhomogeneities in the doping can open preferred conductive paths corresponding to those chip sections with higher doping. This effect can become very important at low temperatures, where small differences in dopant concentration can lead to large differences in resistivity. Normally, this phenomenon is related to doping techniques other than NTD, which are not so reliable in terms of doping uniformity.

As for the second hypothesis, it is remarkable that the self-heating phenomenon is a frequent problem in low-temperature resistance measurements. This is due to the unwanted presence of parasitic powers associated to a large electron-phonon decoupling, which can lead to an electron temperature significantly higher than that of the phonon bath. Looking at the details of the information provided by the factory, it comes out that the change in slope corresponds exactly to measurements taken with a different excitation: from 63 μV to 20 μV. This may be a symptom of some difficulties in that range.

The two mechanisms can be related: in case a), the effective conduction takes place in a small part of the thermistor, with a small volume, and therefore with a lower electron-phonon thermal conductance.

In the following subsection different possible ways to use the calibration data provided by the factory to determine a temperature are discussed.

A first approach is to consider only the data above 90 mK reliable and to fit the calibration points with a VRH-like law, with γ free. Then, this law can be extrapolated down to the lowest temperatures achievable with the cryostat. The related temperature scale will be labelled as *Temperature Scale 1*. This is equivalent to assume of being able to measure correctly the thermometer resistance, without the self-heating problems possibly affecting the factory calibration.

In order to determine the correct parameters for the VRH law, the A. Zabrodskii, K. Zinoveva method (177) has been used, which allows to extract the γ parameter from the data with a useful linearization not involving R_0 and T_0 parameters:

$$\ln\left(\frac{-d\ln(T)}{d\ln(R)}\right) = -\gamma\ln(T) + k$$

4-3

The derivatives can be taken numerically thanks to the reasonably high number of samples in the calibration data, as shown in Figure 4-10. All the calculations have been detailed carried on in (178). The calibration points are consistent with $\gamma = 0.5$ down to ~90 mK (VRH with Coulomb gap), showing even more clearly that there are problems or at least a new phenomenon shows up below this temperature. The *Temperature Scale 1* was fixed by assuming for the thermometer a VRH-like law with the parameters given in

Table 4-5. In this scale the highest resistance readable with the DAQ setup, 2 MΩ[12], corresponds to 25.8 mK.

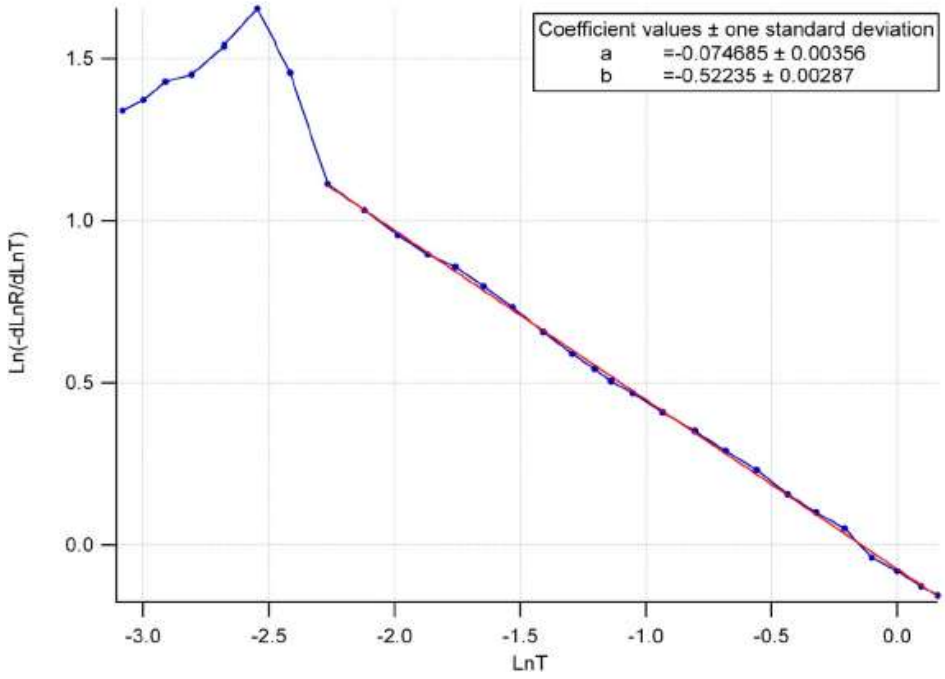

Figure 4-10. Fit of the calibration data with the 4-3. The coefficient "b" in the fit corresponds to the slope parameters (i.e. to γ in the equation), while "a" is the intercepts k.

Calibrated thermometer	
$\mathbf{T_0}$	3.0634 K
$\mathbf{R_0}$	12.482 Ω
$\boldsymbol{\gamma}$	0.52 (fixed)

Table 4-5. The VRH parameters for the calibrated thermometer that define the *Temperature Scale 1.*

[12]2 MΩ is the maximum range achievable with the AVS Bridge. Nevertheless, it was possible to read a resistance of 2.4 MΩ (and stabilizing at the corresponding temperature) using a 2M resistance in parallel to the bridge, during the CUORE thermistor characterization run.

A more conservative approach is to use only data acquired above 50 mK and to rely on the factory calibration in the recommended thermometer range (100 kΩ - 66 Ω). Doing this one obtains another temperature scale labelled as *Temperature Scale 2*.

An extension of this scale is possible using the factory calibration data down to 50 mK and try a phenomenological fit of these data with a function that can be extrapolated down to a thermometer resistance of 2 MΩ. After several attempts, the chosen function was:

$$T = \frac{a}{R^{\alpha}} + b,$$

4-4

with a = 0.47078, b = -0.02822668, α = 0.155905 and T expressed in K and R in Ω.

The negative aspect of this approach is that the chosen interpolation has no physical basis. However in this way one can obtain a third scale, the *Temperature Scale 3*.

Another possibility is to use the well-known Cuoricino thermistor present in the setup (the H31-B25) as a thermometer. It is calibrated with a VRH law with fixed γ = 0.5 with a few points taken above 90 mK with the LakeShore thermometer, in the region where the calibration data look fully reliable (see Figure 4-11), and then the calibration has been extrapolated down to 2MΩ. Because of the inhomogeneous behaviour of CUORE-II data set and the good agreement between the CUORE-0 and CUORE measurements, only the CUORE-I points have been used for calculating the VRH parameters of the H31-B25 thermistor. The results of this calibration are collected in Table 4-6: this is the *Temperature Scale 4*.

The philosophy of this approach is that the NTD thermistors have a reliable uniform doping and therefore their behaviour should be more stable in temperature. In addition, in the Cuoricino configuration, they have a large volume that should protect them from electron-phonon decoupling effects. The negative aspect is that the calibration is performed with a few points where the resistance is very low and possibly affected by imprecision in the determination of the wire resistance.

Finally, a *Temperature Scale 5* can be obtained with the same consideration but using the BIG23H reference thermistor. In this case the discrepancy between the CUORE-I and the CUORE-II measurements is more evident with respect to the H31-B25 thermistor (see 4.2). Nevertheless the good agreement between CUORE-0 and CUORE-I characterisation data ensure the coherence of the BIG23H along different measurements and the calculation of the VRH parameters has been carried on using the CUORE-I resistance data set also in this case. The results of this calibration are also collected in Table 4-6.

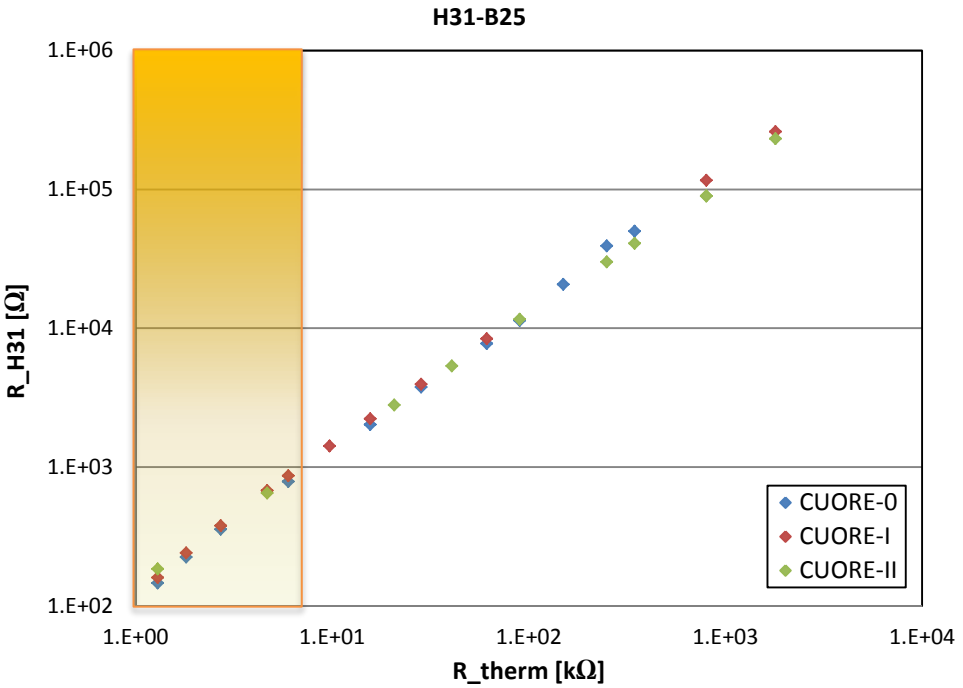

Figure 4-11. Plot of all the data for the Cuoricino reference thermistor H31-B25 collected during both CUORE-0 and CUORE thermistor characterisation runs. On the x axis the thermometer resistance is displayed while on the y axis there is the resistance of the H31-B25 thermistor. The good agreement between the CUORE-0 and CUORE-I data sets can be observed, while the CUORE-II points show some problems in the re-establishing of the initial measurement conditions after the He-leakage during the CUORE thermistor characterisation run (see 4.2). The orange area on the left side of the plot denotes the region of the thermometer resistance values used for building the Temperature Scale 4. Only the CUORE-I data set has been used for the calibration.

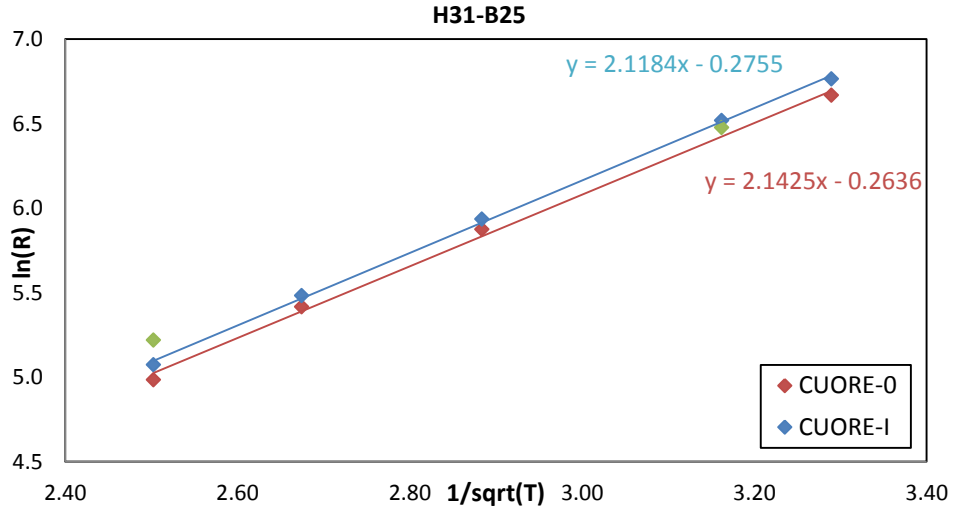

Figure 4-12. Focus on the points used for the calibration of the H31-B25 thermistor, corresponding to the orange region in Figure 4-11. The thermometer resistances are converted in temperature thanks to the Temperature Scale 1 and then the inverse of the square root of the temperature is displayed on the x-axis, while on the y-axis the natural logarithm of the NTD's resistances is taken, in order to perform a linear fit of the data, fixing $\gamma = 0.5$. From the fit parameters the constant R_0 and T_0 are derived.

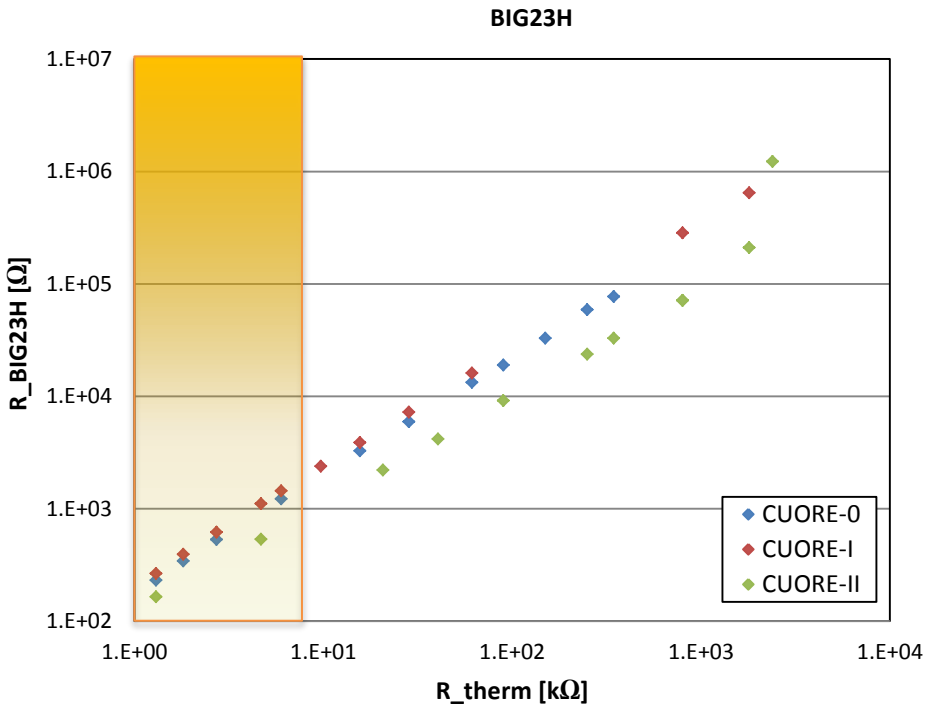

Figure 4-13. Plot of all the data for the BIG23H reference thermistor collected during both CUORE-0 and CUORE thermistor characterisation runs. On the x axis the thermometer resistance is displayed while on the y axis there is the resistance of the BIG23H thermistor. The agreement between the CUORE-0 and CUORE-I data sets can be observed, while the CUORE-II points show problems in the re-establishing of the initial measurement conditions after the He-leakage during the CUORE thermistor characterisation run (see 4.2). The orange area on the left side of the graphic denotes the region of the thermometer resistance values used for building the Temperature Scale 5. Only the CUORE-I data set has been used for the calibration.

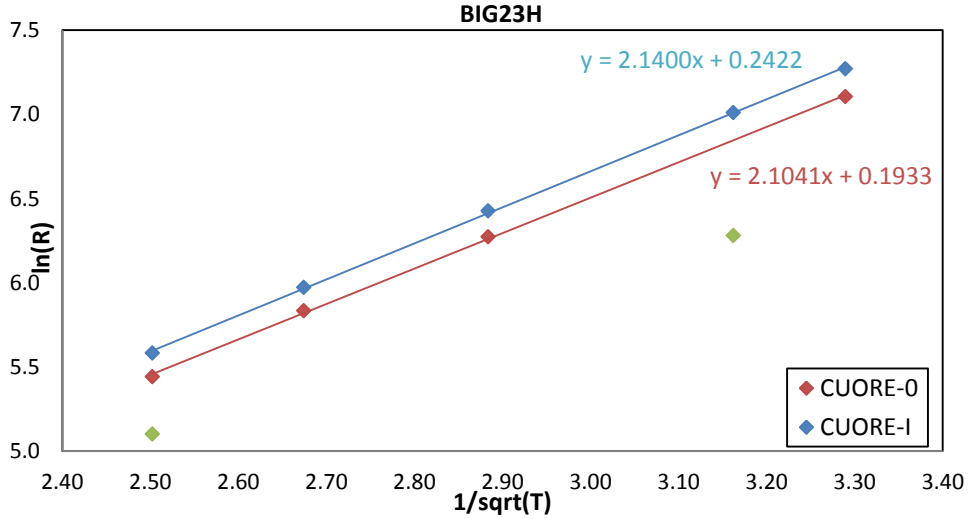

Figure 4-14. Focus on the points used for the calibration of the BIG23H thermistor, corresponding to the orange region in Figure 4-13. The thermometer resistances are converted in temperature thanks to the Temperature Scale 1 and then the inverse of the square root of the temperature is displayed on the x-axis, while on the y-axis the natural logarithm of the NTD's resistances is taken, in order to perform a linear fit of the data, fixing $\gamma = 0.5$. From the fit parameters the constant R_0 and T_0 are derived.

H31-B25	
T_0	4.590 K
R_0	0.768 Ω
γ	0.5 (fixed)

BIG23H	
T_0	4.580 K
R_0	1.274 Ω
γ	0.5 (fixed)

Table 4-6. The VRH parameters for the H31-B25 and the BIG23H thermistor, defining the *Temperature Scale 4* and the *Temperature Scale 5*, respectively. In the calibration the resistance values of the CUORE-I data set corresponding to thermometer temperatures above 90 mK have been used.

Using the five temperature scales, it is now possible to convert the resistance values of the thermometer and of the two reference thermistors into temperature values. The temperature values at which the load curves have been collected during the three NTD characterisation runs are shown in Table 4-7.

Run	R_{therm} [kΩ]	Scale 1 [mK]	Scale 2 [mK]	Scale 3 [mK]	R_{H31} [kΩ]	Scale 4 [mK]	R_{B23H} [kΩ]	Scale 5 [mK]
0, I, II	1.30	159.68	159.99	159.99	0.16	161.16	0.27	160.53
0, I	1.81	139.81	140.02	140.02	0.24	139.01	0.39	139.43
0, I	2.72	120.26	120.01	120.01	0.38	119.45	0.62	119.68
I, II	4.68	100.01	99.942	99.942	0.68	99.797	1.11	99.936
0, I	6.00	92.410	93.117	93.117	0.87	92.924	1.44	92.694
I	9.75	79.999	84.578	84.578	1.42	81.212	2.39	80.584
0, I	15.7	69.954	75.960	75.960	2.23	72.201	3.88	71.175
II	20.7	64.999	71.956	71.956	2.80	68.241	---------	---------
0, I	28.4	60.004	67.339	67.339	3.95	62.852	7.22	61.316
II	40.6	54.999	62.020	62.020	5.36	58.612	---------	---------
0, I	61.3	49.996	56.274	56.274	8.38	53.112	16.1	51.330
0, II	90.0	45.922	51.367	51.367	11.4	49.785	18.9	49.620
0	150	41.241	---------	45.198	20.7	44.104	32.8	44.407
0, II	250	37.248	---------	39.577	39.2	39.060	58.9	39.689
0, II	346	35.006	---------	36.227	49.9	37.370	76.8	37.798
I, II	800	30.087	---------	28.332	116	32.273	285	30.189
I, II	1800	26.262	---------	21.617	260	28.314	645	26.542
II	2400	25.080	---------	19.429	3321	19.662	---------	---------

Table 4-7. The resistance values of the thermometer and the reference thermistors that have been collected during the three NTD characterisation runs are converted into temperature points using the different temperature scales.

4.4. Data analysis

As shown in Table 4-4, eleven temperature points are available for the analysis of the CUORE-0 thermistors, while for the CUORE NTDs the CUORE-I data set is used, including the CUORE-II points that are not already present in the CUORE-I data set. This addition is omitted if there is a clear sign of discordances between the two data sets (see Figure 4-8). When both data sets are used, the points considered for the fit are sixteen at maximum, while they are eleven in the CUORE-I data set only. The point at 2400 kΩ in the CUORE-II data set has not been used because it is not always reliable. In general, the stabilization at resistances higher than 200 kΩ is difficult and the corresponding points are noisy.

The thermistor resistances are put in correspondence with the thermometer resistances converted in temperatures according to a Temperature Scale. Then a fit is performed with a VRH-like law using three free parameters: R_0, T_0 and γ. If γ ranges between 0.4 and 0.6, a new fit is performed fixing γ at 0.5 and recording the corresponding R_0 and T_0. Then, using these values, the NTD resistance is extrapolated down to 15 mK and 10 mK, i.e. the temperatures reached during the runs at LNGS and foreseen for the CUORE-0 and CUORE experiments, to confront the new thermistor behaviour with the old Cuoricino ones.

The procedure is repeated for all the five Temperature Scales and the obtained results allow selecting which one is the most reliable. From Figure 4-15 to Figure 4-19 examples of the fits with different *Temperature Scale* are displayed.

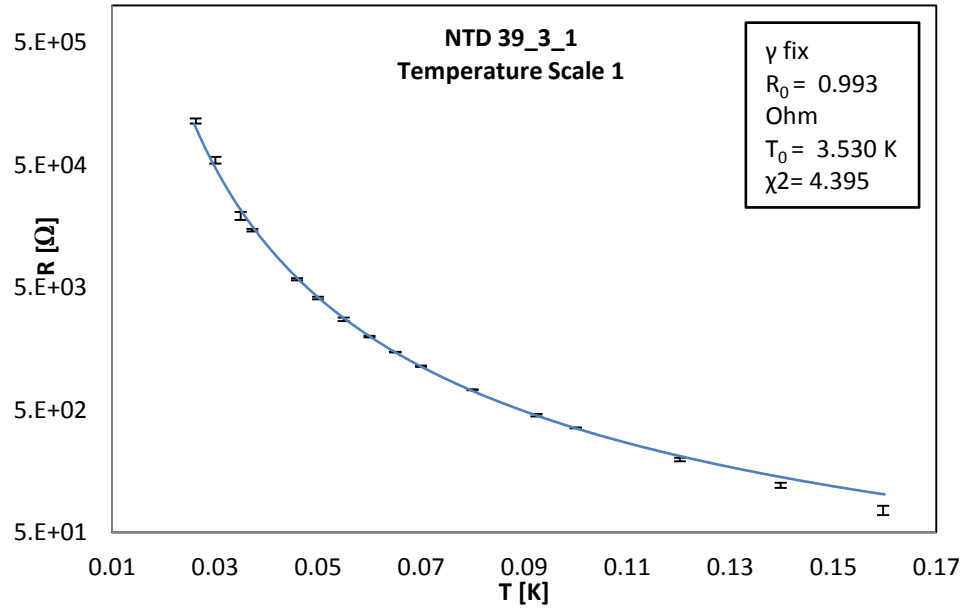

Figure 4-15. Example of a fit for the 39_3_1 CUORE thermistor with *Temperature Scale 1.* The results of the fit are displayed in the box.

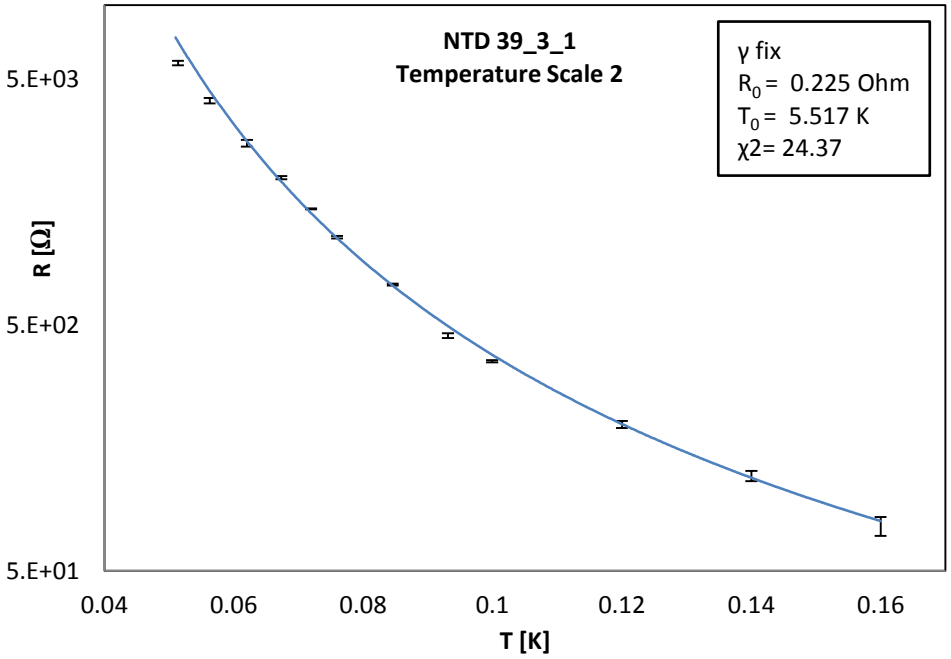

Figure 4-16. Example of a fit for the 39_3_1 CUORE thermistor with *Temperature Scale 2*. The results of the fit are displayed in the box.

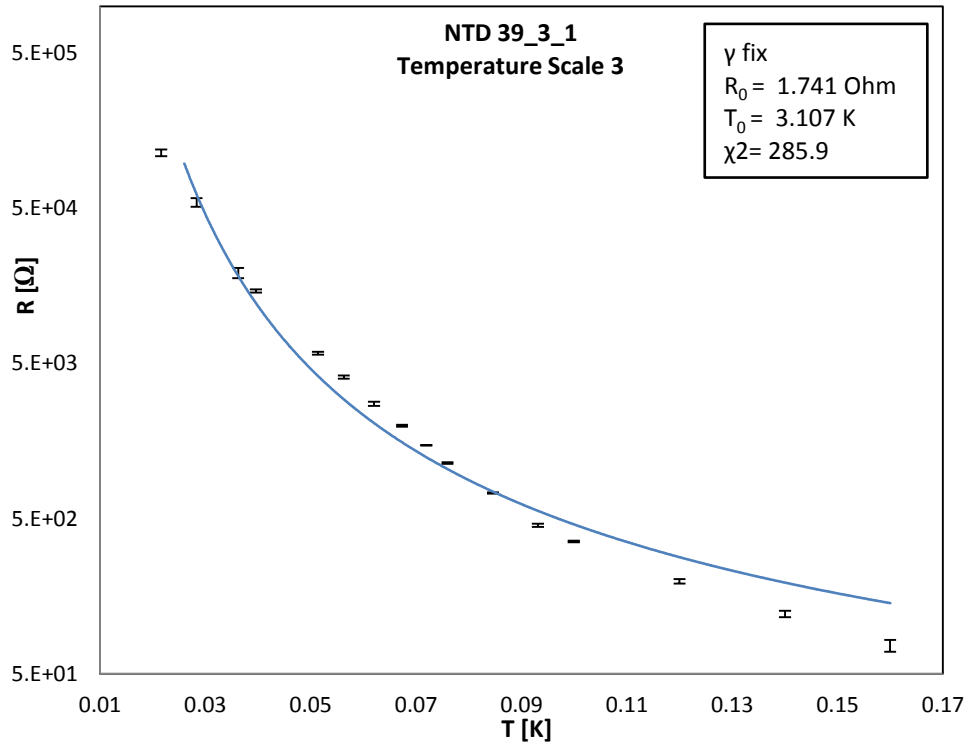

Figure 4-17. Example of a fit for the 39_3_1 CUORE thermistor with *Temperature Scale 3*. The results of the fit are displayed in the box.

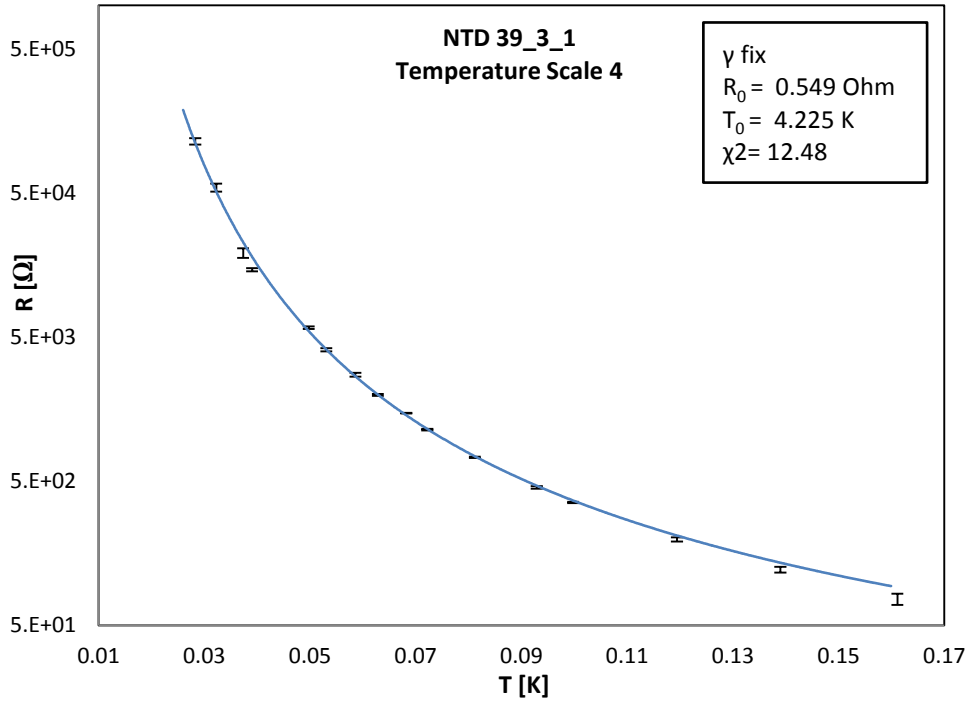

Figure 4-18. Example of a fit for the 39_3_1 CUORE thermistor with *Temperature Scale 4*. The results of the fit are displayed in the box.

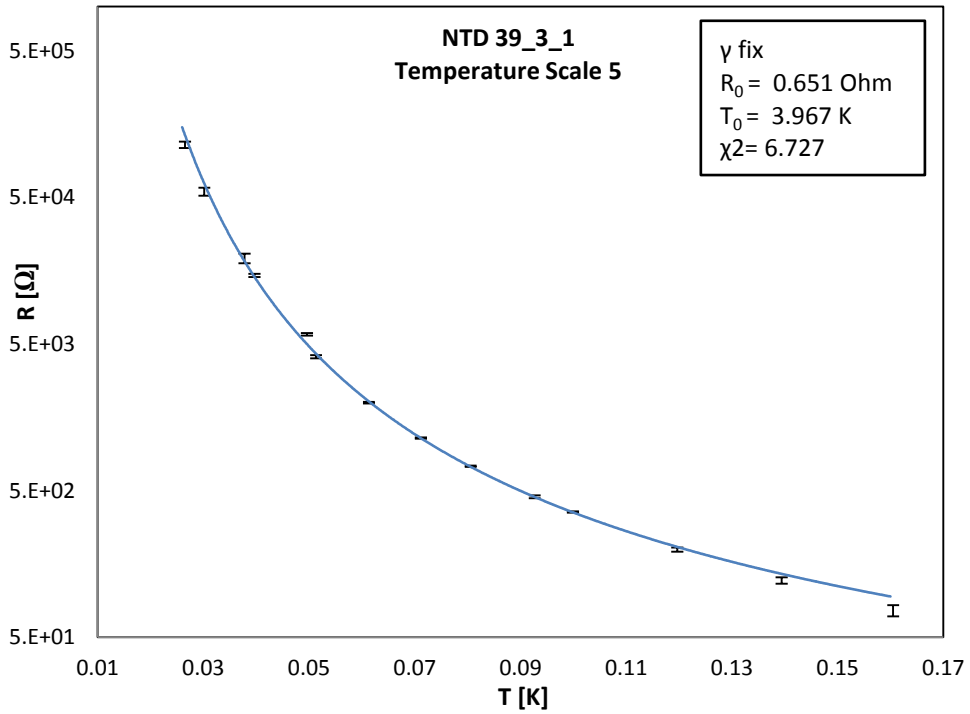

Figure 4-19. Example of a fit for the 39_3_1 CUORE thermistor with *Temperature Scale 5*. The results of the fit are displayed in the box.

BIG23H										
CUORE-0 data	**T1**		**T2**		**T3**		**T4**		**T5**	
	γ free	**γ fixed**	**γ free**	**γ fixed**	**γ free**	**γ fixed**	**γ free**	**γ fixed**	**γ free**	**γ fixed**
γ	0.484	0.5	0.516	0.5	0.476	0.5	0.492	0.5	0.501	0.5
R_0	1.152	1.480	0.889	0.683	0.744	1.033	0.813	0.936	0.734	0.741
T_0	5.037	4.127	4.472	5.425	6.576	4.876	5.383	4.835	5.039	5.061
χ2/dof	4.905	4.020	76.79	58.63	123.1	117.6	14.64	12.95	48.73	42.74
CUORE-I data	**T1**		**T2**		**T3**		**T4**		**T5**	
	γ free	**γ fixed**	**γ free**	**γ fixed**	**γ free**	**γ fixed**	**γ free**	**γ fixed**	**γ free**	**γ fixed**
Γ	0.488	0.5	0.501	0.5	0.462	0.5	0.490	0.5	0.477	0.5
R_0	1.283	1.524	0.504	0.507	0.701	1.650	0.843	0.991	0.897	1.274
T_0	5.001	4.321	6.027	6.044	7.777	4.415	5.592	4.940	6.121	4.580
χ2/dof	10.50	9.989	137.7	118.1	731.6	745.5	17.93	13.41	0.918	4E-06

Table 4-8. Fit results for the reference thermistor BIG23H according to all the *Temperature Scale* and with the parameter γ both free and fixed. The values of the reduced-χ^2 of the fits obtained with the *temperature Scale* created starting from BIG23H data, i.e. *Temperature Scale 5,* are denoted in red.

H31-B25										
CUORE-0 data	**T1**		**T2**		**T3**		**T4**		**T5**	
	γ free	**γ fixed**	**γ free**	**γ fixed**	**γ free**	**γ fixed**	**γ free**	**γ fixed**	**γ free**	**γ fixed**
γ	0.487	0.5	0.509	0.5	0.496	0.5	0.498	0.5	0.500	0.5
R_0	0.845	1.042	0.388	0.334	0.510	0.524	0.559	0.579	0.501	0.507
T_0	4.746	4.040	5.107	5.688	5.272	5.069	4.962	4.841	5.000	4.972
χ^2/dof	19.99	16.54	78.55	65.30	86.88	77.33	5.236	4.532	44.69	39.64
CUORE-I data	**T1**		**T2**		**T3**		**T4**		**T5**	
	γ free	**γ fixed**	**γ free**	**γ fixed**	**γ free**	**γ fixed**	**γ free**	**γ fixed**	**γ free**	**γ fixed**
γ	0.485	0.5	0.511	0.5	0.462	0.5	0.494	0.5	0.485	0.5
R_0	1.011	1.296	0.378	0.316	1.416	2.673	0.687	0.768	0.950	1.216
T_0	4.708	3.887	5.217	5.959	5.501	3.276	4.987	4.590	4.853	4.002
χ^2/dof	9.905	7.743	30.47	26.35	611.5	619.2	0.060	8E-06	3.920	5.638

Table 4-9. Fit results for the Cuoricino reference thermistor H31-B25 according to all the *Temperature Scale* and with the parameter γ both free and fixed. The values of the reduced-χ^2 of the fits obtained with the *temperature Scale* created starting from H31-B25 data, i.e. *Temperature Scale 4,* are denoted in red.

Q0_34C_1A	T1		T2		T3		T4		T5	
	γ free	γ fixed	γ free	γ fixed	γ free	γ fixed	γ free	γ fixed	γ free	γ fixed
γ	0.484	0.5	0.510	0.5	0.483	0.5	0.495	0.5	0.489	0.5
R_0	0.942	1.202	0.341	0.288	0.570	0.689	0.659	0.714	0.588	0.723
T_0	4.902	4.029	5.492	6.216	6.159	5.072	5.071	4.768	5.382	4.662
χ^2/dof	4.813	3.605	67.94	57.06	263.3	244.8	3.103	2.767	61.70	51.35
Q0_34C_1C	**T1**		**T2**		**T3**		**T4**		**T5**	
	γ free	γ fixed	γ free	γ fixed	γ free	γ fixed	γ free	γ fixed	γ free	γ fixed
γ	0.490	0.5	0.498	0.5	0.497	0.5	0.493	0.5	0.492	0.5
R_0	1.521	1.796	0.539	0.551	0.762	0.763	0.743	0.849	0.751	0.884
T_0	5.003	4.389	6.375	6.254	5.987	5.810	5.990	5.451	5.916	5.317
χ^2/dof	5.025	4.660	504.4	421.5	582.9	520.2	41.62	35.97	245.2	212.5

Table 4-10. Fit results for the CUORE-0 34C thermistors according to all the *Temperature Scale* and with the parameter γ both free and fixed.

Q0_34B_5A	T1		T2		T3		T4		T5	
	γ free	γ fixed	γ free	γ fixed	γ free	γ fixed	γ free	γ fixed	γ free	γ fixed
γ	0.486	0.5	0.511	0.5	0.502	0.5	0.496	0.5	0.501	0.5
R_0	1.064	1.361	0.471	0.386	0.927	0.831	0.703	0.755	0.581	0.576
T_0	5.018	4.170	5.284	6.068	4.814	5.033	5.257	4.997	5.207	5.267
χ^2/dof	24.40	19.23	170.7	141.1	323.6	282.6	8.811	7.439	161.6	144.2
Q0_34B_5B	**T1**		**T2**		**T3**		**T4**		**T5**	
	γ free	γ fixed	γ free	γ fixed	γ free	γ fixed	γ free	γ fixed	γ free	γ fixed
γ	0.477	0.5	0.506	0.5	0.493	0.5	0.505	0.5	0.493	0.5
R_0	1.078	1.600	0.412	0.381	0.633	0.722	0.962	0.880	0.737	0.852
T_0	5.916	4.362	6.091	6.529	6.139	5.581	4.878	5.215	5.742	5.217
χ^2/dof	28.03	21.08	193.1	162.8	206.1	184.9	27.01	25.27	127.8	109.4
Q0_34B_5C	**T1**		**T2**		**T3**		**T4**		**T5**	
	γ free	γ fixed	γ free	γ fixed	γ free	γ fixed	γ free	γ fixed	γ free	γ fixed
γ	0.515	0.5	0.505	0.5	0.484	0.5	0.494	0.5	0.578	0.5
R_0	1.703	1.336	0.459	0.430	1.016	1.288	0.707	0.800	1.686	0.480
T_0	3.560	4.266	5.803	6.150	5.842	4.786	5.475	5.027	2.340	5.495
χ^2/dof	20.33	20.91	189.9	142.1	514.9	471.6	11.16	7.998	133.4	189.6

Table 4-11. Fit results for the CUORE-0 34B thermistors according to all the *Temperature Scale* and with the parameter γ both free and fixed.

39A										
39A_1	**T1**		**T2**		**T3**		**T4**		**T5**	
CUORE-I data	**γ free**	**γ fixed**	**γ free**	**γ fixed**	**γ free**	**γ fixed**	**γ free**	**γ fixed**	**γ free**	**γ fixed**
γ	0.495	0.5	0.518	0.5	0.475	0.5	0.506	0.5	0.497	0.5
R_0	0.662	0.737	0.180	0.127	0.656	0.880	0.383	0.345	0.551	0.580
T_0	5.904	5.495	6.745	8.457	7.243	5.393	6.199	6.679	6.074	5.871
χ^2/dof	25.49	21.17	96.36	83.69	957.0	873.7	11.44	11.46	1.322	0.991
39A_3	**T1**		**T2**		**T3**		**T4**		**T5**	
	γ free	**γ fixed**	**γ free**	**γ fixed**	**γ free**	**γ fixed**	**γ free**	**γ fixed**	**γ free**	**γ fixed**
γ	0.497	0.5	0.537	0.5	0.471	0.5	0.513	0.5	0.508	0.5
R_0	0.671	0.710	0.311	0.154	0.483	0.754	0.435	0.342	0.515	0.450
T_0	5.240	5.039	4.768	7.539	7.492	5.178	5.204	6.142	5.185	5.705
χ^2/dof	14.33	12.95	125.9	108.8	758.6	738.7	20.91	20.32	52.90	49.19

Table 4-12. Fit results for the CUORE 39A thermistors according to all the *Temperature Scale* and with the parameter γ both free and fixed. For the 39A_1 NTD only the CUORE-I data set has been used, while the fits for the 39A_3 thermistor are made with both CUORE data sets.

39C										
	T1		**T2**		**T3**		**T4**		**T5**	
39C_1	**γ free**	**γ fixed**	**γ free**	**γ fixed**	**γ free**	**γ fixed**	**γ free**	**γ fixed**	**γ free**	**γ fixed**
γ	0.490	0.5	0.515	0.5	0.477	0.5	0.501	0.5	0.499	0.5
R_0	0.570	0.675	0.256	0.194	0.957	1.203	0.363	0.356	0.386	0.392
T_0	4.722	4.145	5.006	6.040	4.806	3.743	4.959	5.018	4.902	4.844
χ^2/dof	5.308	4.841	34.96	30.10	354.0	336.0	12.35	11.44	24.80	22.74
39C_2	**T1**		**T2**		**T3**		**T4**		**T5**	
	γ free	**γ fixed**	**γ free**	**γ fixed**	**γ free**	**γ fixed**	**γ free**	**γ fixed**	**γ free**	**γ fixed**
γ	0.491	0.5	0.513	0.5	0.479	0.5	0.503	0.5	0.499	0.5
R_0	0.706	0.832	0.361	0.286	1.012	1.413	0.477	0.451	0.579	0.593
T_0	5.000	4.448	5.257	6.177	5.418	4.132	5.126	5.338	5.041	4.955
χ^2/dof	57.43	51.33	52.41	46.01	437.6	438.3	35.01	32.73	17.72	16.32

Table 4-13. Fit results for the CUORE 39C thermistors according to all the *Temperature Scale* and with the parameter γ both free and fixed.

39_3										
39_3_1	T1		T2		T3		T4		T5	
	γ free	γ fixed	γ free	γ fixed	γ free	γ fixed	γ free	γ fixed	γ free	γ fixed
γ	0.482	0.5	0.506	0.5	0.478	0.5	0.491	0.5	0.488	0.5
R_0	0.708	0.933	0.255	0.225	1.231	1.741	0.475	0.549	0.536	0.651
T_0	4.435	3.530	5.072	5.517	4.135	3.107	4.730	4.225	4.632	3.967
χ^2/dof	4.431	4.395	27.63	24.37	286.5	285.9	12.74	12.47	6.812	6.727
39_3_2	T1		T2		T3		T4		T5	
	γ free	γ fixed	γ free	γ fixed	γ free	γ fixed	γ free	γ fixed	γ free	γ fixed
γ	0.486	0.5	0.508	0.5	0.447	0.5	0.493	0.5	0.458	0.5
R_0	0.668	0.840	0.278	0.240	0.838	1.693	0.489	0.549	0.324	0.694
T_0	4.548	3.793	5.091	5.636	6.440	3.247	4.800	4.387	7.316	4.065
χ^2/dof	12.99	12.23	16.28	14.31	238.3	255.8	14.66	13.93	5.998	8.830

Table 4-14. Fit results for the CUORE 39_3 thermistors according to all the *Temperature Scale* and with the parameter γ both free and fixed.

40										
40_1	T1		T2		T3		T4		T5	
	γ free	γ fixed	γ free	γ fixed	γ free	γ fixed	γ free	γ fixed	γ free	γ fixed
γ	0.486	0.5	0.508	0.5	0.413	0.5	0.444	0.5	0.424	0.5
R_0	0.548	0.583	0.213	0.162	0.236	0.892	0.180	0.409	0.160	0.505
T_0	2.954	2.604	3.628	4.157	8.265	2.375	6.378	3.028	7.932	2.756
χ^2/dof	6.990	6.555	6.578	5.577	24.56	28.88	5.466	6.369	6.367	7.684
40_2	T1		T2		T3		T4		T5	
	γ free	γ fixed	γ free	γ fixed	γ free	γ fixed	γ free	γ fixed	γ free	γ fixed
γ	0.476	0.5	0.498	0.5	0.413	0.5	0.487	0.5	0.495	0.5
R_0	0.602	0.739	0.145	0.141	0.205	0.746	0.440	0.511	0.492	0.495
T_0	3.015	2.337	4.254	4.220	8.352	2.439	3.127	2.733	2.834	2.725
χ^2/dof	4.173	3.996	2.767	2.485	12.49	13.87	4.828	4.287	3.699	3.369

Table 4-15. Fit results for the CUORE 40 thermistors according to all the *Temperature Scale* and with the parameter γ both free and fixed.

Table 4-8 and Table 4-9 contain the fit parameters relative to the two reference thermistors, Table 4-10 and Table 4-11 are related to the CUORE-0 NTDs, while Table 4-12, Table 4-13, and Table 4-14 give the results for the top-offs of the CUORE #39 thermistors and Table 4-15 collects the data for the CUORE NTDs of series #40.

Observing the reduced χ^2 of the fits (see Figure 4-21) it is easy to notice that these values are generally high with respect to what expected for good fits. This means that the fitting law is not correct or that there is an underestimation of the errors of the fitted points.

Presently the resistance uncertainties have been calculated as the standard deviation of the resistance values in the plateau of each load curve (see 4.2), that is quite equivalent to measure several times the same resistance during a single run of the cryostat. But this doesn't take into account some systematic effect introduced by the cool down (different amount of He penetrating the IVC and so on) that are not under control during the measurement.

To check this kind of uncertainty one should repeat several cool downs with the same thermistors and averaging the different resistance values obtained for the same NTD at each temperature point during the different runs, and taking the corresponding standard deviation as the error. For distinguish the previously calculated statistical quantities from these new ones, the former will be named "time average" and "time standard deviation" and the latter "ensemble average" and "ensemble standard deviation" (shortened respectively in T.Av., T.St.D., E.Av., E.St.D.).

Because of the unwanted He-leakage into the IVC during the CUORE thermistor calibration run, that split the measurement in two parts, there is the unwilling possibility to have an idea of the ensemble average and standard deviation for the CUORE thermistor; as can be seen from Table 4-4, the CUORE-I and CUORE-II data sets have some common temperature points, even if they are few (four at maximum) and situated at the extremities of the temperature range, therefore it is possible to confront the single NTD measured resistances for these temperature points.

Moreover, there are two NTDs that took part to all the characterisation run, i.e. the two reference thermistors. Excluded the BIG23H that showed unexplained discrepancies between CUORE-I and CUORE-II runs, the H31-B25 NTD has eleven temperature points shared between CUORE-I/CUORE-II and CUORE-I/CUORE-0 data sets.

To understand the different weight of the two kinds of uncertainties, the ratio between the time standard deviation from CUORE-I data set and the average standard deviation from CUORE-I/CUORE-II and CUORE-I/CUORE-0 data sets has been calculated for the H31-B25 and the CUORE thermistors, with the exception of 39A_1, that showed some

discrepancies between the two CUORE data sets, even if smaller with respect to the BIG23H NTD.

The ratios, collected inTable 4-16, show that the T.St.D. is very often lower than E.St.D., indicating that using just the time standard deviation the uncertainties on the resistances are undervalued.

To understand better the effect of this underestimate, it is possible to perform an R-T fit for the H31-B25 data (the only NTD with a reasonable number of temperature point from the "ensemble" point of view), where T is given as usual from the different Temperature Scales, R is the ensemble average of the resistance among the characterisation runs for a fixed temperature and the corresponding standard deviation is the uncertainty on R.

The fits, with $\gamma = 0.5$, are displayed in Figure 4-20, while the corresponding VRH parameters are collected in the central part of Table 4-17, that in its part shows also, as comparison, the results previously obtained with "time quantities" from the CUORE-I data (see Table 4-9) and a third set of parameters coming from fitting the "time averaged" CUORE-I resistances with the ensemble standard deviations as uncertainties.

T.St.D / E.St.D								
NTD / **R_{therm}**	**H31**	**39A_3**	**39C_1**	**39C_2**	**39_3_1**	**39_3_2**	**40_1**	**40_2**
1.301	0.73	0.23	0.27	0.41	0.56	0.23	0.77	2.07
1.814	0.53	0.44	3.38	0.36	0.64	0.80	------	------
2.722	0.30	------	------	------	------	------	------	------
6.000	0.16	------	------	------	------	------	------	------
15.66	0.12	------	------	------	------	------	------	------
28.41	0.17	------	------	------	------	------	------	------
61.28	0.36	------	------	------	------	------	------	------
800.0	0.91	0.33	1.08	1.92	8.82	0.32	------	------
1800	0.55	------	0.52	1.29	1.67	------	------	------

Table 4-16. The ratio between the Time Standard Deviation from CUORE-I data set and the Average Standard Deviation from CUORE-I/CUORE-II and CUORE-I/CUORE-0 data sets. The 39A_1 thermistor has been omitted because of unexplained discrepancies between CUORE-I and CUORE-II data. The results show that the T.St.D is seldom higher than the E.St.D..

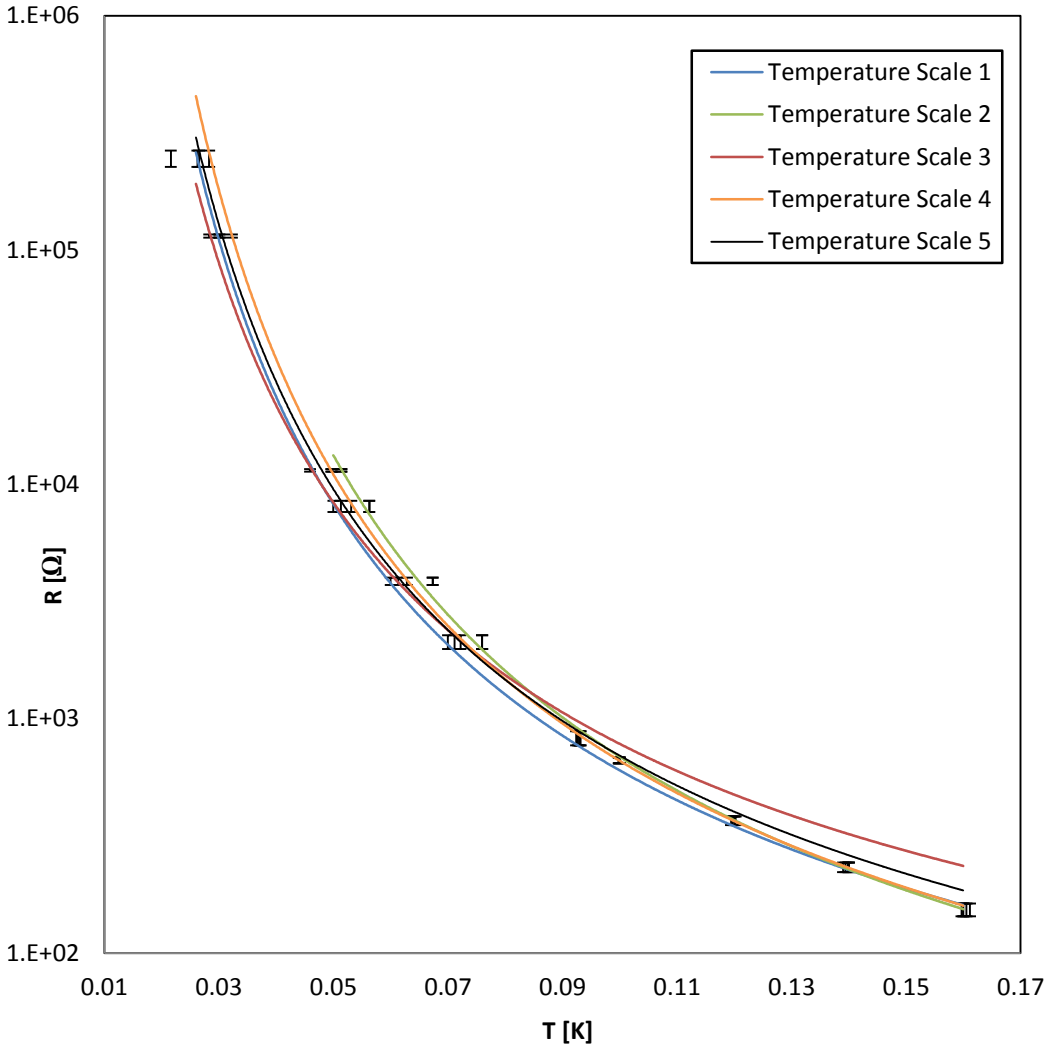

Figure 4-20. The fits of the "ensemble" H31-B25 thermistor using all the Temperature Scales are displayed. The resistance values at certain temperature come from the average of the NTD resistance among different characterisation runs, while the corresponding standard deviation is the resistance uncertainty.

The VRH parameters obtained using E.St.D. as uncertainties have reduced χ^2 values definitely smaller with respect to those obtained from the previous fit of the CUORE-I data set, even if the weight for each *Temperature Scale* is the same (number 3 has the highest χ^2 and number 4 the lowest).

The fit outputs of the three data sets are similar according to the *Temperature Scale*; in particular, fitting time averaged CUORE-I resistance with ensemble standard deviation, give the same parameters but with more meaningful χ^2, indicating that the problem of having high reduced χ^2 depends more on a underestimation of the uncertainties rather than using a wrong law. From this consideration, it is still possible to use the χ^2 values obtained from time

averaged resistances and the corresponding time standard deviation to select which, among the five candidates, is the most reliable *Temperature Scale.* This selection will be carried out in the next section.

4.4.1. Some consideration on the Temperature Scales

The primary step of the analysis should be the determination of a unique *Temperature Scale* for having a single set of calibration parameters for each NTD.

A first exclusion of certain scales can be done by looking at the reduced χ^2 of the fits. The values of the reduced χ^2 obtained for all the fits for each *Temperature Scale* are collected in the spectrum displayed in Figure 4-21. As can be easily seen, *Temperature Scale 3* results very often in extremely high χ^2, indicating that these fits are not good. Probably the phenomenological extrapolation (Eq. 4-4) of the calibration data is not reliable. Also the *Temperature Scale 2* can be excluded by looking at the χ^2 distribution. In this case the fits are not so bad as in the previous one, but this calibration suffers the fact that it is based only on data points not lower than 50 mK, excluding the points closer to the actual operating temperatures of the NTDs.

H31-B25					
"T.Av" CUORE-I data	**T1**	**T2**	**T3**	**T4**	**T5**
R_0	1.296±0.063	0.316±0.009	2.673±0.048	0.768±0.038	1.216±0.009
T_0	3.887±0.050	5.959±0.037	3.276±0.017	4.590±0.056	4.002±0.007
χ^2/dof	7.743	26.35	619.2	8E-06	5.638
E.Av. data	**T1**	**T2**	**T3**	**T4**	**T5**
R_0	1.132±0.070	0.396±0.100	2.114±0.096	0.730±0.052	1.135±0.067
T_0	3.994±0.051	5.581±0.359	3.317±0.034	4.619±0.065	4.014±0.049
χ^2/dof	1.100	2.091	54.34	0.092	0.815
T.Av. CUORE-I data with E.St.D	**T1**	**T2**	**T3**	**T4**	**T5**
R_0	1.190±0.068	0.409±0.047	2.199±0.137	0.768±0.074	1.193±0.096
T_0	3.970±0.047	5.581±0.163	3.303±0.046	4.590±0.088	3.989±0.068
χ^2/dof	0.419	1.154	27.48	1E-06	0.441

Table 4-17. VRH parameters for the H31-B25 thermistor obtained from fitting "time" and "ensemble" data, with all the *temperature Scales* and γ fixed to 0.5. In the first part of the table, denoted with "T.Av. CUORE-I data", the "time quantities" from the CUORE-I data have been used (see Table 4-9); the second part of the table, indicated by "E.Av. data", collects the results from fitting the ensemble averaged resistances from different characterisation runs; in the last part T.Av. CUORE-I data with E.St.Dev. have been used.

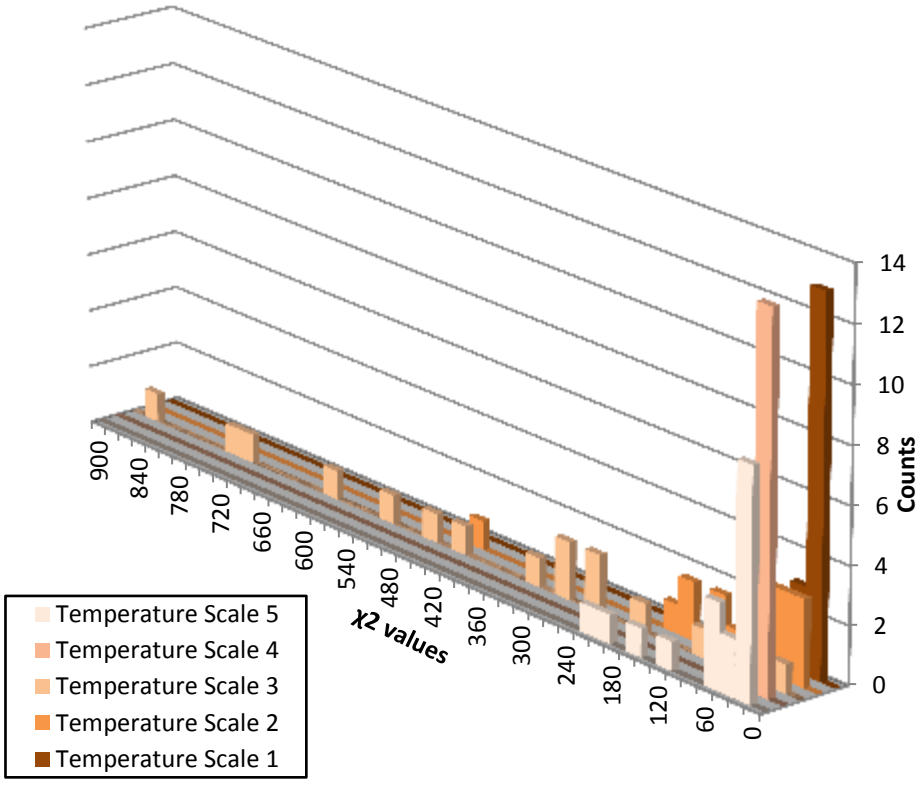

Figure 4-21. For each Temperature Scale, the spectrum of the reduced χ2 values obtained for the fits with γ=0.5 is displayed.

Among the remaining *Temperature Scale*, the number 5, obtained by fitting the BIG23H thermistor, is the worst one. Looking in detail to the fits results obtained with this scale, it can be seen that the highest reduced χ^2 values come from the fits of the CUORE-0 measurements. In particular, there is a huge difference in the results obtained fitting the BIGH23H with this "own" scale if the CUORE-I or CUORE-0 data are used: in the first case the outcome of the fit coincides exactly with the calibration parameters (see column 10 of Table 4-8 and right side of Table 4-6), in the second case the difference is very high. On the contrary, for the other reference thermistor, the H31-B25 the fits results obtained with both data sets are comparable (see column 8 of Table 4-8 and left side of Table 4-6).

Considering also that the BIG23H thermistor is the one that was mostly affected by the re-cooling during CUORE NTD characterisation run (see Figure 4-13), it can be deduced that this NTD suffers of some systematic problem, probably connected to its link to the holder, making its performances slightly different from one run to another. For this reason, the calibration made with this thermistor is not reliable.

H31-B25	T1		T4	
$\gamma = 0.5$	CUORE-0 data	CUORE-I data	CUORE-0 data	CUORE-I data
R_0 [Ω]	1.480	1.296	0.579	0.768
T_0 [K]	4.127	3.887	4.841	4.590
χ^2/dof	4.020	7.743	4.532	8E-06
R [MΩ] (T=15mK)	13.96	12.70	36.66	30.39
R [MΩ] (T=10mK)	558.0	473.0	2077	1549

Table 4-18. Fit results for the H31-B25 Cuoricino thermistor according to the *Temperature Scale 1* and the *Temperature Scale 4*, with γ = 0.5. The resistance values at 15 and 10 mK, calculated from each set of parameters are also reported.

Let's now compare the two remaining scales, the one made with the calibrated thermometer (*Temperature Scale 1*) and the other based on the Cuoricino reference NTD (*Temperature Scale 4*). Both provide reasonably fits for all the samples, with γ close to 0.5 when let it free. However, they result in different fit parameters for all the thermistors.

To decide which one has to be considered the most reliable, the results obtained for the fit with γ = 0.5 of the H31-B25 Cuoricino NTD have been compared and also its resistance values extrapolated down to 15-10 mK (see Table 4-18).

The fit results obtained with the *Temperature Scale 1* are closer to the ones obtained with previous calibration of the Cuoricino NTD and the extrapolation of the VRH law to temperatures in the range 10-15 mK provides resistance values very close to those observed in the Gran Sasso refrigerator runs. On the contrary, the extrapolation results carried out for the VRH parameters obtained with Temperature Scale 4 are too high. This is probably due to the fact that the calibration of H31-B25 used as thermometer is made with too few points, in a too high temperature range and with too low resistance values, close to the wire resistance.

After all these considerations, *Temperature Scale 1* is taken as the most reliable.

CUORE-0 thermistors						
NTD	**Q0-34C**		**Q0-34B**			**H31-B25**
	1A	**1C**	**5A**	**5B**	**5C**	
T_0 [K]	4.029	4.389	4.170	4.362	4.266	4.127
R_0 [Ω]	1.202	1.796	1.361	1.600	1.336	1.480
R [MΩ] (T=15mK)	15.76	48.17	23.71	40.77	28.15	13.96
R [MΩ] (T=10mK)	627.0	2250	1005	1883	1246	558.0

Table 4-19. Results for the fits of the CUORE-0 thermistor using *Temperature Scale 1* and γ = 0.5. With the obtained parameters the NTD resistance values have been extrapolated down to the usual thermistor operational temperatures.

CUORE thermistors					
NTD	**39A**		**39C**		**H31-B25**
	1	**3**	**1**	**2**	
T_0 [K]	5.495	5.039	4.145	4.448	3.887
R_0 [Ω]	0.737	0.710	0.675	0.832	1.296
R_0' [Ω]	0.890	0.858	0.815	1.005	1.296
R [MΩ] (T=15mK)	182.9	78.28	13.51	30.27	12.70
R [MΩ] (T=10mK)	13503	4816	566.6	1452	473.0
NTD	**39_3**		**40**		**H31-B25**
	1	**2**	**1**	**2**	
T_0 [K]	3.530	3.793	2.604	2.337	3.887
R_0 [Ω]	0.933	0.840	0.583	0.739	1.296
R_0' [Ω]	1.127	1.016	0.704	0.893	1.296
R [MΩ] (T=15mK)	5.175	8.187	0.372	0.246	12.70
R [MΩ] (T=10mK)	162.6	291.9	7.181	3.895	473.0

Table 4-20. Results for the fits of the CUORE thermistors using *Temperature Scale 1* and γ = 0.5. With the obtained parameters, scaled to thermistor with the real CUORE size, the NTD resistance values have been extrapolated down to the usual thermistor operational temperatures.

4.4.2. General comments on the results

The fit results for all the NTDs using *Temperature Scale 1* with γ fixed to 0.5, and the extrapolation of the VRH law in the usual operational temperature range are summarized in Table 4-19 and Table 4-20. For the case of the CUORE thermistors, the extrapolation has been done considering NTDs with the pad distance foreseen for CUORE (see Section 3.3.1.1).

Concerning the CUORE-0 thermistors, what emerges from the collected data is that the samples are similar according to their series numbers. For each temperature point the NTD resistance is between 1 and 3 times the resistance measured for the H31-B25 Cuoricino reference thermistor (Figure 4-22.).

Also the ratio between the CUORE-0 NTD and the H31-B25 resistances extrapolated to the CUORE-0 experiment working temperatures ranges between 1 and 4 (see the first columns of Table 4-21). That means that the final expected CUORE-0 thermistor resistances will be around some hundreds of MΩ, as desired.

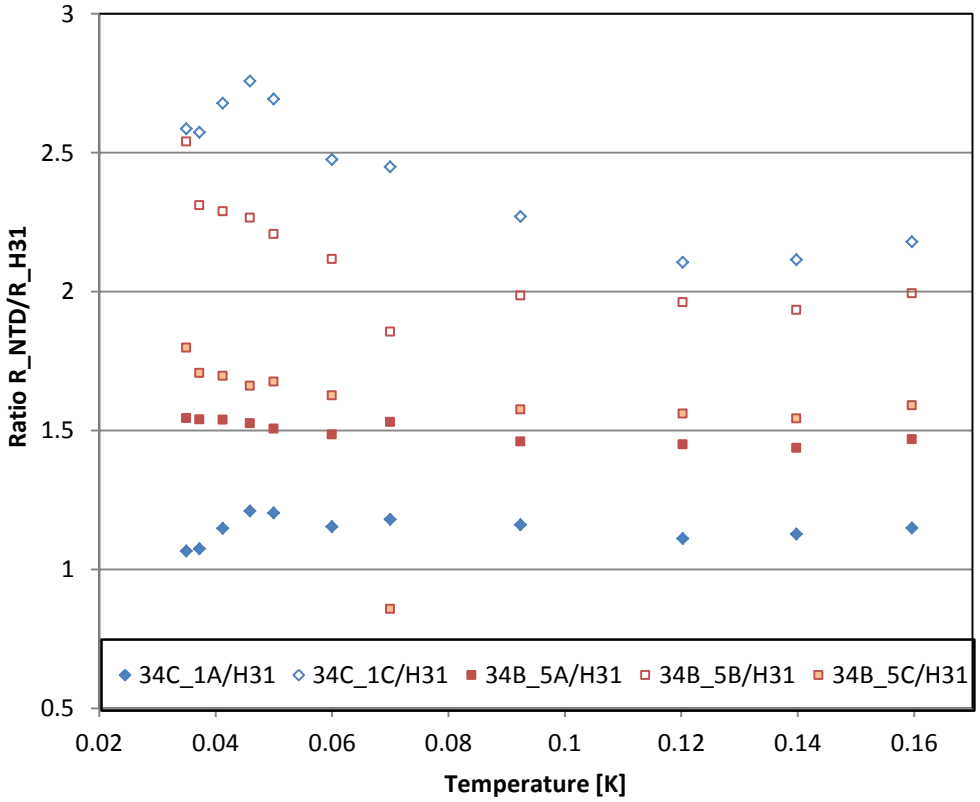

Figure 4-22. The ratios between each CUORE-0 thermistor and the H31-B25 Cuoricino reference NTD for all the temperature points collected during the CUORE-0 characterisation run.

NTD	$R_{Q0NTD}/R_{H31-B25}$ @ CUORE-0 working T		|ΔT| for $R_{H31-B25}(T_{work}+\Delta T) = R_{Q0NTD}(T_{work})$		T_{Q0NTD} for R equal to min and max value allowed by the electronics	
	15 mK	10 mK	15 mK	10 mK	50 MΩ	500 MΩ
Q034C_1A	1.13	1.12	0.40 mK	0.28 mK	13.1 mK	10.2 mK
Q034C_1C	3.45	4.03	2.21 mK	1.41 mK	14.9 mK	11.6 mK
Q034B_5A	1.70	1.80	1.10 mk	0.72 mK	13.7 mK	10.7 mK
Q034B_5B	2.92	3.38	1.96 mK	1.27 mK	14.6 mK	11.4 mK
Q034B_5C	2.07	2.23	1.38 mK	0.92 mK	14.0 mK	10.9 mK

Table 4-21. The first part shows the ratios between each CUORE-0 thermistor and the H31-B25 Cuoricino reference NTD for the working temperatures foreseen for the CUORE-0 experiments. The thermistor resistance values have been extrapolated from the VRH law obtained with the Scale Temperature 1 with γ = 0.5. The central part of the table shows show how much the temperature of the H31-B25 thermistor should change with respect to the working temperature in order that this NTD reaches the CUORE-0 NTD resistance at the working temperature. In the last two columns there are the temperatures to which the CUORE-0 thermistors should be cooled down for having a resistance corresponding to the minimum and the maximum value allowed by the CUORE-0 electronics (50 MΩ and 500 MΩ respectively).

NTD	$R_{QNTD}/R_{H31-B25}$ @ CUORE working T		ΔT for $R_{H31-B25}(T_{work}+\Delta T) = R_{QNTD}(T_{work})$		T_{QNTD} for R equal to min and max value allowed by the electronics	
	15 mK	10 mK	15 mK	10 mK	50 MΩ	500 MΩ
39A_1	14.4	28.6	3.96 mK	2.70 mK	16.9 mK	13.3 mK
39A_3	6.16	10.2	2.89 mK	2.00 mK	15.4 mK	12.1 mK
39C_1	1.06	1.20	0.12 mK	0.18 mK	12.6 mK	9.9 mK
39C_2	2.38	3.07	1.50 mK	1.05 mK	13.9 mK	10.9 mK
39_3_1	0.41	0.34	1.82 mK	1.18 mK	11.1 mK	8.7 mK
39_3_2	0.65	0.62	0.85 mK	0.51 mK	11.8 mK	9.3 mK

Table 4-22. The first part shows the ratios between each CUORE thermistor of the top-off of #39 series and the H31-B25 Cuoricino reference NTD for the working temperatures foreseen for the CUORE-0 experiments. The thermistor resistance values have been extrapolated from the VRH law obtained with the Scale Temperature 1 with γ = 0.5. The central part of the table shows how much the temperature of the H31-B25 thermistor should change with respect to the working temperature in order that this NTD reaches the CUORE-0 NTD resistance at the working temperature. In the last two columns there are the temperatures to which the CUORE thermistors should be cooled down for having a resistance corresponding to the minimum and the maximum value allowed by the CUORE electronics (50 MΩ and 500 MΩ respectively).

NTD / R_{therm}	34B_1A	34C_5A	39A_3	39C_1	39_3_1	40_1
1.301	0.07	0.18	0.21	0.12	0.50	1.02
1.814	0.03	0.11	0.10	0.11	0.43	0.77
2.722	0.02	0.10	0.10	0.07	0.30	0.95
4.68	------	------	0.03	0.04	0.11	0.68
6	0.01	0.03	0.02	0.03	0.19	0.89
9.705	------	------	0.03	0.01	0.08	0.90
15.66	0.01	0.06	0.03	0.02	0.09	0.90
20.73	------	------	0.04	0.02	0.05	0.31
28.41	0.01	0.02	0.03	0.02	0.11	0.51
40.63	------	------	0.05	0.15	0.25	0.54
61.28	0.02	0.05	0.03	0.06	0.17	2.21
90	0.04	0.05	0.06	0.03	0.15	1.00
150	0.01	0.01	------	------	------	------
250	0.02	0.07	0.07	0.04	0.15	1.56
346	0.06	0.07	0.24	0.09	0.39	1.00
800	------	------	0.09	0.14	0.46	0.88
1800	------	------	0.36	0.08	0.21	------

Table 4-23. The ratio between the time standard deviation of the first thermistor of each group and the error used for the last fit is shown.

This can be better understood by calculating the temperature variation of the H31-B25 NTD with respect to the working point to reach the CUORE-0 NTD resistance at the operating temperature (Table 4-21, central columns): the ΔT is very small, around one mK for all the thermistors, underlining again how the CUORE-0 and the Cuoricino NTDs are compatible. This is confirmed also by the temperatures the NTDs should reach in case their resistance is the minimum or the maximum value allowed by the CUORE-0 electronics, i.e. 50-500 MΩ. As can be seen from last columns of Table 4-21, these temperatures range from 10 to 15 mK for all the CUORE-0 NTDs and are normally reachable with the LNGS cryostats.

Regarding the CUORE NTDs, also in this case the samples are similar in pairs, according to their series numbers. The analysis confirms that the doping of series #40 is not suitable for the CUORE purpose. The three top-off types of series #39 look different, with a dose increasing in this sense: 39A, 39C, 39_3.

The 39A thermistors are quite far from the behaviour of the Cuoricino NTDs, while the samples closer to the Cuoricino thermistors are those of the series 39_3. The difference

between the 39C and the 39_3 NTDs results strange, because in principle they belongs to the same wafer, being the 39_3 a witness pieces of the 39C.

Among the causes of this discrepancy one can be the presence of some systematics in the characterisation process: as pointed out in Section 4.2 (see in particular Figure 4-8), after the re-cooling occurred during the CUORE thermistor characterisation run, all the NTDs re-established their initial condition except the BIG23H and, in a minor way, the first of the 39A thermistors. This discrepancy in the thermistor behaviour seems to be dependent on the position of the NTD on the copper holder, but it has been not understood yet, also because no "position effects" appeared in the characterisation of the CUORE-0 thermistors.

For the 39C and 39_3 thermistors the ratio between the NTDs resistances and the Cuoricino thermistor resistances at the CUORE working temperature ranges between 0.4 and 3, corresponding to a change in the H31-B25 temperature of about 1-2 mK with respect to the operating point for having the same resistance of the 39C and 39_3 NTDs at the working temperature. The limit resistances allowed by the electronics converted in temperature are compatible with the temperature reachable by the LNGS cryostat, even if for the 39_3 they are a little bit smaller (see Table 4-22). From these considerations the 39C top-off (and perhaps also the 39_3) comes out to be surely usable for CUORE.

The last step of this section will be deriving a unique set of VRH parameters for each thermistor group (34C, 34B, 39A, 39C, 39_3 and 40). In doing that the *Temperature Scale 1* has been used for converting the thermometer data and the fits have been done fixing $\gamma = 0.5$.

The NTDs of each group have been considered as the same sample, measured twice (or three times in case of 34B) during a single characterisation run. Where possible, the resistance points from both CUORE-I and CUORE-II runs have been used. The thermistor resistance values used in the fits are the average of the points described before and the corresponding standard deviation has been taken as uncertainty. The inhomogeneity in behaviour among the thermistors belonging to the same series arises because of possible differences in the way they are glued to the holder.

As can be seen from Table 4-23, the ratio between the usual time standard deviation and this new error is very small, smaller also with respect to the ratio T.St.D./E.St.D., (Table 4-16) ensuring that there is no underestimation of the errors. The fits are displayed in Figure 4-23 and the related parameters are collected in Table 4-24.

The global fits of the two CUORE-0 series give very similar results and the ones for the CUORE NTDs confirm the previous outcomes. To confirm this result however, a test of these NTDs on a real bolometer is mandatory, for checking also the quality of the signal obtained. This will be discussed in the next Chapter.

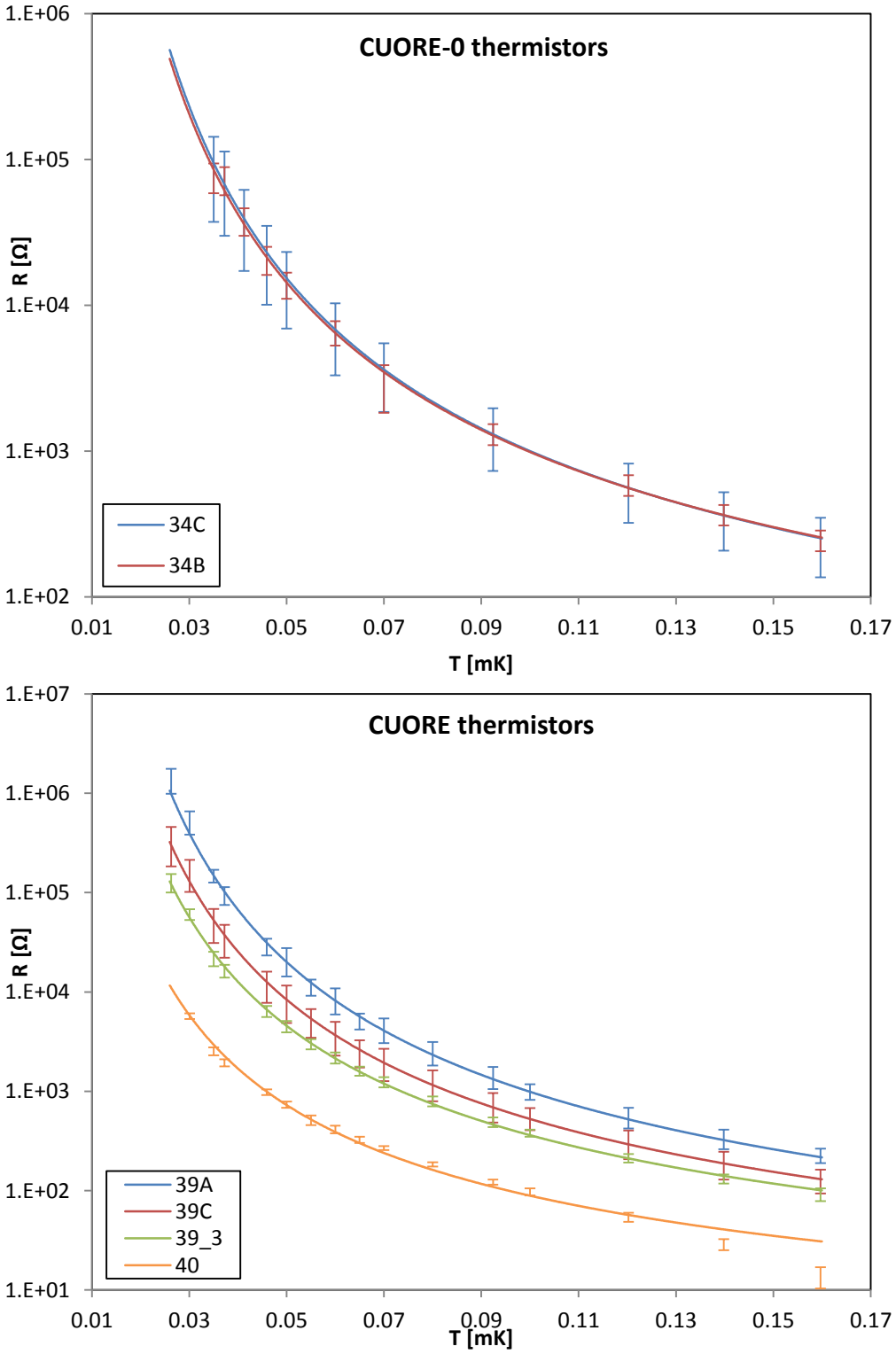

Figure 4-23. Global fit with a γ= 0.5 VRH law of the CUORE-0 and CUORE thermistors (upper and lower plot, respectively) using Temperature Scale 1 and averaging on all the NTDs of each series.

	R_0	T_0	χ^2	R'
34C	1.378±0.826	4.342±0.644	0.004	1.378
34B	1.549±0.499	4.170±0.341	0.163	1.549
39A	0.694±0.330	5.274±0.524	0.230	0.838
39B	0.662±0.348	4.460±0.554	0.037	0.800
39_3	0.796±0.144	3.744±0.177	0.263	0.962
40	0.558±0.078	2.572±0.107	4.792	0.674

Table 4-24. VRH parameters obtained from fitting the CUORE-0 and CUORE thermistor series considering all the thermistors of each series as different measurements of a single NTDs and using *Temperature Scale 1*. R' is the R_0 parameter scaled for thermistors with the real CUORE-0/CUORE size.

Chapter 5.
CUORE-0/CUORE CRYSTAL AND THERMISTOR VALIDATION

"Four fried chickens and a Coke".[13]

As described in Chapter 3, an extremely high level of cleanliness and radio-purity of the detector materials is required, in order to reach the desired background level for the CUORE experiment. Careful attention is devoted to the control of each phase of the crystal growth (described in Section 3.2.3) including raw materials, reagents, intermediary products, consumables and equipment. Some steps are particularly relevant: the validation of crystal seeds, for example, which are used for many growth cycles.

Several techniques are used for the certification of the CUORE crystals, the last being a bolometric test with some sample of the final production. These last measurements and their results are the subject of this Chapter; moreover, some of the test crystals are equipped with CUORE-0 and CUORE thermistors, whose characterization is described in the previous Chapter, allowing a more complete validation of the future CUORE Single Module elements.

5.1. Validation protocol for the CUORE crystal production

The entire production process is subject to a complex validation protocol illustrated in Figure 5-1 which includes radio-purity certification procedures to be applied in each production phase and immediate actions to be taken in case of failure, including the halt of crystal production until the problem is solved. Different techniques are applied for the radio-purity certification: Inductively Coupled Plasma Mass Spectrometry (ICP-MS) and Gamma spectroscopy with HPGe detectors were devoted to the test of all the raw materials used in the crystal growth, while alpha spectroscopy with Surface Barrier Detectors (SBD) is used to prevent contamination of the crystal surfaces after the final phases of their production.

[13] (224)

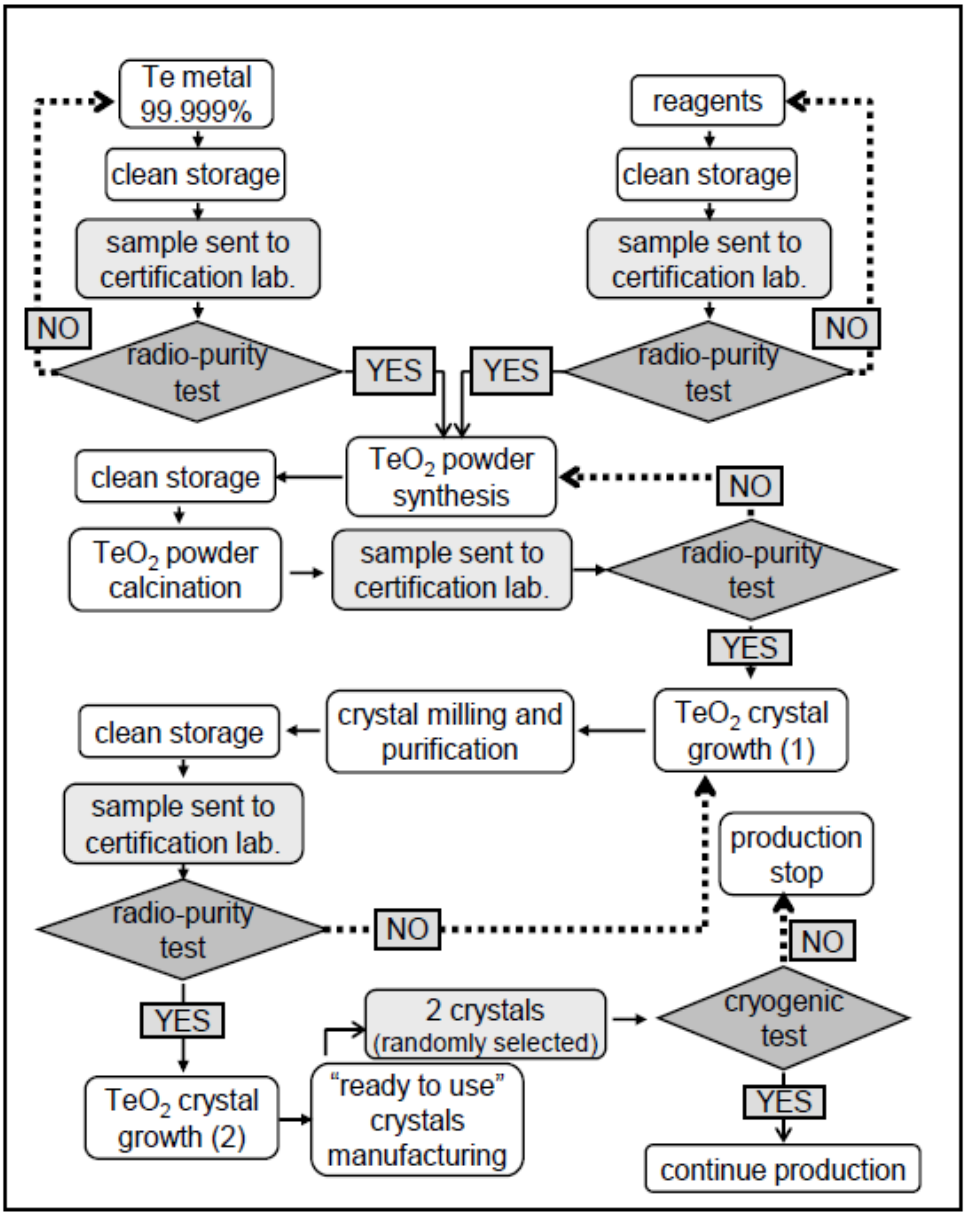

Figure 5-1. Radio-purity certification protocol applied for TeO_2 crystals.

An ICP-MS combines a high temperature Inductively Coupled Plasma source with a Mass Spectrometer. The sample is typically introduced in the ICP plasma as an aerosol, either by aspirating a liquid or dissolved solid sample into a nebulizer or by converting directly solid samples to the aerosol form using a laser: after introduction, its elements are converted first into gaseous atoms and then ionized towards the end of the plasma. Ions are collimated into a beam by a system of electrostatic lenses and focused into the entrance of the mass

spectrometer, where they are separated by their mass-to-charge ratio. The most commonly used type of mass spectrometer is the quadrupole mass filter.

ICP-MS measurements were performed at LNGS on all raw materials and intermediary products for the CUORE crystal growth; results were systematically crosschecked following the same measurement protocol on twin samples at the Shanghai Institute of Applied Physics (SINAP), in China, and at the Lawrence Berkeley National Laboratory (LBNL), in the USA. Dedicated sample preparation protocols (different procedures depending on the nature of samples) were developed, in order to enhance the sensitivity, and applied in all laboratories for cross-check measurement.

The sensitivities on the investigated radio-nuclides (see Section 3.2.3 and Table 5-1) obtained with this measurement protocol and dedicated samples treatment conditions are very high: $2 \cdot 10^{-10}$ g/g for ^{232}Th and ^{238}U in solid raw materials and consumables (Te, TeO_2, Al_2O_3, SiO_2), 10^{-12} g/g in H_2O and 10^{-11} g/g in all other reagents. For the other contaminants measured, the sensitivities were 10^{-9} g/g for ^{195}Pt and ^{209}Bi in solid samples and 10^{-11} g/g for Bi and Pb in the reagents (10^{-12} g/g in the case of H_2O). The only exception was the low 10^{-6} g/g sensitivity reached for 40K, which was improved by means of the second certification technique, i.e. gamma spectroscopy with HPGe detectors.

This technique allow determining the contaminant concentration in a given sample by direct measurement of the energy of γ-ray photons emitted by radio-nuclides as a consequence of their α and β-decays. It is extremely sensitive thanks to a good energy resolution for distinguishing different gamma ray lines, intrinsic low radioactive contamination of the measurement system, and to effective shielding of the detector from environmental radioactivity. In particular, the HPGe measurements related to the production process of TeO_2 crystals took place at LNGS, were the sensitivity of measurements is enhanced by the reduced cosmic ray background due to the underground location.

Sensitivities of the order of 10^{-10} were achieved on the U and Th chains in ~2 kg samples, which are deemed sufficient for the certification of raw materials and consumables in the synthesis of TeO_2 crystals: although lower limits could be obtained by increasing measurement times, the choice was made to stick to response times of a few weeks in order to give prompt answers without delaying the schedule of crystal production.

These two techniques were devoted to the radio-purity certification of raw materials, reagents, consumables and intermediate products that could be sources of bulk radioactivity in the final TeO_2 crystals. For certification activities aimed at preventing surface contamination the final phase of the crystal production (cutting and shaping, surface processing, packaging and shipment) the Surface Barrier Detector (SBD) technique was used

because able to reach a very low level counting in the alpha decay energy range. Alpha decay is a good indicator of possible surface contamination from the ^{238}U and ^{232}Th chains. Especially in the ^{232}Th decay chain there are isotopes that can emit particles which produce an important background for the final detector. Measurements with SBDs were conducted at the Milano-Bicocca University environmental radioactivity laboratory.

Despite all of these measurements (whose results are detailed in (147)), a validation of the ready-to-use crystals is still necessary to verify the contamination levels of the final product and can be performed only by means of cryogenic tests in an R&D setup with conditions close to those of the final experiment are met. This is the purpose of the CUORE Crystal Validation Runs.

5.2. CUORE Crystal Validation Runs

The goal of the CUORE Crystal Validation Runs (shortened in CCVRs) is to measure the bulk and surface contaminations of the new crystals produced by SICCAS after the definition of the new growth procedure. The allowed radioactive contamination limits of the crystals (Table 5-1) are extremely low; therefore the only way to verify them is to use the bolometric technique, i.e. using the crystals as absorbers in bolometers. Moreover, because often the thermistors coupled to the crystal belong to the CUORE-0 or CUORE batches, CCVRs can give a hint of the bolometric performances of the future CUORE detectors.

A CCVR run is made of four crystals randomly chosen from a single CUORE batch coming from SICCAS, each equipped with two thermistors and one heater for the energy stabilization, assembled in a Cuoricino-like Single Module and operated at cryogenic temperatures. The detector construction followed the manual procedure used for the Cuoricino detector that will be entirely presented in Section 5.2.1.

Isotope	Allowed contamination	Decays/crystal at the allowed contamination level
^{238}U	$< 3 \cdot 10^{-13}$ g/g	0.24/day
^{232}Th	$< 3 \cdot 10^{-13}$ g/g	0.079/day
^{210}Pb	$< 1 \cdot 10^{-5}$ Bq/kg	0.65/day
^{60}Co	$< 1 \cdot 10^{-6}$ Bq/kg	0.065/day
^{210}Po	< 0.1 Bq/kg	270/h

Table 5-1. The contamination limits imposed to SICCAS for the final product, i.e. the CUORE crystals. As a reference, the last column shows the decay rates if the crystals have contaminations at the contract limits.

Run	Crystals	Duration	Live time [days]
CCVR-I	007, 011, 039, 041	Dec 20, 2008 – Mar 9, 2009	59.9
CCVR-II	007, 011, 076, 096	Jun 6, 2009 – Jun 30, 2009	19.4
CCVR-III	180, 190, 229, 236	Nov 11, 2009 – Jan 4, 2010	43.05
CCVR-IV	313, 340, 354, 380	Mar 31, 2010 – May 17, 2010	25.8
CCVR-V	416, 421, 436, 455	Aug 11, 2010 - Oct 1, 2010	30.3
CCVR-VI	447, 476, 546, 547	Jan 22, 2011 - Feb 8, 2011	11.8

Table 5-2. Summary of CCVR data taking periods and live times.

All the CUORE crystals (and therefore the one used in CCVRs) moves from China to LNGS by ship, to avoid cosmic activation due to the travel in the high atmosphere. The only exception are the four crystals used in CCVR-I (two of them were also re-tested in CCVR-II) that reached LNGS by plane in order to ensure a fast response on the radioactivity level of the initial crystal production. Table 5-2 collect a summary of the CCVR detector operation.

Most of the CCVRs have been assembled during this PhD thesis and the results of the first five runs in terms of radioactive contaminations will be presented in Section 5.1. For what concerns the bolometric performances of these detectors, the attention will be focused on CCVR-IV, CCVR-V and CCVR-VI, containing the CUORE-0 and CUORE NTDs in Section 5.4.

5.2.1. Manual detector assembly

The construction of a CCVR detector follows the procedure used for the assembly of the Cuoricino Single Module. In particular, for the coupling of the sensor to the absorber the same tools designed for Cuoricino are used, while the copper treatment and some in the final set-up are different. The manual thermistor-to-crystal connection and its problematic will be discussed here, in order to understand some difficulties in the CCVRs data analysis (above all in the detector performance evaluation) and the necessity to have a semi-automatic line for the CUORE construction.

The construction of a single CCVR (detailed in (179)) can be divided in three steps:

1) single element preparation;
2) thermistor-to-crystal gluing;
3) detector assembly.

The main room in the initial detector preparation is occupied by the cleaning of the holder Cu parts and by their wrapping in six polyethylene layers, for an overall layer of ~70 μm, according to the prescription used in the best tower of the TTT detector (Section 3.4.1). The other important step is the inspection of the box (Figure 5-2) containing the crystals, packed under vacuum in three plastic bags, in search of damages or unwanted air exposure.

Figure 5-2. (From left to right) A closed box, with its proper barcode; the crystal box is open, revealing it Polystyrene holder for the crystals; a single packed crystal: on each plastic bag the barcode identifying the single crystal is reproduced.

The coupling of the NTD to the crystal is made thanks to the so-called Cuoricino gluing tool, whose elements are presented in Figure 5-3. The main idea behind the procedure is to deposit glue spots on the sensor and not on crystal surface (that, differently from the NTD, cannot be clean) thanks to a matrix of 3x3 tips.

The thermistor (provided with gold wires) is placed in a devoted indentation on the movable cylinder in the centre of the gluing tool basement and held with vacuum. This cylinder is free to move in the vertical direction and can be fixed in a stable position: in particular, thanks to a proper spacer cap, the cylinder holding the thermistor can be lowered in order that the NTD upper surface stays 50 μm lower with respect to the top of the gluing tool, where the crystal will be deposed at the end. This ensures the correct spacing between sensor and crystal and allows working with thermistor of different thickness but, because of the finite dimensions of the recess, NTD larger than the indentation (or with gold wires attached not laterally) should be lifted with a small ring (see Figure 5-4).

In a special cap, able to slide on the gluing tool, the 3x3 matrix of tips (each of them with adjustable vertical position) is mounted. After the 30 second manual mixing of the two glue components (dosed in 1:1 volume ratio by eye) in a Teflon basin and the levelling of the final mixture, the pins are dipped in the basin and then pushed on the upper surface of the sensor thanks to the cap.

Then a proper PTFE holder is inserted on the gluing tool, where the TeO_2 crystal is placed and kept in position, and lowered toward the thermistor until the crystal touches the top of the gluing tool. Because of the spacing between the NTD and the gluing tool surface, the crystal will touch only the top of the nine glue dots, preserving the shape of the matrix.

All the stages starting from the gluing mixing must take no more than the three-five minutes corresponding to glue pot life at room temperature; then the detector rests on the PTFE holder for the whole duration of curing time.

Figure 5-3. Counterclockwise: the gluing tool, with the moving central cylinder hosting the recess for the thermistor, and the PTFE crystal holder; the spacer cap for placing the upper face of the NTD 50 μm below the surface of the gluing tool; the cap with the nine tips for the glue deposition; a detail of the 3x3 tip matrix; the TeO_2 crystal placed In the PTFE holder at the end of the gluing procedure.

Figure 5-4. The two cases of thermistor positioning. If the NTD width fits the indentation and the bonding is lateral, the thermistor is simply put in the recess, with the gold wires arranged along the lateral recesses. In case of bigger thermistor and/or with frontal bonding, a small ring is placed to raise the NTD with respect to the indentation.

This brief description is useful to point out all the uncertainties intrinsic to the manual gluing procedure (nevertheless able to bring to the Cuoricino results!), that can rise discrepancies in the CCVR results, in particular in the detector performance such as energy resolution and signal shape. The most important problems connect to this procedure (and therefore arise during the CCVRs assembly) are:

- ✓ thermistor breaking because of dimension too close to the recess ones: when the glue procedure is finished and the glued crystal is removed from the gluing tool, a part of the NTD can remain stuck in the indentation (Figure 5-5);
- ✓ thermistors damaging when the spacer cap for the creation of the 50 μm gap is pressed: the thermistor can be cracked if force is not applied perpendicularly (Figure 5-6 left);
- ✓ thermistor loosing wires in any moment of the assembly;
- ✓ difficulties in positioning the thermistor with respect to the nine-tip matrix if the NTD size is very smaller with respect to the recess (Figure 5-6, right);
- ✓ erosion and dirtiness of the nine tips: uneven quantities of glue are picked up by the pins when they are in different cleaning conditions, leading to a spread in the diameters of spots belonging to the same matrix. This could mean epoxy dots so small that they don't touch crystal surface, as well as spots large enough to merge with the neighbouring ones;
- ✓ manual dosing and mixing of the two glue components: an unequal proportion of resin to hardener leads to a variation in glue properties and manual mixing does not guarantee thorough uniformity in the final result.
- ✓ uncertainties in the crystal placing can cause a not parallel descent of the crystal on the glue spot, therefore the crystal can damage the matrix when deposed on it (Figure 5-7).

In view of the construction of the CUORE, a new thermistor-to-absorber coupling procedure is mandatory, with a higher level of simplicity and reproducibility. The work performed toward this goal will be presented in the next chapter.

The last step of the of the CCVR assembly is the construction of the holder housing the four crystals by mounting the Cu frame (Figure 5-8, left), connecting the gold wires from the thermistors to the Cu pins (Figure 5-8, right), wrapping the entire detector into a 70 μm thick polyethylene layer (Figure 5-9, left), connecting the electrical wires (Figure 5-9, right) and assembly the external Cu shields (Figure 5-10). Particular attention is paid to the cleanliness of all the assembly steps, to avoid introducing of further surface contaminations.

Figure 5-5. NTD broken during the gluing procedure. Its dimensions were too close to the ones of the indentation, therefore, when the glued crystal was removed, a piece of the thermistor remained in the recess.

Figure 5-6. (Left) Broken NTD because of a too high pressure on the spacer cap. (Right) A small NTD is in position for receiving the glue: because it is very small, it can accommodate only six spot, therefore a row of pin has been moved away and the thermistor has been decentred using the small ring in order to fit with the remaining tips.

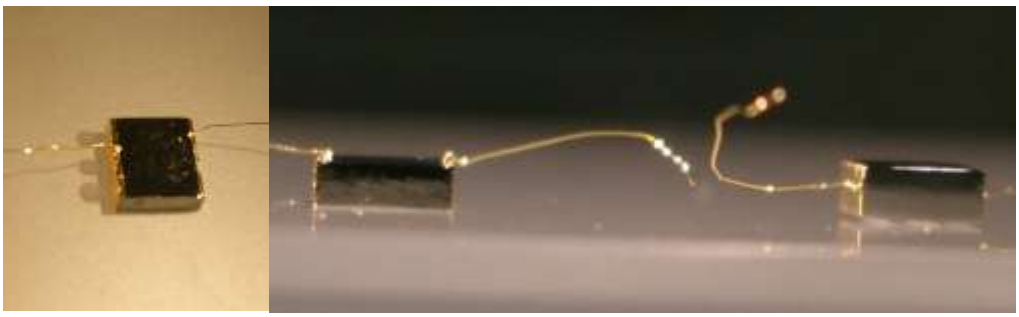

Figure 5-7. (Left) Because of an unwanted moving of the crystal in the PTFE holder, the crystal "skipped" a row of glue spots (visible on the left of the NTD), and squashed the remaining dots in a veil of glue. The difference between this gluing and another successful one is shown in the right.

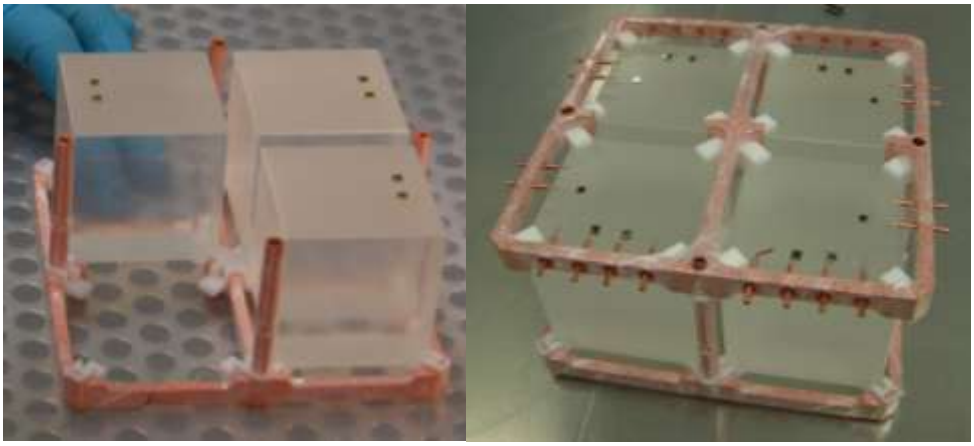

Figure 5-8. Some moments of the CCVR assembly: (left) mounting of the frames; (right) the detector is completed with heaters and gold wires from chips to the Cu pins inserted in the upper frame.

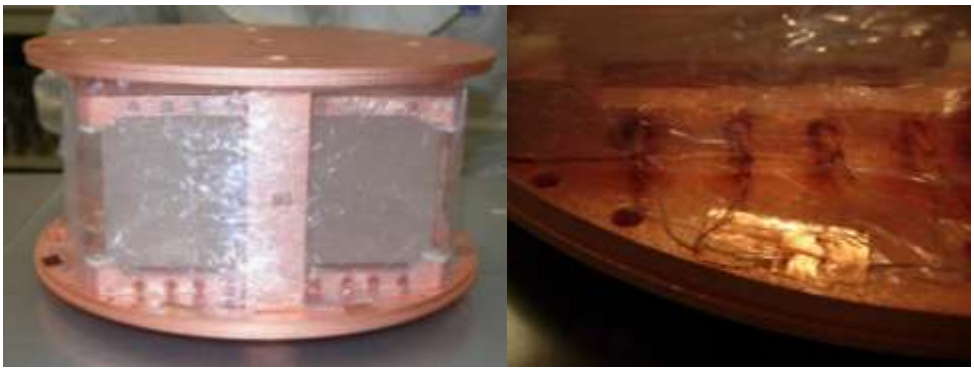

Figure 5-9. Some moments of the CCVR assembly: (left) after the mounting of the top and bottom part of the external shield, the detector is wrapped in ~70 μm thick polyethylene layer; (right) electric wires are connected to the Cu pins trough the Polyethylene layer.

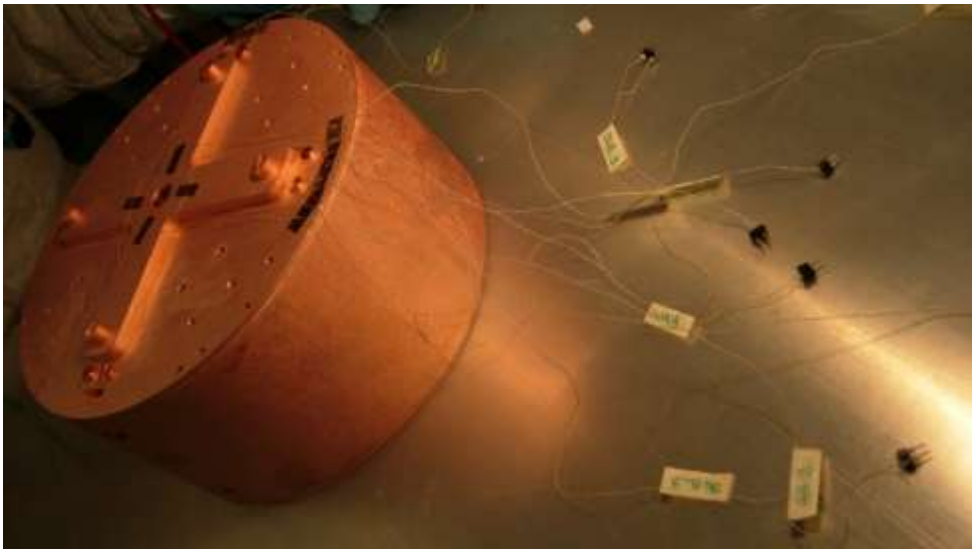

Figure 5-10. Completed CCVR detector.

5.2.2. CCVR spectra

CCVR data processing, aiming to obtain the radioactive spectra of each detector, follows the procedure described in details in (50). The raw data are processed by applying the Optimum Filter (OF) algorithm (180) to maximise the signal-to-noise ratio and to estimate the best amplitude of each recorded pulse. The idea at the basis of the OF technique is to discard the signal frequency components most affected by noise by constructing a proper filter transfer function, determined thanks to the detector response information extracted from a mean pulse and its noise power spectrum density, that are estimated from bolometric pulses and noise baseline (i.e. data samples recorded randomly and without triggered events) by a proper averaging procedure. This technique will be also applied in 7.3.

Besides the amplitude, the OF technique is able to reconstruct other feature of the pulses, such as rise and decay time. They will be used for distinguish real events from spurious ones for constructing the detector spectra (Section 5.2.2) and for discussing the thermistor performances in forming the heat signal (Section 5.4). A list of the most used pulse feature evaluated thanks to the OF is presented in Table 7-6.

Because a heater was not always present on the detector (for inconvenient happened during the assembly), the correction of the measurement instability (section 3.3.2) was done with the 5407.5 keV α line from ^{210}Po, always present in recently grown crystals.

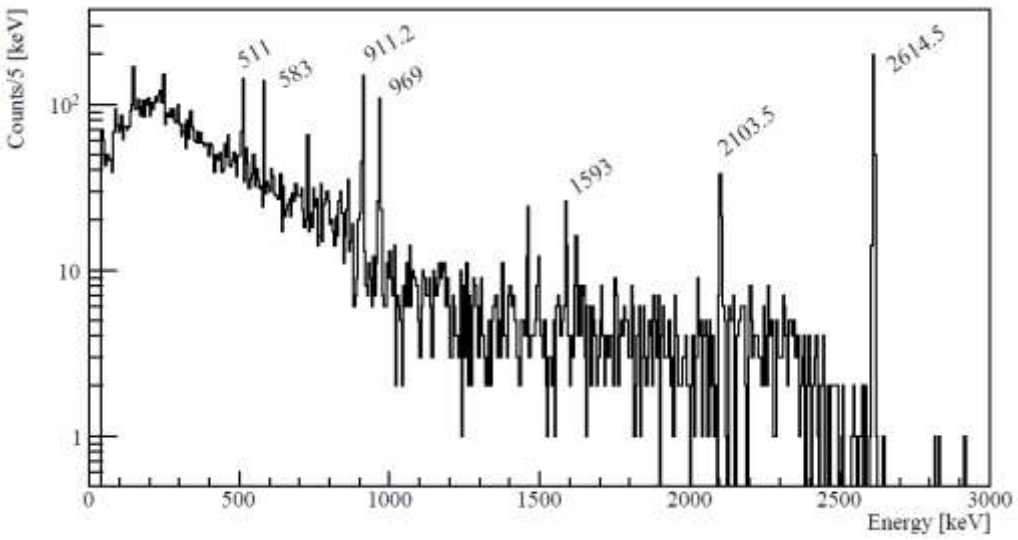

Figure 5-11. An example of a CCVR calibration spectrum (taken from CCVR-I, Channel 2). Gamma lines from the ^{232}Th decay chain are visible in the spectrum. In particular, the 511 keV line corresponds to e^+e^- annihilation, the 911.2 keV and the 969 keV lines are from ^{228}Ac and the 583 keV, the 1593 keV, the 2103.5 keV and the 2614.5 keV lines came from ^{208}Tl.

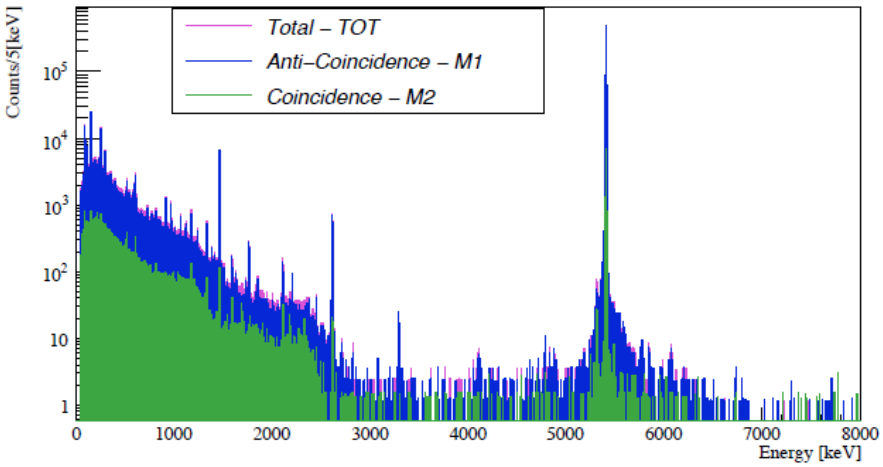

Figure 5-12. Total, anticoincidence (M1) and coincidence (m2) energy spectra for the full CCVR statistics.

	Continuum 2.7-3.2 MeV	**^{190}Pt 3.2-3.4 MeV**	**Continuum 3.4-3.9 MeV**	**U/Th 4.0-5.0 MeV**	**^{210}Po 5.0-6.0 MeV**	**U/Th 6.0-8.0 MeV**
M1	0.13±0.02	0.34±0.04	0.06±0.01	0.13±0.01	-	0.057±0.004
M2	0.02±0.01	0.005±0.004	0.008±0.003	0.014±0.003	-	0.014±0.002

Table 5-3. Count rates of all CCVRs measured in [counts/(keV·kg·y)] after the subtraction of the ^{210}Po counts. Errors are statistical.

The criteria for the selection of the pulses for composing the spectrum (i.e. the rejection of spurious events and so on) are discussed in detail in (181). The calibration of the spectra is performed using a third-order polynomial function and the ^{210}Po peak is used in addition to the ^{232}Th peaks due to ^{232}Th sources inserted inside the external lead cryostat shield. An example of calibration spectrum is shown in Figure 5-11.

A Gaussian fit of some peaks (in particular the 5407.5 keV line of ^{210}Po) is used for evaluating the energy resolution of the detectors, while the distinction of single site events (i.e. happened in just one crystal) and coincident pulses (recorded by two detectors) allows creating multiplicity 1 (M1 or anti-coincidence) and multiplicity 2 (M2 or coincidence) spectra, that are used to extract the level of bulk and surface contamination. The coincidence of two pulses is defined in a time window of 100 ms. An energy threshold of 50 keV is chosen for all CCVRs. The energy spectra of the total CCVR statistics are shown in Figure 5-12.

Six energy regions of interest are identified in the spectra:

- ✓ 2.7–3.2 MeV: this continuum region is of great interest, being immediately above the Q-value of the neutrinoless double beta decay of ^{130}Te;

- ✓ 3.2-3.4 MeV: here the contribution of the α-line from ^{190}Pt is expected, due to an almost unavoidable contamination in TeO^2 crystals, as explained in Sec. 5;
- ✓ 3.4-3.9 MeV: continuum region;
- ✓ 4.0-8.0 MeV: here the contribution of the various α lines from U and Th decay chains is expected. This region is divided in two subsets (4.0-5.0 MeV and 6.0-8.0 MeV), for taking into account that the 5.0-6.0 MeV region is also affected by the ^{210}Po contamination (see Sec. 5.1); it produces not only a peak at the energy of the Po α line at 5407.5 keV but also a broad background over the entire region due to mis-identified pile-up events (above the peak energy) or to the escape of the α that releases part of its energy in a inert material (below the peak energy). An indication of the rate in this region is of no particular interest, also because of the relative short half-life of ^{210}Po (138.38 days) that guarantees a huge reduction of this count rate when CUORE will start the data taking.

The corresponding count-rates for each spectrum are calculated. Because of the presence of ^{210}Po, an excess of count rate could arise in the M1 and M2 spectra below the energy of the 5407.5 keV α-line, if the contamination of ^{210}Po is close enough to the surface for the alpha to escape and release part of its energy in an inert material (M1 spectrum) or in a nearby detector (M2 spectrum). This contribution has been evaluated and subtracted from both M1 and M2 spectra (181) and the resulting count rates are collected in Table 5-3.

		Continuum 2.7-3.9 MeV	**U/Th 4.0-5.0 MeV**	**^{210}Po 5.0-6.0 MeV**	**U/Th 6.0-8.0 MeV**
CCVR	M1	0.09±0.02	0.13±0.01	-	0.057±0.004
	M2	0.015±0.007	0.014±0.003	-	0.014±0.002
TTT-1	M1	0.05±0.01	0.28±0.02	1.3±0.1	0.025±0.004
	M2	0.009±0.003	0.02±0.005	0.09±0.1	0.005±0.002
Cuoricino	M1	0.107±0.001	0.5±0.003	0.87±0.004	0.102±0.001
	M2	0.009±0.001	0.008±0.001	0.16±0.002	0.0163±0.0004
(CCVR/TTT-1)	M1	1.80	0.46	-	2.28
	M2	1.67	0.70	-	2.80
(CCVR/Qino)	M1	0.84	0.26	-	0.56
	M2	1.67	1.75	-	0.86

Table 5-4.The count rates of all CCVRs after the subtraction of the ^{210}Po counts are compared with the ones of the best tower of the TTT test (see Section 3.4.1) and the Cuoricino detector. Rates are expressed in [counts/(keV·kg·y)]. Errors are statistical. The notation (2.7-3.9) refers to the combination of both the continuum region (2.7, 3.2) MeV and (3.4, 3.9) MeV, excluding the ^{190}Pt energy region of (3.2, 3.4) MeV. The ratio between the rates of CCVR and the other detectors are also presented.

The count rates in the different energy region can be then confronted with the rates obtained with Cuoricino and with other detector, such as the best tower in the TTT run. This comparison is collected in Table 5-4. The CCVR background rate shows a reduction with respect to the one measured in CUORICINO in all the considered energy regions.

5.1. Bulk contamination of the CUORE crystals

Bulk contaminations in CUORE crystals are expected from:

- ✓ ^{210}Po, as a result of the chemical affinity between polonium and tellurium;
- ✓ natural contaminants, like ^{238}U, ^{232}Th with their radioactive chains and the β/EC decaying isotope ^{40}K;
- ✓ ^{210}Pb, as a result of the deposition of lead nuclei produced by ^{222}Rn decays, during the crystal handling in free atmosphere;
- ✓ ^{190}Pt, due to the fact that platinum is used in several phases of the crystal production cycle. Platinum crucibles are used for the calcination of TeO_2 powder used for the crystal growth and the growth crucibles are made of platinum foil. The central part of the as-grown crystal ingot is selected for the CUORE crystals in order to avoid the risk of platinum contamination on the surface of the crystal due to possible diffusion during the growth process. Possible Pt contaminations are therefore in the bulk of the CUORE crystals.

For ^{210}Po the activity is determined from a fit to the rate vs. time behaviour (see Section 5.1.1). For ^{238}U and ^{232}Th (see Section 5.1.2), the level of contamination (mainly an upper limit) is determined from the intensities of the α-peaks in the M1 spectrum of all crystals, or from integrals centred at the peak position if the peaks are not visible. This is because an α decay from bulk contamination releases the entire Q-value of the reaction (α energy + nuclear recoil) in a single crystal. Finally, for ^{210}Pb, the limit on bulk contamination is determined from a fit in the energy region (40, 60) keV in a subset of CCVR data with high statistics and low threshold (see Section 5.1.4).

5.1.1. ^{210}Po bulk activity

The activity of ^{210}Po can be measured from the 5407.5 keV α line: the events are selected in a ±20 keV window around the energy of the α-line and the corresponding global rate of ^{210}Po events over time for each CCVR is fitted with a pure exponential function:

$$r(t) = r_0 e^{-ln2 \cdot t/T_{1/2}},$$

5-1

where r_0 is the rate at the beginning of the measurement and $T_{½}$ is the ^{210}Po half-life.

An example of fit is shown in while the fit results for all CCVRs are collected in

The half-life of the exponential decay for all CCVRs is in good agreement (1σ) with the half-life of ^{210}Po (138.38 d), as can be seen in Table 5-5. This indicates that the ^{210}Po contamination is out of equilibrium and it is not being fed by ^{210}Pb.

From the value of r_0 returned by the fit for each CCVR and for each crystal the ^{210}Po activity A at the beginning of the measurement is extracted as follows:

$$A[Bq/kg] = \frac{r_0}{86400[s/day] \cdot m[kg]},$$

5-2

where m is the crystal mass. Knowing the time elapsed since the "crystal birth date" (growth completed, before the cut and shape) and the start of the measurement, the ^{210}Po activity at production is computed. The ^{210}Po activities for each CCVR and for all crystals are reported in Table 5-6 and in Figure 5-14. The results for crystals 007 and 011, measured first in CCVR-I and again in CCVR-II, are consistent. All crystals tested in the first five CCVR are well below the limit of 0.1 Bq/kg imposed to the crystal producers.

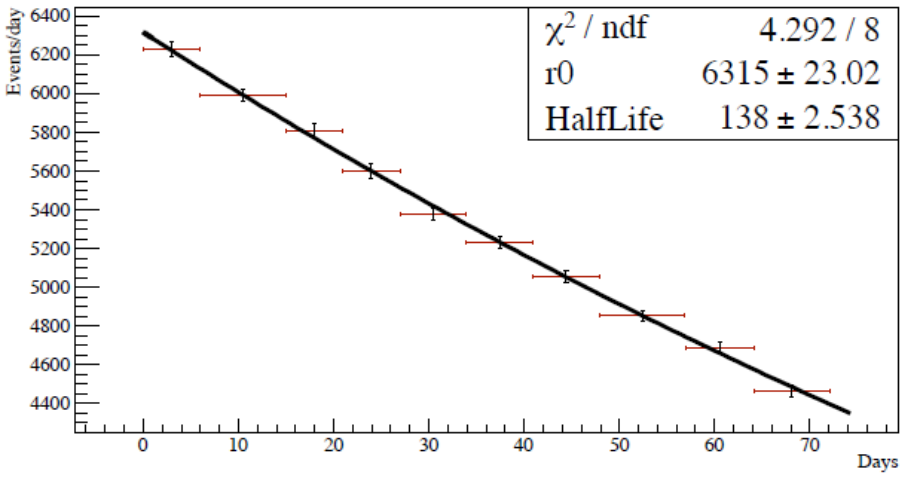

Figure 5-13. Global rate of ^{210}Po events over time for CCVR-I. The units on the x-axis are days since the start of the first background measurement. Each point represents a run or a group of runs. Holes in the distributions are due to calibration measurements or to interruptions in the data taking. The horizontal error bars indicate the beginning and the end of each group of runs, they are for visualization only. Fit results are superimposed to the points.

	CCVR-I	CCVR-II	CCVR-III	CCVR-IV	CCVR-V
r_0	6315±23.02	4214±32.32	2788±17.58	3384±24.48	2437±18.34
Half-life [d]	138±2.538	132.3±14.66	139.4±6.27	137.8±11.46	136.6±9.119

Table 5-5. Fit results of the global rate of ^{210}Po events over time for each CCVR. The half-life of the exponential decay is in good agreement (1σ) with the half-life of ^{210}Po (138.38 d).

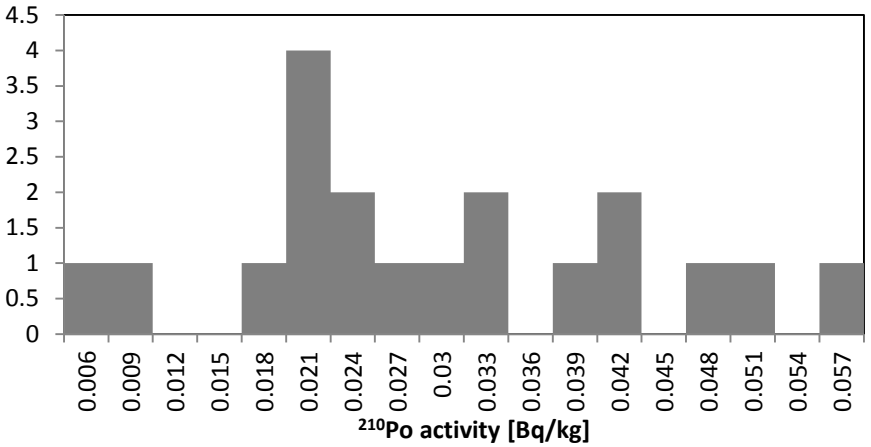

Figure 5-14. Distribution of the ^{210}Po activity at production time for all CCVR crystals.

CCVR	Crystal	^{210}Po activity [Bq/kg]
1	007	0.0414±0.0004
	011	0.0510±0.0005
	039	0.0229±0.0001
	041	0.0257±0.0001
2	007	0.047±0.015
	011	0.07±0.02
	076	0.021±0.004
	096	0.055±0.006
3	180	0.0203±0.0008
	190	0.0078±0.0005
	229	0.0283±0.0008
	236	0.0159±0.0005
4	313	0.005±0.001
	340	0.032±0.004
	354	0.039±0.004
	380	0.040±0.004
5	416	0.024±0.003
	421	0.020±0.003
	436	0.032±0.003
	455	0.019±0.002

Table 5-6. ^{210}Po activity at production time for all the crystals measured in CCVRs I to V.

5.1.2. U/Th bulk contaminations

^{238}U and ^{232}Th bulk contaminations are evaluated from the M1 sum spectrum of all CCVR runs. For each α peaks of the U and Th chain (reported in Table 5-7), the number of counts within an energy window of 6σ around the Q-value is estimated, where σ=2.2 keV corresponds to the average between the values of the σ of the ^{210}Po peak for each CCVR, weighted by the corresponding lifetime of that run (see Tab. 8 for details). Using the Feldman-Cousins procedure with 0 expected background counts (182), the 90% C.L. intervals for the number of counts ($N_{low} \div N_{up}$) are obtained (see Table 5-7).

The activity for each nuclide is calculated as:

$$A[Bq/kg] = \frac{N_{low} \div N_{up}}{t[s] \cdot m[kq]}.$$

5-3

In the previous formula, t is the CCVR live time, m is the crystal mass and it has been assumed that the observed counts for each nuclide are entirely due to a bulk contamination of that precise nuclide, i.e. that each single site event is total contained in the crystals. This is a conservative hypothesis since there is not a clear indication (for example a line) that such a bulk contamination actually exists and that the observed counts are not due to background of some other origin. The activity calculated for the different nuclides of the U and Th chains are collected in the last column of Table 5-7.

Chain	Nuclide	Q-value [keV]	Half-life	$N_{low} \div N_{up}$ 90% C.L.	90% C.L. interval [Bq/kg]
^{238}U	^{238}U	4270.0	$4.47 \cdot 10^{9}$ y	3.6 - 11.5	$7.7 \cdot 10^{-8}$ - $2.5 \cdot 10^{-7}$
	^{234}U	4858.8	$2.45 \cdot 10^{5}$ y	9.5 - 21.5	$2.1 \cdot 10^{-8}$ - $4.7 \cdot 10^{-7}$
	^{230}Th	4770.0	$7.54 \cdot 10^{4}$ y	12.5 - 26.2	$2.7 \cdot 10^{-8}$ – $5.7 \cdot 10^{-7}$
	^{226}Ra	4870.6	1599 y	15.8 - 31.0	$3.4 \cdot 10^{-8}$ - $6.7 \cdot 10^{-7}$
	^{218}Po	6114.7	3.05 min	1.5 - 7.4	$3.2 \cdot 10^{-8}$ - $1.6 \cdot 10^{-7}$
^{232}Th	^{232}Th	4082.8	$1.4 \cdot 10^{10}$ y	1.1 - 5.9	$2.4 \cdot 10^{-8}$ - $1.3 \cdot 10^{-7}$
	^{212}Bi	6207.1	60.55 min	4.4 - 14.0	$9.4 \cdot 10^{-8}$ - $3.0 \cdot 10^{-7}$

Table 5-7. For several nuclides of the U and Th chain the Q-value and the half-life of the α decay are shown (third and fourth columns) together with the 90% C.L. intervals on the number of events (fifth column) and the corresponding 90% C.L. intervals on the bulk activity (last column) ascribed to these nuclides.

Chain	Nuclide	90% C.L. interval [g/g] secular equilibrium	90% C.L. interval [g/g] non-equilibrium
^{238}U	^{238}U	$6.3\cdot10^{-15}$ - $2.0\cdot10^{-14}$	$6.3\cdot10^{-15}$ - $2.0\cdot10^{-14}$
	^{234}U	$1.7\cdot10^{-14}$ - $3.8\cdot10^{-14}$	$8.9\cdot10^{-19}$ - $2.0\cdot10^{-18}$
	^{230}Th	$2.2\cdot10^{-14}$ - $4.6\cdot10^{-14}$	$3.6\cdot10^{-19}$ - $7.4\cdot10^{-19}$
	^{226}Ra	$2.8\cdot10^{-14}$ - $5.4\cdot10^{-14}$	$9.3\cdot10^{-21}$ - $1.8\cdot10^{-20}$
	^{218}Po	$2.6\cdot10^{-15}$ - $1.3\cdot10^{-14}$	$3.1\cdot10^{-30}$ - $1.5\cdot10^{-29}$
^{232}Th	^{232}Th	$5.9\cdot10^{-15}$ - $3.2\cdot10^{-14}$	$5.9\cdot10^{-15}$ - $3.2\cdot10^{-14}$
	^{212}Bi	$2.3\cdot10^{-14}$ - $2.1\cdot10^{-13}$	$1.7\cdot10^{-28}$ - $5.6\cdot10^{-28}$

Table 5-8. 90% C.L. intervals on the bulk contamination of U and Th decay chains in the hypothesis of secular equilibrium and of non-equilibrium.

The 90% C.L. intervals for U/Th bulk contaminations are then calculated in two ways: in a first approach, secular equilibrium within the uranium and thorium decay chains is assumed. If the activity of all daughter nuclides is equal to the activity of the chain parent, the 90% C.L. intervals for ^{238}U and ^{232}Th chains are set just considering the relative branching ratios. The second approach is to assume that the nuclides are being fed from an isotope above it in the chain, but they are not necessarily in secular equilibrium with ^{238}U and ^{232}Th. Results for the total CCVR data considering both hypotheses are collected in Table 5-8.

Maintaining a conservative approach, the bulk contamination limit on ^{238}U and ^{232}Th is set considering the most active nuclide for each chain. The following intervals at 90% C.L. for uranium and thorium bulk contamination are then obtained:

$$2.8\cdot10\text{-}14 < {}^{238}\text{U} < 5.4\cdot10\text{-}14 \text{ [g/g]}$$
$$2.3\cdot10\text{-}14 < {}^{232}\text{Th} < 2.1\cdot10\text{-}13 \text{ [g/g]} \qquad 5\text{-}4$$

Both values of the upper limits are within the contract specification of $3\cdot10^{-13}$[g/g]. For the ^{238}U decay chain, the contribution from ^{210}Pb is treated separately (see Section 5.1.4).

5.1.3. ^{40}K bulk contamination

Because of the low Q-value of ^{40}K (1311.1 keV for β^- decay and 1504.9 keV for β^+/EC decay), eventual crystal bulk contamination of this nuclide does not contribute to the background in the energy region of $0\nu\beta\beta$ ^{130}Te but could be dangerous in the low energy region, thus affecting the potential of CUORE to look for dark matter and axions (183).

A limit on the ^{40}K contamination of the crystals can be evaluated from the intensity of the 1460.8 keV gamma line, which is clearly visible in all CCVR spectra and can be due to potassium contamination in the materials surrounding the detectors or to contamination in the detector itself. The discrimination between these two possibilities (as well as a sensitive limit on the contamination) can be derived from the study of the continuum associated to the beta decay. The 90% C.L. upper limit on the bulk ^{40}K bulk contaminations according to the two different signatures are:

$$^{40}\mathrm{K} < 1.1 \cdot 10^{-2}\ [\mathrm{Bq/kg}]\ (1460.8\ \gamma\ \mathrm{line})$$
$$^{40}\mathrm{K} < 1.9 \cdot 10^{-3}\ [\mathrm{Bq/kg}]\ (\beta\ \mathrm{continuum})$$

5-5

The most stringent limit comes from the continuum, for the intensity of the 1460.8 keV line can be increased also by bulk ^{40}K contamination of the other experimental materials.

5.1.4. ^{210}Pb activity

A small contamination in ^{210}Pb (bulk or surface) might occur in the CUORE crystals despite the great efforts for minimizing the exposure to air, to avoid contamination from radon and its daughter. Even if the soft beta (16.5 keV and 63 keV) and γ (46.5 keV) radiation from ^{210}Pb is generally self-absorbed, energetic β rays from the daughter ^{210}Bi induced bremsstrahlung can give rise to a continuum up to 1.16 MeV. Moreover, the α decay of the daughter ^{210}Po can contribute to the continuum back ground in the 0νββ energy region.

Because the ^{210}Po contamination in CCVRs is out of equilibrium, as deduced in Section 5.1.1, it cannot be used for estimating the ^{210}Pb contamination. The only available signature is a combination of a β spectrum (end point 16.96 keV) with a de-excitation energy of 46.5 keV (most of the cases through a conversion electron). This produces a broad signature in the 40-60 keV energy region, whose shape depends on the location of the Pb contamination.

As expressed in Section 5.2.2, the selected threshold for CCVRs is 50 keV, so the search of the ^{210}Pb contamination requires a reprocessing of the data with a lower threshold. This has been performed with CCVR-I dataset, being this run the one with high statistics and good bolometric performances (see Section 5.4).

Several simulations have been performed both for a bulk and for a surface contamination with exponential density profile and contamination depth varying from 0.01 μm to 10 μm. Then the energy spectrum between 40 and 60 keV of the CCVR-I has been fitted with an exponentially decreasing background and allowing the presence of a ^{210}Pb

spectrum with shape taken from Monte Carlo simulation. The free parameters of the fit are the two of the exponential background and the total number of counts from ^{210}Pb. An example can be found in Figure 5-15. The fit is repeated for each Monte Carlo signature, resulting in a number of ^{210}Pb events compatible with zero within the error for all signatures.

The upper limit at 90% C.L. on the number of ^{210}Pb counts is $N_{up}=1.644\sigma$, where σ is the error on the number of counts returned from the fit. The bulk contamination is computed using Eq. 5-3 with $N_{low}=0$.

The surface contamination is extracted using the following formula:

$$A[Bq/cm^2] = \frac{N_{low} \div N_{up}}{\varepsilon_{MC} \cdot t[s] \cdot S[cm^2]},$$

5-6

where ε_{MC} is the Monte Carlo detection efficiency, t is the live time, S=150 cm^2 is the surface of a crystal and $N_{low}=0$. Results are shown in Table 5-9.

The upper limit on the activity for bulk contamination is below the contract limit of 10^{-5} Bq/kg.

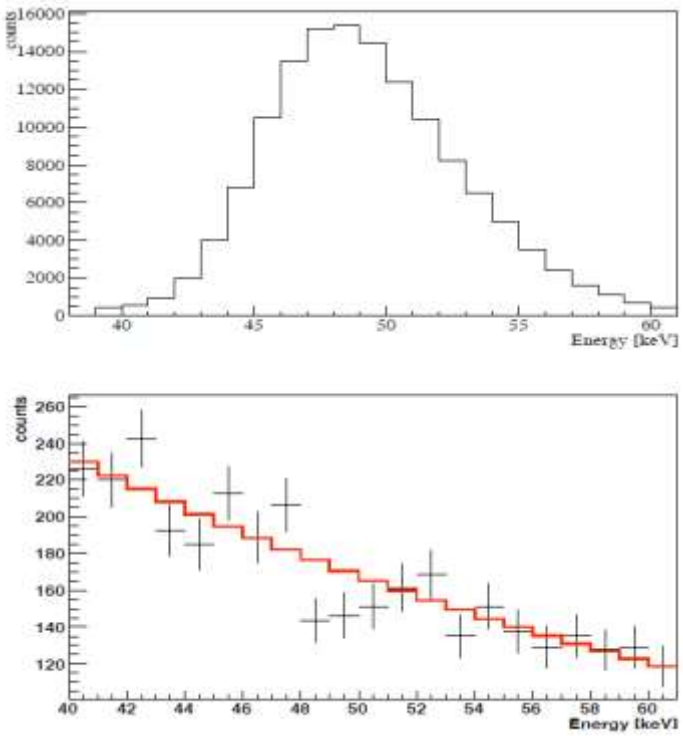

Figure 5-15. Top: Monte Carlo simulation of a ^{210}Pb bulk contamination in CCVR-I. Bottom: CCVR I low energy M1 spectrum (40-60 keV). The energy threshold is set to 40 keV. The red line represents the fit to the spectrum with an exponential background and allowing the presence of a ^{210}Pb bulk contamination with the above shape. No hint of such contamination is found.

Contamination	Upper limit 90% C.L.
Surface 0.01 μm	$9.8 \cdot 10^{-07}$ [Bq/cm^2]
Surface 0.1 μm	$3.8 \cdot 10^{-08}$ [Bq/cm^2]
Surface 0.2 μm	$2.2 \cdot 10^{-08}$ [Bq/cm^2]
Surface 1 μm	$9.2 \cdot 10^{-09}$ [Bq/cm^2]
Surface 5 μm	$5.6 \cdot 10^{-09}$ [Bq/cm^2]
Surface 10 μm	$4.9 \cdot 10^{-09}$ [Bq/cm^2]
Bulk	$3.3 \cdot 10^{-06}$ [Bq/kg]

Table 5-9. Upper limits on the activity of bulk and surface contamination of ^{210}Pb. Bulk contamination is given in [Bq/kg], surface contaminations are given in [Bq/cm^2].

5.2. Surface contamination of the CUORE crystals

Surface contaminations of CUORE crystals are expected from all the nuclides discussed until now except for ^{190}Pt, which is all in the bulk. Uranium and thorium surface contaminations can be investigated by means of coincident events in two facing crystals. In this case the spectrum of the sum energy of multiplicity 2 events ($M2_{sum}$) is used (see Figure 5-16). Considering the case of an α decay so near to the surface of a crystal, both the energy of the α particle (E_α) in the facing crystal and the corresponding nuclear recoil energy (E_r) in the original crystal are detected and the variable $E_{sum}=E_\alpha+E_r$ is plotted in the $M2_{sum}$ spectrum. Therefore surface contamination of an α-decaying nuclide should appear in $M2_{sum}$ as a peak at the Q-value of the . At the same time, if the surface contamination is deep enough, the α particle can be absorbed by the crystal, giving rise to the same signature of a bulk event.

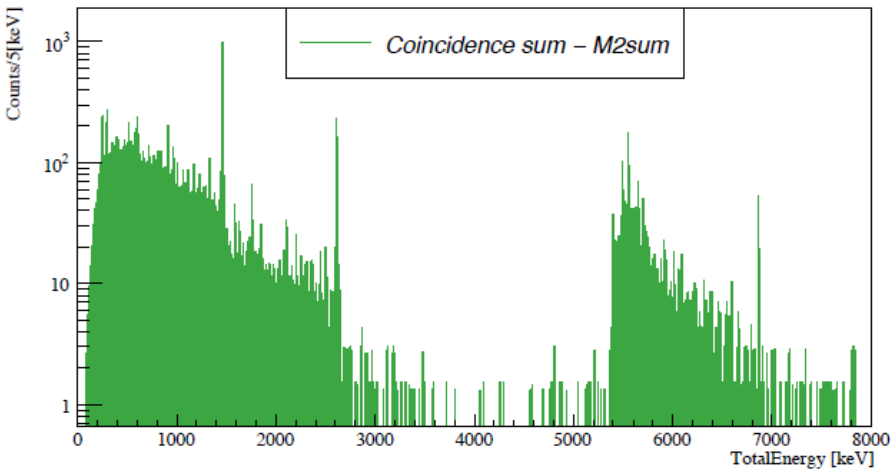

Figure 5-16. Sum energy spectrum of multiplicity 2 events ($M2_{sum}$) for all the CCVR statistics.

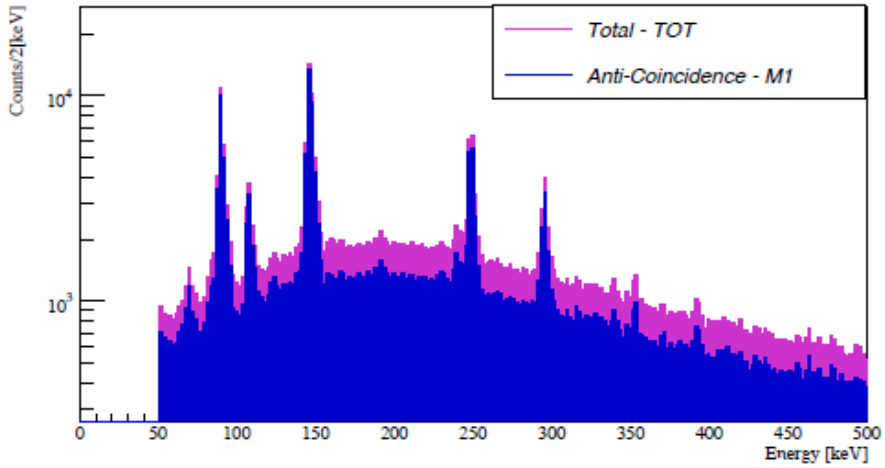

Figure 5-17. Total and anti-coincidence spectra in the region 0-500 keV: low energy lines from Te metastable isotopes are clearly visible.

Te isotope	Energy [keV]	Coincident peak with 5407.5 keV ^{210}Po line [keV]
^{127}Te	88.3	5495.8
^{129}Te	105.5	5513
^{125}Te	144.8	5552.3
^{123}Te	247.5	5655
^{121}Te	294	5701.5

Table 5-10. Energy of the γ lines from Tellurium metastable isotopes and the corresponding sum energy when emitted in coincidence with a ^{210}Po event.

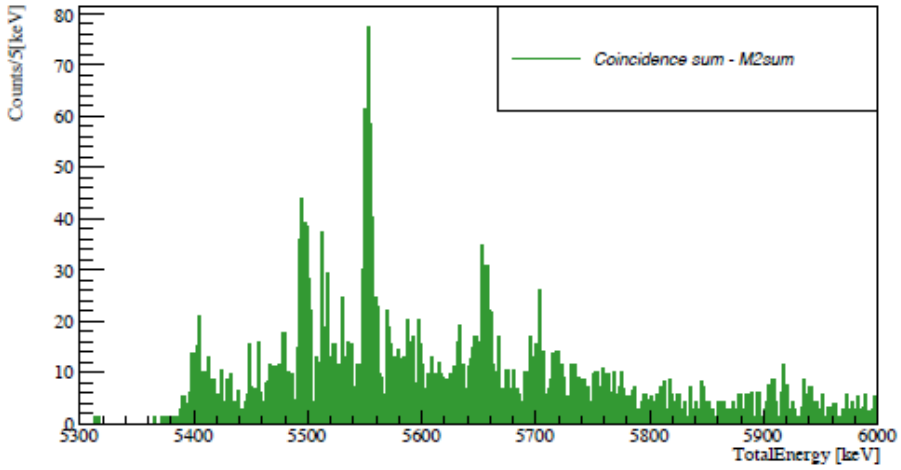

Figure 5-18. A closer look to the $M2_{sum}$ spectrum in the region above the 5470.5 keV α line of ^{210}Po. Here the peaks resulting from coincidences between the ^{210}Po α line and low energy γ line due to Tellurium metastable isotopes are visible.

5.2.1. U/Th surface contaminations

The presence of Tellurium metastable isotopes decaying in low-energy γ lines (see Figure 5-17 and Table 5-10) create a huge background in the CCVR $M2_{sum}$ spectrum for energies above the polonium 5407.5 keV α line because of random coincidences between ^{210}Po and these low energy events (Figure 5-18)

Because of these coincidences, only those nuclides having a Q-value lower than 5407.5 keV are used for surface contamination analysis. ^{218}Po and ^{212}Bi are therefore discarded. For each of these nuclides, the numbers of counts is computed from the $M2_{sum}$ energy spectrum in an energy window of ±6σ around the Q-value and divided by ε^2 (where ε is the efficiency of the event-based cuts), since two coincident events have independent probabilities of passing the cuts. The corresponding 90% C.L. intervals, computed using the Feldman-Cousins procedure with 0 expected background counts, are reported in Table 5-11.

Monte Carlo spectra for ^{238}U and ^{232}Th contamination on the crystal surface are generated with exponential profile and various penetration lengths. For each contamination depth, the detection efficiency is calculated in a ±6σ interval around the Q-value of each nuclide both for the $M2_{sum}$ spectrum and for the M1 spectrum. The results (collected in Figure 5-19) show that for penetration length of 0.01 and 0.1 μm the higher containment efficiency comes from the $M2_{sum}$ spectrum, whereas for depths of 1, 5 and 10 μm this arises from the M1 spectrum. The efficiency containment value for 0.2 μm depth is very similar both for M1 and $M2_{sum}$ spectrum.

The 90% C.L. intervals for the surface activity of each nuclide are evaluated using Eq. 5-6, where N_{low} (N_{up}) is the 90% C.L. lower (upper) limit on the number of observed events from the $M2_{sum}$ or the M1 spectrum (taken from Table 5-11 and Table 5-7 respectively) and ε is the Monte Carlo average efficiency for the corresponding spectrum ($M2_{sum}$ or M1) and for the given signature.

Chain	Nuclide	Q-value [keV]	Half-life [y]	Energy range [keV]	$N_{low} \div N_{up}$ 90% C.L.
^{238}U	^{238}U	4270.0	$4.47 \cdot 10^9$	4257 - 4283	0.5 - 4.4
	^{234}U	4858.8	$2.45 \cdot 10^5$	4845 - 4871	0.5 - 4.4
	^{230}Th	4770.0	$7.54 \cdot 10^4$	4757 - 4783	0.5 - 4.4
	^{226}Ra	4870.6	1599	4857 - 4883	3.6 - 11.5
^{232}Th	^{232}Th	4082.8	$1.4 \cdot 10^{10}$	4069 - 4095	0 - 2.4

Table 5-11. 90% C.L. intervals on the number of counts ascribed to several nuclides from uranium and thorium decay chain from the $M2_{sum}$ spectrum. For each nuclide is also shown the half-life of the α decay.

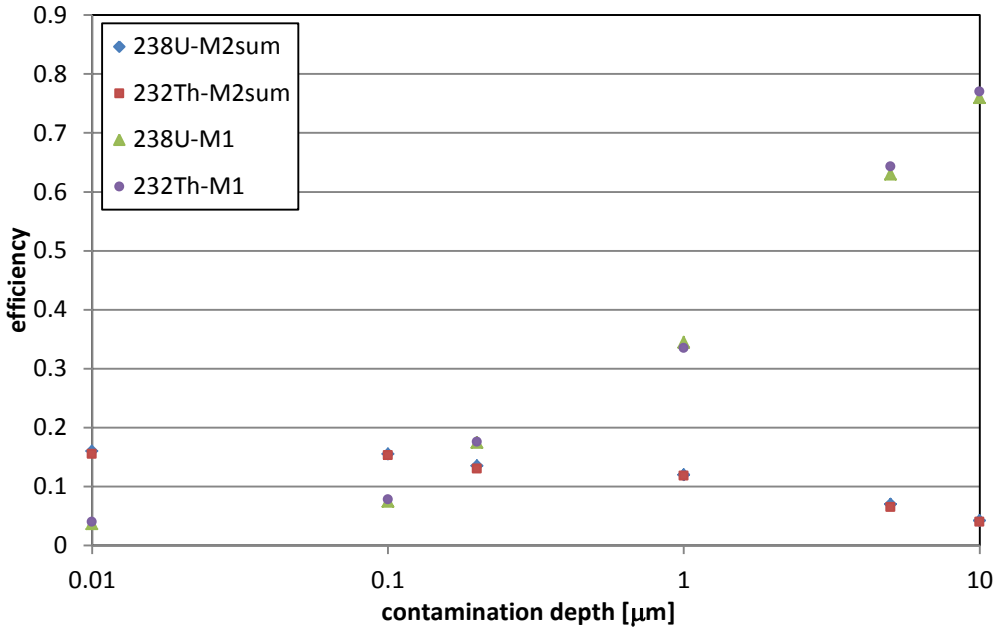

Figure 5-19. For each penetration length, the containment efficiency of surface events is computed for both M1 and $M2_{sum}$ Monte Carlo spectra. For small penetration length (0.01 and 0.1 μm) the higher containment efficiency comes from the $M2_{sum}$ spectrum, whereas for higher depths (1, 5 and 10 μm) this arises from the M1 spectrum. The efficiency containment value for 0.2 μm depth is very similar both for M1 and $M2_{sum}$ spectrum.

The confidence intervals for surface activity contaminations are calculated for both the $M2_{sum}$ and M1 spectra (normalizing each signature with the corresponding Monte Carlo efficiency) and the signature giving the most stringent result is taken into account. For surface contaminations of 0.01, 0.1 and 0.2 μm depths, the most stringent limits come from the $M2_{sum}$ spectrum, since in this case the alpha particle is more likely to escape and produce a double coincidence; on the contrary, for depth 1, 5 and 10 μm the surface activity reduces practically to a bulk activity and the M1 signature produces the most stringent limits. As for the bulk contaminations, these confidence intervals are calculated under the conservative hypothesis that the observed counts for each nuclide are entirely due to a surface contamination of that nuclide in the corresponding depth.

For the ^{238}U chain, the surface contamination is evaluated for the peak of the chain parent itself and for ^{226}Ra, being the most active line both in M1 and $M2_{sum}$ spectra. In the case of the ^{232}Th chain, only one line is left for the analysis, i.e. the peak of the parent. This means that there is no way of testing the portion of the chain below ^{220}Rn and take into account a possible non-equilibrium of the chain, as done for the bulk contamination. The results are collected in Table 5-12.

Depth [μm]	Nuclide	90% C.L. interval [Bq/cm²]
0.01	^{238}U	$3.6\cdot10^{-10}$ – $2.9\cdot10^{-9}$
	^{226}Ra	$2.1\cdot10^{-9}$ – $2.9\cdot10^{-9}$
	^{232}Th	0 – $2.9\cdot10^{-9}$
0.2	^{238}U	$4.5\cdot10^{-10}$ – $2.9\cdot10^{-9}$
	^{226}Ra	$2.6\cdot10^{-9}$ – $2.9\cdot10^{-9}$
	^{232}Th	0 – $2.1\cdot10^{-9}$
1	^{238}U	$4.7\cdot10^{-10}$ – $2.9\cdot10^{-9}$
	^{226}Ra	$5.3\cdot10^{-9}$ – $2.9\cdot10^{-8}$
	^{232}Th	$3.5\cdot10^{-10}$ – $2.9\cdot10^{-9}$
5	^{238}U	$2.6\cdot10^{-10}$ – $2.9\cdot10^{-9}$
	^{226}Ra	$2.9\cdot10^{-9}$ – $2.9\cdot10^{-9}$
	^{232}Th	$1.9\cdot10^{-10}$ – $2.9\cdot10^{-9}$
10	^{238}U	$2.1\cdot10^{-10}$ – $2.9\cdot10^{-9}$
	^{226}Ra	$2.3\cdot10^{-9}$ – $2.9\cdot10^{-9}$
	^{232}Th	$1.6\cdot10^{-10}$ – $2.9\cdot10^{-10}$

Table 5-12. 90% C.L. intervals for surface contamination, for different penetration length values.

5.3. Extrapolation to CUORE background

From CCVRs no indication of a bulk or surface contamination from uranium and thorium decay chains, as well as from ^{210}Pb (out of equilibrium), is found. The contamination levels resulting from the CCVR data can be then used to extrapolate the crystal contribution to the CUORE background. To do that, a simulation both for bulk and surface contamination, reproducing the CUORE geometry and studying the contribution to DBD energy region has been performed. Since the interest is in a conservative upper limit to the CUORE background, only the upper bounds of the 90% confidence intervals calculated for the bulk and surface contaminations are used for the extrapolation.

The CUORE geometrical efficiency for a uniform crystal bulk contamination in ^{210}Pb, ^{238}U and ^{232}Th is estimated via Monte Carlo, and the corresponding CUORE background at the DBD energy region in a window of ±30 keV around the Q-value is obtained with the formula:

$$bkg_{CUORE} = \frac{A_{CCVR.bulk} \cdot \varepsilon_{MC}^{CUORE.bulk}}{\Delta E}, \qquad 5\text{-}7$$

where $A_{CCVR.bulk}$ are the values of ^{210}Pb, ^{238}U and ^{232}Th activities calculated in the previous sections (from Table 5-7 and Table 5-9), $\varepsilon^{CUORE.bulk}{}_{MC}$ is evaluated from Monte Carlo simulation and ΔE = 60 keV. The results are shown in Table 5-13.

In the most conservative approach, considering the most active line (^{212}Bi), the upper limit to the CUORE background at the DBD energy due to bulk contamination of crystals is:

Chain	Nuclide	Upper limit [counts/(keV·kg·y)]
	^{210}Pb	$2.6 \cdot 10^{-5}$
^{238}U	^{238}U	$7.9 \cdot 10^{-7}$
	^{232}U	$1.5 \cdot 10^{-6}$
	^{230}Th	$1.8 \cdot 10^{-6}$
	^{226}Ra	$2.1 \cdot 10^{-6}$
	^{218}Po	$5.1 \cdot 10^{-7}$
^{232}Th	^{232}Th	$1.7 \cdot 10^{-5}$
	^{212}Bi	$1.2 \cdot 10^{-4}$

Table 5-13. Extrapolation to CUORE background from CCVR bulk contamination limits calculated in the previous sections and collected in Table 5-7 and Table 5-9. The highest limit is highlighted.

$$1.2 \cdot 10^{-4} \text{ counts/(keV·kg·y)}. \quad \text{5-8}$$

In a similar way, the CUORE geometrical efficiency for a surface contamination for several depths is estimated and the corresponding CUORE background is extrapolated from:

$$bkg_{CUORE} = \frac{A_{CCVR.\text{surf}} \cdot \varepsilon_{MC}^{CUORE.\text{surf}} \cdot S}{\Delta E \cdot M_{CUORE}}. \quad \text{5-9}$$

Here $A_{CCVR.surf}$ are the surface contamination vaules calculated in the previous section (from Table 5-12 and Table 5-9), $\varepsilon^{CUORE.surf}_{MC}$ is evaluated from Monte Carlo simulation, again ΔE = 60 keV, S is the surface of the CUORE crystals and the mass of CUORE, M_{CUORE}, is 0.75·988 kg. The results are shown in Table 5-14.

Based on these results, in the most conservative approach, the upper limit of the CUORE background due to the surface contamination of the crystals would be:

$$3.5 \cdot 10^{-3} \text{ counts/(keV·kg·y)}. \quad \text{5-10}$$

This value is strictly dependent on the density profile assumed for the contaminants distribution, as can be seen in Figure 5-20, where lower and upper bounds of the 90% C.L. intervals for the rate in the DBD energy region (computed on ^{226}Ra line) are plotted in function of contamination depth. It has to be noticed that, while the limit expressed by Eq. 5-8 is an upper limit in strict sense, the limit of Eq. 5-10 is the upper limit of a range. This means that a contribution to the CUORE background due to the crystal surface contamination must be expected, even if it will be well below the experiment goal.

Depth [μm]	Nuclide	Upper limit [counts/(keV·kg·y)]
0.01	^{210}Pb	$1.6 \cdot 10^{-3}$
	^{238}U	$8.4 \cdot 10^{-5}$
	^{226}Ra	$2.9 \cdot 10^{-4}$
	^{232}Th	$4.6 \cdot 10^{-5}$
0.2	^{210}Pb	$2.3 \cdot 10^{-4}$
	^{238}U	$3.7 \cdot 10^{-4}$
	^{226}Ra	$8.4 \cdot 10^{-4}$
	^{232}Th	$1.5 \cdot 10^{-4}$
1	^{238}U	$3.8 \cdot 10^{-4}$
	^{210}Pb	$1.2 \cdot 10^{-3}$
	^{226}Ra	$3.5 \cdot 10^{-3}$
	^{232}Th	$4.5 \cdot 10^{-4}$
5	^{210}Pb	$4.3 \cdot 10^{-4}$
	^{238}U	$1.2 \cdot 10^{-3}$
	^{226}Ra	$3.5 \cdot 10^{-3}$
	^{232}Th	$4.8 \cdot 10^{-4}$
10	^{210}Pb	$2.9 \cdot 10^{-4}$
	^{238}U	$7.0 \cdot 10^{-4}$
	^{226}Ra	$1.9 \cdot 10^{-3}$
	^{232}Th	$3.0 \cdot 10^{-4}$

Table 5-14. Extrapolation to CUORE background from CCVR bulk contamination limits calculated in the previous sections and collected in Table 5-12 and Table 5-9. The highest limit is highlighted.

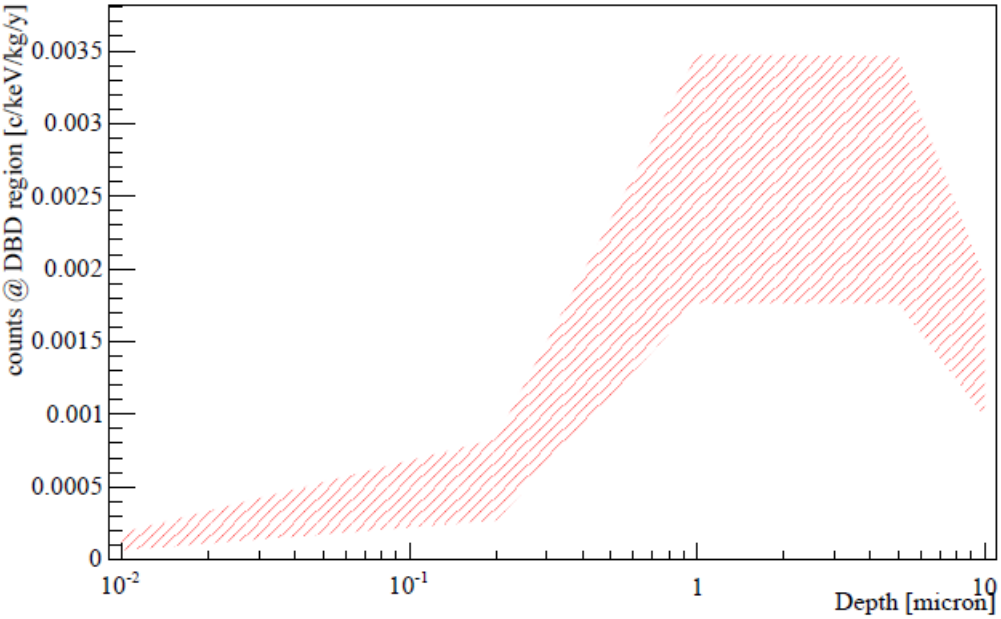

Figure 5-20. For each penetration depth, the lower and upper bounds of the 90% C.L. intervals for the count rate at the DBD energy region are plotted. Values computed on ^{226}Ra line.

5.4. Performances of CCVR bolometers

CCVR bolometers are made with (in principal) identical absorbers but different sensors: in fact, there is no a unique set of thermistors constantly used in the several runs. This is because at the beginning the CCVRs were deputed only to the crystal contamination measurement, but after the characterisation of the CUORE-0 and CUORE NTDs it was decided to utilise the CCVRs also to evaluate the sensor performances. In addition, because of the difficulties during the assembly (see Section 5.2.1), it is not easy to have more than one or two bolometers made with the same kind of thermistor in the same run, reducing the possibility of a direct confrontation. Moreover, the cryostat devoted to the CCVRs met with difficulties in reaching a low base temperature in some runs.

All the above considerations give the idea how not trivial is to confront the performances of different bolometers and, moreover, to understand where is the source of eventual discrepancies among the detectors. The main problem is that, even if dealing with the same bolometer components, their assembly is done manually; for example, two NTD with the same VRH parameters and size, applied to the same crystal, can result in different pulses for the same deposed energy because of difference in the gluing (bigger or smaller dots, a veil instead of a perfect matrix and so on). Avoiding this kind of uncertainties is the main goal of the new CUORE thermistor-to-absorber assembly line, as will be discussed in Chapter 6.

An immediate way to examine the bolometric behaviour is to evaluate its energy resolution (Section 5.4.1) but in general it is not easy to confront the performances of different detectors. An immediate criterion can be the comparison of the respective pulse amplitude for a fixed energy deposition, but it must be considered that high-sensitive thermistor will results in higher pulses but also in high sensitivity to spurious noise. Even the operation of a given detector at a lower base temperature gives high pulses, but at the price of a higher resistance and therefore of worse spurious noise. A not-intuitive tool for solving the problem is the so-called “Pirro Curve” that will be described in Section 5.4.2. The attention will be then focused on the performance of bolometers with CUORE-0 and CUORE NTDs, i.e. CCVR-V and CCVR-VI, in the attempt to evaluate the new thermistor behaviour.

5.4.1. Energy resolution of CCVRs

The energy resolution of the CCVR bolometers is calculated from the FWHM of three peaks (if the number of events collected for the peak were enough): 1460 keV of ^{40}K, 2615

keV of ^{208}Tl and 5407 keV of ^{210}Po; the results are collected in Figure 5-22. The values achieved with some bolometers are amazing. One over all, crystal 007 equipped with a 34B thermistor, used in both CCVR-I and CCVR-II has a FWHM at the ^{208}Tl 2615 keV peak of 3.05 and 2.2 keV, while it is 2.78 and 2.4 keV for the 5407 keV line of ^{210}Po: they are the best energy resolution ever obtained with a bolometer on a high energy gamma line and the best ever obtained with any detector on an alpha line (see Figure 5-21). On the contrary, there are detectors with a worse energy resolution, in particular the ones of CCVR-IV, that mostly suffered of assembly problems.

Notice that the number of thermistors per run is equal or more than four (see Table 5-15), meaning that there are some crystals with two thermistors instead of one: this was done both for "safety reason" (in principle, all the crystals had two thermistors, but not all survived, even if there were always an alive channel per each absorber) and for direct comparison of two kind of NTDs. Particular attention was given to CCVR-V and CCVR-VI, because they host CUORE-0 and CUORE NTDs.

The different kinds of thermistor used in CCVRs are collected in Table 5-15. *34B* refers to witness NTDs cut from the 34B wafer (see Section 3.3.1.1) with lateral gold pad, while *Q0_34B* are from the CUORE-0 batch, having lateral and frontal pad (as for the *Q0_34C*). The *39C* and *39_3* are the CUORE witness pieces tested in the characterisation run in Como (see Chapter 4), having only lateral gold pad and smaller size with respect to all the others NTDs (2.4x3x1 mm^3 instead of 3x3x1 mm^3); notice that because of their reduced surfaces, they can be glued with only 6 glue dots instead of nine. Because these arose some controversial results, other NTDs were produced from the CUORE wafer, with the correct size: they are the *Q39C* thermistors and have with both lateral and frontal pad. *WA* stays for Wrap Around and refers to the first samples cut from the 34B/C wafers with both lateral and frontal gold pads, for testing their operation (160). *Cuoricino* refers to the NTDs used in the experiment.

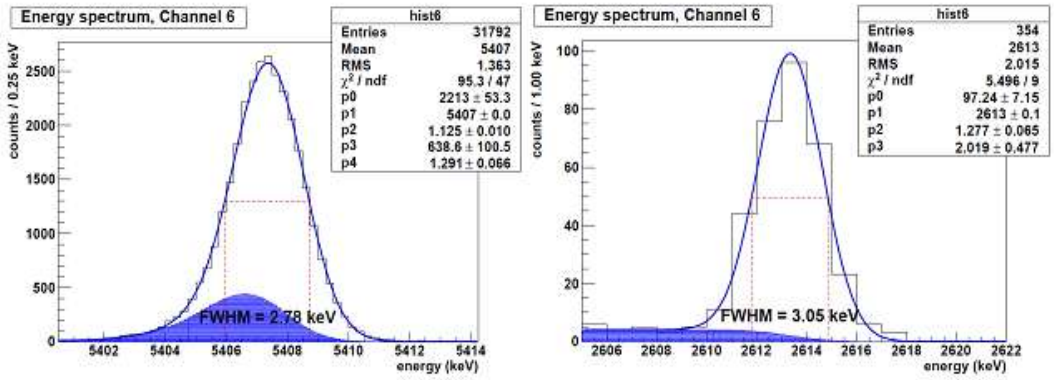

Figure 5-21. Energy resolution of crystal 007 with a 34B thermistor in CCVR-I. Left: 5407 keV ^{210}Po alpha line. Right: 2615 keV ^{208}Tl gamma line.

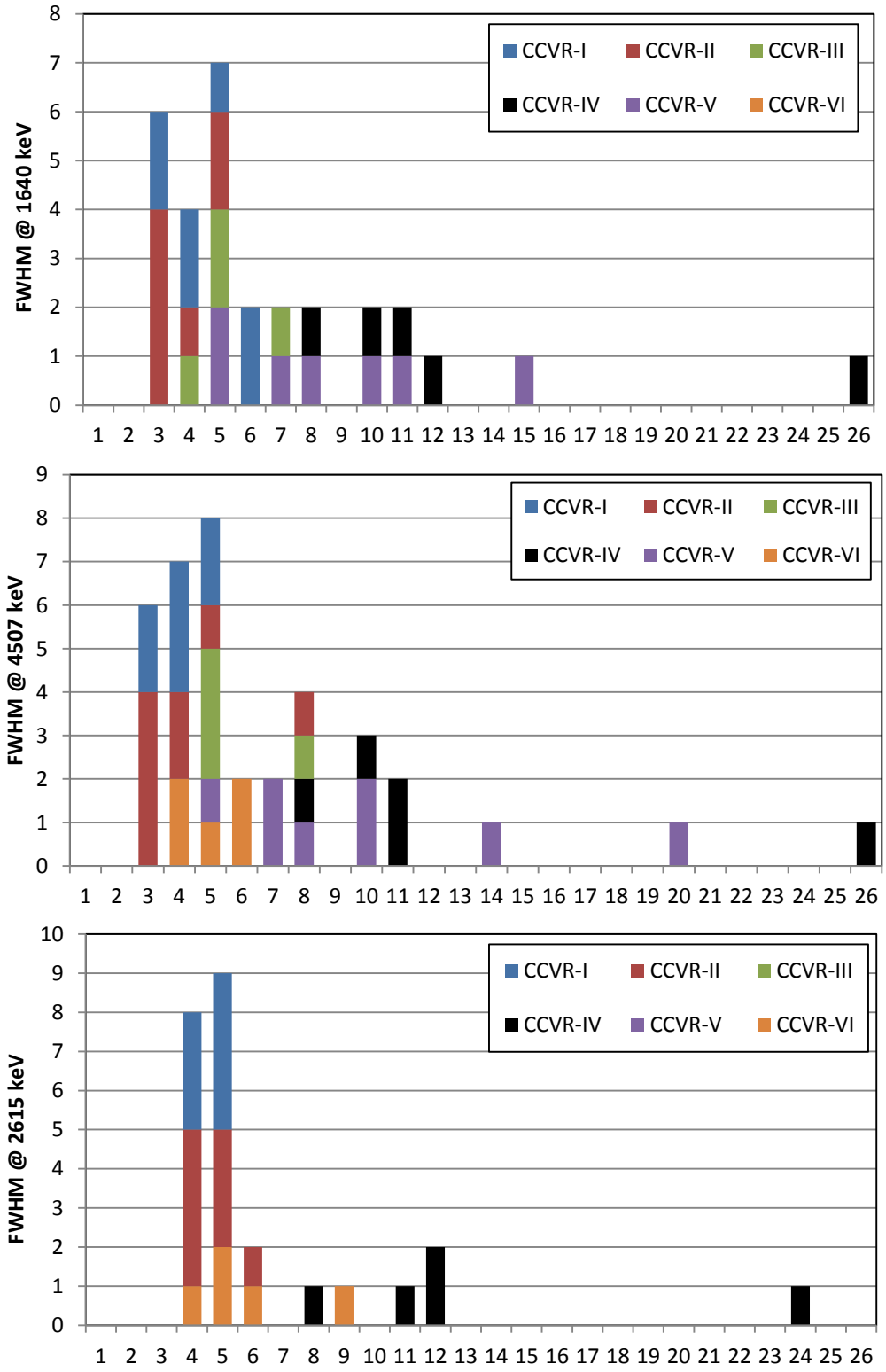

Figure 5-22. Distribution of the energy resolution of all the bolometers of CCVR-I to CCVR-IV, measured as the FWHM of three peaks: 1460 keV of ^{40}K (top), 2615 keV of ^{208}Tl (middle) and 5407 keV of ^{210}Po.

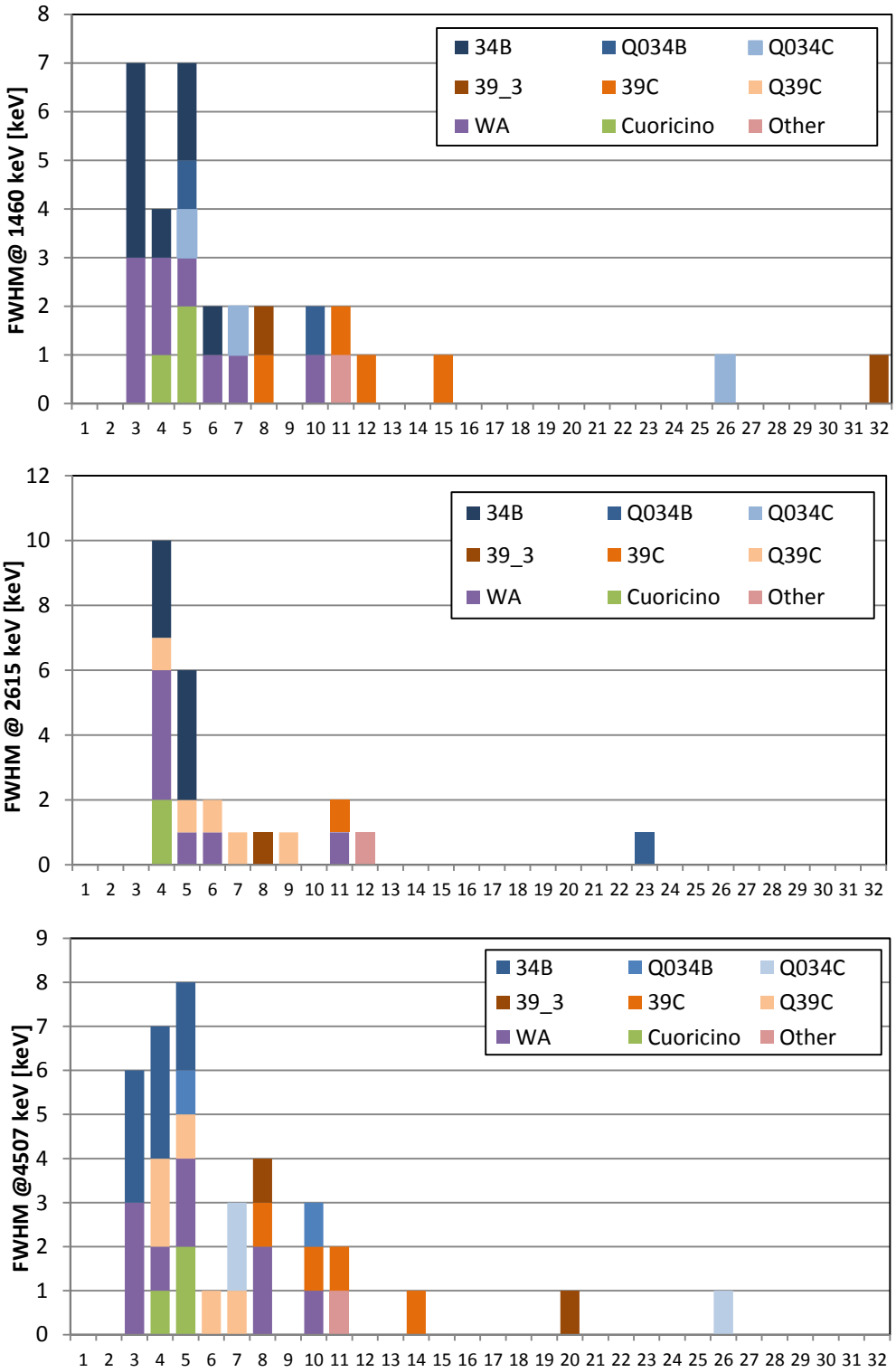

Figure 5-23. Distribution of the energy resolution of all the bolometers of CCVR-I to CCVR-IV, grouped according to the NTD type, measured as the FWHM of three peaks: 1460 keV of 40K (top), 2615 keV of ^{208}Tl (middle) and 5407 keV of ^{210}Po (bottom).

NTD type	#	CCVR-I	CCVR-II	CCVR-III	CCVR-IV	CCVR-V	CCVR-VI
34B	8	X	X	X			
Q0_34B	2					X	
Q0_34C	3				X	X	
39C	4				X	X	
39_3	2				X	X	
Q39C	5						X
WA	9	X	X	X	X		
Cuoricino	3		X	X			
Other	1				X		

Table 5-15. The different kinds of thermistors used in CCVR bolometers.

It is therefore possible to sketch out a distribution of the energy resolutions according to the kind of thermistor used. The results are collected in Figure 5-23. A first glance to the three distributions highlights how the energy resolution behaviour does not depend on the peak examined, therefore only the 4507 keV line of ^{210}Po will be considered from now on.

Grouping the NTDs according to the wafer they were cut from and their size (Figure 5-24) and excluding the one from the 34B/C-WA group with the highest FWHM value (that belongs to CCVR-IV), it appears that the small 39C/3 thermistors, i.e. the witness ones investigated in Chapter 4, have the worst energy resolution. Because the 39C (from the same wafer but with the right size) don't show the same problem, this fact can be connected to the different thermistor-to-crystal coupling of the small NTDs. Therefore they will not been considered in calculating the average FWHM for each CCVR. These results, collected in Table 5-16, values are consistent among the different CCVRs, with the exception of CCVR-IV for the reasons expressed before.

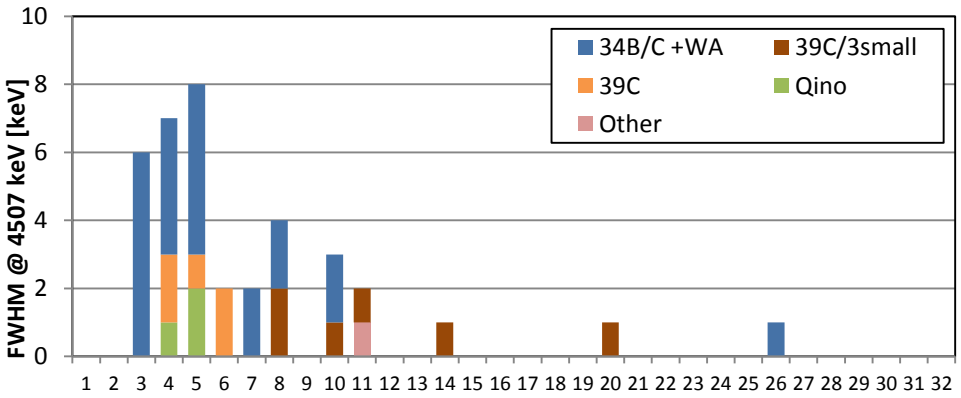

Figure 5-24. Distribution of the energy resolution of all the bolometers of CCVR-I to CCVR-IV, grouped according to the wafer their NTDs were cut from and their NTD size, measured as the FWHM of the 5407 keV peak of ^{210}Po.

Run	Live time [days]	# of channels	FWHM @ 1460 [keV]	%	FWHM @ 2615 [keV]	%	FWHM @ 5407 [keV]	%
CCVR-I	59.9	7	4.1	0.28	4.0	0.15	3.7	0.068
CCVR-II	19.4	8	3.2	0.22	4.0	0.15	3.6	0.066
CCVR-III	43.05	4	4.6	0.32	-	-	5.2	0.096
CCVR-IV	25.8	5	13.1	0.90	12.8	0.5	13.0	0.24
CCVR-V	30.3	8	5.6	0.38	-	-	6.1	0.11
CCVR-VI	11.8	5	-	-	6.1	0.23	4.6	0.085

Table 5-16. Summary of CCVR live time and average energy resolution for the 1460 keV ^{40}K, 2615 ^{208}Tl and 5407 keV ^{210}Po peaks.

5.4.2. Pirro curves

"Pirro curves" (from the name of the physicist that started using them) are a significant way for defining a merit figure for a bolometer (184).

The idea is to collect for each detector a family of load curves (Section 3.3.1.2), each with is working point determined thanks a reference pule amplitude (from a pulser or a known radioactive peak) and to collect the thermistor resistance at working point (R_w) and the absolute signal amplitude, (A, usually expressed in μV/MeV) corresponding to the maximum pulse amplitude for a given heat sink temperature. The plot of A vs R_w for each temperature will give the "Pirro curve", usually expected to be linear in the log-log plot.

A detector usually shows a very similar behaviour in terms of S/N ratio along a "Pirro curve"; this mean that working at a slightly high or lower heat sink temperature doesn't change so much: what is lost in term of signal, is gained in terms of noise and vice versa. Usually, it is better to avoid the extremities of the curve, which lead to too high spurious noise or to too small signals.

Comparing the "Pirro curve" of two different bolometers is a way to understand which one is better: the best detector will be the one providing the highest signal for the same resistance value, i.e. the one having its "Pirro curve" lying systematically above the other in the R_w-A space.

In the case of CCVR, the absolute signal amplitude is determined using the 4507 keV peak of ^{210}Po as for the shape parameters of the pulses, as will be discussed in the next session.

The “Pirro Curves” have been plotted grouping the bolometers according to different criteria.

In Figure 5-25 the detectors are divided according to the run number. This plot highlights how the best performances were obtained with CCVR-II detectors, as pointed out also by energy resolution considerations, being their points in the most upper left part of the graphic, above all the other points.

A second grouping (Figure 5-26) divides the bolometers in two subsets, according to the contact geometry of their thermistors, i.e. wrap-around and lateral. It appears that there is no correlation between the position of the pads and the detector performances.

Then the bolometers are divided in two groups thanks to the size of their NTDs (Figure 5-27): the small NTDs are the witness pieces from the top-off of the 39 wafer measured during the characterisation in Como (39C and 39_3, see Chapter 4), while the remaining thermistors form the set of the big ones. It is evident from the graphic that the bolometers equipped with the small thermistors belong to the “worse” detectors because their points lie lower with respect to the others, as expected because of their reduced sensor-to-absorber coupling.

To understand if this fact is related just the smaller size of the CUORE witness thermistors, a fourth grouping have been done, according to the wafer from where the NTDs were cut from without taking care about their size or contact geometry (Figure 5-28). The two main groups are the one containing the 34B, the Q034B, the Q034C and the WA, and the one with the small 39C and the Q39C; the 39_3 and the Cuoricino points are also plotted in the graphic. It appears that not only the small thermistors lie on a lower line with respect to the others but also the “right-size” Q39C NTDs have the same trend, lying on the same lower line. The 39_3 points don’t add further information, while the Cuoricino points are in agreement with the 34B ones.

A fit of the two data sets have been performed, resulting in:

$$\log_{10}(A_{34B}) = 0.910 \log_{10}(R_{work}) + 0.752$$
$$\log_{10}(A_{39C}) = 0.827 \log_{10}(R_{work}) + 0.429$$

5-11

This points out a slight pulse height deficit in the #39C series thermistors with respect to the #34B/C probably due to the difference in the irradiating dose in the wafer. Nonetheless they are suitable to be used in CUORE.

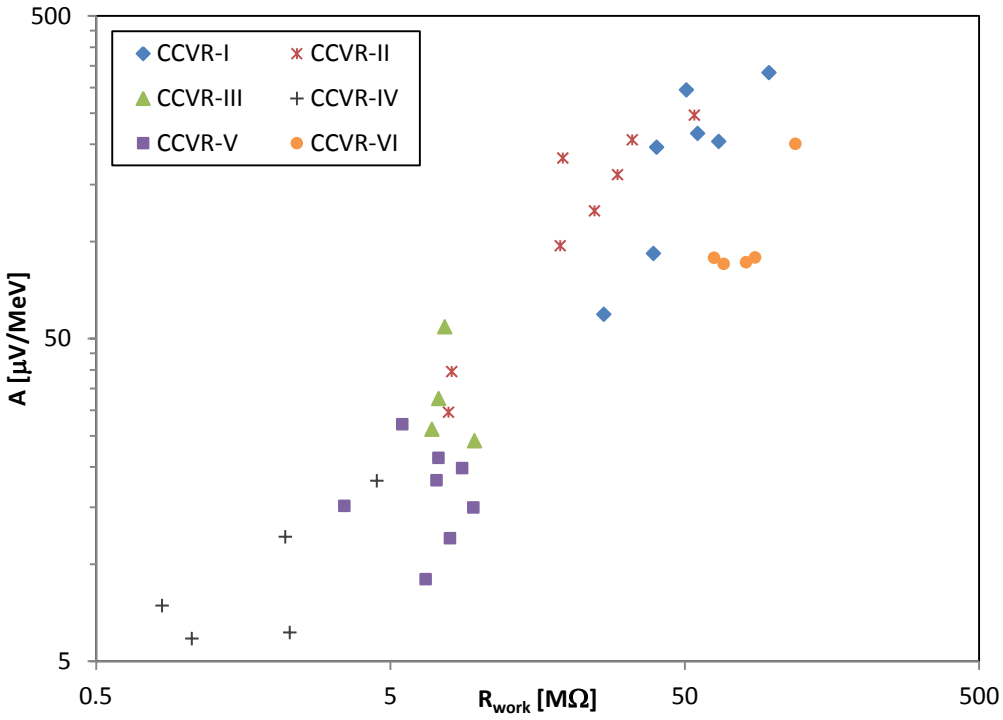

Figure 5-25. "Pirro curves" of all the CCVRs.

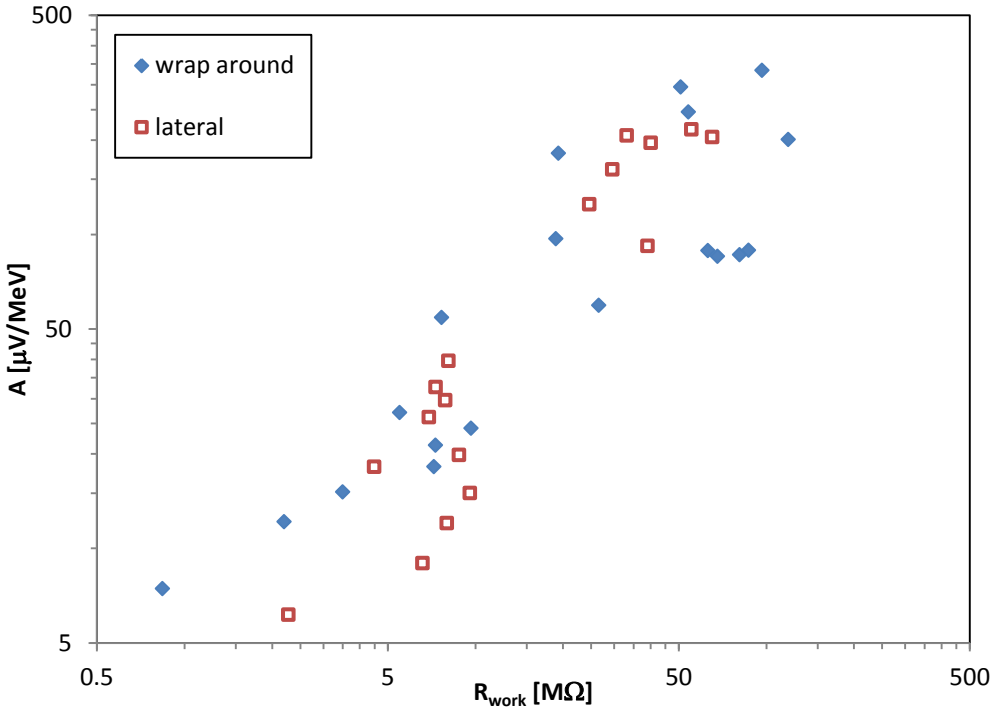

Figure 5-26. "Pirro curves" of all the CCVR detectors divided according to the contact geometry of their NTDs (wrap-around gold pad or only lateral gold pad).

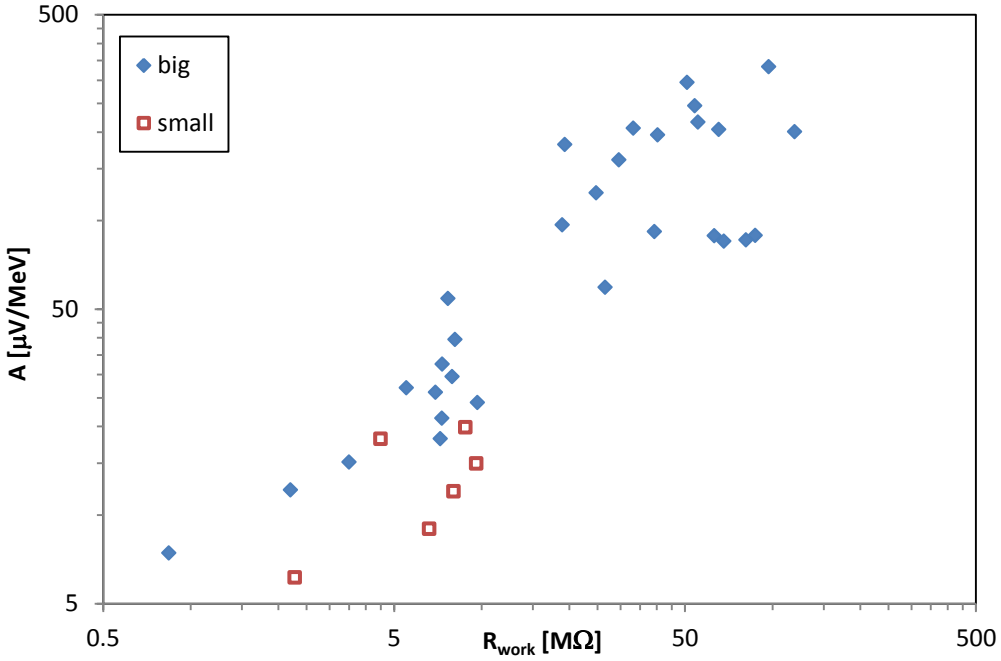

Figure 5-27. "Pirro curves" of all CCVR detectors divided according to the size of their NTDs. All the detectors belong to the "big" set except the ones having the NTDs from the top-offs of wafer 39.

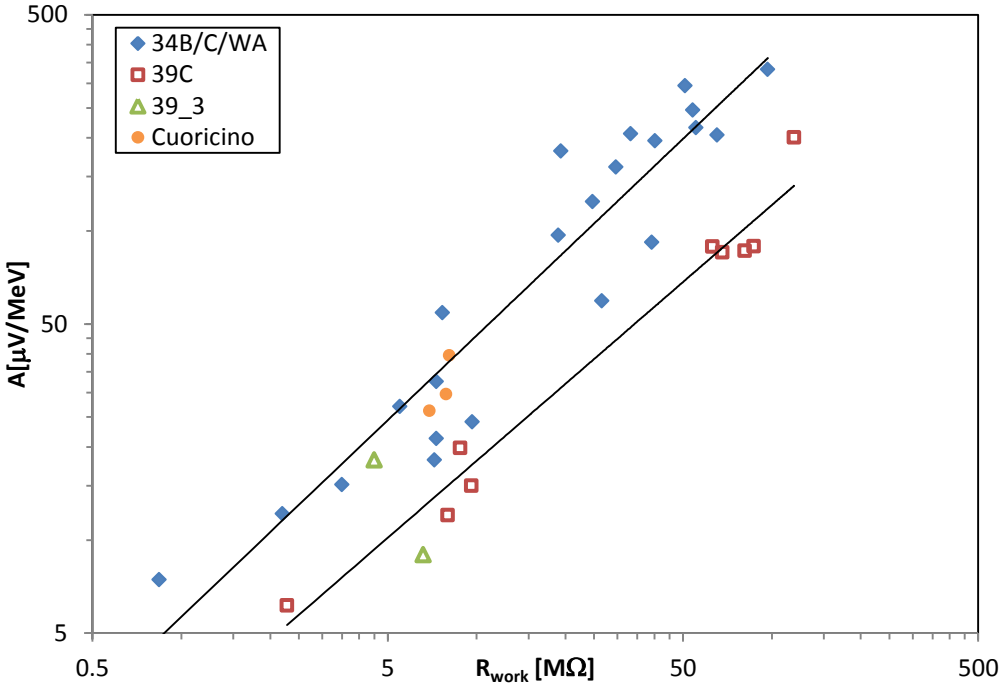

Figure 5-28. "Pirro curves" of all the CCVR detectors divided according to the wafer their NTDs were cut from. Two main data sets appear: the 34B one, collecting the A-R_{work} points of the bolometers equipped with 34B, Q034B, Q034C and WA NTDs, and the 39C, with the detectors having thermistors of small 39C or Q39C type. Other two groups are reported for comparison: the Cuoricino and the 39_3. The two lines correspond to the fit of the 34B group (the upper one) and of the 39C set (the lower one) whose results are presented in Eq. 5-11.

5.4.3. Pulse shapes

The last considerations about the performances of the CUORE-0/CUORE thermistors regard the shape of the pulses they generate after collecting events, described in terms of rise and decay time (see Table 7-6). This two shape parameters have been calculated for each detector from CCVR-I to CCVR-IV by using the average pulse at 5407 keV peak.

A first glance to the distribution of the rise time (Figure 5-29) shows a small spread, while the variation in the decay time (Figure 5-30) is not so big.

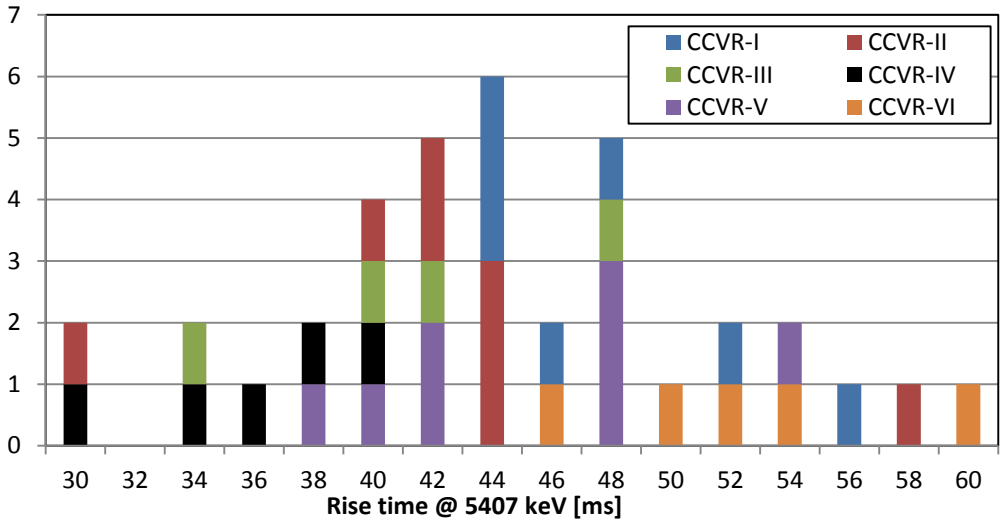

Figure 5-29. Rise time distribution of the 5407 keV average pulses of all CCVR detectors (from I to VI).

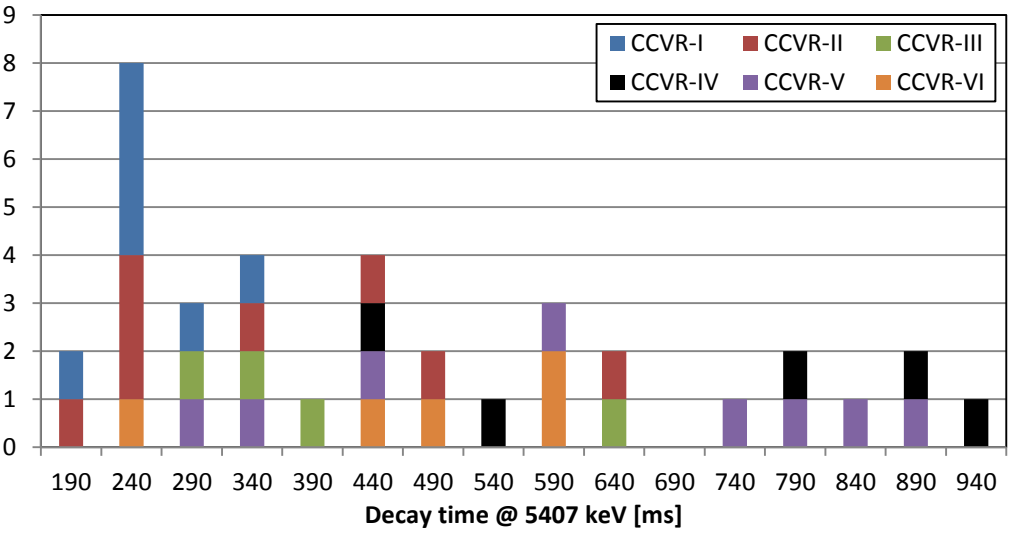

Figure 5-30. Decay time distribution of the 5407 keV average pulses of all CCVR detectors (from I to VI).

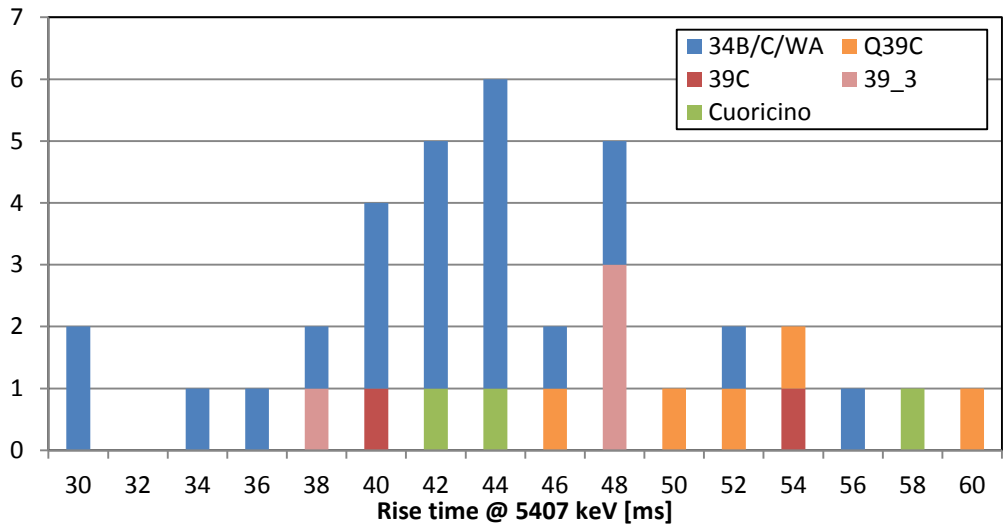

Figure 5-31. Rise time distribution of the 5407 keV average pulses of all CCVR detectors (from I to VI), divided according to the wafer from which the thermistors were cut.

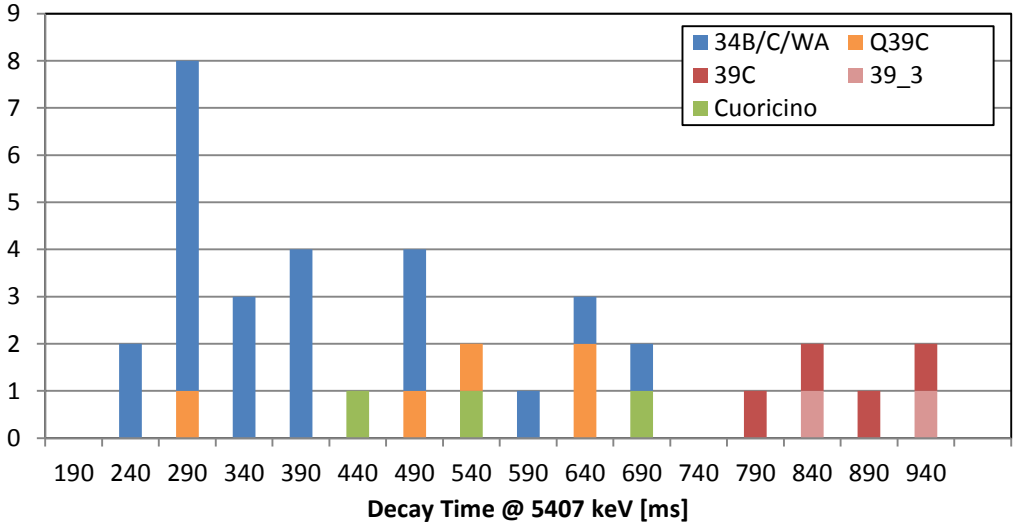

Figure 5-32. Decay time distribution of the 5407 keV average pulses of all CCVR detectors (from I to VI), divided according to the wafer from which the thermistors were cut.

Grouping the detectors according to the wafer from which their thermistors have been cut, no real correlation appear with the rise time (Figure 5-31), while the smallest 39 NTD show to have the longest decay time (Figure 5-32).

Using data from CCVR-V crystals it is possible to make a direct comparison between the pulses from the smallest thermistors and the 34B/C ones from the CUORE-0 batch (Figure 5-33). It appears as if the pulses from 34B/C thermistors have two components in their decay, one fast and one slower, while in the pulses from 39 NTDs, only the slower component is present. The same observation is valid also for the Q39C wrap-around NTD.

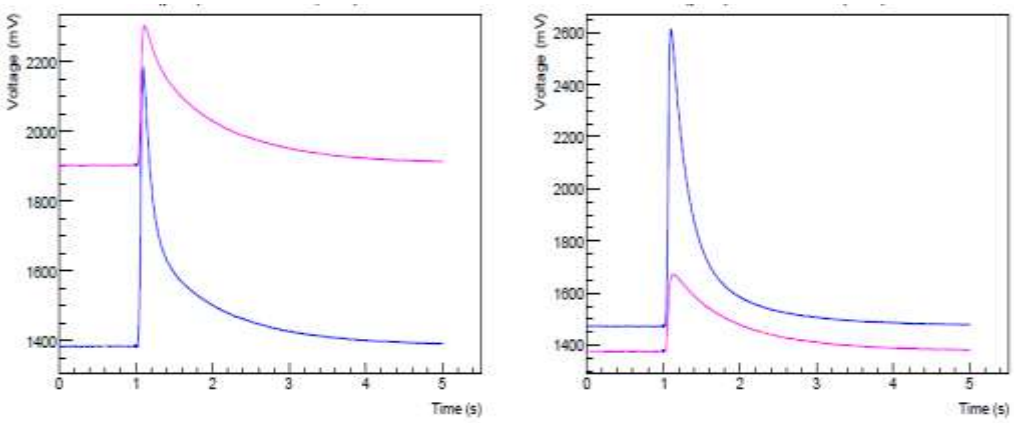

Figure 5-33. Example of pulses from CCVR V. Blue pulses are from a Q034C and a Q034B thermistor, while the pink ones are from a 39_3 and a 39C thermistor.

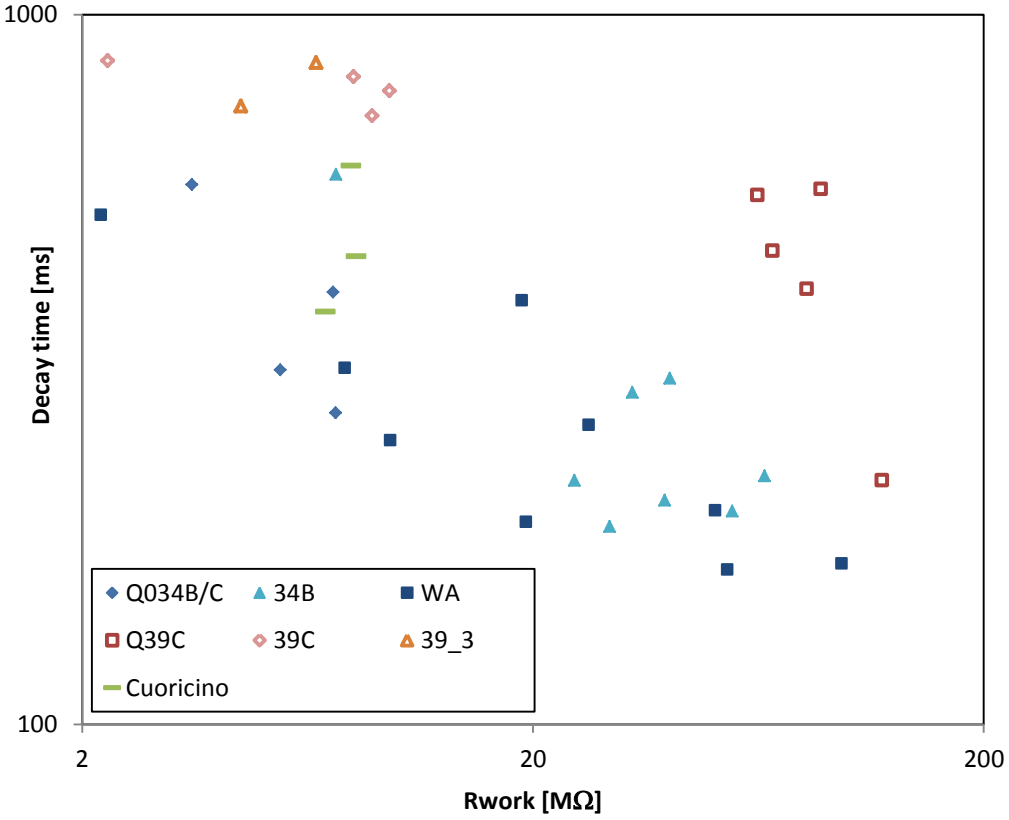

Figure 5-34. Decay time of the 5407 keV average pulses of all CCVR detectors (from I to VI) versus the corresponding resistance at the working point.

Also the plot of the decay time versus the resistance at the working point of each bolometer show a different trend in the detectors made with the thermistors from the two wafers, as if the lie on two separated lines.

This difference is not yet understood, that's because it is not so clear which parameters of the bolometric model can have a so strong influence on the decay time. For example, it is known that the irradiating dose received by the thermistors fixes the T_0 of the NTD and, through it, the dependence of the thermistor on the temperature (VRH Eq. 3-1) or its electron-phonon decoupling (Eq. 2-29) or the specific heat of its electron system. But simulations based on the composite bolometric model ran varying these parameters (an example is in Figure 5-35) don't show the difference observed in the real pulses.

Besides this consideration, it is necessary to underline also that this kind of analysis is complicated by the fact that the gluing of the thermistor to the absorber is not as reproducible as desired, because it is "manually" done (see Section 5.2.1), therefore some differences in the behaviour of the thermistors can be enhanced or reduced by slight (or not so) discrepancies in the sensor-to-absorber coupling.

This problem can be avoided by the use for the future CCVR tests the semi-automatic gluing line, presently almost ready in the underground CUORE clean room at LNGS and that will be described in the next Chapter.

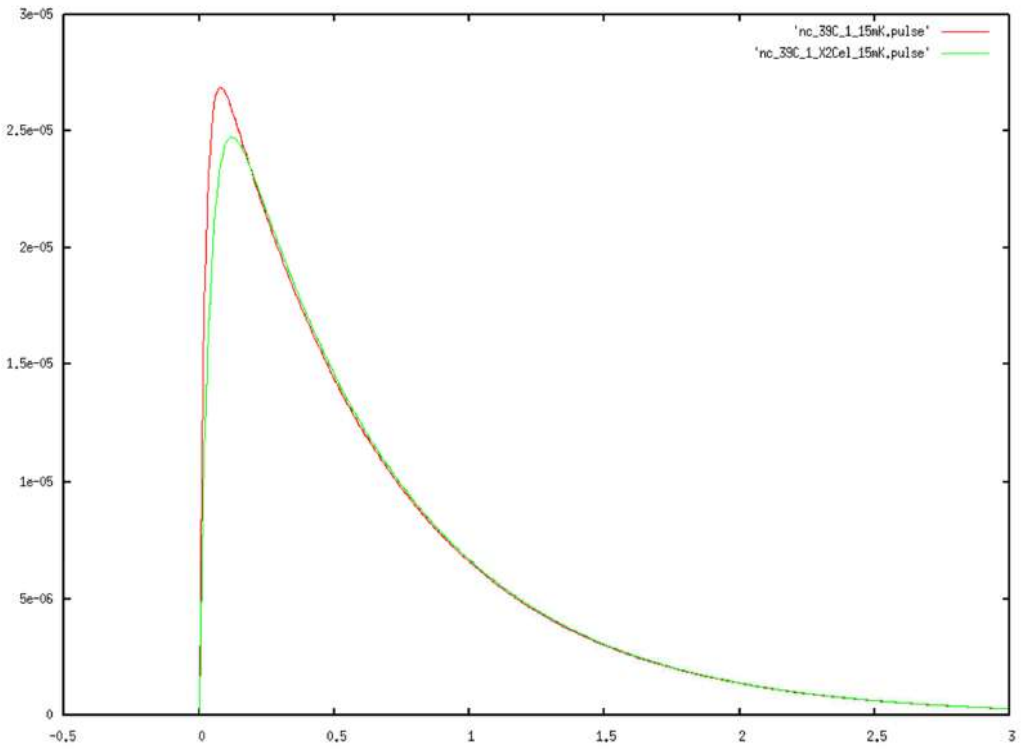

Figure 5-35. Simulated pulses from a 39C thermistor. The simulation is based on the composite model of bolometers (see 2.4): the green pulse has a double C_{el} with respect to the red pulse.

Chapter 6.
THERMISTOR-TO-ABSORBER COUPLING

It – could – work![14]

As stated many times in this PhD thesis, a sensitive point that must be taken into account in reviewing the Cuoricino Single Module toward the CUORE-0/CUORE SM is the connection of the Ge sensor to the TeO_2 crystal absorber. In fact this coupling (both thermal and mechanical) has a relevant role in defining the quality of detector performance, as will be pointed out in Section 6.1. A huge work has been performed in order to improve the totally manual gluing procedure described in Section 5.2.1, and many aspects of the procedure have been optimised (Section 6.2), resulting in the design of a semi-automatic line for absorber connection to both Ge thermistor and Si heater that will be firstly used in the CUORE-0 construction and then in the CUORE assembly.

This Chapter is dedicated to present all the innovation introduced in the sensor-to-absorber coupling procedure. Although the final system involves heater connection as well, explicit mention of it will be omitted in this review and focus will be given to the sole thermistor-to-crystal coupling; in fact, the technical considerations and solutions developed for the NTDs will be easily extended to the heater itself. No loss of generality is expected, as the following paragraphs will show that, when it comes to absorber coupling, the most sensitive point is the Ge sensor, therefore any direct reference to heaters will be omitted.

6.1. Need to change

A first, trivial reason for requiring a new sensor-to-absorber coupling (as well as a new assembly line for the construction of the entire tower) is a matter of time. The gluing of the detectors took about two months for the Cuoricino array (62 crystals), about three months for the TTT run (36 crystals) and about a week for each CCVR detector (4 crystals). A quick extrapolation suggests that the realization of just the sensor-to-absorber couplings for

[14] (222)

the whole CUORE will take about two-three years, if carried out with the same rate, a solution completely impractical. Therefore a revising of the procedure in order to cut on time is mandatory.

Besides this practical motivation there are important scientific reasons for improve the coupling of the bolometer components, because this coupling influence the overall bolometric performance, that, as discussed in Section 5.4, can be evaluated in terms of energy resolution and pulse shape.

Chapter 5 shows as even if considering a set of bolometers built with the same elements and cooled down in the same run a spread in the the energy resolution of the detectors appears. Figure 6-1 and Figure 6-2 (left) gives a sample of this problem, that is a constant in Cuoricino as well as in the following R&D detectors. Such a distribution of the detectors performances can be related to the heterogeneous quality of sensor-to-absorber couplings among different bolometers. As for the issue of pulse shape, a specific discussion will be made to deduce a definite link between variable characteristics of thermistor-to-absorber couplings and non-uniform detector responses, so that reproducibility of couplings may be seen as a mandatory aim to improve experimental results.

First of all, the variation in pulse shapes obtained by different detectors is a fact observed in both Cuoricino and the following R&D runs. As evidence of this experimental circumstance, the right side of Figure 6-2 reports the distribution of amplitudes in μV/MeV for the Cuoricino tower and Figure 6-3 shows a selection of pulses from a sample of Cuoricino detectors: neat differences in heights, rise times, decay times can be noticed in the pulses reported, and variations in other shape parameters from one signal to the other are evidenced by data analysis.

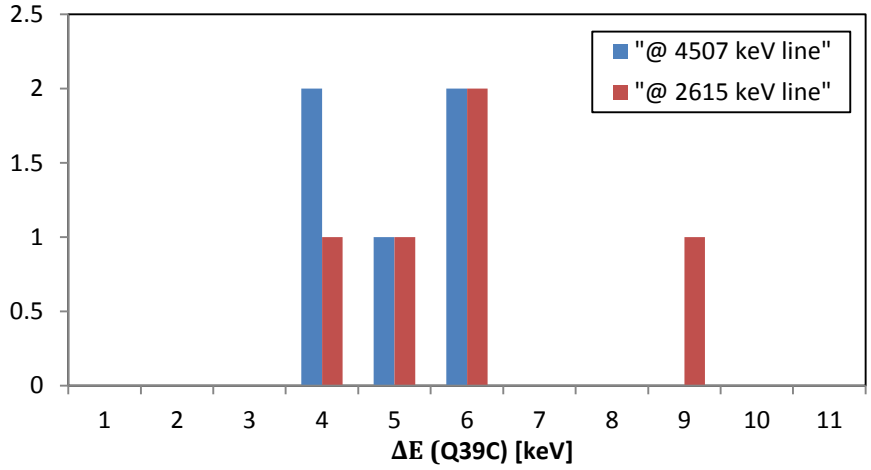

Figure 6-1. Energy resolution of the CCVR-VI bolometers measured at the 2615 keV γ line of ^{208}Tl and at the 4507 keV α line of ^{210}Po for all the channels.

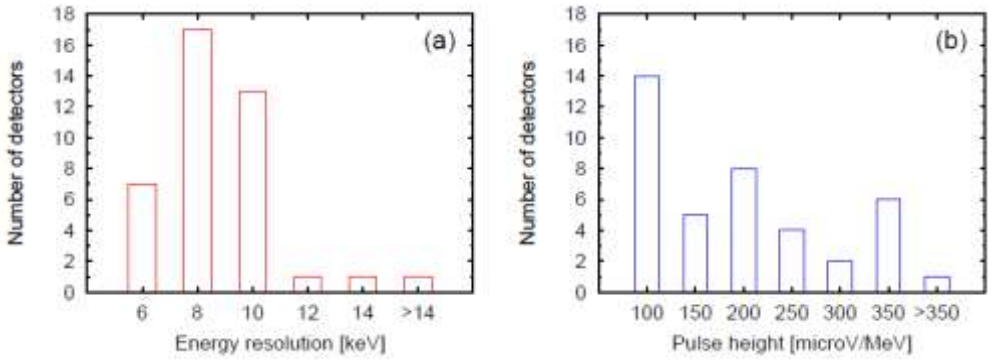

Figure 6-2. Examples of distributions of detector performance parameters for the 5×5×5 cm^3 bolometers in the Cuoricino tower; the data in the histograms is taken from a 3 days ^{232}Th calibration which took place during Run II on the 40 surviving big detectors. (a) FWHM resolutions at 2615 keV. (b) Pulse heights in μV/MeV.

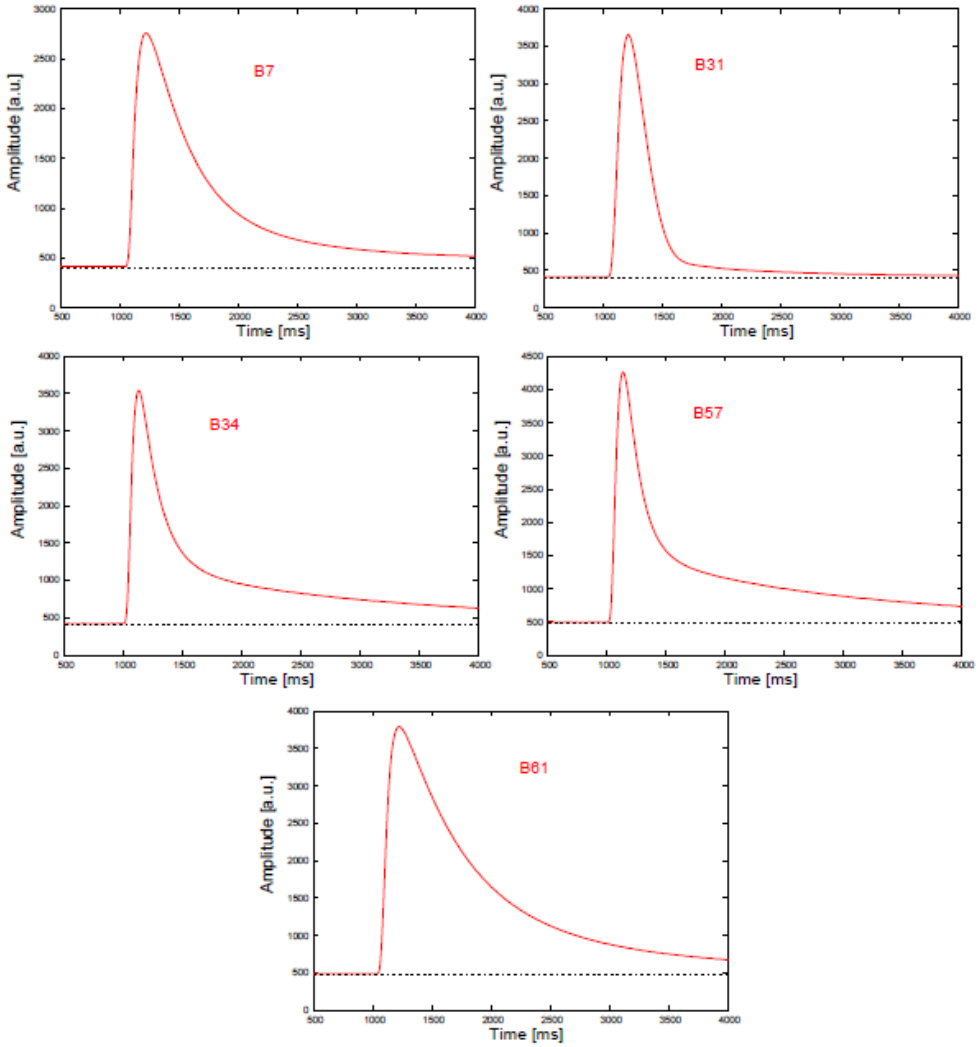

Figure 6-3. Examples of pulses from selected bolometers in the Cuoricino tower (B7, B31, B34, B57, B61) featuring variations in shape parameters.

Two main reasons justify concern on the spread in pulse shapes when comparing several identical bolometers in the same run. The first point regards the overall comprehension of the detector behaviour: the unexpected shape variations hint at a shallow understanding of some aspects in the thermal model, which have to be clarified because of the obvious consideration about non-predictable elements in the responses meaning that full control on the bolometer has not been reached yet.

The second point involves data analysis: the huge number of the bolometers in the CUORE detector requires to automate certain steps in the analysis process: for instance, discrimination of those groups of signals that cannot be due in principle to 0νββ events, such as thermistor pulses or non-flagged heater pulses; or, again, recognition and discard of pile-up signals. These classes of events can be distinguished by specific rejection parameters, which are linked to the shape of signals and change accordingly to the aforementioned variations. In order to develop software tools so that part of the data analysis process is handled by automatic procedures, the unpredictability introduced by the overall spread in pulse shape parameters in the same run has to be reduced: the more similarly bolometers respond, the faster and more reliable is data analysis.

In light of the previous considerations and enlarging the view from the behaviour of a lone bolometer to arrays constituted by multiple detectors, achieving global uniformity of performance should be definitely seen as a plus.

The bolometric model in Figure 6-4, already examined briefly in Chapter 2, is used as a reference to discuss which components are candidate to be responsible for pulse shape variations and to which extent; for the values of the capacities and conductances listed here, refer to Section 3.5.

The first element analysed is the phonon-electron conductance (G_{ph-el}, 1). Thermistors in the Cuoricino experiment were obtained from the same wafer and were exposed to the same irradiation: variations in the HEM conductance from one detector to the other are therefore expected not because of doping differences but only from tolerance on dimension, as G_{ph-el} grows linearly with thermistor volume. Such contribution is negligible: the precision is estimated as ±75 μm in all directions, which corresponds to a variation of order lower than 0.1h in conductance value for Cuoricino 3×3×1 mm^3 thermistors.

The previous consideration applies also to the conductance of read-out wires (G_{pad}, 2), which is a Kapitza conductance whose value, at fixed temperature, depends linearly on the contact surface in the Au/Ge interface. Here the only variation is introduced by tolerance on the dimension of pads for electric contact, and again the contribution is negligible (1% on G_{pad} for Cuoricino thermistors with 3×1 mm^2 pads).

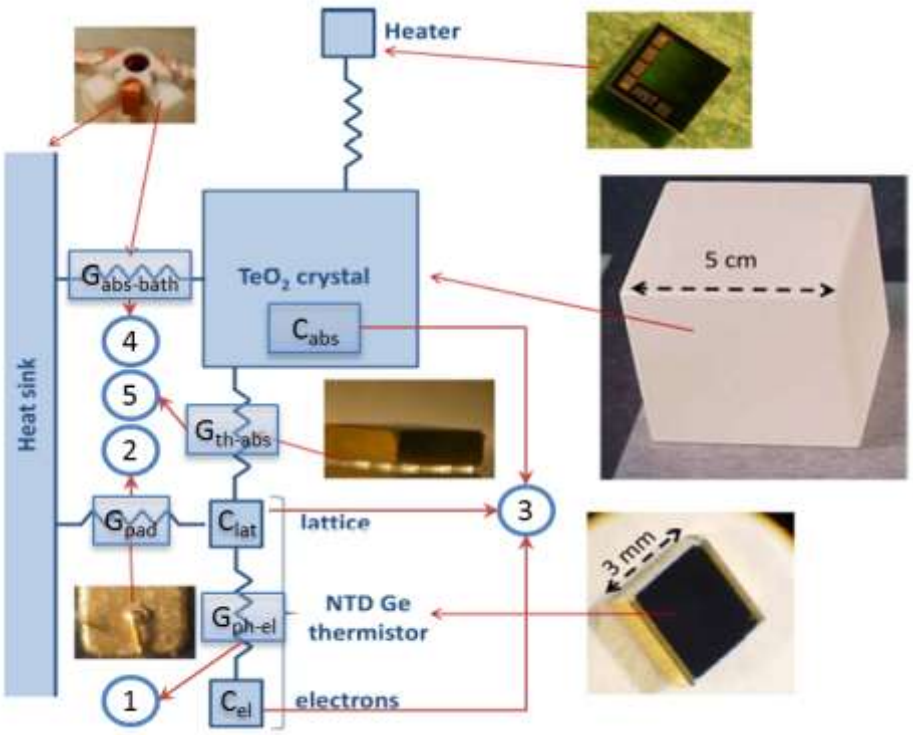

Figure 6-4. Bolometric model of reference for the discussion on pulse shape variations. The parameters taken into account as possible sources of the variations are enumerated with the same notation in the figure and in the list in Section 6.1.

Because the variation on the sensor volume is 1% at worst, the contribution of C_{lat} and C_{el} (3), can be also neglected while a few more words should be spent for the C_{abs} term. Section 3.2 reported the optimization conducted on the production of TeO_2 crystals, which aimed specifically at uniforming the purity, the reliability and the geometry of the batches of absorbers for future use in CUORE-0 and CUORE. According to the results of the work done, the spread in the heat capacity values of crystals is negligible (one part in a billion) and no consequent appreciable contributions to the origin of pulse shape variations in different detectors are expected.

In the frame of the R&D activity focused on background reduction, an investigation was made regarding exotic contributions to the counting rate in the $0\nu\beta\beta$ region of the energy spectrum: the study aimed at verifying the possibility for PTFE crystal holders to release heat in the absorbers as a consequence of thermal relaxation processes, mimicking particle interactions. This idea has already been mentioned in Sec. 3.1.2, and is beyond the goal of this thesis. However, this work, offers insight on why the absorber-to-heat bath coupling ($G_{abs-bath}$, 4): this term should not be considered a candidate for the origin of pulse shape variations from one detector to the other.

The results of the attempted substitution of PTFE holders prove the point under discussion. Eight detectors, which had already been tested and constituted a performance benchmark, were reassembled in the frame of their last test keeping the setup identical apart from PTFE holders, replaced by copper clamps: all the other elements (NTD thermistors, read-out wires, crystals, thermistor-to-absorber couplings) and working conditions (base temperature, electronics) remained comparable. The data obtained suggests that the difference between pulse shapes, from the mounting with PTFE holders to the one with Cu clamps, is negligible (185).

The last candidate among the parameters of the thermal model used here is the connection between the Ge sensor and its crystal (G_{th-abs}, 5). As a general remark, there is an obvious influence of this conductance on pulse shape: the fraction of heat which reaches the thermistor following energy deposition in the absorber depends on the value of G_{th-abs}, and this is reflected on pulse height and rise time; the simulation work developed during Cuoricino R&D shows that when sensor-to-absorber coupling gets larger, the detector optimum pulse amplitude initially increases and eventually reaches saturation due to electron-phonon HEM decoupling becoming the limiting factor (132).

Besides this immediate consideration, evidence of the link between Gth−abs and pulse shape can be extracted by the analysis of bolometers with a pair of equal thermistors connected to the absorber: in this case, the only distinguishing factor in the pair is thermistor-to-absorber coupling, because the crystal is the same and all the other parameters in the model are equal or have negligible variations according to the considerations exposed previously.

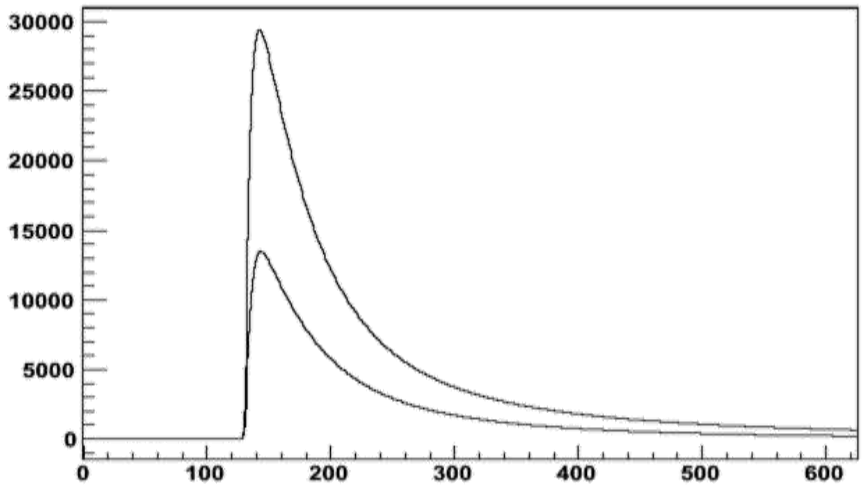

Figure 6-5. Pulses from the two 39C thermistors glued on one of the crystal (#547) of the CCVR-VI detector (see Chapter 5). Each pulse is generated by the same particle deposition in the corresponding absorber, and is seen by a different thermistor.

As an example, a pairs of pulses coming from one of the crystal (#547) of the CCVR-VI detector (see Chapter 5) which is equipped with two 39C thermistors, are reported in Figure 6-5; each pulse is generated by the same particle deposition in the corresponding absorber and is seen by a different thermistor: pulses read by thermistors on the same crystal show differences in shape.

As a last remark, another feature hints at the importance of thermistor-to-absorber coupling in the definition of detector performance. In the calibrated energy spectra of two thermistor of the same kind glued on the same crystal, the notable peaks due to particle energy depositions have a good superimposition while an energy shift of the heater peak of can be observed from one spectrum to the other. A possible explanation is that the mechanism of signal development differs slightly for heater and particle depositions. This is due to the contribution of those athermal phonons that hit the sensor-absorber interface and are transmitted to the thermistor, where their energy is thermalized quickly through interaction with the conduction electrons (details on the conversion of particle energy to thermal phonons have already been given in Chapter 2). In other words, heater depositions generate signals that constitute a stand-alone class and have a different athermal component than usual particle depositions in the bulk.

The probability that an athermal phonon is absorbed by the sensor is $p=\alpha(\sigma/S)$, where S is the surface of the crystal, σ is the surface offered by the thermistor-to-absorber coupling and α is the transmission coefficient of the high energy phonons: however, α does not take into account an effect that could explain the observed energy shift between heater peaks, which is thermistor-to-absorber coupling acting as a selection filter for phonon energy. This would change the ratio of athermal to thermal contribution in the heater pulse, in function of variations in the thermistor-to-absorber coupling.

For completeness, other possible motivations should be mentioned: a position effect, for example, due to one thermistor (TR) being nearer to the heater as compared to the other one. The previous considerations on the link between G_{th-abs} and the shift in heater lines should be therefore considered a hypothesis.

The last considerations regard the treatment of crystal surfaces, even if this item is not integrated in the thermal model used here; however, a brief treatment of its possible contributions to the subject under discussion is required for completeness. R&D tests (160) pointed out that the treatment of crystal surfaces can be determinant for the quality of bolometric performance. The underlying mechanism of the observed behaviour has still to be cleared. Nonetheless, the same protocol of surface treatment is now applied equally to all

crystals; it also cannot account for pulse shape variations seen in signals read by two equal thermistors connected to the same absorber (as detailed in the previous item of this list).

Summing up, the optimization of the sensor-to-absorber coupling preliminary to CUORE-0 is focused on reproducibility. Following the principles fixed by the Cuoricino R&D on the physical characteristics of the conductance, this is mainly a technological problem: all the steps in the realization of the coupling have to be reviewed and standardized, getting rid of those actions which are intrinsically not reproducible. As simple as it may seem, the task hides a good collection of tricky points. This is due to various restrains which will be listed right after and constituted the starting point for the work done.

6.2. Constraints to the gluing process

There are several fixed points that the thermistor-to-absorber coupling for the CUORE bolometers must undergo, independently on the way it is performed, set from years of R&D starting before Cuoricino itself was built. They concern several aspect of the coupling, ranging from the type of glue to be used to the shape of the glue dots and to the room conditions where the operations are made.

The primary requirement is that the thermistor-to-absorber coupling is made thanks to a matrix of glue dots instead of a veil. In fact the distribution in separate spots compensates the differential thermal contractions between the material of each sensor and TeO_2, so that no fractures or detachment of the elements happen at low temperatures. The number of dots giving the most efficient results is nine for a ~3x3 mm^2 thermistor and five for a ~2.4x2.4 mm^2 heater. These dots must have a diameter of ~700 μm while their height is determined by imposing a 50 μm gap between the TeO_2 crystals and the chips.

The glue used for that purpose therefore must have a density high enough to avoid the merging of the dots after their deposition (which happens on the chip surface and not on the crystal one because the chips are easy-to-clean, in case of errors, while for cleaning the crystal a new lapping procedure is required) and of course it has to work at cryogenics temperatures. The chosen one, since Cuoricino, is the Araldite Rapid glue, a DIY bi-component epoxy with an extremely short pot-life (3 minutes), whose radioactive contaminations showed to be very low, as required by the CUORE needs.

Because of the dependence of the glue curing with the temperature and the necessity to reduce the detector component exposure to air, to avoid recontamination, the gluing procedure has to be done in controlled atmosphere, i.e. in a dedicated glove box.

6.2.1. The glue

The glue for the thermistor-to-absorber coupling is the bi-component epoxy Araldite Rapid, actually produced by Huntsman Advanced Materials (186). This kind of epoxies come in two different components, an epoxy resin and a catalysing agent (commonly called hardener), whose exothermic chemical reaction results in a thermosetting polymer.

The resin is made of monomers or short-chain polymers with an epoxy group at each end; the hardener is constituted by polyamine monomers. As the two components are mixed with fixed ratio and for a given time, the aminic and epoxy groups react and a covalent bond is set up: the resulting polymer is highly cross-linked. The features of the polymerization process, known as curing, endow epoxy glues with high adhesion, chemical and thermal resistance and electric insulation. The specific use for bolometers additionally requires the chosen epoxy to withstand the severe conditions found at cryogenic temperatures: the adhesive properties of the fully cured glue should resist a complete down-to-10 mK thermal cycle and compensate differential thermal contractions between the glued items, which can be relevant for the Ge-TeO_2 couple, so that detachments and fractures are avoided.

As thermosetting polymers, the properties of epoxies depend on the curing environment but also on their thermal and environmental history. The temperature at which the curing process develops sets various features of epoxy adhesives. For instance, these materials are characterized by a so-called glass transition temperature T_g, that is the temperature under which the polymer goes from a rubber like state to a hard, glass like state; T_g varies according to the curing degree and the water content. Various studies in literature (i.e. (187)) show that glue vitrifies when its curing is performed at temperatures lower than the ultimate glass transition of the completely cross-linked epoxy: the epoxy will then be vitrified but under polymerized, so that the cross-linking reaction slows down drastically and a long time may occur for the adhesive to reach its final properties. One should then pay due attention to the choice of curing temperature.

Curing times may vary consistently for different bi-component epoxies. This process is the results of several steps, that can be described in terms of the following parameters: mix ratio, pot life, handling time and curing time. The mix ratio is the ratio of resin to hardener, in volume or weight, needed to start the polymerization reaction.

The pot life is time available for glue application before it gets unusable. The end of pot life is marked by a steep rise in both the mixture viscosity and temperature. Moving the glued items after this time limit implies breaking the forming macromolecules and preventing the correct development of curing. Pot lives range from a few minutes to hours

depending on epoxy and environmental parameters. The intermediate time threshold after which the glued system can be moved without risking that vibrations abort curing is the handling time. However, more time is needed for the epoxy to reach its full qualities. The curing time is the total time necessary for the epoxy to gain its specific final gluing properties.

All these times are functions of temperature T. A general behaviour of epoxies is the reduction of pot life and curing time corresponding to a growth in T; moreover, the degree of curing reached by the epoxy features a strong correlation to viscosity (188): as an example, Figure 6-6 shows the dependence of viscosity on curing time at three different temperatures for the Araldite 2014 glue, a kind of Araldite with longer pot life and curing time than the Araldite Rapid used in this application (189).

Such behaviour forces operators to balance the conditions for glue dispensing: higher T means lower viscosity, which makes epoxy application easier, but it also implies shorter time to complete the operation. The previous consideration is useful mainly for that class of epoxies with the shortest pot lives (a few minutes). The Araldite Rapid glue extensively tested in bolometer assembly for the Cuoricino experiment and CUORE-0 R&D runs is a short pot life epoxy; it can be cured at room temperature.

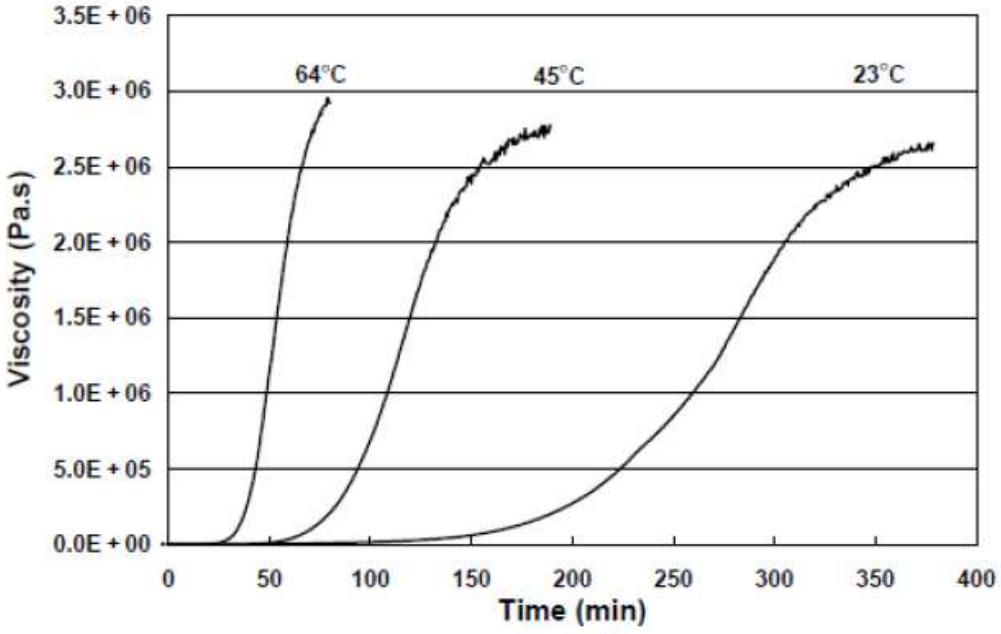

Figure 6-6. Correlation between the degree of conversion and the viscosity of the epoxy Araldite 2014, belonging to the same family of Araldite Rapid but with longer pot life, at three curing temperatures (189).

Mix ratio	1:1 volume
Colour (visual)	Pale yellow
Relative density	ca 1.18
Viscosity at 25 °C	25-35 Pas
Pot life (100g at 25°C)	5 min
Shelf life (2-40 °C)	3 years
Cure time for reaching lap shear strength > 1 MPa	20 min at 25 °C
Cure time for reaching lap shear strength > 10 MPa	60 min at 25 °C

Table 6-1. List of chemical, mechanical and thermal properties for the epoxy Araldite 2012, the industrial version of Araldite Rapid (190), after the mixing of its two components. Although a 5 minutes pot life is quoted, the experimentally observed work life of the epoxy is shorter (approximately 3 minutes at room temperature), due to the rapid growth in viscosity which reduces its usability.

Araldite Rapid takes different names according to the country of distribution, which is Switzerland for the product used in this application; it shows variations in colour within different batches, mainly in the hardener which can vary from white to yellow, even sometimes light orange, according to the site of production and the source of the production materials (Figure 6-7). As guaranteed by the producer, these differences have no influence on the ultimate mechanical performance; however, radio-purity at the levels required by the CUORE collaboration was tested and approved only for the batches of Araldite Rapid selected by CERN laboratory in Geneve. Therefore, this is the supplier of the epoxy we are currently using and intend to use in both CUORE-0 and CUORE.

Since Araldite Rapid is distributed as a common do-it-yourself product, in order to gain detailed information on glue properties one has to refer to technical data sheets of its industrial version, which goes under the name of Araldite 2012. A selection of its chemical, mechanical and thermal properties is presented in Tab. 6.1.

The reported pot life of a few minutes may be reputed very short for the requirements of this application: in particular, it makes quite complex the phase of glue distribution, whose peculiar geometry will be discussed in the following subsection. In spite of the disadvantaging brief time window available for gluing operations, Araldite Rapid has been extensively tested in terms of bolometric performance and radio-purity: both evaluations are excellent and supported by the large statistics collected (191). The epoxy Araldite Rapid was chosen for CUORE-0 and CUORE assembly because of its reliability in these fields and its outstanding mechanical properties throughout cryogenic thermal cycles that compensate possible complexities in the assembly.

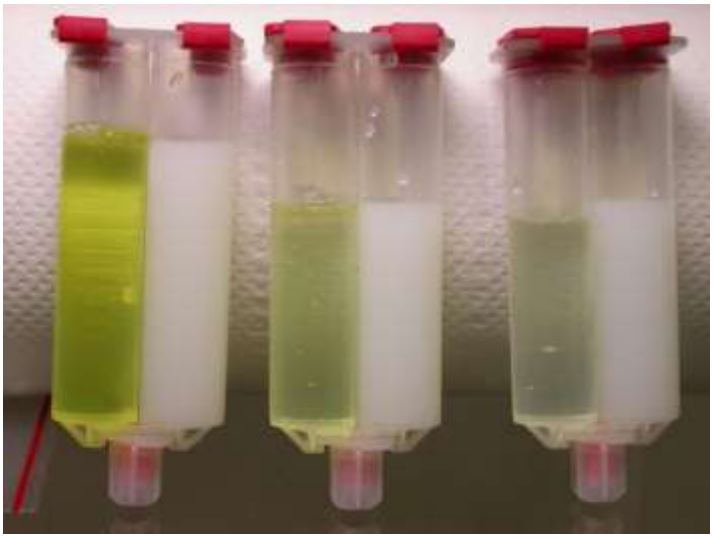

Figure 6-7. The content of DIY Araldite Rapid tubes coming from different producers. The one used for CUORE is on the right.

6.2.2. The geometry of the epoxy interface

The most intuitive way to glue a sensor to the corresponding crystal is, probably, to deposit a homogeneous epoxy layer between the two surfaces: one can easily picture the procedure to be fast and compatible with short pot lives; even performing the operation manually inside a glove-box would not complicate it strongly. This is not the case, however.

Epoxy deposition in form of a homogeneous layer, as thin as it may be, is excluded for reasons of mechanical performance at cryogenic temperature. Experimental evidence says that, throughout a low temperature thermal cycle, a thin layer of Araldite Rapid is not elastic enough to compensate differential thermal contractions in the Ge/TeO_2 and Si/TeO_2 pairs: fractures in crystal absorbers may often happen. The interface should then be designed with the aim of a higher elasticity. The epoxy distribution most successful for this application is a dot matrix. The single-spot dimension and the total number of spots in one matrix were decided during Cuoricino R&D.

Glue spots deposited with the Cuoricino assembly system have diameters ranging from 0.5 mm to 0.8 mm; spot height is fixed at 50 μm by using an appropriate spacer and pressing together sensor/absorber pairs. If neighbouring epoxy dots merge together when pressed, a layer can form. 50 μm, the chosen height, is a limit value: if pressed under this value, the largest spots merge with their neighbours due to an excessive growth in their diameters.

The change in dimensions that glue dots undergo when pressed can be estimated roughly by a simple geometrical model. According to the model, a not-pressed epoxy dot can be approximated by a spherical cap: when the sensor and the crystal are pushed together, the dot is pressed and an amount of epoxy corresponding to a smaller spherical cap is moved to its sides; the pressed dot becomes therefore a spherical segment.

A reasonable estimation for the average height of not-pressed spots is ~100 μm, based on the experience made during the assembly of both Cuoricino and R&D tests; in this case, if a 800 μm large epoxy dot is reduced to a 50 μm height, according to this model the growth of its diameter is ~200 μm. The value acquires meaning once the amount of epoxy dots requested in the coupling is known: a dedicated simulation work was performed in the Cuoricino R&D phase to identify the number of spots leading to the highest pulse amplitude for a given energy deposition in the absorber, and taking into account the size of thermistor footprint, the optimum was found to be nine epoxy dots (132). Therefore, a 200 μm growth in the diameter of larger spots, corresponding to the 50 μm height reduction, is the limit value before neighbouring epoxy dots in a 3×3 matrix merge together and form a layer.

The heat conductance of the average Cuoricino Araldite spots was measured in Milan and the phenomenological relation:

$$2.6 \times 10^{-4}(\mathrm{T[K]})^3\,[\mathrm{W/(K \cdot spot)}], \qquad 6\text{-}1$$

already quoted in Sec. 2.1.6, was found (171). This is coherent with the interpretation of a thermal boundary conductance with phonon heat transmission (192).

The left side of Figure 6-8 shows a typical Cuoricino nine-dots matrix deposited on a 3x3 mm^2 surface thermistor. Once the crystal is deposited on the glue spots, because of the current opacity of surface-treated crystals, the resulting matrix cannot be visually inspected easily and different methods to check its quality, such as mechanical tests, must be used.

6.2.3. Restrains on environmental conditions

The third and last category of preliminary restrains on sensor-to-absorber coupling regards environmental conditions in the gluing site.

The importance of temperature control has already been discussed in Section 6.2.1. A growth in temperature leads to higher fluidity of the epoxy, but at the same time it may reduce dramatically the time window available for gluing because of fast polymerization. As in this case short pot life combines to complex dispensing, the preferable choice is to keep

the temperature a bit lower than room temperature (around 19–20 °C) in order to slow down the process; pushing temperature under this range could lead to alterations in epoxy properties, as already stated in 6.2.1. Of course, the temperature should be kept constant until gluing operations, curing included, are over. As a final remark, another reason for not having excessive temperature variation in both directions is that TeO_2 crystals are sensitive to sudden temperature variations, which can result in cracks due to thermal contractions.

Humidity should also be supervised. Cured resins are quite sensitive to water, considering the highly polar and hydrogen-bonding character of epoxies: in high humidity conditions, water disrupts the inter-chain hydrogen bonding and the net effect of this physical hydrolysis is a lowering of tensile strength. Therefore, an increasing water content in the epoxy with exposure time can compromise the mechanical properties of glue. Usually, water works as a plasticizer leading to a softening of the material (193), (194).

This effect has been witnessed regularly in clean-room assembly tests at humidity levels high as 70%: the epoxy does not reach the required levels of lap shear strength even days after the end of regular cure time; it stays in a rubber-like state.

There is also another evidence of how humidity affects gluing, this time coming from a property of the crystal absorber: black signs emerge in the points where the glue dots and the surface of the TeO_2 crystal are in contact, as shown in right side of Figure 6-8. Two mechanisms lie behind this phenomenon. First of all, the catalysing agent of the epoxy reacts with the oxygen of the TeO_2 material: tellurium is freed and forms a black layer on the crystal's surface. Then, TeO_2 is slightly dissolved by H_2O and this enhances the effect, as in presence of high humidity levels greater amounts of TeO_2 are freed on the surface and can interact with the hardener forming the black layer.

However, humidity in the gluing site is automatically regulated when another restrain is satisfied: the assembly procedure must take place inside a glove-box where nitrogen gas is constantly flushed to avoid radon contamination. The N_2 atmosphere does not compromise epoxy polymerization. The curing of the bi-component glue used is a pure reaction between an epoxy resin and an amine hardener, therefore it does not need any oxygen or moisture like other products. The curing occurs unaltered under a nitrogen atmosphere. Glove-box assembly also helps to minimize the contact of assembled bolometers with possible sources of radioactive contamination. Operators must handle instrumentation and detector elements only inside a protected environment, where materials whose levels of radio-purity have not been guaranteed by previous certification cannot be introduced.

Figure 6-8. A typical Cuoricino nine-dots matrix deposited on a 3x3 mm^2 surface thermistor (left) and an example of the effect of high humidity in the gluing environment: black epoxy spots (right).

6.3. Innovations in the CUORE-0/CUORE gluing line

The semi-automatic gluing system for CUORE-0 and CUORE detectors was developed to obtain a highly reproducible sensor-to-absorber coupling procedure. The work on the new line started in 2007 at Insubria University with the idea of designing a system for CUORE-0 as a prototype for the CUORE final set-up but then the work forces converged in the project of a unique set-up. Most of the innovations introduced by the Como group, studied during this PhD work, especially in the glue handling and in the relative positioning of the thermistor with respect to the crystal, have been used in the final project of the CUORE gluing line, which is presently underground in a dedicated clean-room in Hall A at LNGS and it is quite ready for gluing the 52 bolometers of the CUORE-0 tower.

The final CUORE gluing system has been designed to be reliable and fast despite limitations due to the glue short curing time. Each step of the new procedure has been optimized according to the following lines of action:

- ✓ Sensor positioning –design of a non-intrusive method to fix the 50 μm gap with an error of the order of 1 μm.
- ✓ Epoxy mixing –better dosing of the resin-to-hardener ratio and more homogeneous mixing.
- ✓ Epoxy dispensing –calibration of the single-spot volume to reach uniformity in the nine-dot matrix and definition of the environmental parameters to get a reasonable trade-off between epoxy viscosity and pot life duration.
- ✓ Crystal deposition –design of an error-free placement system with limited contact between the absorber and other materials.

Moreover, the general philosophy of the project is to remove as much as possible the variability introduced by manual work: operator dependant stages are, wherever allowed, automated. Automation of certain steps also gives the advantage of precise timing, which is useful considering the short time window of epoxy use. A final note regards the implications of radio-purity restrains. First of all, detector elements cannot touch materials whose radio-purity has not been proved (PTFE and specific types of steel are allowed). Second, as a general rule, contact is minimized. The final choices for new system are a dedicated glue dispenser plus a set of devices for XYZ precise positioning of the chips, while the movement of the crystal and the chips is managed by an anthropomorphic robotic arm. The following subsections detail the performed optimization work in order to reach this final set-up.

6.3.1. Mixing of the bi-component epoxy

In the initial phase of the project study, two ways were considered for epoxy mixing: a dynamic and a static solution. The first idea consists in using a laboratory mixer supplied with mixing rods suitable to stir average viscosity fluids. This path was abandoned mainly because pouring epoxy from the mixing site to the dispensing container proved to be inconvenient, for this process lead easily to incorporating unwanted air in the mixture, and also because of the possibility of glue contamination with small particles of material originated by some degree of rod erosion; moreover, a solution for two-components dosing had yet to be found.

Figure 6-9. (Left) 50 ml dual cylinder syringe with bleeding-valve pistons to contain resin and hardener. The cartridge is filled in N_2 atmosphere. (Right) tested static mixers. The effectiveness of mixing for a given epoxy depends on the diameter of the tubular housing, as well as on the number and shape of mixing elements. From top to bottom, the inner diameter and the number of elements for each mixer are: 6.3 mm×21, 5.4 mm×21, 3.0 mm×17, 3.0 mm×7, 5.3 mm×24. The top four mixers have an internal helix, while the last one is square shaped.

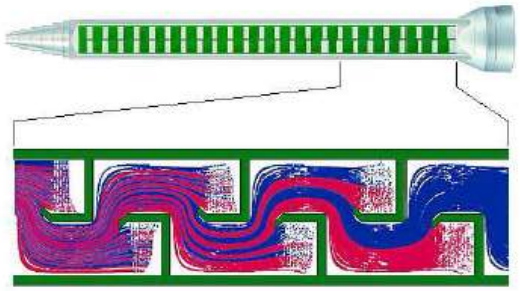

Figure 6-10. Principles of operation of the static mixer selected for the Araldite Rapid epoxy glue. The resin and the hardener are mixed mainly by the mechanisms of division and conversion. The specific geometry allows building the mixer in a very compact and short way.

The winning choice was the so-called static mixing, which is both a very simple and effective method. A dual cylinder syringe in nylon or polypropylene with side-by-side barrels is used (Figure 6-9, left). The barrels, with equal capacities in order to satisfy the 1:1 proportion, are filled separately each with one epoxy component; when the syringe opening is still closed, two bleeding-valve pistons are pushed into the cartridges so that air is drained out. Barrel filling may take place in nitrogen atmosphere. As bleeding valves are sealed, a plunger is inserted and the syringe is ready for use. The mixing is then performed by connecting to the syringe opening a static mixer, which is a tubular housing with an internal system of plastic baffles.

The diameter of the tip and the number of internal mixing elements are selected according to epoxy requirements. Provided that a small initial quantity of processed material is rejected, the resin and the hardener are automatically dosed.

The resulting epoxy is thoroughly mixed through three processes: in the division process, the fluid is split in half every time it passes through an element; in the conversion process, the fluid, which glides along the inner walls of each element, moves from the central area of the housing to the walls and vice versa, being sorted in the meantime; in the inversion process, the fluid changes direction of rotation in each element and is consequently agitated. For fluids whose viscosity is similar to Araldite Rapid, the division and the conversion processes prevail. Another advantage intrinsic to this procedure is simplicity in filling containers for the following step of glue dispensing. Of course, static mixers are disposable due to Araldite Rapid's short pot life. A selection of static mixers with different lengths, diameters, shapes and internal mixing elements has been tested during the project study (Figure 6-9, right). The selected mixer has a 5.3 mm wide tubular housing which contains 24 elements, whose square shape guarantees a more effective mixing comparing to the common internal helix: Figure 6-10 depicts its principles of operation.

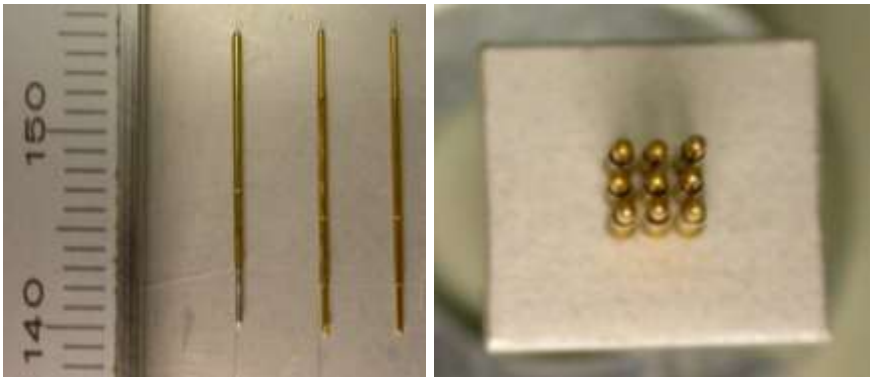

Figure 6-11. Pogo-pins for use in the nine-pins array gluing procedure. Tested types of Pogopins (left) and Pogo-pins mounted in the fixed array (right).

6.3.2. Dispensing of the mixed epoxy

Epoxy dispensing represented an intriguing challenge in the optimization process but eventually outstanding results were reached. The first attempt was based on an evolution of the nine-pins array procedure. Some problems were initially solved by substituting common pins with Pogo-pins. These devices have application in electronics to establish contact between printed circuit boards: single-tip Pogo-pins, the type we used, are small cylinders containing a sharp, spring-loaded tip. Pogo-pins with variously shaped tips and different lengths were tested in the preliminary study, as shown in Figure 6-11.

The advantage of Pogo-pins as opposed to the common ones is the spring-loaded mechanism, which leads to an automatic adjustment of the array pressure on sensor surface; moreover, when force is applied, the outer cylinder of the pin pushes glue off the retracting tip, contributing thus to uniform epoxy deposition. Encouraging results were obtained, although characterized once again by problems in reproducibility among different depositions and in dot-dimension equality inside the same matrix. A series of matrices deposited with the same array of Pogo-pins is shown in Figure 6-12.

A study of spot size was conducted during the testing of Pogo-pins. The average increase in dot diameter following height reduction down to the 50 μm requirement was evaluated (an estimation based on a simple geometrical model has already been proposed in Section 6.2.2). Figure 6-13 reports an example. This study is compatible with previous estimations and leads to the conclusion that the average increase in spot diameter is ~100-150 μm. Ideal spots in 9-dots matrices have an initial diameter of ~0.7 mm, which turns to approximately 0.8 mm after height reduction. A superior limit for the diameter of not-pressed spots should be fixed at 0.85 mm, because the probability of merging for neighbouring dots in the same matrix becomes relevant.

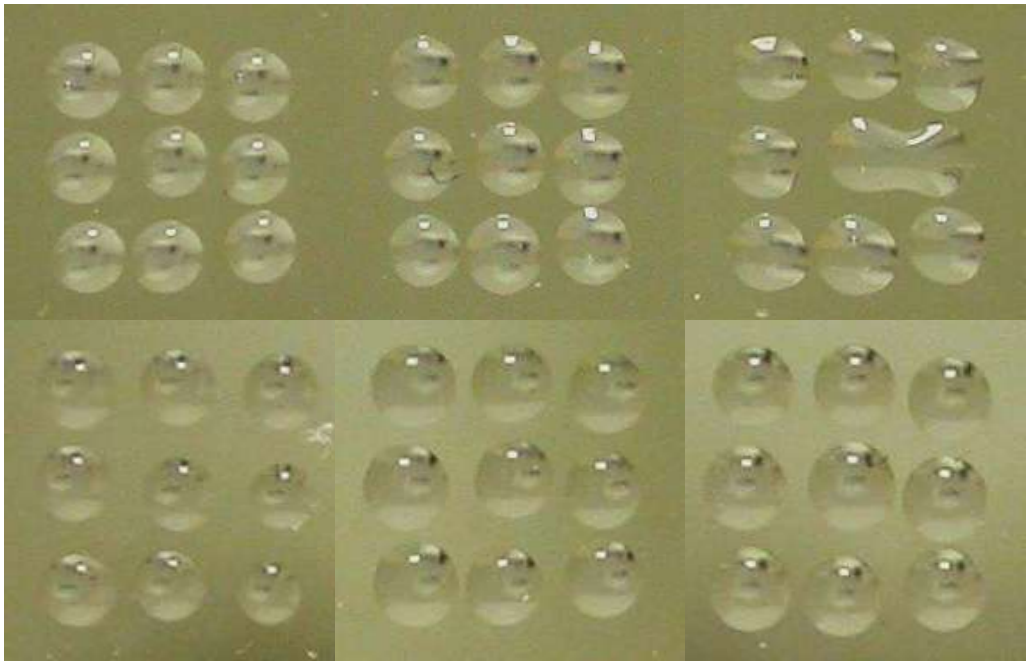

Figure 6-12. Nine-dots matrices made with the same array of Pogo-pins. Pogo-pins were cleaned with ethanol between depositions, and a new amount of freshly mixed glue was used for each matrix. Slight variations in both position and dimension of dots can be seen from one matrix to the other. The tests were performed in the same conditions, at ~21 °C and few seconds after epoxy mixing.

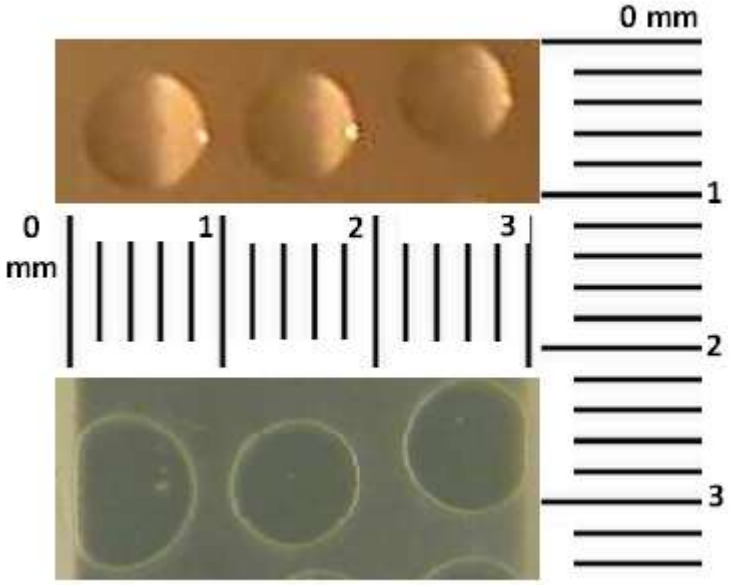

Figure 6-13. Example of diameter enlargement in a row of a nine-dots matrix due to height reduction at 50 µm. The same row of spots was photographed before and after thermistor application on the transparent side of a TeO_2 crystal.

Because the desired level of uniformity and reproducibility was not reached (as testified by the variation of spot size and position in Figure 6-12), Pogo-pin arrays started to be regarded as a backup solution and another dispensing strategy became appealing.

The chosen path is epoxy single-dot micro-dispensing. The term micro-dispensing refers to the technique of producing liquid media dosages in volumes smaller than 1 μl. The common industrial application of this system is to deposit adhesives in small quantities as well as in extremely precise and repeatable patterns: as this is the same challenge of the CUORE gluing line project, the introduction of micro-dispensing seemed a viable option. The idea is to deposit matrices dot by dot and in principle this approach allows spot size definition by controlling the amount of glue released singularly.

A micro-dispensing system is constituted by two main elements: an automatic dispenser with an electronic controller to perform glue distribution and a controlled system for syringe displacement. The dispenser has a syringe as barrel reservoir and is programmed to control the parameters for glue expulsion, which are very different according to the dispensing technique (mainly, pneumatic or air-free). The syringe is moved in this case with a cartesian coordinate robot, an industrial machine whose three axes of control are linear and at right angles to each other: the syringe translates across an XY plane following the pattern of the nine-dots matrix and is moved vertically along the Z-axis for glue deposition.

However, the effectiveness of micro-dispensing depends largely on epoxy properties, and works well if the parameters controlled by the automatic dispenser can be kept constant throughout the deposition process. This is generally easier with long pot lives, when epoxy viscosity does not show appreciable variations for a reasonable time. As the viscosity of Araldite Rapid increases drastically in about three minutes, micro-dispensing can be applied provided that a set of conditions is satisfied: the whole dispensing must be performed in a time window shorter than pot life; a limited number of matrices can therefore be deposited; any non-replaceable part of the dispenser should be kept out of contact with glue to avoid rapid sticking. A remark on the first point is that pot life is slightly reduced by epoxy containment inside a syringe. In fact, a concentrated mass will cure faster than epoxy spread out over a large flat area because heat cannot be dispersed easily.

Overall, the dispensing process can be divided in four phases:

1) Zero-point location. The zero-point Z_0 is the Z-position of contact between the syringe needle and the upper surface of the sensor. Disposable plastic syringes are characterized by high tolerances on their dimensions which are incompatible with the total ±10 μm required by this positioning, so that zero-point search must take place anew for every gluing. The operation is scheduled before epoxy

mixing in order to save on the available time; however, it may be necessary to remove the syringe from the cartesian robot, fill it and fix it back: in this case, zero-point is lost unless mechanical connection to the robot is provided by a specific joint that allows repeatability. In our tests, the zero-point is found by verifying electric contact between the steel needle of the syringe and a thin strip of aluminium fixed on the test slab. The actual height Z_d of single-spot deposition is $Z_0+\Delta Z$, where ΔZ varies according to the dispensing technique.

2) Syringe filling. As mentioned in the previous item, syringe removal from the robot is usually necessary before filling. This is what happened during tests at the Cryogenics Laboratory in Como, although a system for syringe filling avoiding removal is being considered for the ultimate gluing line. The syringe is generally filled at less than one half of its volume to avoid that large epoxy mass concentration accelerates curing time. While filling, epoxy should not be dropped directly into the needle in order to avoid clogging.
3) Purge. It is the process of pushing epoxy through the needle right after syringe filling: as explained later, it is complicated by the viscosity of Araldite Rapid.
4) Single-dot deposition. According to the dispensing technique, glue can be pushed out of the syringe with continuity or in singularities. This process is described by a set of parameters whose interplay leads to the required spot size.

Dispensing tests with automatic dispensers at the Cryogenics Laboratory in Como were performed using the table-top cartesian robot WR300, shown in Figure 6-14, by the Italian company AEB Robotics. Its main specifics are reported in Table 6-2. The XYZ robot selected for the final system instead is different, for the reason discussed in Section 6.4.1.

As for the automatic dispenser, two systems were selected for testing: an air-free model produced by Fishman Corporation and a pneumatic pressure-driven one by Loctite, part of Henkel International. Other technologies, such as Archimedes valves, which incorporate an auger, and positive displacement piston pumps, are commercially available: they are however unsuitable for Araldite Rapid use because of cleaning issues. Figure 6-15 presents the difference in syringe configuration between the two techniques.

Pneumatic dispensers are simple in design: they consist primarily of a piston sliding within the syringe under air pressure, which can be continuous or pulsating. The volume dispensed depends on the viscosity of the material, air pressure and amount of time the pressure is applied, and epoxy flow is controlled by the size of the dispense tip. So easiness of use is balanced by the impossibility of having full initial control on the volume dispensed.

WR300 by AEB Robotics	
Movement	520 mm along X,Y, 150 mm along Z
Repeatability	±20 μm
Minimum resolution	6 μm
Maximum load	10 kg on working surface, 5 kg on the moving arm
Axis speed	1-600 mm/s along X,Y and Z

Table 6-2. Technical characteristics of the table-top cartesian robot used in the Como dispensing tests.

Figure 6-14. The table-top cartesian robot WR300 used in Como dispensing tests.

On the other hand, the air-free model works with a linear actuator-driven mechanical lead screw. The head of the screw is inserted in a disposable piston and moves it out on command from a microprocessor control unit. With this kind of dispensing, control is achieved with the linear drive system and is not given by the size of the needle. The shot is delivered volumetrically: after system calibration at the beginning of the process, the control unit, instructed on barrel capacity, automatically calculates the distance the plunger must travel forward and backward for the correct shot size. In addition to that, drawback of the plunger may be programmed to prevent material drip. More control on the single dot is achieved in principle, at price of more complications which will be discussed later on.

The aim of dispenser testing in Como was to select the model for the ultimate gluing line at LNGS. Matrix quality being comparable, fastness of the dispensing procedure was used as a choice standard. Higher easiness of processing was also preferred, as the selected dispenser is meant for use inside a glove-box. Tests have not been performed in a tightly controlled environment due to their selective purpose, even if they were done in clean-room: the final tuning of parameters will take place in the CUORE clean room at LNGS. The behaviour of tested instruments in the four phases of glue dispensing is presented in the following Sections.

6.3.2.1. The air-free dispenser

The air-free dispenser is the Fishman Corp. model LDS9000-SDAV (Figure 6-16). This instrument achieves dot volumes as small as 2.5×10^{-4} cc at 3σ for the 3 cc syringe used in the tests. The principles of this kind of air-free dispensing have already been described in the previous paragraph. The dispenser has two operative modes: a manual mode, which gives the operator real-time control on the duration of screw extension and retraction, and an automatic mode, whose parameters are fixed to gain the desired dot size. A mechanical joint connects the syringe to the robot, so that the reservoir may be filled and reinstalled keeping Z_d within a 10 μm error. Approximately 1 cc of glue is used for each test.

The most delicate phase is purge. Epoxy is pushed through the needle by screw extension until a drop forms. If the process is too quick, however, the high viscosity fools the system into believing that syringe bottom has been reached, and extension is blocked by an automatic control: gluing is aborted and a new syringe must be used. This forces to proceed with small, subsequent screw extensions that consume about 1 min of the available time. Some drawback follows successful purge to lower internal pressure and prevent dripping.

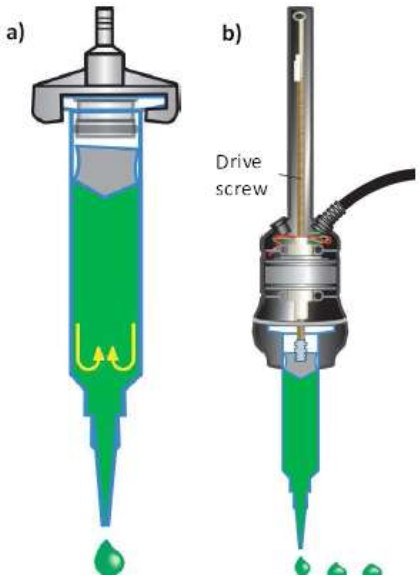

Figure 6-15. (Left) Syringe configuration in the pneumatic dispensing system: the barrel is connected to a pressure supply (N_2 in this case) controlled by the dispenser. (Right) Syringe configuration in the air-free model: the inner piston is mounted on the head of the drive screw, whose extension and retraction is controlled by the dispenser according to the desired drop volume.

All the previous operations are performed by manual control of the dispenser, then the system is ready for single-spot deposition and the dispenser is switched to automatic mode.

The cartesian robot takes the syringe at the coordinates (X_1, Y_1, Z_d) of the first point and stays in position while single-spot dispensing is completed. A set of parameters, regarding both the robot and the dispenser, proved to be particularly relevant for this type of air-free dispensing. They are:

- ✓ ΔZ: tests with ΔZ ranging from 30 μm to 300 μm were performed: examples of matrices are the B/B' cases shown in Figure 6-17. The optimum Z_d is found 200 μm higher than zero-point.
- ✓ Shot size: the volume of each shot is fixed according to the diameter requested for the deposited dot. Approximating the shape of the epoxy drop released to half of a sphere, a 700 μm diameter corresponds to a volume of the order of 10^{-4} cc. Shot size is fixed at the smallest value achieved by the dispenser: 2.3×10^{-4} cc. This does not mean that larger spots are deposited, as both needle size and viscosity contribute in shaping the glue dot.
- ✓ Dispensing rate: when the speed of screw extension is too high, the needle clogs due to Araldite Rapid viscosity. In order to save on working time, the dispensing rate is fixed at the limit value before clogging manifests: 0.135 cc/s.

Figure 6-16. The air-free Fishman LDS9000-SDAV epoxy dispenser with its dispensing gun.

- ✓ Drawback: screw retraction, known as drawback, is relevant right after purge as well as following each single-spot deposition. In the first case, drawback is used manually to control the heavy flow of epoxy caused by purge (Figure 6-17, case A, shows what happens when not enough drawback is applied). In the second case, automatic drawback helps preventing the formation of glue filaments that compromise matrix quality. The value of automatic drawback following each single-spot deposition is fixed at its maximum: 500 steps.
- ✓ Single-point working time: this parameter is determined by the amount of time necessary for screw extension and drawback in single-spot deposition. With dispensing rate equal to 0.135 cc/s and drawback fixed at 500 steps, the necessary time window is 3 s.
- ✓ Point-to-point rise: after single-spot deposition is complete, the syringe moves to the following point in the matrix. Movement along the X and Y axes should be preceded by a vertical rise. Due to Araldite Rapid viscosity, in the detachment of the needle from the deposited dot a glue filament forms and smears on the surface if an immediate X or Y translation follows: this may result in adjacent epoxy dots merging together. An increase in point-to-point rise helps breaking the filament with no surface remnants. This parameter has small influence on air-free dispensing, as depositions are volumetrically quantified and drawback helps relieving internal pressure. Figure 6-17 reports examples of matrices (C and C') with a different point-to-point rise. The ultimate value chosen is 15 mm.

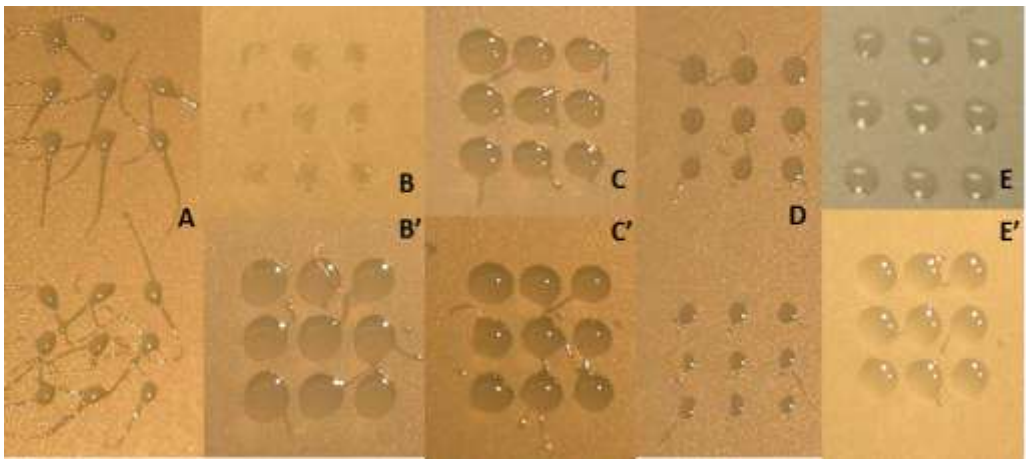

Figure 6-17. Selection of nine-dots matrices realized with the air-free dispensing technique. Pair of matrices indicated by the same capital letter illustrate each the effect of a peculiar dispensing condition or the variation due to the tuning of one parameter. Filaments and small size in the A matrices are due to insufficient after-purge drawback; matrix B was dispensed with ΔZ=30 μm, B' with ΔZ=200 μm; matrices C and C' are characterized by point-to-point rise equal respectively to 12 mm and 15 mm; the D matrices were dispensed in row at advanced pot life (2 min after mixing) and show reduction in spot size due to viscosity increasing steeply; matrices E and E' were dispensed by needles with different inner diameter: 0.20 mm and 0.25 mm. For all cases, the unmentioned parameters are equal to the ordinary values listed in the text.

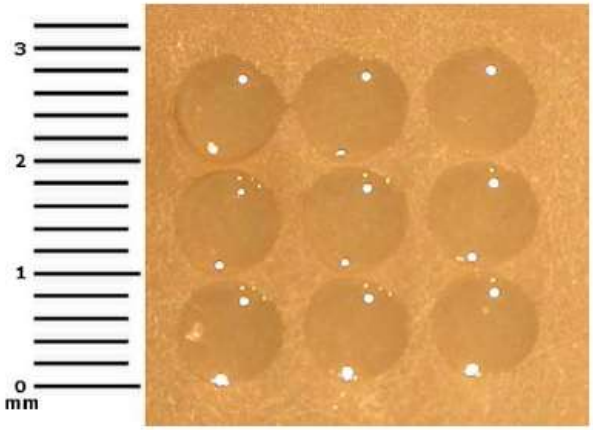

Figure 6-18. Nine-dots matrix dispensed by air-free technique with the set of parameters defined as optimal: ΔZ=200 μm, shot size=2.3×10^{-4} cc, dispensing rate=0.135 cc/s, drawback=500 steps, single-point working time=3 s, point-to-point rise=15 mm.

In addition to the previous list, two stainless steel needles with 12.7 mm long tips and different inner diameters (0.20 mm and 0.25 mm) were tried: the E/E' pair in Figure 6-17 shows the difference in matrices dispensed by the two kinds. Requested spot diameter is given by the second type, the 0.25 mm needle, which is adopted also for use with the pneumatic dispenser.

When air-free dispensing is performed as described, a "calibration" dot and two subsequent nine-dots matrices are done with a single syringe filling. Epoxy dots satisfy size requirements. A reproducible example of matrix dispensed with the optimal set of parameters previously listed is reported in Figure 6-18.

6.3.2.2. The pneumatic glue dispenser

The pneumatic dispenser is the Loctite 98666 model, pictured in Figure 6-19. As already pointed out, the technique does not give the operator full power on the volume dispensed. However, this feature can be counterbalanced, and control on epoxy flow is obtained by tuning the parameters of the cartesian robot. Compared to air-free dispensing, the procedure is remarkably simpler.

Figure 6-19. The pneumatic Loctite 98666 epoxy dispenser.

After zero-point determination, the syringe, now with 10 cc capacity, is removed and filled; approximately 2 cc of epoxy are used (one fifth of the overall volume); then a disposable piston should be inserted in the syringe, to ensure a uniform distribution of the pressure: because the small amount of glue in the syringe, this step can be omitted. Finally the pneumatic tube commanded by the dispenser is attached: N_2 gas is used instead of air due to environmental requirements described in Section 6.2.3

Repositioning that keeps the syringe at Z_d within a 10 μm error is guaranteed by a mechanical joint different from the one used in the Fishman case. Purge is a straightforward operation because the pneumatic dispenser has not pressure controls that stop epoxy expulsion. Pressure is opened at the beginning of the dispensing process and then supplied continuously while matrices are composed.

The following parameters proved to be relevant in pneumatic dispensing.

- ✓ ΔZ: the optimal Z_d is 100 μm higher than the zero-point. A selection of tests done with changing ΔZ is presented in Figure 6-20, cases A and A'.
- ✓ Dispensing pressure: the maximum pressure reachable in the experimental setup at Como Laboratory is 2.8 bar. Working with higher pressures is advisable because of the resistance opposed by epoxy viscosity (Figure 6-20, B and B').
- ✓ Single-point working time: as opposed to air-free dispensing, this time window is not fixed by other parameters but plays a relevant role. This happens because pressure is supplied continuously and not on a point-by-point basis. Other parameters being equal, higher single-point working times result in larger epoxy dots. After tests ranging from 0 to 4 s (see C and C' in Figure 6-20), the 1 s time interval was selected.
- ✓ Point-to-point rise: this parameter, which has limited influence in air-free dispensing, is relevant in pneumatic dispensing because no drawback is applied. Lifting the syringe vertically in the X-Y transfer from one point of the matrix to the following limits the formation of epoxy filaments. Point-to-point rise is fixed at the maximum value obtainable by the cartesian robot: 150 mm.
- ✓ Z-axis speed: if a glue filament forms when the needle is lifted from the deposited spot, slow movements of the robot keeps it from smearing on the matrix. The value v_z=600 mm/s is adopted. An example is the D/D' pair in Figure 6-20.

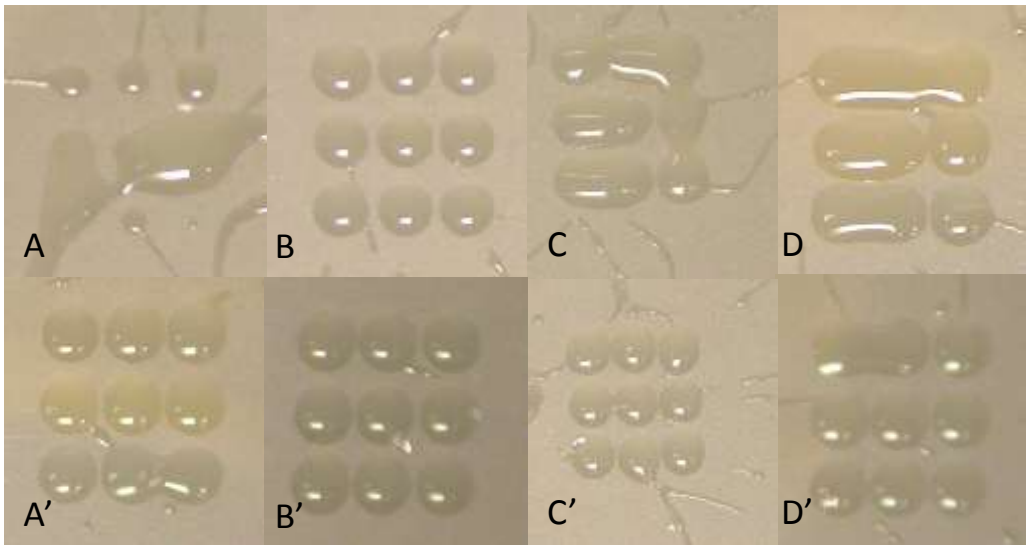

Figure 6-20. Selection of nine-dot matrices realized with the pneumatic dispensing technique. Pairs of matrices indicated by the same roman number were obtained with an equal set of parameters apart from one: ΔZ for pair A, dispensing pressure for pair B (lower P corresponds to smaller spots, while filament production remains unaltered), single-point working time for pair C and Z-axis speed for pair D. The complete set of parameters for each pair is reported in Table 6-3.

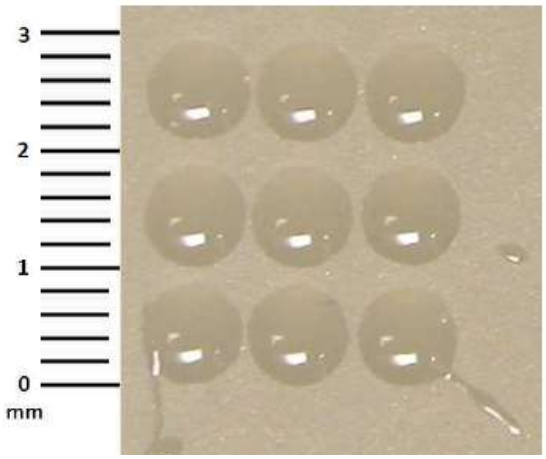

Figure 6-21. Nine-dots matrix dispensed by pneumatic technique with the set of parameters defined as optimal: ΔZ=100 μm, dispensing pressure=2.8 bar, single-point working time=1 s, point-to-point rise=150 mm, Z-axis speed=600 mm/s. Final parameter tuning will take place in the ultimate gluing site at LNGS to get rid of the epoxy filaments visible in the picture.

Matrix number	ΔZ [μm]	Dispensing pressure [bar]	Single point working time [s]	Z-axis speed [mm/s]
A	500	2.8	1	600
A'	100	2.8	1	600
B	100	2.0	1.2	600
B'	100	2.8	1.2	600
C	200	2.8	3	600
C'	200	2.8	2	600
D	100	2.8	1	600
D'	100	2.8	1	200

Table 6-3. List of dispensing parameters for the selection of epoxy matrices in Figure 6-20. Only matrices belonging to the same pair should be compared. For all matrices, epoxy dispensing is performed with the inner diameter of 0.25 mm needle and 150 mm point-to-point rise.

One should note that, as opposed to air-free dispensing, the previous parameters are strongly interconnected. For instance, higher single-point working time leads to larger spots but can be counterbalanced by lowering dispensing pressure; or again, high point-to-point rise helps limiting the problem of glue filaments unless v_z is too high. A total of one "calibration" spot and two nine-dots matrices whose size satisfies requirements are deposited with one syringe filling. A reproducible example of matrix dispensed with the optimal set of parameters previously listed is reported in Figure 6-21.

6.3.3. Comparison between dispensing techniques

Air-free and pneumatic dispensing gave satisfying results in terms of spot dimension. The behaviour of both dispensers is understood and the fine tuning of parameters will be performed in the ultimate gluing site, at LNGS.

The two techniques have fundamental differences. Air-free allows volumetric dosage of each spot at price of handling complications originated by Araldite Rapid being a short pot life, high viscosity epoxy; in particular, the most difficult operations are the syringe filling and the purge, the latter for the reasons described in Section 6.3.2.1, the former because inserting the cap that prevents the screw to touch the glue (see Figure 6-15) risks to create an unwanted amount of air between the glue and the cap. Both procedures require time and precise actions of the operator, slowing down the entire process.

	Air-free dispenser	Pneumatic dispenser
Model	Fishman LDS9000-SDAV	Loctite 98666
T range	20-21 °C	
Syringe capacity	3 cc	10 cc
Volume of epoxy used	~1 cc	~2 cc
Needle inner diameter	0.25 mm	
Needle length	12.7 mm	
Dispensing mode	Point-to-point	Continuous
ΔZ	200 μm	100 μm
Shot size	2.3×10^{-4} cc	-
Dispensing rate	0.135 cc/s	-
Drawback	500 steps	-
Dispensing pressure	-	2.8 bar
Single point working time	3 s	1 s
Point-to-point rise	15 mm	150 mm
Z-axis speed	600 mm/s	
Average purging time	60 s	30 s
Average deposition time (one spot+two nine-dots matrices)	57 s	19 s

Table 6-4. Comparison between dispensing techniques: best parameters for epoxy deposition as deduced by Como tests. The temperature range reported accounts for the testing environment in Como not being tightly controlled. Items eight to ten are parameters of the cartesian robot.

The pneumatic dispenser showed to be able to work properly without the piston, i.e. with the N_2 flux pressing directly on the glue, making the syringe filling extremely easy. On the other hand, the control on spot size is not so precise and it is allowed only by joining up the parameter of the dispenser with those of the cartesian robot.

Table 6-4 reports a quantitative overview on dispensing parameters for both techniques. The pneumatic technique has simpler application and requires shorter time windows. Results being comparable, the choice of the Como group is oriented on the Loctite 98666 model, provided that the fine-tuning of the parameters in the final set-up allows avoiding the glue filaments across the dots in the singe matrix.

6.3.4. Sensor positioning

As anticipated in Section 6.3, the optimization of sensor positioning consists in designing a non-intrusive method to fix within an error lower than 5 μm error the 50 μm-gap between sensor and crystal. The project was guided by the following principles:

1) use of a single tool to position sensors, support them during epoxy dispensing and host the glued crystal until expiration of curing time (see Section 6.2.1);
2) no dependency of the gluing process on sensor thickness. The precision on the height of 34B/C NTDs for CUORE-0 is 0.89±0.075 mm and for the 39C CUORE

thermistors it is 0.9±0.050 mm, while the variation in height of heaters at 3σ is 0.525±0.010 mm for chips from the same wafer and ±0.015 mm for chips from different wafers (see Section 3.3.1.1 and Section 3.3.2.1);

3) for each crystal, one-shot gluing of both the thermistor and the heater. The sensor must be glued on the same crystal side due to assembly requirements on the bonding of signal read-out wires, although positioning standards on the XY plane had yet to be fixed by the CUORE Assembly at the time of prototype design;
4) no pressure on the sensors during positioning to avoid breakage (Section 5.2.1);
5) concerning radio-purity, use of safe materials to build the outer shell of the tool (stainless steel 303/304, PTFE), no oils that could undergo de-gasification or particulate production, and possibility of easy cleaning. The use of aluminium is accepted provided that no contact with detector elements takes place;
6) limited contact of the crystal with any mechanical parts, and in any case only with the stainless steel and PTFE elements.

The idea for the tool, called Z-positioner or, shortly, Z-pos, was developed in Como and a prototype was accordingly designed and built. In the prototype, the 50 μm-gap is obtained by putting in mechanical contact a zero reference plane with a mobile plane, which has an integrated spacer 50 μm lower than the zero surface (Figure 6-22-c). Two chip holders are mounted on the heads of inner vertical ratchet-stop micrometers that move along the Z-axis. The operator regulates manually and independently the position of each micrometer (Figure 6-22-a). The sensors are placed in the insets on the chip holders, where they are firmly held by vacuum, and lowered under the zero-plane level (Figure 6-22-b).

The mobile plane is moved on the zero plane and fixed by two screws. The chip holders are raised and thanks to the ratchet stop mechanism, the extension of the micrometers is blocked when the upper surface of each sensor touches the spacer: the 50 μm-gap is therefore fixed without causing any damage to the sensors, due to the limited force applied (Figure 6-22-d); the error on positioning depends on micrometer tolerance as well as on the quality of both the zero plane and the mobile plane, which must undergo precision grinding. The mobile plane is unscrewed and removed after the gap is set, leaving the upper surface of the sensors free for glue deposition. At the end of dispensing, the crystal is laid upon a PTFE frame, which is lowered until the TeO_2 lower surface rests on the epoxy dots and on a set of steel pedestals 50 μm higher than the zero surface, making the crystal plane: the position of the pedestals compensates the possibility of a slight curvature of crystal surface, mainly because of lapping.

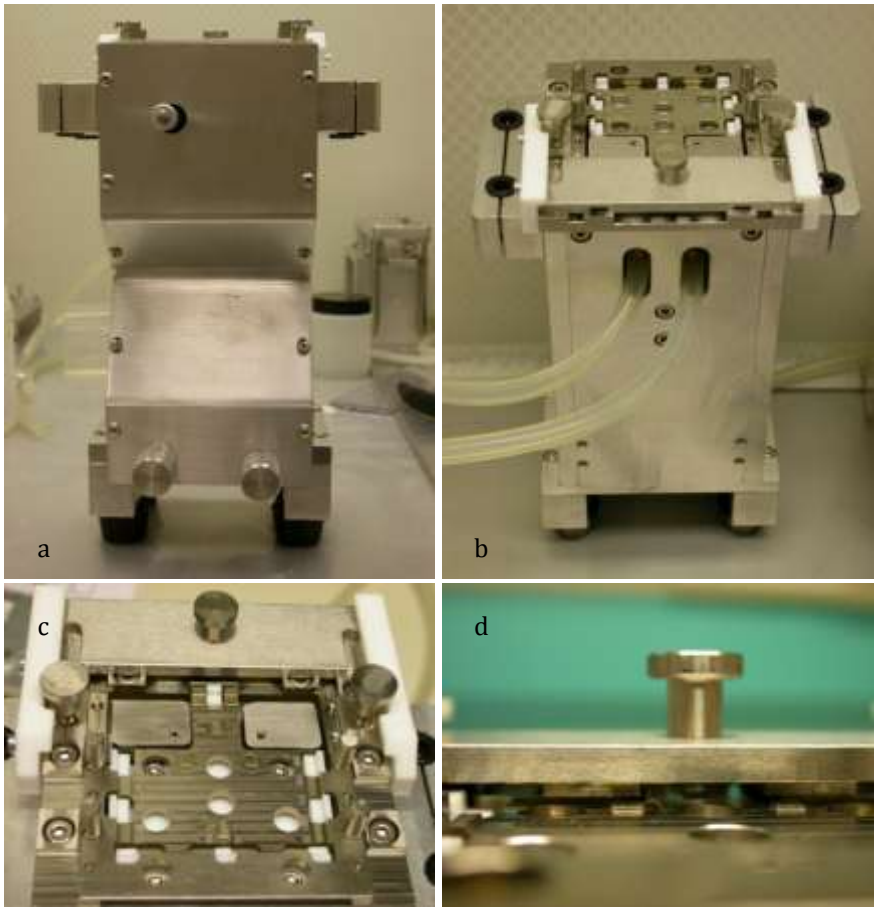

Figure 6-22. The Como prototype of Z-positioner. (a) Front view: the two handles for vertical adjustment of the chip holders and the handle for displacement of the crystal PTFE frame are visible. (b) Rear view: the vacuum tubes reach the chip holders and are connected to a small pump. (c) View of the zero plane, the chip holders, the PTFE frame and the mobile plane on the back. (d) Zoom on the mobile plane in its rest site, prior to positioning on the chip holders: the 50 μm spacers are visible.

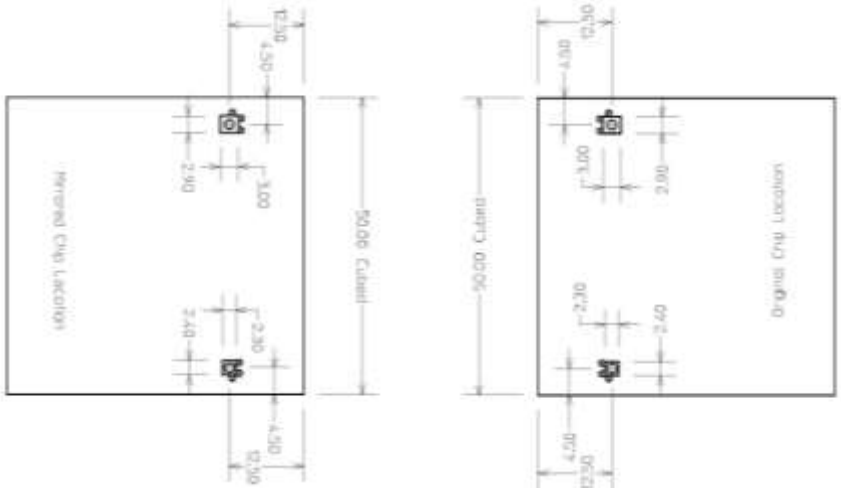

Figure 6-23. Position of thermistor and heater on the crystal surface in the standard defined by the CUORE Assembly Working group. Notice that, for reason connected to the carrying of the electrical connection outside the cryostat, two mirrored positioning are necessary: this requires two Z-pos for the final system.

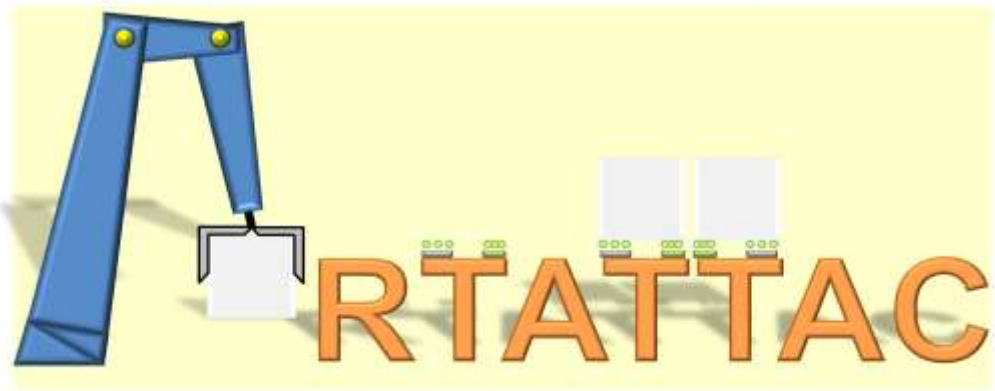

Figure 6-24. The logo of the new CUORE gluing line. The acronym stays for "A Robotic Tool for A Thermistor-To-Absorber Coupling".

The assembled detector is left on the Z-positioner until curing time is over. The prototype, shown in Figure 6-22, was built in 2008 and underwent several positioning tests. The idea behind the functioning of the prototype Z-positioner proved to be successful and remained basically unaltered. Some features, however, were revised to improve global tolerance and repeatability, as well as to meet the new requirements on sensor position on crystal surface (see Figure 6-23) and those originated by the parallel development of the other stages of the gluing procedure (e.g. integration with automated elements, see Section 6.4.3). The development of the ultimate model of Z-positioner was entrusted to LLNL.

6.4. The final CUORE-0/CUORE gluing line

The work performed for the optimisation of the glue handling and chip positioning is just the initial step toward the definitive sensor-to-absorber coupling line for the CUORE experiment (whose logo is depicted in Figure 6-24).

The fine tuning of the dispensing technique, as well as the design of the final Z-pos requires thinking these tools not as stand-alone objects but as devices integrated in a more complex set-up. Moreover, almost all the steps in the tests described in the previous sections are strictly operator-dependent (syringe filling, start of the glue dispensing, chip positioning…), while the goal for the new gluing is to have an automatic line.

In fact, as already stated in Section 6.3, the introduction of automated steps comes from the necessity of a definite timing for the gluing procedure as well as of reducing the lack of reproducibility intrinsic to human intervention. Nonetheless, the realization of a totally automatic system is out of purpose in this case: there are operations in the procedure whose

results are not improved in precision and may be, in specific cases, even complicated by automation. A semi-automatic approach, with automated and manual stages cohabiting, allows for a more straightforward approach. The new elements introduced in the CUORE gluing line, their integration and the fine-tuning of the working parameters are the subject of the next sections.

6.4.1. Introduction of automated elements

As mentioned in Section 6.3.2, syringe displacement and epoxy dispensing are both automated: while the three-axis cartesian robot is programmed to move the glue barrel along a fixed sequence of coordinates depending on the ultimate layout of the gluing line, the epoxy dispenser performs dot deposition according to a memorized set of predetermined parameters. The cartesian robot used during Como tests will not be incorporated in the ultimate gluing line at LNGS because its dimensions and portal configuration imply restrictions on the layout; a three-axes system by Jenny Science AG, commonly called simply Jenny (Figure 6-25, left), allowing a versatile assembly of the independent linear axes and easier integration with the other components of the layout, will be used. Compared to the robot used in Como tests, the final cartesian system has also higher technical standards, as shown in Table 6-5. A vision system constituted by a camcorder and an image acquisition software will provide check on the quality of epoxy dots (Figure 6-25, right).

Besides the dispensing, all the other operations involving the glue are automatic performed too. A pneumatic gun is used for extruding the mixed glue from the bi-cartridge equipped a static mixer (see Section 6.3.1) and filling the syringe; the adopted model is the Loctite 97042 pneumatic gun: it has a manual trigger which is bypassed by integrating a flow valve for automatic gas supply (N_2) (Figure 6-26).

Another automation element is introduced in the placement of sensors and crystals. The gluing line will incorporate the six-axes anthropomorphic robot IRB 140 produced by ABB Robotics, which has maximum payload 5 kg, 810 mm reach and ±30 μm position repeatability (Figure 6-27, top). It has been equipped with two tools: a clamp mounted on the robot's arm, covered with the same gloves used in the glove box, for grabbing and moving the crystals (Figure 6-27, bottom-left) and a PTFE suction cap for picking up the sensors by vacuum (Figure 6-27, bottom-right). The robotic arm eliminates the operator contact with cleaned detector elements and allows reaching positioning repeatability and precision which would manually be unobtainable.

	Jenny Science AG
Movement	520 mm along X,Y, 150 mm along Z
Repeatability	±2 μm
Minimum resolution	1 μm
Maximum load	10 kg on working surface, 5 kg on the moving arm
Axis speed	1-2500 mm/s along X,Y and Z

Table 6-5. Technical characteristics of the table-top cartesian robot used in the final gluing line.

Figure 6-25. The three-axes system by Jenny Science AG (left) and the camera for the glue dots inspection placed on it (right).

Figure 6-26. The Loctite 97042 pneumatic gun with a bi-cartridge and its static mixer.

Figure 6-27. The ABB anthropomorphic robot (top) and the tools it has been equipped with (bottom): the clamp for handling the crystals (left) and the vacuum cap for picking up NTDs and heaters (right).

6.4.2. Optimisation of the glue handling

As described in Section 6.3.3, the chosen dispensing technique is the pneumatic one, because of the easiness in the syringe filling, but provided that the glue filaments appearing around the dots, that can cause glue dots merging as well as dirty the Z-pos, are eliminated.

These filaments are due to the fact that the N_2 flux is continuously injected in the syringe, so there is no neat separation between one spot and the following for the dispenser; therefore the glue filaments can be avoided only thanks to a precise tuning of the cartesian robot movements. To understand how this is possible, it is necessary to focus on the syringe displacements required for performing a single dot.

Let's suppose that the needle is above the chip, with the right glue amount on its tip (Figure 6-28:1). Then the tip moves towards the chip surface, resting at a ΔZ distance above it: the glue touches the chip and the spot start forming (Figure 6-28:2). Then the tip rise: during this movement, the filament creates (Figure 6-28:3); after that the needle moves to the next spot position, the filaments following the tip direction. If the rise and the displacement in x/y direction are fast enough, the breaking of the filament will happen when the needle is middle way between two spots, spreading away on the chip surface (Figure 6-28:4a). Therefore the way for avoiding the filaments is reducing the speed along the z-axis of the robot: in this way, the glue filament is broken while the needle is moving in the vertical direction and the corresponding amount of glue will fall directly in the glue spot that originates the filament itself (Figure 6-28:4b).

The "right amount of glue" is created on the needle tip by waiting for the proper single point working time (see Section 6.3.2.2); an equivalent way, that gives a further help in breaking the glue filaments, is to continue the syringe rise with a proper speed.

Taking into account all these points, the single glue dot creation can be summarised in the following step:

1) the needle moves to a ΔZ level above the sensor surface;
2) the needle rises for a distance Z' with slow speed v_z' for breaking the filament;
3) the needle rises for a distance Z'' with high speed v_z'' for creating the glue amount for the next spot;
4) the needle moves (x or y direction) to the position for the next stop.

It is evident from this sequence that somewhere there must be a starting dot, but it is should be different from the first spot on the sensor: it consist in the "calibration" spot, already described in Section 6.3.2.2, that follows the needle purging operation. In fact the

purge (needed for let the glue entering the needle) creates an unknown amount of glue on the tips that must be removed and the best way to do that is to perform a certain number of spots before moving to the chip, so that the dispensing procedure can reach a stable regime in terms of glue drops.

These spots, named purge spots, are made on a dedicated platform in the gluing set-up (the purge platform, Figure 6-29, left) hosting a cleanable surface that can be removed after each gluing. Of course the distance between the last spot on the purge platform and the first spot on the sensor is bigger than the distance between two near glue dots on the sensor: to avoid the first spot on the sensor to be bigger than the others, the speed on x and y axes of Jenny Cartesian robot are increased so that the time elapsed from purge to sensor is the same as from spot to spot. This is possible thanks to the high axis maximum speed allowed by this particular three-axis robot. The same speeding-up is applied while the syringe moves from the last dot on the thermistor to the first on the heater, being established that the two chips on the same crystal can be done with the same syringe filling.

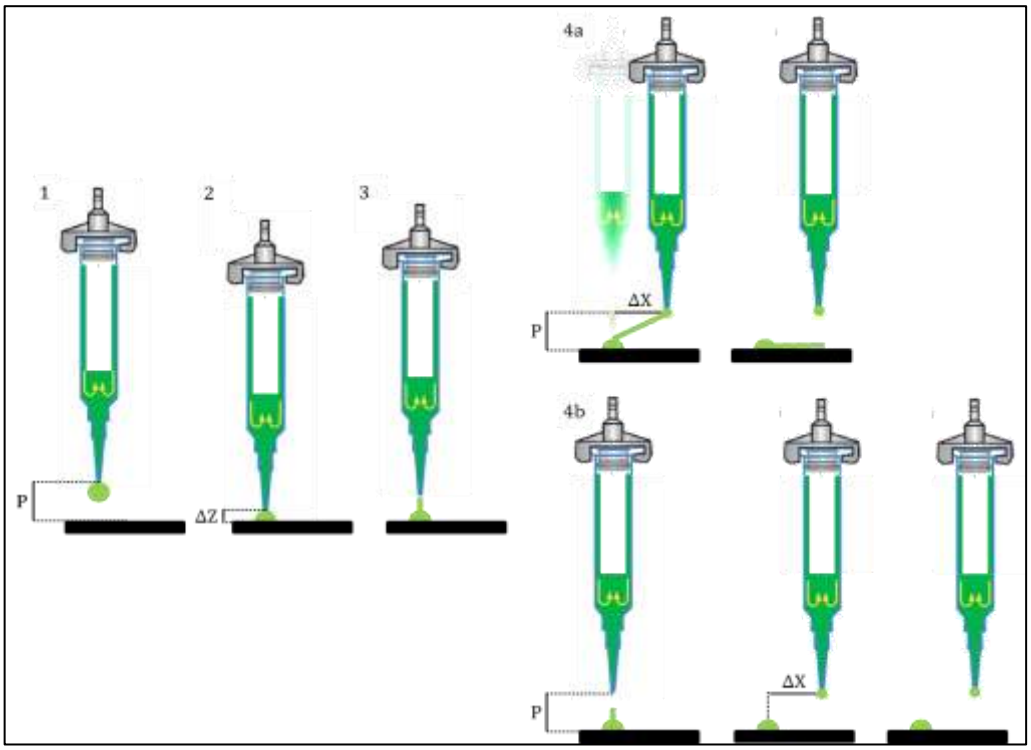

Figure 6-28. Single spot and filament formation with the pneumatic dispensing. 1) The needle is at the point-to-point height (P) with the right amount of glue. 2) The needle move down until it reaches the ΔZ distance from the chip surface: the glue touches the chip and the spot forms. 3) The needle starts rising and the filament creates. 4) Two cases follow: the speed on the vertical axis is fast (a) or slow (b). In the first way the filament is broken while the needle moves towards the next spot and falls onto the chip; in the second one, the slow vertical movement allows the filament breaking and falling onto the spot before the needle moves towards the next spot position.

The start and the end of the N_2 supply is totally controlled by Jenny robot: this means that also the syringe filling and purge operations are automatized. A devoted holder has been designed for the dispensing gun (Figure 6-29, right), in order that, following a specific path, Jenny robot can insert the syringe into the static mixer already applied to the bi-cartridge and then the gun dispenses glue for a fixed amount of time. Then the syringe is moved by Jenny on the purge station and the purging procedure begins: N_2 is flushed in the syringe for a certain number of time intervals, for having the glue exiting the tip. After the right time is elapsed, the gluing sequence can start with the purge spots.

In this way the number of items to be accomplished by a human operator reduces dramatically. These operations consist in placing the syringe in its holder on Jenny robot, inserting the new static mixers on the bi-cartridge (after replacing the cartridge itself if empty), connecting the pneumatic tube to the syringe and checking the quality of the glue dots before the crystal deposition.

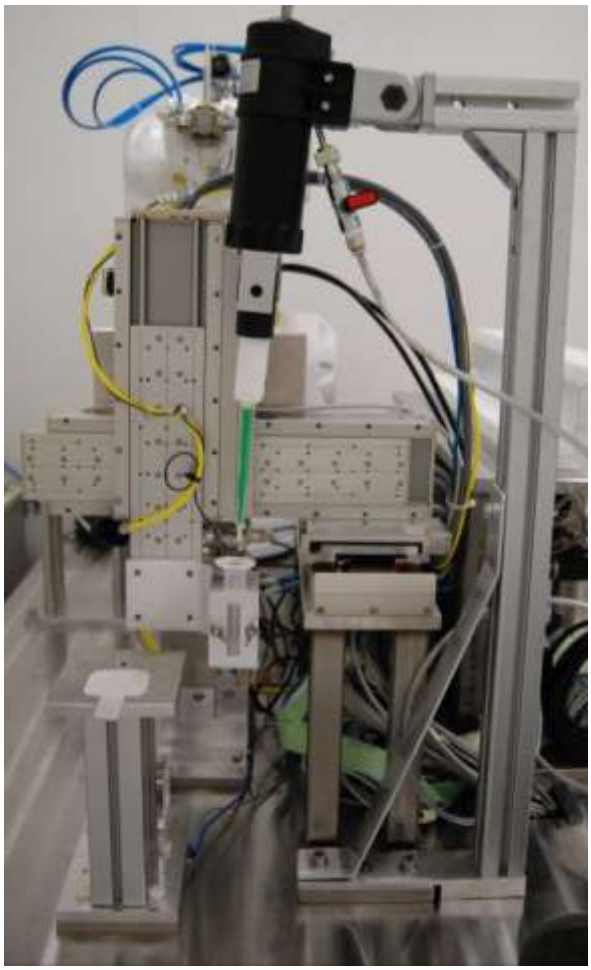

Figure 6-29. The "glue corner" of the system: the purge station (left) the syringe holder connected to Jenny's axis (middle) and the pneumatic gun placed on its holder (right).

6.4.3. Optimization of the Z-pos

Two new Z-positioners were produced for the final set-up because of the necessity to have mirrored crystal (see Figure 6-23). They have several advantages with respect to the prototype. First of all, the chip holders are still on the top of micrometers, but the inset for the chip has been replaced with three reference tips delimiting two adjacent sides of the chip, against with the chip has to be pushed (Figure 6-30, a). In this way there is no limit on the dimension of the chip the holder can accommodate.

Also the slot in which the micrometer moves has been modified, in order to ensure that the chip holder upper surface raises parallel to the zero reference plane (Figure 6-30, b). This plane is created thanks to two couple of three squared grinded teeth surrounding each chip holder. A circular clamp, with grinded bottom surface can be pressed and fixed on each set of teeth and then the micrometer should be rise in order the upper face of the chip touches the clamp (Figure 6-30, c). The contact between the two surfaces is monitored thanks to load cells. Once the clamp is removed, the chip rests in its final position. Tests performed show that the errors on the chip vertical position are 1 μm for the NTD and 0.5 μm for the heater.

The chips are positioned 50 μm lower than the crystal plane, determined by other three grinded teeth on which the crystal will be placed at the end of the gluing procedure (Figure 6-30, e). The number of teeth has been reduced with respect to the previous Z-pos to enhance the precision in the crystal placement. Again the crystal is not directly placed on the crystal plane but in a PTFE holder, but in the new Z-pos the raise and the descent of this holder are controlled by a pneumatic valve (Figure 6-30, d) and the crystal is put down on it thanks to the ABB robotic arm. In this way also the crystal positioning that ends the gluing is perfectly timed.

6.4.4. Optimization of the zero point location

As introduced in Section Figure 6-31.6.3.2, an important parameter in the gluing process is the zero-point, i.e. the vertical position of contact between the syringe needle and the upper surface of the sensor. This position has to be checked every time the syringe is changed because the worst tolerance of this element with respect to the one required by the procedure. As in the Como test, in the final set-up the zero point is found by verifying electric contact between the steel needle of the syringe and a point of the Z-pos and, staring from this value, the vertical position of the chip is determined.

Because the cartesian robot and the Z-pos are in principle two separated system, i.e. has no points in common, also the zero pint along the X and Y axis must be determined, in order Jenny to learn the complete position of the chip in the space.

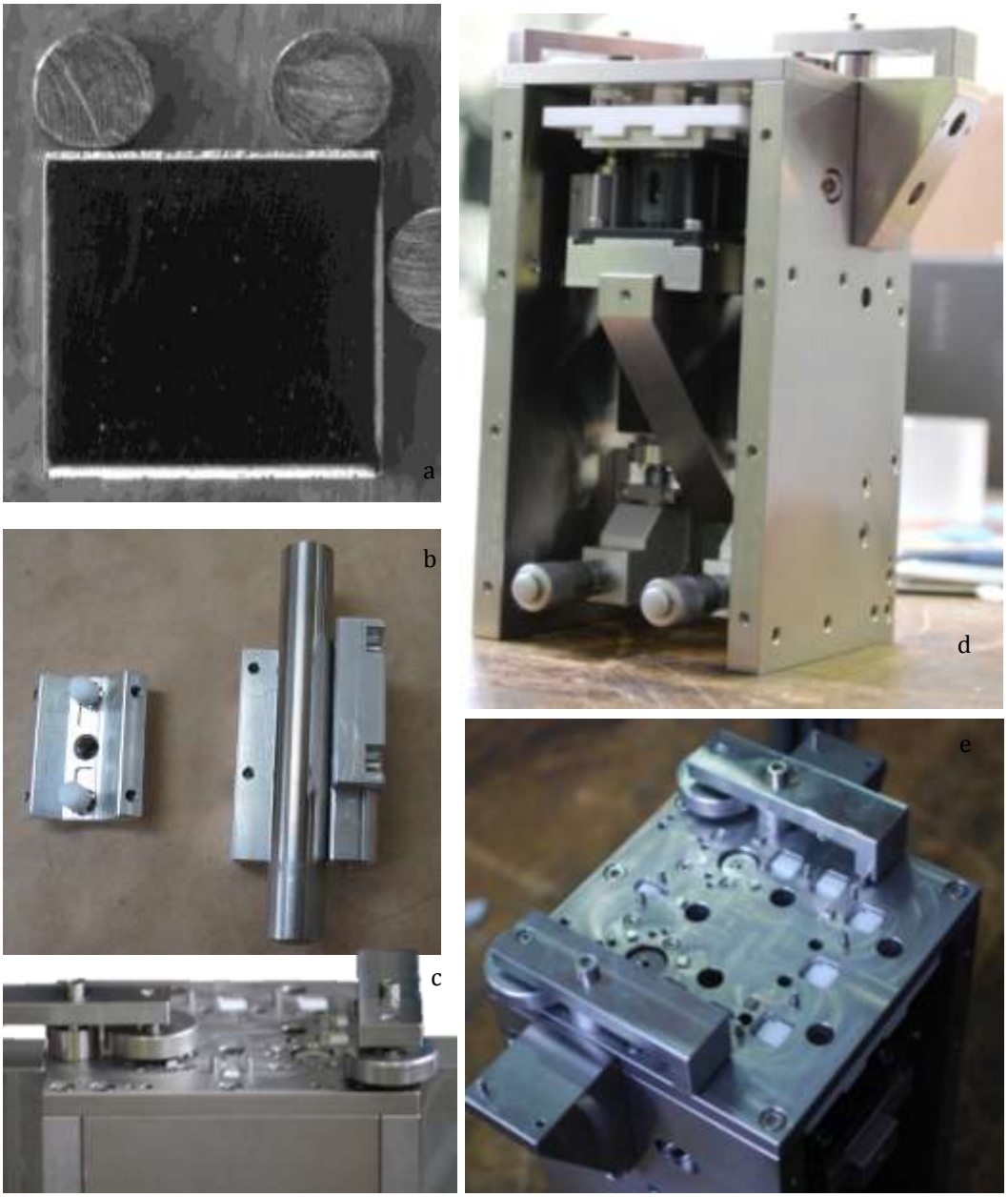

Figure 6-30. Some details of the new Z-positioners: the three tips that fix the position of the chip on the chip holder (a), the pieces ensuring parallel rising of the chip holder with respect to the zero reference plane (b), a detail of the clamp for positioning the chip at the right height (c), the pneumatic control for the PTFE crystal elevator (d) and the top of the Z-pos where the zero reference plane and the crystal plane, made by three group of three teeth each, the latter 50 μm higher than the other two groups, are visible.

To perform the electrical contact search, it is necessary to insulate the Z-pos from the table and set it at a certain voltage potential, while the needle behaves as ground, after connecting it to Jenny robot thanks to a wire (as done in the Como tests). The selection of the wire is a very critical part because of the extreme thinness of the needle: a too much stiff wire can bend the needle while the cartesian axes move, modifying the zero point position.

This problem is avoided by changing the needle with the one having the same tip size but with an aluminium crimping between tip and body (instead of a plastic one); the aluminium part offers a more stable place to which attaching the wire. Moreover, the wire has been replaced with a Cu-Be band, directly connected on the bottom part of the syringe holder, in which the aluminium part of the needle is inserted every time the syringe is placed in its housing. It allows the operator avoiding to connect the wire with the needle each time the syringe is changed, a difficult step to be performed in a glove box environment. The difference between the two kind of needles and wire connections are shown in Figure 6-30. Tests performed show that, using the same needle, the error in the zero point location in two following measurements is ≤2 μm and ≤5 μm after several measurements for all the axes.

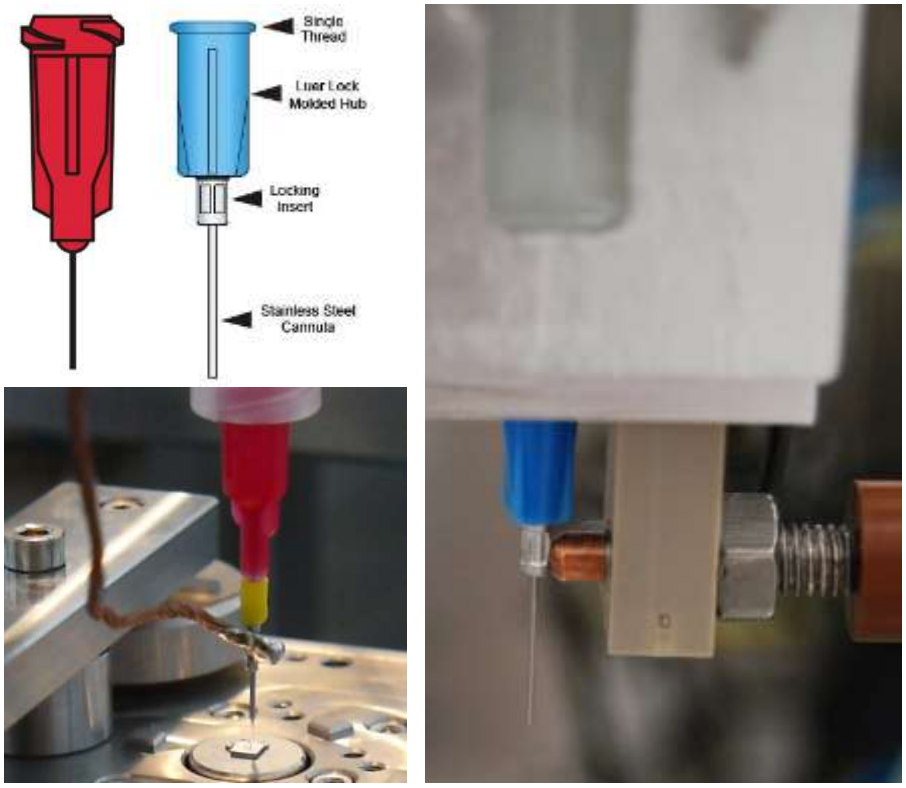

Figure 6-31. (Left-top) The difference between the previously used needle (red) and the new adopted one (blue). (Left-bottom) The old wire-to-needle connection for the zero point location. (Right) The new connection for the zero point location.

6.4.5. The gluing procedure

The integration phase of the semi-automatic gluing line is now completed: all the components individually tested and approved are interfaced to communicate and interact. A PLC serves this purpose. All instruments are mounted in glove box in the CUORE clean room.

Thanks to the presence of two Z-positioners, two detectors can stay in the operational area at the same time. However, gluing runs are performed on one crystal at a time, so that epoxy deposition on different crystals is done with a separate syringe filling: the choice was made not to force working times, which are already short due to the three minutes pot life of Araldite Rapid and to have the same kind of chip (NTD or heater) glued at a precise time after the beginning of the glue mixing; in line of principle, if no unexpected events take place, this guarantees epoxy dots whose quality, on the same as well as on different detectors, is safe from time variations in glue viscosity. Five purge dots, a thermistor nine-dot matrix and a heater five-dot matrix are dispensed with a single syringe filling in less than 3 minutes. An example of gluing is shown in Figure 6-32, while all the parameters required for reach such a result with a temperature of 21-21.5 °C are collected in Table 6-6.

Parameter	Value
Gun pressure	3 bar
Time for static mixer purging	12 s
Time for syringe filling	8 s
Dispenser pressure	1.4 bar
Number of step for syringe purging	5
Time for each purge step	7.5 s
Distance between two dot centres (X/Y)	900 μm
Speed on X/Y axis (between two adjacent spots)	$1 \cdot 10^5$ μm/s
Distance between the needle and the chip surface (ΔZ)	150 μm
Vertical rise for breaking the filament (Z')	5000 μm
Vertical speed for breaking the filament (v_z')	5000 μm/s
Vertical rise (Z'')	5000 μm
Vertical speed (v_z'')	$3 \cdot 10^4$ μm/s

Table 6-6. Parameters to be optimised to perform glue dots with the proper size. The values reported refer to a room temperature ranging between 21 and 21.5 °C and humidity of 30-50%.

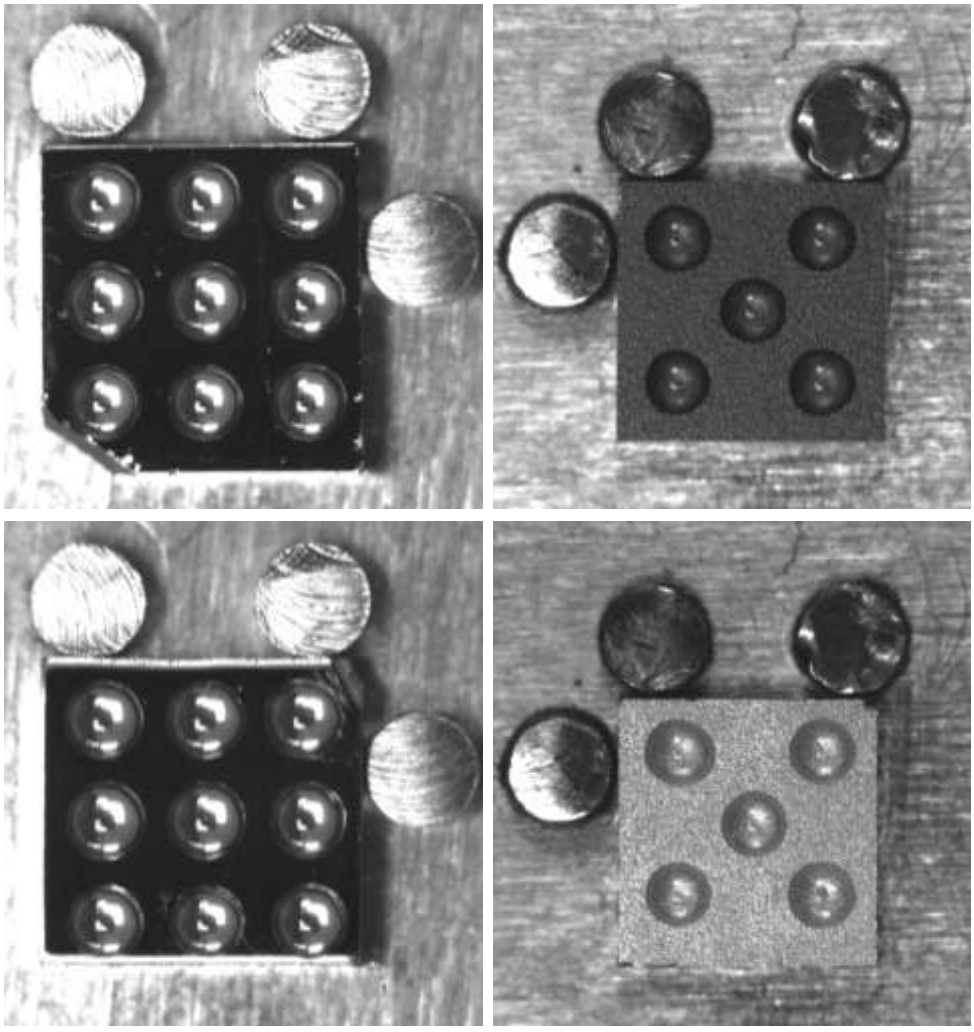

Figure 6-32. Examples of gluing obtained with the new chip-to-absorber coupling line. The pictures are taken with the camera placed on Jenny axis and show two examples of the nine-dot matrix on a thermistor and a five-dot matrix on heater. The thermistor in the upper picture is a real CUORE 39C NTD, while the one in the bottom picture is a 34C.

When the 30 minutes handling time for the first crystal expires, so that no vibrations disturb matrix polymerization anymore, the gluing of the second crystal begins. The first absorber is not removed from the Z-positioner during this procedure and is moved to a storage area only at the end of curing time. The total duration of a gluing run includes system preparation, besides curing time. According to the timetable presented, the gluing line can lead to the daily yield of twelve detectors. For this reason, the system layout includes two repositories containing the twelve crystals (before and after gluing) and the corresponding number of sensors employed in a working day. The former is made in PTFE (Figure 6-33, left) while the latter in stainless steel (Figure 6-33, right) according to the radio-purity requirements.

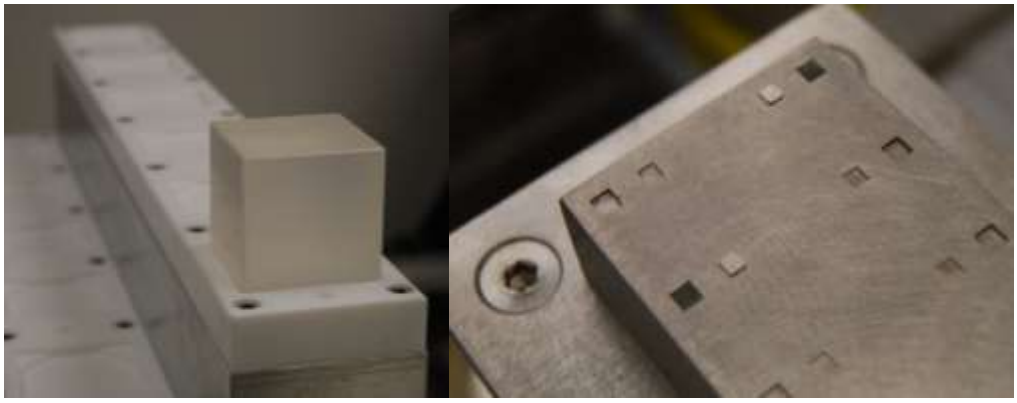

Figure 6-33. Crystal repository with a TeO_2 crystal (left) and chip repository with two NDT-heater couples (right).

Considering an entire working day, the tasks to be accomplished can be divided in two groups: operations to be done once a day (tipically a the beginning and at the end) and operations required for assembly the single bolometer. The tasks belonging to the first group include opening the bare crystal and chip boxes (like the one shown in Figure 5-2) and packing the final detectors, and are done by the operator with the exception of the moving of the items in the gluing area, which is done by the ABB robotic arm.

As for the single detector gluing, the procedure can be also divided in two steps: the positioning of the material required for the single gluing (i.e. thermistor and heater on the Z-pos, static mixer on the bi-cartridge, and syringe in the holder) and the gluing itself. Again, the first part is almost a complete duty of the operator, while the second one is fully automated with the exception of two confirm the operator should give to go on: as a result, thanks to all the innovation developed in the framework of this PhD thesis, the gluing procedure appears to be reproducible and exactly timed.

The use of double-barrel syringes combined with static mixers guarantees reproducible resin and hardener dosing, as well as thorough epoxy mixing; the single-dot micro-dispensing, although a tricky process when short life bi-component epoxies are used, allows full control on the gluing process: the amount of fluid released for each spot is fixed and uniformity of matrices is guaranteed; the use of automation eliminates the human error and quality variation intrinsic to operator-dependant procedures, besides introducing definite timing. The complete set-up is shown in Figure 6-34.

The gluing line has now finished the commissioning phase, and is ready for the first CUORE-0 gluing, which is foreseen to take place in the late July 2011.

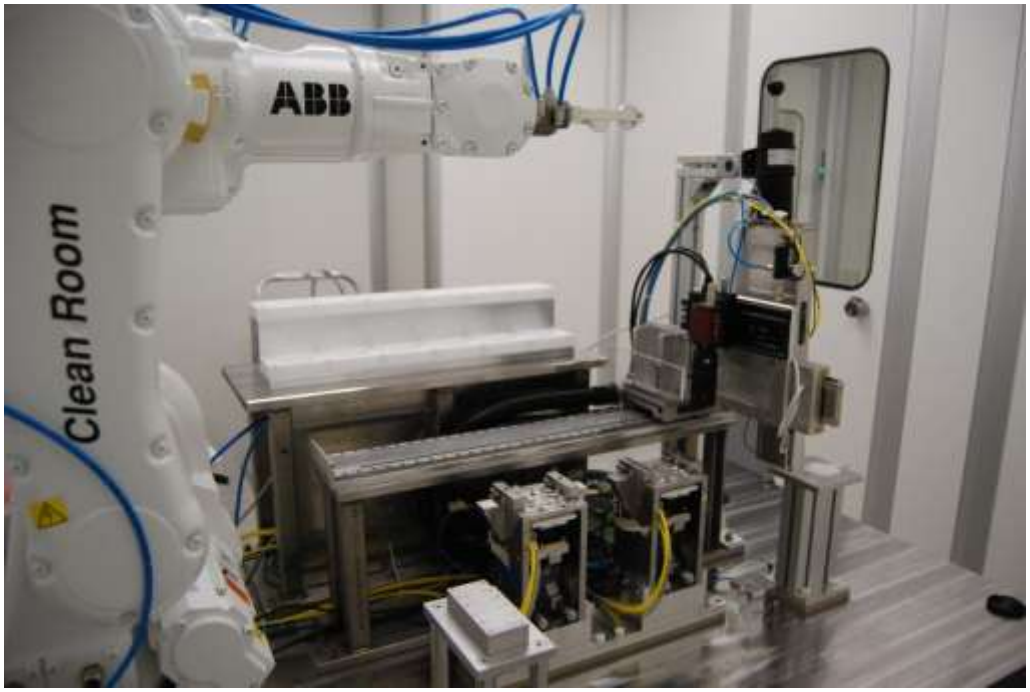

Figure 6-34. The CUORE gluing line.

Chapter 7.
SCINTILLATING BOLOMETERS

MEPHISTO: Verachte nur Vernunft und Wissenschaft,
Des Menschen alleröchste Kraft!
Du Lässest doch von Blend- und Zauberwerken
Dich in dem Quantengeist bestärken!
Pass auf, wie jetzt die Schwierigkeiten schwinden,
Und wunderbar wirst du das Neutron finden![15]

As introduced in Chapter 1, the goal of the next-generation 0νββ experiments is to reach sensitivity on the mass of the neutrino in the order of ~50 meV, to investigate the inverse hierarchy of the mass of the neutrinos. To accomplish this task, according to Eq. 1-31 and Eq. 1-32, excellent energy resolution, low number of background counts in the ROI and a high quantity of the candidate isotope are required.

Among the different kind of detectors available, bolometers (Chapter 2) have provided the best results in terms of energy resolution (FWHM around 0.2–0.5 % at 2800 keV), which is necessary to resolve the searched peak from background. The CUORE experience (Chapter 3) shows how the improvement on this technique can be hardly obtained on this parameter as well as in increasing the source mass and that the effort should be focused in reducing the background level.

The rejection methods adopted in CUORE are almost passive, i.e. based on a high level of radio-purity and cleaning of the materials, with the detector granularity helping in the discrimination of the background thanks to the study of coincidences. The only way for further improving the sensitivity is to add other background rejection tools to the present passive technique.

One of the most promising solutions is represented by scintillating bolometers, which combine the heat detection with independent scintillation read-out: thanks to the different light output of α and γ/β particles, they are able to suppress with high efficiency the background events due to αs.

[15] Mephisto: Despite only reason and science, / Mankind's highest power! / You allow deception and witchcraft / To confirm you in the quantum-mind! / See how now the difficulties dwindle, / And, Wonderful! You will find the Neutrino! (220). For the translation from German, see (221).

Furthermore, using a scintillating bolometer containing a DBD emitter whose transition energy exceeds the natural 2615 keV γ-line of ^{208}Tl (see Figure 1-9) it is possible to reach extremely low levels of background.

A project based on all these elements has been recently proposed: the LUCIFER experiment, with the aim of reducing the background in the 0νββ region of interest to 1 c/(keV·ton·y). The main elements of the experiment, starting from the bolometer absorber, have not been decided yet: during this PhD thesis some cryogenic measurements have been performed in order to increment the number of elements on which this selection should be based. In this chapter the main features of scintillating bolometers will be presented (Section 7.1) together with the LUCIFER experiment (Section 7.2) and the work done in this framework.

7.1. The basic idea

A scintillating bolometer is, in principle, a very simple device. It is composed of a bolometer, whose absorber is a scintillating crystal, and a suitable light detector, facing it, able to measure the emitted photons. Thanks to the fact that different particles (namely β/γ, α and neutrons) have different scintillation yields (or scintillation Quenching Factors, QF), this detector can easily discriminate among them (see Figure 7-1.).

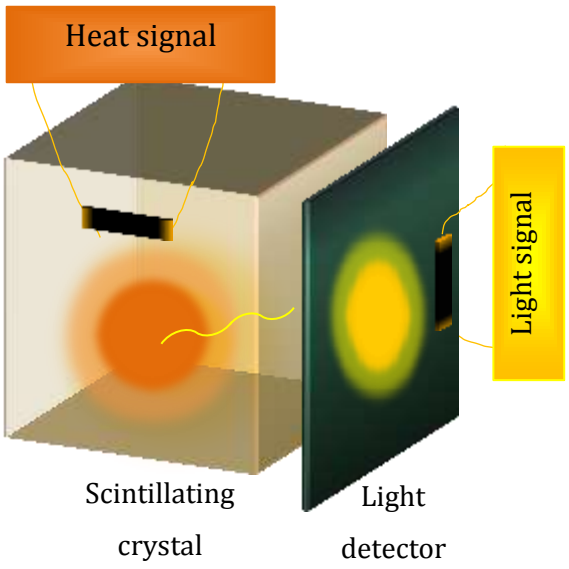

Figure 7-1. The operating principle of a scintillating bolometer. The release of energy inside a scintillating crystal follows two channels: light production and thermal excitation. The heat is read out by a temperature sensor glued on the primary crystal while the light is read by a second crystal (light detector).

When interacting in the absorber, a particle produces basically ionization and excitation, which starts triggering a series of processes that lead to the conversion of almost all the deposited energy into phonons. However it is possible that a fraction of this energy is trapped in long-living excited states or is lost through the emission of photons that escape the absorber. The scintillation mechanism in inorganic solids is the result of a complex series of processes, which are not always fully understood. Basically, it relies on the activation of impurity centres, which form intermediate energy levels: the impinging radiation can cause an electron to pass to the exciton band, just below the conduction band, with the creation of an electron-hole exciton state; the excitons can migrate through the crystal and ionize impurity centres, finally relaxing with the emission of light.

The ratio between the energy emitted in photons and the total deposited energy defines the Light Yield (LY):

$$LY \equiv \frac{dL}{dE}.$$

7-1

In order to account for the reduced LY of heavy particles, a semi-empirical formula has been proposed by Birks (195):

$$\frac{dL}{dr} = \frac{S\frac{dE}{dr}}{1 + kB\frac{dE}{dr}},$$

7-2

where dr is the length of the track of the incident particle, S is the absolute scintillating efficiency, BdE/dr is the density of activation centres along the track and k is a quenching factor; usually kB is referred to as a single parameter, the Birks factor, and is set experimentally after fitting data from the specific scintillator.

In the approximation of low stopping power, such as the case of electron-like events, Eq. 7-2 becomes:

$$\frac{dL}{dr} = S\frac{dE}{dr}$$

7-3

and the LY is equivalent to the absolute scintillating efficiency.

On the other hand, for high stopping power particles, such as alphas, saturation occurs and one has:

$$\frac{dL}{dr} = SkB.$$

7-4

The emitted light is found by integrating along the whole track the previous expressions; the ratio of LY from αs to that of electrons at the same energy defines the Quenching Factor (QF):

$$QF \equiv \left(\frac{dL}{dE}\right)_{\alpha} \Big/ \left(\frac{dL}{dE}\right)_{e}.$$

7-5

The first light/heat measurement with a background discrimination for DBD searches was performed with a thermal bolometer and a silicon photodiode by the Milan group in 1992 (196), (197); this technique however was not pursued because of the difficulties of running such a light detector at low temperatures (~10 mK). The following idea of using a bolometer as light detector was first developed (198) and then optimized (199), (200) for Dark Matter (DM) searches and then successfully applied to DBD (201), (202), (203), (204). From now on a scintillating bolometer will be considered as having a bolometer also for light detection, usually made of a thin crystal of Ge or Si.

Certainly, large-surface bolometric light detectors cannot easily reach the threshold of PMTs (~1 photoelectron, i.e., 3–7 photons, taking into account the quantum efficiency conversion), but they have two important advantages: first of all, they are sensitive over an extremely large band of photon wavelength (depending on the absorber) and, secondly, the overall quantum efficiency can be as good as the one of photodiodes. This means that the energy resolution on the scintillation light, which depends (above threshold) only on the Poisson statistical fluctuation of the emitted photons, will be better for bolometric light detectors with respect to PMTs. The main characteristics of a bolometric light detector should be easy expandability up to ~1000 channels and complete reliability of the composed device (bolometer + light detector) in order to have an almost 100% live time measurement.

On the other hand, there is not the need to have an extremely sensitive detector, as in the case of Dark Matter Searches, since the DBD signal lies in the MeV range. This makes the construction and the operation of such devices extremely easier with respect to the ones developed for DM Searches.

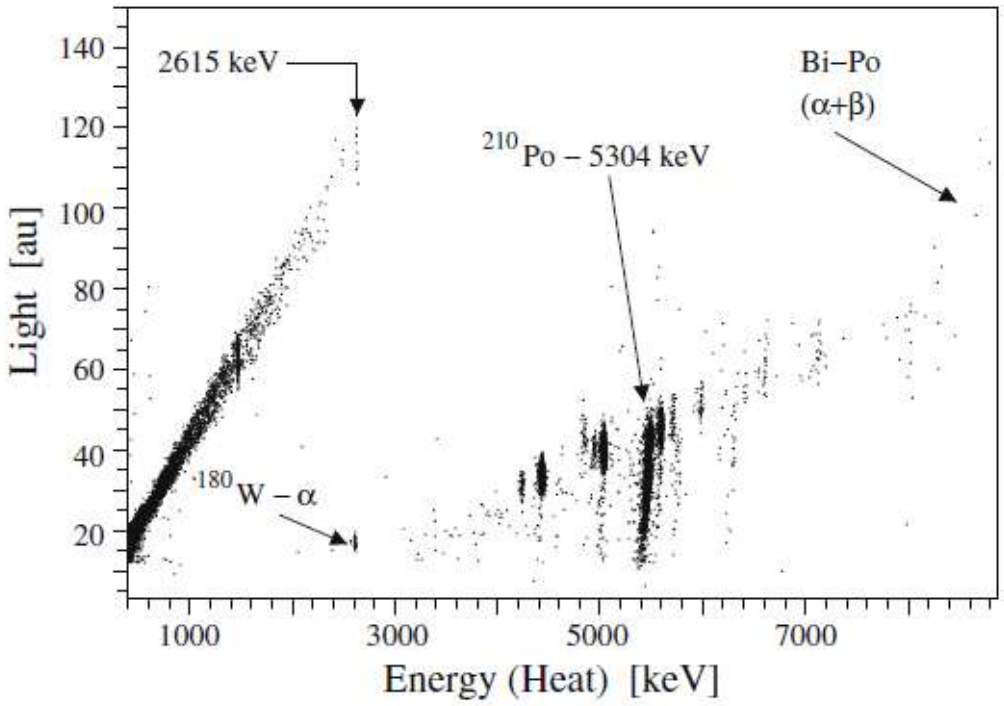

Figure 7-2. Scatter plot of heat (3x3x6 cm^3 $CdWO_4$, 426 g) vs. light (collected by Ge light detector).This plot shows how it is possible to separate very well the background due to α particles from the β/γ region (94).

The small thickness of the light detectors doesn't allow calibrating the detector with an external source. For this reason dedicated measurement should be performed, usually with a calibration source (^{55}Fe) facing the light detector.

An example of α-β/γ discrimination thanks to the different QF is given in Figure 7-2.

An additional help in rejecting the background is given by the fact that, according to the detector material, α or β/γ pulses can have different shape parameters (such as rise or decay time) and can be recognised by pulse-shape analysis.

Considering all these features, a scintillating bolometer appear to be a very sensitive device for the search of 0νββ, that can be improved by using crystals containing high Q-value 0νββ candidate nucleus, such as Cd, Se or Mo, which decay should be outside the natural radioactivity energy region.

A new experiment has been proposed for exploiting this technique, described in the next section.

7.2. The LUCIFER experiment

The Low-background Underground Cryogenics Installation For Elusive Rates (LUCIFER) project (205) is an experiment recently approved by the European Research Council that will search the 0νββ decay with the bolometric technique improved by the use of scintillating bolometers, aiming to reduce the background level to 10^{-3} counts/(keV·kg·y) and below.

LUCIFER is proposed to be located in Hall A at LNGS, in the same cryostat of the Cuoricino and CUORE-0 experiments, which available volume (6000 cm^3) is compatible with the needs of the project. Neither the 0νββ source isotope nor the detector structure has been decided yet, having in both cases a range of two or three appealing proposals that will be discussed in the next sections.

7.2.1. The candidate isotopes

The 0νββ emitter and the absorber compound have to be chosen taking into account, only the nuclei that can be used to fabricate a scintillating crystal (see Table 1-3). Moreover, besides the criteria expressed in Section 1.4.1.1 (high Q-value above the natural radioactivity region, the relative amount of the emitter in the crystal, the enrichment feasibility and cost), for the material selection also the quenching factor and the scintillation yield must be considered.

Practical scintillators can be built out Mo, Cd and Se. The three nuclei are equally good in terms of Q-value (see Figure 1-9), which is beyond the 2615 γ-peak of ^{208}Tl in all cases, and also the isotopic abundance of the three nuclides is comparable (see Figure 1-10): because it is between 5% and 10%, the cost and feasibility of enrichment must be considered. Both Mo and Se have been successfully enriched in comparable quantities to the LUCIFER needs while Cd has additional difficulties and a plausible cost higher by more than a factor 2. In particular, for the case of Se, the enrichment in ^{82}Se has already been investigated in the framework of the Integrated Large Infrastructures for Astroparticle Science (ILIAS JRA2/N4).

Possible good options are Cadmium Tungstate ($CdWO_4$), Zinc Selenide (ZnSe) and Zinc Molibdate ($ZnMoO_4$). $CdWO_4$ is a well-established scintillator, with a rather large light yield and its radiopurity is ‘‘naturally” high. Due to these favourable features this crystal compound was already used to perform a DBD experiment (48) using ‘‘standard” photomultipliers. A large mass experiment, based on enriched $CdWO_4$ crystals, readout by

photomultipliers, was also proposed (206). But this technique, limited by the modest achievable energy resolution, key point of future experiments, is no more pursued. ZnSe is a semiconductor known as a luminescent crystal since many years (207). $ZnMoO_4$ is one of the most promising materials for searching the 0νββ decay of ^{100}Mo (208)because it contains a high concentration of Mo (43% in weight) and recently efforts in the crystal growth show that is possible to have sample with a very low content of radioactive elements (209).

All these compounds were successfully tested as scintillating bolometers, but a reproducible, reliable crystal growth technology has not been developed yet, as well as the possibility of growing crystals of large dimensions (typically 500 g to 1 kg) and of high purity should still be studied.

To reach this goal, preliminary work is needed to the study of the optical properties of the material and their low temperature dependence, taking into account the effect of impurities and local defects. The growth conditions and the post-growth treatment of the crystals will be also examined. A full characterization of the material is foreseen as well, in terms of a systematic measurement of electrical characteristics, photoluminescence, radioluminescence and thermo-stimulated luminescence. These introductive activities will help to define the precise nature of scintillation in undoped crystals. Other aspects that will be examined will be the thermal dependence of scintillation yield, the possible doping, and the technological limits for the purification of the raw material. A second phase will be dedicated to test the limits of possible improvement of the scintillator performance, and the specifications to be asked to potential producers will be defined.

Crystal	**Candidate isotope**	**Isotope weight [kg]**	**Useful material**	**Half-life limit [10^{26} y]**	**Sensitivity to $m_{\beta\beta}$ [meV]**
$CdWO_4$	^{116}Cd	15.1	32%	1.15	65-80
$ZnMoO_4$	^{100}Mo	11.3	44%	1.27	67-73
ZnSe [0]		17.6		2.31	52-65
ZnSe [1]	^{82}Se	20.5	56%	2.59	49-61
ZnSe [2]		27.8		3.20	44-55

Table 7-1. Sensitivity of three experimental options for a 0νββ scintillating bolometer experiment compatible with the experimental volume of the Cuoricino cryostat. ZnSe Option [1] and ZnSe Option [2] foresee an increased ZnSe crystal volume with respect to the baseline [0], achievable thanks to some modification to the LNGS Hall A cryostat and will be discussed in detail in Section 7.2.2.
The 1σ sensitivity (Eq. 1-31, 1-32) is calculated with the Feldman-Cousin approach for 5 year running and a background index b = 10^{-3} c/(keV·kg·y). The matrix elements come from the two most recent QRPA calculations (60), (58), (210); a 5 keV energy window is taken, in comparison with the resolution achieved in TeO_2 macrobolometer and in scintillating bolometer R&D.

Crystal	Candidate isotope	Q-value [keV]	LY [keV/MeV]	QF (α/β)
$CdWO_4$	^{116}Cd	2809	34	0.19
$ZnMoO_4$	^{100}Mo	3034	1.4	0.16
ZnSe	^{82}Se	2996	7.4	4.2

Table 7-2. Light yield (LY) and quenching factor (QF) for interesting scintillating bolometers (211), (203).

The comparison of the three candidates with respect to physics sensitivity for a given mass, relative amount of DBD emitter in the crystal and sensitivity is given in Table 7-1, while transition energy, quenching factor and scintillation yield are reported in Table 7-2.

Because it allows reaching the worst sensitivity and the production costs are the highest, $CdWO_4$ appear to be the worst candidate as crystal for the LUCIFER experiment. On the contrary, ^{82}Se (ZnSe) appear to be the best isotope choice, being the one with the best sensitivity. A possible contraindication for this isotope came from the quenching factor: even if it offers the requested rejection factor, it goes in the opposite direction of what expected: α particles have (much) higher light yield than β particles. Although not really welcome, this unexpected property, according to results of preliminary investigations, to be confirmed by a careful study on the prototype crystals for the experiment, does not degrade the discrimination power of this material compared to the others and makes it compatible with the requirement of this high sensitivity experiment.

Another question mark about the ZnSe is the reproducibility of its features: preliminary tests (212) showed how the quenching factor is different from crystal to crystal, so high effort in the material production should be done.

$ZnMoO_4$ can be a possible compromise solution, being its production nowadays more reliable, but it will lead to a worst sensitivity in comparison to ZnSe.

7.2.2. The LUCIFER detector

The LUCIFER array will be made of tens of individual bolometers arranged in a close-packed configuration and housed by the same cryogenic infrastructure. This approach allows to achieve large masses (~50 kg) keeping the single-crystal mass reasonable (~0.5 kg) and providing a rough granularity, very helpful for background identification and rejection.

The elementary module of the LUCIFER array is very similar to the CUORE-0/CUORE single module described in Chapter 3: four 5 cm side square ZnSe crystals (660g each), provided with NTD Ge sensors and heaters, are held by PTFE pieces in a copper structure.

The main difference is the upper copper frame, where an intrinsic-Si disk-shaped slab 0.5 mm thick and 9.5 cm diameter, acting as a photon absorber for the light detector, is placed. The option to use a square slab with 9.5 cm side (providing larger light collection) will be considered as well.

The Si slab is held above the ZnSe crystals and the PTFE elements supporting them, and will be kept by four PTFE clamps fixed at the frame. Again, a NTD Ge thermistor and a heater will be glued on the Si slab. This configuration allows the light detector to see the four crystals underneath, and to offer its upper face to the adjacent EM with its four ZnSe crystals. A scheme of the LUCIFER single module is sketched in Figure 7-3.

Twelve modules will be stacked to form the LUCIFER tower (see Figure 7-4), starting from below with an additional isolated frame similar to the single module upper frame and containing a light detector. The total tower height will be 85 cm, fully exploiting the available space in the Cuoricino cryostat in the present internal shielding arrangement. The total bolometric mass will be 31.7 kg and the corresponding enriched material mass is 17.6 kg.

This configuration is very conservative and based on the preservation as complete as possible of already tested structures. However, other possibilities can be taken into consideration, with the aim to increase the total detector mass without moving to another cryostat. For instance:

1) The internal lead shielding placed between the mixing chamber and the detector can be reduced or removed, creating room for two more floors of crystals. This possibility, corresponding to ZnSe option 1 in Table 7-1, would increase the total mass to 36.9 kg and the enriched one to 20.5 kg.
2) The lateral lead shield can be removed, making possible to increase to 6 cm the side of the crystal cube, leading to a single crystal mass of about 1.1 kg. In this case, named ZnSe option 2 in Table 7-1, the total mass would be 50 kg and enriched mass 27.8 kg. Of course this possibility requires rescaling opportunely the frames of the single module and depends of course on the success of the crystallization R&D and on the bolometric performance or very large mass ZnSe detectors, but looks quite reasonable.

The removal or the reduction of the internal shields may look dangerous. However, the gamma activity is not so harmful for scintillating bolometers as for common bolometers and, moreover, the Cuoricino cryostat is realized with low radioactivity materials. A Monte Carlo validation of the new proposed structures will be necessary anyhow.

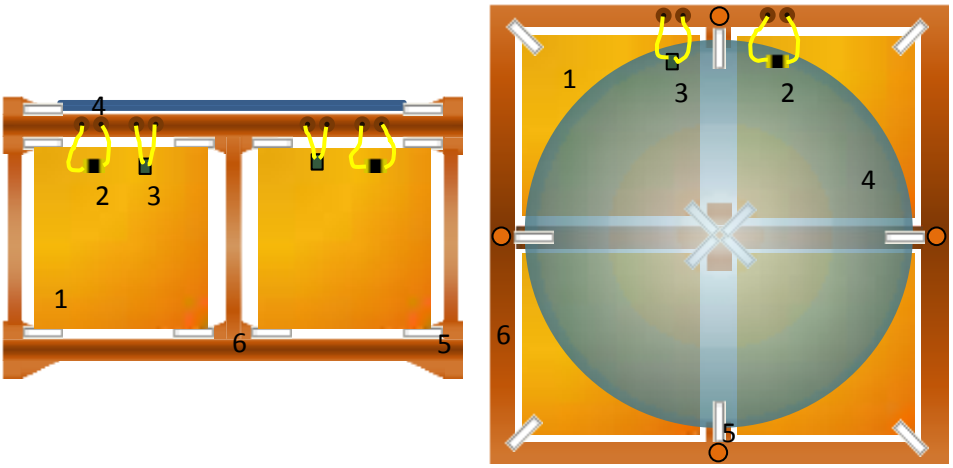

Figure 7-3. Lateral (left) and upper (right) view of the LUCIFER single module. 1) ZnSe Crystal; 2) NTD Ge thermistor; 3) heater; 4) Si- slab acting as light detector; 5) PTFE spacer; 6) copper frame.

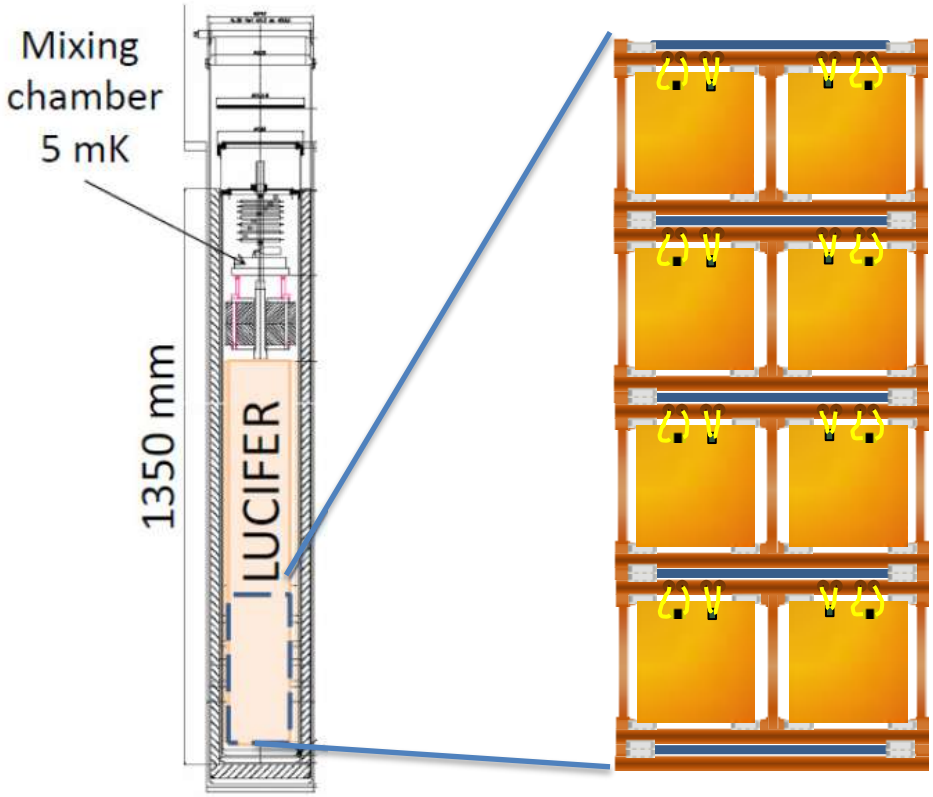

Figure 7-4. The LUCIFER tower inside the former Cuoricino/CUORE-0 cryostat. A detail of the tower, comprising four elementary modules, is shown on the right.

Whatever the detailed configuration will be, having each ZnSe crystal sandwiched between two light detectors (both collecting light when energy is deposited in the main bolometer) defines a very well characterized event class to which the double-beta-decay signal belongs, unlike alpha events and multiple-scattering gamma or neutron events:

1) a triple-coincidence signal in a ZnSe crystal and in the two light detectors which surround it;
2) simultaneous signal in none of the remaining channels;
3) a light-to-heat signal amplitude ratio compatible with beta-like or gamma-like events;
4) a pulse shape in the light and heat channels compatible with beta-like or gamma-like events.

The tower will be surrounded by a copper thermal shield and suspended using the same method developed for Cuoricino, and also the front end electronics, the post-amplifiers and the DAQ system will be exactly those used for Cuoricino. The calibration of the detectors will be performed with external gamma sources, as in Cuoricino.

7.3. Detectors: Three Different Ones

To check the main options in terms of scintillating crystals and light detectors for the LUCIFER experiment a dedicated set-up has been prepared in the cryogenic laboratory at Insubria University.

The aim of these low-temperature tests is not only to select the best combination of materials for a scintillating bolometer for double beta decay search, but also to verify if this kind of measurement can be efficiently performed also in an aboveground site.

In order to easily compare the data from several cool downs with different bolometer elements the mounting has been designed allowing a fast change of the detector components and a high-reproducible assembly.

The holder is made of copper and contains a scintillating crystal and two squared light detectors, facing two opposite sides of the main crystal; all the elements are equipped with a "T-shaped" 34B type NTD thermistor (size: 3×1×0.6 mm^3, ρ_0 = 1.2 Ω/mm, T_0 = 3.95 K) with 50 micron diameter wires, and held by Teflon pieces. Because the data taking is planned to be aboveground, the size of the bolometers should be small, to avoid a huge rate of cosmic rays.

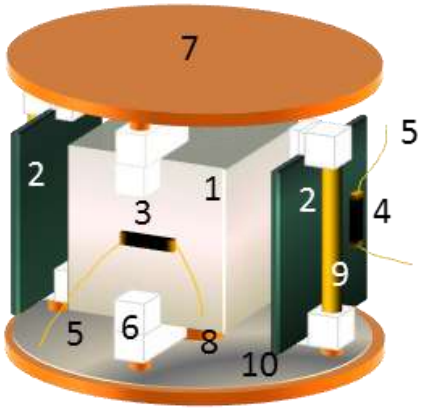

Figure 7-5. A scheme of the scintillating bolometer setup tested at Insubria cryogenic laboratory: 1) the scintillating crystal; 2) the light detectors; 3) the heat thermistor. On the opposite crystal face a heater is also present; 4) the light thermistor; 5) gold wires for thermistor readout; 6) Teflon parts holding the bolometers and providing the conductance to the thermal bath; 7) copper structure; 8) hole in the holder bottom plane for placing the Uranium source; 9) column holding the light detectors, on which the Iron source will be attached; 10) scintillating foil that cover all the copper parts and surrounds the entire detector for enhancing the light collection.

The connection between absorbers and thermistors is made with a single spot of Araldite Rapid glue. The scintillating crystal is also equipped with a heater. All the copper parts facing the bolometers are covered with a scintillating foil, to enhance light collection. A scheme of the detector is depicted in Figure 7-5.

Radioactive sources are applied to the holder for the bolometer calibration: a depleted uranium source is placed in correspondence of a hole in the bottom plate of the holder, facing the downside face of the scintillating crystal, while two iron sources are applied close to the external side of the light detectors. All the sources were prepared from a liquid solution by depositing drops (weighted with a precision scale) on a piece of copper tape. The copper tape with the Fe source was covered with a thin layer of transparent tape for stopping the Auger electrons. The isotopes contained in the sources are listed in Table 7-3.

Source	Decay mode	Decay energy	B.R.
^{238}**U**	Alpha	4.15 MeV	20.9%
		4.20 MeV	79.0%
^{234}**U**	Alpha	4.77 MeV	71.4%
		4.72 MeV	28.4%
^{55}**Fe**	K_α X rays from EC	5.9 keV	
	K_β X rays from EC	6.5 keV	

Table 7-3. The isotopes contained in the calibration sources with their decay modes and decay energies.

Crystal	Size [mm^3]	Mass [g]	0νββ isotope	$Q_{\beta\beta}$ value [keV]
ZnSe	10×10×10	5.34	^{82}Se	3034
$ZnMoO_4$	15×15×5	5.07	^{100}Mo	2995

Table 7-4. The main features of the two crystals assembled for the scintillating bolometer tests.

Two different scintillating crystals have been tested: a 10×10×10 mm^3 Zinc Selenide and a 15×15×5 mm^3 Zinc Molybdate, containing respectively ^{82}Se and ^{100}Mo as double beta decay sources. The main characteristics of the two crystals are collected in Table 7-4 and Table 7-5.

The ZnSe crystal belongs to a series was produced by Alkor Technologies (Saint-Petersbourg, Russia) and is undoped (usually ZnSe is doped with Te). Its X-ray induced luminescence has been recently measured from room temperature down to 10 K, resulting in a dominant emission in the red region (610 and 645 nm) and a smaller component in the infrared region (970 nm) (212). The series was already used for a scintillating bolometer test performed at LNGS (212). The crystals show a colour variation not fully understood, that could be ascribed to a different stoichiometry (212), and resulted having also different light output. Among the series, the crystal selected for the measurement performed in the framework of this PhD thesis is the one with the highest light output.

The $ZnMoO_4$ is a complete new crystal, growth in the Nikolaev Institute of Inorganic Chemistry (Novosibirsk, Russia) by the low-thermal-gradient Czochralski technique in platinum crucible (224). Differently from previously produced crystals, which have a pinkish hue, this $ZnMoO_4$ is clear and has a better quality, being the number of impurity reduced in the growth procedure. Transmittance measurements confirm significant improvement of the material that has been tested as a scintillating bolometer for the first time in the framework of this thesis. X-ray luminescence was also investigated at 8, 118 and 290 K. The emission spectrum exhibits a broad band in the visible region with a maximum at 610 nm at room temperature, which shifts to 625 nm at 8 K. The integral luminescence is strongly quenched at room temperature, reaches a maximum around 110-140 K and then drops with cooling, tending to stabilize below 60 K at a factor ~5 higher than at room temperature. The luminescence results are in agreement with the data of previous investigations. Thermo-stimulated luminescence at ~75 K and phosphorescence indicates the presence of defects and impurities in the crystal, showing that there is still a considerable potential to improve the quality of the material.

The light detectors used are a couple of 15 mm side and 0.5 mm thickness Ge slabs and a couple of Si slabs of the same size. Figure 7-6 collects pictures of all these elements.

	ZnSe	$ZnMoO_4$
Density [g/cm³]	5.27 (213)	4.3 (214)
Debye temperature [K]	271 K (215)	
Molecular weight	65.38+78.96	65.38+95.94+15.60
Number of moles	0.037	

Table 7-5. Some properties of the ZnSe and $ZnMoO_4$ crystals.

Three detectors have been assembled: one containing the ZnSe crystal and the Ge slabs, the second with the same ZnSe crystal and the two Si slabs and the last with the $ZnMoO_4$ crystal and the Ge slabs again. From now on they will be named ZnSe-Ge, ZnSe-Si, $ZnMoO_4$-Ge. The first mounting was cooled down alone, while the ZnSe-Si and the $ZnMoO_4$-Ge were measured in the same cryogenic run. Figure 7-7, Figure 7-8, and Figure 7-9 display some moment of the detector assembly.

The cool downs of the three detectors for the aboveground measurements were done in the TBT refrigerator of Insubria cryogenic lab and are almost identical: the detectors reached a base temperature of ~25 mK. Before the data acquisition, load curves have been collected for the main bolometer and the light detectors and then the optimal working points have been selected. The corresponding working temperatures for each bolometer and the parameters of the electronic system are collected in Table 7-7, Table 7-12 and Table 7-13.

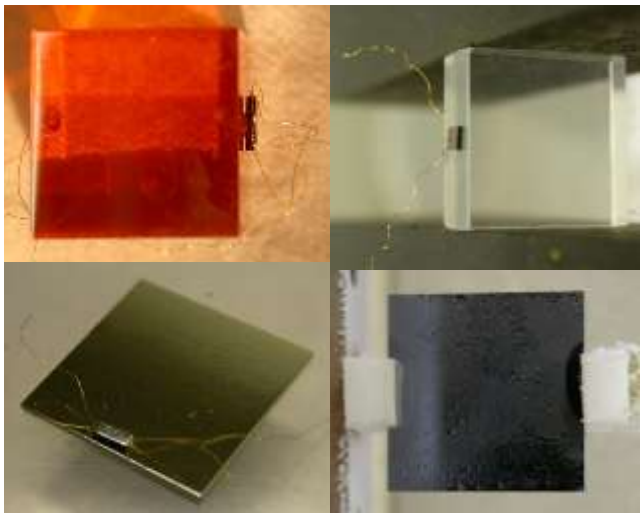

Figure 7-6. The main elements of the ZnSe-Ge, ZnSe-Si and $ZnMoO_4$ scintillating bolometers. From left up corner, clockwise: the ZnSe crystal equipped with a 3×1×0.6 mm³ NTD; the Zn MoO_4 crystal equipped with a heater; a Si slab after a test in liquid Nitrogen to check the thermal contraction of the slab holder; a Ge slab equipped with a 3×1×0.6 mm³ NTD.

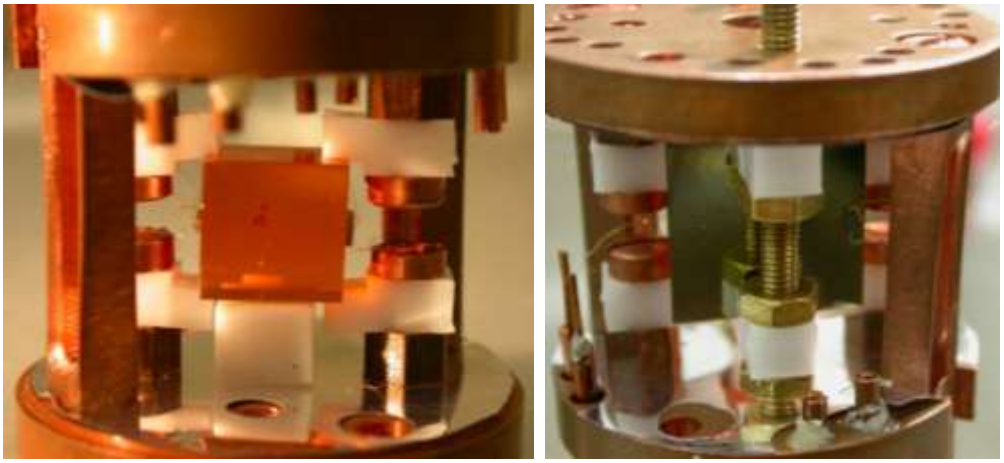

Figure 7-7. ZnSe-Ge detector. (Left) The ZnSe crystal, equipped with a 3x1x1 mm^3 thermistor (on the left) and a heater (on the right) is held by the Teflon part in the copper frame. (Right) A thermistor-equipped Ge slab, held in position by a sequence of brass nuts and Teflon pieces, covers one side of the ZnSe crystal.

Figure 7-8. (Left) The 15×15×5 mm^3 $ZnMoO_4$ crystal is placed in the copper holder between the two Ge slabs. (Right) The same picture from a different point of view: in the central hole of the bottom copper plate (already covered with the scintillating foil) the calibrating Uranium source can be seen (green spot).

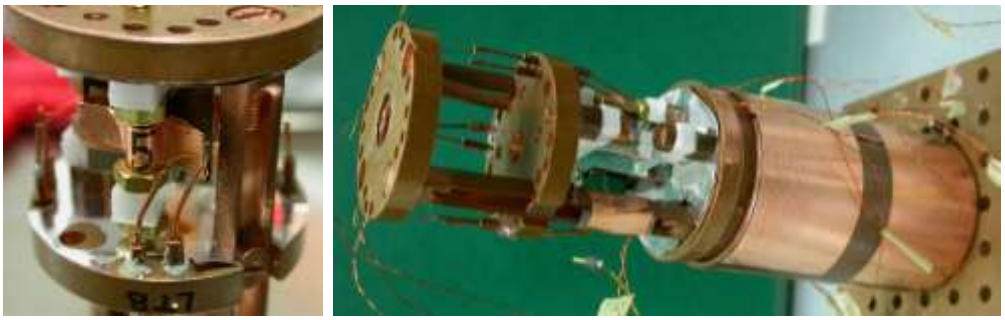

Figure 7-9. (Left) An iron source (numbered with "5") is placed in front of the slab. (Right) The $ZnMoO_4$-Ge detector is placed onto the ZnSe-Si detector, already completed with the copper shield.

Data were acquired with a dedicated DAQ system. The measurement sampling frequency is 20 kHz and the number of sampling point is 1024, because the pulse time scale is of the order of 50 ms. The pre-trigger, i.e. the time elapsed before each triggered pulse, is 1/8 or 1/4 of the time window. The trigger signal was duplicated by mean of a multiplexer and AC coupled in order to reduce the noise. It was not independent for each channel, so pulses collected are always in temporal coincidence. Using the heater, a reference pulse has been generated in the scintillating crystal for the measurement stabilisation (Section 3.3.2).

Several sets of measurement were performed, mostly with the trigger on the heat channel (the few performed with the trigger on the light channels were for calibration reasons), and the best in terms of duration and noise are selected for the analysis. Baselines (i.e. the data recorded in absence of pulses) were also collected to evaluate the noise spectra of the measurements, allowing applying the optimum filter technique to reconstruct the pulses from the raw data.

Also the data analysis of the three detectors will follow always the same line, made by two subsequent steps performed thanks to dedicated software.

In the first part of the analysis the raw data acquired with the ADC are processed by applying the Optimum Filter (OF) algorithm (180), already described in Section 5.2.2 to maximise the signal-to-noise ratio and to estimate the best amplitude of each recorded pulse. Together with the pulse amplitude, the OF allows to determine a certain number of parameters, such as arrival, rise and decay time, describing the pulses. All the parameters are then collected in a vector, the so-called n-tuple. A list of the most used n-tuple parameters is collected in Table 7-6.

The second step is the processing of the n-tuple for selecting pulses with desired features thanks to pulse shape analysis or identifying trends by analysing of the n-dimensional parameter space. This is also the time for performing the off-line stabilisation, i.e. the correction of the eventual temperature fluctuations occurred during the measurement, thanks to the presence of heater reference pulses (see Section 3.3.2).

The first output of this procedure are the calibrated energy spectra for both heat and light channels, by measuring the ratio Voltage/Energy for some reference radioactive peaks, from which the detector energy resolution is determined by evaluating the FWHM of the peaks fitted by a Gaussian. Then a bi-dimensional scatter-plot of amplitude the heat-light coincident pulse is performed, to discriminate between alpha and beta/gamma events. This discrimination in performed also applying the pulse shape analysis to the heat and/or light channel. From the two calibrated spectra and the heat-light amplitude scatter-plot the Quenching Factor (Eq. 7-5) and the Light Yield (Eq. 7-1) are finally determined.

Parameter	Meaning
Time	absolute arrival time of the pulse
Amplitude (time or frequency domain)	amplitude of the filtered signal in both time and freq. domain
Delay	difference of the pulse to the average pulse arrival time
Baseline value	DC level obtained averaging over a certain sample of points in the pre-trigger interval
Baseline RMS	
Rise time	time needed for the signal to rise from 10% to 90% of its maximum amplitude
Decay time	the time needed for the signal to lower from 90% to 30% of its maximum amplitude
Test Value Left and Right (TVL, TVR)	mean square difference between the i^{th} point of the pulses, taken from its left/right part (s_i) and the average pulse (a_i)
	$TVL = \frac{1}{N/2}\sum_{i=1}^{N/2}(s_i - a_i)^2; TVR = \frac{1}{N/2}\sum_{i=(N/2)+1}^{N}(s_i - a_i)^2$ 7-6
Test Value (AF)	mean square difference to the average pulse, which is the parameter employed in the adaptive filter (AF) technique

Table 7-6. Most used pulse parameters collected in a n-tuple after the application of the Optimum Filter.

7.4. ZnSe-Ge detector

The ZnSe-Ge detector was cooled down in the TBT cryostat of Insubria cryogenic lab in May 2010. After the data collection it was decided to move the detector to LNGS, to directly compare the performances of the same detector (not only of the same crystal) aboveground and underground.

7.4.1. ZnSe-Ge aboveground: the COMO run

The ZnSe-Ge detector was cooled down to a base temperature of about 25 mK. Details of the electronic system and of the detector working point are collected in Table 7-7. From a

rough comparison of the load curves it is possible to see that the behaviour of the light bolometers is slightly inhomogeneous, requiring an improved assembling procedure. This is confirmed also by the scatter plot (Figure 7-13) that displays the amplitudes of the pulses in coincidence on heat channel and on each light channel. An example of coincident pulses is shown in Figure 7-10. Using the heater, a 10 mHz frequency reference pulse has been generated in the scintillating crystal.

During the measurement, a helium leakage into the IVC occurred, warming up the system and requiring a new cool down. After the re-cooling, the setup stabilized in the same condition as before the leakage, allowing continuing the measurement as nothing has happened. The cryostat warm up can be seen in the baseline versus time plot for the heat channel displayed in Figure 7-12 while the correspondence of the working point before and after the re-cooling comes out by checking the load curves in the two moments (Figure 7-11). The details of the measurements selected for the data analysis are collected in Table 7-8.

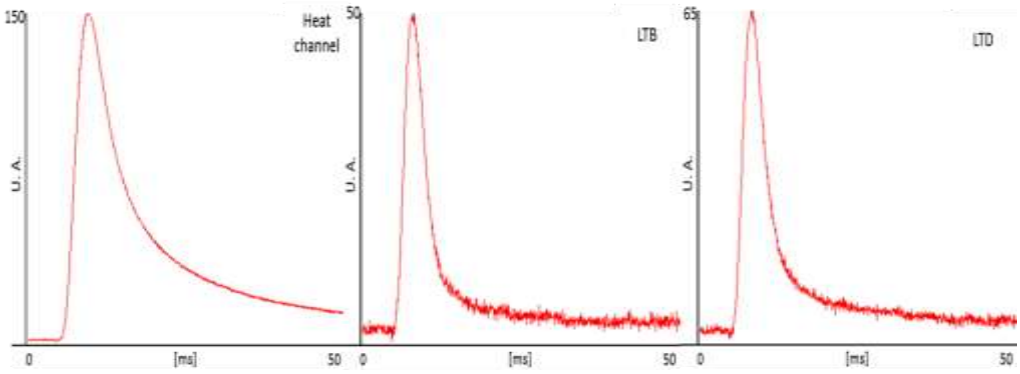

Figure 7-10. Example of coincident pulses collected with the ZnSe-Ge detector. The pulse on the heat channel is about three times higher than the same event on the light channels. The pulses time scale is 50 ms.

Channel	R_{Load} [MΩ]	Pretrigger [bsln]	Bessel cut off freq [Hz]	V_{bias} @ working point [V]	Gain	R_{work} [kΩ]	T_{work} [mK]
ZnSe	200	1/8	125	1.187	1931.0	395	32.1
LTB	200	1/8	125	3.999	3304.3	290	34.2
LTD	200	1/8	125	1.973	3304.3	244	31.6

Table 7-7. Electronic parameters and temperatures for the three thermistors in the aboveground measurement of the ZnSe-Ge detector: ZnSe is the heat channel from the scintillating crystal, while LTB and LTD are the light channels from the two Ge-slabs named B and D respectively. The temperatures were calculated with the doping parameters from the 34B series derived in Chapter 4 (see Table 4-24).

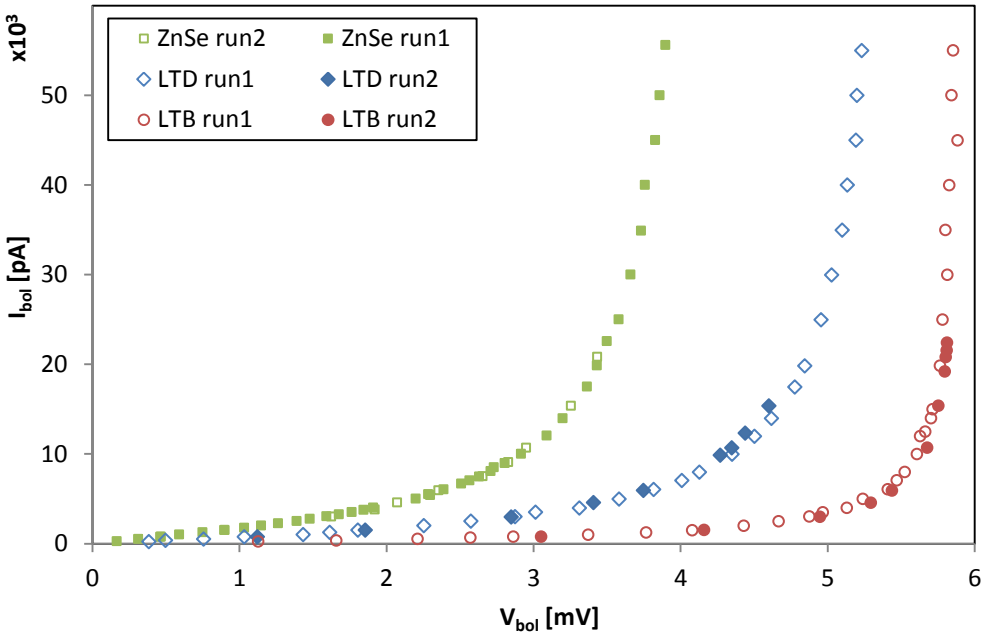

Figure 7-11. Static characterization of the three bolometers of the ZnSe-Ge detector: the load curves are identical before (run1) and after re-cooling (run2) even if there are difference between the two light detectors. This indicates a slight inhomogeneity in the single detector components, however the performances are stable in time.

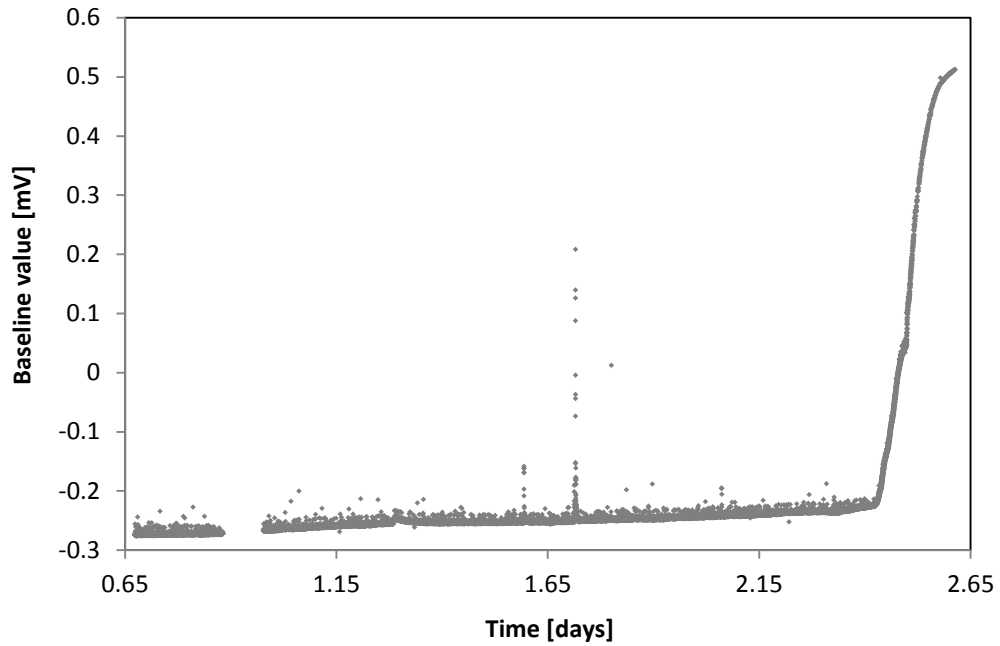

Figure 7-12. Baseline level versus time for the heat channel of the ZnSe-Ge detector. The steep rise in the right part of the graph corresponds to the sudden warm up of the cryostat due to the He leakage in the IVC. The gap between 0.8 and 0.9 days corresponds to the time interval during which the measure was stopped in order to acquire the noise spectrum.

Triggering channel	Full scale [V]	Measurement duration [h]
ZnSe	200	50.414
LTB	10	16.126
LTD	10	6.656

Table 7-8. Trigger configuration for the best data set of the aboveground measurements of ZnSe-Ge.

7.4.1.1. Event identification

The plot of the amplitudes of the coincident pulses on the heat (i.e. ZnSe) channel and each light channels (LTB and LTD) is shown in Figure 7-13. As already noticed from the load curves, the two light detectors have similar but not equal performances, even if in both case the discrimination between α and β/γ particles is clearly visible: two different bands are in fact distinguishable, however part of them are the result of random triggers. Because the ADC configuration allowed triggering only on one channel, the rejection operation of spurious coincidences can be carried out only by means of shape parameters. In this plot no cut have been applied yet on the shape of the pulses so saturated or spike events are still present. In particular, the group of points at about 350 mV on the heat channel and 0 on the light channels corresponds to the events generated by the heater on the ZnSe, used for stabilizing the measurement.

A preliminary identification and rejection of distorted pulses, e.g. energy saturated or pure ionization events, is possible using shape parameters (such as TVL, TVR and AF –see Table 7-6) of the heat channel: part of the spurious coincidences is then rejected (Figure 7-14). Then, through an analysis of the shape parameters of the light channel, further discrimination is achievable. In this case, the TVR was especially useful: in Figure 7-15 three different event families are discernible. These correspond to the pure ionization events on LTB (TVR<3), the α events (3<TVR<7.5) and β/γ events (TVR>7.5), as shown in Figure 7-16.

7.4.1.2. Energy calibration of the heat channel

From the measurement triggered by the heat channel, a background spectrum is obtained: ^{40}K, ^{208}Tl double escape and ^{208}Tl peaks were identified and a calibration of the spectrum was performed with a quadratic polynomial (Figure 7-17). Energy resolutions FWHM were obtained from the fits of the three peaks (Figure 7-18); unfortunately, the statistic is poor because of the cited cryogenics problems and energy resolutions at high energies worsen (see Table 7-9). For the same reason and because of the low-activity of the U calibrating source, no α-peaks are visible in the spectrum.

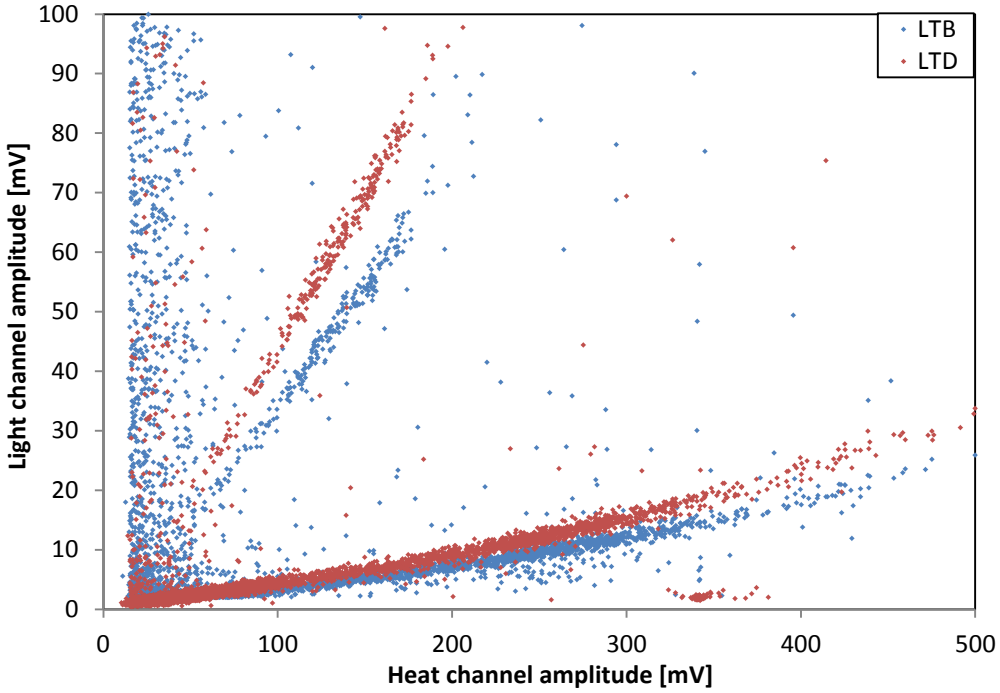

Figure 7-13. Plot of the amplitude of the coincidence events on the heat channel (x-axis) and both light channels (y-axis): red for LTD and blue for LTB. As already noticed from the static characterization (Figure 7-11), the two detectors have similar but different performances.

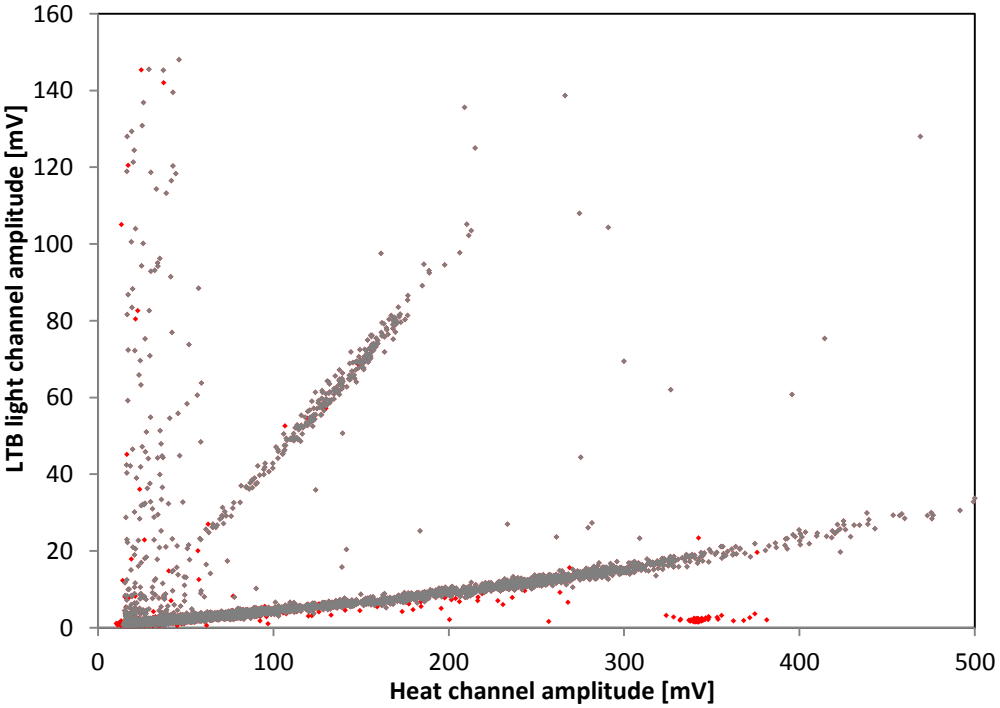

Figure 7-14. The amplitude of the heat channel versus the amplitude of the LTB light channel. In red the events selected by operating cuts on on the TVR of ZnSe: part of the pure ionization events as well as the pulses due to the heater are rejected.

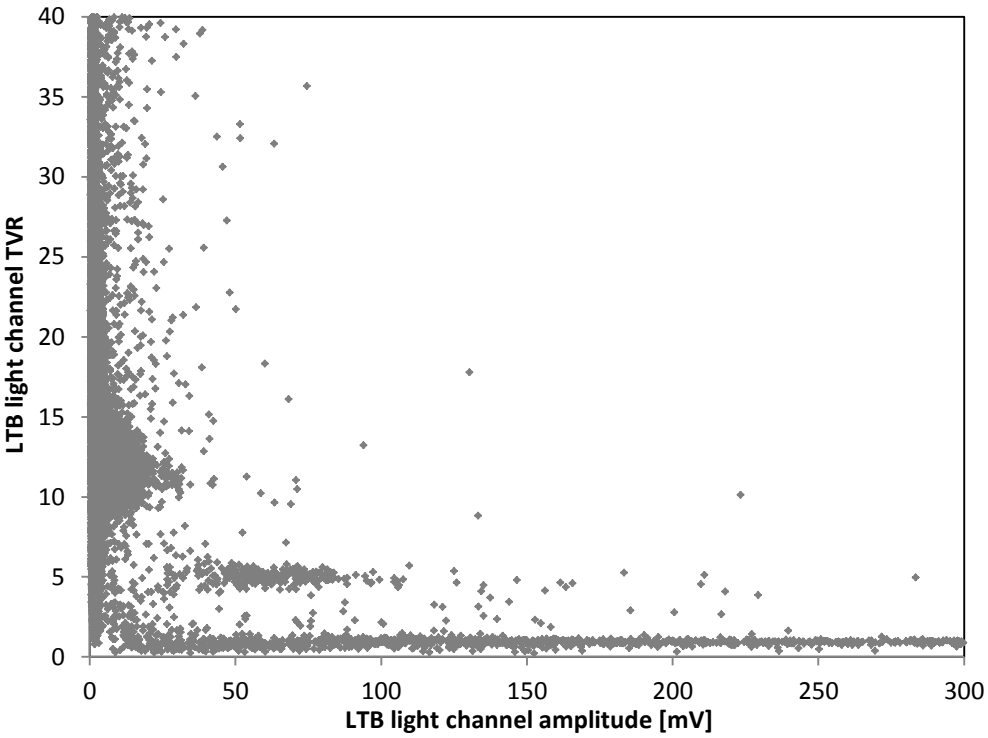

Figure 7-15. TVR versus amplitude for the LTB light channel. Discrimination among different event categories is appreciable.

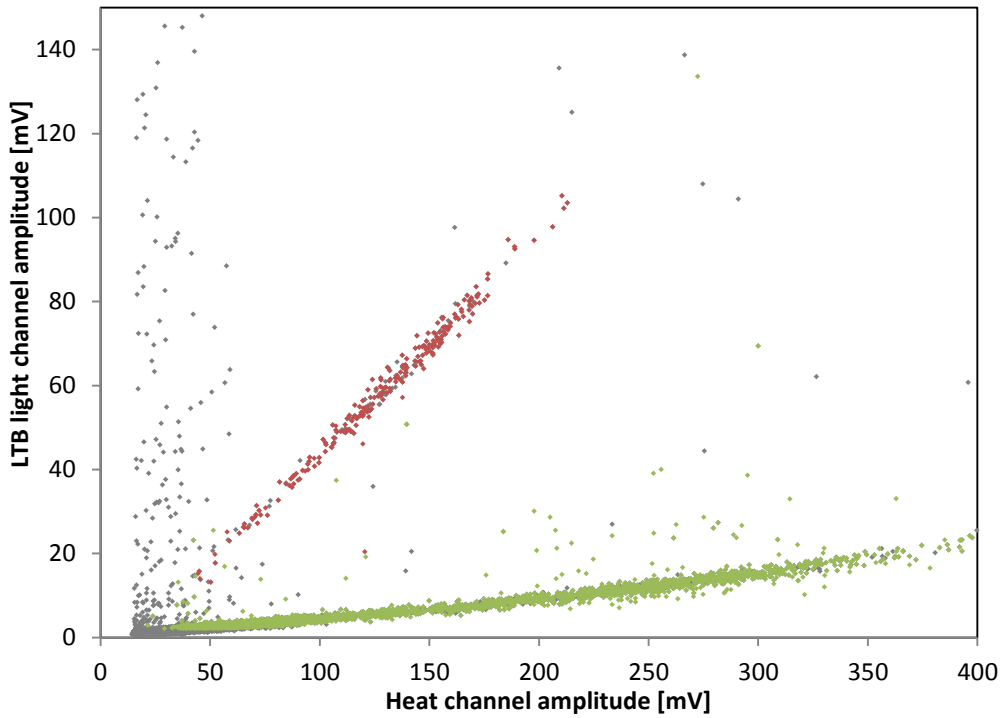

Figure 7-16. Plot of ZnSe-LTB coincidences: in blue, residual pure ionizing events; α and βγ events (in red and in green respectively) are discriminated thanks to the cuts on the TVR of LTB light channel.

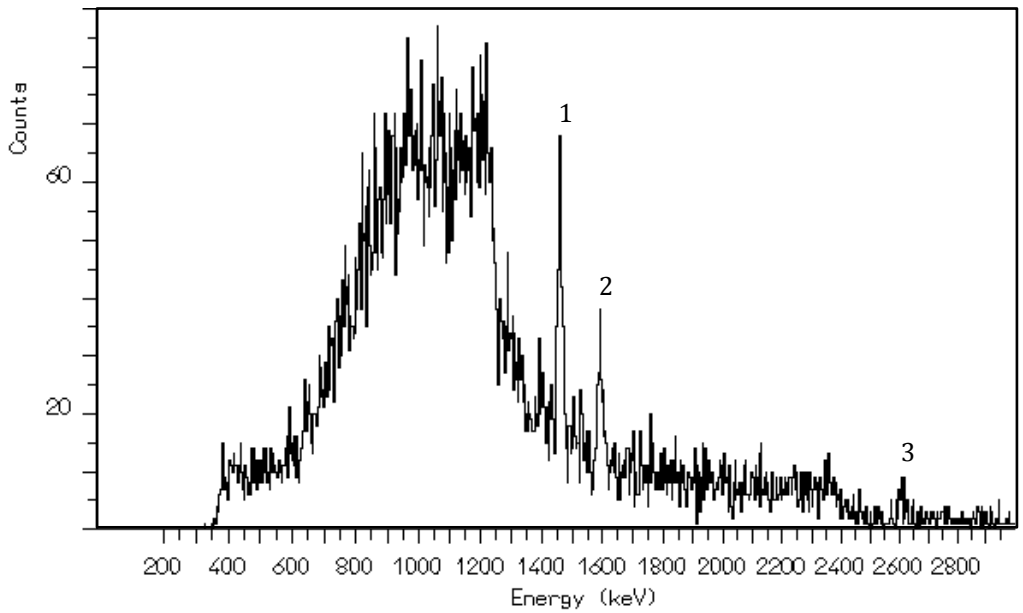

Figure 7-17. Calibrated γ spectrum of ZnSe bolometer. The three numbered peaks correspond to the 1460 keV line of ^{40}K (1), the 1590 keV line of ^{208}Tl double escape (2) and the 2615 keV line of ^{208}Tl (3).

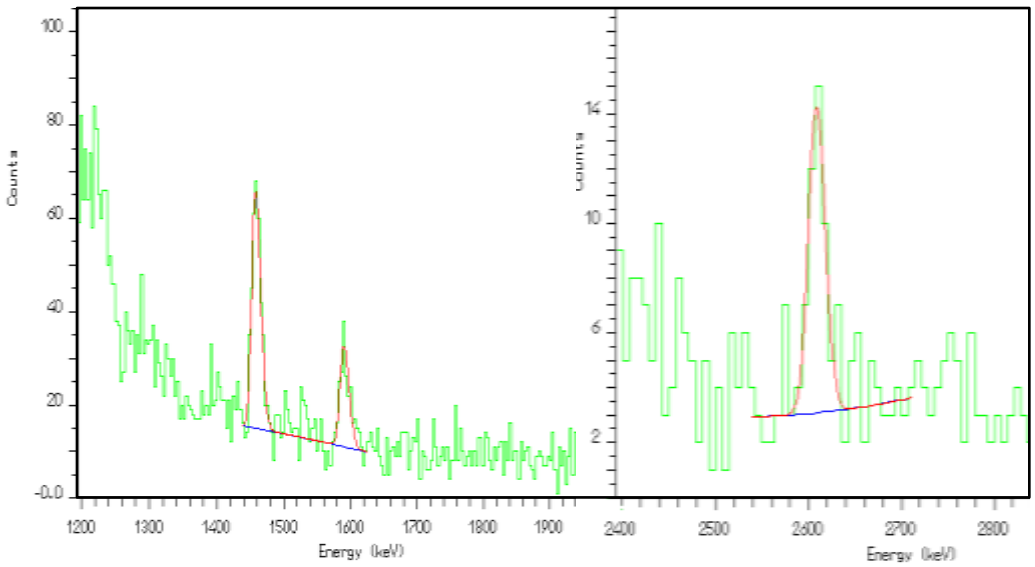

Figure 7-18. Fits of the three identified lines: ^{40}K, ^{208}Tl double escape and ^{208}Tl. The FWHM of each peak is reported in Table 7-9.

Peak	Energy [keV]	FWHM [eV]	Error on FWHM [eV]
^{40}K	1459.0	14.5	1.2
^{208}Tl double escape	1591.0	14.5	1.2
^{208}Tl	2609.6	18.6	5.4

Table 7-9. Calibration of the heat channel. The energy value and the energy resolution are obtained from the fit shown in Figure 7-18.

The voltage pulse at the ^{40}K peak energy is 58.4 mV: considering that it is amplified by electronics with a gain of 1931 (see Table 7-7), the pulse height is then 20.7 μV/MeV (one order of magnitude less than for a typical TeO_2 5x5x5 cm^3 crystal, as shown in Section 5.4.2); using Eq. 3-6, being the logarithmic sensitivity at the operation point A=5.55, it is possible to extract the temperature rise corresponding to an energy deposition of 1460 keV: ΔT=2.29 mK. From this the heat capacity can be obtained in a naïve way as $C=\Delta E/\Delta T=1.02\cdot10^{-10}$ J/K.

From the theoretical point of view, the expected lattice heat capacity for ZnSe at 32 mK is $2.84\cdot10^{-11}$ J/K (using Eq. 2-11 and data from Table 7-5), to be summed with the heat capacity of the thermistor: as seen in Section 3.5, $c(T) = 1.1\cdot10^{-9}\cdot T[K]$ [J/(K·mm^3)], leading to 6.34×10^{-11} J/K at the working temperature. The total expected heat capacity is therefore $9.18\cdot10^{-11}$ J/K, very close to the roughly deduced one, on the base of experimental parameters: this is well symptomatic of a good thermalization of the crystal.

For what concerns the energy resolution, the peak FWHM can be confronted with the theoretical resolution achievable with the OF, which is 0.271 μV FWHM for the frequency interval up to 125 Hz (the Bessel cut-off frequency) and corresponds to 13 keV; the two values are compatible, indicating that at this level, no further contribution worsening the energy resolution is observable, such as trapping mechanisms in the crystal.

7.4.1.3. Rejection efficiency and quenching factor

According to the calibration, the 0νββ peak of ^{82}Se, which is expected at 2995 keV, corresponds to about 120 mV for the amplitude on the heat channel scale. As can be seen from Figure 7-13, the discrimination power between α and β is extremely good in that region. In the attempt of quantifying the discrimination power, the β/γ band in the heat-light scatter plot (the green one in Figure 7-23) has been fitted with a line. Using the fit parameters, for each amplitude of β/γ event measured by the heat channel the corresponding theoretical value on the light channel has been computed (a_t) and then this result has been divided for the data really collected by the light channel (a_s). Still using the same parameters, the calculation has been repeated for the α events.

Plotting the value of the ratio a_s/a_t versus the amplitudes collected by the heat channel (Figure 7-19), it appears that the α and β/γ events are grouped around two well separated lines almost parallel to the x-axes (red and green point, respectively). The distribution of the two a_s/a_t index for the two kind of event is also plotted on the graphic (orange for αs and blue for β/γs). The central values of the two distributions are 9.2 for alphas and 0.89 for betas.

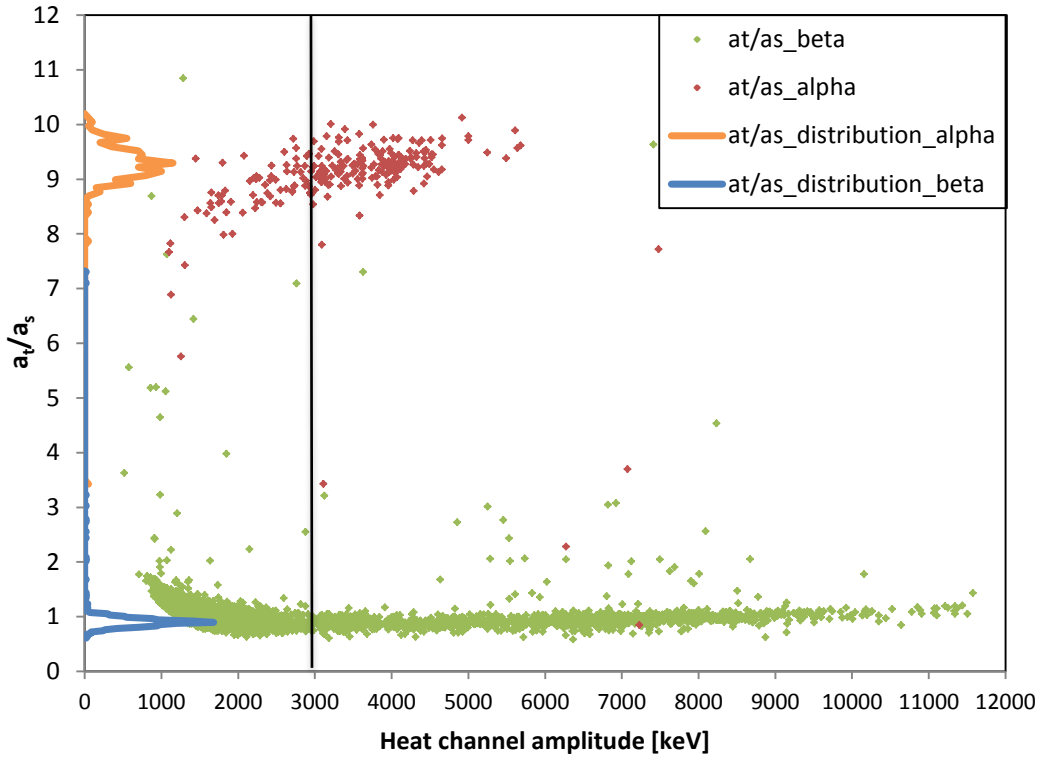

Figure 7-19. a_t/a_s index versus heat channel amplitude and a_t/a_s index distribution for α (red dot and orange line) and β/γ event (green dot and blue line). The central limits of the $(a_s/a_t)_\alpha$ and $(a_s/a_t)_{\beta/\gamma}$ distributions are 9.2 and 0.89 respectively. The vertical black line indicates the energy value corresponding to the 0νββ peak of ^{82}Se.

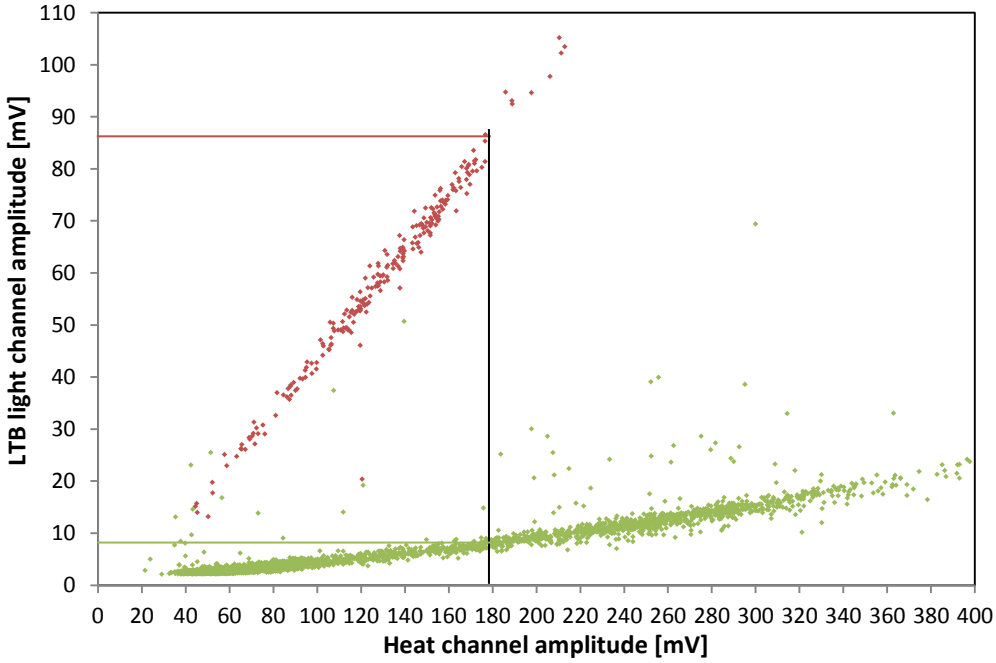

Figure 7-20. Rough identification of the alpha end-point, corresponding to 4.2 MeV, and, as a consequence, of the QF from the LTB-ZnSe coincidence plot.

The ratio of the central values of the distributions of the a_s/a_t index for beta and alpha results in QF~9. It is confirmed also by the scatter plot of heat-light amplitudes: because of the absence of alpha-peaks, the 4.2 MeV end-point of the alpha region, corresponding to 180 meV, will be used for evaluating the quenching factor. The resulting QF is the same value found out with the same crystal in a previous underground run. The result excludes QF dependence on the detector configuration and on the coating of the germanium slabs, which in other cases were darkened through the deposition of a 600 Å layer of SiO_2 on the surface facing the scintillating absorber.

7.4.2. ZnSe-Ge underground: the LNGS run

The ZnSe-Ge detector was cooled down in the 1K-pot fridge of Hall C at LNGS during Summer 2010 at a base temperature of 18 ~mK, to confront its performances with the previous aboveground measurement and in particular to verify possible dependence of the QF on the temperature. Unfortunately, the electrical contact to the heater was lost during the cooling down, making impossible to perform a stabilization of the measurement, neither a static characterization; the working point was chosen after acquisition and comparison of several background spectra.

The data were acquired for 40 hours, with 4 kHz sampling frequency and 12 Hz Bessel cut-off frequency; the trigger was set independently on each channel, with a 10 mV threshold on the heat channel and 17 mV threshold on the light channels. All the details of this run are given in (168).

The acquisition parameters and the working point for each detector are collected in Table 7-10. Here, a huge discrepancy between the temperatures of the two light detectors appears, the LTD's resistance being one order of magnitude smaller than LTB's. Indeed, all over the data-taking, the LTD appeared severely affected by noise, making its data totally unusable for the analysis.

Channel	R_{Load} [MΩ]	Bessel cut off freq [Hz]	Gain	R_{work} [MΩ]	T_{work} [mK]
ZnSe	54	12	3237	5.90	20.7
LTB	54	12	7520	30.7	16.6
LTD	54	12	8217	0.92	27.7

Table 7-10. Electronic parameters and temperatures for the three thermistors in the underground measurement of the ZnSe-Ge detector: ZnSe is the heat channel from the scintillating crystal, while LTB and LTD are the light channels from the two Ge-slabs named B and D respectively. The temperatures were calculated with the doping parameters from the 34B series derived in Chapter 4 (see Table 4-24).

This behaviour (and the loss of the heater) is probably the consequence of a corruption of the detector during transport and mounting operations at LNGS. The different detector performances can be clearly seen in Figure 7-21, where the amplitudes of the light-heat coincidence events are plotted.

7.4.2.1. Event Discrimination

For each detector channel, the collected data have been cleaned from spurious coincidence by mean of cuts on the shape parameters. Then, the analysis of the shape parameters of the survived light detector allows the alpha-beta/gamma event discrimination on the heat channel.

The discrimination can be carried out from the pattern in the test value versus amplitude plot of light channel: the long horizontal band in the Figure 7-22 corresponds to alphas, while the big spot denotes the β/γ events, and the remaining are the pure ionization events, as highlighted in Figure 7-23.

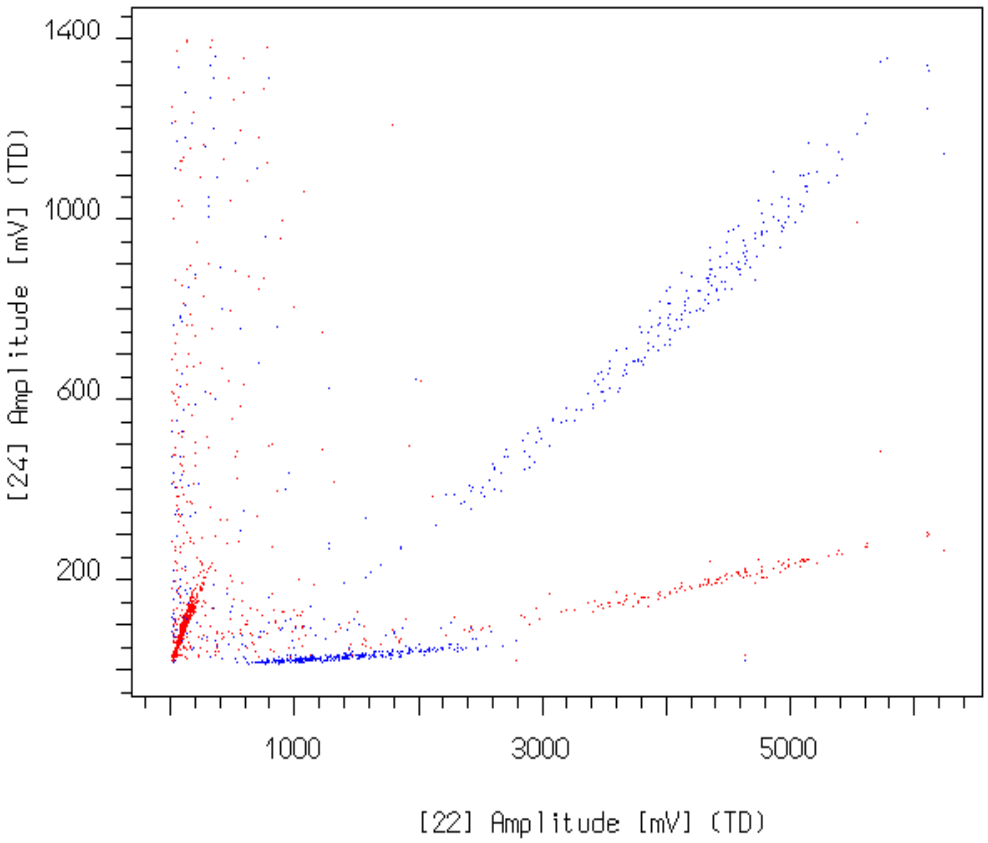

Figure 7-21. Light versus heat of both Ge-slabs: LTB in blue and LTD in red. The performances of the two detectors are very different from each other; in particular, the LTD is strongly affected by noise and pile-up.

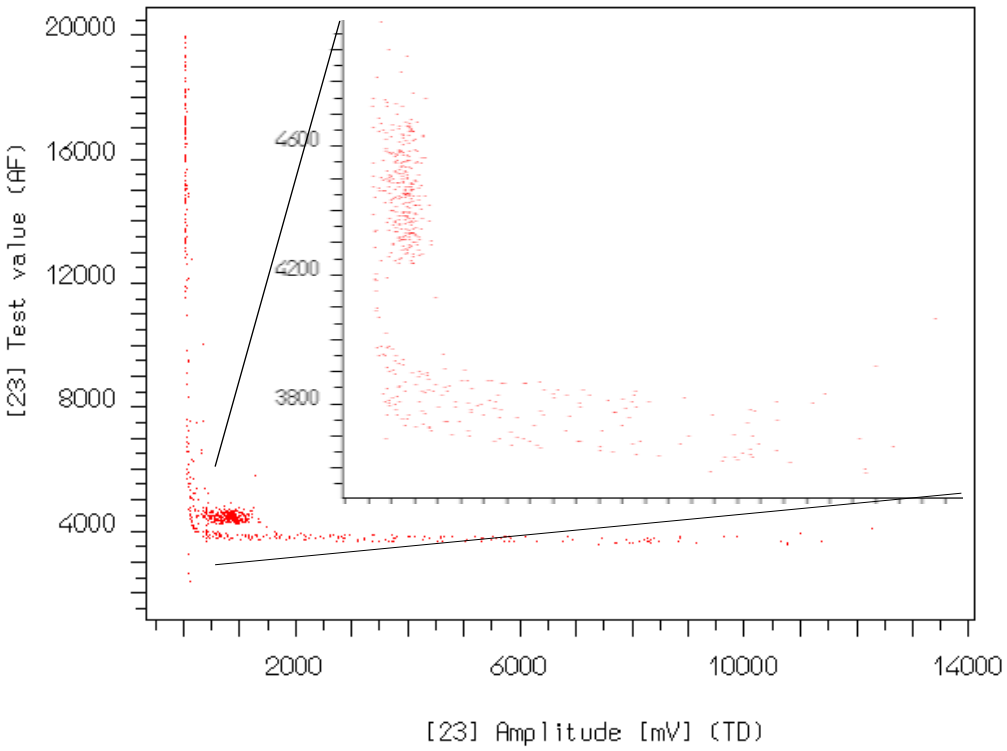

Figure 7-22. Test value (AF) versus amplitude for the LTB light detector. The test value band below 4000 corresponds to alphas, while the big spot between 4200 and 4800 identifies the β/γ events.

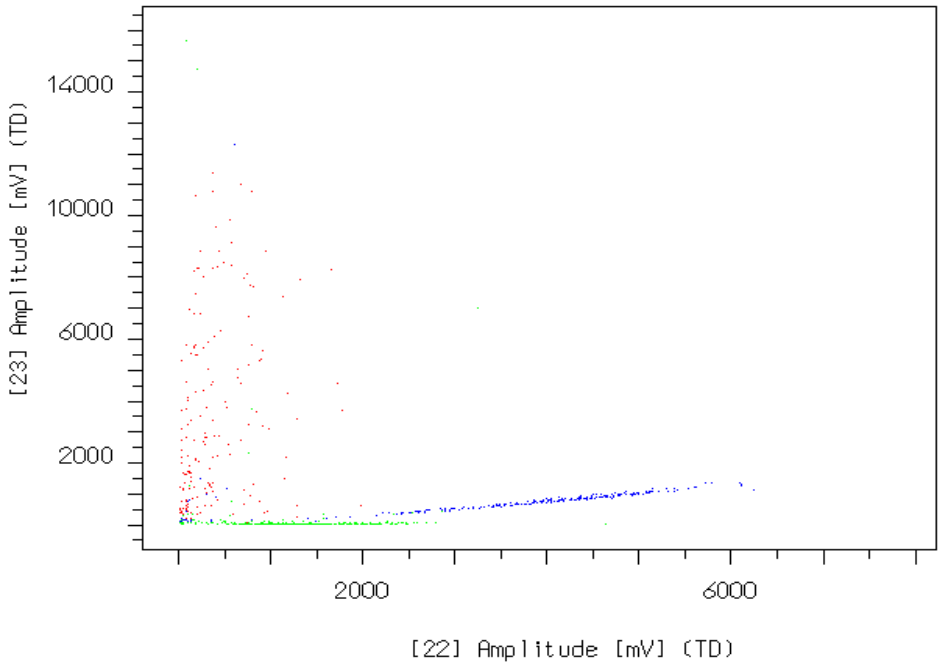

Figure 7-23. Heat and light coincidences: β/γ events (green) are identified by the cut between 4200 and 4800 on the Test Value of the LTB light channel; alpha events (blue) correspond to the Test Value below 4000 and the remaining are the pure ionization events (red).

Similar results can be obtained using the Test Value Right or the decay time of the light channel: in both cases the three families of events are recognizable and identifiable into the light-heat coincidence plot. Also in this measurement the QF results to be around 10, even if the operating temperature of the detector was about 10 mK lower with respect to the aboveground run: this exclude possible temperature dependence of the QF values.

7.4.2.2. Light Detector

The trigger configuration allowed to identify the ^{55}Fe events exploiting the anticoincidence method: in fact the source is placed in front of the Ge slab and it is completely absorbed by the light detector, so by setting a time anticoincidence of 1 ms between the light and the heat channel permits to discern the pure LTB events.

The amplitude spectrum of the LTB light channel is displayed in Figure 7-24: in blue the anticoincidence events are plotted without cuts; the red spectrum corresponds to a cut on TVR (TVR<17.5) is applied, in order to discard the noise contribution; in green the spectrum of events in coincidence with the heat channel is showed for a comparison, confirming that radiation from the ^{55}Fe source is entirely absorbed by the light detector.

The two peaks appearing in Figure 7-24 corresponds to ^{55}Fe K-lines (see Table 7-3). An energy calibration has been performed (Figure 7-25) to obtain the value and the FWHM of the peaks. The results are collected in Table 7-11. The energy resolutions are compatible with the standard range usually measured for light detectors in previous tests (216), indicating a good quality of the light detector. The calibration of the light channel allows calculating relative LYs, not corrected for the photon collection efficiency, which is very difficult to estimate. In a very rough approximation, taking the end-point of the α region at the 4.2 MeV energy of the uranium source and the γ end-point of natural radioactivity at the 2615 keV of the ^{208}Tl peak, the relative LY for alphas is about 20.5 keV/MeV, while for β/γs it is around 1.6 keV/MeV, yielding a QF of about 12. Considering the approximations on the end-points, the relative LY_{α} and $LY_{\beta/\gamma}$ are compatible with the values of 3 keV/MeV and 40 keV/MeV obtained in the previous test of the same ZnSe crystal, taking into account that the LYs in the present case are reduced to one half, as the light detectors are two instead of one.

Peak	Energy [keV]	FWHM [keV]	Error on FWHM [eV]
K_{α}	5.80	0.54	16
K_{β}	6.48	0.54	16

Table 7-11. Peaks and energy resolutions from the fit of the ^{55}Fe spectrum collected with the light detector.

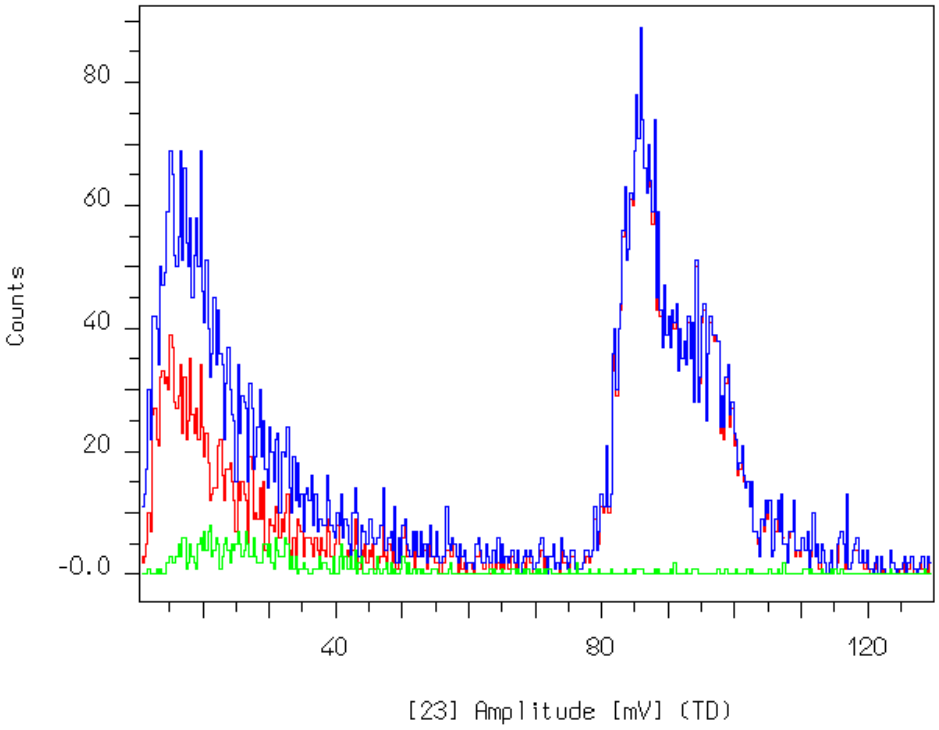

Figure 7-24. Amplitude spectrum of the LTB light detector with 1 ms anticoincidence with the heat channel; the blue shape is the entire spectrum (no cuts), while in the red case a cut on the light detector TVR < 17.5 is applied. The green shape corresponds to the coincidences with the heat channel: the absence of the peak in the latter case shows how the whole ^{55}Fe contribution is detected by the light detecting slab.

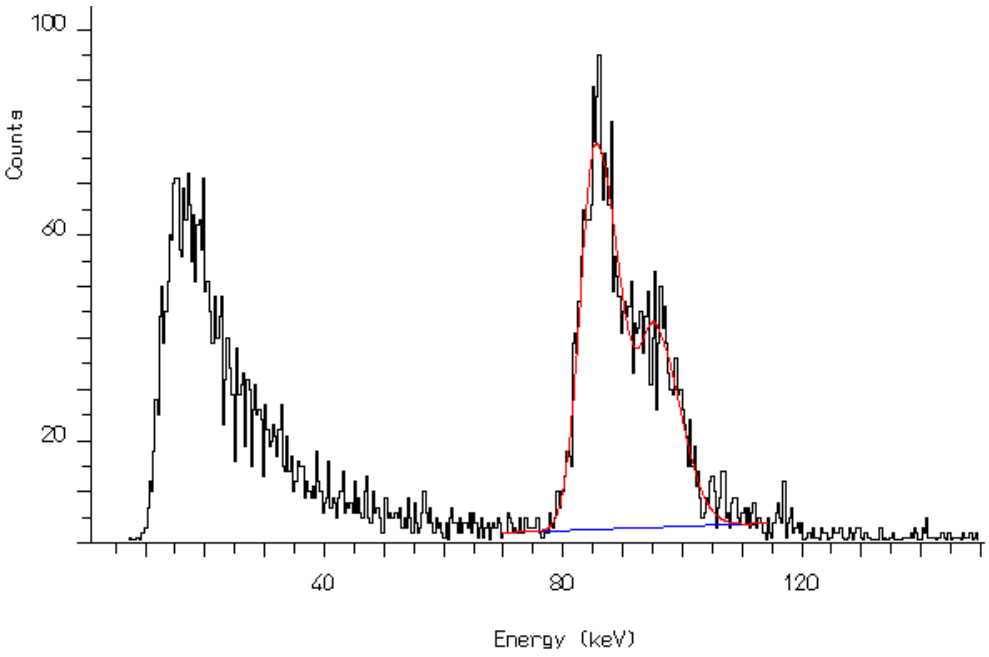

Figure 7-25. Energy spectrum of LTB and fit of the ^{55}Fe X-ray peaks.

Channel	R_{Load} [MΩ]	Bessel cut off freq [Hz]	V_{bias} @ working point [V]	Gain	R_{work} [MΩ]	T_{work} [mK]
ZnSe	200	125	1.187	1931.0	0.31	33.5
LT3	200	125	1.979	9971.8	0.35	32.7
LT4	200	160	0.600	9971.8	0.62	29.6

Table 7-12. Electronic parameters and temperatures for the three bolometers in the ZnSe-Si detector: ZnSe is the heat channel from the scintillating crystal, while LT3 and LT4 are the light channels from the two Si-slabs. The temperatures were calculated with the doping parameters from the 34B series derived in Chapter 4 (see Table 4-24).

7.5. ZnSe-Si detector

The purpose of this cool-down is just to evaluate the efficiency of the Si slab in detecting the light from the ZnSe and to confront the result with the one for the Ge slabs. Therefore only a short measurement (~14 h) with the trigger on the heat channel has been taken. The instabilities of the cryogenic setup (see Figure 7-26) did not really affect the data taking. The details of the channel configuration are given in Table 7-12.

The two light detectors show different behaviours, as can be seen from their load curves in Figure 7-27, confirming the problem in the connection of the small slab with the holder. Only the best Si light detector is used in the comparison with the Ge light detector.

The scatter plot of the light versus heat amplitude of the ZnSe-Si detector is displayed in Figure 7-28, with the β/γ-events well separated from the α-events. The identification of the 4.2 MeV end point of the alpha radioactivity at ~40 mV, besides calculating the QF, allows determining how differently the light output of the ZnSe scintillating crystal is detected by the Si or Ge slabs.

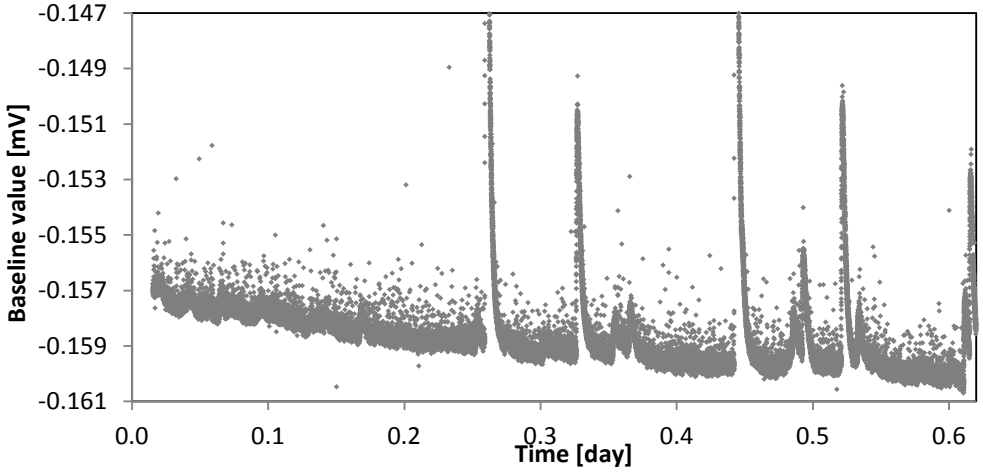

Figure 7-26. Baseline level versus time for the heat channel of the ZnSe-Si detector, showing the temperature instabilities during the measurement.

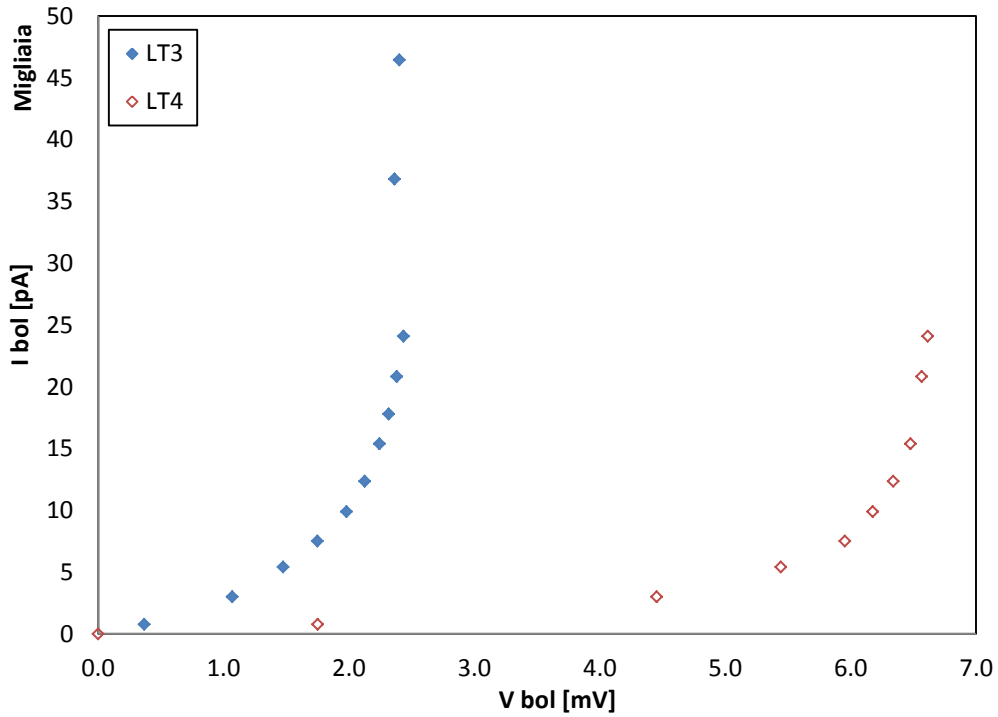

Figure 7-27. Static characterization of the two light channels of the ZnSe-Si detector, named LT3 and LT4.

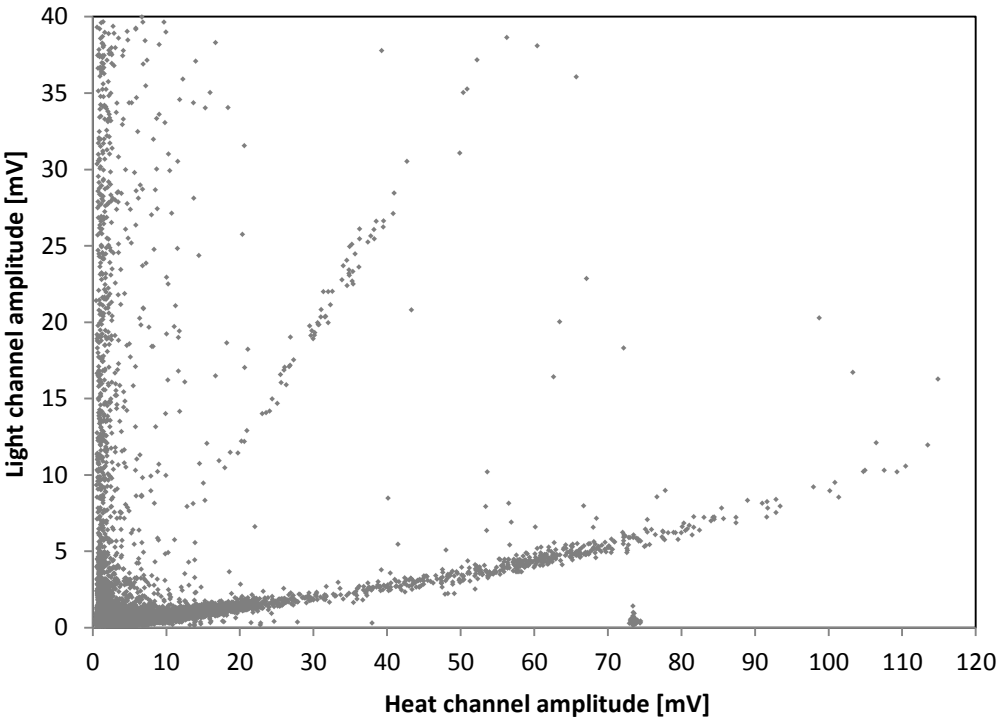

Figure 7-28. The amplitude of the heat channel versus the sum of the amplitudes of the two light channels for the ZnSe-Si detector.

The ratio of the Si and Ge light channel amplitude corresponding to 4.2 MeV, divided by the gain (see Table 7-7 and Table 7-12), for both β/γ and α particles is:

$$\frac{(LightAmpl/Gain)_{Si}}{(LightAmpl/Gain)_{Ge}} \cong 0.1. \qquad 7\text{-}7$$

This result confirms how the Ge slabs are better light detector than the Si slab.

7.6. $ZnMoO_4$-Ge detector

The 15×15×5 mm^3 $ZnMoO_4$ crystal produced at Novosibirsk with two Ge slab previously used in ZnSe-Ge detector has been cooled down in December 2010 to a base temperature of ~22 mK. The details about the electronic system and the detector working point are given in Table 7-13.

The cryostat showed in several instabilities during the run (that are appreciable in the plot of the baseline versus time for the heat channel for one of the measurement set chosen for the data analysis, reported in Figure 7-29) and the cool down ended with a suddenly warm up during the data taking for the light channel calibration (see Figure 7-41). For this reason just one measurement was taken having the trigger on one light detector (LTD). The details of the measurements selected for the data analysis are collected in Table 7-14.

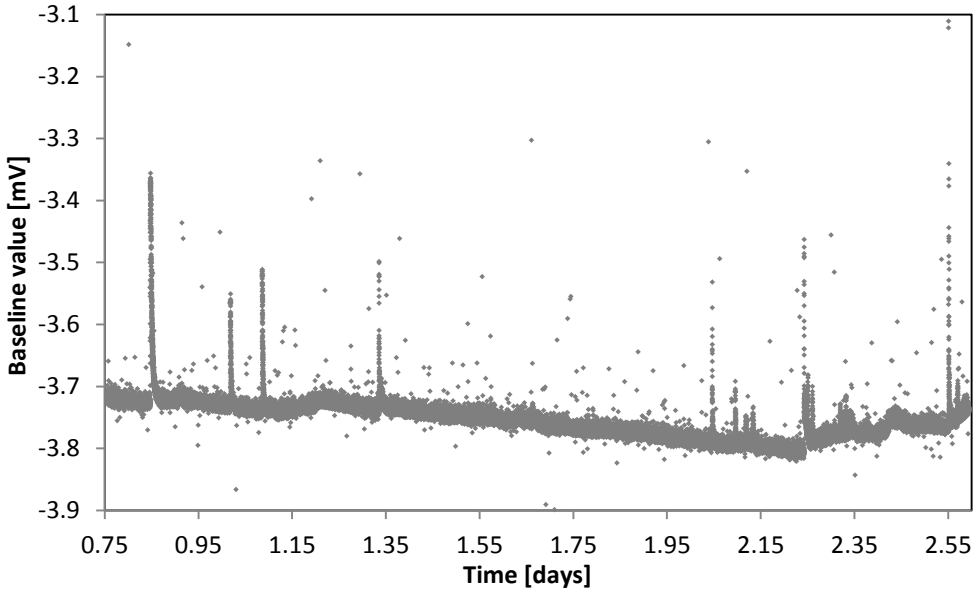

Figure 7-29. Baseline level versus time for the heat channel of the $ZnMoO_4$-Ge detector. The spikes denote the sudden warm-up of the cryostat.

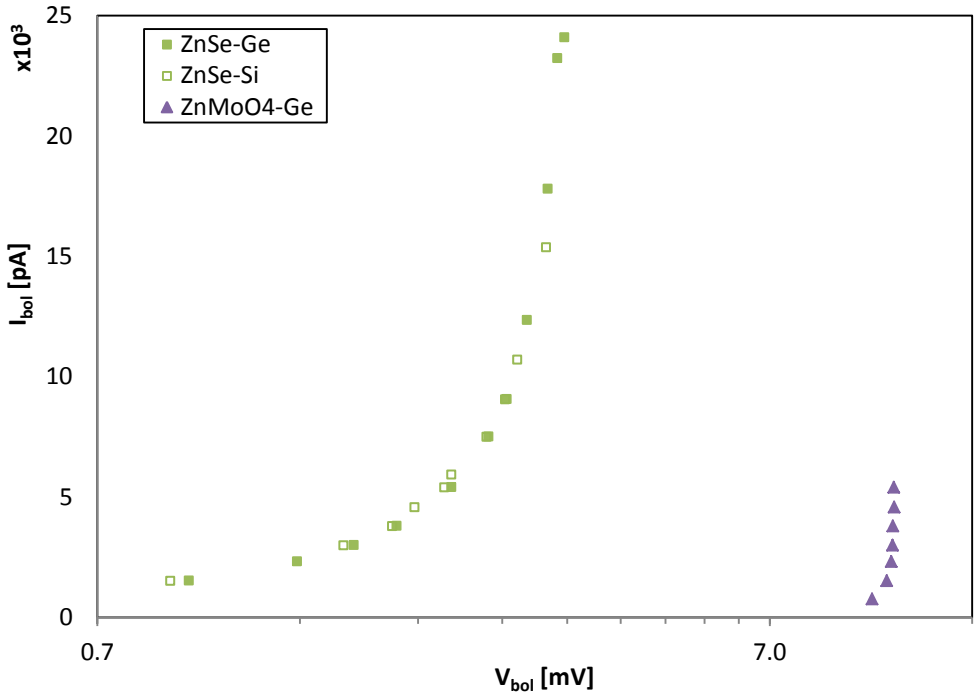

Figure 7-30. Load curves of the scintillating crystals. The ZnSe behaviour is constant among the different cool-downs (ZnSe-Ge and ZnSe-Si) while a huge difference appears between the two crystal measured in the same run (ZnSe-Si and $ZnMoO_4$-Ge).

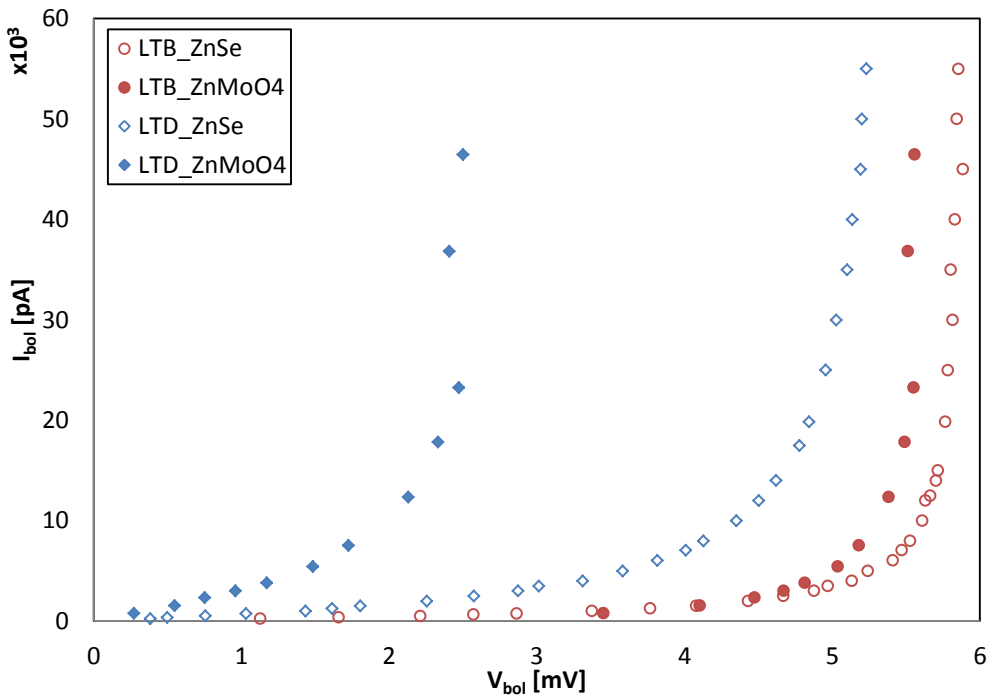

Figure 7-31. The static characterization of the two light detectors of $ZnMoO_4$-Ge (solid points) is compared with the results obtained for the ZnSe-Ge detector (empty points): the load curves of LTB light detector are quite similar among the two runs, but the behaviour of LTD Ge-slab varies a lot.

Channel	R_{Load} [MΩ]	Bessel cut off freq [Hz]	V_{bias} @ working point [V]	Gain	R_{work} [MΩ]	T_{work} [mK]
$ZnMoO_4$	200	125	0.304	1931.0	7.25	20.3
LTB	200	125	1.502	3304.3	2.70	23.3
LTD	200	125	0.304	3304.3	0.23	35.5

Table 7-13. Electronic parameters and temperatures for the three thermistors in the $ZnMoO_4$-Ge detector: $ZnMoO_4$ is the heat channel from the scintillating crystal, while LTB and LTD are the light channels from the two Ge-slabs named B and D respectively. The temperatures were calculated with the doping parameters from the 34B series derived in Chapter 4 (see Table 4-24).

Triggering channel	Full Scale [V]	Measurement duration [h]
$ZnMoO_4$	10	44.4
LTD	4	74.2

Table 7-14. Trigger configuration for the best data set of the aboveground measurements of $ZnMoO_4$-Ge.

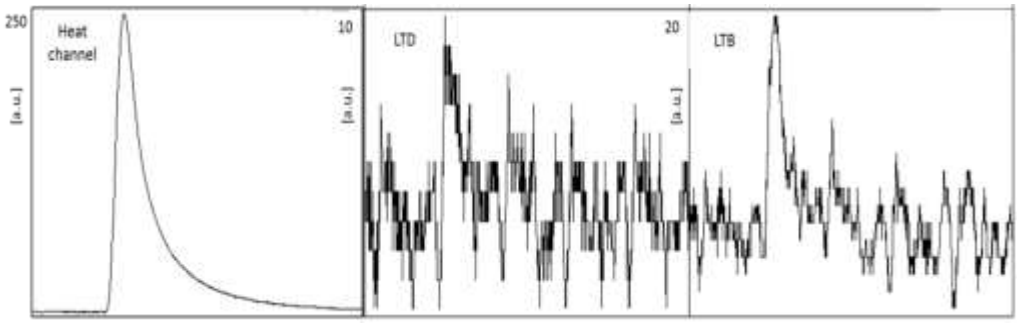

Figure 7-32. Example of coincident pulses collected with the $ZnMoO_4$-Ge detector. The pulse on the heat channel is about three times higher than the same event on the light channels, which are not identical, being one slightly smaller. The pulses time scale is 50 ms.

An example of coincident pulses on all channels is reported in Figure 7-32. The pulses on LTD appear to be smaller than the one from LTB. The inhomogeneity in the behaviour of the light detectors is confirmed by looking at the load curves (Figure 7-31), which are very different from one detector to another and also with respect to the previous run where LTB and LTD Ge-slab were used. This points out a problematic in the assembly of the light detectors probably due to the way they are mounted on the copper frame.

As it appears confronting its working point and its load curve with the ones of the other bolometers present in the cool-down (Figure 7-30) the $ZnMoO_4$ crystal seems to be very cold. This discrepancy of the detector temperature can be due to extreme different thermal contraction between the crystal and its NTD.

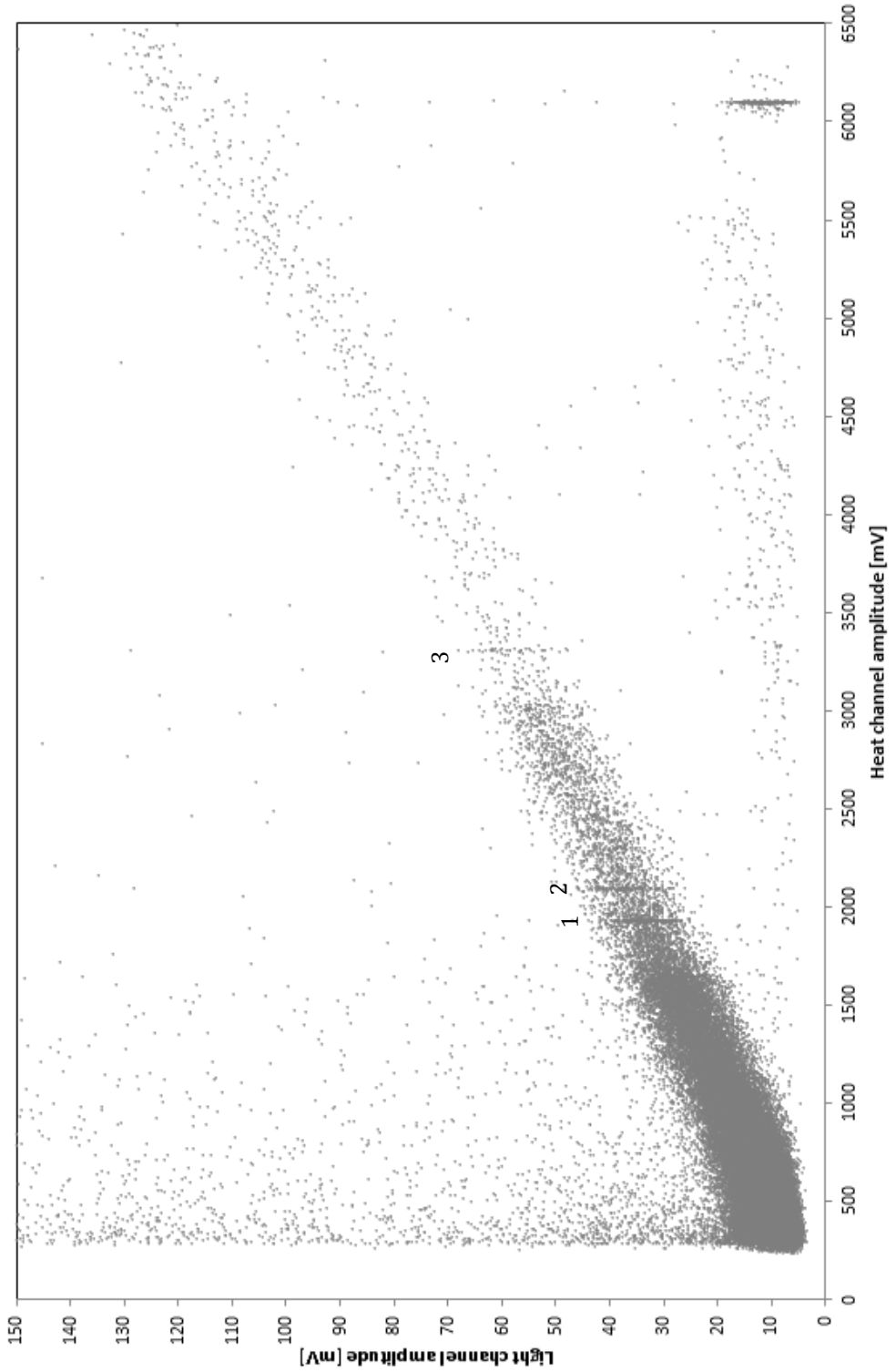

Figure 7-33. The amplitude of the heat channel versus the sum of the amplitudes of the two light channels for the $ZnMoO_4$-Ge detector. The separation between alpha and beta/gamma events is clearly visible. Three lines of natural radioactivity are evident: the 1640 keV of ^{40}K (1), the 1592 keV of ^{208}Tl double escape (2) and the 2615 keV of ^{208}Tl (3). The line at the end of the alpha region represents the pulser events.

7.6.1.1. Event identification

Differently from the ZnSe-Ge detector, the $ZnMoO_4$-Ge doesn't show any correspondence between shape parameters on the light channel and different event type (beta/gamma or alpha). It is therefore possible to sum the contribution of the two light channels and plot the result versus the amplitude of the heat channel, as shown in Figure 7-33, after the removal of some spurious events. The discrimination between α and β/γ particles is clearly visible, even if the $ZnMoO_4$ resulted to be a poor scintillator: two different bands are distinguishable, even if part of them are the result of random triggers.

Looking at the pulse shape parameters on the heat channel, what comes out is that, besides removing unwanted events (such as the heater signals, thanks to a cut on decay time - Figure 7-34), they can be used for discriminating β/γ and α pulses; in particular the Test Value resulting from the application of the Adaptive Filter technique (see Figure 7-35 and Table 7-6) allows to identify different event families. These correspond to α events (48<AF<56) and β/γ plus ionisation events (AF>56). Because of the shape of the AF parameter when plotted versus the amplitude, a precise distinction between beta/gamma and ionisation event is possible only for amplitude on the heat channel higher than 1800 mV (that corresponds to energy higher than 1400 keV, as derived in the next Section).

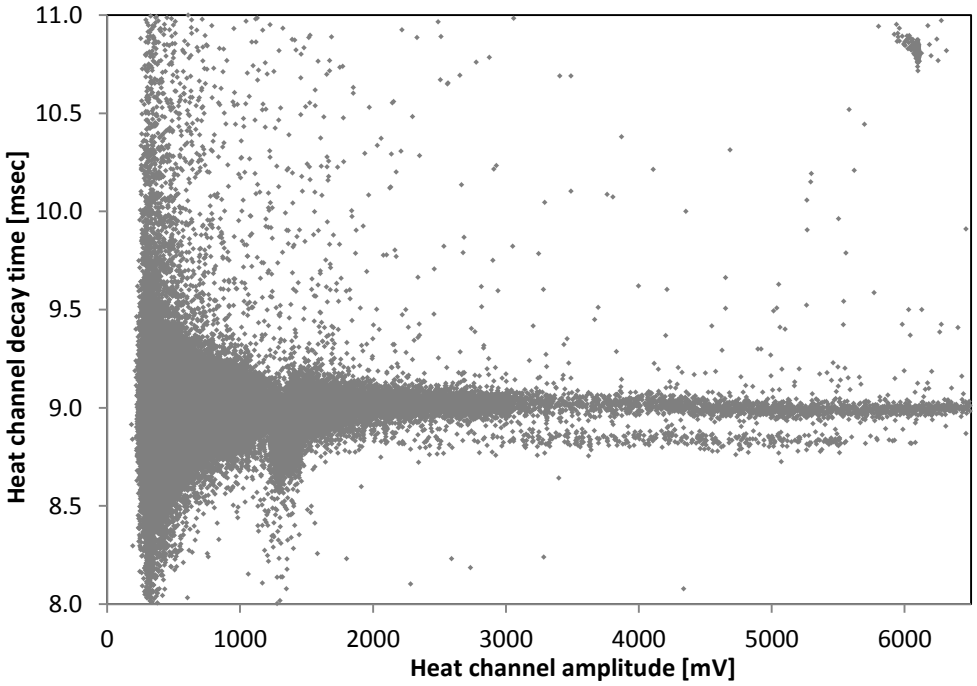

Figure 7-34. Decay time versus amplitude of the pulses detected on the heat channel. The two parallel lines correspond to beta/gamma (above) and alpha (below) events. The collection of points in the upper right corner of the plot corresponds to the pulser events: a cut on the decay time can exclude these signals from the light versus heat scatter plot.

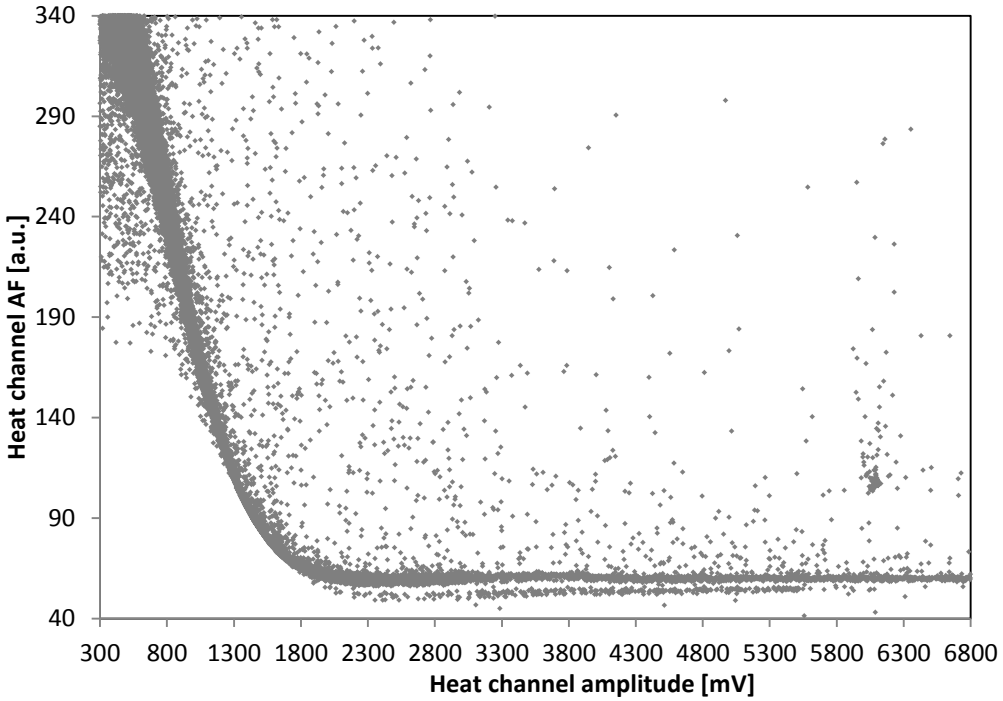

Figure 7-35. The shape parameter AF (see Table 7-6) versus the amplitude of the pulses collected on the heat channel. The two lines denoting beta/gamma and alpha events are clearly distinguishable.

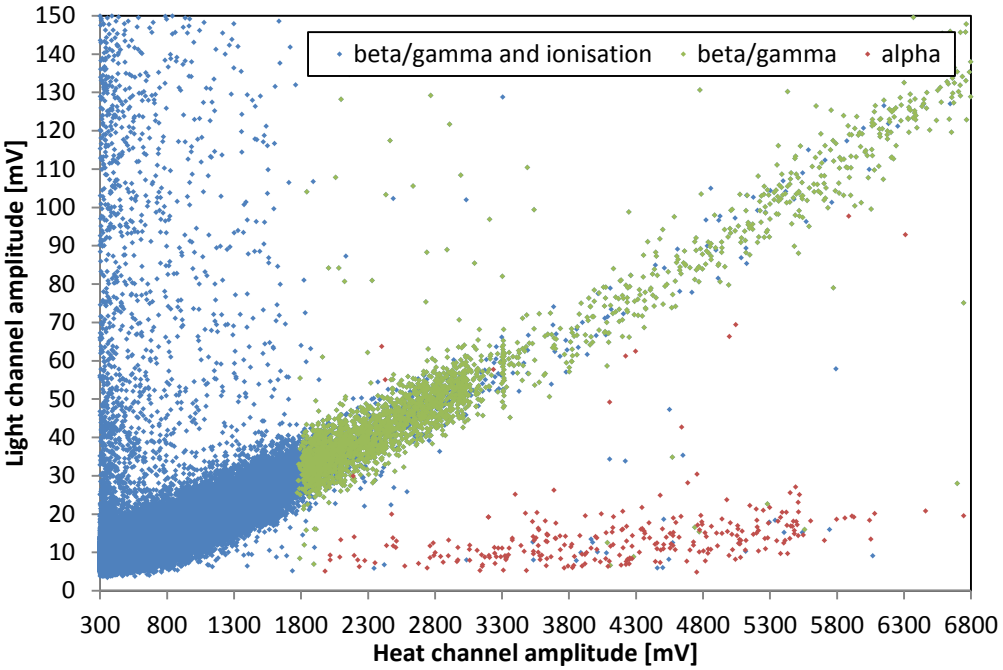

Figure 7-36. Plot of $ZnMoO_4$-Light coincidences: alpha events (in red) are discriminated from residual pure ionizing and β/γ events (in blue) thanks to the cuts on the AF of heat channel. The green dots correspond to the β/γ events alone.

7.6.1.2. Energy calibration of the heat channel

In the background spectrum collected for the heat channel ^{40}K and ^{208}Tl double escape are were easily identifiable and usable to perform a calibration with a quadratic polynomial (Figure 7-37). Then other peaks are identified, all belonging to the Thorium chain, and the corresponding energy resolutions are obtained from fitting and collected in Table 7-15. There is no correction of the non-linearity of the spectrum. As for the ZnSe-Ge detector, no alpha peaks are visible.

7.6.1.1. Rejection efficiency and quenching factor

According to the calibration, the 0νββ peak of ^{100}Mo, which is expected at 3034 keV, corresponds to about 3800 mV for the amplitude on the heat channel scale. As can be seen from Figure 7-13, the discrimination power between α and β is extremely good in that region, and the problem in the distinction of ionisation event from β/γ events doesn't affect the identification of the two classes of event. Again, as in the case of the ZnSe-Ge detector, for quantify the discrimination power, the β/γ band in the heat-light scatter plot above 1300 keV (the green one in Figure 7-23) has been fitted with a line and, using the fit parameters, the ratio between the theoretical an real value of the light channel amplitude (a_s/a_t) has been calculated for both alpha and beta/gamma events. The $(a_s/a_t)_{\beta/\gamma}$ and $(a_s/a_t)_{\alpha}$ ratios versus the amplitudes collected by the heat channel are displayed in Figure 7-39 together with the distribution of the two a_s/a_t index (orange for αs and blue for β/γs). The central value of the $(a_s/a_t)_{\alpha}$ distribution is 0.14 while it is 0.99 for the $(a_s/a_t)_{\beta/\gamma}$ distribution. The ratio of the two central values results in a QF~0.14. It is confirmed also by the scatter plot of heat-light amplitudes: because of the absence of alpha-peaks, the 4.2 MeV end-point of the alpha region, corresponding to 5300 meV, will be used for evaluating the quenching factor. This result confirms what already observed with $ZnMoO_4$ scintillating bolometers (Table 7-2).

Peak	Expected energy [keV]	Energy [keV]	FWHM [keV]	Error on FWHM [keV]
^{40}K	1460	1464.8	6.0	0.45
^{208}Tl double escape	1592	1591.0	6.0	0.45
^{208}Tl	510	529.0	3.8	0.48
^{208}Tl	583	602.4	3.8	0.48
^{214}Bi	609	628.5	3.8	0.48
^{208}Tl	2615	2511.2	3.8	1.12

Table 7-15. Identified peaks in the gamma spectrum of the $ZnMoO_4$ heat channel (see Figure 7-38). The first two lines refer to the peaks used for the calibration.

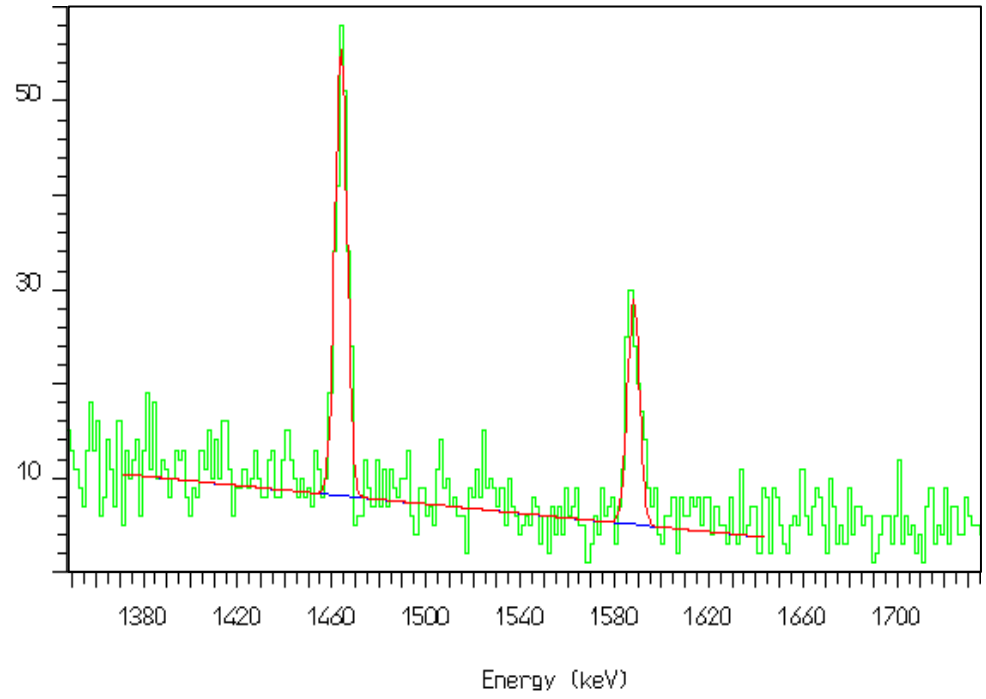

Figure 7-37. Fits of the ^{40}K and ^{208}Tl double escape peaks. The peak FWHMs are reported in Table 7-15.

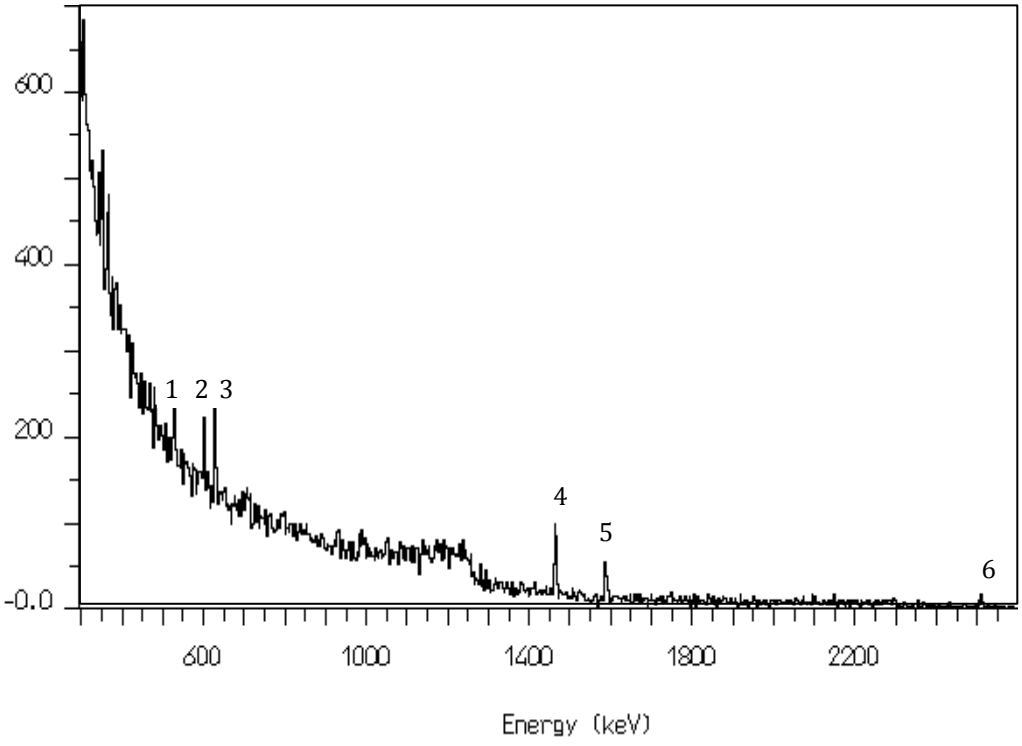

Figure 7-38. Calibrated γ spectrum of $ZnMoO_4$ bolometer. The numbered peaks correspond to: 510 keV (1), 583 keV (2), 1592 keV double-escape (5), 2615 keV (6) line of ^{208}Tl, the 609 line of ^{214}Bi (3), and the 1460 keV line of ^{40}K (5).

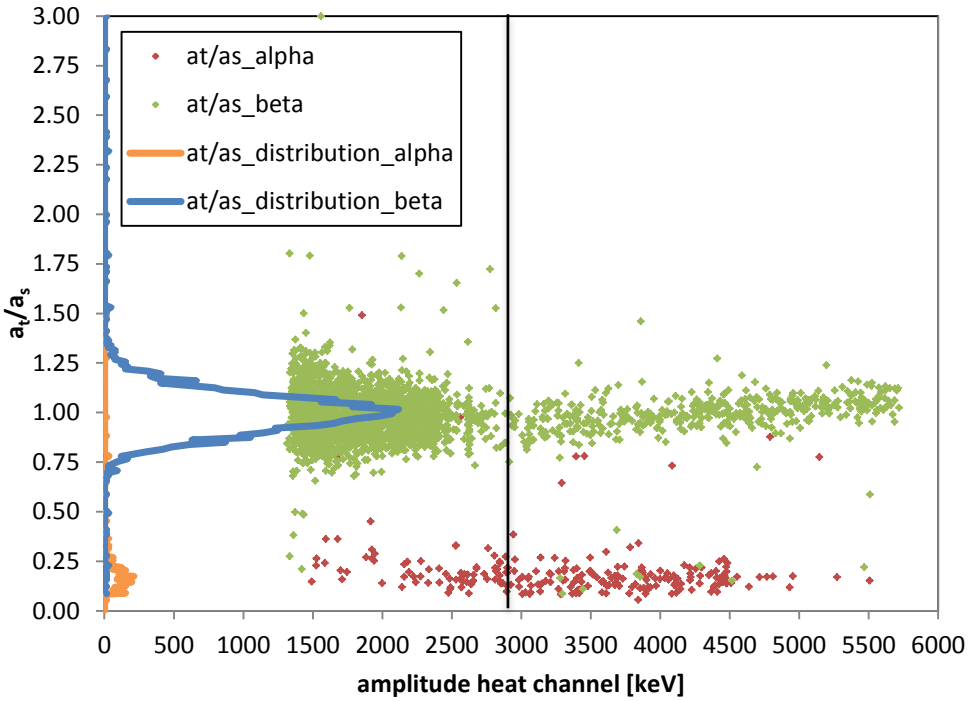

Figure 7-39. a_t/a_s index versus heat channel amplitude and a_t/a_s index distribution for α (red dot and orange line) and β/γ event (green dot and blue line). The central limits of the $(a_s/a_t)_\alpha$ and $(a_s/a_t)_{\beta/\gamma}$ distributions are 0.14 and 0.99 respectively. The vertical black line indicates the energy value corresponding to the 0νββ peak of ^{100}Mo.

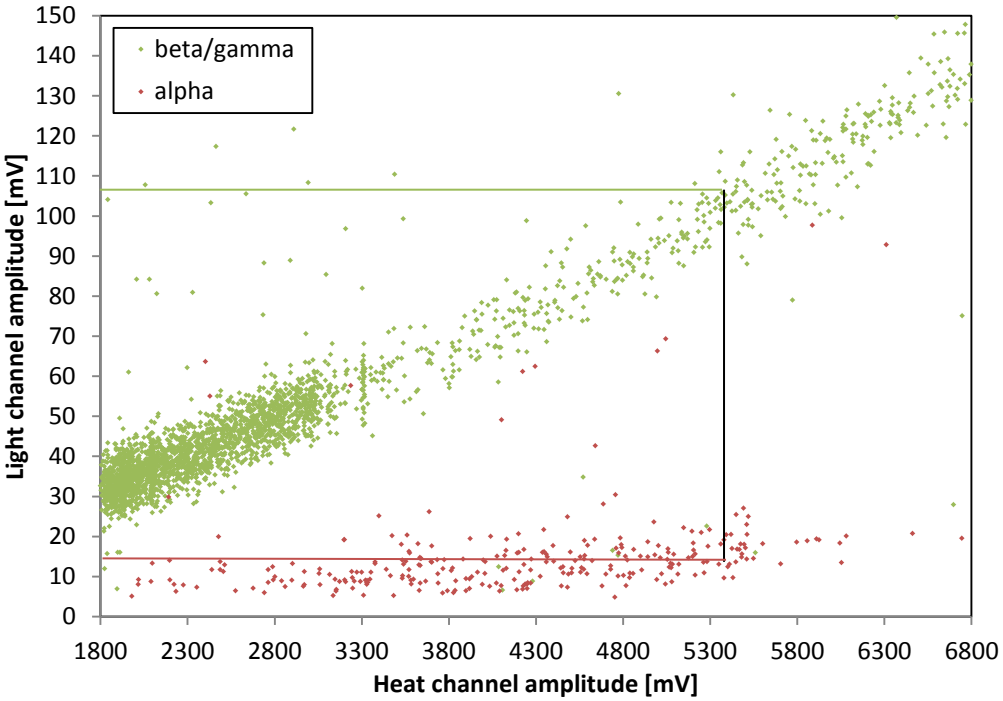

Figure 7-40. Rough identification of the alpha end-point, corresponding to 4.2 MeV, and, as a consequence, of the QF from the LTB-$ZnMoO_4$ coincidence plot. The resulting QF is about 0.14.

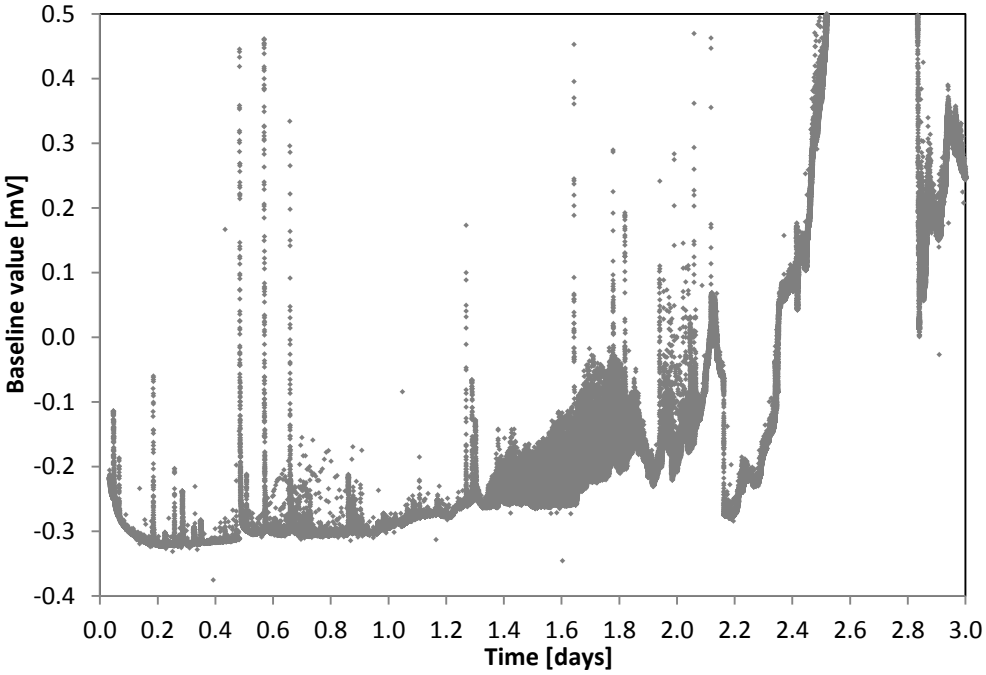

Figure 7-41. Baseline value versus time of the LTD light detector, showing the sudden warming-up of the cryogenic system occurred during the measurement.

7.6.1.1. Light detector

Because of the unwanted warming-up of the cryostat, it was possible to make just one measurement having the trigger on a light channel (LTD, i.e. the worst), but also the main part of that sample is unusable for the great instability of the baseline; the remaining data are not enough to obtain a clear background spectrum of the light channel, in which the ^{55}Fe peaks of the calibration source are identifiable (**Errore. L'origine riferimento non è stata trovata.**).

The LY of the $ZnMoO_4$-Ge has been obtained after another cool-down of the detector, without any modification, in a different cryostat (217). The resulting LY beta/gamma and alpha particles are 1.66 keV/MeV and 0.33 keV/MeV, respectively. These values, consistent with previous measurements, take into account the light collected by both light detectors (which is the same in each of them for the same event in the $ZnMoO_4$ crystal within the light detector energy resolution), but do not account for the light collection efficiency. Therefore, they have to be taken as an inferior limit.

CONCLUSIONS

The Ph.D. work presented in this thesis focused on the optimization of bolometric detector for the 0νββ decay search in the framework of CUORE-0/CUORE and LUCIFER experiments, investigating, in both cases, the elements constituting the core of the detector.

For the CUORE experiment, the attention was initially concentrated on the temperature sensor. A final characterisation of the CUORE-0 thermistors has been performed, allow fixing once for all the VRH parameters that determine the sensor resistance dependence on the temperature. The same characterisation was done also for the different CUORE NTD series leading to the identification of the best wafer among the ones suitable for CUORE. The performances of these thermistors in terms of signal formation have also been tested, pointing out a lack in the pulse height for the CUORE thermistors, as well as difference in the pulse shape with respect to the CUORE-0 and Cuoricino sensors. These discrepancies have not been understood yet and require a deeper investigation of the bolometric model of the CUORE detectors. Then a protocol, in terms of radio-purity, dimensions and crystallographic orientation, has been validated for the growth and surface treatment of TeO_2 crystal absorbers: the final results show how the radioactive contaminations of the CUORE crystals are very low: 1the upper limit for crystal bulk and surface contaminations are $.2 \cdot 10^{-4}$ and $3.5 \cdot 10^{-3}$ counts/(keV·kg·y) respectively. Finally, the realization of the thermistor-to-absorber coupling, which is limited by strong constraints, was studied thoroughly for an appreciable increase in its reproducibility among different detectors: the design of the semi-automated gluing line based on the guidelines defined here is now being completed at LNGS.

Regarding the LUCIFER detector, an experimental set-up has been developed for combining different scintillating crystals and light detectors and performing a direct comparison of their performances in terms of light yield and the discrimination capability between α and β/γ events. Ge and Si light detectors have been coupled to a well-known scintillating crystal, in order to select the one with best performances. ZnSe and $ZnMoO_4$ crystals, both containing a 0νββ candidate, have been also measured: in both cases a good discrimination between alpha and beta/gamma events has been achieved, demonstrating, in particular the feasibility of this kind of measures also in aboveground laboratories.

List of abbreviations

0νββ	Neutrinoless double beta decay
2νββ	Two-neutrino double beta decay
BR	Branching Ratio
CCVR	CUORE Crystal Validation Run
CTAL	CUORE Tower Assembly Line
CUORE	Cryogenic Underground Observatory for Rare Events
DBD	Double Beta Decay
E.Av.	ensemble average
E.St.D.	ensemble standard deviation
FFC	Flexible Flat Cable
GB	Glove Box
GERDA	GERmanium Detector Array
GUT	Great Unification Theory
HEM	Hot Electron Model
HM	Heidelberg-Moscow
HPGe	High Purity Germanium
IBM	Interacting Boson Model
ICP-MS	Inductively Coupled Plasma Mass Spectrometry
ISM	Interacting Shell Model
ITC-irst	Istituto Trentino per la Cultura-Italian Research Center on Semiconductors
LBL	Lawrence Berkeley Laboratory
LLNL	Lawrence Livermore National Laboratory
LNGS	Laboratori Nazionali del Gran Sasso
LTD	Low Temperature Detector
LUCIFER	Low-background Underground Cryogenic Installation For Elusive Rates
LY	Light Yield

m.w.e.	meters of water equivalent
MIT	Metal-to-Insulator Transition
MIT-NRL	Massachusetts Institute of Technology Nuclear Research Laboratory
MURR	Missouri University Research Reactor
NEMO	Neutrino Ettore Majorana Observatory
NME	Nuclear Matrix Elements
NTD	Neutron Transmutation Doping
OF	Optimum Filter
PMD	Phonon Mediate Detector
PMNS	Pontecorvo Maki Nakagawa Sakata matrix
QD	Quasi-Degenerated (hierarchy)
QF	Quenching Factor
QRPA	Quasi Random Phase Approximation
R&D	Research and Development
ROI	Region Of Interest
SBD	Surface Barrier Detector
SICCAS	Shanghai Institute of Ceramics Chinese Academy of Science
SM	Standard Model (Chap. 1) or Single Module (from Chap. 2 on)
SNO	Subdury Neutrino Observatory
ST	Semiconductor Thermistor
T.Av.	time average
T.St.D.	time standard deviation
TTT	Three Towers Test
TVL	Test Value Left
TVR	Test Value Right
UWP	Universal Working Plane
VRH	Variable Range Hopping

List of Figures

Figure 1-1. Measurement of the cross section of hadron production at the Z resonance. The curves show the expected cross section for two, three and for neutrino families coupled with Z in the SM, assumed neutrino mass to be negligible (16). 15

Figure 1-2. The ν_e survival probability $P(\nu_e \rightarrow \nu_e)$ (Eq. 1-3) in the 2-neutrino scenario as a function of the neutrino energy for L=180 km, $\Delta m^2=7.0\cdot10^{-5}$ eV^2 and $\sin^2 2\theta=0.84$ (32). 19

Figure 1-3. Three neutrino mass squared spectrum in case of normal (left) and inverted (right) hierarchy, with the estimation of the flavour components of each mass eigenstate, according to oscillations data (33). 20

Figure 1-4. Feynman diagrams for the 2νββ (a) and 0νββ (b) decay channels. In the latter, an antineutrino is produce at the vertex 1 and a neutrino is absorbed at vertex 2. 27

Figure 1-5. Spectra of the sum of the two electron kinetic energies, K_e: he 2νββ (dotted curve) is normalised to 1, while the 0νββ (solid curve) is normalised to 10^{-2} (10^{-6} in the inset, to underline the contribution of the 2νββ as a background to the 0νββ). All spectra are convolved with energy resolution of 5% (56). 28

Figure 1-6. 99% CL expected ranges as function of the lightest neutrino mass for mββ (here m_{ee}) using recent data from oscillation experiments. The green region corresponds to the inverted hierarchy ($m_{light} = m_3$) while the red one is for the normal hierarchy ($m_{light} = m_1$). The darker regions at the centre of both areas show how the ranges would shrink if the oscillation values were known with negligible errors (36). 29

Figure 1-7. 0νββ nuclear matrix elements calculated for some 0νββ candidates with the Microscopic Interacting Boson Model (IBM-2) (61), the Quasiparticle Random Phase Approximation (QRPA) in both renormalized QRPA (58) and proton-neutron QRPA (59) frameworks, and in a recent work taking into account nuclear deformation for the ^{150}Nd (62), and the Interacting Shell Model (ISM) (60). When a range is present, the central mark for each NME range indicates only the mean of the maximum and minimum values of the range, and is intended solely to guide the eye. The range limits are obtained identifying the minimum and the maximum NME values among the two NME ranges calculated with Jastrow and UCOM Short Range Correlation, and the central value is obtained averaging the range limits. All matrix elements are in dimensionless units. The three coloured bands highlight the isotopes considered in this PhD work. 30

Figure 1-8. Phase-space factors for some 0νββ candidates, calculated from the electron wavefunctions according to (63) with r_0=1.1 fm and g_A=1.25 for the blue-round series (Simkovic, (64), (65)) and with r_0=1.2 fm and g_A=1.25 for the green-square series (Suhonen-1998, (66)); the yellow-rhomb series (Tomoda) is obtained from (67), with r_0=1.2 fm and g_A=1.25: the value listed in (67) are in [y^{-1}fm^2] unit, being multiplied by a factor $4R^2$ ($R= r_0A^{1/3}$) to match the definition of the nuclear matrix element and the neutrino potential in (67). The phase space factors in the red-squared series (Suhonen-2009) are deduced from the decay time $T_{1/2}$ reported in (59) with r_0=1.2 fm and g_A=1.00. The three coloured bands highlight the isotopes considered in this PhD work. 30

Figure 1-9. Q-values of some candidate nuclei to 0νββ (69), (70). The three coloured bands highlight the isotopes relevant in this PhD work. As a reference, the red line denotes the 2.6 MeV γ-peak of ^{208}Tl, corresponding to the end-point of natural radioactivity. 35
Figure 1-10. The isotopic abundance of some nuclei candidate to 0νββ (71), (72). The three coloured bands highlight the isotopes relevant in this PhD work. 35
Figure 1-11. Q-value versus isotopic abundance for some 0νββ candidate nuclides 36
Figure 1-12. Nuclear form factors (defined by Eq. 1-33) for some 0νββ candidates. As in the NME plot (Figure 1-7), the central mark of each F_N range indicates the mean of the maximum and minimum values of the range, and is intended solely to guide the eye. The error bars show the full extent of each range. The reference used for the calculation are: IBM-2: (61) ($M_{0\nu}$), and (66), (67) ($G_{0\nu}$); (R)QRPA: (58) ($M_{0\nu}$) and (64), (65) ($G_{0\nu}$); pnQRPA: (59) ($M_{0\nu}$) and (66), deduced from $T_{1/2}$ in (59) ($G_{0\nu}$) ISM: (60) ($M_{0\nu}$) and (66) ($G_{0\nu}$). For details see the caption of Figure 1-7 and Figure 1-8. 36
Figure 1-13. Energy spectrum measured by the Heidelberg-Moscow experiment in the $Q_{\beta\beta}{}^{0\nu}$ region (78). 38
Figure 1-14. (a) Energy sum spectrum of the two electrons, (b) angular distribution of the two electrons, and (c) single energy spectrum of the electrons, after background subtraction from ^{100}Mo with 7.369 kg·yr exposure. The solid line corresponds to the expected spectrum from 2νββ simulations and the shaded histogram is the subtracted background computed by Monte Carlo simulations. The signal contains 219 000 ββ events and the signal-to-background ratio is 40 (90). 39
Figure 1-15. The thirteen floors of the Cuoricino tower. Eleven floors are made with four bolometers whose absorber size is 5x5x5cm^3, while the remaining two are composed by six 3x3x6cm^3 detectors. Among these small crystals, two have been enriched at 82% in ^{130}Te and other two at 75% in ^{128}Te. 40
Figure 1-16. Best fit, 68% and 90% confidence intervals for the total statistics superimposed on the Cuoricino sum spectrum in the 0νββ region (50). 41
Figure 1-17. Comparison between the Cuoricino limit on ^{130}Te $T^{0\nu}{}_{½}$ and the ^{76}Ge claim from the HM experiment claim expressed in terms of $T^{0\nu}{}_{½}$ (^{130}Te) as stated from Eq. 1-35. The orange horizontal line represents the Cuoricino limit where the blue columns are the range of the limit of the ^{130}Te obtained from the ^{76}Ge claim by using nuclear factor taken from IBM-2, (R)QRPA, pnQRPA and ISM nuclear matrix element calculation (see Figure 1-12 for the details of the F_N calculation and references). 42
Figure 2-1. The status of the actual 0νββ searches in terms of explored neutrino mass hierarchy regions. Being the present experimental sensitivity to the effective Majorana mass about 500 meV, only the Quasi-Degenerate hierarchy region has been probed, as shown by the yellow band. The black line denotes the central value of the HM claim. 44
Figure 2-2. High energy β-γ decays of the ^{238}U and ^{232}Th chains preceded (or followed) by an α emission. Using delayed α coincidences, β-γ decays can be identified (94). 46
Figure 2-3. Schematic model of a bolometer. 50
Figure 2-4. Simplified diagram of the energy flow due to incident radiation within an absorber. S_n is the nuclear channel while S_e is the electronic one. Only the energy appearing as heat at the bottom of the diagram will contribute to the phonon creation (125). 54
Figure 2-5. Model of the thermalisation process of phonons after their production in the absorber. 55
Figure 2-6. Typical average phonons energy versus time (a1) and (a2) recoil of electrons and nuclei with creation of electron–hole pairs and mostly high-energy optical and Debye phonons; (b) rapid decay of phonons by successive creation of lower energy pair of acoustic phonons, each process

conserving both energy and momentum. At the end of (b), phonons propagate ballistically and reach the surface of the absorbing crystal; (c) interaction with the surface, creation of athermal signal, (d) rise of thermal signal; (e) is the return to equilibrium temperature (34). 55
Figure 2-7. A scheme of the tunnelling hopping conduction mechanism in semiconductor mediated by phonon in case of doping slightly below the MIT concentration 58
Figure 2-8. A sketch of the basic thermistor bias circuit. 60
Figure 2-9. Composite thermal model with three nodes. The sign of powers flowing in the system is not known in principle, and they are fixed by convention. 62
Figure 2-10. Bias circuit for the voltage read-out of the thermistor, corrected by the presence of a parasitic capacitance in parallel with the sensor's resistance. 67
Figure 3-1. Picture of a Cuoricino Single Module. 71
Figure 3-2. Anticoincidence total energy spectrum of all Cuoricino detectors (black). The most prominent peaks are labelled and come from known radioactive sources such as: e^+e^- annihilation (1), ^{214}Bi (2), ^{40}K (3), ^{208}Tl (4), ^{60}Co (5) and ^{228}Ac (6). The total energy spectrum of all Cuoricino detectors during calibration measurements is also shown (colour). For convenience, it is normalized to have the same intensity of the 2615 keV line of ^{208}Tl as measured in the non-calibration spectrum 72
Figure 3-3. Drawing of a CUORE Single Module connected to the top plate of a tower. 74
Figure 3-4. Sketch of a CUORE bolometer, with all its elements: 1) the TeO_2 crystal absorber; 2) the NTD-Ge thermistor, with wrap-around style gold pads; 3) the Si heater; 4) the copper frame acting as thermal bath; 5) the PTFE spacers, linking the absorber to the bath; 6) the gold wires, 7) the copper pad and 8) the wire tray for carrying out the electrical signal. 74
Figure 3-5. Pictures of the 5x5x5 cm^3 TeO_2 crystal produced by SICCAS for the CUORE-0 and CUORE experiments. 76
Figure 3-6. A scheme of the two successive crystal growth procedures. 80
Figure 3-7. Microdistribution of the resistivity of reference resistances prepared from germanium by NTD method (1) and metallurgical method (2) (156). 83
Figure 3-8. Sketch of a CUORE-0/CUORE thermistor. W is the width, i.e. the distance between the lateral gold pads (~2.95 mm); L is the length and (~2.90 mm); H is the height (~0.9 mm); P is the width of the gold pads (~0.2 mm). 85
Figure 3-9. A box of CUORE-0 thermistors (left), a sample of 34B CUORE-0 thermistor (middle) and a sample of 34C CUORE-0 thermistor (right). 86
Figure 3-10. Spread in the size of the 34C CUORE-0 NTDs. The average values of the height, width and length are: <H> = 0.893 cm; <W>=2.745 cm; <L> = 2.895 cm. For the meaning of H, W, L, see Figure 3-8. 87
Figure 3-11. Sketch of the wafer holder for Ge wafer the irradiation at MIT-NRL. The location of the wafers (large circles) and the monitor isotopes (small circles) are shown. 88
Figure 3-12. Spectrum from the radioactivity measurements of #39 and #40 wafers. In the inset, only the region above 600 keV is shown. The 1077 keV ^{68}Ge line, the 1115 keV ^{65}Zn line, the 657 keV ^{110m}Ag line and the 1173 keV ^{60}Co line are observed. 88
Figure 3-13. A sketch of the electronic readout system for the thermistor characterisation. 89
Figure 3-14. Simulated I-V curves at different temperatures of a Ge NTD thermistor having T_0 = 3.3 K, R0=1.15 (164). 90
Figure 3-15. Left: T_0 measured by Milan and Florence for the NTD series irradiated at MURR. Right: T_0 measured by Milan and Florence as a function of the neutron fluence, as quoted from the MURR and calculated from the monitors. 91

Figure 3-16. T_0 as a function of the neutron fluence measured by monitors. The lines correspond to the fits of the first three points (#33, #34, #35) together with the CUORE series (#39, #40) –all the points are labelled in bold. The fitted function is T_0=a+fluence·b and the parameters obtained are a=44.315±0.887, b=-1.1869·10^{-17}±2.93·10^{-19} for the Florence data and a=37.907±0.719, b=-1.0225·10^{-17}±2.38·10^{-19} for the Milan data. 92
Figure 3-17. N_{net} doping for 0.5%, 1.0%, 1.6% and 5% epithermal flux for the wafers irradiated at MURR and at MIT-NRL. 93
Figure 3-18. The structure of a heater of the CUORE production made at ITC-irst. The resistive meander is visible and the dimension and the ratio length/width are reported (165). 96
Figure 3-19. Samples of Si heaters from the CUORE production. 96
Figure 3-20. Examples of wafer mapping realized at ITC-irst using the results of room temperature characterisation: "bad-select" map, "shades" map and coloured map for wafer 2, measuring the heater resistances between pad 1 and 2 with 1 V of bias voltage (165). 97
Figure 3-21. Examples of thermistors glued with nine glue dots made with a nine tip matrix. 98
Figure 3-22. A wrap-around thermistor provided with frontal bonded gold wires. 99
Figure 3-23. (Left) A Cuoricino style wiring: the 50 μm gold wires of the thermistors, attached before the gluing, are inserted and crimped in the small copper pins, which are on they turns connected to the copper holder. (Right) A CUORE-style wiring: the 25 μm gold wires are bonded to the heaters after their gluing and have to reach the Cu pad of the FFC stepping over the frame. The different lengths of the wire path can be observed. 100
Figure 3-24. Drawings of the CUORE frames. From left to right: lower and upper frame for a four-crystal floor, detail of the plug for the PTFE pieces and a column. 101
Figure 3-25. The three towers. From left to right: T1, wrapped in polyethylene, T2 cleaned at LNGS, T3 cleaned at Legnaro National Laboratory. 102
Figure 3-26. Schematic diagram of a CUORE bolometer, with a photo of each of its components. 104
Figure 3-27. Scheme of a single CUORE tower. 107
Figure 3-28. (Left) Layout scheme of the 19 towers of CUORE (top view). (Right) Drawing of the CUORE cryostat in cross-section, revealing the shielding and the array of towers. 108
Figure 3-29. A mock-up tower closed in the Garage, with at the top the UWP (left) and the mock-up tower lifted from the Garage into the Storage Box thanks to the elevator (right). 110
Figure 3-30. Schematic drawing of the Mech Box (top view). 111
Figure 3-31. Sketch of the Cabling Box (left) and the real GB on the top of the Garage (right). 111
Figure 3-32. (Top) The instrumentation of the Bonding Box with the vertical bonding machine on the left and the camera and the screen on the right. (Bottom) A detail of the ceramic capillary approaching the mock-up tower for bonding tests. 112
Figure 3-33. The CUORE sensitivity to the 0νββ half-life of ^{130}Te as a function of the measuring time, assuming a 5 keV FWHM energy resolution, in case of the realistic CUORE background of 10^{-2} counts/(keV·kg·y) (green, lower line) and of a target, optimistic background of 10^{-3} counts/(keV·kg·y) (blue, upper line). 114
Figure 3-34. The inverted hierarchy region of neutrino mass spectra corresponds to an effective Majorana mass range between 50 meV and 10 meV (see Figure 1-6). Here this mass interval has been translated into ^{130}Te life-time using the nuclear form factors obtained from different nuclear matrix element calculations (see Figure 1-12) and is represented by the vertical orange bands.

The CUORE sensitivities in case of a realistic background of 10^{-2} counts/(keV·kg·y) and of an optimistic background of 10^{-3} counts/(keV·kg·y) are superimposed onto these intervals (blue line and red dotted line respectively); assuming the realistic background, CUORE will be able to touch the inverted hierarchy region in most of the cases (i.e. according to three over four nuclear matrix element calculations) while it will deep explore this mass pattern in case the improvement on the reduction of the background will reach its optimistic target. 115

Figure 3-35. The CUORE-0 sensitivity to the 0νββ half-life of ^{130}Te as a function of the measuring time of the experiment assuming 5 keV FWHM as energy resolution in case of the realistic CUORE-0 background of 0.12 counts/(keV·kg·y) (blue, lower line) and in case the background is due only to the irreducible component derived from the cryostat (green, upper line). The Cuoricino limit is given as a reference (red, straight line). 116

Figure 4-1. The complete set of the "witness" thermistors of the CUORE production. 118

Figure 4-2. A CUORE "witness" thermistor. Its size (3×2.4×1 mm^3) is smaller than a standard CUORE-0 or CUORE thermistor and has only lateral gold pad instead of being wrap around type. Here 50 μm gold wires have already been bonded to the gold pads. 118

Figure 4-3. (Left/Middle) A scheme of both sides of the holder for the thermistor characterisations. Six thermistors can be accommodated on one side and five on the opposite one, for a total of eleven slots. The long, grey lines denote the common pad, while pads named A, B, C, D are the four contacts devoted to the calibrate thermometer four-wires read-out. (Right) A picture of one side of the holder. The top part is the one to be connected to the cryostat mixing chamber, while the bottom one is the thermometer holder. 120

Figure 4-4. (Left) The calibrate thermometer is placed in its dedicated holder. (Right) The thermometer holder is fixed to the entire mounting. The Indium cold welding of the wires can be seen for both thermistors and thermometer. 120

Figure 4-5. A scheme of the electronic readout system. The load resistance R_L can assume values from 0.01 MΩ to 2.07 GΩ. The temperatures at which each part of the circuit operates are also displayed. 121

Figure 4-6. Typical V-I and R-P curves. In the R-P plot the plateau corresponds to the ohmic region. 122

Figure 4-7. The resistance values for all the thermistors in the CUORE-0 characterisation run versus the thermometer resistance values are displayed. 124

Figure 4-8. The resistance values for all the thermistors in both CUORE-I and CUORE-II characterisation runs versus the thermometer resistance values are displayed. The thermistors behave in the same way during the two runs except the BIG23H and, in a minor way, the 39A-1. 124

Figure 4-9. The calibration data for the Ge thermometer provided by the LakeShore company. A clear change in the slope of the curve is clearly observable at ~90 mK. 126

Figure 4-10. Fit of the calibration data with the 4-3. The coefficient "b" in the fit corresponds to the slope parameters (i.e. to γ in the equation), while "a" is the intercepts k. 128

Figure 4-11. Plot of all the data for the Cuoricino reference thermistor H31-B25 collected during both CUORE-0 and CUORE thermistor characterisation runs. On the x axis the thermometer resistance is displayed while on the y axis there is the resistance of the H31-B25 thermistor. The good agreement between the CUORE-0 and CUORE-I data sets can be observed, while the CUORE-II points show some problems in the re-establishing of the initial measurement conditions after the He-leakage during the CUORE thermistor characterisation run (see 4.2). The orange area on the left side of the plot denotes the region of the thermometer resistance values used for building the Temperature Scale 4. Only the CUORE-I data set has been used for the calibration. 130

Figure 4-12. Focus on the points used for the calibration of the H31-B25 thermistor, corresponding to the orange region in Figure 4-11. The thermometer resistances are converted in temperature thanks to the Temperature Scale 1 and then the inverse of the square root of the temperature is displayed on the x-axis, while on the y-axis the natural logarithm of the NTD's resistances is taken, in order to perform a linear fit of the data, fixing $\gamma = 0.5$. From the fit parameters the constant R_0 and T_0 are derived. 130

Figure 4-13. Plot of all the data for the BIG23H reference thermistor collected during both CUORE-0 and CUORE thermistor characterisation runs. On the x axis the thermometer resistance is displayed while on the y axis there is the resistance of the BIG23H thermistor. The agreement between the CUORE-0 and CUORE-I data sets can be observed, while the CUORE-II points show problems in the re-establishing of the initial measurement conditions after the He-leakage during the CUORE thermistor characterisation run (see 4.2). The orange area on the left side of the graphic denotes the region of the thermometer resistance values used for building the Temperature Scale 5. Only the CUORE-I data set has been used for the calibration. 131

Figure 4-14. Focus on the points used for the calibration of the BIG23H thermistor, corresponding to the orange region in Figure 4-13. The thermometer resistances are converted in temperature thanks to the Temperature Scale 1 and then the inverse of the square root of the temperature is displayed on the x-axis, while on the y-axis the natural logarithm of the NTD's resistances is taken, in order to perform a linear fit of the data, fixing $\gamma = 0.5$. From the fit parameters the constant R_0 and T_0 are derived. 131

Figure 4-15. Example of a fit for the 39_3_1 CUORE thermistor with *Temperature Scale 1.* The results of the fit are displayed in the box. 133

Figure 4-16. Example of a fit for the 39_3_1 CUORE thermistor with *Temperature Scale 2*. The results of the fit are displayed in the box. 134

Figure 4-17. Example of a fit for the 39_3_1 CUORE thermistor with *Temperature Scale 3*. The results of the fit are displayed in the box. 134

Figure 4-18. Example of a fit for the 39_3_1 CUORE thermistor with *Temperature Scale 4.* The results of the fit are displayed in the box. 135

Figure 4-19. Example of a fit for the 39_3_1 CUORE thermistor with *Temperature Scale 5*. The results of the fit are displayed in the box. 135

Figure 4-20. The fits of the "ensemble" H31-B25 thermistor using all the Temperature Scales are displayed. The resistance values at certain temperature come from the average of the NTD resistance among different characterisation runs, while the corresponding standard deviation is the resistance uncertainty. 142

Figure 4-21. For each Temperature Scale, the spectrum of the reduced $\chi 2$ values obtained for the fits with $\gamma=0.5$ is displayed. 144

Figure 4-22. The ratios between each CUORE-0 thermistor and the H31-B25 Cuoricino reference NTD for all the temperature points collected during the CUORE-0 characterisation run 147

Figure 4-23. Global fit with a $\gamma= 0.5$ VRH law of the CUORE-0 and CUORE thermistors (upper and lower plot, respectively) using Temperature Scale 1 and averaging on all the NTDs of each series. 151

Figure 5-1. Radio-purity certification protocol applied for TeO_2 crystals. 154

Figure 5-2. (From left to right) A closed box, with its proper barcode; the crystal box is open, revealing it Polystyrene holder for the crystals; a single packed crystal: on each plastic bag the barcode identifying the single crystal is reproduced. 158

Figure 5-3. Counterclockwise: the gluing tool, with the moving central cylinder hosting the recess for the thermistor, and the PTFE crystal holder; the spacer cap for placing the upper face of the NTD 50 μm below the surface of the gluing tool; the cap with the nine tips for the glue deposition; a detail of the 3x3 tip matrix; the TeO_2 crystal placed In the PTFE holder at the end of the gluing procedure. 159
Figure 5-4. The two cases of thermistor positioning. If the NTD width fits the indentation and the bonding is lateral, the thermistor is simply put in the recess, with the gold wires arranged along the lateral recesses. In case of bigger thermistor and/or with frontal bonding, a small ring is placed to raise the NTD with respect to the indentation. 159
Figure 5-5. NTD broken during the gluing procedure. Its dimensions were too close to the ones of the indentation, therefore, when the glued crystal was removed, a piece of the thermistor remained in the recess. 161
Figure 5-6. (Left) Broken NTD because of a too high pressure on the spacer cap. (Right) A small NTD is in position for receiving the glue: because it is very small, it can accommodate only six spot, therefore a row of pin has been moved away and the thermistor has been decentred using the small ring in order to fit with the remaining tips 161
Figure 5-7. (Left) Because of an unwanted moving of the crystal in the PTFE holder, the crystal "skipped" a row of glue spots (visible on the left of the NTD), and squashed the remaining dots in a veil of glue. The difference between this gluing and another successful one is shown in the right. 161
Figure 5-8. Some moments of the CCVR assembly: (left) mounting of the frames; (right) the detector is completed with heaters and gold wires from chips to the Cu pins inserted in the upper frame. 162
Figure 5-9. Some moments of the CCVR assembly: (left) after the mounting of the top and bottom part of the external shield, the detector is wrapped in ~70 μm thick polyethylene layer; (right) electric wires are connected to the Cu pins trough the Polyethylene layer. 162
Figure 5-10. Completed CCVR detector. 162
Figure 5-11. An example of a CCVR calibration spectrum (taken from CCVR-I, Channel 2). Gamma lines from the ^{232}Th decay chain are visible in the spectrum. In particular, the 511 keV line corresponds to e^+e^- annihilation, the 911.2 keV and the 969 keV lines are from ^{228}Ac and the 583 keV, the 1593 keV, the 2103.5 keV and the 2614.5 keV lines came from ^{208}Tl 163
Figure 5-12. Total, anticoincidence (M1) and coincidence (m2) energy spectra for the full CCVR statistics 164
Figure 5-13. Global rate of ^{210}Po events over time for CCVR-I. The units on the x-axis are days since the start of the first background measurement. Each point represents a run or a group of runs. Holes in the distributions are due to calibration measurements or to interruptions in the data taking. The horizontal error bars indicate the beginning and the end of each group of runs, they are for visualization only. Fit results are superimposed to the points. 167
Figure 5-14. Distribution of the ^{210}Po activity at production time for all CCVR crystals. 168
Figure 5-15. Top: Monte Carlo simulation of a ^{210}Pb bulk contamination in CCVR-I. Bottom: CCVR I low energy M1 spectrum (40-60 keV). The energy threshold is set to 40 keV. The red line represents the fit to the spectrum with an exponential background and allowing the presence of a ^{210}Pb bulk contamination with the above shape. No hint of such contamination is found. 172
Figure 5-16. Sum energy spectrum of multiplicity 2 events ($M2_{sum}$) for all the CCVR statistics 173
Figure 5-17. Total and anti-coincidence spectra in the region 0-500 keV: low energy lines from Te metastable isotopes are clearly visible. 174

Figure 5-18. A closer look to the $M2_{sum}$ spectrum in the region above the 5470.5 keV α line of ^{210}Po. Here the peaks resulting from coincidences between the ^{210}Po α line and low energy γ line due to Tellurium metastable isotopes are visible. 174
Figure 5-19. For each penetration length, the containment efficiency of surface events is computed for both M1 and $M2_{sum}$ Monte Carlo spectra. For small penetration length (0.01 and 0.1 μm) the higher containment efficiency comes from the $M2_{sum}$ spectrum, whereas for higher depths (1, 5 and 10 μm) this arises from the M1 spectrum. The efficiency containment value for 0.2 μm depth is very similar both for M1 and $M2_{sum}$ spectrum. 176
Figure 5-20. For each penetration depth, the lower and upper bounds of the 90% C.L. intervals for the count rate at the DBD energy region are plotted. Values computed on ^{226}Ra line. 179
Figure 5-21. Energy resolution of crystal 007 with a 34B thermistor in CCVR-I. Left: 5407 keV ^{210}Po alpha line. Right: 2615 keV ^{208}Tl gamma line. 181
Figure 5-22. Distribution of the energy resolution of all the bolometers of CCVR-I to CCVR-IV, measured as the FWHM of three peaks: 1460 keV of ^{40}K (top), 2615 keV of ^{208}Tl (middle) and 5407 keV of ^{210}Po. 182
Figure 5-23. Distribution of the energy resolution of all the bolometers of CCVR-I to CCVR-IV, grouped according to the NTD type, measured as the FWHM of three peaks: 1460 keV of 40K (top), 2615 keV of ^{208}Tl (middle) and 5407 keV of ^{210}Po (bottom). 183
Figure 5-24. Distribution of the energy resolution of all the bolometers of CCVR-I to CCVR-IV, grouped according to the wafer their NTDs were cut from and their NTD size, measured as the FWHM of the 5407 keV peak of ^{210}Po. 184
Figure 5-25. "Pirro curves" of all the CCVRs. 187
Figure 5-26. "Pirro curves" of all the CCVR detectors divided according to the contact geometry of their NTDs (wrap-around gold pad or only lateral gold pad). 187
Figure 5-27. "Pirro curves" of all CCVR detectors divided according to the size of their NTDs. All the detectors belong to the "big" set except the ones having the NTDs from the top-offs of wafer 39. 188
Figure 5-28. "Pirro curves" of all the CCVR detectors divided according to the wafer their NTDs were cut from. Two main data sets appear: the 34B one, collecting the A-R_{work} points of the bolometers equipped with 34B, Q034B, Q034C and WA NTDs, and the 39C, with the detectors having thermistors of small 39C or Q39C type. Other two groups are reported for comparison: the Cuoricino and the 39_3. The two lines correspond to the fit of the 34B group (the upper one) and of the 39C set (the lower one) whose results are presented in Eq. 5-11. 188
Figure 5-29. Rise time distribution of the 5407 keV average pulses of all CCVR detectors (from I to VI). 189
Figure 5-30. Decay time distribution of the 5407 keV average pulses of all CCVR detectors (from I to VI). 189
Figure 5-31. Rise time distribution of the 5407 keV average pulses of all CCVR detectors (from I to VI), divided according to the wafer from which the thermistors were cut. 190
Figure 5-32. Decay time distribution of the 5407 keV average pulses of all CCVR detectors (from I to VI), divided according to the wafer from which the thermistors were cut. 190
Figure 5-33. Example of pulses from CCVR V. Blue pulses are from a Q034C and a Q034B thermistor, while the pink ones are from a 39_3 and a 39C thermistor. 191
Figure 5-34. Decay time of the 5407 keV average pulses of all CCVR detectors (from I to VI) versus the corresponding resistance at the working point. 191
Figure 5-35. Simulated pulses from a 39C thermistor. The simulation is based on the composite model of bolometers (see 2.4): the green pulse has a double C_{el} with respect to the red pulse. 192

Figure 6-1. Energy resolution of the CCVR-VI bolometers measured at the 2615 keV γ line of ^{208}Tl and at the 4507 keV α line of ^{210}Po for all the channels. 194
Figure 6-2. Examples of distributions of detector performance parameters for the 5×5×5 cm^3 bolometers in the Cuoricino tower; the data in the histograms is taken from a 3 days ^{232}Th calibration which took place during Run II on the 40 surviving big detectors. (a) FWHM resolutions at 2615 keV. (b) Pulse heights in μV/MeV. 195
Figure 6-3. Examples of pulses from selected bolometers in the Cuoricino tower (B7, B31, B34, B57, B61) featuring variations in shape parameters. 195
Figure 6-4. Bolometric model of reference for the discussion on pulse shape variations. The parameters taken into account as possible sources of the variations are enumerated with the same notation in the figure and in the list in Section 6.1. 197
Figure 6-5. Pulses from the two 39C thermistors glued on one of the crystal (#547) of the CCVR-VI detector (see Chapter 5). Each pulse is generated by the same particle deposition in the corresponding absorber, and is seen by a different thermistor. 198
Figure 6-6. Correlation between the degree of conversion and the viscosity of the epoxy Araldite 2014, belonging to the same family of Araldite Rapid but with longer pot life, at three curing temperatures (189). 202
Figure 6-7. The content of DIY Araldite Rapid tubes coming from different producers. The one used for CUORE is on the right. 204
Figure 6-8. A typical Cuoricino nine-dots matrix deposited on a 3x3 mm^2 surface thermistor (left) and an example of the effect of high humidity in the gluing environment: black epoxy spots (right). 207
Figure 6-9. (Left) 50 ml dual cylinder syringe with bleeding-valve pistons to contain resin and hardener. The cartridge is filled in N_2 atmosphere. (Right) tested static mixers. The effectiveness of mixing for a given epoxy depends on the diameter of the tubular housing, as well as on the number and shape of mixing elements. From top to bottom, the inner diameter and the number of elements for each mixer are: 6.3 mm×21, 5.4 mm×21, 3.0 mm×17, 3.0 mm×7, 5.3 mm×24. The top four mixers have an internal helix, while the last one is square shaped. 208
Figure 6-10. Principles of operation of the static mixer selected for the Araldite Rapid epoxy glue. The resin and the hardener are mixed mainly by the mechanisms of division and conversion. The specific geometry allows building the mixer in a very compact and short way. 209
Figure 6-11. Pogo-pins for use in the nine-pins array gluing procedure. Tested types of Pogopins (left) and Pogo-pins mounted in the fixed array (right). 210
Figure 6-12. Nine-dots matrices made with the same array of Pogo-pins. Pogo-pins were cleaned with ethanol between depositions, and a new amount of freshly mixed glue was used for each matrix. Slight variations in both position and dimension of dots can be seen from one matrix to the other. The tests were performed in the same conditions, at ~21 °C and few seconds after epoxy mixing. 211
Figure 6-13. Example of diameter enlargement in a row of a nine-dots matrix due to height reduction at 50 μm. The same row of spots was photographed before and after thermistor application on the transparent side of a TeO_2 crystal. 211
Figure 6-14. The table-top cartesian robot WR300 used in Como dispensing tests. 214
Figure 6-15. (Left) Syringe configuration in the pneumatic dispensing system: the barrel is connected to a pressure supply (N_2 in this case) controlled by the dispenser. (Right) Syringe configuration in the air-free model: the inner piston is mounted on the head of the drive screw, whose extension and retraction is controlled by the dispenser according to the desired drop volume. 216

Figure 6-16. The air-free Fishman LDS9000-SDAV epoxy dispenser with its dispensing gun. 217
Figure 6-17. Selection of nine-dots matrices realized with the air-free dispensing technique. Pair of matrices indicated by the same capital letter illustrate each the effect of a peculiar dispensing condition or the variation due to the tuning of one parameter. Filaments and small size in the A matrices are due to insufficient after-purge drawback; matrix B was dispensed with ΔZ=30 μm, B' with ΔZ=200 μm; matrices C and C' are characterized by point-to-point rise equal respectively to 12 mm and 15 mm; the D matrices were dispensed in row at advanced pot life (2 min after mixing) and show reduction in spot size due to viscosity increasing steeply; matrices E and E' were dispensed by needles with different inner diameter: 0.20 mm and 0.25 mm. For all cases, the unmentioned parameters are equal to the ordinary values listed in the text. 218
Figure 6-18. Nine-dots matrix dispensed by air-free technique with the set of parameters defined as optimal: ΔZ=200 μm, shot size=2.3×10^{-4} cc, dispensing rate=0.135 cc/s, drawback=500 steps, single-point working time=3 s, point-to-point rise=15 mm 218
Figure 6-19. The pneumatic Loctite 98666 epoxy dispenser. 219
Figure 6-20. Selection of nine-dot matrices realized with the pneumatic dispensing technique. Pairs of matrices indicated by the same roman number were obtained with an equal set of parameters apart from one: ΔZ for pair A, dispensing pressure for pair B (lower P corresponds to smaller spots, while filament production remains unaltered), single-point working time for pair C and Z-axis speed for pair D. The complete set of parameters for each pair is reported in Table 6-3. 221
Figure 6-21. Nine-dots matrix dispensed by pneumatic technique with the set of parameters defined as optimal: ΔZ=100 μm, dispensing pressure=2.8 bar, single-point working time=1 s, point-to-point rise=150 mm, Z-axis speed=600 mm/s. Final parameter tuning will take place in the ultimate gluing site at LNGS to get rid of the epoxy filaments visible in the picture 221
Figure 6-22. The Como prototype of Z-positioner. (a) Front view: the two handles for vertical adjustment of the chip holders and the handle for displacement of the crystal PTFE frame are visible. (b) Rear view: the vacuum tubes reach the chip holders and are connected to a small pump. (c) View of the zero plane, the chip holders, the PTFE frame and the mobile plane on the back. (d) Zoom on the mobile plane in its rest site, prior to positioning on the chip holders: the 50 μm spacers are visible. 225
Figure 6-23. Position of thermistor and heater on the crystal surface in the standard defined by the CUORE Assembly Working group. Notice that, for reason connected to the carrying of the electrical connection outside the cryostat, two mirrored positioning are necessary: this requires two Z-pos for the final system 225
Figure 6-24. The logo of the new CUORE gluing line. The acronym stays for "A Robotic Tool for A Thermistor-To-Absorber Coupling". 226
Figure 6-25. The three-axes system by Jenny Science AG (left) and the camera for the glue dots inspection placed on it (right) 228
Figure 6-26. The Loctite 97042 pneumatic gun with a bi-cartridge and its static mixer. 228
Figure 6-27. The ABB anthropomorphic robot (top) and the tools it has been equipped with (bottom): the clamp for handling the crystals (left) and the vacuum cap for picking up NTDs and heaters (right). 229
Figure 6-28. Single spot and filament formation with the pneumatic dispensing. 1) The needle is at the point-to-point height (P) with the right amount of glue. 2) The needle move down until it reaches the ΔZ distance from the chip surface: the glue touches the chip and the spot forms. 3) The needle starts rising and the filament creates. 4) Two cases follow: the speed on the vertical axis is fast (a) or

slow (b). In the first way the filament is broken while the needle moves towards the next spot and falls onto the chip; in the second one, the slow vertical movement allows the filament breaking and falling onto the spot before the needle moves towards the next spot position..... 231
Figure 6-29. The "glue corner" of the system: the purge station (left) the syringe holder connected to Jenny's axis (middle) and the pneumatic gun placed on its holder (right). 232
Figure 6-30. Some details of the new Z-positioners: the three tips that fix the position of the chip on the chip holder (a), the pieces ensuring parallel rising of the chip holder with respect to the zero reference plane (b), a detail of the clamp for positioning the chip at the right height (c), the pneumatic control for the PTFE crystal elevator (d) and the top of the Z-pos where the zero reference plane and the crystal plane, made by three group of three teeth each, the latter 50 μm higher than the other two groups, are visible. 234
Figure 6-31. (Left-top) The difference between the previously used needle (red) and the new adopted one (blue). (Left-bottom) The old wire-to-needle connection for the zero point location. (Right) The new connection for the zero point location. 235
Figure 6-32. Examples of gluing obtained with the new chip-to-absorber coupling line. The pictures are taken with the camera placed on Jenny axis and show two examples of the nine-dot matrix on a thermistor and a five-dot matrix on heater. The thermistor in the upper picture is a real CUORE 39C NTD, while the one in the bottom picture is a 34C. 237
Figure 6-33. Crystal repository with a TeO_2 crystal (left) and chip repository with two NDT-heater couples (right). 238
Figure 6-34. The CUORE gluing line. 239
Figure 7-1. The operating principle of a scintillating bolometer. The release of energy inside a scintillating crystal follows two channels: light production and thermal excitation. The heat is read out by a temperature sensor glued on the primary crystal while the light is read by a second crystal (light detector)..... 241
Figure 7-2. Scatter plot of heat (3x3x6 cm^3 $CdWO_4$, 426 g) vs. light (collected by Ge light detector).This plot shows how it is possible to separate very well the background due to α particles from the β/γ region (94). 244
Figure 7-3. Lateral (left) and upper (right) view of the LUCIFER single module. 1) ZnSe Crystal; 2) NTD Ge thermistor; 3) heater; 4) Si- slab acting as light detector; 5) PTFE spacer; 6) copper frame. 249
Figure 7-4. The LUCIFER tower inside the former Cuoricino/CUORE-0 cryostat. A detail of the tower, comprising four elementary modules, is shown on the right..... 249
Figure 7-5. A scheme of the scintillating bolometer setup tested at Insubria cryogenic laboratory: 1) the scintillating crystal; 2) the light detectors; 3) the heat thermistor. On the opposite crystal face a heater is also present; 4) the light thermistor; 5) gold wires for thermistor readout; 6) Teflon parts holding the bolometers and providing the conductance to the thermal bath; 7) copper structure; 8) hole in the holder bottom plane for placing the Uranium source; 9) column holding the light detectors, on which the Iron source will be attached; 10) scintillating foil that cover all the copper parts and surrounds the entire detector for enhancing the light collection. 251
Figure 7-6. The main elements of the ZnSe-Ge, ZnSe-Si and $ZnMoO_4$ scintillating bolometers. From left up corner, clockwise: the ZnSe crystal equipped with a 3×1×0.6 mm^3 NTD; the Zn MoO_4 crystal equipped with a heater; a Si slab after a test in liquid Nitrogen to check the thermal contraction of the slab holder; a Ge slab equipped with a 3×1×0.6 mm^3 NTD..... 253

Figure 7-7. ZnSe-Ge detector. (Left) The ZnSe crystal, equipped with a 3x1x1 mm^3 thermistor (on the left) and a heater (on the right) is held by the Teflon part in the copper frame. (Right) A thermistor-equipped Ge slab, held in position by a sequence of brass nuts and Teflon pieces, covers one side of the ZnSe crystal. 254
Figure 7-8. (Left) The 15×15×5 mm^3 $ZnMoO_4$ crystal is placed in the copper holder between the two Ge slabs. (Right) The same picture from a different point of view: in the central hole of the bottom copper plate (already covered with the scintillating foil) the calibrating Uranium source can be seen (green spot)..... 254
Figure 7-9. (Left) An iron source (numbered with "5") is placed in front of the slab. (Right) The $ZnMoO_4$-Ge detector is placed onto the ZnSe-Si detector, already completed with the copper shield. 254
Figure 7-10. Example of coincident pulses collected with the ZnSe-Ge detector. The pulse on the heat channel is about three times higher than the same event on the light channels. The pulses time scale is 50 ms..... 257
Figure 7-11. Static characterization of the three bolometers of the ZnSe-Ge detector: the load curves are identical before (run1) and after re-cooling (run2) even if there are difference between the two light detectors. This indicates a slight inhomogeneity in the single detector components, however the performances are stable in time..... 258
Figure 7-12. Baseline level versus time for the heat channel of the ZnSe-Ge detector. The steep rise in the right part of the graph corresponds to the sudden warm up of the cryostat due to the He leakage in the IVC. The gap between 0.8 and 0.9 days corresponds to the time interval during which the measure was stopped in order to acquire the noise spectrum..... 258
Figure 7-13. Plot of the amplitude of the coincidence events on the heat channel (x-axis) and both light channels (y-axis): red for LTD and blue for LTB. As already noticed from the static characterization (Figure 7-11), the two detectors have similar but different performances. 260
Figure 7-14. The amplitude of the heat channel versus the amplitude of the LTB light channel. In red the events selected by operating cuts on on the TVR of ZnSe: part of the pure ionization events as well as the pulses due to the heater are rejected..... 260
Figure 7-15. TVR versus amplitude for the LTB light channel. Discrimination among different event categories is appreciable. 261
Figure 7-16. Plot of ZnSe-LTB coincidences: in blue, residual pure ionizing events; α and βγ events (in red and in green respectively) are discriminated thanks to the cuts on the TVR of LTB light channel. 261
Figure 7-17. Calibrated γ spectrum of ZnSe bolometer. The three numbered peaks correspond to the 1460 keV line of ^{40}K (1), the 1590 keV line of ^{208}Tl double escape (2) and the 2615 keV line of ^{208}Tl (3)..... 262
Figure 7-18. Fits of the three identified lines: ^{40}K, ^{208}Tl double escape and ^{208}Tl. The FWHM of each peak is reported in Table 7-9. 262
Figure 7-19. a_t/a_s index versus heat channel amplitude and a_t/a_s index distribution for α (red dot and orange line) and β/γ event (green dot and blue line). The central limits of the $(a_s/a_t)_\alpha$ and $(a_s/a_t)_{\beta/\gamma}$ distributions are 9.2 and 0.89 respectively. The vertical black line indicates the energy value corresponding to the 0νββ peak of ^{82}Se. 264
Figure 7-20. Rough identification of the alpha end-point, corresponding to 4.2 MeV, and, as a consequence, of the QF from the LTB-ZnSe coincidence plot..... 264
Figure 7-21. Light versus heat of both Ge-slabs: LTB in blue and LTD in red. The performances of the two detectors are very different from each other; in particular, the LTD is strongly affected by noise and pile-up..... 266

Figure 7-22. Test value (AF) versus amplitude for the LTB light detector. The test value band below 4000 corresponds to alphas, while the big spot between 4200 and 4800 identifies the β/γ events. 267
Figure 7-23. Heat and light coincidences: β/γ events (green) are identified by the cut between 4200 and 4800 on the Test Value of the LTB light channel; alpha events (blue) correspond to the Test Value below 4000 and the remaining are the pure ionization events (red). 267
Figure 7-24. Amplitude spectrum of the LTB light detector with 1 ms anticoincidence with the heat channel; the blue shape is the entire spectrum (no cuts), while in the red case a cut on the light detector TVR < 17.5 is applied. The green shape corresponds to the coincidences with the heat channel: the absence of the peak in the latter case shows how the whole ^{55}Fe contribution is detected by the light detecting slab. 269
Figure 7-25. Energy spectrum of LTB and fit of the ^{55}Fe X-ray peaks. 269
Figure 7-26. Baseline level versus time for the heat channel of the ZnSe-Si detector, showing the temperature instabilities during the measurement. 270
Figure 7-27. Static characterization of the two light channels of the ZnSe-Si detector, named LT3 and LT4. 271
Figure 7-28. The amplitude of the heat channel versus the sum of the amplitudes of the two light channels for the ZnSe-Si detector. 271
Figure 7-29. Baseline level versus time for the heat channel of the $ZnMoO_4$-Ge detector. The spikes denote the sudden warm-up of the cryostat. 272
Figure 7-30. Load curves of the scintillating crystals. The ZnSe behaviour is constant among the different cool-downs (ZnSe-Ge and ZnSe-Si) while a huge difference appears between the two crystal measured in the same run (ZnSe-Si and $ZnMoO_4$-Ge). 273
Figure 7-31. The static characterization of the two light detectors of $ZnMoO_4$-Ge (solid points) is compared with the results obtained for the ZnSe-Ge detector (empty points): the load curves of LTB light detector are quite similar among the two runs, but the behaviour of LTD Ge-slab varies a lot. 273
Figure 7-32. Example of coincident pulses collected with the $ZnMoO_4$-Ge detector. The pulse on the heat channel is about three times higher than the same event on the light channels, which are not identical, being one slightly smaller. The pulses time scale is 50 ms. 274
Figure 7-33. The amplitude of the heat channel versus the sum of the amplitudes of the two light channels for the $ZnMoO_4$-Ge detector. The separation between alpha and beta/gamma events is clearly visible. Three lines of natural radioactivity are evident: the 1640 keV of ^{40}K (1), the 1592 keV of ^{208}Tl double escape (2) and the 2615 keV of ^{208}Tl (3). The line at the end of the alpha region represents the pulser events. 275
Figure 7-34. Decay time versus amplitude of the pulses detected on the heat channel. The two parallel lines correspond to beta/gamma (above) and alpha (below) events. The collection of points in the upper right corner of the plot corresponds to the pulser events: a cut on the decay time can exclude these signals from the light versus heat scatter plot. 276
Figure 7-35. The shape parameter AF (see Table 7-6) versus the amplitude of the pulses collected on the heat channel. The two lines denoting beta/gamma and alpha events are clearly distinguishable. 277
Figure 7-36. Plot of $ZnMoO_4$-Light coincidences: alpha events (in red) are discriminated from residual pure ionizing and β/γ events (in blue) thanks to the cuts on the AF of heat channel. The green dots correspond to the β/γ events alone. 277
Figure 7-37. Fits of the ^{40}K and ^{208}Tl double escape peaks. The peak FWHMs are reported in Table 7-15. 279

Figure 7-38. Calibrated γ spectrum of $ZnMoO_4$ bolometer. The numbered peaks correspond to: 510 keV (1), 583 keV (2), 1592 keV double-escape (5), 2615 keV (6) line of ^{208}Tl, the 609 line of ^{214}Bi (3), and the 1460 keV line of ^{40}K (5). 279
Figure 7-39. a_t/a_s index versus heat channel amplitude and a_t/a_s index distribution for α (red dot and orange line) and β/γ event (green dot and blue line). The central limits of the $(a_s/a_t)_\alpha$ and $(a_s/a_t)_{\beta/\gamma}$ distributions are 0.14 and 0.99 respectively. The vertical black line indicates the energy value corresponding to the 0νββ peak of ^{100}Mo..... 280
Figure 7-40. Rough identification of the alpha end-point, corresponding to 4.2 MeV, and, as a consequence, of the QF from the LTB-$ZnMoO_4$ coincidence plot. The resulting QF is about 0.14. 280
Figure 7-41. Baseline value versus time of the LTD light detector, showing the sudden warming-up of the cryogenic system occurred during the measurement..... 281

List of Tables

Table 1-1. Best fit values with 1σ errors and the 3σ allowed intervals for the three-flavour oscillation parameters from global data including solar, atmospheric, reactor (KamLAND and CHOOZ) and accelerator (K2K and MINOS) experiments (31). 18

Table 1-2. Summary of the most sensitive direct searches for 2νββ and 0νββ. Limits are at 90% C.L. All the 2νββ half-lives come from (53), except the limit on ^{136}Xe, that is taken from (54). The references for the 0νββ half-lives are reported directly in the table. 27

Table 1-3. Successfully tested bolometric materials for DBD search; the compounds written in bald are good scintillators at low temperatures. 37

Table 2-1. Several proposed next generation 0νββ experiments: for each proposal, the isotope that will be used, together with estimates for detector performance parameters (FWHM energy resolution, detection efficiency and background rate per unit of energy, time and 0νββ isotope mass) are given. The background estimates and the 0νββ source mass include both a reference ® and an optimistic (O) scenario (116). 47

Table 3-1. Concentration limits for radioactive isotopes requested for raw materials, reagents, consumables and intermediary products used for the production of TeO_2 crystals (147). 78

Table 3-2. Reactions occurring in the NTD process for a Ge wafer. In the first reaction Ga acceptor form, while the second and the third lead to donors and double donor respectively. σ_T and σ_E are the thermal and epithermal neutron capture cross section. 83

Table 3-3. Comparison of fluence data for 34B wafers reported from MURR and calculating using both thermal and epithermal neutron flux or considering only thermal fluence from the ^{59}Fe 1099 keV line. 85

Table 3-4. Thermal and resonant cross sections for neutrons and the half-life of their products via (n,γ) reactions for isotopes used for neutron monitoring for the MURR irradiation. 86

Table 3-5. Reaction for the fast-neutron monitors. 86

Table 3-6. Comparison of the fluence data for #39 and #40 series from MIT-NRL and from the monitors. 88

Table 3-7. Results of the characterisation of the 34B series performed by the Milano and Florence group. 91

Table 3-8. T_0 resulting from the characterisations of the #39 and #40 series performed by the Milan and Florence group. 91

Table 3-9. Splitting of the 15 CUORE wafers according to the implant dose. 97

Table 3-10. Values of the composite model parameters applied to the Cuoricino bolometers, considering 5x5x5 cm^3 absorbers and 3x3x1 mm^3 thermistors. 106

Table 3-11. Radioactivity levels of the detector major components and their effect on the 0νββ counting rate as predicted by the Monte Carlo simulation. In all cases there are only upper limits on the contaminations. 113

Table 4-1. The doses for the three top-offs of the series #39. The dose of the 34B NTDs is $3.41 \cdot 10^{18}$. 117

Table 4-2. The channel map of CUORE-0 NTD characterisation run. "S" stays for shorted contacts used for evaluating the wire resistance. Channel 4 was lost during the cool down. 125

Table 4-3. The channel map of CUORE NTD characterisation run. Channel 4 was not used because it was broken during the CUORE-0 characterisation run. 125

Table 4-4. The thermometer resistance values at which the thermistor load curves have been collected, for each characterisation run. 125
Table 4-5. The VRH parameters for the calibrated thermometer that define the *Temperature Scale 1.* 128
Table 4-6. The VRH parameters for the H31-B25 and the BIG23H thermistor, defining the *Temperature Scale 4* and the *Temperature Scale 5*, respectively. In the calibration the resistance values of the CUORE-I data set corresponding to thermometer temperatures above 90 mK have been used. 132
Table 4-7. The resistance values of the thermometer and the reference thermistors that have been collected during the three NTD characterisation runs are converted into temperature points using the different temperature scales. 132
Table 4-8. Fit results for the reference thermistor BIG23H according to all the *Temperature Scale* and with the parameter γ both free and fixed. The values of the reduced-χ^2 of the fits obtained with the *temperature Scale* created starting from BIG23H data, i.e. *Temperature Scale 5,* are denoted in red. 136
Table 4-9. Fit results for the Cuoricino reference thermistor H31-B25 according to all the *Temperature Scale* and with the parameter γ both free and fixed. The values of the reduced-χ^2 of the fits obtained with the *temperature Scale* created starting from H31-B25 data, i.e. *Temperature Scale 4,* are denoted in red. 136
Table 4-10. Fit results for the CUORE-0 34C thermistors according to all the *Temperature Scale* and with the parameter γ both free and fixed. 137
Table 4-11. Fit results for the CUORE-0 34B thermistors according to all the *Temperature Scale* and with the parameter γ both free and fixed. 137
Table 4-12. Fit results for the CUORE 39A thermistors according to all the *Temperature Scale* and with the parameter γ both free and fixed. For the 39A_1 NTD only the CUORE-I data set has been used, while the fits for the 39A_3 thermistor are made with both CUORE data sets. 138
Table 4-13. Fit results for the CUORE 39C thermistors according to all the *Temperature Scale* and with the parameter γ both free and fixed. 138
Table 4-14. Fit results for the CUORE 39_3 thermistors according to all the *Temperature Scale* and with the parameter γ both free and fixed. 139
Table 4-15. Fit results for the CUORE 40 thermistors according to all the *Temperature Scale* and with the parameter γ both free and fixed. 139
Table 4-16. The ratio between the Time Standard Deviation from CUORE-I data set and the Average Standard Deviation from CUORE-I/CUORE-II and CUORE-I/CUORE-0 data sets. The 39A_1 thermistor has been omitted because of unexplained discrepancies between CUORE-I and CUORE-II data. The results show that the T.St.D is seldom higher than the E.St.D. 141
Table 4-17. VRH parameters for the H31-B25 thermistor obtained from fitting "time" and "ensemble" data, with all the *temperature Scales* and γ fixed to 0.5. In the first part of the table, denoted with "T.Av. CUORE-I data", the "time quantities" from the CUORE-I data have been used (see Table 4-9); the second part of the table, indicated by "E.Av. data", collects the results from fitting the ensemble averaged resistances from different characterisation runs; in the last part T.Av. CUORE-I data with E.St.Dev. have been used. 143
Table 4-18. Fit results for the H31-B25 Cuoricino thermistor according to the *Temperature Scale 1* and the *Temperature Scale 4*, with γ = 0.5. The resistance values at 15 and 10 mK, calculated from each set of parameters are also reported. 145

Table 4-19. Results for the fits of the CUORE-0 thermistor using *Temperature Scale 1* and γ = 0.5. With the obtained parameters the NTD resistance values have been extrapolated down to the usual thermistor operational temperatures. 146
Table 4-20. Results for the fits of the CUORE thermistors using *Temperature Scale 1* and γ = 0.5. With the obtained parameters, scaled to thermistor with the real CUORE size, the NTD resistance values have been extrapolated down to the usual thermistor operational temperatures. 146
Table 4-21. The first part shows the ratios between each CUORE-0 thermistor and the H31-B25 Cuoricino reference NTD for the working temperatures foreseen for the CUORE-0 experiments. The thermistor resistance values have been extrapolated from the VRH law obtained with the Scale Temperature 1 with γ = 0.5. The central part of the table shows show how much the temperature of the H31-B25 thermistor should change with respect to the working temperature in order that this NTD reaches the CUORE-0 NTD resistance at the working temperature. In the last two columns there are the temperatures to which the CUORE-0 thermistors should be cooled down for having a resistance corresponding to the minimum and the maximum value allowed by the CUORE-0 electronics (50 MΩ and 500 MΩ respectively). 148
Table 4-22. The first part shows the ratios between each CUORE thermistor of the top-off of #39 series and the H31-B25 Cuoricino reference NTD for the working temperatures foreseen for the CUORE-0 experiments. The thermistor resistance values have been extrapolated from the VRH law obtained with the Scale Temperature 1 with γ = 0.5. The central part of the table shows how much the temperature of the H31-B25 thermistor should change with respect to the working temperature in order that this NTD reaches the CUORE-0 NTD resistance at the working temperature. In the last two columns there are the temperatures to which the CUORE thermistors should be cooled down for having a resistance corresponding to the minimum and the maximum value allowed by the CUORE electronics (50 MΩ and 500 MΩ respectively). 148
Table 4-23. The ratio between the time standard deviation of the first thermistor of each group and the error used for the last fit is shown 149
Table 4-24. VRH parameters obtained from fitting the CUORE-0 and CUORE thermistor series considering all the thermistors of each series as different measurements of a single NTDs and using *Temperature Scale 1.* R' is the R_0 parameter scaled for thermistors with the real CUORE-0/CUORE size. 152
Table 5-1. The contamination limits imposed to SICCAS for the final product, i.e. the CUORE crystals. As a reference, the last column shows the decay rates if the crystals have contaminations at the contract limits. 156
Table 5-2. Summary of CCVR data taking periods and live times. 157
Table 5-3. Count rates of all CCVRs measured in [counts/(keV·kg·y)] after the subtraction of the ^{210}Po counts. Errors are statistical. 164
Table 5-4.The count rates of all CCVRs after the subtraction of the ^{210}Po counts are compared with the ones of the best tower of the TTT test (see Section 3.4.1) and the Cuoricino detector. Rates are expressed in [counts/(keV·kg·y)]. Errors are statistical. The notation (2.7-3.9) refers to the combination of both the continuum region (2.7, 3.2) MeV and (3.4, 3.9) MeV, excluding the ^{190}Pt energy region of (3.2, 3.4) MeV. The ratio between the rates of CCVR and the other detectors are also presented. 165
Table 5-5. Fit results of the global rate of ^{210}Po events over time for each CCVR. The half-life of the exponential decay is in good agreement (1σ) with the half-life of ^{210}Po (138.38 d). 168
Table 5-6. ^{210}Po activity at production time for all the crystals measured in CCVRs I to V. 168

Table 5-7. For several nuclides of the U and Th chain the Q-value and the half-life of the α decay are shown (third and fourth columns) together with the 90% C.L. intervals on the number of events (fifth column) and the corresponding 90% C.L. intervals on the bulk activity (last column) ascribed to these nuclides. 169
Table 5-8. 90% C.L. intervals on the bulk contamination of U and Th decay chains in the hypothesis of secular equilibrium and of non-equilibrium. 170
Table 5-9. Upper limits on the activity of bulk and surface contamination of ^{210}Pb. Bulk contamination is given in [Bq/kg], surface contaminations are given in [Bq/cm^2]. 173
Table 5-10. Energy of the γ lines from Tellurium metastable isotopes and the corresponding sum energy when emitted in coincidence with a ^{210}Po event. 174
Table 5-11. 90% C.L. intervals on the number of counts ascribed to several nuclides from uranium and thorium decay chain from the $M2_{sum}$ spectrum. For each nuclide is also shown the half-life of the α decay. 175
Table 5-12. 90% C.L. intervals for surface contamination, for different penetration length values. 177
Table 5-13. Extrapolation to CUORE background from CCVR bulk contamination limits calculated in the previous sections and collected in Table 5-7 and Table 5-9. The highest limit is highlighted. 178
Table 5-14. Extrapolation to CUORE background from CCVR bulk contamination limits calculated in the previous sections and collected in Table 5-12 and Table 5-9. The highest limit is highlighted. 179
Table 5-15. The different kinds of thermistors used in CCVR bolometers. 184
Table 5-16. Summary of CCVR live time and average energy resolution for the 1460 keV ^{40}K, 2615 ^{208}Tl and 5407 keV ^{210}Po peaks. 185
Table 6-1. List of chemical, mechanical and thermal properties for the epoxy Araldite 2012, the industrial version of Araldite Rapid (190), after the mixing of its two components. Although a 5 minutes pot life is quoted, the experimentally observed work life of the epoxy is shorter (approximately 3 minutes at room temperature), due to the rapid growth in viscosity which reduces its usability. 203
Table 6-2. Technical characteristics of the table-top cartesian robot used in the Como dispensing tests. 214
Table 6-3. List of dispensing parameters for the selection of epoxy matrices in Figure 6-19. Only matrices belonging to the same pair should be compared. For all matrices, epoxy dispensing is performed with the inner diameter of 0.25 mm needle and 150 mm point-to-point rise. 222
Table 6-4. Comparison between dispensing techniques: best parameters for epoxy deposition as deduced by Como tests. The temperature range reported accounts for the testing environment in Como not being tightly controlled. Items eight to ten are parameters of the cartesian robot. 223
Table 6-5. Technical characteristics of the table-top cartesian robot used in the final gluing line. 228
Table 6-6. Parameters to be optimised to perform glue dots with the proper size. The values reported refer to a room temperature ranging between 21 and 21.5 °C and humidity of 30-50%. 236
Table 7-1. Sensitivity of three experimental options for a 0νββ scintillating bolometer experiment compatible with the experimental volume of the Cuoricino cryostat. ZnSe Option [1] and ZnSe Option [2] foresee an increased ZnSe crystal volume with respect to the baseline [0], achievable thanks to some modification to the LNGS Hall A cryostat and will be discussed in detail in Section 7.2.2. 246
Table 7-2. Light yield (LY) and quenching factor (QF) for interesting scintillating bolometers (211), (203). 247
Table 7-3. The isotopes contained in the calibration sources with their decay modes and decay energies. 251
Table 7-4. The main features of the two crystals assembled for the scintillating bolometer tests. 252
Table 7-5. Some properties of the ZnSe and $ZnMoO_4$ crystals. 253
Table 7-6. Most used pulse parameters collected in a n-tuple after the application of the Optimum Filter. 256

Table 7-7. Electronic parameters and temperatures for the three thermistors in the aboveground measurement of the ZnSe-Ge detector: ZnSe is the heat channel from the scintillating crystal, while LTB and LTD are the light channels from the two Ge-slabs named B and D respectively. The temperatures were calculated with the doping parameters from the 34B series derived in Chapter 4 (see Table 4-24)..... 257
Table 7-8. Trigger configuration for the best data set of the aboveground measurements of ZnSe-Ge..... 259
Table 7-9. Calibration of the heat channel. The energy value and the energy resolution are obtained from the fit shown in Figure 7-18..... 262
Table 7-10. Electronic parameters and temperatures for the three thermistors in the underground measurement of the ZnSe-Ge detector: ZnSe is the heat channel from the scintillating crystal, while LTB and LTD are the light channels from the two Ge-slabs named B and D respectively. The temperatures were calculated with the doping parameters from the 34B series derived in Chapter 4 (see Table 4-24)..... 265
Table 7-11. Peaks and energy resolutions from the fit of the ^{55}Fe spectrum collected with the light detector..... 268
Table 7-12. Electronic parameters and temperatures for the three bolometers in the ZnSe-Si detector: ZnSe is the heat channel from the scintillating crystal, while LT3 and LT4 are the light channels from the two Si-slabs. The temperatures were calculated with the doping parameters from the 34B series derived in Chapter 4 (see Table 4-24)..... 270
Table 7-13. Electronic parameters and temperatures for the three thermistors in the $ZnMoO_4$-Ge detector: $ZnMoO_4$ is the heat channel from the scintillating crystal, while LTB and LTD are the light channels from the two Ge-slabs named B and D respectively. The temperatures were calculated with the doping parameters from the 34B series derived in Chapter 4 (see Table 4-24)..... 274
Table 7-14. Trigger configuration for the best data set of the aboveground measurements of $ZnMoO_4$-Ge..... 274
Table 7-15. Identified peaks in the gamma spectrum of the $ZnMoO_4$ heat channel (see Figure 7-38). The first two lines refer to the peaks used for the calibration..... 278

Bibliography

1. *Letter to L. Meitner.* **Pauli, W.** 1930, http://cdsweb.cern.ch/record/83282/files/.
2. *Tentativo di una teoria dei raggi beta.* **Fermi, E.** Nuovo Cimento - 1934.
3. *Detection of the Free Neutrino: A Confirmation.* **Cowan C.L, Jr., Reines F., Harrison F.B., Kruse H.W., McGuire A.D.** Science 124 (3212):103 - 1956.
4. *Parity Nonconservation and a Two-Component Theory of the Neutrino.* **Lee T.D., Yang C.N.** Phys. Rev. 105, 1671–1675 (1957).
5. *Experimental test of parity conservation in beta decay.* **Wu C.S., Ambler E., Hayward R.W., Hoppes D.D., Hudson, R.P.** Phys. Rev. 105, 1413–1415 (1957) .
6. *Helicity of neutrinos.* **Goldhaber M., Grodzins L., Sunyar A.W.** Phys Rev. 109, Nr. 3, 1975, S. 1015-1017.
7. *Experiments with neutrinos emitted by mesons.* **Pontecorvo, B.** Zh.Eksp.Teor.Fiz.39:1166,1960.
8. *Observation of high-energy neutrinos reactions and the existence of two kinds of neutrinos.* **Danby G., Gaillard J-M., Goulianos K., Lederman L.M., Mistry N., Schwartz M., Steinberger J.** Phys. Rev. Lett. 9, 36 (1962). .
9. **Hasert F.J., et al.** Phys. Lett. 46B (1973) 138.
10. **Glashow, S.L.** Nucl. Phys. 22 (1961) 279.
11. *A Model of Leptons.* **Weinberg, S.** Phys. Rev. Lett. 19, 1264–1266 (1967).
12. **Salam, A.** Phys. Rev. 127 (1962) 331.
13. *Search for elastic muon neutrino electron scattering.* **Hasert F.J., et al.** Phys. Lett. B, 46 (1973) 121-124.
14. *Observation of neutrino-like interactions without muon or electron in the Gargamelle neutrino experiment.* **Hasert F.J., et al.** Phys. Lett. B, 46 (1973) 138-140.
15. *Experimental observation of isolated large transverse energy electrons with associated missing energy at $\sqrt{s}$ = 540GeV.* **Arnison G., et al. (the UA1 collaboration).** Phys. Lett. B, Vol 122, 1 (1983) 103-116 .
16. *Precision Electroweak Measurements on the Z Resonance.* **The ALEPH, DELPHI, L3, OPAL, SLD Collaborations; The LEP Electroweak Working Group; The SLD Electroweak and Heavy Flavour Groups.** 2006, hep-ex/0509008 v3.
17. **Davis D., Harmer R., Hoffman K.** Phys. Rev. Lett. 20, 1205 (1968).
18. **Bahcall J.N., Fowler W.A., Iben I., Sears R.L.** 1963, ApJ, 137, 344.
19. **Bellerive, A.** International Journal of Modern Physics A 19, 8 (2004).
20. *Neutrino Experiments and the Problem of Conservation of Leptonic Charge.* **Pontecorvo, B.** Sov. Phys. JETP 26: 984 (1968).
21. **Ahmad Q.R., et al.** Phys. Rev. Lett. 87, 071301 (2001).
22. **The KamiokaNDE collaboration.** Phys. Rev. Lett. 81 (1998) 1562.
23. *First Results from KamLAND: Evidence for Reactor Anti-Neutrino Disappearance.* **The KamLAND collaboration.** Phys. Rev. Lett. 90 (2003) 021802.
24. *Measurement of Neutrino Oscillation by the K2K Experiment.* **The K2K collaboration.** Phys.Rev.D74:072003,2006.
25. *Search for neutrino oscillations on a long base-line at the CHOOZ nuclear power station.* **Apollonio M., et al.** Eur. Phys. J., C27:331–374, 2003.

26. *Measurement of Neutrino Oscillations with the MINOS Detectors in the NuMI Beam.* **Adamson P., et al.** arXiv:0806.2237.
27. *The CKM quark-mixing matrix.* **Nakamura K., et al. (Particle Data Group).** J. Phys. G 37, 075021 (2010).
28. **Bilenky S.M., Hosek J., Petcov S.T.** Phys. Lett. B94, 495 (1980).
29. **Cabibbo, N.** Phys. Lett. B72, 333 (1978).
30. **Barger V., et al.** Phys. Rev. Lett. 45, 2084 (1980).
31. *Three-flavour neutrino oscillation update.* **Schwetz T., Tórtola M., Valle J.W.F.** arXiv:0808.2016.
32. **Goswami S., et al.** Nucl. Phys. (Proc. Supp.) B143, 121 (2005).
33. *Neutrino mass hierarchy, vacuum oscillation, and vanishing ue3.* **de Gouvea A., Jenkins J.,Kayser B.** 2005, arXiv:hep-ph/0503079 v2.
34. **Bonn J., et al.** Nucl.r Phys. B Proc. Suppl. 91, 273 (2001).
35. **Fogli G.L., et al.** Phys. Rev. D78, 033010 (2008).
36. *Neutrino masses and mixings, 2010.* **Strumia A., Vissani F.**
37. *Violation of CP in variance, C asymmetry, and baryon asymmetry of the universe.* **Sakharov, A. D.** 1991 Sov. Phys. Usp. 34 392.
38. *Baryogenesis without Grand Unification.* **Yanagida T., Fukugita M.** Phys. Lett. B 174, 45 (1986).
39. *Heavy Majorana neutrinos and baryogenesis.* **Pilaftsis, A.** arXiv:hep-ph/9812256v3, 1999.
40. *Towards a complete theory of thermal leptogenesis in the SM and MSSM.* **Giudice G.F., Notari A., Raidal M., Riotto A., Strumia A.** arXiv:hep-ph/0310123v2, 2004.
41. *Double Beta-Disintegration.* **Goeppert-Mayer, M.** Phys. Rev. 48, 512.
42. **Brudanin V.B., Rukhadze N.I., Briancon Ch., Egorov V.G., Kovalenko V.E., Kovalik A., Salamatin A.V., Stekl I., Tsoupko-Sitnikov V.V., Vylov Ts., Cermak P.** Phys. Lett. B 495, 63 (2000).
43. **Klapdor-Kleingrothaus H.V., et al.** Eur. Phys. J. A, 12 (2001) 147.
44. **Aalseth C.E., et al. (IGEX).** Phys. Rev. D65 (2002) 092007.
45. *NEMO-3 DOUBLE BETA DECAY EXPERIMENT: LASTEST RESULTS.* **Barabash, A. S.** arXiv:hep-ex/0610025v1 (2006).
46. *Double beta decay of 96Zr.* **Arnold R., et al.** Nucl. Phys. A 658, 299 (1999).
47. *Phys. Rev. C, 63 (2001) 065501.* **Ejiri H., et al.**
48. *Search for 2β decay of cadmium and tungsten isotopes: Final results of the Solotvina experiment.* **Danevich F.A., et al.** Phys. Rev. C 68 (2003) 035501.
49. **Alessandrello A., Brofferio C., Cremonesi O., Fiorini E., Giuliani A., Nucciotti A., Pavan M., Pessina, G., Pirro S., Previtali E., Vanzini M., Zanotti L., Bucci C., Pobes C.** Phys. Lett. B 486, 13 (2000).
50. *130Te neutrinoless double-beta decay with CUORICINO.* **Andreotti E., Arnaboldi C., Avignone III F.T., Balata M., Bandac I., Barucci M., Beeman J.W., Bellini F., Brofferio C., Bryant A., Bucci C., Canonica L., Capelli S., Carbone L., Carrettoni M., Clemenza M., Cremonesi O., Creswick R.J., Di Domizio S., Dolinski M.J., Ejzak L., Faccini R., Farach H.A., Ferri E., Fiorini E., Foggetta L., Giachero A., Gironi L., Giuliani A., Gorla P., Guardincerri E., Gutierrez T.D., Haller E.E., Kazkaz K., Kraft S., Kogler L., Maiano C., Maruyama R.H., Martinez C., Martinez M., Newman S., Nisi S., Nones C., Norman E.B., Nucciotti A., Orio F., Pallavicini M., Palmieri V., Pattavina L., Pavan M., Pedretti M., Pessina G., Pirro S., Previtali E., Risegari L., Rosenfeld C., Rusconi C., Salvioni C., Sangiorgio S., Schaeffer D., Scielzo N.D., Sisti M., Smith A.R., Tomei C., Ventura G., Vignati M.** Astr. Phys. 34 (2011) 822 - arXiv:1012.3266v1.
51. **Bernabei R., et al.** Phys. Lett. B, 546 (2002) 23.
52. *Measurement of the Double Beta Decay Half-life of 150-Nd and Search for Neutrinoless Decay Modes with the NEMO-3 Detector.* **The NEMO collaboration.** arXiv:0810.0248v2.

53. *Precise half-life values for two-neutrino double-β decay.* **Barabash, A. S.** Phys. Rev. C 81, 035501 (2010).
54. *Results of a search for the two neutrino double β decay of 136Xe with proportional counters.* **Gavriljuk Ju.M., Kuzminov V.V., Osetrova N.Ya., Ratkevich S.S.** Phys. Rev. C 61, 035501 (2000).
55. **Schechter J., Valle J.W.F.** Physics Review D25, 2951 (1982).
56. **Elliott S.R., Vogel P.** 2002, Annu. Rev. Nucl. Part. Sci. 52,115.
57. *Double beta decay, Majorana neutrinos, and neutrino mass.* **Avignone III F.T., Elliott S.R., Engel J.** Reviews of Modern Physics, vol 80, April–June 2008.
58. **Šimkovic F., Faessler A, Rodin V., Vogel P., Engel J.** Phys. Rev. C 77, 045503 (2008).
59. *Nuclear Matrix Elements for Double Beta Decay in the QRPA approach: a critical review.* **Civitarese O., Suhonen J.** J. Phys.: Conf. Ser. 173, 012012 (2009).
60. **Menendez J., Poves A., Caurier E., Nowacki F.** Nucl. Phys. A 818, 139-151 (2009).
61. **Barea J., Iachello F.** Phys. Rev. C 79, 044301 (2009).
62. *Neutrinoless double beta decay of 150Nd accounting for deformation.* **D. Fang, A. Faessler, V. Rodin.** arXiv:1009.5579v2 [nucl-th] 2010.
63. **Doi M., Kotani T., Takasugi E.** Prog. Theor. Phys. Suppl. 83, 1 1985.
64. **Šimkovic F., Pantis G., Vergados J.D., Faessler A.** Phys. Rev. C 60, 055502 (1999).
65. **Pantis G., Simkovic F., Vergados J.D., Faessler A.** Phys. Rev. C 53, 695-707 (1996).
66. **Suhonen, J. e Civitarese, O.** Phys. Rept. 300, 123-214 (1998).
67. **Tomoda, T.** Rep. Prog. Phys. 54, 53-126 (1991).
68. *Neutrinoless double-beta decay: impact, status and experimental techniques.* **Giuliani, A.** Measurements of Neutrino Mass, Proceedings of the International School of Physics "Enrico Fermi", Varenna on Lake Como, Villa Monastero, 17-27 June 2008.
69. **Audi G., Wapstra A.H., Thibault C.** Nuclear Physics A 729, 337–676 (2003).
70. **Tretyak V.I., Zdesenko Yu.G.** Atomic Data and Nuclear Data Tables 80, 83–116 (2002).
71. **Rosman K.J.R., Taylor P.D.P.** Pure and Appl. Chem. 70, 217 (1998).
72. **Firestone R.B., Ekström L.P.** ToRI, Version 2.1, February 1999.
73. **Klapdor-Kleingrothaus H.V., et. al.** Eur. Phys. J. A, 12 (2001) 147.
74. **Klapdor-Kleingrothaus H.V., Krivosheina, A. Dietz I.V., Chkvorets O.** Mod. Phys. Lett. A16, 2409 (2001).
75. **Klapdor-Kleingrothaus, H.V.** arXiv:hep-ph/0205228.
76. **Klapdor-Kleingrothaus, H.V.** Found. of Phys. 32 (2002) 1181.
77. **Klapdor-Kleingrothaus H.V., et al.** Nucl. Instrum. Meth. A511 (2003) 335 (arXiv:hep-ph/0309157).
78. **Klapdor-Kleingrothaus H.V., Krivosheina, A. Dietz I.V., Chkvorets O.** Physics Letters B586, 198 (2004).
79. **Klapdor-Kleingrothaus H.V., et al.** arXiv:hepph/0404062.
80. **Klapdor-Kleingrothaus H.V., Krivosheina I.V.** Mod. Phys. Lett. A21 (2006) 1545.
81. **Feruglio F., Strumia A., Vissani F.** Nucl. Phys. B637 (2002) 345 (arXiv:hepph/0201291).
82. **Aalseth C.E., et al.** Mod. Phys. Lett. A17 (2002) 1475 (arXiv:hep-ex/0202018).
83. **Zdesenko Y.G., Danevic F.A., Tretyak V.I.** Phys. Lett. B546 (2002) 206.
84. **Harney, H.L.** Mod. Phys. Lett. A16 (2001) 2409.
85. **Bakalyarov A.M., et al.** Phys. Part. Nucl. Lett. 2 (2005) 77 (arXiv:hep-ex/0309016).
86. *GERDA proposal to LNGS P38/04 (2004).* **The GERDA collaboration.**
87. **Arnold R., et al. (NEMO Collaboration).** Nucl. Instr. and Meth. in Phys. Res. A536 (2005) 79.

88. *Double Beta Decay: Historical Review of 75 Years of Research.* **Barabash, A.S.** arXiv:1104.2714v2 (2011).

89. *Results of NEMO 3 and Status of SuperNEMO.* **Vála L., on behalf of the NEMO and SuperNEMO Collaborations.** arXiv:0901.0473v1 [hep-ex] 2009.

90. *First Results of the Search for Neutrinoless Double-Beta Decay with the NEMO 3 Detector.* **Arnold R., et al. (NEMO Collaboration).** Phys. Rev. Lett. 95 (2005) 182302.

91. *Results from a search for the 0νββ-decay of 130Te.* **Arnaboldi C., et al.** Phys. Rev. C 78, 35502 (2008).

92. **Laubenstein M., et al.** Appl. Radiat. Isotopes 61 (2004) 167.

93. **Pirro S., et al.** AIP Conf. Proc. 785 (2005) 177.

94. *CdWO4 bolometers for double beta decay search.* **Gironi L., Arnaboldi C., Capelli S., Cremonesi O., Pessina G., Pirro S., Pavan M.** Optical Materials 31 (2009) 1388–1392.

95. *CUORE: A cryogenic underground observatory for rare events.* **Arnaboldi C., et al., (CUORE collaboration).** Nucl. Instrum. Meth. A518 (2004) 775-798 [hep-ex/0212053].

96. *From Cuoricino to CUORE: Investigating neutrino properties with double beta decay.* **Sisti M., (CUORE collaboration).** J. Phys. Conf. Ser. 203 (2010) 012069.

97. *Monte Carlo evaluation of the external gamma, neutron and muon induced background sources in the CUORE experiment.* **Bellini F., et al.** Astropart. Phys. 33 (2010) 169-174 [arXiv:0912.0452].

98. *Status of EXO-200.* **Ackerman N., (EXO Collaboration).** arXiv:0909.1826.

99. *Double beta decay in liquid xenon.* **Gornea R., (EXO Collaboration).** J. Phys. Conf. Ser. 179 (2009) 012004.

100. *Correlated fluctuations between luminescence and ionization in liquid xenon.* **Conti E., et al., (EXO Collaboration).** Phys. Rev. B68 (2003) 054201, [hep-ex/0303008].

101. *Detection of very small neutrino masses in double-beta decay using laser tagging.* **Danilov M., et al.** Phys. Lett. B480 (2000) 12-18 [hep-ex/0002003].

102. *A new Ge-76 double beta decay experiment at LNGS.* **Abt I., et al. (GERDA Collaboration).** hep-ex/0404039.

103. *Operation of a GERDA Phase I prototype detector in liquid argon and nitrogen.* **Barnabé Heider M., et al.** arXiv:0812.3976.

104. *Shielding of the GERDA experiment against external gamma background.* **Barabanov I., et al.** Nucl. Instrum. Meth. A606 (2009) 790-794.

105. *The GERDA experiment at Gran Sasso.* **Zuzel G., (GERDA Collaboration).** Acta Phys. Polon. B41 (2010) 1469.

106. *R&D for possible future improvements of KamLAND.* **Terashima A., et al., (KamLAND Collaboration).** J. Phys. Conf. Ser. 120 (2008) 052029.

107. *KamLAND double beta decay experiment using 136Xe.* **Koga, M.** in International Conference on High Energy Physics (ICHEP), (Paris), July, 2010.

108. *NEXT, a HPGXe TPC for neutrinoless double beta decay searches.* **Grañena F., et al., (NEXT Collaboration).** arXiv:0907.4054.

109. *High-pressure xenon gas electroluminescent TPC for 0nu beta beta-decay search.* **Nygren, D.** Nucl. Instrum. Meth. A603 (2009) 337-348.

110. *The SNO+ Experiment.* **Chen M.C., (SNO+ Collaboration).** arXiv:0810.3694.

111. *Robust Signal Extraction Methods and Monte Carlo Sensitivity Studies for the Sudbury Neutrino Observatory and SNO+ Experiments.* **A., Wright.** PhD thesis, Queen's University, 2009.

112. *The rich neutrino programme of the SNO+ experiment.* **Kraus C., Peeters J.M., (SNO+ Collaboration).** Prog. Part. Nucl. Phys. 64 (2010) 273-277.

113. *Topological detection of double beta decay with NEMO3 and SuperNEMO.* **Saakyan R.,**

(NEMO/SuperNEMO Collaboration). J. Phys. Conf. Ser. 179 (2009) 012006.

114. *A Search for Neutrinoless Double Beta Decay: from NEMO-3 to SuperNEMO.* **Shitov Y.A., (NEMO/SuperNEMO Collaboration).** arXiv:1006.4775.
115. *Probing New Physics Models of Neutrinoless Double Beta Decay with SuperNEMO.* **Arnold R., et. al., (SuperNEMO Collaboration).** arXiv:1005.1241.
116. *Sense and sensitivity of double beta decay experiments.* **Gómez-Cadenas J.J., et al.** arXiv:1010.5112v3 [hep-ex] (2010).
117. **Simon, F.E.** Nature 135, 763 (1935).
118. **Andrews D.H., et al.** Phys. Rev. 76, 154 (1949).
119. **Fiorini E., Niinikoski T.O.** Nucl. Instr. Meth. A 224, 83 (1984).
120. **Fano, U.** Phys. Rev. 70 (1946) 44.
121. *Phonon propagation with frequency down-conversion.* **Levinson, Y.B.** in Nonequilibrium Phonons in Nonmetallic Crystals, edited by W. Eisenmenger and A. Kaplyanskii, chap 3, pp. 91-143, Elsevier Science Publisher B.V., Amsterdam, 1986.
122. **Maris, H.J.** J. Low Temp. Phys. 93 (1993) 355.
123. *Imaging Phonons, Acoustic Wave Propagation in Solids.* **Wolfe, P.** Cambridge University Press, Cambridge, 1998.
124. *Phys. Rev. Lett. 49, 416 (1969).* **Taylor B., Maris H., Elbrum C.**
125. **Andersen, H.H.** Nucl. Instr. and Meth. B 15 (1986) 722.
126. *Temperature dependence of the energy gap in semiconductors.* **Varshni, Y.P.** Physica 34, 149-154 (1967).
127. **Mott N.F., Davies J.H,.** Phil. Mag. B 42, 845 (1980).
128. *Electronic Properties of Doped Semiconductors.* **Shklovskii B., Efros A.** Springer, Berlin 1984.
129. **McCammon, D.** physics/0503086 (2005).
130. **Shklovskii B., Efros A.** Sov. Phys. JETP 33, 468 (1971).
131. *Phys. Rev. B 57, 4472 (1998).* **Zhang J., et al.**
132. *The single module for Cuoricino and CUORE detectors: tests, construction and modelling.* **Pedretti, M.** PhD thesis, Insubria University, 2004.
133. **Mather, J.C.** Appl. Opt. 21, 1125 (1982).
134. *CUORE: a Cryogenic Underground Observatory for Rare Events.* **Fiorini, E.** Physics Reports 307 (1998) 309.
135. *CUORE: A Cryogenic Underground Observatory for Rare Events.* **Ardito R., et al.** arXiv:hep-ex/0501010.
136. *Muon-induced backgrounds in the CUORICINO experiment.* **Andreotti E., et al.** Astropart. Phys.34:18-24,2010, arXiv:0912.3779 [nucl-ex].
137. **Coplen T.B., et al.** Pure and Applied Chemistry, 74-10, 1987 (2002).
138. *Double-beta decay Q values of 130Te, 128Te, and 120Te.* **Scielzo N.D., et al.** Physical Review C 80, 025501 (2009).
139. *Measurement of Low Temperature Specific Heat of Crystalline TeO2 for the Optimization of Bolometric Detectors.* **Barucci M., Brofferio C., Giuliani A., Gottardi E., Peroni I., Ventura G.** Journal of Low Temperature Physics 123 (2001) 303-314.
140. *Thermal properties of paratellurite (TeO2) at low temperatures.* **White G.K., Collocott S.J., Collins J.G.** J. Phys.: Condens. Matter 2 (1990) 7715 - 7718.
141. *Einkristallzüchtung von Paratellurit (TeO2).* **Liebertz, J.** Kristall und Technik, 4 (1969) 221-225.
142. *Technology of tellurium dioxide single crystal growth.* **Pu Zhifen, Ge Zengwei.** Patent: CN85107803 (A), 1987-04-15.
143. *The crystal structure of tellurium dioxide. A redetermination by neutron diffraction.* **Leciejewicz, J.** Zeitschrift für Kristallographie, Kristallgeometrie, Kristallphysik, Kristallchemie 116 (1961) 345-353.
144. *An electron spin resonance study of vanadium-doped α-TeO2 single crystals.* **Edwards G.J., Gilliam O.R., Bartram R.H., Watterich A.,**

Voszka R., Niklas J.R., Greulich-Weber S., Spaeth J-M. J. Phys.: Condens. Matter 7 (1995) 3013-3022.

145. *Optical Properties of Single-Crystal Paratellurite (TeO2).* **Uchida, Naoya.** Physical Review B 4(1971) 3736-3745.

146. *New CUORICINO results on the way to CUORE.* **Gorla P., et al.** Physica Scripta T127 (2006) 49-51, doi: 10.1088/0031-8949/2006/T127/018.

147. *Production of high purity TeO2 single crystals for the study of neutrinoless double beta decay.* **Arnaboldi C., Brofferio C., Bryant A., Bucci C., Canonica L., Capelli S., Carrettoni M., Clemenza M., Dafinei I., Di Domizio S., Ferroni F., Fiorini E., Ge Z., Giachero A., Gironi L., Giuliani A., Gorla P., Guardincerri E., Kadel R., Kazkaz K., Kogler L.**

148. *Growth of the high quality and large size paratellurite single crystals.* **Yaoqing Chu, Yaogang Li, Zengwei Ge, Guoqing Wu and Hongzhi Wang.** Journal of Crystal Growth 295 (2006), 158-161.

149. *Growth of Φ4'' Li2B4O7 single crystals by multi-crucible Bridgman method.* **Jiayue Xu, Shiji Fan, Baoliang Lu.** Journal of Crystal Growth, 264 (2004) 260-265.

150. **Downey P.M., Jeffries A.D., Meyer S.S., Weiss R., Bachner F.J., Donnelly J.P., Lindley W.T., Mountain R.W., Silversmith D.J.S.** Appl. Opt. 23, 910 (1984).

151. *Sensitive germanium thermistors for cryogenic thermal detector of Tokyo dark matter search programme.* **Ootani W., Ito Y., Nishigaki K., Kishimoto Y., Minowa M.** arXiv:hep-ex/9510008v1 (1995).

152. **Itoh K.M, et al.** J. Low Temp. Phys. 93 (1993) 307.

153. **Haller E.E., et al.** *in Neutron Transmutaion Doping of Semiconductor Materials.* s.l. : R. D. Larrabee (Plenum Press, New York, 1984), p21.

154. **Fritzsche H., Lark-Horovitz K.** Phys. Rev. 113 (1959) 999.

155. **Fritzsche H., Cuevas M.** Phys. Rev. 119 (1960) 1238.

156. *Neutron transmutation doping in semiconductors: science and applications.* **I.S., Shlimak.** Phys. Solid State 41 (5), 1999.

157. *Measurements of residual radioactivity in neutron transmutation doped thermistor.* **Alessandrello A., Brofferio C., Camin D.V., Cremonesi O., Fiorini E., Giuliani A., Pavan M., Pessina G., Previtali E., Zanotti L.** Nucl. Instr. & Meth. B, vol. B93, 322 (1994).

158. **Haller, E.E.** Infrared Physics and Technology 35, 127 (1994).

159. **Harman, G.** *Wire Bonding in Microelectronics - Third Edition.* s.l. : McGraw-Hill, 2009.

160. **Salvioni, C.** *Optimization of the single moduel of detection for the CUORE-0 experiment.* s.l. : PhD Thesis, 2010.

161. *Precision Production of Neutron Transmutation Doped Germanium Thermistors for CUORE.* **Maruyama, R.** Cuore internal report -2008.

162. **Alessandrello A., et al.** Nuclear Instruments and Methods in Physics Research Section B: Beam Interactions with Materials and Atoms 93, 322 (1994).

163. *Fabrication and low-temperature characterization of Si-implanted thermistor.* **Alessandrello A., Brofferio C., Cattadori C., Cavallini R., Cremonesi O., Ferrario L., Giuliani A., Margesin B., Nucciotti A., Pavan M., Pessina G., Pignatel G., Previtali E., Sisti M.** J. Phys. D: Appl. Phys. 32 (1999) 3099–3110.

164. *The temperature stabilization system of CUORICINO: an array of macro bolometers.* **Arnaboldi C., Bucci C., Capelli S., Gorla P., Guardincerri E., Nucciotti A., Pessina G., Pirro S., Sisti M.** IEEE TRANSACTIONS ON NUCLEAR SCIENCE, 52-5 (2005) 1630-1637.

165. *Production, characterization, and selection of the heating elements for the response stabilization of the CUORE bolometers.* **Andreotti E., Brofferio C., Foggetta L., Giuliani A.,**

Margesin B., Nones C., Pedretti M., Rusconi C., Salvioni C., Tenconi M.

166. *Methods for response stabilization in bolometers for rare decays.* **Alessandrello A., et al.** Nucl. Instr. and Meth. Phys. Res. A 412, 454 (1998).
167. **Andreotti, E.** *Application of doped semiconductor devices to the development of bolometric detectors to be used in experiments for the measurement of the neutrino mass.* 2009. Vol. PhD thesis.
168. **Tenconi, M.** *Advanced bolometric techniques to reveal the neutrino nature.* s.l. : Tesi di Laure Specialistica, 2010.
169. **Heusser, G.** Annu. Rev. Nucl. Part. C 45, 543 (1995).
170. **The CUORE collaboration.** Internal note in progress.
171. **Alessandrello A., et al.** Czechoslovak Journal of Physics 46-S5, 2893 (1996).
172. **Alessandrello A., et al.** NIM B 142 (1998) 163-172.
173. *The Programmable Front-End System for CUORICINO, An Array of Large-Mass Bolometers.* **Arnaboldi C., Bucci C., Campbell J.W., Capelli S., Nucciotti A., Pavan M., Pessina G., Pirro S., Previtali E., Rosenfeld C., Sisti M.** IEEE Transactions on nuclear science, vol. 49, no. 5, October 2002.
174.
175. **Lakeshore.** http://www.lakeshore.com/pdf_files/sensors/Manuals/F020-00-00.pdf. [Online]
176. http://www.picowatt.fi/. [Online]
177. *Low-temperature conductivity and metal-insulator transition in compensated n-Ge.* **A. Zabrodskii, K. Zinoveva.** Soviet physics. JETP, vol.59 - 1984, pp.425-433.
178. **Mancuso, M.** *Caratterizzazione a temperature criogeniche di termistori drogati tramite trasmutazione neutronica per l'esperimento CUORE-0.* s.l. : Tesi di Laurea Triennale, 2009.
179. *Detector assembly procedure.* **Nones C., Rusconi C.** CUORE collaboration internal note.
180. *Processing the Signals from Solid-State Detectors in Elementary-Particle Physics.* **Gatti E., Manfredi P.F.** Rivista del Nuovo Cimento vol9, n1 (1986).
181. *The CUORE Crystals Validation Runs (CCVR). Results on radioactive contamination and extrapolation to the CUORE background.* **Alessandria F., et al. (the CUORE collaboration).** (draft).
182. *A Unified approach to the classical statistical analysis of small signals.* **Feldman G.J., Cousins R.D.** Phys. Rev. D57 (1998) 3873 - arXiv:physics/9711021v2.
183.
184. *A thermal model for large mass TeO2 bolometers with NTD Ge thermistors.* **Giuliani, A.** 1998, Internal report.
185. *Characterization of cryogenic bolometers and data acquisition system for the CUORE experiment.* **Giachero, A.** PhD thesis, Genova University, 2008.
186. **materials, huntsman advanced.** http://www.huntsman.com/advanced_materials/. [Online]
187. **Sinclair, J.W.** Journal of Adhesion 38, 219 (1992).
188. **Imaz J.J., Markaide N., Jurado M.J.** European Polymer Journal 28(3), 299 (1992).
189. **Lapique F., Redford K.** International Journal of Adhesion and Adhesives 22, 337 (2002).
190. Araldite 2012 technical data sheet. *https://www.huntsmanservice.com/.* [Online]
191. **Salvini A., et al.** Journal of Physics: Conference Series 41, 417 (2006).
192. *Matter and Methods at Low Temperatures, Third edition - Springer(2007).* **Pobell, F.**
193. *Physical, mechanical properties of cured resins.* **Kaelble D.H., Moacanin J., Gupta A.** Epoxy Resins. Chemistry and Technology - Second edition, Marcel Dekker Inc., 1988.
194. **Prolongo S.G., del Rosario G., Urena A.** International Journal of Adhesion and Adhesives 26, 125 (2006).
195. **Birks, J.B.** Proc. Phys. Soc. A 64 (1951) 874.

196. **Alessandrello A., et al.** Nucl. Phys. B (Proc. Suppl.) 28A (1992) 233.

197. **Alessandrello A., et al.** IEEE Trans. Nucl. Sci. 39–34 (1992) 610.

198. **Bobin C., et al.,.** Nucl. Instrum. Meth. A 386 (1994) 453.

199. **Angloher G., et al.** Astropart. Phys. 23 (2005) 325.

200. **Cebrian S., et al.** Phys. Lett. B 563 (2003) 48.

201. **Pirro S., et al.** nucl-ex/0510074 (2005).

202. **Gorla P., et al.** J. Low Temp. Phys. 151, 854 (2008).

203. **Gironi L., et al.** nucl-ex/0809.5126v1 (2008).

204. **Gironi, L.** nucl-ex/0911.1061v1 (2009).

205. *LUCIFER proposal.* (2009).

206. *High sensitivity quest for Majorana neutrino mass with the BOREXINO counting test facility .* **Bellini G., et al.** Phys. Lett. B 493 (2000) 216.

207. *Influence of growth non-stoichiometry on optical properties of doped and non-doped ZnSe grown by chemical vapour deposition.* **Krause E., et al.,.** J. Crystal Growth 138 (1994) 75.

208. *Performance of ZnMoO4 crystal as cryogenic scintillating bolometer to search for double beta decay of molybdenum.* **Pirro S., et al.** submittet to J. Instr.

209. *Growth and properties of ZnMoO4 single crystals.* **Ivleva L.I., et al.** Crystallography Reports 53 (2008):1087.

210. **Suhonen J., et al.** Int. J. Mod. Phys. E17 (2008) 1.

211. *Scintillating double-beta-decay bolometers.* **Pirro S., et al.** Physics of Atomic Nuclei 69 (2006):2109.

212. *Low Temperature Scintillation in ZnSe Crystals.* **Dafinei I., Fasoli M., Ferroni F., Mihokova E., Orio F., Pirro S., Vedda A.** Nuclear Science, IEEE Transactions on Volume: 57 , Issue: 3 , Part: 2, Page(s): 1470 - 1474, 2010.

213. Zinc selenide (ZnSe) density, melting point, hardness. *SpringerMaterials - The Landolt-Börnstein Database (http://www.springermaterials.com). DOI: 10.1007/10681719_481.* [Online]

214. **Ivleva, L.I., et al.** 2008, Cristallography Report 53, p. 1087.

215. **Madelung O., Rassler U., Schulz, M.** SpringerMaterials – The Landolt-Brönstein Database. *<http://www.springermaterials.com> doi:0.1007/10681719_480.* [Online]

216. *ZnSe scintillating bolometers for Double Beta Decay.* **Arnaboldi C., et al.** nucl-ex 0058338 (2010).

217. *Potential of a next generation neutrinoless double beta decay experiment based on ZnMO4 scintillating bolometers.* **Danevich F.A., Degoda V.Ya., Dmitruk I.M., Galashov E.N., Giuliani A., Marnieros S., Nones C., Pessina G., Olivieri E., Rusconi C., Shlegel V.N., Tretyak V.I., Vasiliev Ya.V.** Preprint submitted to Phys. Lett. B -2011.

218. *Sakharov Conditions for Baryogenesis.* **Perepelitsa, D. V.** 2008.

219. *Observation of Tau Neutrino Interactions.* **DONUT collaboration.** 2002.

220. *Blegdamsvej Faust.* 1932.

221. **Gamow, G.** *Thirty Years That Shook Physics.* 1966.

222. **Brooks, Mel.** *Young Frankenstein.* 20th Century Fox, 1974.

223. **Gilbert, Ron.** *Monkey Island 2: LeChuck's Revenge.* s.l. : LucasArts, 1991.

224. **Landis, John.** *The Blues Brothers.* Universal Studios, 1980.

225. **Tolkien, J.R.R.** Firiel's song. 1940.

226. **Gabriel, Peter.** The Tower That Ate People. *OVO.* s.l. : Real World Music Ltd, 2000.

227. **Pink Floyd.** Comfortably numb. *The Wall.* 1979.

228. *The Enemy (Star Trek: The Next Generation Season 3, Episode 7).* Paramount Pictures, 1989.

THE END

"Optimisation of the bolometric performances of the CUORE-0/CUORE and LUCIFER detectors for the neutrinoless double beta decay search"

Previously known as:

"Several species of bolometric detectors gathered together in a cave at grooving at low T"

"OK, that's it, turn off your computer and do something constructive.
Like play a little racquetball.
Or wash your car.
Or cook dinner.
Or join a funk band.
Or travel to a foreign country.
Or run for president.
Or talk to a member of the opposite sex.
Or lube your car.
Or host a weenie roast.
Or dig for buried treasure.
Or milk a cow.
Or have a yelling contest with your neighbor's dog.
Or perform brain surgery.
Or paint a yellow line in the center of your driveway.
Or write your name in the snow.
Or teach basket weaving to clams.

Or sing Welsh folk songs at the bank.

Or plant trees on public property.

Or confuse the person next to you.

Or make a triangular table.

Or hop, skip and jump.

Or ride a train.

Or organize your sock drawer alphabetically.

Or go bowling with your mom.

Or train potato bugs to do tricks.

Or make a quilt.

Or publish a magazine about pencil shavings.

Or eat lime jello with pineapple in it.

Or pave a freeway.

Or learn to draw.

Or take up photography.

Or learn to tell time.

Or photocopy money.

Or go out for pasta.

Or sew a dress.

Or bathe your iguana.

Or go fishing.

Or paint a stranger's house in the middle of the night.

Or take up windsurfing.

Or change your hair style.

Or sharpen your whiteboard markers.

Or feed a toucan.

Or enjoy the sun.

Or do a crossword puzzle.

Or buy some cool clothes.

Or go to the beach.

Or play croquet with your dad.

Or water your plants.

Or build a doll house.

Or invite some friends over for salmon and white wine.

Not!"[16]

[16] (223)